



HAL
open science

**Melt transport and assimilation-precipitation processes
through the heterogeneous lower oceanic crust :
microstructural and petro-geochemical constraints from
drill cores**

Carlotta Ferrando

► **To cite this version:**

Carlotta Ferrando. Melt transport and assimilation-precipitation processes through the heterogeneous lower oceanic crust : microstructural and petro-geochemical constraints from drill cores. Earth Sciences. Université Montpellier, 2017. English. NNT : 2017MONTT156 . tel-01735772

HAL Id: tel-01735772

<https://theses.hal.science/tel-01735772>

Submitted on 16 Mar 2018

HAL is a multi-disciplinary open access archive for the deposit and dissemination of scientific research documents, whether they are published or not. The documents may come from teaching and research institutions in France or abroad, or from public or private research centers.

L'archive ouverte pluridisciplinaire **HAL**, est destinée au dépôt et à la diffusion de documents scientifiques de niveau recherche, publiés ou non, émanant des établissements d'enseignement et de recherche français ou étrangers, des laboratoires publics ou privés.

THÈSE POUR OBTENIR LE GRADE DE DOCTEUR DE L'UNIVERSITÉ DE MONTPELLIER

En Sciences de la Terre

École doctorale GAIA

Unité de recherche Géosciences Montpellier

Transport de magma et processus d'assimilation- précipitation dans la croûte océanique inférieure hétérogène: contraintes microstructurales et pétro- géochimiques de forages océaniques

Présentée par Carlotta FERRANDO
Le 6 Décembre 2017

Sous la direction de Marguerite GODARD
et Benoît ILDEFONSE

Devant le jury composé de

Mme. Catherine MEVEL, Directeur de Recherche émérite, CNRS, IPGP, Paris

M. Georges CEULENEER, Directeur de Recherche, CNRS, GET, Toulouse

M. Johan LISSEBERG, Maître de conférences, School of Earth and Ocean Sciences, Université de Cardiff

M. Jean-Louis BODINIER, Directeur de Recherche, CNRS, Université de Montpellier

Mme. Marguerite GODARD, Directeur de Recherche, CNRS, Université de Montpellier

M. Benoît ILDEFONSE, Directeur de Recherche, CNRS, Université de Montpellier

Rapporteur

Rapporteur

Examinateur

Président

Directrice de Thèse

Co-directeur de Thèse



UNIVERSITÉ
DE MONTPELLIER

THESIS FOR THE DEGREE OF DOCTOR OF PHILOSOPHY FROM THE UNIVERSITY OF MONTPELLIER

in Earth Science

GAIA Doctoral School

Research laboratory Géosciences Montpellier

**Melt transport and assimilation-precipitation processes
through the heterogeneous lower oceanic crust:
microstructural and petro-geochemical constraints from
drill cores**

**Defended by Carlotta FERRANDO
The 6th December 2017**

**Under the supervision of Marguerite GODARD
and Benoît ILDEFONSE**

In front of the thesis jury composed of

Mrs. Catherine MEVEL, Director of Research, CNRS, IPGP, Paris

Mr. Georges CEULENEER, Director of Research, CNRS, GET, Toulouse

Mr. Johan LISSEBERG, Senior Lecturer, School of Earth and Ocean Sciences, Cardiff University

Mr. Jean-Louis BODINIER, Director of Research, CNRS, Université de Montpellier

Mrs. Marguerite GODARD, Director of Research, CNRS, Université de Montpellier

Mr. Benoît ILDEFONSE, Director of Research, CNRS, Université de Montpellier

Reviewer

Reviewer

Examiner

President

Supervisor

Co-supervisor



**UNIVERSITÉ
DE MONTPELLIER**



ABYSS has received funding from the People programme (Marie Curie Actions) of the European Union's FP7/2007-2013/ under REA Grant Agreement n°608001

Acknowledgments

I acknowledge the European Commission for funding the ABYSS Initial Training Network under the Seventh Framework Programme for Research and Technological Development (FP7).

Alice asked to the white rabbit, 'how long is forever?', and the white rabbit answered, 'sometimes just one second'. Three years ago I began my PhD and thought I would have so much time ahead of me to learn, to understand the secrets of the ocean, to meet people, to travel... Suddenly (or at least that's how it feels), I find myself writing the last few (or maybe more) sentences of my manuscript. Looking back I realize the incredible stock of knowledge I take with me. The intense scientific work, learning and amazing experiences all went by in the blink of an eye. These achievements probably would have not been so successful without the aspiring guidance, or constructive criticism, friendly advice and immense support I received from many people: I thank you all!

I first would like to acknowledge the members of my thesis committee. George Ceuleneer and Catherine Mével for agreeing to evaluate my manuscript, and for your positive and helpful thesis reports. Johan Lissenberg and Jean-Louis Bodinier for accepting to read the manuscript and to participate in the defense of my thesis. Special thanks are due to Jean-Louis for his advises on chemical numerical modeling and for providing always clear explanation.

I sincerely thank my supervisor Margot Godard for her guidance, encouragements and advices she has provided throughout my thesis. Thank you Margot for always pushing me over, what I thought to be, my limits! Scientific discussions with you have been and I believe will be very constructive, thanks to your 'all round' view of the topics concerning my work. Your expertise in geochemistry was precious for the development of my study, and I appreciate the time you spent to teach me and correct my mistakes. I thank my co-supervisor Benoit Ildefonse for his encouragements and for being there whenever I had questions. Thank you Benoit for your many advices on the structural geology aspects of my thesis and for your precious support.

I am particularly grateful to Margot and Benoit for allowing me to board on the Joides Resolution and giving me the opportunity to actively participate in the IODP program... thanks for making my dream come true! An unforgettable experience!

I would like to thank all the participants of the IODP Expedition 360 from the scientists to the whole cruise staff. Thanks to the co-chiefs Henry and Chris and to Peter for making sure that the work on board was fluent and for getting our spirits up when drilling was not going as expected. Gus, Jeremy, Oliver and Mike I thank you for sharing ideas and teaching me so much during our working shift every day. Jürgen and Lyderic thank you for the discussions we had on board, but also for your helpful advises on my thesis and future work. Marion, Alessio, Gus, Tomo, Chanzu, Cho, Jason, James and many others I really appreciated the time shared with you on the JR, you helped making this experience 'amazing'!

I would like to thank all Geosciences Montpellier. J'aimerais remercier Jose Alberto pour ses conseils sur la diffusion des éléments et son bon humour. Karoly pour avoir m'aideé au tout

début avec le analyses EBSD et ses conseils sur le traitement des données. Je remercie également tous qui s'occupent de lime minces, Christophe Nevado et Doriane Delmas, faire tourner les machines, en particulier Fabrice Barou et Olivier Bruguier, notre bibliothécaire Sylvie, et Anne pour le service de infographiste.

Constructive and fundamental discussions with the team of the DISTAV department in Genova, including Betta Rampone, Laura Crispini and Val Basch, helped me understanding my scientific questions and mature my research skills. Most important I really appreciate their support. Grazie Betta per avermi condotto nel mondo della ricerca, per avermi insegnato le fondamenta della petrologia e petrografia, per essere stata presente e disponibile per una riflessione o discussione, ma soprattutto per trasmettermi la voglia di ricercare e scoprire. Probabilmente se non ti avessi incontrata nel mio percorso, sin dal secondo anno di Laurea Triennale, non sarei qui ora, e per tutto questo ti ringrazio. Grazie anche a te Laura per il tuo spirito sempre sorridente e la tua frenetica voglia di fare, le tue idee e consigli sono stati frutto d' ispirazione. Un immenso grazie a Val... merci pour ta présence et réponses à chaque petit question que je t'ai posée (et il en avait beaucoup...), pour toutes les discussions que on a eu toujours inspirantes; un grosse merci pour ta patience surtout le dernier mois !

Special thanks are due to the ABYSS group and network. Meetings have been important opportunities to exchange, communicate and discuss about our scientific subjects, and have been a source of scientific brain-stimulation for myself. Many thanks to Barbara, Zeudia, Sofia, Rachael, Karin, Kristina, Aurelien, Tom, Adriana, Justine, Manuel, Pavel. Thanks to Manos and Val for sharing some of the best moments during these three years. This network and the organization of all ABYSS activities would have not been possible without two patient managers: thank you Cloe and Alida for your hard work.

Je tiens à remercier tous les doctorants a GM qui m'ont accueillie à partir de mon premier jour ici et m'ont accompagnée pendant ces trois année. Merci donc à Romain, Manon, Audrey, Ben (cit.: 'ciao, io sono un bel ragazzo'), Robin, Anaïs, Laure, Max, Sam, Sven, Poujol, Fatna, Nori, Alizia, Gianluca, Lucan, Manuel, Carol, Céline, Julie, Asma, Enora, Alex, Justine, Tancredi (j'ai surement oublié quelqu'un, je suis désolée !)... Cyp et Olivier (bah vous n'étiez pas de doctorants mais bon)... pour tous les super moments et activités partagée avec vous. Anita (ou bien Anitax), Séverine et Barbara parce que vous étiez toujours là pour tout et n'importe quoi, Anita en particulier pour son aide avec MATLAB et Word ! Vanessa, Arianna, Stefania et Sonia pour avoir bien rigolée ensemble. Unas gracias especiales a mi compañera de despacho Sofía con la que compartimos buena parte de nuestro doctorado, y varios viajes en avión infinito... Te agradezco por haberme soportado estos últimos meses y por procurarme comida!

Ringrazio immensamente tutta la mia famiglia. Mia mamma, che sempre è stata e sarà l'esempio di forza e tenacia da cui imparare, grazie! Mio papà che non mi lascia nemmeno per un secondo, accanto a me per ogni decisione (e devo dire che a volte sembra essere lui da lassu' a prendere certe decisioni prima di me..). Mia sorella, a lei devo l'inizio di questo percorso...lei per prima mi ha spinto ad iniziare geologia, lei che sempre crede in me, un supporto su cui so di poter contare! Ringrazio i miei zii che con il loro affetto appoggiano le mie decisioni incondizionatamente.

E come non poter ringraziare la banda di geologi che a Genova si riunisce per le feste...Fil per non esserti rotto ancora del tutto, ma (siamo sinceri) il tuo maggior dono è quello essere sempre e comunque presente; Miki per credere in me e farmi sempre il tifo; Michi per il tuo essere genovese e mugugnare piu' di me, a volte mi manca; Ector per la tua calma in ogni situazione che tranquillizza tutti; Campo per trasmettermi il tuo interesse nella geologia.

Un grazie a te, Adri. Senza troppo seguire tutti i miei spostamenti, riesci ad affiancarmi, appoggiarmi, supportarmi in qual si voglia idea che mi passi per la mente. Gracias por animarme cuando ya ves que mi camino se va por un lado o al otro...gracias!

A mio papà...

Abstract

About 80% of present-day oceanic crust is formed at slow-spreading mid-ocean ridges. There, the lower oceanic crust is extremely heterogeneous, and partly composed of serpentinized mantle rocks intruded by multiple magmatic bodies. Studies of these plutonic sequences have shown that, to some extent, melt-rock interactions must be invoked to explain their formation. To constrain the relative contribution of crystallization processes and melt-rock interactions on the geochemical budget and architecture of the oceanic crust at slow spreading ridges, I investigated two gabbroic sequences sampled *in situ* at the Atlantis Massif (30°N, Mid-Atlantic Ridge, MAR) and the Atlantis Bank (32°S, 57°E, Southwest Indian Ridge, SWIR), where gabbros are exposed on the seafloor by long-lived detachment faults (Oceanic Core Complexes).

I performed (i) a multi-scale petro-structural, geochemical and numerical modeling study of primitive gabbroic rocks drilled at the Atlantis Massif, and (ii) a petrographic and geochemical study of olivine gabbros recovered at the Atlantis Bank.

Atlantis Massif was drilled during IODP Expeditions 304/305. The heterogeneous lower oceanic crust recovered at Site U1309 presents discrete intervals of olivine-rich troctolites. They are distinguished by partially dissolved olivines with relatively high forsterite (86) and Ni contents (2000-2800 ppm), and they are characterized by the co-precipitation of high Mg# (86-88) clinopyroxene and plagioclase (An=74-81). These characteristics suggest that olivine-rich troctolites result from extensive impregnation of an olivine-rich protolith by a melt undersaturated in olivine. The flat Mg#, Ni, Mn and Li geochemical profiles across olivine and adjacent minerals suggest that the composition of the protolith was modified by, and re-equilibrated with this impregnating melt. Yet, elements hosted in olivine (i.e., Ni, Li and Co) display extremely variable compositions at constant olivine Mg#, suggesting that they are affected by the signature of the precursor material. Chemical modeling indicates that these chemical variations are likely inherited from a mantle matrix of composition similar to Site U1309 harzburgites. Laboratory experiments show that melt distribution and paths in infiltrated porous mantle is controlled by the mineral modal distribution of pyroxenes. We posit that the variations in mineral modal and chemical compositions of the U1309D olivine-rich troctolites result from the heterogeneous distribution of orthopyroxene in the precursor harzburgitic mantle, which locally drives the abundance and flow of impregnating melt. This in turn controls different extents of orthopyroxene dissolution, leading to generation of variably olivine-undersaturated melts and subsequent local olivine dissolution. Geochemical modeling indicates that the protracted melt percolation and assimilation of about 5% of a mantle protolith can explain the structure and composition of the olivine-rich troctolites. One of the main consequences of this reactive process in Hole U1309D is a local shift of melt compositions toward apparent high pressure fractionation. Nevertheless, no high pressure chemical signature is observed in MORBs from the Atlantis Massif, although it is recorded at nearly amagmatic regions, as for example in the easternmost region of the SWIR (61°-67°E).

Atlantis Bank was drilled during IODP Expedition 360 in 2016. The recovered lower oceanic crust is dominated by olivine gabbros (75%) and oxide gabbros (20%). The section is in places

intensively deformed. Shipboard studies have documented textures of plagioclase assimilation, as evidenced by resorbed grain boundaries, by an invading melt crystallizing clinopyroxene. Compositions of olivine gabbros cover a wide range of trace element contents up to relatively evolved signature ($Yb = 3-10 \times C1\text{-chondrite}$; MORB $Yb = 19$). Previous studies on olivine gabbros from Atlantis Bank showed that their formation could be ascribed to processes of oceanic crust assimilation by clinopyroxene-saturated trace element enriched melts. This model is under further investigation.

The study of Atlantis Massif and Atlantis Bank evidence melt-rock interactions and mineral assimilation associated to melt transport through the accreting lower oceanic crust. Similar textural and chemical features are observed at Kane (24°N, MAR) and in analogous ophiolite complexes (e.g., Alpine and Apennine ophiolites). These various evidences indicate that melt-rock interaction processes are probably ubiquitous, and contribute significantly to shaping the lower oceanic crust at slow-spreading ridges. Furthermore, the characterization of gabbroic rocks drilled at Hess Deep suggests that melt-rock interactions may take place also at fast-spreading ridges. Melt transport and associated mineral assimilation processes likely play a major role in the building of the oceanic crust overall. Their contribution to the MORB plumbing system is considerable at nearly amagmatic spreading centers, while it seems negligible at magmatic ridge segments, thereby indicating that their effect on MORBs is likely controlled by melt productivity in the upwelling mantle.

Résumé

La croûte océanique formée aux rides océaniques lentes a une composition extrêmement hétérogène, et pour expliquer sa formation, il est nécessaire d'invoquer des processus d'interactions magma-roche. Afin de contraindre la contribution relative des processus de cristallisation fractionnée et d'interaction magma-roche sur le budget géochimique et l'architecture de la croûte océanique formée aux dorsales lentes, j'ai étudié deux séquences gabbroïques échantillonnées in situ à l'Atlantis Massif (30°N, Dorsale Médio-Atlantique, MAR) et l'Atlantis Bank (32°S, 57°E, Dorsale Sud-Ouest Indienne, SWIR), où des gabbros sont exhumés par des failles de détachement.

J'ai effectué (i) une étude multi-échelle pétro-structurale et géochimique, combinée à une modélisation numérique, de gabbros primitifs forés à l'Atlantis Massif, et (ii) une étude pétrographique et géochimique de gabbros à olivines forés à l'Atlantis Bank.

L'Atlantis Massif a été foré pendant l'expédition IODP 304/305. La croûte océanique inférieure hétérogène échantillonnée au Site U1309 présente des intervalles discrets de troctolites riches en olivines (Ol-T). Ils se distinguent par des olivines partiellement dissoutes, relativement riches en Forsterite (Fo86) et en Ni (>2000ppm), ainsi que par la co-précipitation de clinopyroxènes riches en magnésium (Mg# = 86-88) et de plagioclases. Ces caractéristiques suggèrent que les Ol-T sont le résultat de l'imprégnation d'un protolithe riche en olivines par un magma sous-saturé en olivine. Les profils géochimiques plats entre l'olivine et les minéraux adjacents suggèrent que la composition du protolithe a été modifiée par le magma entrant. Pourtant, le Ni, Li et Co montrent des compositions extrêmement variables à Mg# de l'olivine constant, ce qui suggère qu'ils préservent la signature géochimique du matériel préexistant. La modélisation géochimique indique que ces variations compositionnelles sont héritées d'une hétérogénéité dans les harzburgites du Site U1309D. Les expériences de percolations en laboratoire ont démontré que la distribution de magma en milieux poreux est contrôlée par la composition modale de la roche percolée à échelle locale. La distribution hétérogène d'orthopyroxène dans le protolithe mantellique contrôle la quantité de magma entrant, et ainsi la quantité d'olivine dissoute, comme indiqué par les variations modales et compositionnelles observées dans les Ol-T à l'Atlantis Massif. La modélisation géochimique indique que la formation des Ol-T peut être expliquée par la percolation de magma et l'assimilation de 5% de protolithe mantellique. Une conséquence de ce processus de réaction au Site U1309D est le décalage des compositions du magma à l'Atlantis Massif vers des compositions apparentes généralement attribuées à des processus de cristallisation fractionnée à haute pression. Pourtant, aucune signature géochimique de haute pression n'est observée dans les MORBs à l'Atlantis Massif, alors qu'elles sont observées dans les MORBs d'une portion amagmatique de la dorsale sud-ouest indienne (61°-67°E).

L'Atlantis Bank a été foré au cours de l'expédition IODP 360. La croûte océanique inférieure échantillonnée est faite principalement de gabbros à olivines (75%) et de gabbros à oxydes (20%), et est par endroits intensément déformée. Les études à bord du bateau de forage ont mis en évidence des textures indiquant l'assimilation de plagioclase par un magma d'imprégnation, ainsi que la cristallisation de clinopyroxènes. Les gabbros à olivines montrent

des compositions de roche totale relativement évoluées ($Yb = 3-10 \times C1\text{-chondrite}$; MORB $Yb = 19 \times C1\text{-chondrite}$). Des études précédentes des gabbros à olivines de l'Atlantis Bank ont montré que leur formation peut être attribuée à l'assimilation de la croûte océanique par un magma saturé en clinopyroxène et enrichi en éléments en traces.

Les études de l'Atlantis Massif et de l'Atlantis Bank révèlent des processus d'interactions magma-roche et d'assimilations de minéraux, associés au transport de magma dans la croûte océanique inférieure à la dorsale. Des caractéristiques texturales et géochimiques similaires ont été documentées à Kane Megamullion (24°N , MAR) et dans les ophiolites Alpines-Appennines. Elles indiquent que les interactions magma-roche sont probablement omniprésentes et contribuent à façonner la croûte océanique inférieure aux dorsales lentes. L'étude de roches gabbroïques forées à Hess Deep (East Pacific Rise) suggèrent que les interactions magma-roche interviennent également aux dorsales rapides. Le transport réactif de magma dans la croûte océanique joue un rôle majeur dans le processus de formation de la croûte océanique dans son ensemble. Leur contribution dans la composition des MORBs est probablement contrôlée par la production de magma durant la remontée mantellique.

Table of contents

Introduction	5
Chapter I – Overview on the building of the heterogeneous lower oceanic crust ...	11
1. Formation of the lower oceanic crust at slow- and fast- spreading ridges	13
1.1 In situ sampling at modern ridges	13
1.2 Structure of ridges and oceanic crust	17
1.3 Models of lower oceanic crust accretion.....	25
1.4 Genesis and crystallization of Primary MORB-type melts	29
2. Melt transport from the mantle to the oceanic crust: a petrological and geochemical perspective	40
2.1 Transport of melts: a physical perspective	41
2.2 Melt extraction	45
2.3 Lower oceanic crust processes: reaction with the infiltrating melt	51
3. Element transport: a modeling perspective	56
3.1 Crystal-melt reactions in magmatic systems	57
3.2 Melt-rock interaction modeling.....	65
3.3 Partition coefficients.....	68
3.4 Diffusion coefficients	73
Chapter II – Analytical methods.....	79
1. Introduction	81
2. Sample preparation	82
3. Microstructural and Petrological study	83
3.1 Microstructural analyses.....	83
3.2 Mineral major element analyses	92
4. Geochemistry	95
4.1 Inductively Coupled Plasma Mass Spectrometry	95
4.2 Bulk analyses.....	102
4.3 In situ trace element analyses	104
5. Development of new standards adapted to high quality in situ geochemical data	106
5.1 Sample selection and preparation.....	108
5.2 Analytical procedure	109
5.3 Results and discussion	112
5.3.1 Results	112
5.3.2 Two standards for LA-ICP-MS analyses	118

Chapter III	121
1. Introduction.....	123
2. Melt transport and mantle assimilation at Atlantis Massif (IODP Site U1309): Constraints from geochemical modeling.....	124
2.1 Introduction	125
2.2 Geological setting	128
2.3 Petrologic overview of U1309D olivine-rich troctolites	130
2.4 Analytical methods	132
2.5 Results.....	134
2.5.1 Downhole characteristics of Olivine-rich troctolites in the 1100-1300 mbsf interval	134
2.5.2 Mineral geochemistry.....	137
2.5.3 Geochemical profiles	143
2.6 Discussion	146
2.6.1 Evidence of reactive Olivine-rich troctolites	146
2.6.2 Numerical simulations of compositional variations	149
2.6.3 Chemical equilibrium in U1309D olivine-rich troctolites	156
2.6.4 Genesis of Olivine-rich troctolites at Atlantis Massif	158
2.6.5 The geodynamic context of Olivine-rich troctolites	161
2.6.6 The effect of olivine assimilation on MORB compositions.....	163
2.7 Conclusions	165
Acknowledgements	167
Appendix A. Supplementary data.....	167
References	172
3. Ca and REE chemical profiles: a record of subsolidus re-equilibration in Olivine-rich troctolites from Hole U1309D?.....	180
3.1 Introduction	180
3.2 Results.....	182
3.3 Discussion and conclusions.....	188
 Chapter IV.....	 193
1. Introduction.....	195
2. Geological setting	196
2.1 The Atlantis Bank	198
3. IODP Expedition 360	202
3.1 The rationale behind IODP Expedition 360	203
3.2 Scientific objectives	205
3.3 IODP Hole U1473A.....	206
3.3.1 Igneous petrology.....	209
3.3.2 Downhole magmatic fabric and igneous layering	212
3.3.3 Are there evidences of melt-rock interactions?	214

4. Whole rock geochemistry of olivine gabbros from IODP Hole U1473A: Data report	215
4.2 Post-cruise geochemical analyses.....	219
4.2.1 Sampling strategy and analytical method	219
4.2.2 Results	219
5. Comparison with Atlantis Massif (30°N, Mid-Atlantic Ridge)	222
<i>Discussion</i>	229
<i>Conclusions and perspectives</i>	241
<i>References</i>	251
<i>Appendix</i>.....	287
<i>Curriculum Vitae - Carlotta Ferrando</i>	

Introduction

The continuous cycle of solid Earth begins at mid-ocean ridges where the ascent of magmas forms the oceanic crust, which later is destined to return to the mantle at subduction zones. Formation of oceanic crust represents the main contribution of mass flow from the Earth's interior to the surface, as it accounts for about 88% of global produced Earth surface over time (Bird, 2003). The building of the oceanic crust is commonly modeled as the product of a simple differentiation suite forming a layered structure comprising, from top to bottom, a basaltic volcanic crust and sheeted dyke complex, and in the lower section a plutonic sequence typically composed of gabbroic rocks (e.g., Coogan, 2014). Oceanographic and drilling expeditions revealed that the structure and chemistry of the lithosphere change with variation of the spreading rate (e.g., Ildefonse *et al.*, 2014). At fast-spreading ridges (>90 mm/a) the constant magma supply leads to the formation of a relatively homogeneous layered magmatic crust ('Penrose Model', Penrose field Conference Participants, 1972). In contrast, the oceanic lithosphere accreted at slower-spreading ridges (<50 mm/a) has laterally and vertically heterogeneous lithologies, comprising magmatic components as well as serpentinized mantle, due to the extremely variable melt production (e.g., Cannat, 1993; Dick *et al.*, 2003).

About 80% of the 66,000 km extended ocean ridges spread at rates less than ~50 mm/yr. Along slow-spreading centers, sections of plutonic rocks are exhumed on the seafloor by long-lived detachment faults often associated with uplifted domal structure of Oceanic Core Complexes (OCCs). The OCCs are a unique tectonic window that provide direct access and sampling of the deeper gabbroic rocks, and can account for the occurrence of locally shallower mantle-crust boundary. Investigations of OCCs are essential to understand the processes that build the lower oceanic crust at a slow-spreading center.

Studies of gabbroic rocks recovered at OCCs, together with studies of ophiolite analogues (Lagabrielle and Cannat, 1990; Lagabrielle *et al.*, 2015), questioned the origin of the lower oceanic crust as whether it is the result of simple magmatic differentiation processes, or it is affected by migration of melts that may react with the pre-existing mantle or plutonic rock thereby changing its composition and rheology. Specifically, the occurrences of olivine-rich gabbroic rocks in the lower oceanic crust accreted at slow-spreading ridges seem to prove that such melt-rock interactions play a fundamental role in the formation of the oceanic crust (e.g., Drouin *et al.*, 2009, 2010; Sanfilippo and Tribuzio, 2013; Sanfilippo *et al.*, 2014; Rampone *et al.*, 2016). However, their

effect on the global geochemical budget and structure of the lower oceanic crust is yet to be assessed (e.g., Lissenberg and MacLeod, 2017; O'Neill and Jenner, 2012).

The study presented in this manuscript aims at understanding the relative contribution of fractional crystallization and reactive melt percolation on the geochemical budget and architecture of the lower oceanic crust formed at slower-spreading ridges. For this I studied samples from two of the most well know OCC, the Atlantis Massif at 30°N of the Mid-Atlantic Ridge (MAR) and the Atlantis Bank at 32°S, 57°E of the Southwest Indian Ridge (SWIR).

At Atlantis Massif IODP Site U1309 was drilled during Integrated Ocean Drilling Program (IODP) Expeditions 304/305 (Blackman *et al.*, 2006), and a 1415.5 m thick gabbroic sequence was recovered at Hole U1309D. Mantle relicts were found only within the first 200 m of the central dome as isolated intervals of maximum 1 m thick within the gabbroic section, while abundant olivine-rich rocks were sampled downhole U1309D. The mantle intervals are impregnated by melts that successively crystallized the associated gabbroic rocks (Tamura *et al.*, 2008). Olivine-rich troctolites (> 70% olivine) formed by multiple and more extensive melt impregnation of pre-existing olivine-rich lithologies (Drouin *et al.*, 2009, 2010). The nature of the olivine-rich protolith, from which olivine-rich troctolites formed, is discussed and characterized in this work to constrain the impact of olivine assimilation on the structure and geochemistry of the oceanic crust.

In order to document the scale of modal and chemical heterogeneities in Hole U1309D olivine-rich troctolites, the least altered interval (<1% serpentinization) in the borehole (1100-1300 mbsf) was described in detail at the IODP Bremen Core Repository (Germany). For a complete microstructural and geochemical characterization of olivine-rich troctolites representative samples were selected from those described in previous studies (Drouin *et al.*, 2009, 2010), and implemented with new samples from Bremen Core Repository. I realized a multi-scale microstructural and petro-geochemical study, supported by numerical modeling of magmatic and reactive processes investigated. Geochemical profiles across adjacent phases were performed to investigate the effect of melt-rock interactions. Rim-to-rim geochemical compositions in olivine were analyzed along the principal crystallographic axes to account for anisotropic element diffusion in olivine.

International Ocean Discovery Program (IODP) Expedition 360 drilled Hole U1473A at the Atlantis Bank. Olivine gabbros represent the most primitive lithology, and they compose more than

75% of the recovered gabbroic sequence (MacLeod *et al.*, 2017). My participation to Expedition 360 allowed me to collect olivine gabbros from another heterogeneous lower crustal section analogous to Atlantis Massif, but geochemically different. My work off-shore is here summarized. It consisted in describing the magmatic structural features of recovered cores. My on-shore contribution is reported in this thesis and focuses on the whole rock characterization of the olivine gabbros, olivine-bearing gabbros and disseminated gabbros.

The work presented in this thesis comprises numerous analytical techniques.

- *Qualitative and quantitative analyses of microstructures* at the thin section scale by *Electron Backscattered Diffraction (EBSD)* to identify heterogeneous textures, deformed and undeformed crystals, and to define the orientation of the principal crystallographic axes of olivine in olivine-rich troctolites from the Atlantis Massif. EBSD analyses allowed me to provide new quantitative data on the deformation mechanisms recorded by olivine-rich troctolites. The results of microstructural analyses are reported in Chapter III and Appendix 1.
- *In situ major and trace elements* compositions of rock-forming minerals determined by *Electron Probe Micro Analyser (EPMA)* and *Inductively Coupled Plasma Mass Spectrometer coupled with laser ablation system (LA-ICP-MS)*. Olivine, plagioclase and clinopyroxene in olivine-rich troctolites from Hole U1309D were characterized. The geochemical data permit to constrain the equilibrium or disequilibrium signature among phases, thus providing information on the origin and processes that formed the olivine-rich troctolites. Mineral major and trace elements compositions are reported in Chapter III and Appendix 2.
- *Whole rock analyses by Inductively Coupled Plasma Mass Spectrometer (ICP-MS)* of olivine gabbros from the Atlantis Bank to characterize their trace element compositions. These geochemical data permit to hypothesize the petrological evolution of the olivine gabbros. Trace elements geochemical analyses are in Appendix 3 and discussed in Chapter IV.

I performed also a geochemical study to develop new standards adapted to high quality *in situ* geochemical data. This side-project arised from the need of matrix-matched secondary standards to avoid analytical problems and discrepancies in the quality control of LA-ICP-MS acquired data, which are due to matrix dependent elements fractionation (e.g., Jochum *et al.* 2007). I selected

minerals of different compositions mainly corresponding to those analysed in this thesis, which include olivine and clinopyroxene (and chromite).

This manuscript is composed of four main Chapters:

- I. Bibliographic synthesis of the formation of the lower oceanic crust at both slower- and faster-spreading ridges. Here I propose an overview of present-day knowledge of the composition and architecture of the lower oceanic crust, together with models of crustal accretion. Processes of magma crystallization, (melt and element) transport and reaction, which are involved in the building of crustal sections, are also treated as support to the discussion developed in the following Chapters.
- II. Detailed description of the different analytical methods implemented in this thesis. In Chapter II.5 I report the parallel study aimed to develop mineral secondary standards for *in situ* geochemical data.
- III. Microstructural and petro-geochemical study of olivine-rich troctolites recovered at Atlantis Massif. The first section corresponds to the article intitled “Melt transport and mantle assimilation at Atlantis Massif (IODP Site U1309): evidence from chemical profiles along olivine crystallographic axes” that I submitted for publication on the Special Issue ‘Reactive Geological Systems from the Mantle to the Abyssal sub-seafloor’ in *Lithos*. The second section documents Ca and Rare Earth Elements profiles across clinopyroxenes and olivines from U1309D olivine-troctolites.
- IV. Summary of the main results of IODP Expedition 360 at the Atlantis Bank, with particular detail on my contribution off-shore. I also describe the first outcome of my geochemical on-shore study. A comparison between Atlantis Bank OCC and Atlantis Massif OCC concludes this Chapter.

Finally, I discuss the principal outcomes of my work in a general conclusion, and I propose future studies to further understand the formation of the lower oceanic crust at the global scale.

Chapter I

Overview on the building of the heterogeneous

lower oceanic crust

Observations and models

1. Formation of the lower oceanic crust at slow- and fast-spreading ridges

1.1 *In situ* sampling at modern ridges

Before the late '60s, when marine geology at mid-ocean ridges became significantly active, the study of the formation of oceanic lithosphere was centred on ophiolite complexes. Ophiolites represent a unique access to the internal structure of the lithosphere, and provide essential insights on the three dimensional architecture and chemical composition of the oceanic crust. Although they represent remnants of oceanic lithosphere likely formed at spreading centres, they may retain signatures of subduction during the closure of the paleo-ocean, where they originally formed, and emplacement on land (e.g., Boudier *et al.*, 1985; Rollinson *et al.*, 2014; Lagabrielle *et al.*, 2015). It is essentially over the last 70 years that *in situ* oceanic crust at mid-ocean ridges has gained attention, and has been investigated by geophysical and geological expeditions. This greatly improved our knowledge on the nature and formation of the oceanic lithosphere. The advantage of studies at modern spreading ridges lays on the fact that the young oceanic lithosphere records processes of early formation by cooling of magmas, and that these features are not overprinted by those processes occurring at subduction zones, which instead partially affect ophiolite complexes.

At fast-spreading ridges plutonic rocks compose the deeper section of oceanic crust, thus they are the most challenging to sample. Advances in drilling techniques allowed penetrating to deep parts of the oceanic crust during the scientific drilling programs Deep Sea Drilling Project (DSDP), Ocean Drilling Program (ODP), Integrated Ocean Drilling Program (IODP), and International Ocean Discovery Program (IODP). Fast-spread crust has been recovered to the base of the upper crust and the uppermost gabbro (IODP Hole 1256D, East Pacific Rise; Figure I.1). Alternatively, access to deeper part of the oceanic crust has been possible in tectonic windows, for example at Hess Deep where lower crust layered gabbros and troctolites were drilled into fast-spread crust for the first time (Site U1415, East Pacific Rise; Figure I.1). Along slow- and ultraslow-spreading ridges, the heterogeneous oceanic lithosphere (definition reported in Chapter I.1.2) is exhumed by long-lived detachment faults, providing a unique tectonic window for sampling of the *in situ* oceanic crust, from the upper part to the deeper section. Gabbroic sequences with associated serpentinized

mantle exposed on the seafloor have been dredged and drilled along the Mid-Atlantic Ridge (e.g., 30° N, IODP Site U1309; 24°N, Kane area; 15°20'N, ODP Sites 1268-1275; Figure I.1), and Southwest Indian Ridge (57°E, Holes IODP U1473A and ODP 735B) where dominantly mantle rocks were also sampled in some ridge segments (e.g., 61°-67°E; Figure I.1) by dredging expeditions (Cannat *et al.*, 2006; Sauter *et al.*, 2013). Figure I.2 shows a compilation of drilling results over the past 50 years (Ildefonse *et al.*, 2007a, 2014). It should be noted that although more than 6000 m of oceanic crust have been recovered, a complete and continuous section of intact oceanic crust down to the crust-mantle boundary has yet to be drilled at both slow- and fast-spreading centres. Samples of oceanic lithosphere were collected *in situ* not solely by drilling, but also during dredging and submersible expeditions (e.g., Dick *et al.*, 1984; Tucholke and Lin, 1994; Cannat *et al.*, 1995; MacLeod *et al.*, 1998, 2002; Fujiwara *et al.*, 2003).

Holes Drilled in Ocean Crust (1974-2016)

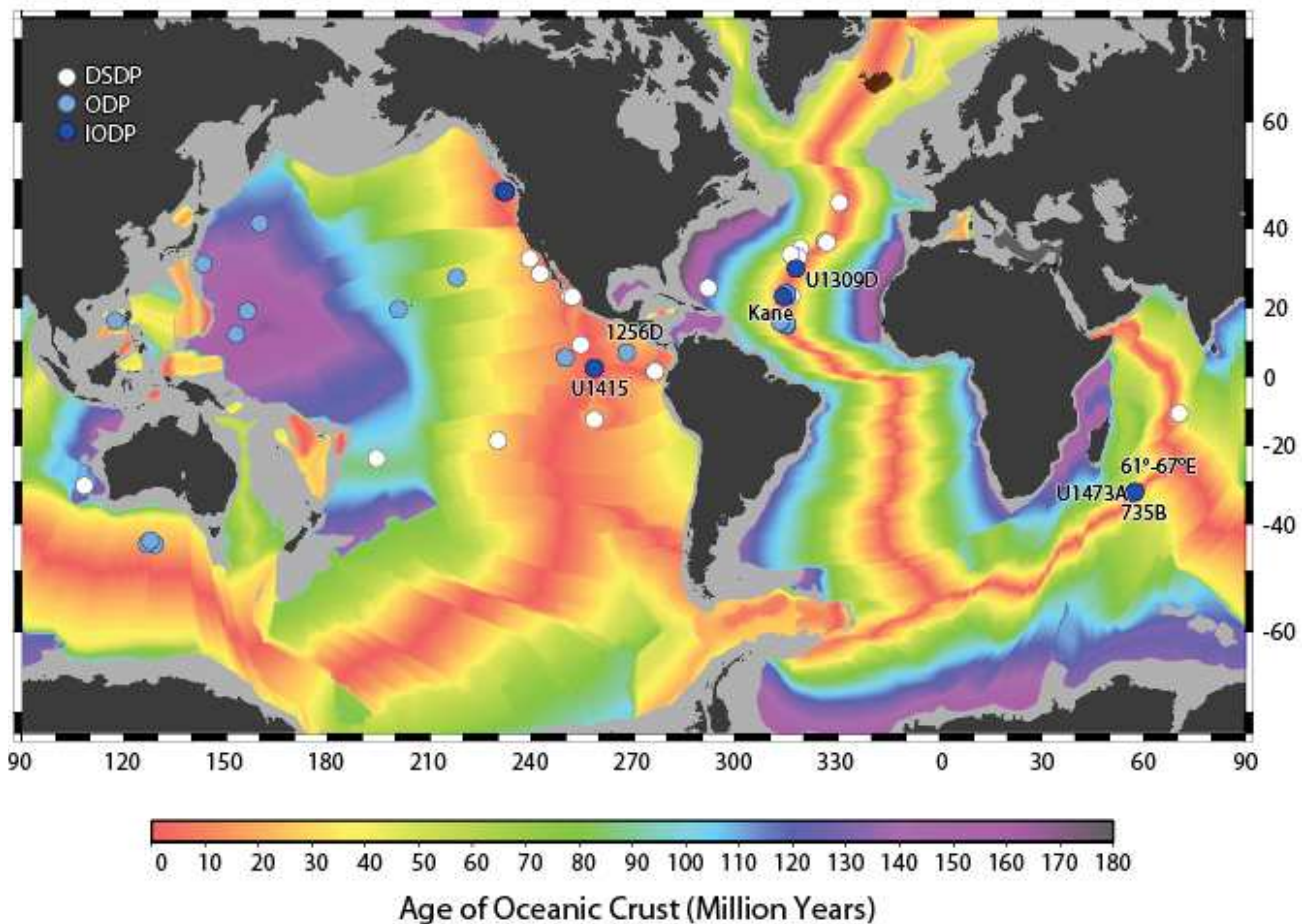


Figure I.1 - DSDP, ODP, and IODP holes drilled in ocean crust >100 mbsf from 1974 to 2016 (modified after Ildefonse *et al.*, 2014), mainly along active spreading centres. Sites labelled are cited in the text.

Table I.1 – Estimated number of samples of gabbroic and peridotite rocks from active spreading centres, forearc, backarc and ophiolites. Source: PetDB (<http://www.earthchem.org/petdb>)

Type rock sample	Spreading centres	Forearc	Backarc	Ophiolite	TOT
Gabbro	1911	22	24	167	2124
Troctolite + Dunite + Wherlite	325	17	24	268	634
Peridotite	1218	56	61	581	1916

Our understanding of the formation of oceanic crust comes from a relatively limited number of samples in comparison with the vast area that ocean floor covers worldwide (70% of Earth surface). The geochemical composition was characterized for a selection of these samples of mantle and oceanic crustal rocks, of which numbers are reported in Table I.1 for different locations including spreading centres, forearc and backarc basins, and ophiolite complexes.

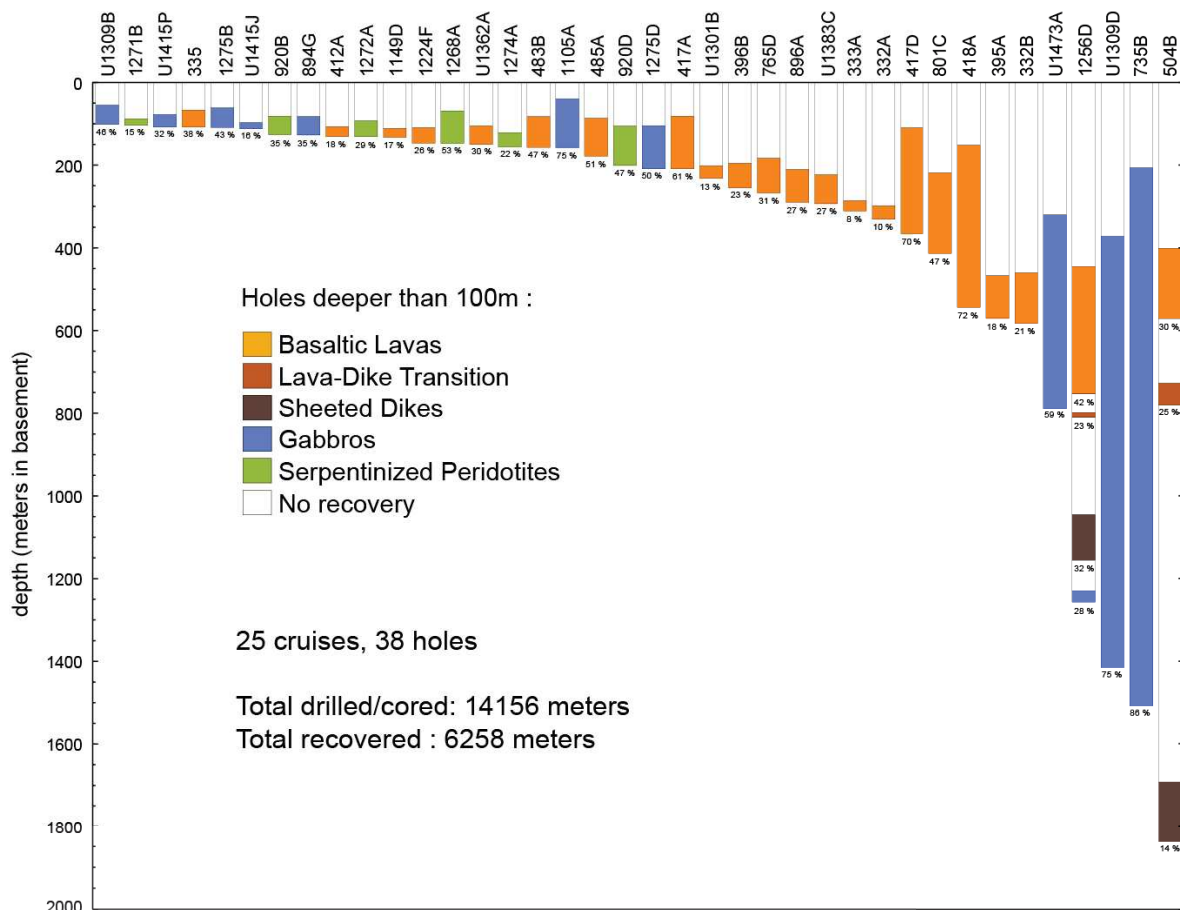


Figure I.2 - Compilation chart showing holes drilled >100 m in oceanic crust >100 mbsf from 1974 to 2016 (modified after Ildefonse et al., 2014), mainly along active spreading centres. Percentages indicate recovery.

Despite this, a lot was learned from studies of samples of oceanic lithosphere from active spreading centres and ophiolites. Various accretion models have been proposed over the years, and they are still debated. Different ridge morphologies and oceanic crust architectures have been identified between fast- and slow-spreading ridges. In the following I report their major characteristics.

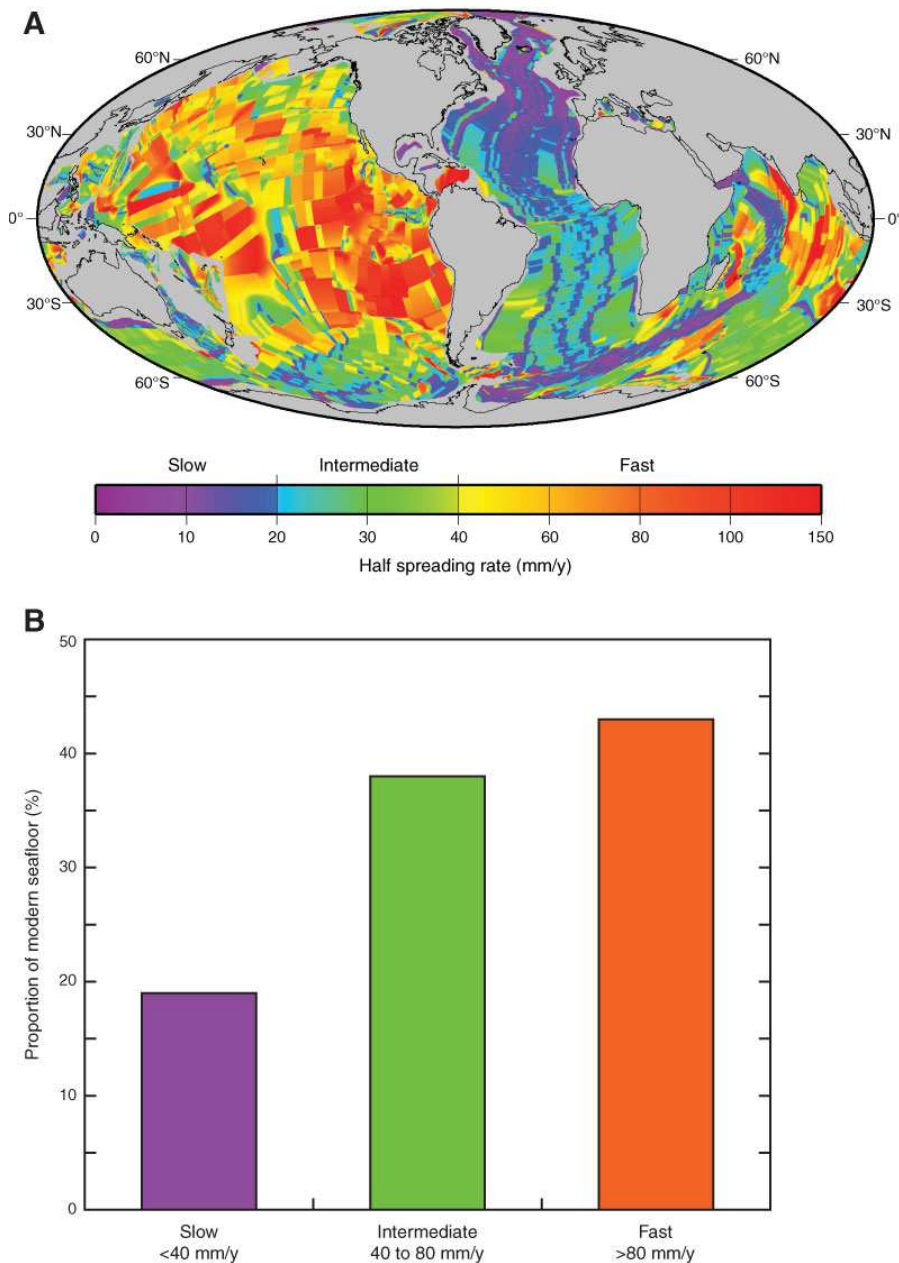


Figure 1.3 – a) Global view of ocean crust formation coloured by half-spreading rate; b) histogram comparing the proportions of the present-day ocean crust (Teagle et al., 2012)

1.2 Structure of ridges and oceanic crust

The oceanic crust is continuously generated along mid-ocean ridges that separate two divergent plates (Figure I.3; e.g., Bird, 2003). The mid-ocean ridge system is divided, at the global scale, into long segments of variable spreading rate. Fast-rates of seafloor renewal account for spreading along ~13000 km of the ~67000 km ridge system (e.g., Bird, 2003; Teagle *et al.*, 2012). Slower-rates account for 80% of global mid-ocean ridge spreading: ~34000 km is intermediate- and slow-spreading, and ~20000 km is ultraslow-spreading (e.g., Bird, 2003; Dick *et al.*, 2003). Each of these portions of the mid-ocean ridge systems have distinctive morphologic characteristics and oceanic crust architecture (see reviews by Dick *et al.*, 2003; Buck *et al.*, 2005; Coogan, 2014; Ildefonse *et al.*, 2014; White and Klein, 2014; Dunn, 2015).

Morphology

Mid-ocean ridges are tectonically segmented by a hierarchy of transform and nontransform offsets (Figure I.4). First order segments reach 300-500 km in length of various shorter lived

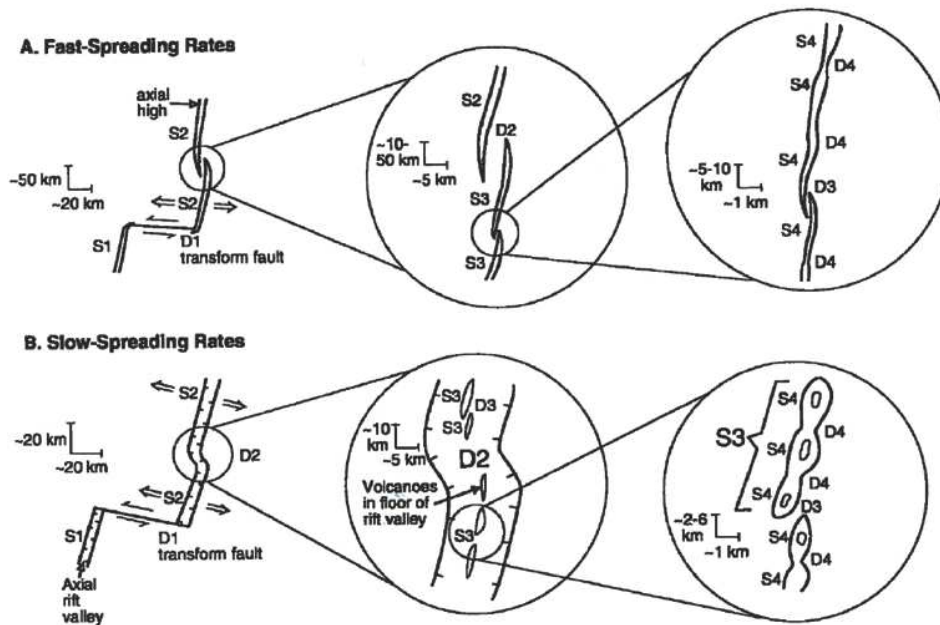


Figure I.4 – Hierarchy of ridge-axis discontinuities proposed by Macdonald *et al.* (1993a) for a) fast-spreading ridges and b) slow spreading ridges. S1, 2, 3, 4 are ridge segments of first, second, third and fourth order, respectively. D1, 2, 3, 4 are ridge-axis discontinuities of first, second, third and fourth order, respectively.

segments (second order segments; Macdonald et al., 1993a, 1993b), and are delimited by major transform faults that offset the ridge by up to hundreds of kilometres. Second order discontinuities persist for 1-2 million years, and are different between those at slow- and fast-spreading ridges (Figure I.4). At fast-spreading ridges, they are overlapping spreading centers, while at slow spreading ridges they are generally amagmatic non-transform offsets (Macdonald et al., 1993a, 1993b; Dick et al., 2003). Even shorter lived ridge segments are described as third and fourth order, being responsible for smaller offsets (White and Klein, 2014; Dunn, 2015, and references therein).

As full-spreading rate decreases, the average depth of ridge axes becomes greater and more variable, more segmented, and more heavily rifted (Figure I.5; Buck et al., 2005; Dunn, 2015). Fast-spreading centres, where plates diverge at a rate faster than 8 cm/yr, such as the East Pacific Rise

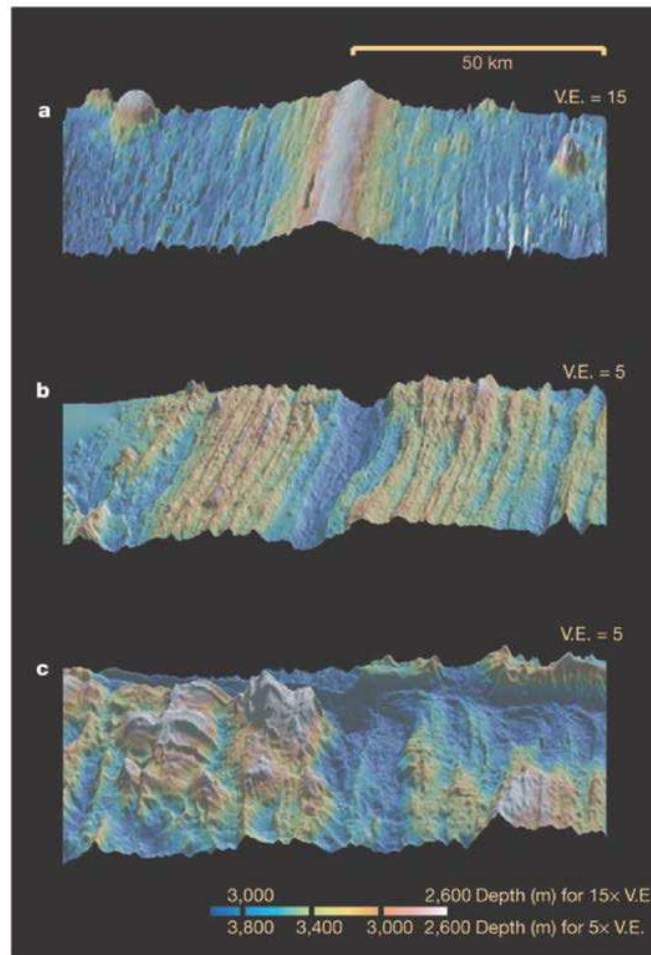


Figure I.5 – Shaded relief images of bathymetry (Buck et al., 2005) over 40 km along the ridge axis and 110 mm across the axis of representative a) fast-spreading ridge, East Pacific Rise; b) intermediate-spreading ridge, Southeast Indian Ridge; c) slow-spreading ridge, Mid-Atlantic Ridge.

(EPR; e.g., Müller *et al.*, 2008), are characterized by a smooth topography that result from the fact that spreading is dominantly accommodated by magmatism (Detrick, 1987; Solomon and Toomey, 1992; Kent *et al.*, 1993; White *et al.*, 2002,2009; White and Klein, 2014). The ridge exhibits broad axial highs, which were classified in axial 'troughs' (Fornari *et al.*, 1988), and axial summit 'graben' of primarily tectonic origin. It is distinguished by long straight magmatic segments (e.g., Fornari *et al.*, 1988; White *et al.*, 2002) and second order segments are delimited by overlapping spreading centres that offset the ridge by 5-10 km (Macdonald *et al.*, 1993a, 1993b). Fast-spreading ridges have high magma flux that produce on the seafloor high volumes of lava at high effusion rates along axial troughs (e.g., Fornari *et al.*, 1988; White *et al.*, 2002, 2009).

Slower-spreading centres exhibit more irregular and rough topography, due to the characteristic ductile to brittle deformation that accommodates divergence (brittle–ductile transition at 4 km depth; Barclay *et al.*, 2001), compared to fast-spreading ones. Slow-spreading ridges are characterized by full-spreading rates slower than 40 mm/yr, such as the Mid-Atlantic Ridge (MAR). Slower spreading velocities characterize the ultraslow-spreading ridges in the Arctic Ocean (Gakkel Ridge) and the Southwest Indian Ridge (SWIR), with maximum rates of 18 mm/yr (Dick *et al.*, 2003). A prominent 5 to 20 km wide axial valley marks the plate boundary that is typically 1 km or more deep. Within the axial valley, pillow lavas form the axial volcanic ridge. Seismic and geochemical data suggest that individual eruptions are generally larger but less frequent at slow- spreading ridges than at faster ones (Perfit and Chadwick, 1998; Tolstoy *et al.*, 2001; Soule *et al.*, 2007; Goss *et al.*, 2010). Segmentation is denser at slow-spreading ridges: second-order segments are commonly less than 100 km in length and are delimited by oblique shear zones that offset the ridge 15–30 km (Macdonald *et al.*, 1993a, 1993b; Sempéré *et al.*, 1993; Figure I.4).

Intermediate-spreading ridges, with spreading rates between 40 and 80 mm/yr, have morphologies that vary between those typical of fast- and slow-spreading ones. One example of intermediate-spreading centre is Juan de Fuca Ridge that has segments exhibiting the full range of morphologies (Carbotte *et al.*, 2006; Stakes *et al.*, 2006).

Along slow-spreading ridges magma flux is lower than beneath faster-spreading centres. Magma supply decreases at ultraslow-spreading ridges where magmatic segments alternate with amagmatic regions (Dick *et al.*, 2003). This results in variable architectures of oceanic crust beneath spreading centres.

Architecture

The architecture of oceanic crust was first reconstructed after profiles of seismic velocities (e.g., Raitt, 1963; Christensen, 1970; Christensen and Shaw, 1970; Christensen and Salisbury, 1975; Miller and Christensen, 1997). Seismic data reported by Raitt (1963), based on the results of seismic-refraction experiments in the 1950s at the Mid-Pacific (review in Prodehl *et al.*, 2013), showed a gradient of P-wave velocities (V_p) at increasing depth through the oceanic crust. Variations in seismic velocities were divided in three main layers (Raitt, 1963; Christensen and Salisbury, 1975) that, by analogy to ophiolites and dredged hauls, were interpreted as characteristic lithologic units composing the oceanic crust (Conference Participants, 1972).

Ocean Ridge Crustal Accretion Models

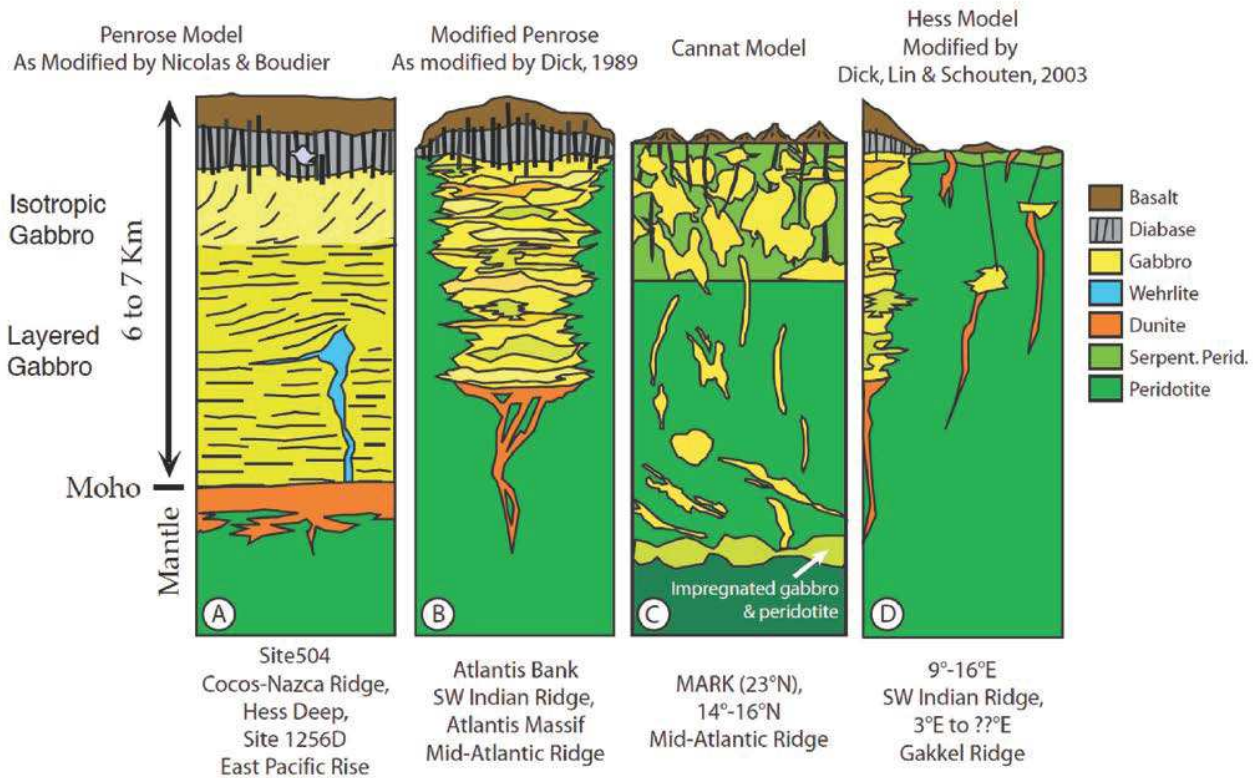


Figure I.6- Models for crustal accretion at ocean ridges as synthesized by Dick *et al.* (2006). a) Interpretation of the Penrose Model for a fast-spreading ridge based on the Oman Ophiolite. c) Penrose model as modified for slow-spreading ridges based on the abundance of peridotite and frequent absence of gabbro at seafloor along the Southwest Indian Ridge and Mid-Atlantic Ridge. c) Model for the anomalous 14°–16°N area of the Mid-Atlantic Ridge as proposed by Cannat *et al.* (1997). d) Model for magmatic and amagmatic accretionary segments at ultraslow-spreading ridges.

Based on this and supported by the uniform composition of dredged basalts along ocean ridges (Engel *et al.*, 1965), attendees of the Penrose field conference (Conference Participants, 1972) elaborated a layered model for the vertical structure of oceanic crust that is composed of, from top to bottom (Penrose Model, Figure I.6):

- Basaltic lava: extrusive layer formed by pillow lava, which display high porosity and low density as evidence of hydrothermal alteration and fracturing. It corresponds to seismic layer 2A ($V_p = 3\text{-}4 \text{ km s}^{-1}$);
- Sheeted dike complex: characterized by mafic vertical dikes that form seismic layer 2B ($V_p = 3\text{-}4 \text{ km s}^{-1}$);
- Gabbroic complex: isotropic (top) and layered (bottom) gabbroic rocks that are underlined by ultramafic cumulates. The gabbroic sequence form seismic layer 3 ($V_p = 6.7\text{-}7.7 \text{ km s}^{-1}$);
- Mantle peridotite: composed by lherzolite, harzburgite and dunites in variable proportions ($V_p = 8 \text{ km s}^{-1}$).

Basaltic lava and sheeted dikes (seismic layer 2) form the upper oceanic crust, whereas the gabbroic complex makes up the lower oceanic crust (seismic layer 3). The seismic boundary underlying the seismic layer 3 is the Mohorovicic Discontinuity (Moho). The Moho corresponds to a compressional V_p velocity increase from 6.7 km s^{-1} to 8.6 km s^{-1} (e.g., Miller and Christensen, 1997), typically located at $\sim 6\text{-}7 \text{ km}$ beneath ocean floor (review in Dunn, 2015). The Moho has been interpreted as the seismic boundary between the lower oceanic crust and upper mantle, thus it has been studied to retrieve the thickness of oceanic crust (Figure I.7), which varies locally depending upon melt supply (e.g., Dick *et al.*, 2003; Carbotte and Scheirer, 2004; Cannat *et al.*, 2009; review in Dunn, 2015). Since the early 1970s, seafloor mapping, geophysical data and first deep drilling along MAR (DSDP Leg. 37, Aumento *et al.*, 1977; DSDP Leg. 45, Melson *et al.*, 1979) have demonstrated that a layered oceanic crust may not apply to the global oceanic crust. Whereas the Penrose Model is widely accepted to represent the crust accreted at fast-spreading centres, such as the Oman Ophiolite (Boudier and Nicolas, 1985) and EPR (recovered upper oceanic crust, Wilson *et al.*, 2003; Alt *et al.*, 2007; Teagle *et al.*, 2006, 2012), this is not always the case for slow- and ultraslow-spreading centres (Figure I.6 and I.8). Hereafter the lower oceanic crust is referred to as the seismic lower oceanic crust, delimited by slower V_p on top and faster at the bottom. In contrast, the term 'magmatic' lower oceanic crust implies gabbroic to gabbroic assemblages (reviews in Bedard

et al., 2000; Coogan, 2014), thus comprising magmatic components exclusively, which applies only to fast-spreading crust (Figure I.8).

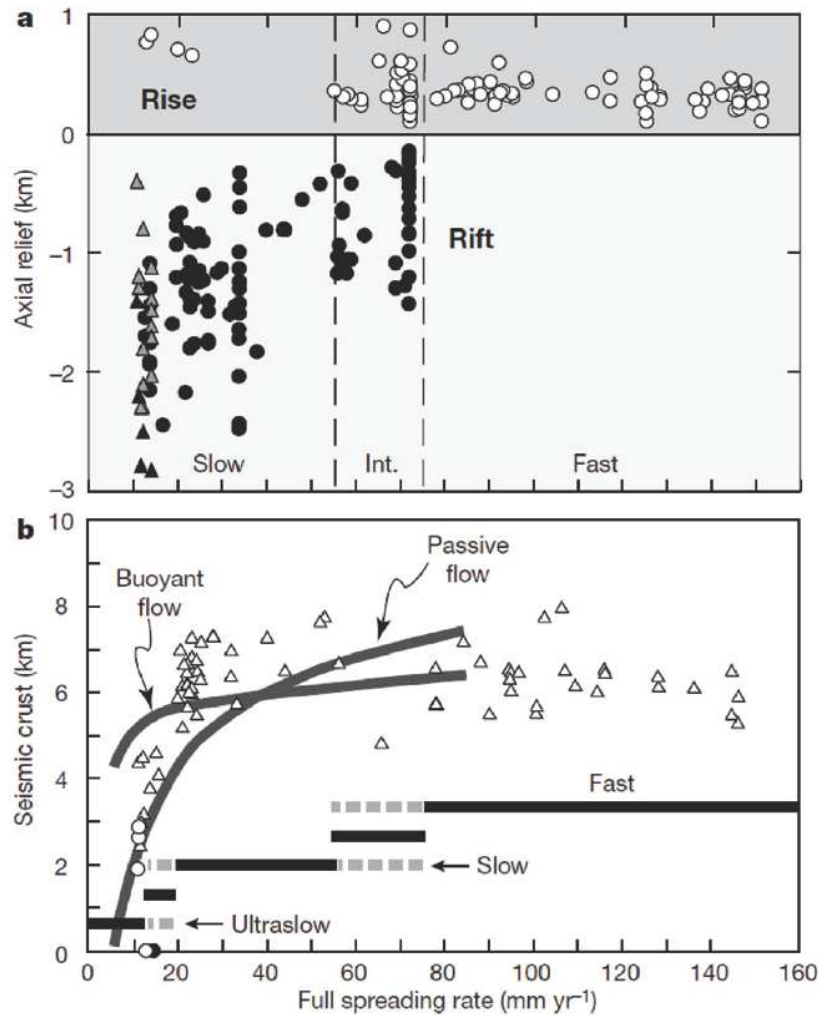


Figure I.7 – Ridge properties as a function of spreading rate as reported by Dick et al. (2003). a) Axial relief of axial rises (white circles) and axial rifts (black circles); triangles represent data of accretionary segments at Gakkel ridge and Southwest Indian Ridge (grey triangles = amagmatic, black triangles = magmatic). b) Seismic crustal thickness; heavy black straight lines show ridge classification; broken grey lines are overlapping spreading rates.

Dredged samples of peridotites associated to gabbros and basalts along the MAR (Bonatti et al., 1971) revealed that heterogeneous oceanic crust forms at slow- and ultraslow- spreading ridges. From the 1980s to the early 2000s seafloor geological studies and geophysical surveys, in addition to scientific ocean drilling expeditions, documented emplacement of mantle rocks at surface associated to small gabbro intrusions overlain by a thin or absent extrusive section (Figure I.6 and

I.8; e.g., MAR and analogous ophiolites, Karson and Elthon, 1987; Lagabrielle and Cannat, 1990; Cannat, 1993, 1996; Cannat et al., 1995, 1997; Canales et al., 2000; Kelemen et al., 2004; SWIR and Gakkell Ridge, Dick, 1989; Dick et al., 2003; Cannat et al., 2006; Sauter et al., 2013). Geophysical data at non-volcanic regions of slow-spreading ridges indicate that the top 4 km of oceanic crust show high porosity suggesting that it is pervaded by faults and fractures (e.g., Barclay et al., 1998; Canales et al., 2000; Dunn et al., 2005). The heterogeneous oceanic crust observed at slower-spreading ridges is thus composed of gabbroic sequences associated to serpentized mantle rocks (review in Coogan, 2014). At decreasing magma supply, crystallization of gabbroic rocks become of minor or negligible importance, especially at magma poor ridge regions (e.g., Cannat, 1993; Cannat *et al.*, 2006; Sauter *et al.*, 2013), where serpentinite is the most abundant lithology exposed at oceanic crustal surface (Figure I.6 and Figure I.9; e.g., Cannat, 1993; Dick et al., 2003; Mével, 2003; D’Errico et al., 2016). Magma supply is generally poor toward ridge segment ends where spreading is tectonically accommodated (e.g., Cannat, 1993; Gracia *et al.*, 1999; Tucholke and Lin, 1994), while it is more robust beneath the central region of single segments (e.g., Canales *et al.*, 2000a; Dunn *et al.*, 2005). The latter axial sections are dominated by magmatic processes, which can locally form oceanic crust of fundamentally similar vertical structure to that of fast-spreading

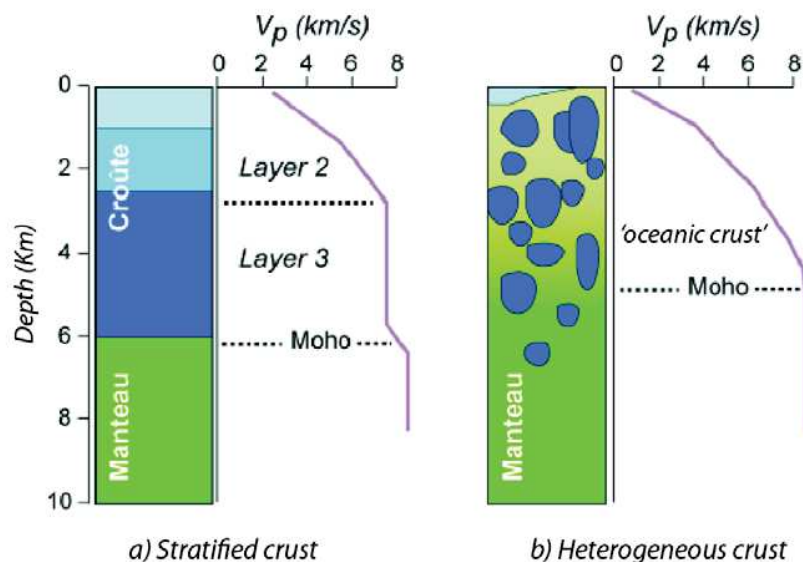


Figure I.8 - Schematic representation of the two types of oceanic crust based on seismic signal (velocity of P waves, V_p ; Mével, 2003): a) stratified oceanic crust composed of magmatic rocks as proposed in the Penrose model; b) slow-spread heterogeneous oceanic crust composed of serpentized mantle intruded by gabbros. Light blue = basalts, blue = dike complex, dark blue = gabbro, green = mantle peridotites.

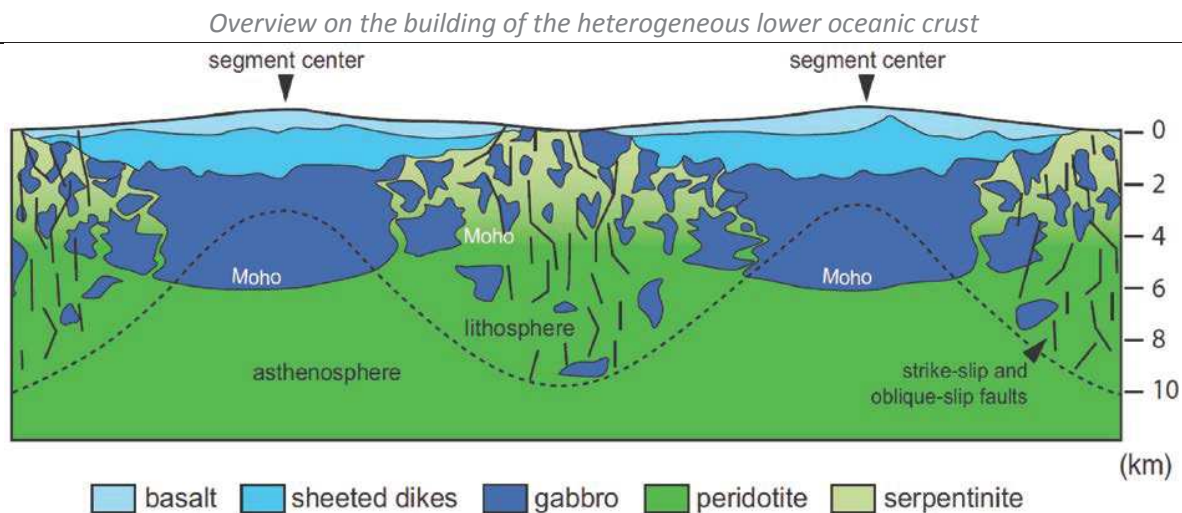


Figure I.9 – Simplified interpretation of lower crustal composition along the axis of slow-spread crust (Ildefonse *et al.*, 2007; modified from Cannat *et al.* (1995)).

ridges (37° 18' N MAR, Singh *et al.*, 2006). A continuous lateral change along the axis thus distinguishes the oceanic crust created along slow- (and ultraslow-) spreading centres. Here, laterally and vertically heterogeneous oceanic crust predominates over the simple layered oceanic crust of fast-spreading ridges, and is commonly characterized by mantle rocks intruded by gabbroic lithologies (Figure I.9; Dick, 1989; Cannat, 1993; Cannat *et al.*, 1997; Dick *et al.*, 2003; Ildefonse *et al.*, 2007a; Kelemen *et al.*, 2007b; Blackman *et al.*, 2011; Sauter *et al.*, 2013; Lagabrielle *et al.*, 2015).

Although a melt lens was detected beneath MAR (37° 18' N MAR, Singh *et al.*, 2006), magma chambers are believed to not persist beneath slower-spreading ridges over the duration of the opening of the ocean (Figure I.8 Figure I.9; e.g., Tucholke *et al.*, 1997; Gracia *et al.*, 1999; Dick *et al.*, 2003; Mével, 2003; Cannat *et al.*, 2006). Thus the magmatic plumbing system is variable in time and space along slower-spreading centres. This and the occurrence of mantle sections at the oceanic crust surface make it challenging to understand the nature of the Moho, early interpreted as the boundary between oceanic crust and mantle. In the early 1960s, H. Hess (1962) argued that the Moho could represent the transition between serpentinized peridotites (having seismic velocities similar to those of gabbros) and underlying mantle rocks, marking an alteration front at the 500°C isotherm. The Moho could represent the hydration boundary between a heterogeneous partially magmatic oceanic crust and the mantle, as evidenced by the occurrence of serpentinites on the seafloor (e.g., Ildefonse *et al.*, 2007a; Canales *et al.*, 2008), but this hypothesis has never

been tested. To date, this seismic discontinuity (Moho) has been a symbolic goal for many geologists. Understanding of its nature is one of the main objectives of several deep drilling projects, including the recent IODP Expeditions 360 (MacLeod *et al.*, 2017b).

1.3 Models of lower oceanic crust accretion

The formation of the oceanic crust is generally modelled as cooling of focused magmas at ridge axes that are previously generated at depths by partial melting of upwelling mantle. Some melts cool slowly in a (or multiple) magma chamber(s) leading to formation of the plutonic gabbroic rocks that make up the lower oceanic crust. After partial crystallization (and magma differentiation) a portion of magma is extracted to form the overlying dikes and lavas (see overview from Coogan, 2014). This simple magmatic crystallization process forms the layered crust described by the Penrose Model and typically observed at fast-spreading ridges (e.g., Boudier and Nicolas, 1985). Permanent magma chambers are assumed in this model in contrast with the episodic magma cooling observed at slow-spreading ridges (Figure I.6, I.8 and I.9). Since the first oceanic accretion model, the so-called ‘infinite onion model’ of a steady-state large molten chamber (Cann, 1974), different alternative models have been proposed for the formation of oceanic crust at fast- and slow- spreading centres. Models for oceanic crust accretion at fast-spreading ridges were elaborated based on geophysical studies along modern ridges (e.g., Detrick, 1987; Kent *et al.*, 1993; Collier and Singh, 1998; Dunn *et al.*, 2000; Van Ark *et al.*, 2007; Canales *et al.*, 2009; Marjanović *et al.*, 2014) and field data in the Oman ophiolite (e.g., Pallister and Hopson, 1981; Boudier *et al.*, 1996; Kelemen *et al.*, 1997c; Nicolas *et al.*, 1988, 2000; Umino *et al.*, 2003). Most recent models for fast-spreading accretion predict that the upper crust is fed by a shallow and thin melt-rich magma chamber (first observed using thermal constrained, Sleep, 1975). Below this magma lens a melt-poor magmatic mush expands vertically over about 4 km (e.g., Detrick, 1987; Dunn *et al.*, 2000), where crystallization of gabbroic rocks occur. Two competing models are proposed for the formation of this lower domain (Figure I.10). In the ‘gabbro glacier model’, crystallization occurs in a shallow magma lens where heat is transferred to the overlying hydrothermal system, and a flow of mushy material downward and outward form the lower crust (e.g., Henstock *et al.*, 1993; Morgan and Chen, 1993; Quick and Denlinger, 1993). In contrast, the ‘sheeted sill model’, based on the observation of sill-like plutonic bodies in the upper mantle

section of the Oman ophiolite (Boudier *et al.*, 1996), involve in situ crystallization of partial (e.g., Boudier *et al.*, 1996), or almost the entire, lower oceanic crust (e.g., Kelemen *et al.*, 1997c; Korenaga and Kelemen, 1997). This model requires extensive hydrothermal cooling along the sides of the mush zone in order to remove heat (e.g., Chen, 2001; MacLennan *et al.*, 2005).

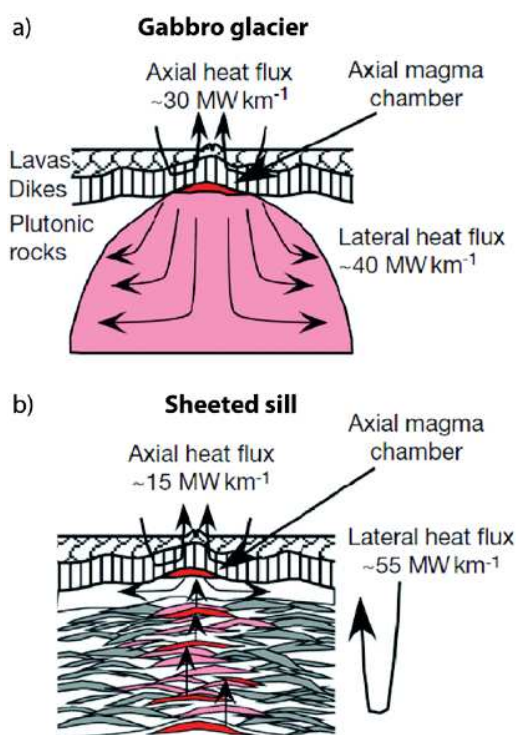


Figure 1.10 – Models for the formation of lower oceanic crust along fast-spreading ridges (Coogan, 2014).

a) 'gabbro glacier' model (Henstock *et al.*, 1993; Morgan and Chen, 1993; Quick and Denlinger, 1993) in which the magma crystallizes in a small steady-state magma chamber at the base of the sheeted dike complex. b) 'sheeted sill' model (Boudier *et al.*, 1996; Kelemen *et al.*, 1997c) in which magma crystallization takes place in multiple sills.

The building of slow-spreading crust was first modeled after studies of ophiolite complexes analogous to present-day oceanic crust (e.g., Lagabrielle and Cannat, 1990; Lagabrielle *et al.*, 2015, and references therein), and later supported by seafloor observations. The absence of a sheeted dike complex and the occurrence of gabbroic intrusions in mantle rocks were explained as the result of magmatic crystallization in plutons at different depths within the oceanic lithosphere (Cannat, 1993, 1996; Lagabrielle *et al.*, 2015). Mechanisms of oceanic crust accretion become extremely dependent on magma production and flux. Central portions of ridge segments, where magma supply is higher (e.g., Blackman and Forsyth, 1989), are expected to be magmatically

accommodated similar to fast-spreading centres (e.g., Toomey *et al.*, 1988; Barclay *et al.*, 1998; Dunn *et al.*, 2005; Singh *et al.*, 2006). In contrast, the ends of ridge segments are characterized by lower melt fluxes, and tectonics become predominant in the accommodation of spreading (e.g., Cannat, 1993; Cann *et al.*, 1997; Gracia *et al.*, 1999; Cannat *et al.*, 2006; Ildefonse *et al.*, 2007a; Escartín *et al.*, 2008; Blackman *et al.*, 2011). Along ridge sections, where magmatic activity is greater seafloor accretion is symmetrical with subsidiary high-angle faulting and the formation of abyssal hills on both flanks (Figure I.11; e.g., Cannat *et al.*, 2006; Escartín *et al.*, 2008). At decreasing magma supply large offsets normal faults are inferred to develop preferentially in one ridge flank, producing asymmetrical accretion (Figure I.11). These large normal faults are deep-reaching but shallowly inclined detachment faults, which are responsible for unroofing and exposure of upper mantle and gabbroic rocks to the seafloor (e.g., Cannat, 1993, 1996; Tucholke and Lin, 1994; Escartín *et al.*, 2003, 2008; Tucholke *et al.*, 1998, 2008).

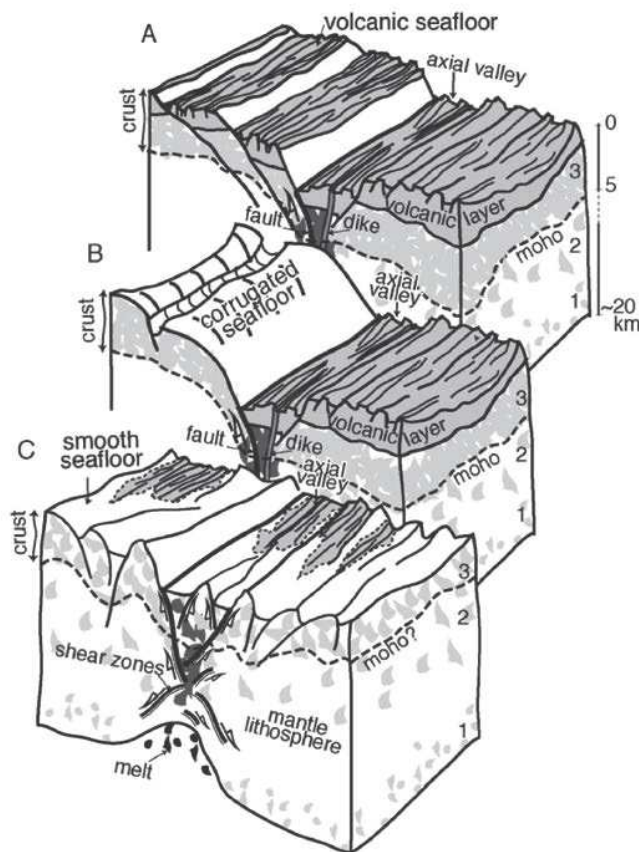


Figure I.11 – Conceptual sketches of axial accretion along slow- and ultraslow-spreading ridges at decreasing melt supply (Cannat *et al.*, 2006) from a) and b) more magmatically robust segments to c) regions with little or absent volcanism.

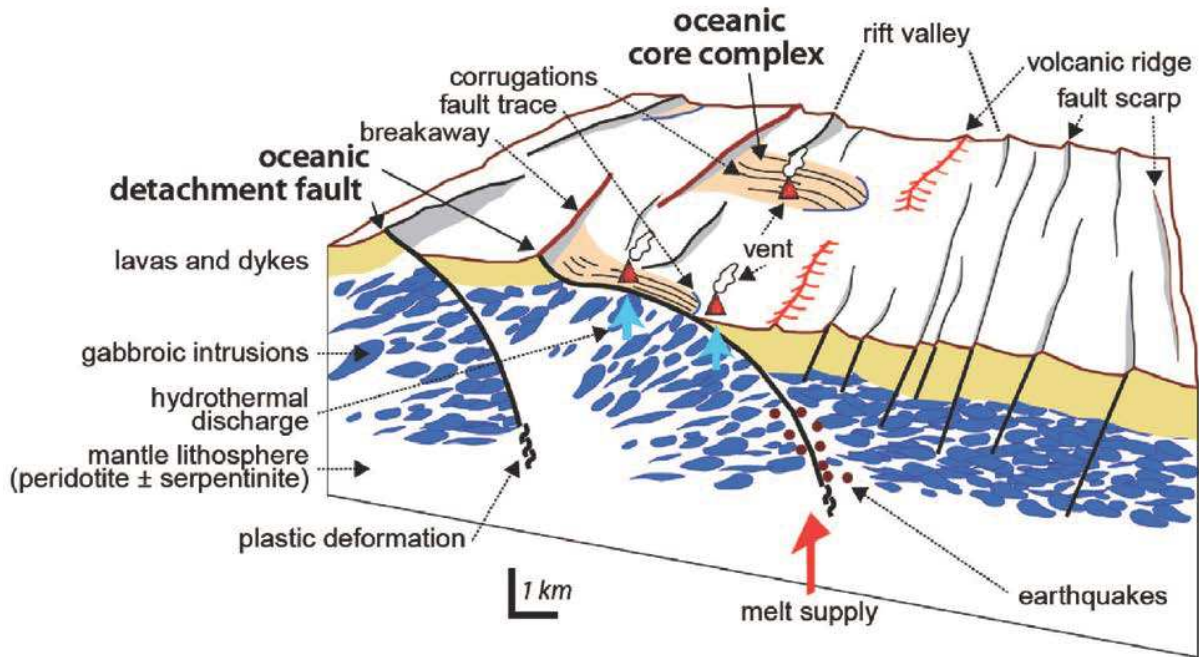


Figure I.12 - Conceptual sketch of lithospheric accretion at slow-spreading ridges: representation of the tectono-magmatic evolution of a heterogeneous lithosphere and emplacement of mantle rocks on the seafloor as detachment faulting progresses and OCCs are formed (Ildefonse, 2014a).

Large, long-lived detachment faults also expose sections of the lower oceanic crust forming domal highs known as Oceanic Core Complexes (OCC; Figure I.12), named after their resemblance with the ‘metamorphic core complexes’ found in extending continental regions (e.g., John, 1987; Dinter and Royden, 1993; Bozkurt and Park, 1994). In OCC the exposure of intrusive crust is often associated with serpentinitized peridotite (e.g., Blackman *et al.*, 2002, 2006; Cann *et al.*, 1997; Dick *et al.*, 1991a; Ildefonse *et al.*, 2007a; MacLeod *et al.*, 2002, 2009). They generally develop at the end of spreading segments, on the ‘insider corner’ of the interception between a transform fault and the ridge axis (Cann *et al.*, 1997; Tucholke *et al.*, 1998, 2001; Tucholke and Lin, 1994), but they have also been identified in other location at slow-spreading ridges (e.g., Smith *et al.*, 2006, 2008; Andreani *et al.*, 2014). The surface of OCC is distinguished by striations parallel to the spreading direction that mark the continuous slip of detachment fault plane developed over a spreading period of 1–2 Ma (Tucholke *et al.*, 1998; MacLeod *et al.*, 2002, 2009; Escartin *et al.*, 2017). The vertical structure of OCC has been studied *in situ* by geophysical investigations (e.g., review in Blackman *et al.*, 2009) and drilling. Among deep drilling expeditions, five have penetrated into

more than 500 mbsf lithospheric sections of two domal cores of OCCs along the Mid-Atlantic Ridge (30°N, Atlantis Massif, IODP Site U1309, Expedition 304/305 [Blackman *et al.*, 2006]), and the Southwest Indian Ridge (57°E, Atlantis Bank, ODP Hole 735B, Leg 118/176 [Pettigrew *et al.*, 1999; Dick *et al.*, 2000] and IODP Hole U1473A, Expedition 360 [MacLeod *et al.*, 2017]). More than 95% of total recovery comprises gabbroic rocks suggesting higher magma supply in comparison with the surrounding spreading sections. Accordingly, Ildefonse *et al.* (2007a) proposed a model whereby the development of OCCs is the result of strain focused in rheologically weaker serpentinised mantle lithosphere around the stronger solidified gabbro intrusions; thus formation of OCCs appear to be associated with relatively enhanced periods of magma supply (Ildefonse *et al.*, 2007b) in an overall magma-poor region. This hypothesis is supported by numerical models that predict 30-50% of total extension being accommodated by magmatic accretion (Tucholke *et al.*, 2008).

1.4 Genesis and crystallization of Primary MORB-type melts

Mantle melting

Magmas forming the plutonic lower oceanic crust are generated at depths under mid-ocean ridges by partial melting of the upwelling mantle, in response to plates spreading (e.g., Langmuir and Forsyth, 2007; Coogan, 2014 and references therein). Melting is the result of pressure decrease as upper mantle rises (e.g., Bowen, 1928; Oxburgh, 1980; Langmuir *et al.*, 1992) following an adiabatic gradient of 1° to 2°C of temperature drop for each kilobar of pressure release (Langmuir *et al.*, 1992). The ascending mantle inevitably intersects the solidus and begins to melt at given pressure and temperature conditions (Figure I.13) within the mantle-melting region ('melting regime', Oxburgh, 1980). The amount of melt that can be produced is proportional to the depth at which mantle rises after crossing the solidus (Figure I.13), increasing up to a rate of about 1-2% of melt generated at each kbar of pressure decrease (e.g., Langmuir *et al.*, 1992). Experimental studies and numerical simulations have demonstrated that overall MORB-type melts are generated by ~5–20% partial melting of fertile peridotite primarily in the depth range between 10 km and 70 km (e.g., Takahashi and Kushiro, 1983; Kinzler and Grove, 1992, 1993; Takahashi *et al.*, 1993; Walter and Presnall, 1994; Gudfinnsson and Presnall, 2000; Presnall *et al.*, 2002; Workman and Hart, 2005). The pressure at which mantle melting begins, at the base of the triangular shaped melting regime (e.g., Oxburgh, 1980; McKenzie and Bickle, 1988; Figure I.13), is

controlled by the overall temperature of the mantle (e.g., Schilling, 1973; McKenzie, 1984; McKenzie and Bickle, 1988). Hot mantle intersects the solidus deeper thus it begins to melt earlier than cooler mantle (Figure I.13), thereby generating abundant melt (e.g., Schilling, 1973; McKenzie, 1984; Langmuir *et al.*, 1992).

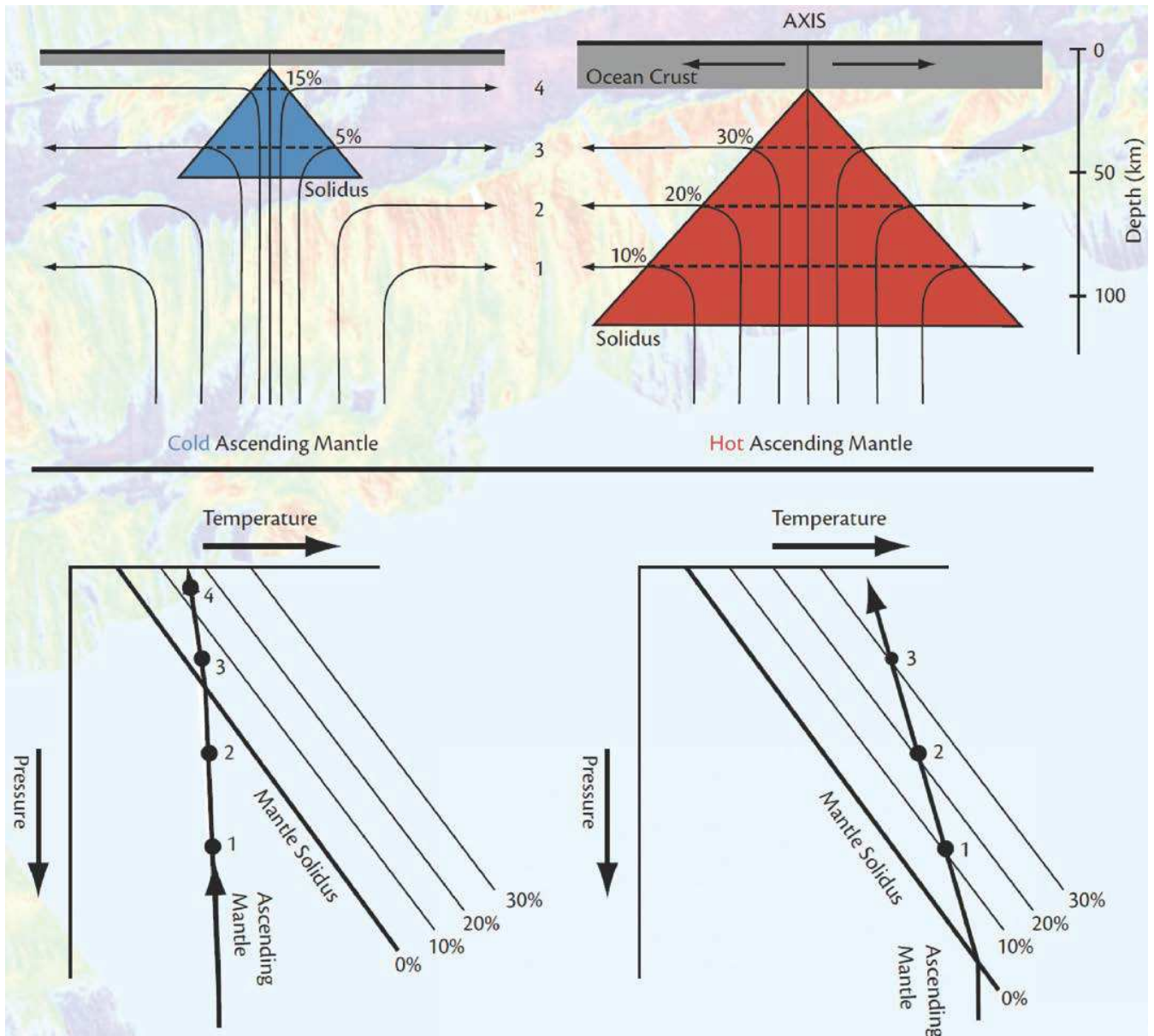


Figure I.13 – Schematic view of melting of the upwelling mantle and melting regime in hot and cold mantle (Langmuir and Forsyth, 2007). Diagrams show schematic boundaries between melt absent and melt present represented by the mantle solidus for different degrees of melting (reported in percentage). Melting begins as the ascending mantle crosses the solidus at different pressures (depths) over a limited range of temperatures. Note that hot mantle begins to melt deeper leading to a larger melting regime (red triangle) and a thicker oceanic crust compared to cold mantle (melting regime = blue triangle).

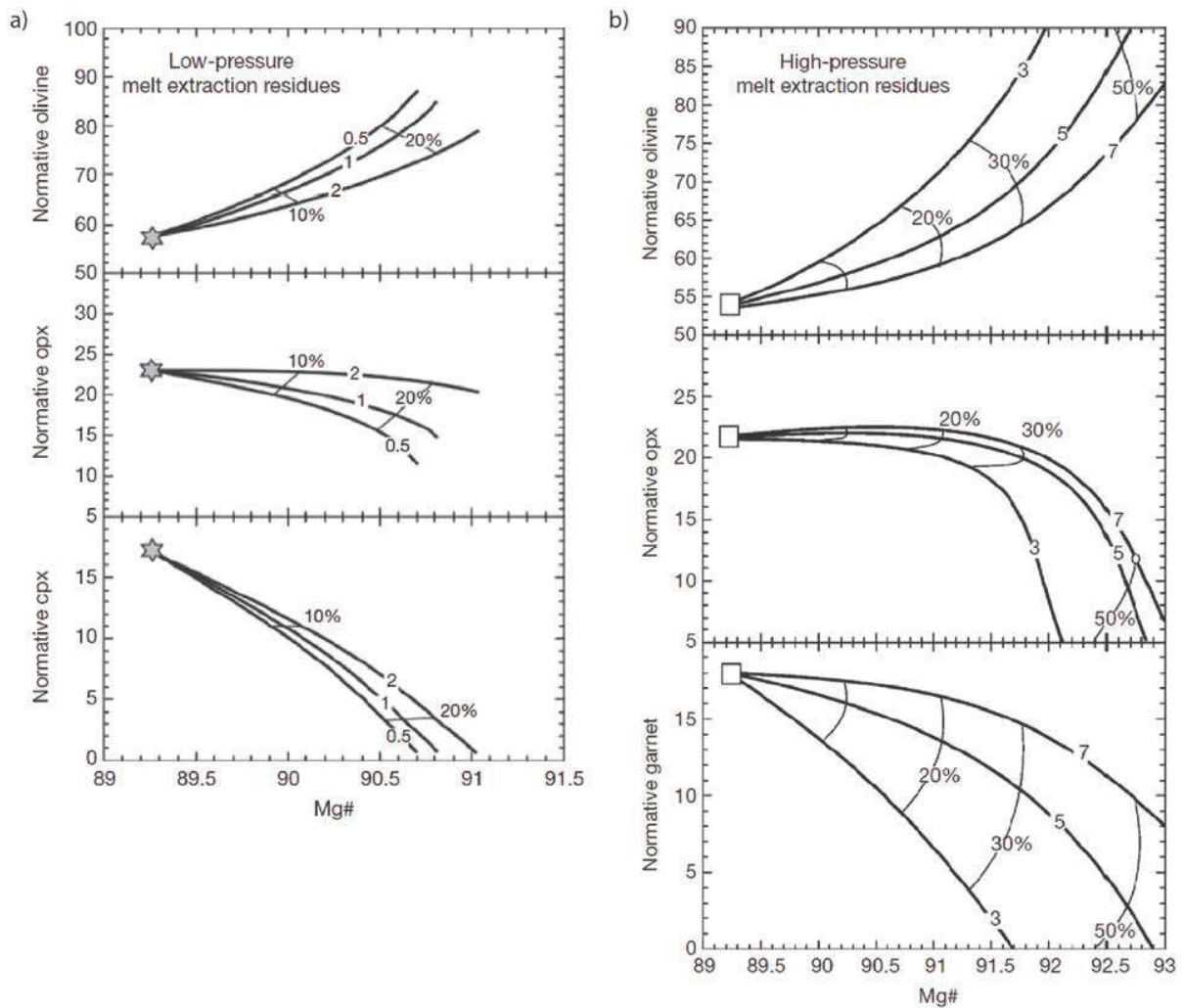


Figure 1.14 – Variations of normative mineral abundances (wt%) of mantle residue during batch partial melt extraction (0–25%) as a function of Mg# (molar Mg/(Fe+Mg)) at a) low pressure where spinel lherzolite is stable, and b) high pressure conditions where garnet lherzolite is stable (Walter, 2014). Starting materials (star in a) and square in b)) are fertile peridotites. Numbered curves are calculated at different pressures: a) 0.5 GPa, 1 GPa, and 2 GPa, and b) 3 GPa 5 GPa and 7 GPa.

Because melts generated are less dense than the surrounding mantle, they tend to move upward while melting proceeds. This process has been widely modeled as near-fractional melting consisting of batches of less than 2% melt that are removed from the mantle as it rises (e.g., McKenzie, 1984; Klein and Langmuir, 1987; Mckenzie and Bickle, 1988; Langmuir *et al.*, 1992). Many different melts are generated from primarily fertile peridotite. As the melting process continues, the composition of the mantle source progressively changes toward depletion in the

most incompatible elements that tend to concentrate preferentially in the melt (see Chapter sections I.3.1 and I.3.3). As melting is pressure and temperature dependent (Figure I.13), mantle mineral abundances (Figures I.14 and I.15) and compositions change in function of the thermodynamic conditions (e.g., Takahashi, 1986; Johnson *et al.*, 1990; Takahashi *et al.*, 1993; Walter and Presnall, 1994; Zhang and Herzberg, 1994; Gudfinnsson and Presnall, 2000; Presnall *et al.*, 2002). Melting, and the composition of its products, is also influenced by the presence of water and CO₂, which reduce the melting point of mantle rocks enhancing mantle melting (e.g., Dasgupta *et al.*, 2007, 2013). In the following I will consider exclusively anhydrous and CO₂-free systems.

The alumina phase and clinopyroxene are the first minerals to melt (Figure I.14). Whether melting occurs at low or high pressures, the residue of melt extraction becomes progressively richer in modal olivine while modal clinopyroxene strongly decreases. This leads to progressive enrichments in Mg component of the mantle source (Figure I.14).

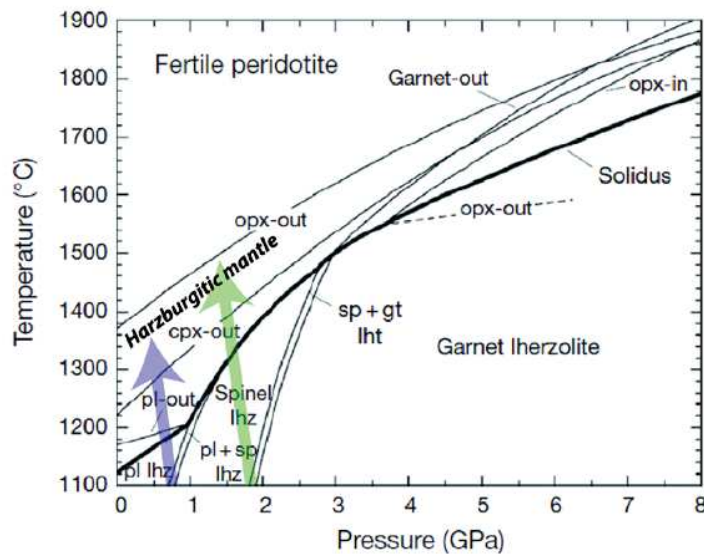


Figure I.15 – Temperature vs pressure generalized phase relations for fertile peridotite from 1 atm to 8 GPa and between 1100° and 1900°C (modified after Walter, 2014). Blue arrow represents melting path at low pressures (<1 GPa). Green arrow indicate melting at moderate pressures (<2.5 GPa). ‘out’ = P-T conditions at which a phase is dissolved; Pl = plagioclase, cpx = clinopyroxene, opx = orthopyroxene, lhz = lherzolite.

The diagram reported in Figure I.15 shows phase relations and solidus curve for fertile peridotite mantle. At low pressures (less than 1 GPa) the stable aluminous phase is plagioclase, which is the first phase consumed during batch partial melting followed progressively by

clinopyroxene, orthopyroxene, and olivine with increase in temperature (Figure I.15). Spinel is stable at moderate pressures (~1-2.5 GPa) and during partial melting first becomes progressively more refractory, as indicated by an increase in Cr/Al ratio (review in Walter, 2014 and references therein), then is generally exhausted at degrees of melting similar to clinopyroxene (~22% melting, Gudfinnsson and Presnall, 2000). The composition of mantle residue at pressures <2.5 GPa is mostly closed to harzburgitic mantle composed of olivine, as the most abundant phase, and orthopyroxene (e.g., Takahashi, 1986; Kinzler and Grove, 1993; Presnall *et al.*, 2002; Green and Falloon, 2005; Figures I.14 and I.15).

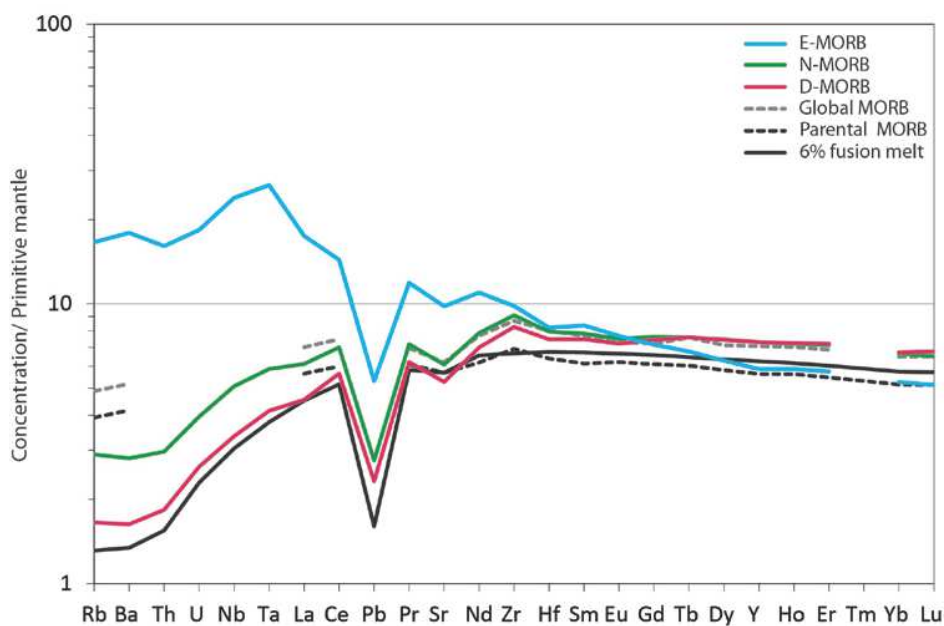


Figure I.16 - Diagram of Primitive mantle-normalized trace element concentrations of MORBs: Enriched- (E-), Normal- (N-), Depleted- (D-) MORB from compilation in Gale *et al.* (2013); Global MORB and Parental MORB from Su and Langmuir (2002); calculated Primary MORB after 6% aggregated fractional melting of a Depleted MORB Mantle (Workman and Hart, 2005).

Melts generated at mid-ocean ridges by progressive melting of the adiabatic upwelling mantle were defined as 'primary magmas' (e.g., Elthon, 1979; Stolper, 1980). Similarly to variations in compositions of mantle residue, the compositions of primary magmas depend on thermodynamics condition at which melting takes place (e.g., Klein and Langmuir, 1987; Langmuir *et al.*, 1992; Gale *et al.*, 2014), but also they vary as function of primary compositional mantle heterogeneity (e.g., Niu and O'Hara, 2008; Shen and Forsyth, 1995). The concentrations of moderately incompatible elements (i.e., Na, Al and Ti) in mantle melts are roughly inversely proportional to the extent of

melting (e.g., Jaques and Green, 1980; Dick *et al.*, 1984; Langmuir *et al.*, 1992; Gudfinnsson and Presnall, 2000), whereas Fe is found to positively correlate with variations in pressure of melting (Langmuir and Hanson, 1980). Primary magmas produced at spreading centres, or primary Mid Ocean Ridge Basalts (MORBs), have primitive compositions defined by relatively high Mg contents ($Mg\# = 100 \times \text{cationic Mg} / (\text{Mg} + \text{Fe}) \geq 71$, e.g., Kinzler and Grove, 1993; Presnall and Hoover, 1987) and are in equilibrium with olivine of the mantle source ($Fo \geq 89$; Dick and Bullen, 1984; Green and Falloon, 2005; Presnall *et al.*, 2002). In contrast, the majority of basalts collected along mid-ocean ridges have lower Mg# ($Mg\# < 70$; Gale *et al.*, 2013; Green and Falloon, 2005) and generally more evolved compositions (TiO_2 wt% ~ 1.5 in MORBs and < 1 in Primary MORB; for trace elements see Figure I.16; Presnall and Hoover, 1987; Kinzler and Grove, 1993; Gale *et al.*, 2013). Their compositions indicate that Primary magmas must undergo some processes of magma differentiation, and magmatic crystallization, upon their ascent to the active spreading centre (e.g., Grove *et al.*, 1992; O'Hara and Herzberg, 2002; Herzberg, 2004; Herzberg *et al.*, 2007).

Magmatic crystallization

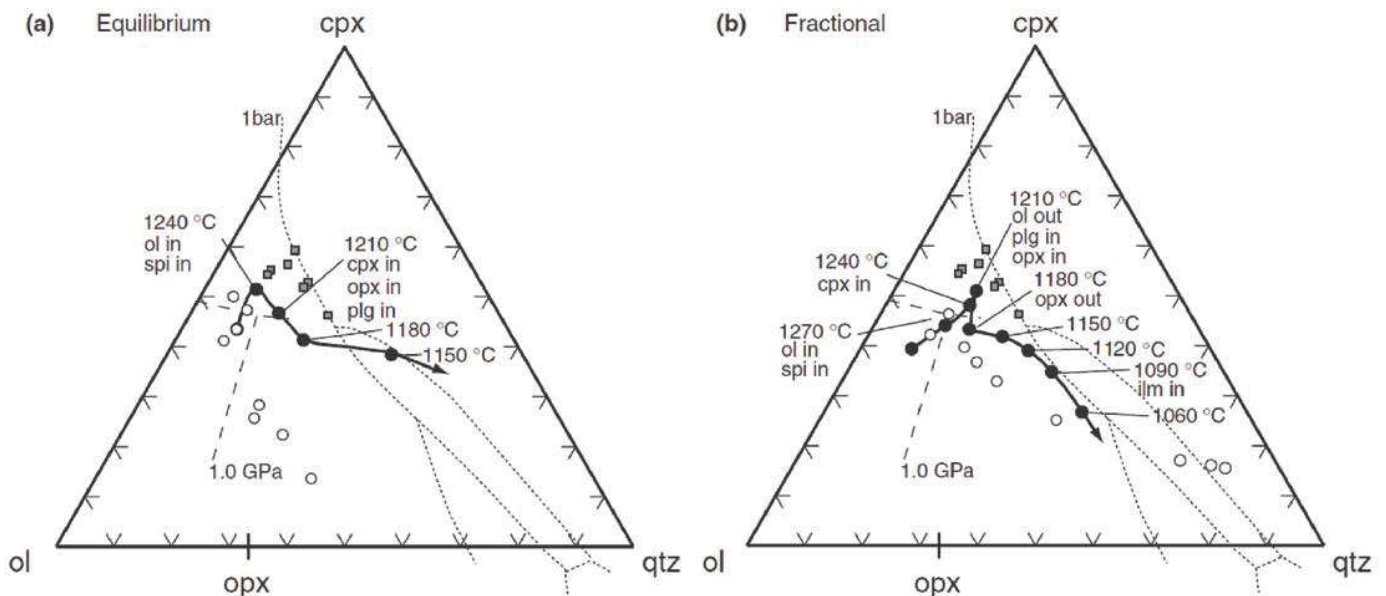


Figure I.17 - Normative pseudo-ternary clinopyroxene (cpx) – olivine (ol) – quartz (qtz) diagram, illustrating the compositions of glass obtained after anhydrous a) equilibrium and b) fractional crystallization experiments (Villiger *et al.*, 2007). Experimental data are reported for 1 bar (squared symbols) 0.7 GPa (filled circle symbols), and 1.0 GPa (open circle symbols). Phase boundaries are at 1 bar (dotted lines) 1.0 GPa (dashed lines). 'in' = phase appearance; 'out' = phase disappearance.

Studies on large datasets of MORB glasses and experimental investigations (e.g., Michael and Cornell, 1998; Herzberg, 2004; Villiger *et al.*, 2004, 2007a, 2007b; O'Neill and Jenner, 2012; Coogan, 2014) have shown that crystallization in the lower oceanic crust occurs at variable depths beneath spreading ridges. Although crystallization pressures are estimated to vary inversely with plate spreading rates (with P up to ~10 kbar under slow-spreading ridges; e.g., Grove *et al.*, 1992; Michael and Cornell, 1998; Villiger *et al.*, 2007a), locally slow-spreading lower oceanic crust forms at relatively low pressures, as observed in OCCs (e.g. ~2 kbar at Atlantis Massif, Mid-Atlantic Ridge, Grimes *et al.*, 2008). At pressures lower than 7-8 kbar (depending on magma composition) the typical crystallization sequence of a primary MORB with a tholeiitic composition (Figure I.17) is as follows (e.g., Presnall *et al.*, 1978; Grove *et al.*, 1992; Herzberg, 2004; Villiger *et al.*, 2007b):

Melt±spinel → melt+olivine±spinel → melt+olivine+plagioclase → olivine+plagioclase+clinopyroxene

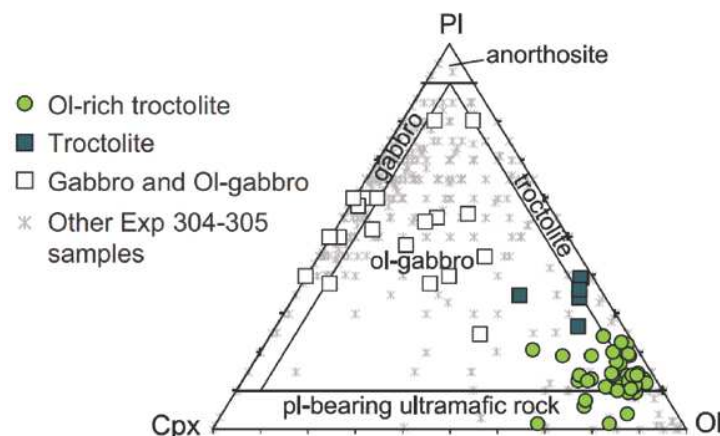


Figure I.18 – Streckeisen diagram of samples drilled at IODP Hole U1309D (Drouin *et al.*, 2009) on the Atlantis Massif (30°N, Mid-Atlantic Ridge). Note that some samples are characterized by high modal contents of olivine (>70%) and their compositions fall between troctolite and dunite: they were defined olivine-rich troctolites during Expeditions 304/305 (Blackman *et al.*, 2006).

This crystallization sequence leads to the formation of gabbroic bodies from the most primitive troctolite (10-30% olivine, 40-70% plagioclase, <10% clinopyroxene) and olivine gabbro (>5% olivine) to the most evolved gabbro and oxide gabbro (>5% oxides), which have been all sampled *in situ* at active spreading centres (Figure I.18; e.g., Atlantis Massif, MAR, IODP Expeditions 304/305, Blackman *et al.*, 2006; Atlantis Bank, SWIR, ODP Expeditions 118/176 and IODP Expedition 360, Dick *et al.*, 2000; MacLeod *et al.*, 2017). The gabbroic rocks have typical textures showing euhedral

to subhedral cumulus phases, which are the first to precipitate as generally olivine and plagioclase, and interstitial to poikilitic intercumulus phases, as typically clinopyroxene (e.g., Donaldson, 1977; Irvine, 1982; O'Driscoll *et al.*, 2007).

Crystallization of magmas from the lower oceanic crust, where plutonic rocks are formed, to the upper crust, where basalts form, is induced by cooler surroundings and drives the magmatic differentiation. Different geochemical models have been developed to explain chemical and modal composition of solids and melts during magmatic differentiation and crystallization. Fractional and equilibrium crystallization are the principal processes controlling chemical trends of mineral compositions in a closed-system (e.g., Elthon *et al.*, 1992; Grove *et al.*, 1992; Coogan, 2014; Figure I.17 and I.19). Fractional crystallization involves removal of newly formed crystals from the melt avoiding reaction between phases (e.g., Bowen, 1928), while during equilibrium crystallization crystals remain in contact with the melt and continuously react with it (Shaw, 1970). Assuming that closed-system crystallization occurs in a magmatic chamber, melt and mineral compositions may also be affected by chemical reaction with an interstitial melt continuously added at the margins of the magmatic chamber, where cooling is assumed to occur. This process of fractional crystallization and concomitant reaction is referred to as *in situ* crystallization (Langmuir, 1989).

Models of fractional crystallization generally reproduce mineral chemical compositions of gabbroic sequences. The positive correlations of the An content of plagioclase and the Mg# of clinopyroxene define the compositional evolution from the most primitive end-member characterized by high An and high clinopyroxene Mg#, to progressively lower contents in more evolved gabbros (Figure I.19a). Variations of TiO₂ wt%, Na₂O wt% (Figure I.19c-d) and trace elements contents (Figure I.20) in clinopyroxene are also commonly used to track rock chemical evolution during fractional crystallization. They generally show an inverse correlation with the Mg# of clinopyroxene due to their affinity for the melt as governed by their low partition coefficients ($K < 1$, see Chapter I.3.1 and I.3.2). Clinopyroxene formed at low pressure (<6-7 kbar) has Mg# ~83 (e.g., Tormey *et al.*, 1987; Yang *et al.*, 1996; Grove *et al.*, 1992), which results from the early crystallization of olivine that buffers and decrease Mg content of the melt (e.g., Villiger *et al.*, 2004, 2007b). In contrast, oceanic gabbros formed at slow-spreading ridges have high Mg# clinopyroxene (Mg# > 88), which may suggest that they crystallized after a primitive melt. Such high Mg# clinopyroxene coexists with plagioclase showing extremely variable An contents that range

between An_{30} and An_{95} (e.g., Elthon *et al.*, 1992; Dick *et al.*, 2002; Miller *et al.*, 2009; Coogan, 2014). These compositions cannot be explained by low pressure fractional crystallization. Instead, high Mg# clinopyroxene may represent the early product of moderate to high pressure

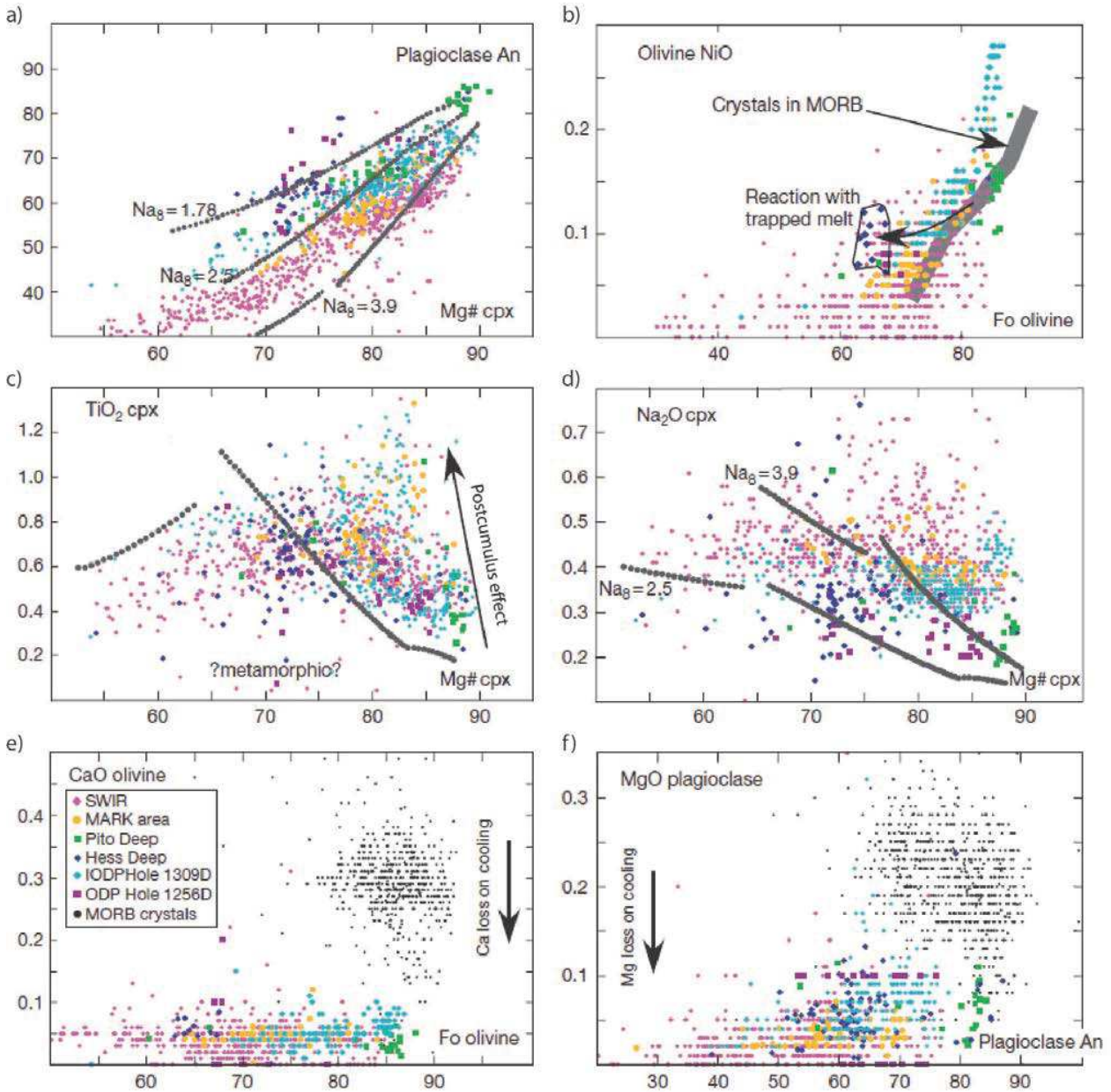


Figure 1.19 – Major element compositions of minerals in oceanic gabbros (Coogan, 2014) from SouthWest Indian Ridge (SWIR), Mid-Atlantic Ridge (Kane area, MARK; IODP Hole U1309D, Atlantis Massif), Pacific Ocean (Pito Deep; Hess Deep; ODP Hole 1256D), and of phenocrystals in MORB. Fractional crystallization modeling trends (small gray symbols) are reported for different melt starting materials labelled with values of Na_8 (Na_{20} wt% recalculated for 8 wt% of MORB MgO). a) Plagioclase An content versus clinopyroxene Mg#. b) Variation in olivine Fo and Ni contents. The gray line shows the trend followed by ‘phenocrysts’ in

MORBs; reaction with trapped melt (black curve) cause the significant decrease in Mg#. c) TiO₂ wt% versus Mg# in clinopyroxene; the postcumulus reaction with trapped melts increases Ti contents of clinopyroxene rims and most interstitial crystals. d) Na₂O wt% versus Mg# in clinopyroxene. e) CaO versus Fo of olivine: the highly Ca depleted signature of oceanic gabbros is related to subsolidus re-equilibration. f) MgO wt% versus An content of plagioclase showing that plagioclase in oceanic gabbros is highly MgO depleted, again suggesting subsolidus re-equilibration.

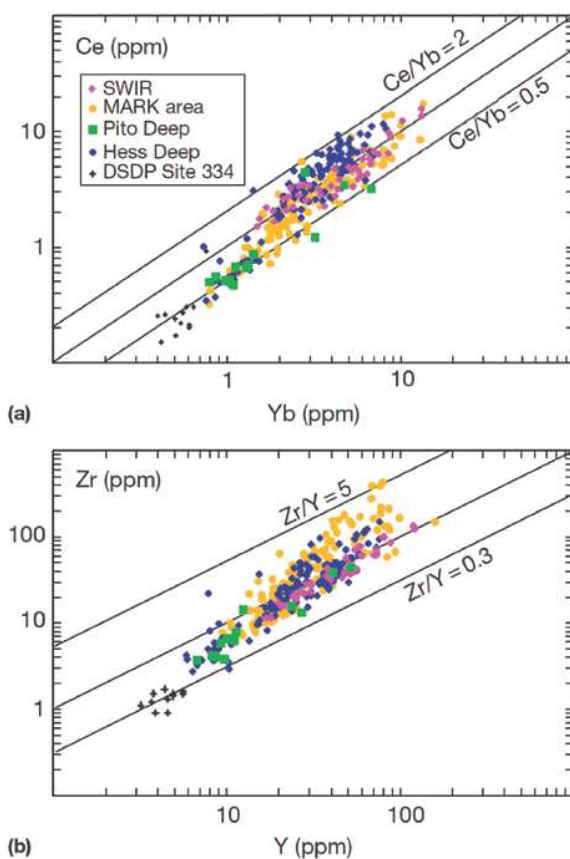


Figure 1.20 – Trace element abundances in clinopyroxene in oceanic gabbros (Coogan, 2014; see Figure 1.21 for details on location of samples) for a) Ce (ppm) and b) Zr (ppm) versus Y (ppm). More-to-less incompatible element ratios (Ce/Yb and Zr/Y) are reported.

fractionation of MORB-type melts, which also lead to high An contents in coexisting plagioclase (e.g., Meyer *et al.*, 1989; Elthon *et al.*, 1992; Dick *et al.*, 2002). At increasing pressure of magmatic crystallization (over 7-10 kbar) the stability field of clinopyroxene increases (Figure 1.21) at the expenses of olivine and plagioclase (e.g., Presnall *et al.*, 1978; Grove *et al.*, 1992; Herzberg, 2004). This leads to early crystallization of clinopyroxene, prior to that of plagioclase and olivine, which buffers the Mg of the melt. Yet, the positive correlation of the Ni and Forsterite content of olivine

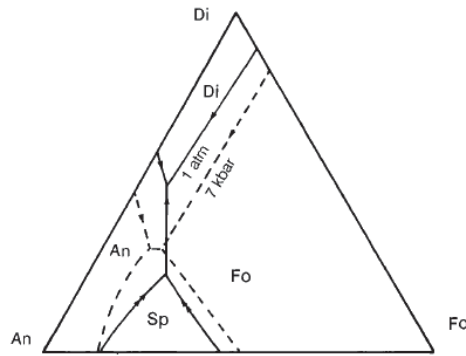


Figure 1.21 – Normative ternary diopside (Di) – anorthite (An) – forsterite (Fo) diagram (Grove et al., 1992). Phase relations are shown for 1 atm (full curves) and 7 kbar (dotted curves); Sp= spinel.

agrees with compositional variations of MORB phenocrysts, and denotes early crystallization of olivine in the most primitive gabbroic rocks with the highest Fo₈₈-Fo₉₀ and ≥ 0.2 NiO wt% (Figure 1.19b). This suggests that fractional crystallization may not represent the solely process controlling mineral and melt compositions. Alternative interpretations are presented in Chapter section 1.2.3.

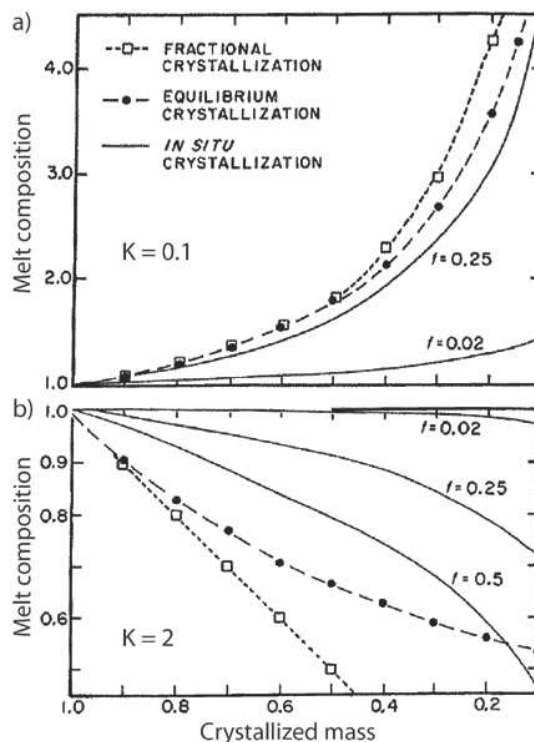


Figure 1.22 – Evolution of melt composition during fractional, equilibrium and in situ crystallization (Langmuir, 1989) for a) incompatible element, b) compatible element. 'f' indicates the proportion of magma addition during in situ crystallization.

In situ crystallization can account for evolved compositions of phases as sometimes observed in primitive gabbroic rocks (e.g., O'Hara and Fry, 1996). Variations of compatible elements ($K > 1$), notably major elements, upon *in situ* crystallization approach those obtained by a near-equilibrium crystallization process (Figure I.22). Incompatible elements ($K < 1$), notably trace elements, are subjected to greater variations (Figure I.22) resulting in enrichments in these elements at almost constant major element compositions.

Later stage processes can modify composition of a partially molten crystal mush. Enrichments in incompatible elements at rims of interstitial and intercumulus poikilitic phases have been explained by reaction between crystals and trapped melts (e.g., Meyer *et al.*, 1989; Elthon *et al.*, 1992; Natland and Dick, 2001; Borghini and Rampone, 2007). This late stage postcumulus process takes place during the final crystallization of interstitial melt and concerns those phases crystallizing last as plagioclase and clinopyroxene. It accounts for chemical zoning marked by higher trace elements (e.g., REE, Ti, Zr) at constant Mg# of clinopyroxene rims (Figure I.19c) coupled with LREE depletion, but enrichments of all REE in plagioclase.

Subsolidus processes occur during cooling of the lower oceanic crust. They can lead to the redistribution of elements between adjacent phases, such as Ca and Mg. The equilibrium partitioning of Ca between olivine and clinopyroxene decreases with temperature, driving migration of Ca out of olivine into clinopyroxene and may changing the overall composition of these phases (Figure I.19e). This temperature effect has been used to calculate the total time of cooling and the temperature reached after the subsolidus process (e.g., Coogan *et al.*, 2002). A similar behaviour is observed for Mg in plagioclase (Figure I.19f) that tends to migrate from plagioclase into the surrounding primary phases during release of heat from the rock (e.g., Faak *et al.*, 2014).

2. Melt transport from the mantle to the oceanic crust: a petrological and geochemical perspective

Melting induced by decompression of upwelling mantle generates melts that segregate and ascend through the residual solid matrix due to differences in density, to cool at shallower depths

and eventually on the seafloor. Driving forces for melt migration include compaction (e.g., McKenzie, 1984; Spiegelman, 1993; Connolly *et al.*, 2009) and tectonic deformation (e.g., Stevenson, 1989; Dick *et al.*, 1991a, 2000). Theory of melt extraction and transport are based on a two-phase system composed of a deformable solid and a fluid phase that occupies pores between crystals (McKenzie, 1984). It requires that melt flows through a connected network of grain scale channels by porous flow (e.g., Kohlstedt and Holtzman, 2009, and references therein). Paths and efficiency of melt transport are controlled by a series of physical properties (i.e., porosity and permeability) that, in turns, depend on the composition of the partially molten rock. In the mantle, melt is first produced along grain boundaries by progressive partial melting of the most thermodynamically instable phases (i.e., plagioclase and pyroxenes depending on pressure conditions; Figure I.15). Therefore, the modal distribution of phases in the mantle source drives the distribution of certain volumes of melt (i.e., porosity), but also plays a role in the melt flow through interconnected pores (i.e., permeability).

Here, I first summarize the basic concepts of porosity and permeability, and the effect of mineral modal distribution on melt transport. Following, I report a brief overview on our understanding of melt extraction and transport in the lower oceanic crust, focusing on melt-rock interactions.

2.1 Transport of melts: a physical perspective

Porosity

Porosity (ϕ) is the volume fraction of melt in a partially molten rock, and it quantifies the grain scale melt distribution. It is defined by the ratio:

$$\phi = \frac{\text{melt volume}}{\text{total volume}}$$

Porosity is distinguished in two types. The volume fraction of isolated pockets of melt is generally referred to as the unconnected or isolated porosity, which do not contribute to melt flow (i.e., permeability). The interconnected porosity is the volume of melt that forms connected network of grain scale channels. Contrarily to the isolated porosity, the interconnected porosity contributes to the permeability (Turcotte and Morgan, 1992).

Permeability

Permeability is the physical property of a partially molten rock that reflects the ability to transmit melts. The parameter describing permeability, k , is usually approximated by the relationship between permeability and porosity (e.g., McKenzie, 1984; von Bargen and Waff, 1986; Wark and Watson, 1998; Connolly *et al.*, 2009; Pec *et al.*, 2017):

$$k = \frac{d^2(\phi)^n}{C}$$

where d is the grain size, n is the melt fraction exponent, and C is a geometrical constant that depends on the shape and spatial distribution of melt channels network (Riley and Kohlstedt, 1991). The geometry of pores is governed by the mineral phases that intersect to form the pore, as defined by the wetting or dihedral angles (e.g., Faul, 1997; von Bargen and Waff, 1986) and it is, therefore, function of the mineral modal composition of the rock. Permeability is a macroscopic property that can evolve upon melt migration by reaction of the melt with the host rock (e.g., Kelemen, 1990; Aharonov *et al.*, 1995; Spiegelman *et al.*, 2001; Pec *et al.*, 2017).

Effect of mineral modes

The mineral modal distribution in a rock controls the formation of preferential paths for melt transport, by creating higher permeability. This is explained in terms of geometry of the solid-liquid interface in pores by considering the wetting (dihedral) angle. The latter is the angle between two intersecting walls of a pore, and is determined by the relative values of the solid-solid and solid-liquid interfacial energies (e.g., von Bargen and Waff, 1986; Watson and Brenan, 1987; Faul, 1997; Wark and Watson, 1998). For wetting angles lower than 60° melt occupies a connected network of channels and can be mobilized at all melt fractions, whereas for angles higher than 60° melt is distributed in isolated pockets (Figure I.23).

Experimental studies have reported that olivine-olivine wetting angles are between 20° and 50°, and thus the formation of an interconnected melt network is possible at melt fractions lower than 1% (e.g., von Bargen and Waff, 1986; Riley and Kohlstedt, 1991; Faul, 1997; Kloe *et al.*, 2000; Figure I.24). In contrast, pyroxene-olivine wetting angles are higher and exceed the 60° angle (e.g.,

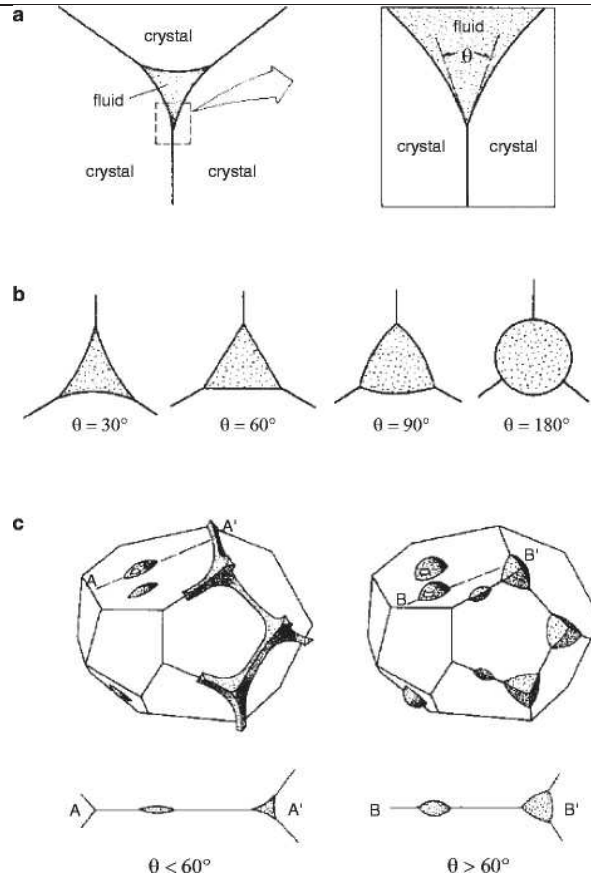


Figure 1.23 – Schematic representation (e.g., Watson and Brenan, 1987) of a) cross-sectional representation of melt(fluid)-filled channel at the junction of three grains (θ = wetting angle); b) channel cross-section for different values of θ ; c) perspective drawings illustrating the distribution of melt for $\theta < 60^\circ$ and $\theta > 60^\circ$.

Toramaru and Fujii, 1986; von Bargen and Waff, 1986). Melt is preferentially distributed in isolated pockets at the corners of pores (Figure 1.24), and about 30% of melt volume must be attained to form interconnected melt channels between the isolated pockets (e.g., Toramaru and Fujii, 1986). Thus olivine-rich rocks are more permeable than pyroxene-rich rocks.

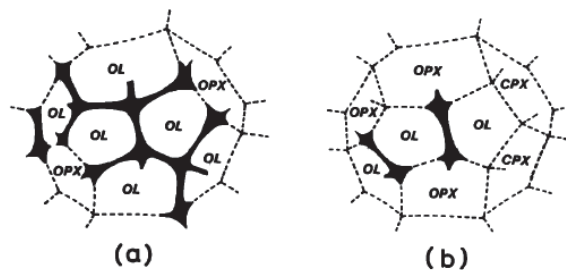


Figure 1.24 – Schematic illustration of two typical cases of the melt interconnection on an olivine grain when a) high olivine modal composition; b) low olivine modal composition (Toramaru and Fujii, 1986).

The effect of mineral modal distribution and, therefore, that of wetting angles on melt migration is observed in the cool oceanic lithosphere beneath spreading centres. The porous network in mantle rocks allows melts to rise buoyantly (e.g., Miller *et al.*, 2014). When these melts enter the thermal boundary layer in the cold lithosphere, they begin to crystallize. If the crystallization is fast enough the pore space is filled by clinopyroxene and plagioclase crystals, thereby decreasing porosity. The precipitation of clinopyroxene, which is characterized by high wetting angles, and the drop in porosity reduce drastically the matrix permeability leading to the formation of a nearly impermeable layer, the permeability barrier (e.g., Sparks and Parmentier, 1991; Spiegelman, 1993; Korenaga and Kelemen, 1997; Hebert and Montési, 2010). At mid-ocean ridges, a permeability barrier forms at the multiple saturation point of clinopyroxene and plagioclase, which occurs when melt temperature decreases (Hebert and Montési, 2010). Therefore, it is also a crystallization front that is shallower at the ridge axis and deepens away from the axis as a function of the changing thermal profile (Figure I.25; e.g., Hebert and Montési, 2010). The permeability barrier can prevent some melts to migrate toward the surface. Beneath this barrier melts may accumulate and crystallize in gabbroic sills as those observed in the Oman Ophiolite (e.g., Ceuleneer and Rabinowicz, 1992; Boudier and Nicolas, 1995; Boudier *et al.*, 1996; Korenaga and Kelemen, 1997; Rabinowicz and Ceuleneer, 2005).

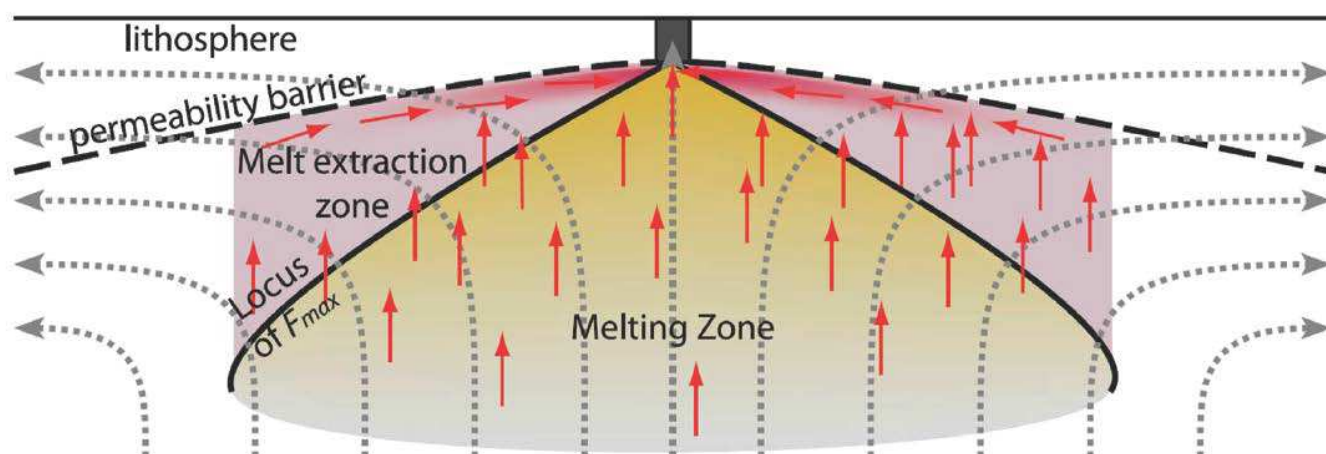


Figure I.25 – Schematic illustration of melt focusing beneath spreading centres (Hebert and Montési, 2010). The permeability barrier is represented by the dashed black line and deepens away from the axis. Red arrows indicate melt flux.

Percolation threshold and Darcy's Law

Melt is extracted from the mantle source when the 'percolation threshold' is achieved (e.g., McKenzie, 1984; Toramaru and Fujii, 1986; von Bagen and Waff, 1986; Turcotte and Morgan, 1992; Spiegelman, 1993). The percolation threshold depends on the matrix permeability, and is function of porosity, grain size and mineral distribution. It is $\geq 3\%$ and decreases in depleted harzburgitic matrices where permeability is enhanced by progressive melting of orthopyroxene (e.g., Nicolas, 1986; Riley and Kohlstedt, 1991; Kelemen *et al.*, 1997a).

The theory of melt transport is based on the assumption that a partially molten rock is a two-phase continuum composed of a deformable solid and a fluid, with different viscosities (McKenzie, 1984). Melt transport is function of the connected porosity, permeability, density of solid (ρ_s) and melt (ρ_l), melt fraction and melt viscosity (e.g., Turcotte and Morgan, 1992; Kelemen *et al.*, 1997a). It has been modeled as a porous flow mechanism using Darcy's law for flow in a porous medium (e.g., McKenzie, 1984; Stevenson, 1989; Turcotte and Morgan, 1992; Spiegelman, 1993; Faul, 1997; Kelemen *et al.*, 1997a; Spiegelman *et al.*, 2001; Miller *et al.*, 2014; Pec *et al.*, 2017):

$$q = \frac{-k}{\mu} \nabla P$$

where q is the Darcy flux, μ is the melt viscosity, and ∇P is the pressure gradient that drives the vertical fluid flow. Melt viscosity controls the velocity of the melt to move in the porous media. At lower viscosity magma flows more freely so that less connected porosity and, therefore, permeability is needed for the melt to migrate upward (Turcotte and Morgan, 1992).

2.2 Melt extraction

Porous flow is considered the principal mechanism of melt extraction and transport through the mantle to the oceanic crust (e.g., Daines and Kohlstedt, 1994; Sparks and Parmentier, 1991; Spiegelman, 1993; Spiegelman *et al.*, 2001). If melt porous flow of large amounts of melt occurs through the interconnected pores, in principle it would lead to extensive chemical exchanges and continuous equilibration with the surrounding peridotite mantle (e.g., Spiegelman and Kenyon, 1992; Hart, 1993).

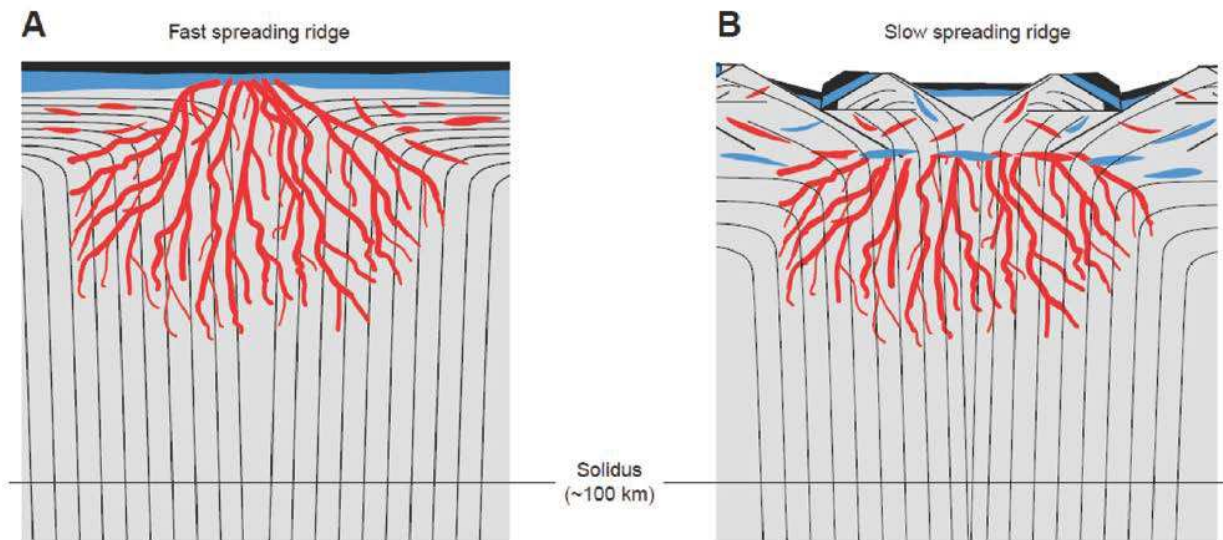


Figure 1.26 – Schematic illustration of melt extraction and igneous accretion beneath a) fast-spreading and b) slow-spreading ridge (Kelemen *et al.*, 2007a). Red lines represent high-porosity dunite channels. a) impregnated peridotites and gabbroic plutons are rare and the oceanic crust is layered. b) impregnated peridotites and gabbroic plutons begin to form at the base of the thermal boundary layer (or conductive boundary layer); brittle faults develop and accommodate spreading.

MORB compositions, however, indicate that they are not in equilibrium with residual mantle (e.g., O'Hara, 1965; Stolper, 1980). Indeed, they are far from saturation in orthopyroxene, which is instead an abundant phase in shallow peridotites (harzburgite and lherzolite), and they are overall enriched in incompatible trace elements while most abyssal peridotites and ophiolitic mantle have depleted signatures (review in Bodinier and Godard, 2014). This indicates that melt fractions must be extracted from their source without interacting with the mantle, most likely by focusing in spatially restricted conduits (Kelemen *et al.*, 1997a). The geological evidence of these conduits is the occurrence of replacive dunite channels (> 90% modal olivine and minor spinel) within the mantle having irregular contacts that are locally discordant with the crystallographic lineation in the hosting mantle (e.g., Kelemen, 1990; Ceuleneer and Rabinowicz, 1992; Kelemen *et al.*, 1995, 1997, 2000; Higgin and Tommasi, 2012). They form during ascent of high-pressure olivine-saturated melts in low-pressure mantle peridotite. Disequilibrium between melt and mantle causes dissolution of mantle pyroxenes producing an increase in liquid mass and, therefore, in porosity, which in turn leads to higher permeability and major focused melt flow (e.g., Kelemen, 1990; Kelemen *et al.*, 1995; Morgan and Liang, 2005; Lambart *et al.*, 2009; Van den Bleeken *et al.*, 2010,

2011). This process, which is termed 'reactive infiltration instability' (e.g., Aharonov *et al.*, 1995; Daines and Kohlstedt, 1994; Kelemen *et al.*, 1995; Spiegelman *et al.*, 2001), results in rapid dissolution and concomitant precipitation of olivine forming the high-porosity dunite channels elongated in the direction of fluid flow (e.g., Kelemen *et al.*, 1995, 1997a; Lambart *et al.*, 2009). Dunite channels range in width from 3 mm to a few meters and grow exponentially with fluid flow. They form a coalescing channel network in which the finer permeable channels feed the above growing channels, leading to a decreasing number of more widely spaced features upward toward the oceanic crust (Figure I.26; Kelemen *et al.*, 1995, 2000). Olivine in dunite channels have Mg# very similar to those in associated mantle peridotites (e.g., Kelemen, 1990; Kelemen *et al.*, 1995), which evidence the replacive nature of dunites.

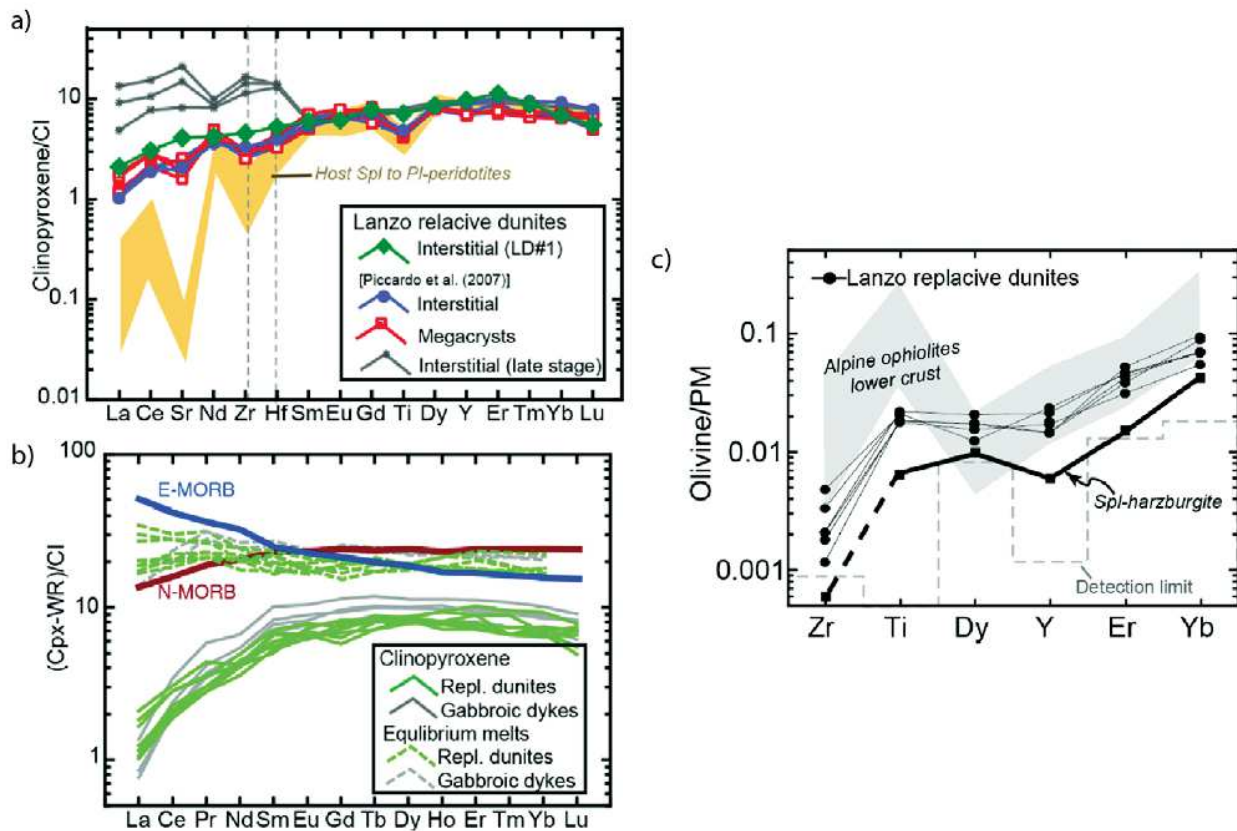


Figure I.27 – Trace element compositions of a) interstitial clinopyroxene in replacive dunites compared to the porphyroclastic clinopyroxene in host spinel to plagioclase peridotites from Lanzo South Massif; b) clinopyroxene (REE) from the Lanzo replacive dunites and gabbroic dykes with calculated equilibrium melts; c) olivines in the Lanzo replacive dunites and other sections in the Alpine ophiolites (Sanfilippo *et al.*, 2017).

Recent geochemical studies on replacive dunites in the Alpine Ophiolites (Sanfilippo *et al.*, 2014, 2017) confirm that their compositions are in disequilibrium with the residual mantle, but are in equilibrium with MORB-type melts (e.g., Kelemen *et al.*, 1995). Compared to clinopyroxene from the host peridotite, clinopyroxene in the replacive dunite is less depleted in the most incompatible elements similarly to MORB signature, and is in equilibrium with gabbroic dikes (Figure I.27a-b). Trace elements in olivine from the replacive dunites have higher absolute values than those measured in the mantle peridotite, and are comparable to olivines from the most primitive gabbros (Figure I.27c). These observations together are evidence of melt extraction through high-porous channels where melts are delivered to the oceanic crust avoiding chemical re-equilibration with the shallower mantle (e.g., Kelemen, 1990; Kelemen *et al.*, 1995, 2000).

In the shallower upper mantle melt transport may also occur as diffuse reactive porous flow, also referred to as reactive crystallization (Collier and Kelemen, 2010), or reactive equilibrium porous flow (Asimow, 1999). The diffuse reactive porous flow is typically evidenced by precipitation of olivine, orthopyroxene and plagioclase, and locally clinopyroxene, at the expenses of primary minerals. These textural features are observed in abyssal (e.g., Dick, 1989; Tartarotti *et al.*, 2002; Seyler *et al.*, 2007; Tamura *et al.*, 2008; Loocke *et al.*, 2013) and orogenic and ophiolitic mantle (e.g., Kelemen *et al.*, 1992; Rampone *et al.*, 1997; Godard *et al.*, 2000; Dijkstra *et al.*, 2001; Rampone and Borghini, 2008; Müntener *et al.*, 2010), and reproduced in laboratory experiments (e.g., Van Den Bleeken *et al.*, 2010, 2011; Saper and Liang, 2014). This process involves interaction between mantle peridotite and silicate melts infiltrating along grain boundaries (e.g., Kelemen, 1990), which lead to compositional variations in the percolated solid and the percolating melt (e.g., Niu, 2004) and, ultimately, to the formation of impregnated mantle. At depth where olivine is stable, the incoming olivine-saturated silicate melt tends to dissolve primary mantle Ca-rich pyroxene and simultaneously precipitate olivine to eventually produce dunites at relatively high melt/rock ratios (e.g., Kelemen *et al.*, 1992; Rampone and Borghini, 2008). This melt-rock interaction process modifies the melt composition, which is progressively enriched in silica and undersaturated in olivine. Further porous flow migration of the Si-rich modified melts, toward shallower depths, lead to crystallization of plagioclase and rims of clinopyroxene and orthopyroxene, thus forming impregnated mantle peridotites at low melt/rock ratios (Dick *et al.*, 1984; Boudier and Nicolas, 1995; Dick and Natland, 1996; Rampone *et al.*, 1997; Tamura *et al.*, 2008). The Si-rich melt may early crystallize new orthopyroxene at decreasing melt mass forming a

harzburgitic matrix (e.g., Kelemen *et al.*, 1992). Alternatively, near-fractional melting have been invoked to explain the formation of olivine-rich abyssal peridotite: it involves dissolution of pyroxenes+spinel, followed by migration of the generated melt that precipitate olivine during decompression of the upwelling mantle (Niu, 1997).

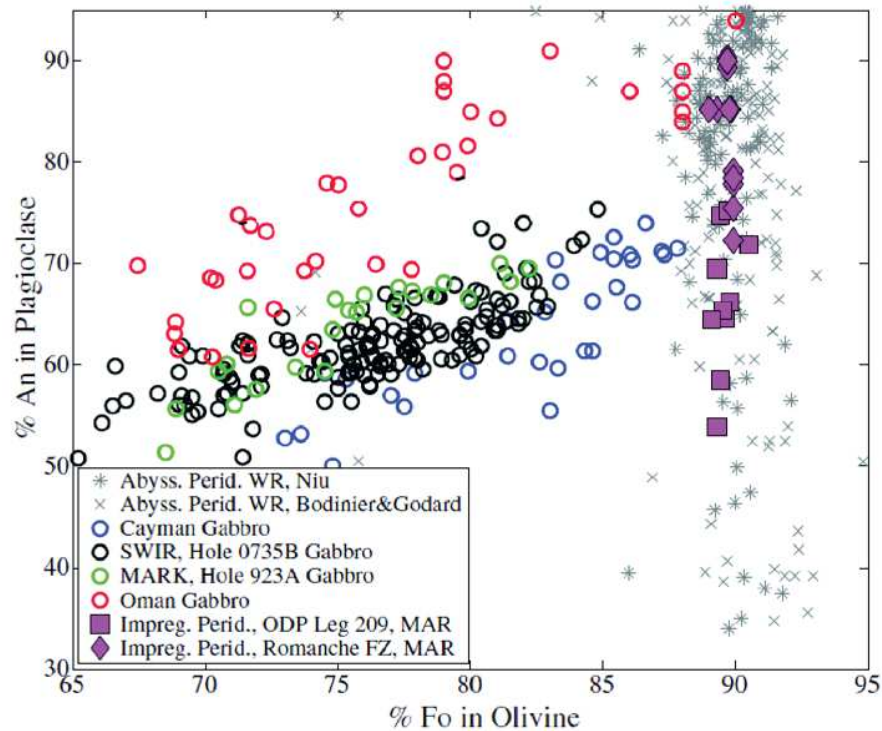


Figure 1.28 – Comparison of An content in plagioclase vs Fo content in olivine in impregnated abyssal peridotites and gabbros sequences sampled along slow-(MAR) and ultraslow-(SWIR) spreading ridges (compilation and graph from Collier and Kelemen, 2010). Abyssal peridotites show significant variations in An at constant Fo, while variations in oceanic gabbros indicate a trend of fractional crystallization.

One of the principal chemical evidence of reactive porous flow is the significant increase of modal olivine at relatively constant or slightly decreasing whole rock Mg# (e.g., Bedini *et al.*, 2002; Bodinier and Godard, 2003). Impregnation of mantle peridotites at shallow depths produces an overall enrichment in incompatible elements (e.g., Na and Ti or trace elements such as M- to HREE) and depletion in bulk Mg component (e.g., Bodinier and Godard, 2003; Godard *et al.*, 2008; Tursack and Liang, 2012), indicative of chemical interaction with a rather Si-rich basaltic melt (e.g., Niu, 2004; Godard *et al.*, 2008). A striking mineral chemical feature of impregnated peridotites is the significant variability of plagioclase anorthite content at nearly constant olivine Mg# (Figure 1.28) and Ni contents (e.g., Borghini *et al.*, 2007; Kelemen *et al.*, 2007b). This results from the role

of olivine to buffer exchanging reactions of Mg, Fe, and Ni, whereas the abundance of incompatible elements, such as Na, increases with decreasing melt mass (i.e., decreasing An; Kelemen, 1986). The chemical reaction of mantle rocks with the impregnating melt also change composition of primary mantle clinopyroxene: while Ti and Na contents increase, Al decreases (e.g., Kelemen *et al.*, 1992; Rampone *et al.*, 1997; Tamura *et al.*, 2008). Reacted clinopyroxene generally displays enrichments in M- to H-REE contents compared to clinopyroxene in non-reacted mantle sections (e.g., Rampone *et al.*, 1997; Seyler *et al.*, 2007; Tamura *et al.*, 2008; Figure I.30). At comparable Cr# (Cr# =Cr/(Cr+Al), atomic ratio) of spinels, the clinopyroxenes in impregnated peridotites show higher HREE contents than those predicted by fractional melting models (e.g., Yb, Figure I.29). These enriched compositions of clinopyroxenes are similar to those of residual clinopyroxene at low degrees of mantle melting, but display significant variations (Figure I.29).

The melt produced beneath mid-ocean ridges must be focused toward the ridge axis, where the oceanic crust begins to form in a neovolcanic zone (e.g., Macdonald, 1982). Gravity and Darcy's law account only for the vertical transport of melt, but do not govern its lateral migration (e.g., Morgan, 1987; Sparks and Parmentier, 1991; Turcotte and Morgan, 1992; Spiegelman, 1993).

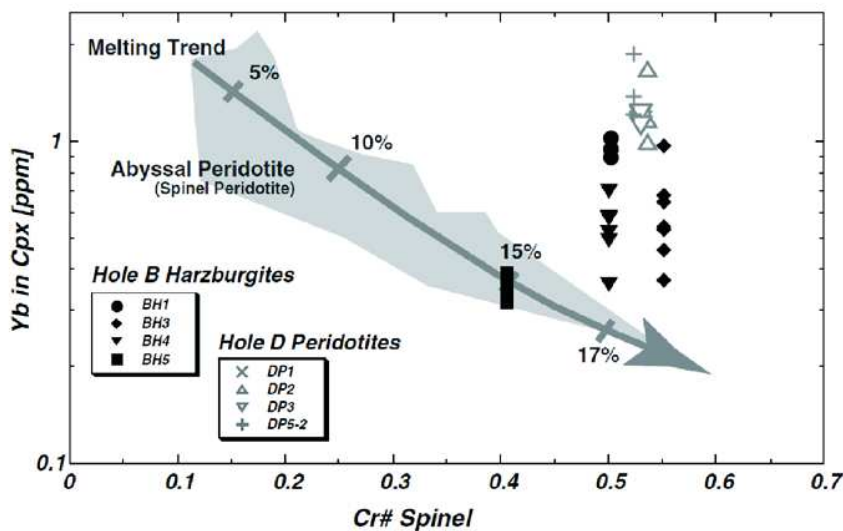


Figure I.29 – Comparison of Yb contents (ppm) in clinopyroxenes vs Cr# of spinels in impregnated peridotites from Hole U1309B (Atlantis Massif, 30°N, MAR). Data compilation and graph from Tamura *et al.* (2008). Clinopyroxenes in impregnated peridotites show enrichments in Yb compared to those predicted by the fractional melting model.

Various mechanisms have been proposed for focused ridge magmatism including large pressure gradients (e.g., Morgan, 1987; Spiegelman and McKenzie, 1987) or convection driven by lateral differences in melt content (Rabinowicz *et al.*, 1984; Buck and Su, 1989); however both require higher viscosities or lower porosities than those estimated under spreading ridges (e.g., Turcotte and Morgan, 1992; Spiegelman, 1993; Hebert and Montési, 2010). Alternatively, melt focusing can be driven by high porosity conduits, or channels, that form underneath the permeability barrier (e.g., Sparks and Parmentier, 1991; Spiegelman, 1993; Rabinowicz and Ceuleneer, 2005; Hebert and Montési, 2010; Figure I.25; Chapter section I.1.2.1). Beneath fast-spreading ridges a permeability barrier forms (e.g., Kelemen and Aharonov, 1998). In contrast, the model computed by Hebert and Montési (2010) indicate that at slower spreading rates (<10 mm/yr half spreading rate) the weak crystallization front precludes the formation of a permeability barrier. Beneath slow- and ultraslow-spreading ridges melts generated at depth may preferentially migrate by diffuse porous flow; they react with the lithospheric mantle and form impregnated peridotites (e.g., Rampone *et al.*, 1997; Kelemen *et al.*, 2004; Tamura *et al.*, 2008), and finally crystallize gabbroic bodies (e.g., Atlantis Massif, IODP Site U1309; Blackman *et al.*, 2011; Drouin *et al.*, 2009, 2010; Godard *et al.*, 2009).

2.3 Lower oceanic crust processes: reaction with the infiltrating melt

Reactive porous flow processes between migrating melts and a pre-existing solid matrix have been observed not solely in the mantle but also within the magmatic lower oceanic crust. Several authors have highlighted that such reactions may modify mineral compositions (e.g., Meyer *et al.*, 1989; Bedard *et al.*, 2000; Dick *et al.*, 2002; Lissenberg and Dick, 2008; Lissenberg *et al.*, 2013) and melt signature (e.g., Kvassnes and Grove, 2008; Lissenberg and Dick, 2008; Lissenberg *et al.*, 2013).

Petrological studies of gabbroic sequences suggest that their textures are commonly modified significantly by processes of melt-rock interactions (e.g., Hunter, 1996; Coogan *et al.*, 2000; Blackman *et al.*, 2006; Lissenberg and Dick, 2008). Typically in gabbroic rocks enriched in olivine (i.e., olivine gabbro to troctolite), clinopyroxene crystals have been observed to occur interstitially between grains of olivine (Figure I.30a) or as coarser grains enclosing plagioclase with lobate and resorbed grain boundaries (Figure I.30b-c, e.g., Blackman *et al.*, 2006; Lissenberg and Dick, 2008).

Resorbed, or corroded grain boundaries suggest disequilibrium during crystallization between the phases in contact, and are generally defined disequilibrium textures (e.g., Donaldson, 1976; O'Driscoll *et al.*, 2007; Holness *et al.*, 2012, 2013). They are evidence of reactive porous flow triggered by the partial dissolution of the pre-existing oceanic crustal rock, likely composed of plagioclase and olivine, and crystallization of clinopyroxene as interstitial and poikilitic phase (Lissenberg and Dick, 2008). The dissolution-precipitation processes invoked involve migration of a MORB-type melt that induce the crystal mush - melt interaction (Lissenberg and Dick, 2008; Lissenberg *et al.*, 2013; Lissenberg and MacLeod, 2017). The variable modal content of clinopyroxene is proportional to the extent of olivine and plagioclase dissolution (e.g., Hunter, 1996; Coogan *et al.*, 2000; Lissenberg and Dick, 2008). When clinopyroxene occurs interstitially between coarser olivine crystals and plagioclase is more equidimensional (Figure I.30a), reaction is limited. Instead, the occurrence of little to negligible fine grained olivine and plagioclase crystals, showing curved grain boundaries, embayed in abundant poikilitic clinopyroxene suggest significant extents of melt-rock interactions (Figure I.30b to I.30c).

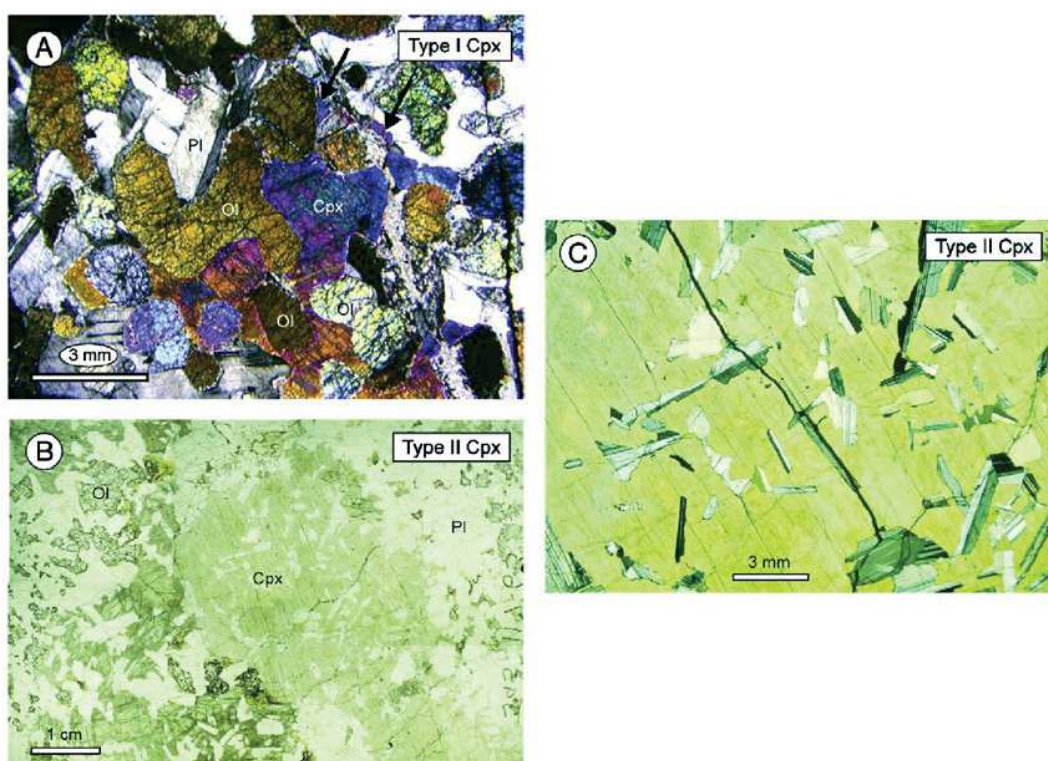


Figure I.30 – Photomicrographs of typical textural occurrences of interstitial clinopyroxene in disequilibrium with olivine and plagioclase in gabbros from Kane Megamullion (Lissenberg and Dick, 2008). a) interstitial clinopyroxene (type I) crystallizes at the expenses of olivine; b) poikilitic clinopyroxene (type II) encloses plagioclase; c) resorbed grain boundaries of plagioclase embayed in poikilitic clinopyroxene.

Reactive processes have been invoked to explain the occurrence of high Mg# (up to 88) clinopyroxene in gabbroic rocks from both ophiolite plutonic sections (e.g., Bédard, 2001; Sanfilippo *et al.*, 2015b) and active spreading centres (Mid-Atlantic Ridge, e.g., Elthon *et al.*, 1992; Lissenberg and Dick, 2008; Southwest Indian Ridge, e.g., Meyer *et al.*, 1989; Kvasnes, 2004; East Pacific Rise, Lissenberg *et al.*, 2013). High Mg# clinopyroxene has been earlier inferred to high pressure crystallization, but geochemical and textural features drive against this hypothesis (see Chapter I.1.4). Furthermore, the high Mg# clinopyroxene often coexists with plagioclase that extends to quite low anorthite contents, in contrast to the positive Mg#-An correlation predicted from high-pressure to low-pressure crystallization (e.g., Grove *et al.*, 1992 and see Chapter I.1.4). The Mg enrichments in clinopyroxene, coupled with enrichments in Cr (Figure I.31), are believed to result from olivine (Mg) and spinel (Cr) dissolution, which increases contents of these elements in the migrating melt upon reactive porous flow (e.g., Kvasnes and Grove, 2008; Lissenberg and Dick, 2008). Forsterite in coexisting olivine is in chemical equilibrium with high Mg# clinopyroxene (Figure I.31a).

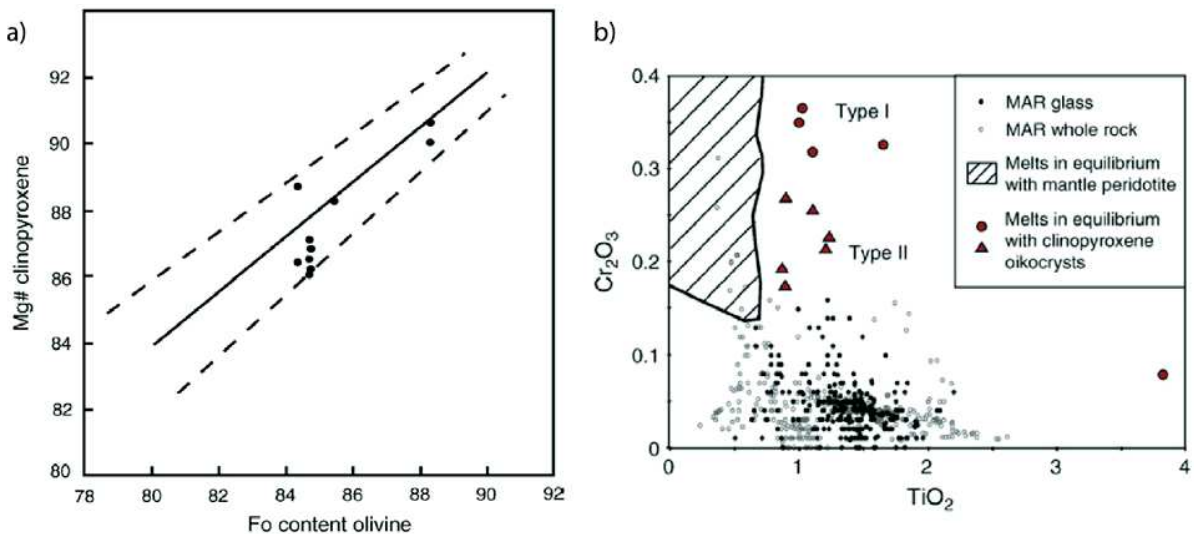


Figure I.31 – Mineral compositions of troctolites from Kane Megamullion (Lissenberg and Dick, 2008). a) Mg# of clinopyroxene vs Fo content of olivines (lines illustrate olivine-clinopyroxene equilibrium); b) Cr₂O₃ vs TiO₂ of melts in equilibrium with clinopyroxenes (types as reported in Figure I.30) compared with MAR glasses and mantle peridotites.

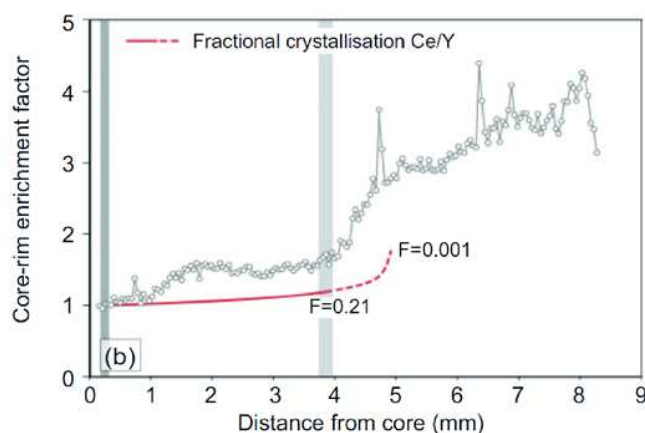


Figure I.32 – Ce/Yb enrichments from core (0) to rim (9) of a clinopyroxene in olivine gabbro from ODP Hole 735B compared to fractional crystallization modeling (Lissenberg and MacLeod, 2017).

The decoupling of the abundances of elements with differing compatibilities in rock-forming minerals is a geochemical evidence of reactive porous flow in crystal mushes (e.g., Coogan *et al.*, 2000; Lissenberg and Dick, 2008; Sanfilippo *et al.*, 2015b; Lissenberg and MacLeod, 2017). Due to differences in element velocities during reaction and melt transport (i.e., ‘chromatographic effect’; e.g., Navon and Stolper, 1987), compatible elements as Mg and Cr (i.e., major elements), which are relatively slower than incompatible elements, are strongly buffered by the matrix during reactive porous flow. This leads to the high major element contents of the solid as described above.

Trace elements show systematic over-enrichment in the most incompatible elements relative to less incompatible trace elements toward the rims of clinopyroxene (e.g., Lissenberg and Dick, 2008; Lissenberg *et al.*, 2013; Lissenberg and MacLeod, 2017). For example, Lissenberg and MacLeod (2017) observed increasing significant trace element fractionations (e.g., high Ce/Y ratios) from core to rim of a clinopyroxene crystal (Figure I.32) in olivine gabbro from ODP Hole 735B (Atlantis Bank, SWIR). Since the most incompatible elements are buffered by the migrating melt, high contents in these elements indicate a progressively more evolved melt as reaction takes place. The latter could ultimately crystallize the incompatible trace elements enriched rims of clinopyroxene.

Studies by Lissenberg and co-workers (Lissenberg and Dick, 2008; Lissenberg *et al.*, 2013; Lissenberg and MacLeod, 2017) have shown that reactive porous flow in the lower oceanic crust is partially responsible for the evolution of plutonic rocks from troctolites to olivine gabbro to

gabbro, and may contribute to the formation of Fe-Ti oxide gabbros (e.g., ODP Hole 735B, Atlantis Bank, SWIR, Dick *et al.*, 2000; Natland and Dick, 2001). The same reactive process must change the

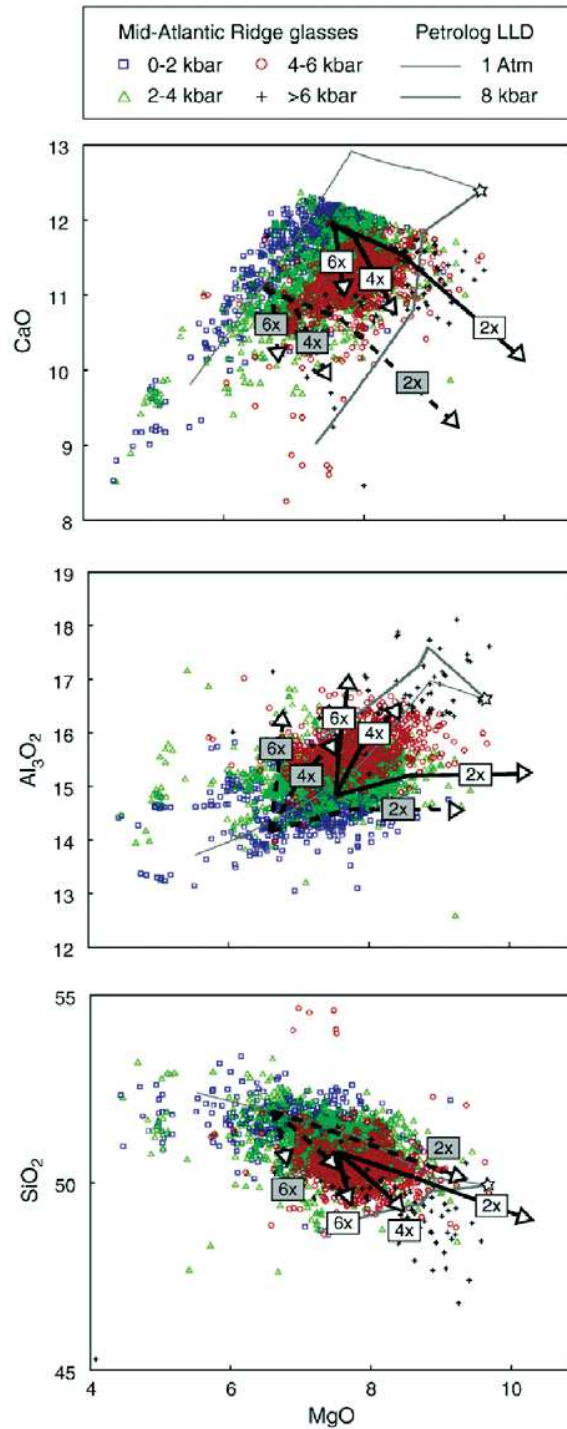


Figure 1.33 – MgO vs SiO₂, Al₂O₃ and CaO compositions of MORB glasses at MAR compared with trends of melt-rock interactions for two starting compositions and with different plagioclase/olivine ratios (6x = 6:1; 4x = 4:1, 2x = 2:1); also reported low-(thin lines) and high-pressure (thick lines) fractional crystallization trends (Lissenberg and Dick, 2008).

composition of migrating melts due to dissolution-precipitation (e.g., Lissenberg and Dick, 2008; Lissenberg *et al.*, 2013; Lissenberg and MacLeod, 2017) or melting of a pre-existing gabbroic component and mixing with the incoming mantle derived melt (g., Bedard *et al.*, 2000; Kvasnes and Grove, 2008). Chemical investigations coupled with numerical models, together with laboratory experiments, have shown that assimilation of a primitive plutonic rock can increase the Al_2O_3 , FeO and Na_2O content of the migrating melt, and decrease its CaO at a given increase in MgO (Figure I.33; Kvasnes and Grove, 2008; Lissenberg and Dick, 2008); while assimilation of evolved gabbro increases CaO and decreases FeO of the melt (Kvasnes and Grove, 2008). These spreads in melt compositions are evidence of apparent high-pressure fractional crystallization (e.g., Grove *et al.*, 1992; Herzberg, 2004; Villiger *et al.*, 2007a). Such chemical variations suggest that melt-rock interactions in the lower oceanic crust can shift both MORB and gabbroic rocks compositions toward high-pressure signals (Figure I.33; Kvasnes and Grove, 2008; Lissenberg and Dick, 2008). The effect of melt-rock interaction on the trace elements compositions of migrating melts is shown by the over-enrichments in the most incompatible elements at clinopyroxene rims (Lissenberg and MacLeod, 2017).

3. Element transport: a modeling perspective

The effect of melt migration and melt-rock interactions on the composition of minerals and melt is related to the continuous perturbation of chemical equilibrium between phases. This is the consequence of compositional differences between the solid and the migrating melt. In order to better understand how such processes affect the composition of the oceanic lithosphere, dissolution and precipitation mechanisms must be considered at the grain scale. In this thesis manuscript, I investigate chemical equilibrium among rock forming minerals, in order to evaluate the mass exchanges that take place whenever a partial melt and its host matrix are out of chemical equilibrium (Kerr, 1995; Liang, 2003).

In the following, I summarize basic concepts of chemical equilibrium, and disequilibrium, and of kinetics of dissolution and precipitation processes at the grain scale. Mass balance models used in this study are then introduced. Partitioning and diffusion mechanisms play an important role in

reactive magmatic systems by controlling phase compositions; thus an overview of partition and diffusion coefficients is reported. In this study, I focus on anhydrous magmatic systems where temperatures are expected to range between 1000°C and 1250°C, and estimated pressures are 2-5 kbar for depths of ~7-10 km (e.g., Grimes *et al.*, 2008; Drouin *et al.*, 2009; Rioux *et al.*, 2016). A compilation of preferred partition and diffusion coefficients suitable for these conditions is proposed (values reported in Appendix 5).

3.1 Crystal-melt reactions in magmatic systems

On the grain scale (micro- to milli-meter), melt-rock interactions involve partial dissolution of a mineral and subsequent or simultaneously precipitation of another mineral. Mineral dissolution takes place whenever a melt and the host crystal-matrix is out of chemical equilibrium leading to chemical disequilibrium corrosion (Kerr, 1995; Liang, 2003). Before kinetics of dissolution-precipitation processes are treated, the concept of chemical equilibrium must be defined.

Chemical equilibrium and disequilibrium

The equilibrium state is the one toward which a system changes to reach the lowest potential energy, from unstable or metastable states (White, 2013; Figure I.34). In magmatic systems, which depend on thermodynamic conditions (i.e., temperature and pressure), the potential energy is described by the Gibbs free energy (G):

$$dG = VdP - SdT$$

where 'V' is the phase volume, 'dP' and 'dT' are variations in pressure and temperature, respectively, and 'S' is the entropy of the melt or crystalline matrix.

Two phases, including solid-solid, solid-melt and melt-melt, are in equilibrium when their Gibbs free energies are equal (White, 2013). They are, instead, in disequilibrium when their Gibbs free energies differ; in this case, the two phases tend to re-equilibrate. At constant temperature and pressure, re-equilibration is governed by the phase volumes and their compositions (which control S). During melt-rock interactions, dissolution and precipitation act to reach an equilibrium melt fraction and crystal-melt chemical re-equilibration (e.g., Albarede and Bottinga, 1972; Liang, 2003).

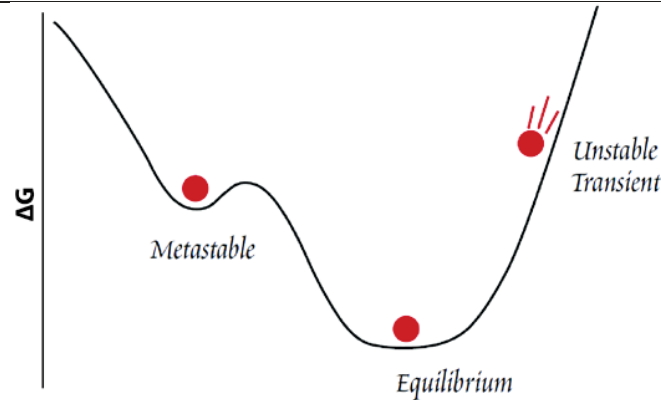


Figure 1.34 – Schematic illustration of the states (red dots) of a system (White, 2013). Equilibrium state has the lowest Gibbs free energy (G); unstable has higher and variable G ; metastable has local lower G .

Kinetics of dissolution-precipitation processes

Upon dissolution, element atoms and molecules are detached from the crystal surface, or grain boundary, and transported into the melt (e.g., Harrison and Watson, 1983, 1984; Donaldson, 1985; Kerr, 1995; Liang, 2000, 2003). A boundary layer (compositional boundary layer) forms around the crystal, between the latter and the melt (Figure 1.35). Within this boundary layer a compositional gradient exists between the two phases, and elements are transported by diffusion from the mineral surface to the melt (desorption) or vice versa (adsorption), as shown in Figure 1.35b). There, the rate of element diffusion is defined by the element diffusion coefficient in the melt.

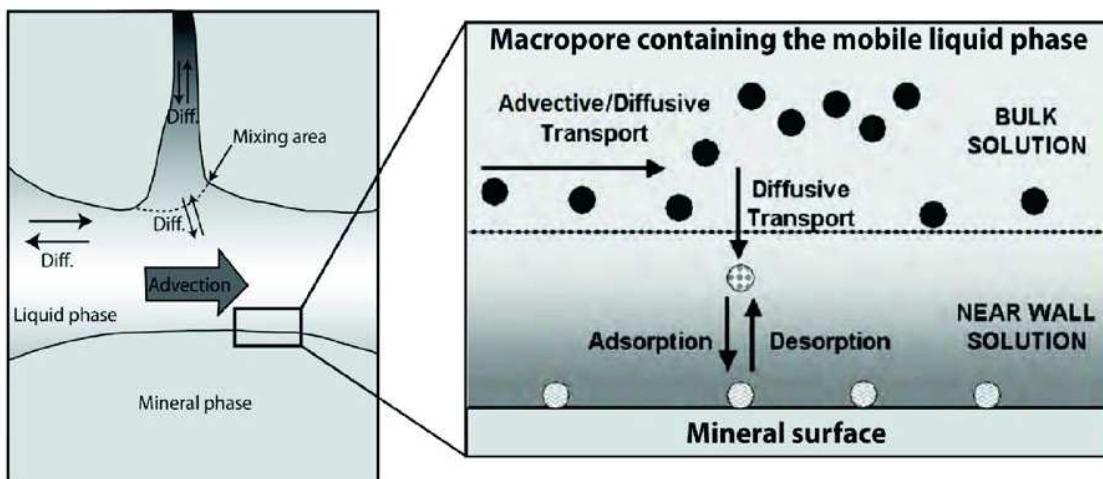


Figure 1.35 – Schematic illustration (Peuble, 2014) of a) mechanisms of melt transport at the grain scale: advection is controlled by the melt velocity, and diffusion occurs when melt velocity is very low or negligible; b) element transport in the compositional boundary layer between mineral surface and mobile melt phase.

When reaction takes place in partially molten silicates (i.e., high temperatures $\geq 1200^\circ\text{C}$), and crystal surface is partially dissolved, transport of elements in the melt is controlled by diffusion (e.g., Zhang *et al.*, 1989; Liang, 1999, 2000) and advection (e.g., Kerr, 1995; Liang, 2003; Chen and Zhang, 2008; Figure I.35a). Diffusive crystal dissolution is the dominant mechanism of element transport when the crystal and melt have similar densities, and thus the melt flows slowly (Zhang *et al.*, 1989). Advection takes place at higher melt velocities, from which it depends, and accounts for element transport away from the crystal-melt interface, where melt composition is maintained homogeneous and constant (Kerr, 1995).

Considering a binary crystal-melt aggregate, the compositional gradient between the two phases lead to dissolution and/or precipitation of the solid. The reaction process is described by the equilibrium melt fraction (ϕ_∞) that is function of melt and crystal compositions (Liang, 2003):

$$\phi_\infty = \frac{C_{s0} - C_{ss}}{C_{ss} - C_{ml}} + \left(\frac{C_{s0} - C_{m0}}{C_{ss} - C_{ml}} \right) \phi_0$$

where ' C_{s0} ' and ' C_{m0} ' are the initial compositions of the solid (crystal) and melt, respectively, ' C_{ss} ' and ' C_{ml} ' are the liquidus and solidus compositions, respectively, and ϕ_0 is the initial melt fraction. The 'equilibrium melt fraction' is the fraction, and composition, of melt at which the crystal and melt reach equilibrium. When $\phi_\infty > \phi_0$ the melt fraction must increase to reach equilibrium, thus dissolution occurs. Precipitation takes place when $\phi_\infty < \phi_0$.

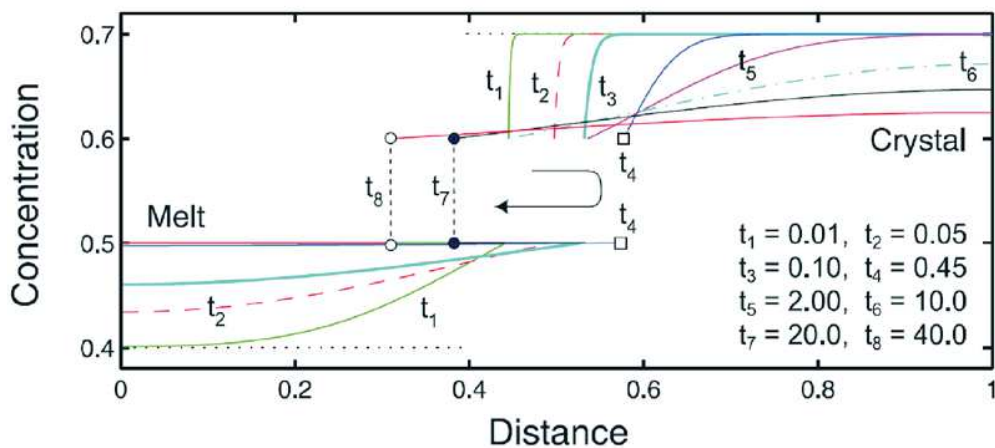


Figure I.36 – Crystal dissolution and precipitation (or growth) in a binary crystal mush (Liang, 2003). Location of the crystal-melt interface is shown at t_4 (square), t_7 and t_8 (dashed lines).

The chemical compositions of the two phases at their interface vary as function of time during the reaction. Experimental studies and numerical simulations (e.g., Kerr, 1995; Dohmen *et al.*, 2003; Liang, 2003; Morgan and Liang, 2005; Chen and Zhang, 2008; Van Den Bleeken *et al.*, 2010; Wang *et al.*, 2013) have shown that dissolution-precipitation processes lead to a continuous change in the position of the crystal-melt interface (Figure I.36), where instantaneous chemical re-equilibration (e.g., Dodson, 1973; Lasaga, 1983) is controlled by element partitioning (see Chapter section I.3.3). Figure I.36 illustrates this ‘moving boundary’ effect (e.g., Liang, 2003). If the melt is initially undersaturated, the crystal dissolves into the melt and the crystal-melt interface progressively moves toward the crystal (from t_1 to t_5 in Figure I.36). Because diffusion in solid is slow (review in Zhang and Cherniak, 2010; see Chapter section I.3.4), the composition of the partially dissolved crystal do not vary at first, but is modified only at the rim (interface) (e.g., Liang, 2003). When the melt becomes saturated, precipitation takes place ($\phi_\infty < \phi_0$; from t_6 to t_8 in Figure I.36).

Diffusion in crystals

The compositional gradient developed in the crystal, hence between the core and the rim, is progressively decreased by the flux of intra-crystalline element diffusion (e.g., Chakraborty, 2008; Brady and Cherniak, 2010). Element diffusion is the transport of chemical components along random pathways (Figure I.37) on very small scales ($< \mu\text{m}$), involving the relative motion of one particle to another (Onsager, 1945). In solids, diffusion is restricted to jumps from one site in the

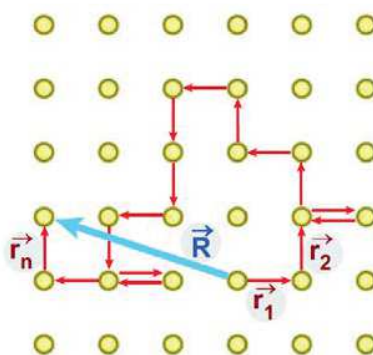


Figure I.37 – Schematic representation (Chakraborty, 2008) of the random pathways (red arrows) in a uniform lattice (yellow dots). The comparison with net displacement (blue arrow) shows that diffusion is inefficient in the long term.

crystal lattice to another, which makes this mechanism efficient only on a short timescale (Chakraborty, 2008). Point defects in the crystal lattice, generally vacancies, create the pathways for the motion of diffusive species (e.g., Tsai and Dieckmann, 2002; Dohmen and Chakraborty, 2007; Chakraborty, 2008).

At high temperature, comparable with those at ocean spreading ridges, volume diffusion dominates over surface diffusion processes (Chakraborty, 2008), thus hereafter we will refer to volume diffusion exclusively. Element diffusion is described by Fick's First Law, according to:

$$J = -D_i \frac{\partial C_i}{\partial x}$$

where the flux J of particles is related to the gradient $\partial C_i / \partial x$ (C_i , concentration of the species 'i'; x , flux direction) and the diffusion coefficient D_i (of element or species 'i', m^2/s), while the negative sign indicates that elements are transported toward the region of lower concentration. The Fick's Second Law expresses the conservation law for the diffusive species:

$$\frac{\partial C}{\partial t} = -\frac{\partial J}{\partial x} = \frac{D \partial^2 C}{\partial x^2}$$

where the first term (time partial derivate) represents the accumulation (or loss) rate of the chemical component, while the second is the balance between the input and output diffusive fluxes. Homogenization of concentration gradients is the manifestation of chemical (or inter-) diffusion, but does not rule it (Chakraborty, 2008, Brady and Cherniak, 2010). The diffusive flux of elements takes place whenever a compositional gradient occurs independently of the process that produced it, whether it is crystal-melt reaction or a drop in temperature. When the compositional gradient is related to crystal-melt reactions, if diffusion is slow, compared to the time of reaction, core-to-rim compositional variations are maintained; at fast diffusivities, instead, the crystal can re-equilibrate completely and its original composition is obliterated.

Partitioning

Partitioning is 'the behavior of an element on its preference, or possibility, to enter a specific lattice site of the different coexisting phases, such as crystals, metals and liquids' (Goldshmidt, 1937). Since the preliminary work of Goldshmidt (1937), several experimental studies and

numerical calculations have quantitatively determined partitioning by element partition coefficients (e.g., Ulmer, 1989; Beattie *et al.*, 1991; Blundy and Wood, 2003; Dohmen *et al.*, 2003; Wood and Blundy, 2003; Bédard, 2005; Agraniar and Lee, 2007; Lee *et al.*, 2007; Evans *et al.*, 2008; Spandler and O'Neill, 2010; Laubier *et al.*, 2014). Partition coefficients (K) relate activity of an element ($a_i = X_i \gamma_i$, where X_i is concentration of element i with the activity coefficient γ_i) in two different coexisting phases.

$$K_i^{\alpha-\beta} = \frac{a_i^\alpha}{a_i^\beta}$$

where α and β are solid and melt respectively, or solid and solid. For values of $K > 1$ an element preferentially enters the solid and its behaviour is referred to as compatible, while an incompatible element has $K < 1$ and is better hosted by the melt structure. The moderately incompatible elements are those with K close to 1.

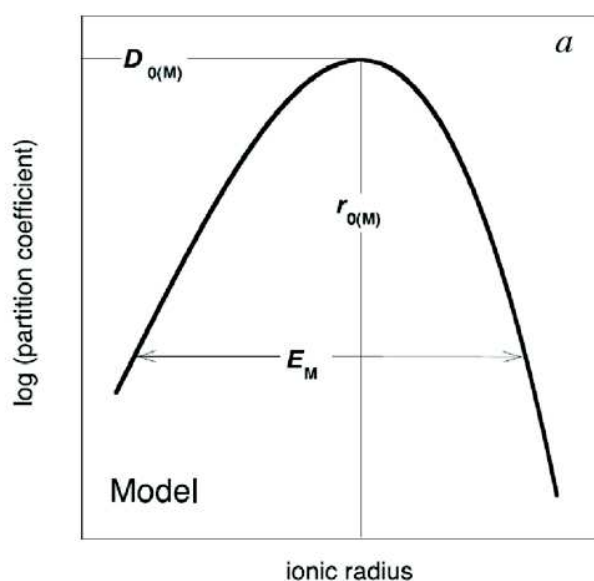


Figure 1.38 – Cartoon illustrating the lattice strain model of element partitioning (Blundy and Wood, 2003).

D_0 is the partition coefficient of a (fictive) ion with the most compatible behaviour, with radius r_0 approaching the radius of the crystal site; E_M is the elastic response of that site (as measured by Young's Modulus) to lattice strain caused by ions that are larger or smaller than r_0 .

The physical properties of each mineral and of the available sites in its crystallographic structure play a fundamental role in element partitioning and represent the bases for lattice strain models (Nagasawa, 1966; Brice, 1975). These Lattice Strain Models (LSM) describe the partitioning

behaviour of isovalent series of ions, represented by a parabolic distribution of logarithmic values of K as function of the ionic radius (Figure I.38). The elastic properties (Young's modulus, E) and the dimension of the crystallographic site of substitution define the LSM isovalent parabola (Figure I.38), in which the best-fit fictive ion have radius r_0 and a corresponding highest partition coefficient (D_0) at the peak of the parabola (e.g., Beattie, 1994; Blundy and Wood, 1994, 2003). D_0 and r_0 vary in function of the cation charge. At given cation charge, elements become more incompatible at increasing distance of ionic radius from r_0 , toward either lower or higher dimensions, that is because strain energy increases (Blundy and Wood, 2003). An example of this misfit in strain energy is the partitioning of rare earth elements (REE) between clinopyroxene and olivine. Since REEs substitute Ca in clinopyroxene and Mg-Fe in olivine, and due to the larger ionic radius of Ca compared to Mg and Fe, REE substitutions in clinopyroxene present lower misfit strain energy than in olivine, leading to major incorporation of REE in clinopyroxene crystals.

Control of thermodynamic variables on partitioning and diffusion

Partitioning and diffusion are the major mechanisms that control element transport during crystal-melt reactions. Temperature and pressure have a significant control on the physical properties of a crystal lattice and, therefore, they rule partitioning and diffusion.

Considering any reaction in magmatic systems (e.g., melting, melt-rock interaction, crystallization), and made some assumptions about the relationship between composition and activity of the considered components (reviews in White, 2013; Wood and Blundy, 2014), the partition coefficient D_0 (Figure I.37) can be related to the equilibrium constant of reaction. From this, a relationship between D_0 and the partition coefficient K can be drawn as follows (White, 2013; Wood and Blundy, 2014):

$$K = D_0 \exp\left(\frac{-\Delta G_{crystal}}{RT}\right)$$

where 'R' is the gas constant. The high of the parabola in Figure I.38, thus D_0 , depends predominantly on the free energy of reaction (ΔG). Since ΔG depends on enthalpy and entropy of the crystal (see *Chemical equilibrium*), which change as function of temperature and pressure, it

follows that the equilibrium constant and, therefore, element partition coefficients depend on the temperature conditions of the system.

I have previously explained that element diffusion is mainly controlled by the availability of vacancies in the crystal lattice. The vacancies can be treated as atoms and ions, and are temperature-dependent (reviews in Chakraborty, 2008; White, 2013). A certain minimum activation energy (E_a) is required to form vacancies and to move an ion from one site to another. Hence E_a controls the activation of the element diffusion process typically expressed as function of temperature ($1/T$) by the Arrhenius equation:

$$D = D_0 e^{\left(\frac{-E_a}{RT}\right)}$$

where ' D_0 ' here is the diffusion coefficient corresponding to the y-axis intercept of the (fitted) line that describe the temperature-dependent variation of diffusion coefficients in the Arrhenius plot (Figure I.39). The slope of this line is E_a/R : for diffusion mechanisms described by a steep slope more energy is needed to initiate element diffusion (e.g., Dohmen and Chakraborty, 2007; Chakraborty, 2008; Brady and Cherniak, 2010). The dominant mechanism of diffusion in most natural silicates is the transition metal-extrinsic diffusion (TaMED) that presents intermediate activation energy between that corresponding to high and low temperatures (Figure I.39).

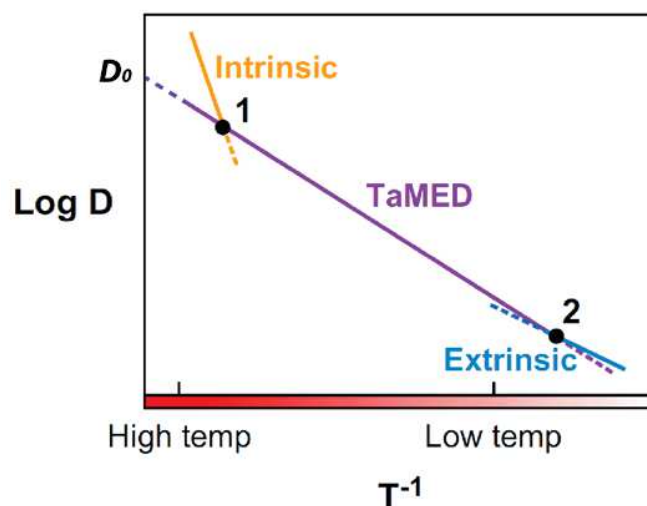


Figure I.39 – Schematic illustration of D (logarithmic scale) versus $1/T$ plot (Chakraborty, 2008): the slope of the line is directly proportional to activation energy for a given process. At highest temperature intrinsic diffusion dominates; in transition metal-bearing materials the TaMED mechanism takes place over a large temperature range; at lower temperatures the extrinsic mechanism is activated. D_0 represents the y-axis intercept of the line. Numbered black dots are the transition temperatures between diffusion mechanisms.

For both partitioning and diffusion, the effect of pressure is restricted to high pressure conditions that are $P > 3\text{GPa}$ for partitioning (e.g., Taura *et al.*, 1998), and $P > 5\text{GPa}$ (over 150 km depths) where diffusivities decrease with increasing pressure (Holzapfel *et al.*, 2007). Exception is made for Fe-Mg exchanges of which mineral/melt partition coefficients are found to decrease with decreasing pressure also at lower pressures (Ulmer, 1989).

3.2 Melt-rock interaction modeling

Assimilation-Fractional Crystallization

Mechanisms of element transport during melt-rock interactions have been often modeled as chemical exchanges resulting from a simple process of mineral assimilation and subsequent fractional crystallization of interstitial phases. Assimilation-Fractional Crystallization (AFC, DePaolo, 1981) is the most common and largely used model to reproduce mineral. It is not thermodynamically constrained since temperature and pressure are not considered as variable parameters. The AFC is a mixing/differentiation model first used to simulate trace element variations during wall-rock assimilation and crystallization in a magma chamber (DePaolo, 1981), then applied to systems of melt-rock interactions in the mantle (Kelemen *et al.*, 1992) and in the lower oceanic crust to reproduce major (e.g., Lissenberg and Dick, 2008; Sanfilippo *et al.*, 2013) and minor and trace elements variations (e.g., Sanfilippo *et al.*, 2014; Rampone *et al.*, 2016). The differential equation that describes this model is function of magma mass, assimilated and crystallized mass, and partitioning, which is the solely mechanism controlling element transport between phases (i.e., melt and minerals). For constant partition coefficient of an element and constant composition of the host rock, the differential equation for AFC was written as (DePaolo, 1981):

$$\frac{C_m}{C_{m0}} = F^{-z} + \left(\frac{r}{r-1}\right) \frac{C_a}{z C_{m0}} (1 - F^{-z})$$

where ' C_m ', ' C_{m0} ' and ' C_a ' are the concentrations of the element in the melt, which is changing upon reaction, in the initial incoming melt and in the host rock, respectively; ' F ' is the fraction of melt, ' z ' is defined by $(r + K - 1)/(r - 1)$, and ' r ' is the mass ratio between mass assimilated and mass crystallized. Neither advection nor diffusion is considered in the AFC model.

Reactive percolation

In this study I used the ‘Plate model’ to simulate the mass transfer between minerals and melt during melt-rock reaction and melt percolation, and to reproduce the associated variations in trace elements and Mg-Fe compositions of mineral phases and melt.

I used the zero-dimension ‘Plate model’ of Vernières *et al.* (1997), which reproduces trace-element fractionation during partial melting and reactive melt transport through a porous media in the Earth’s upper mantle. This model was also adapted to the simulation of Fe-Mg redistribution (Mg# model) in peridotite-melt systems by Bedini *et al.* (2002) using a total inverse method to avoid mineral stoichiometry violation (see Bodinier *et al.*, 2008 and Ionov *et al.*, 2005 for details on the procedure). I used the latter to model variations of mineral Mg# and modal contents in the rock, and MgO and FeO variations in the melt.

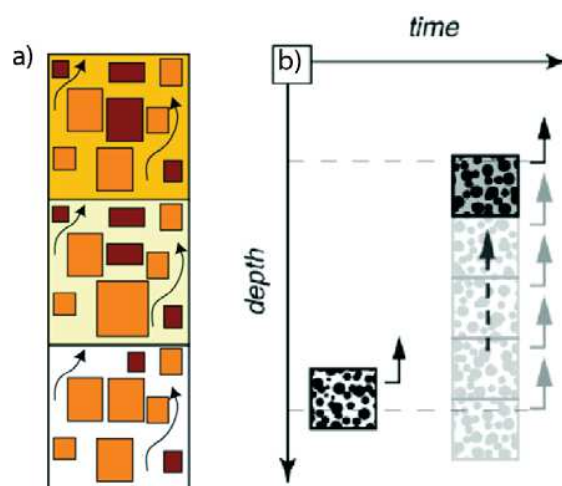


Figure 1.40 – Schematic representation of the reactive process simulated by the nondimensional ‘Plate model’. a) Sketch of the reactive column composed of chemical reactive cells each made of minerals reacted with the migrating melt (orange rectangle) and forming the starting rock (brown rectangle). The direction of migrating melt is indicated by black arrows. Note that the rock-forming minerals at the base of the column are nearly in complete equilibrium with the melt. b) Example of progressive creation of reactive cells at each reaction increment in an open system (Godard *et al.*, 2008).

In the ‘Plate model’, element transport is nondimensional, thus independent of time and distance. Densities of the solid matrix and fluid phase are assumed to be constant throughout the reaction process (Vernières *et al.*, 1997). Porous flow is simulated by the propagation of fluid batches through representative microvolumes of rock (Figure 1.40). The infiltrated medium is

considered as a column made of minerals forming the initial rock, and it is composed of chemical reactive cells (Figure I.40). Based on initial porosity, a certain amount of infiltrating melt reacts with the given initial material from the bottom of the column to the top by creating new reactive cells at each reaction increment (Vernières et al., 1997). Mineral dissolution and precipitation processes are simulated by local-instantaneous equilibrium between phases after sequential partial melting and crystallization, at the scale of a representative volume. This allows control on phase relationships (i.e., phase modal contents) and on their chemical exchanges upon reaction and melt percolation. The step-by-step approach of the 'Plate model' allows reproducing the chemical effects typical of porous flow, such as the chromatographic fractionation of REE (e.g., Navon and Stolper, 1987) during infiltration and transport of the melt (Vernières et al., 1997). The chromatographic effect (e.g., Navon and Stolper, 1987) results from a difference in velocities of element transport through the melt. Indeed, the most incompatible elements move faster and tend to be transported away by the percolating melt, while the more compatibles are slower and are governed by local changes in solid compositions (Navon and Stolper, 1987; Godard et al., 1995; Vernières et al., 1997). Strongly fractionated trace element patterns can be produced by this effect. Chemical equilibrium between phases is controlled by the partition coefficients, but it also depends on the concentration of elements in the melt that can be affected by advection transport. Compared to a batch model (i.e., AFC), the advantage of the 'Plate model' is to consider the effect of melt transport (i.e., the advection mechanism) on element redistribution during reaction.

Diffusion modeling

Element diffusion in solids, and that in the melt, are not taken into account in either AFC model or nondimensional 'Plate model'. Analytical solutions to model element diffusion require fixed initial and boundary conditions including temperature, pressure and chemical composition of crystal core and rim (e.g., Crank, 1975; Chakraborty, 2008). Kinetic processes such as melt-rock interactions account for variations in crystal rim composition changing continuously the boundary conditions of the system. Thus, diffusion mechanism must be considered aside. Minimum re-equilibration time (t_{eq}) can be obtained by using a simple but effective approach (equation by Crank, 1975), whereby the crystal is geometrically approximated to a sphere of radius 'r':

$$t_{eq} = \frac{r^2}{\pi D_i}$$

where t_{eq} depends on the diffusion coefficient (D_i of element 'i') and r . Other equations have been proposed to model element diffusion considering variations of diffusion coefficients with temperature, pressure and mineral element composition as for the case of Fe-Mg diffusion in olivine (e.g., Dohmen and Chakraborty, 2007). In this work I used the following equation (Dohmen and Chakraborty, 2007):

$$\log D_{Fe-Mg} = -9.21 - \frac{201000 + (P - 10^5) * 7 * 10^{-6}}{2.303 RT} + \frac{1}{6} \log \left(\frac{fO_2}{10^{-7}} \right) + 3X_{Fe}$$

Finally, diffusion modeling using two-phases geospeedometer can provide information on temperature and time of re-equilibration during cooling of a rock (e.g., Coogan *et al.*, 2002).

3.3 Partition coefficients

In Chapter section I.3.1 I showed that element partition coefficients depend on the thermodynamic condition of the system, and on the charge and size of the cation for substitution. For the minerals of interest in this thesis, which are olivine, plagioclase and clinopyroxene, LSM models are proposed in literature (e.g., for olivine, Figure I.41a, Beattie, 1994; clinopyroxene, Figure I.41b, Blundy and Wood, 1994; plagioclase, Figure I.41c, Sun *et al.*, 2017). It can be observed that ions of Mg, Fe, Co and Cr plot close to the ideal r_0 for 2+ and 3+ isovalent curves in olivine, while REE are far from it showing higher r than that of the site of substitution. In clinopyroxene Na, Ca, and La are the best fitting ions for 1+, 2+ and 3+ series, respectively. This indicates, for example, the stronger affinity of olivine for Mg, and that of clinopyroxene for Ca and REE. In plagioclase, Ca and Na are also close to r_0 of the relative isovalent curve, but also Sr and Eu; Light-REEs are the closest REE to r_0 of the 3+ series.

The effect that temperature has on the physical properties of crystals, and on the correlated partition coefficients, can be observed for example in olivine and clinopyroxene under subsolidus conditions (<1000°C). The solubility of compatible elements, as for example Ni and Co, increases in olivine at decreasing temperature. As a consequence, their olivine/clinopyroxene partition

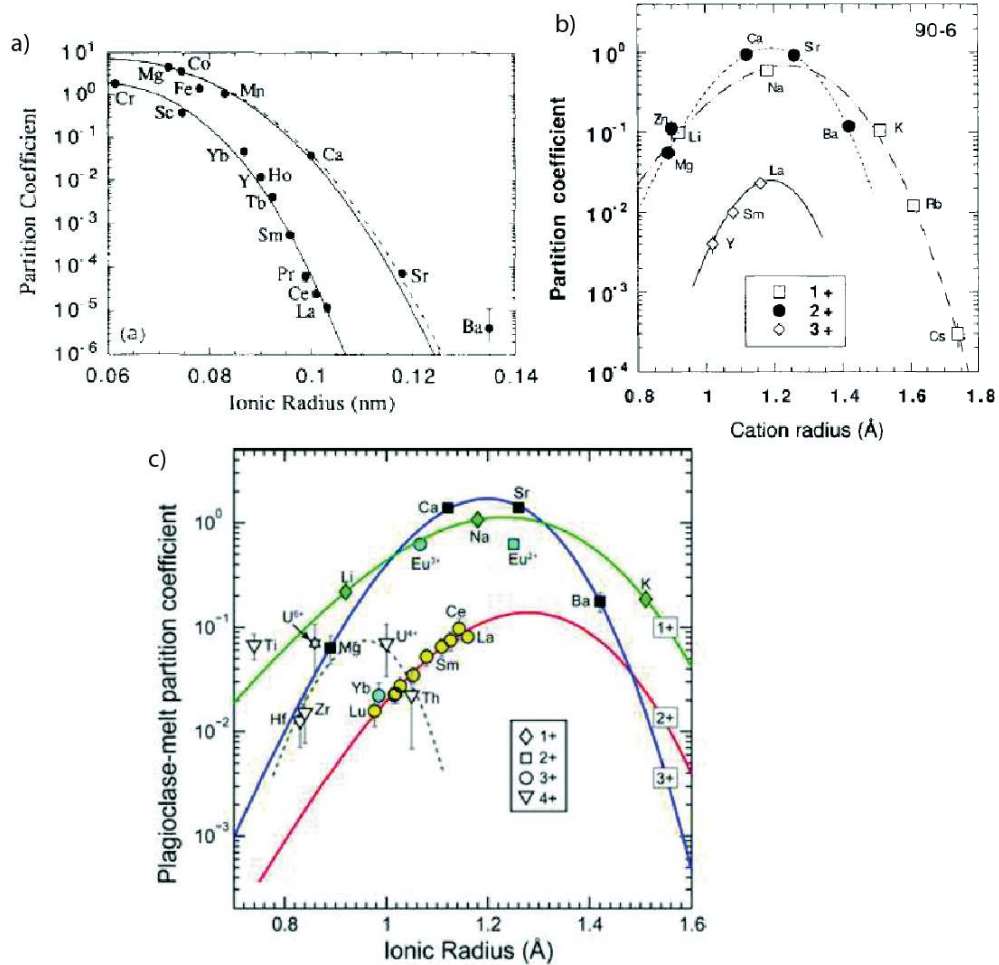


Figure 1.41 – Lattice Strain Models for a) olivine (Beattie, 1994); b) clinopyroxene (Blundy and Wood, 1994); c) plagioclase (Sun et al., 2017).

coefficients increase (Figure 1.42) during cooling of the crystal assemblage (Witt-Eickschen and O'Neill, 2005). In contrast, the solubility of Ca, Y and REE in olivine decreases substantially with the drop of temperature, leading to the migration of these elements outward (e.g., Köhler and Brey, 1990). This phenomenon takes place if adjacent to olivine there is a phase that could act as an infinite reservoir for those elements. In gabbroic systems, as those treated in this study, clinopyroxene is relatively abundant, and has a strong affinity for Ca and a stronger affinity for Y and REE compared to olivine. Thus these elements are redistributed during cooling among the phases, as controlled by the substantial decrease of olivine/clinopyroxene K_{Ca} , K_Y and K_{REE} with temperature (Figure 1.43).

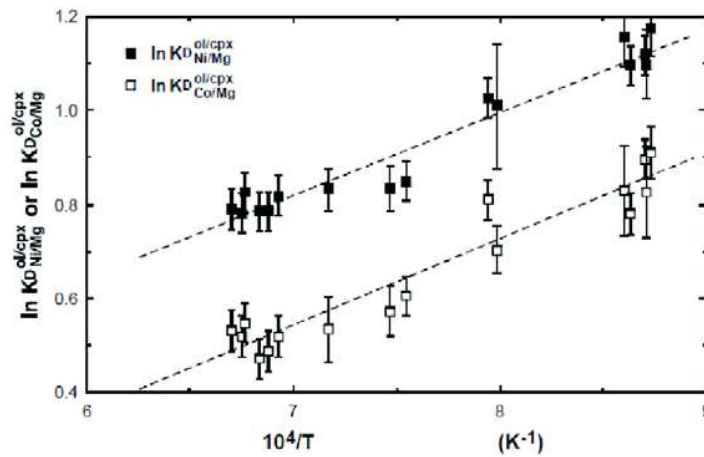


Figure 1.42 – Partitioning of Ni/Mg and Co/Mg between olivine and clinopyroxene as a function of temperature; dashed lines are empirical fits to the data (Witt-Eickschen and O’Neill, 2005). Note the increase in olivine/clinopyroxene partition coefficients at decreasing temperature.

Partition coefficients are also strongly dependent on melt and mineral compositions. The effect of melt composition is generally regarded as the effect of melt structure (e.g., Gaetani, 2004; Mysen and Dubinsky, 2004; Mysen and Shang, 2005). In a silicate melt, this is defined by the possibility of the melt to form a network of SiO₄ tetrahedra units linked by sharing oxygen atoms (i.e., polymerization, Mysen and Richet, 2005). Polymerization of silicate melts decreases with

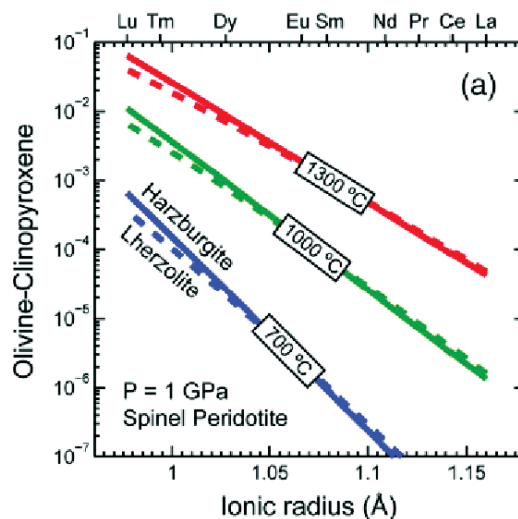


Figure 1.43 – Partitioning of REE between olivine and clinopyroxene (Sun and Liang, 2014). Full lines are for harzburgitic compositions, while dotted are for lherzolite. Note the decrease in partitioning as temperature drops.

decreasing Si content leading to favourable incorporation of metal ions in the melt (Mysen, 1995). Particularly in olivine, variations in MgO and SiO₂ contents in the melt change olivine/melt partition coefficients. More in detail, the decrease of MgO in the melt increases olivine/melt partitioning of major elements (i.e., Fe-Mg, Ulmer, 1989) and Ni (Figure I.44a-b; e.g., Hart and Davis, 1978; Beattie *et al.*, 1991; Bédard, 2005; Mysen, 2007, 2008; Li and Ripley, 2010; Le Roux *et al.*, 2011; Matzen *et al.*, 2013), while minor elements such as Mn and Zn (Figure I.44c) become more incompatible (e.g., Kohn and Schofield, 1994). From an experimental dataset of olivine/melt partition coefficients obtained at different melt compositions, Hart and Davis (1978) quantitatively expressed the variation of Ni partitioning as function solely of MgO content in the melt by proposing the equation:

$$K_{Ni} = 124.13 * \left(\frac{1}{MgO(wt\%)} \right)$$

Similarly, Ulmer (1989) proposed two equations to express the variation of Fe-Mg partitioning in olivine as function of MgO in the melt.

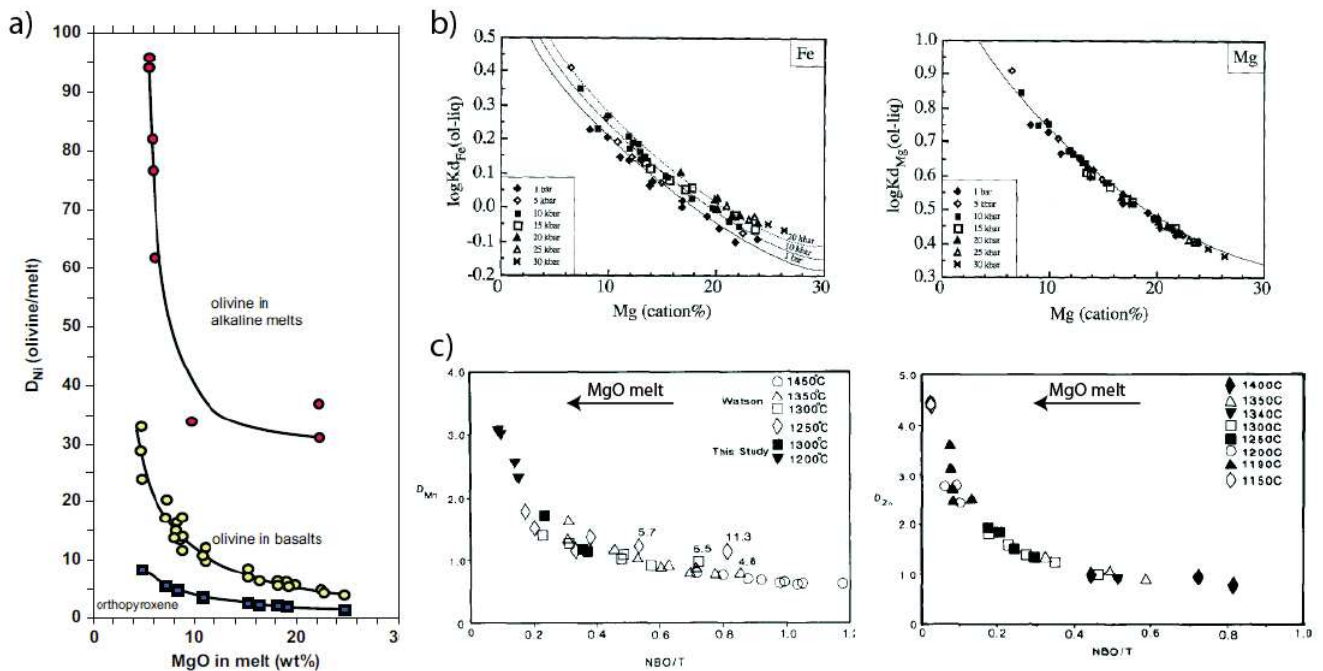


Figure I.44 – Diagrams of olivine/melt partition coefficients vs melt composition. a) Partitioning of Ni vs MgO in the melt for different melt compositions (Foley *et al.*, 2013). b) Partitioning (logarithmic scale) of Fe and Mg vs Mg content in the melt at different pressure conditions (Ulmer, 1989). c) Partitioning of Mn and Zn vs polymerization of the melt (NBO/T, non-binding oxygen) (Kohn and Schofield, 1994); NBO decrease with increasing MgO in the melt.

Conversely, olivine/melt partition coefficients for trace elements are Si-dependent decreasing with increasing SiO₂ contents in the melt (Evans *et al.*, 2008; Tuff and O'Neill, 2010), whereas Zn partitioning appears to be only slightly dependent on melt composition (Le Roux *et al.*, 2011).

On the other hand, the effect of major element composition of the melt on element partitioning in plagioclase and clinopyroxene appears to be indirect through mineral saturation in silicate melt, thus depending on the mineral compositions (e.g., Sun and Liang, 2012; Dygert *et al.*, 2014; Wood and Blundy, 2014; Sun *et al.*, 2017).

Clinopyroxene/melt K_ds depend on clinopyroxene composition in terms of Ca, Al and Na contents (e.g., Hauri *et al.*, 1994; Brenan *et al.*, 1998; Lundstrom *et al.*, 1998; Wood and Blundy, 2001; Sun and Liang, 2012; Liu *et al.*, 2014). At increasing Ca and Al contents partitioning of REE and other trace elements into clinopyroxene increases (e.g., Hauri *et al.*, 1994; Green *et al.*, 2000; Wood and Blundy, 2001; McDade *et al.*, 2003; Sun and Liang, 2012; Dygert *et al.*, 2014). Indeed, the presence of Al, and to a lesser extent that of Ca, in the crystal lattice of clinopyroxene increase the overall size and distortion of the octahedral site where trace elements are preferentially hosted (Wood and Blundy, 2001). The effect of Na₂O is most observed for substitutions with Cu (Liu *et al.*, 2014). Similar to Ca-in-clinopyroxene, also Ca contents of plagioclase affect partitioning of trace elements by increasing plagioclase/melt K_{REE} (Sun *et al.*, 2017).

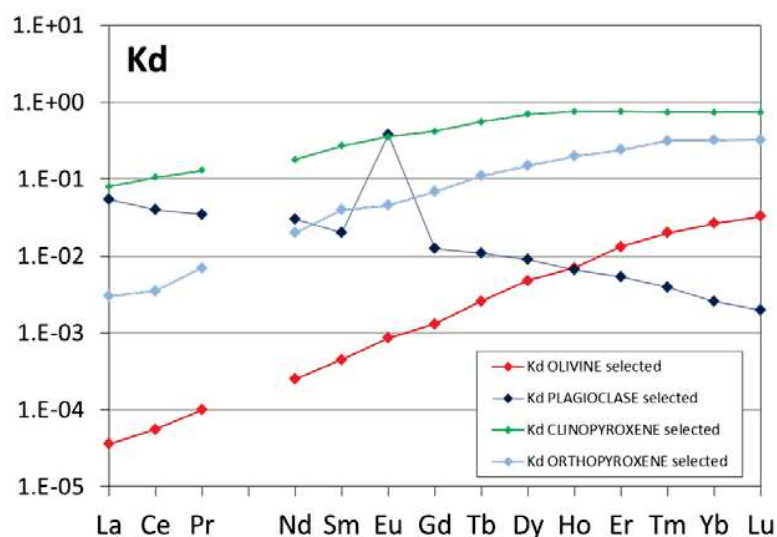


Figure 1.45 – Selection of preferred values of mineral/melt partition coefficients (Appendix 5 for compilation)

Based on these considerations, caution has to be taken when selecting partition coefficients for modeling of petrogenetic processes and element transport. We considered values of K_d obtained under conditions that most closely resemble those of magmatic crystallization at mid-ocean ridges. In Appendix 5 we report a database of mineral/melt K_d s experimentally measured for olivine (Fo_{90}), plagioclase (An_{80} - An_{60}) and pyroxenes (CaO ~20-25 wt%) in basaltic melts, at temperatures between 1100°C and 1300°C. Preferred values used in this study are equally reported and shown in Figure I.45 for olivine, plagioclase and pyroxenes. In order to account for the dependence of partitioning in olivine on variation of melt composition we used the approaches proposed by Hart and Davis (1978) for olivine/melt K_{Ni} ; olivine/melt K_{Fe-Mg} were calculated after Ulmer (1989) using an inverse method (Bedini *et al.*, 2002).

3.4 Diffusion coefficients

I previously discussed the dependence of diffusion coefficients on temperature and pressure. Diffusion is not solely controlled by the thermodynamic variables, but also oxygen fugacity and mineral composition change diffusion coefficients.

The effect of oxygen fugacity (fO_2) on element diffusion rates is correlated to its control on the oxidation state of Fe from Fe^{2+} to Fe^{3+} . The increase of Fe^{3+} in the crystal lattice at increasing fO_2 is charge balanced by the formation of vacancies (Dohmen and Chakraborty, 2007), evidenced by the positive correlation of diffusion coefficients with fO_2 (e.g., Petry *et al.*, 2004; Dimanov and Wiedenbeck, 2006; Chakraborty, 2010). Noteworthy, at temperatures higher than ~1200°C (quartz-fayalite-magnetite, QFM, buffer fO_2 conditions) most element diffusion coefficients of olivine become independent of fO_2 (e.g., Dohmen and Chakraborty, 2007; Tsai *et al.*, 2011; Jollands *et al.*, 2014), made exception for Ti that shows a strong fO_2 dependence even at high temperatures (Jollands *et al.*, 2016).

The formation of vacancies changes between the different crystal lattices and depends also on mineral chemical composition. Overall, olivine shows the highest diffusion coefficients with the lowest activation energies in comparison with clinopyroxene and plagioclase. The crystal lattice of olivine exert an important control on the formation of pathways for element diffusion (e.g., Chakraborty, 1997; Petry *et al.*, 2004; Dohmen *et al.*, 2007; Cherniak, 2010b; Spandler and O'Neill,

2010; Jollands *et al.*, 2014). The oxygen anions form a hexagonal close-packed array that defines the octahedral cation site (M1 and M2) of which half is occupied by the M^{2+} cations. Both M1 and M2 octahedra form serrated chains lying parallel to [001] axis (Figure I.46); Fe occupies M1 sites, whereas Mg prefers the M2 octahedron. As vacancy formation is correlated with Fe, most divalent cations diffuse preferably through a connected and easy path made up of only M1-M1 jumps along [001]. As a consequence, diffusivities along the c -[001] axis are greater than those found for a -[100] and b -[010] axes having similar diffusion rates. In contrast, element diffusion in clinopyroxene is isotropic or little anisotropic. For Ca and Mg diffusion is faster along the c -axis (Zhang *et al.*, 2010), little anisotropy is observed for diffusion of Pb (Cherniak, 2001), whereas Ti and other elements are not sensitive to crystallographic orientation (Cherniak and Liang, 2012). Plagioclase displays little anisotropy for element diffusion (Cherniak, 2010b) showing relatively greater diffusion coefficients along the direction normal to (001). This characteristic is described for monovalent (Na^+ , Cherniak, 2010a and references therein), bivalent cations (Sr^{2+} , Cherniak and Watson, 1994; Ba^{2+} , Cherniak, 2002) and heterovalent cations (Pb^{4+} , Cherniak, 1995; REE^{3+} , Cherniak, 2003), whereas Ca^{2+} and Mg^{2+} show no difference between diffusivities parallel to a -, b - and c -axes (Latourrette and Wasserburg, 1998; Faak *et al.*, 2013; Van Orman *et al.*, 2014).

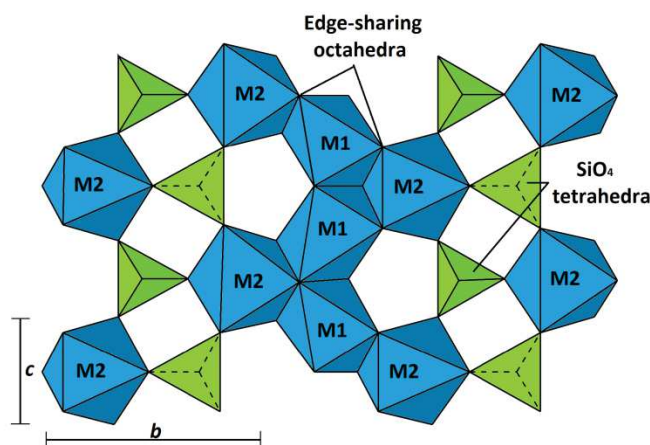


Figure I.46 - Crystal lattice structure of olivine parallel to c - b plane; [100] (a) -axis is perpendicular. M1 and M2 are octahedral lattice sites, tetrahedral sites have triangle shape.

Pure forsterite (Fe_{100}) and mantle olivine (Fe_{90-96}) are used in most studies to investigate the dependence of diffusion coefficients on olivine composition (e.g., Petry *et al.*, 2004; Chakraborty, 2010; Cherniak, 2010b; Cherniak and Liang, 2014; Jollands *et al.*, 2014). The increase in Fe from

pure forsterite to Fe-bearing olivine increases the element diffusion coefficients (for example D_{Ni} , Figure I.47). Similarly, element diffusion coefficients of clinopyroxene depend on the Fe content of crystals. Diffusion in the more iron-rich clinopyroxene is faster with lower activation energy compared to that for the near diopside end-member (Van Orman *et al.*, 2001; Cherniak and Dimanov, 2010). In plagioclase, the effect of composition is controlled by the Ca content: element diffusion coefficients are somewhat faster in slightly more anorthitic plagioclase, than those calculated for the albitic component (Cherniak and Watson, 1994; Latourrette and Wasserburg, 1998; Cherniak, 1995, 2002, 2003; Van Orman *et al.*, 2014).

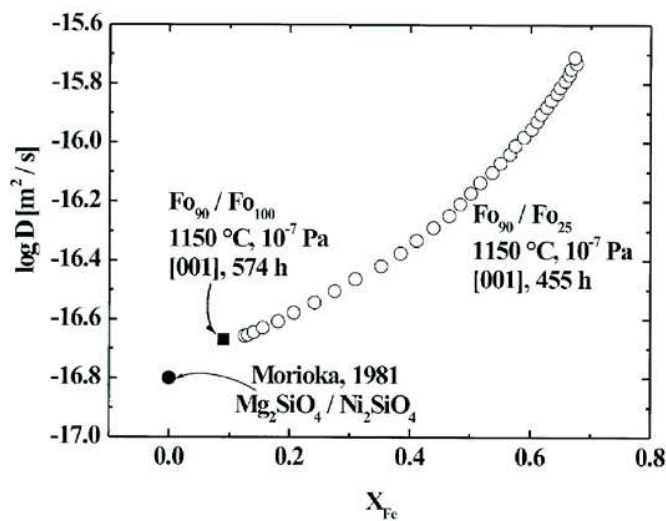


Figure I.47 – Ni diffusion coefficients (logarithmic scale) vs Fe content in olivine (Petry *et al.*, 2004). Note the increase in D_{Ni} with increase of Fe in the crystal.

Ionic radius and charge can also control element diffusion: higher diffusion coefficients are generally found for the smallest cations having the lower charge. For example, Li in olivine can occupy different positions created by point defects due to its small size, thus explaining the fast Li diffusion rates (Dohmen *et al.*, 2010); also, Ni and Fe-Mg show higher diffusion coefficients compared to Ca having respectively smaller and larger ionic radius. While agreement in literature is found for diffusion coefficients of divalent cation in olivine (e.g., Dohmen *et al.*, 2007; Petry *et al.*, 2004; Spandler and O'Neill, 2010), diffusivities of 3+ cations (i.e., REE) differ by more than three orders of magnitude (Figure I.48). Spandler and co-workers (Spandler *et al.*, 2007; Spandler and O'Neill, 2010) obtained diffusion coefficients for trace elements (REE and Ti) close to the fast rates for Fe-Mg diffusion (Dohmen *et al.*, 2007), in contrast to findings of Cherniak and co-workers

(Remmert et al., 2008; Cherniak, 2010; Cherniak and Liang, 2014) who obtained REE diffusivities comparable to the slow rates of silicon and tungsten self-diffusion (Cherniak and VanOrman, 2014). The disparity in REE diffusion coefficients may lie on the effect of different compositions of the material used. The basaltic melt used as diffusion source material by Spandler and O'Neill (2010), is doped with 16 trace elements including Al and Ti, which are found to play an important role in the formation of vacancies in olivine crystals, and therefore they enhance diffusion of REE in olivine (Burgess and Cooper, 2013). However, the studies of Spandler *et al.* (2007) and Spandler and O'Neill (2010) most closely resemble a natural system, thus they are probably the most relevant in terms of providing geologically useful trace element diffusion coefficients (Jollands *et al.*, 2016). For this reason, in this thesis, I selected REE diffusion coefficients provided by Spandler and O'Neill (2010) for diffusion modeling.

In clinopyroxene, Ti and Pb diffusion is comparable to diffusion of the middle to heavy REE, but faster than diffusion of light REE, U and Th (Figure I.48; Cherniak, 1998; Van Orman *et al.*, 1998, 2001; Cherniak and Liang, 2012). Furthermore, Ca, Mg and Fe-Mg interdiffusion are somewhat faster than Ti diffusion (Figure I.48; Cherniak and Liang, 2012; Dimanov *et al.*, 1996; Zhang *et al.*, 2010).

Based on these considerations, we selected diffusion coefficients experimentally obtained under the same conditions reported for partition coefficients and at oxygen fugacity on the QFM buffer (corresponding to the upper mantle – lower oceanic crust transition, Herd, 2008). In Appendix 5 we report a database of D together with preferred values. Arrhenius plots for element diffusion coefficients are in Figure I.48 for olivine and clinopyroxene, and Figure I.49 for plagioclase.

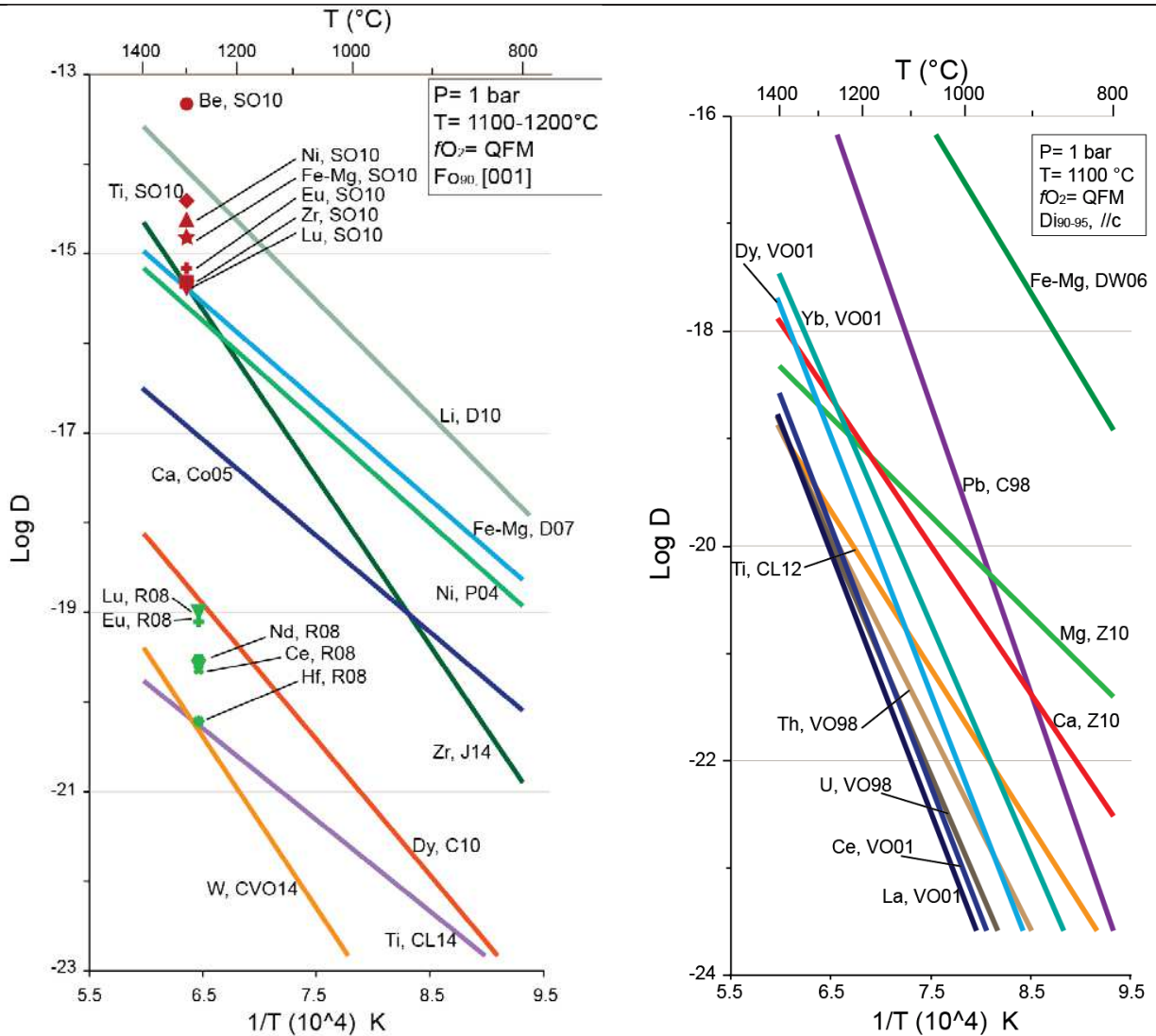


Figure 1.48 – Arrhenius plots of selected diffusion coefficients in olivine (left) and clinopyroxene (right) at constant pressure, temperature, oxygen fugacity, composition, and at anhydrous conditions. Diffusion in olivine is anisotropic: here we report diffusion coefficients calculated along the *c*-axis [001], being the “fastest” axis. Left: J14: Jollands et al. (2014); CL14: Cherniak and Liang (2014); CVO14: Cherniak and Van Orman (2014); SO10: Spandler and O’Neill (2010); C10: Cherniak (2010a); R08: Remmert et al. (2008). D10: Dohmen et al. (2010). D07: Dohmen et al. (2007); Co05: Coogan et al. (2005); P04: Petry et al. (2004). Right: CL12: Cherniak and Liang (2012); Z10: Zhang et al. (2010); DW06: Dimanov and Wiedenbeck (2006); VO01: Van Orman et al. (2001); C98: Cherniak (1998); VO98: Van Orman et al. (1998).

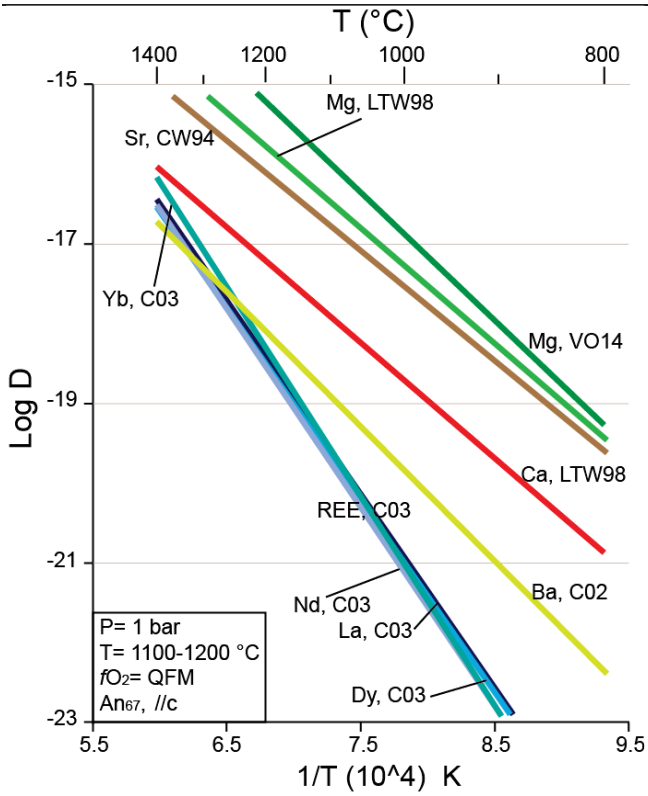


Figure 1.49 - Arrhenius plot of selected diffusion coefficients in plagioclase at constant pressure, temperature, oxygen fugacity, composition, and at anhydrous conditions. VO14: Van Orman et al. (2014); C03: Cherniak (2003); C02: Cherniak (2002); LTW98: Latourrette and Wasserburg (1998); CW94: Cherniak and Watson (1994).

Chapter II

Analytical methods

1. Introduction

Analytical methods implemented in this study include microstructural observations and measurements, petrological analyses as well as bulk rock and *in situ* geochemical analyses. Three main studies were conducted in parallel: a detailed petro-geochemical study of samples collected at Atlantis Massif (30°N, Mid-Atlantic Ridge), bulk-rock analyses of gabbros from Atlantis Bank (32°S, SW Indian Ridge), and geochemical (bulk and *in situ*) analyses of selected minerals to develop new standards for high quality *in situ* geochemical data. Methods will be introduced for each study case in this Chapter, and analyses of standard minerals are treated separately in Chapter section 5 ('Attempt to develop new standards adapted to high quality *in situ* geochemical data').

Microstructural and *in situ* petro-geochemical analyses were performed on samples collected at Atlantis Massif, after careful characterization of textures by Optical Microscopy. *In situ* analytical measurements were performed following a specific order to minimize loss of sample for successive analyses. Polished thin sections were first analysed by Electron Backscattered Diffraction (EBSD) non-destructive technique for microstructural analyses to identify heterogeneous textures, deformed and undeformed crystals. At this stage, regions of interest were selected for petro-geochemical analyses. Thin sections were then carbon coated and chemical measurements were done with non-destructive Electron Probe Micro Analyser (EPMA). Geochemical analyses were finally performed by partially destructive Laser Ablation Inductively Coupled Plasma Mass Spectrometer (LA-ICP-MS). An important feature of our analytical strategy is the choice of a single thin section per sample for all analyses. This avoids uncertainties related to 3D geometrical structure of crystals, which might result in different crystals analysed (and therefore not comparable) over the whole analytical procedure. Petro-geochemical analyses were performed along profiles across different phases. Profiles were done along preferred directions selected parallel to (at least) one of the three principal crystallographic axis of olivine, as defined after microstructural analyses. Generally one axis per olivine grain was selected. Only a few grains have two perpendicular axes parallel to the sample surface: when possible chemical profiles were analysed along both directions. Interstitial phases were analysed along the same profile, in prolongation of the preferred direction in adjacent olivine crystals. Generally, olivine-clinopyroxene and olivine-plagioclase couples were preferred over single olivine grains, in order to

investigate (dis)equilibrium between olivine and neighbouring phases. Olivines were selected after microstructural analyses on the basis of 4 to 6 olivine grains per sample, representative of the textures observed in thin section. Plagioclase, clinopyroxene and, when present, orthopyroxene were selected adjacent to olivine grains. For samples where these phases do not exceed the 10% modal fraction (e.g. 305-U1309D-248R-2W, 22-24cm) and, therefore, olivines are often in contact with other olivine grains, clinopyroxene, plagioclase and orthopyroxene were selected in the closest site to measured olivine. We selected an equal number of olivine in contact with plagioclase and clinopyroxene when possible. Element concentrations were mainly determined from rim_{phase A} to rim_{phase B}; a few profiles were analysed from core_{phase A} to core_{phase B}.

Samples were carefully selected in the least possible altered cores. Core intervals with alteration > 15% were discarded for this study. Oriented thin section billets were available from shipboard sampling during IODP Expeditions 304/305, and additional billets were taken on-shore at IODP Bremen Core Repository (Germany).

Bulk rock compositions were determined for samples of drilled core collected during Expedition 360 at Atlantis Bank. Samples were selected on board among the most fresh intervals, having total alteration <5%. Quarter-core samples of 5 cm to 7 cm length were cut in order to have a representative volume of rock, considering the coarse grain size characteristic of gabbros recovered. Analyses were done by Inductively Coupled Plasma Mass Spectrometer (ICP-MS).

2. Sample preparation

Thin sections

Thin section preparation had to satisfy two requirements: high quality polished surface and appropriate thickness to perform all analyses on the same thin section surface per sample. Thin sections were realized by Christophe Nevado and Doriane Delmas at Geosciences Montpellier. Rock samples exceeding dimensions of 45x30x10 mm were cut. Thin section billets were impregnated with resin under vacuum to avoid holes and reduce surface relief, for about 48 hours. After heating at 50° for 12 hours, the billets were glued to glass stages and levelled in two steps with silicon carbide, first with 220 grit until flat surface was obtained and second with 500 grit for 5 minutes. Thick thin sections of about 100 µm were realized to be thick enough for La-ICP-MS

geochemical analyses. Polishing was done in different steps of 6 μm , 3 μm , 1 μm , 0.25 μm with diamond paste for 45 minutes each. High quality polished surfaces were obtained by an additional preparation step using Chemical-mechanical polishing (CMP). For this a 10 nm silicon particle saturated colloidal NaOH alkaline polishing fluid (SYTON method of Fynn and Powell, 1979) was used for 40-45 minutes.

Rock powders

Powders for bulk rock analyses of drilled core samples were prepared from 40-50 cc sample volume. One slice of 1 cm per sample was conserved for thin section preparation before the procedure of powder griding.

Surface contamination from off-shore drilling operations was first removed by polishing the external sample surface. About 0.5 - 1 mm of material on sample surface was eliminated. Samples were then cut in 0.5 cm slices, placed in sample plastic bag and material was reduced to millimetric cubes by hitting with hammer. The millimetric cubes of sample were grinded at decreasing granulometry (from 2 mm down to 10 μm) with a FRITSCH Agate Mortar Grinder PULVERISETTE 2 to obtain a fine homogeneous powder. Grinding was done in three steps of 15 minutes for each sample. At each step, powder was removed from the mortar and mixed on weighing paper to avoid selected grinding of finer granulometry. The Agate mortar was cleaned three times with Ethanol and let dry before each grinding session.

3. Microstructural and Petrological study

3.1 Microstructural analyses

In this work, the term microstructure describes both morphological textures in terms of dimension and shape of grains, and the distribution of crystallographic axes (crystallographic preferred orientations, CPO) in the rock sample. Microstructures were analytically characterized by using the Electron Backscattered Diffraction (EBSD) technique. EBSD analyses allow defining and quantifying the different structural features at the scale of single crystals. EBSD patterns are

produced by an interaction of electrons with the top few nanometres of sample surface; therefore thin sections are not carbon-coated and must be carefully polished to avoid surface damage and optimize the quality of diffraction patterns.

We performed EBSD analyses using a Scanning Electron Microscope (SEM) JEOL JSM 5600, and a Field Emission Gun (FEG) CamScan X500FE CrystalProbe, both available at Geosciences Montpellier (Université de Montpellier).

Electron Backscattered Diffraction facilities and analytical conditions

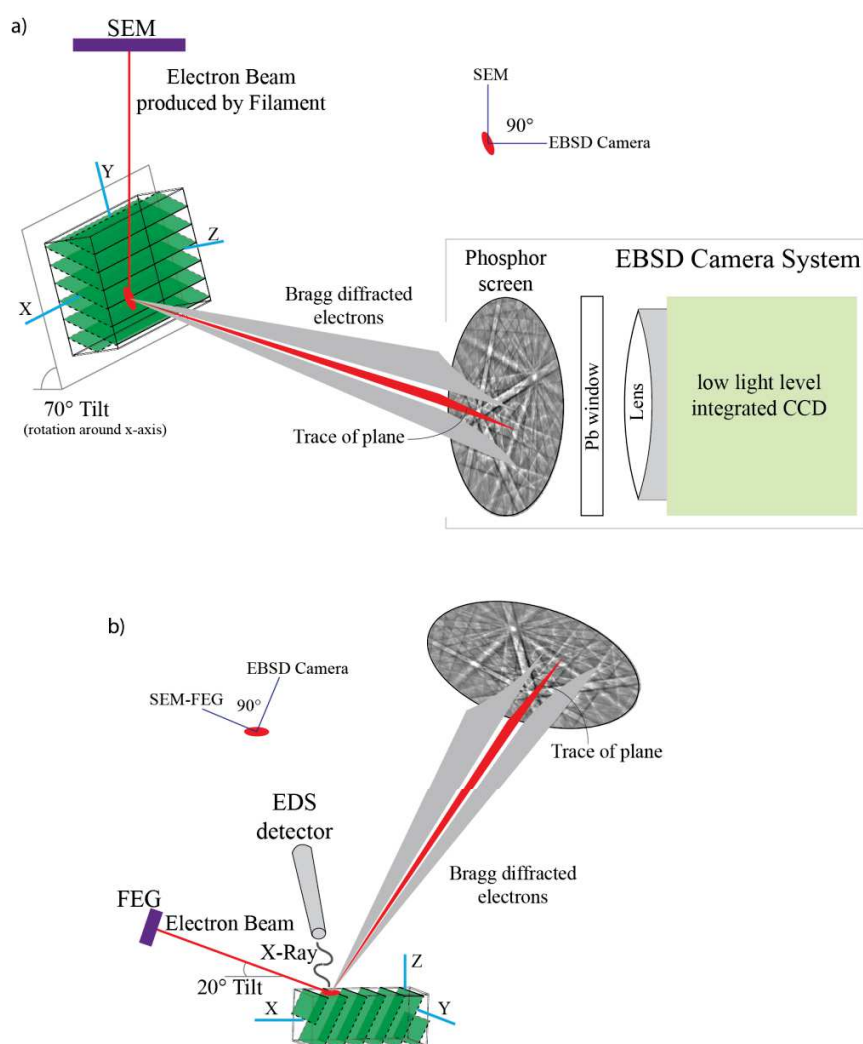


Figure II.1– Schematic representation of EBSD facilities: a) SEM-EBSD JEOL JSM 5600 setting; b) Field Emission Gun (FEG) CamScan X500FE CrystalProbe. The EBSD Camera System reported in a) is installed in both facilities, and composed of a phosphorous screen to detect the Kikuchi patterns, protective lead glass window, lens and low light level integrating CCD camera.

The Electron Backscattered Diffraction (EBSD) technique is an automated microstructure (crystallographic orientations) acquisition equipment installed on scanning electron microscopes (SEMs). Electrons are generated and accelerated in the electron source of SEM. The electrons produced pass through a combination of lenses and apertures to produce a focused beam of electrons that hits the sample surface. EBSD operates by detecting diffracted electrons produced by interaction of the primary electron beam with the crystal lattice. The diffracted electrons form two symmetric cones, the Kikuchi diffraction cones that are detected by a phosphor screen (Figure II.1) installed in the EBSD camera detector. The crystal lattice, unique for each phase, governs the geometry of the Kikuchi diffraction cones producing unique patterns for single minerals analysed.

The formation of diffraction patterns is described by Bragg's Law:

$$n\lambda = 2d \sin \theta$$

where λ is the wavelength of the electron beam energy (correspondent to accelerating voltage), d is the distance between lattice planes, being specific for a certain crystal lattice, and θ (Bragg angle) is the diffraction angle (Figure II.2). Maximum intensity in the diffraction pattern is achieved by capturing the most intense fraction of inelastically scattered electrons, which is obtained by a tilted specimen surface at low angle. An angle of 20° between the electron beam and the sample surface is set, as lower incidence angles would decrease the spatial resolution. The geometry of SEM-EBSD facilities focus the electron beam on the sample surface at low incident angle, resulting in small θ . The small Bragg angle (typically less than 1°) flattens the plane of Kikuchi diffraction cones that appear to be a pair of nearly straight lines, forming the Kikuchi patterns (e.g., Schwarzer, 1997). The signal is recorded and transformed in an image by the

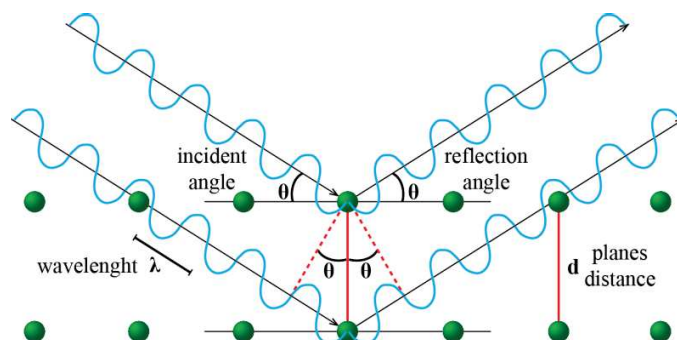


Figure II.2– Schematic representation of Bragg's Law describing the interaction between incident electrons and atoms in the analysed material. Bragg's Law describes the formation of Kikuchi lines in an EBSD diffraction pattern.

EBSA Camera System, a Phototonic Science CoolView CCD, installed perpendicular (90°) to the incident electron beam, with an angular resolution of 0.3°. The image is then analysed by the Oxford Instruments AZtec HKL Acquisition system.

For this study two SEM-EBSA facilities were used: the JEOL JSM 5600 and CamScan X500FE CrystalProbe, both equipped with a digital CCD camera. The analytical differences between the two instruments are given by the type of electron source in each Scanning Electron Microscope, changing the spatial resolution of the instrument. Best spatial resolution depends on the efficiency of the electron source, defined by the beam brightness.

The electron source of JEOL JSM 5600 is a tungsten filament heated at high temperature (~2800 K) that produces an electron beam by thermoelectric effect under vacuum conditions ($<10^{-5}$ Pa). The SEM column is vertical, and the sample stage is tilted at 70° from the horizontal to satisfy the 20° angle between the electron beam and the sample surface (Figure II.1). Analyses were performed at operating conditions of 17 kV accelerating voltage and 0.5 nA beam current, and vacuum condition of the order 10^{-4} Pa.

The CamScan X500FE CrystalProbe is a Field Emission Gun (FEG) - SEM that works with a reduced beam diameter for better beam brightness. Electrons are emitted by an intense electric field applied on a heated (1800 K) tungsten fine tip covered with zirconium oxide ZrO, using the « Schottky » effect. Higher vacuum conditions ($<10^{-7}$ Pa) are needed in the FEG-SEM column. The sample holder is set horizontal in the CrystalProbe, with FEG tilted at 20° to the horizontal (Figure II.1). The tilted column geometry allows a natural division of the column into a domain of high vacuum where electrons are produced, and a lower domain for heated sample stage of low vacuum. Better spatial resolution of 10 nm is obtained with the FEG, compared to a few microns in standard SEMs. The CrystalProbe is equipped with an Energy-Dispersive X-Ray Spectroscopy (EDS) X-MaxN 20mm² detector for qualitative chemical analyses (Figure II.1). Analyses with CrystalProbe were set at operating conditions of 15 kV accelerating voltage, 3.5 nA beam current and a working distance of 20mm under low vacuum conditions (4-5 Pa of gaseous Nitrogen). Good data quality of EBSA analyses are achieved at high hit rates (Element concentrations were recorded during analyses with CrystalProbe. Chemical maps of thirteen elements were collected including C, Na, Mg, Al, Si, S, Cl, K, Ca, Ti, Cr, Mn, Fe and Ni. The AZtec HKL Acquisition system processes single elements chemical maps for the whole area analysed.

Areas of ~ 30x20 mm were scanned for each sample covering almost the entire surface of the thin section. Different sampling step sizes ranged between 13.5 μm for the most altered to 28 μm for the most preserved samples (Table II.1), as a function of the crystal fragments size in single grains. Indexed phases were spinel, olivine, clinopyroxene, plagioclase, orthopyroxene, pargasite, pyrrhotite and chalcopyrite. Generally, pargasite, pyrrhotite and chalcopyrite were present in low modal fractions (ca. 1%) and appear as small grains that were removed during data processing.

Table II. 1 – Sampling step sizes for EBSD analyses.

Sample IODP	Lithology	Depth (mbsf)	Step size (μm)
305-U1309D-227R-3W, 124-126	Olivine-rich Troctolite	1096.17	13
305-U1309D-232R-1W, 116-120	Olivine-rich Troctolite	1116.26	27
305-U1309D-234R-1W, 22-26	Olivine-rich Troctolite	1124.97	15
305-U1309D-241R-2W, 89-91	Olivine-rich Troctolite	1160.66	19
305-U1309D-247R-3W, 16-18	Olivine-rich Troctolite	1190.05	20
305-U1309D-247R-3W, 22-25	Olivine-rich Troctolite	1190.11	28
305-U1309D-247R-3W, 62-66	Olivine-rich Troctolite	1190.51	25
305-U1309D-247R-3W, 76-81	Olivine-rich Troctolite	1190.65	17
305-U1309D-248R-1W, 110-113	Olivine-rich Troctolite	1193	28
305-U1309D-248R-2W, 18-21	Olivine-rich Troctolite	1193.32	20
305-U1309D-248R-2W, 22-24	Olivine-rich Troctolite	1193.36	13.5
305-U1309D-248R-2W, 38-41	Olivine-rich Troctolite	1193.52	30
305-U1309D-248R-2W, 43-48	Olivine-rich Troctolite	1193.57	17
305-U1309D-248R-3W, 29-32	Olivine-rich Troctolite	1194.78	18
305-U1309D-248R-3W, 36-38	Olivine-rich Troctolite	1194.85	25
305-U1309D-248R-3W, 131-134	Olivine-rich Troctolite	1195.8	16
305-U1309D-268R-2W, 83-85	Troctolite	1290.06	23

Data reduction and quality

EBSD data were processed using the CHANNEL5 software from Oxford Instruments HKL. The first stage of post-acquisition data processing consisted of removing isolated single pixels (wild spikes) that are either non-indexed or indexed as a given phase and surrounded by pixels indexed for another phase. The second stage allowed increasing the indexation rate by filling automatically the non-indexed pixel having up to 8 neighbours with identical orientation, and repeating this operation using, respectively, 7 and 6 identical neighbours. At each step, the resulting orientation maps were verified to avoid over-extrapolation of the data. For each olivine crystals systematic indexation errors were identified and corrected automatically. These errors are related to the hexagonal pseudo-symmetry of

olivine crystal lattice, which results in similar diffraction patterns for orientations differing by a rotation of 60° around [100]. Finally, a minimum threshold of grain dimension was set at 5 pixels in average diameter. Small grains with dimensions inferior to this minimum value were considered analytical errors and removed during data processing.

Indexation rates range from 64 % in most altered samples, to 95 % in the most preserved.

Indexed EBSD data were further processed using MTEX, a comprehensive open-source MatLab® toolbox that provides quantitative microstructure analysis covering a wide range of properties such as crystal preferred orientation modelling and pole figure, grain modelling and anisotropic physical properties (Mainprice et al., 2014). MTEX also provide an estimate of phases modal percentage in each selected sample area.

Single grains were reconstructed after EBSD data by automatically selecting adjacent pixels having misorientations $<10^\circ$. The contact between pixels having $>10^\circ$ misorientations represents grain boundary.

Intra- and inter- granular (mis)orientations were calculated:

- crystallographic orientation defined by the three Euler rotation angles φ_1 , ϕ , and φ_2 that are the angles between the three main axes of a crystal and sample coordinates - φ_1 for a-axis, ϕ for b-axis and φ_2 for c-axis (Bunge, 1982);
- misorientation angles between the orientations of each pixel;
- misorientation of each pixel within single grain to the mean orientation of that same grain (Mis2Mean);
- Kernel Average Misorientation (KAM) that is the average angle of every pixel with its four neighbors;

and grain shape, including:

- the aspect ratio (long axis/short axis) of grains;
- the tortuosity of grain boundaries defined as the shape factor (grain perimeter/ perimeter of an equivalent circle of the same surface).

Phases, orientation/misorientation data and grain shapes were represented in EBSD processed maps as complementary dataset to optical observations. EBSD processed phase maps provide

quantitative phase modal compositions and represent a support to textural description. Defined colours were assigned to determined phases (in this study: yellow for chromite, red for olivine, blue for plagioclase, green for clinopyroxene, light blue for orthopyroxene, pink for magnetite and dark green for pargasite amphibole). Crystallographic orientation maps were used to investigate the occurrence of preferred orientation of single phases or to identify random fabrics.

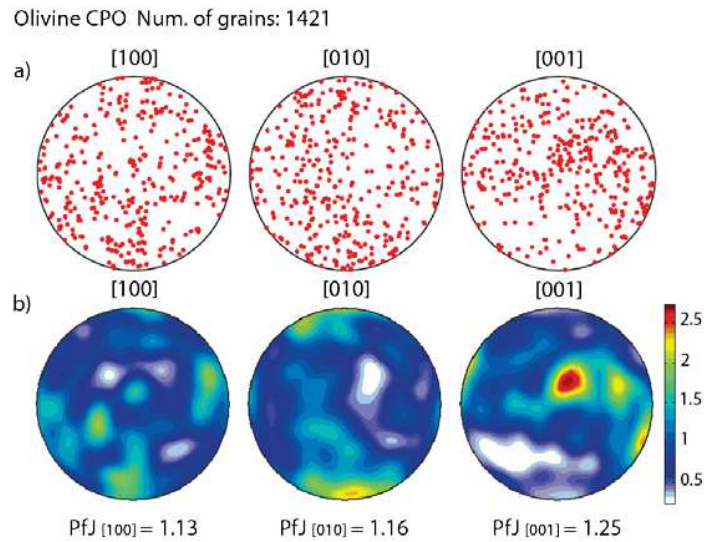


Figure II.3 – Example of olivine crystallographic preferred orientation represented in pole figures. Pole figures are generated as equal-area, lower hemisphere stereographic projection of the orientation of three principal crystallographic axes of all crystals for each phase individually. Single pole figure represents the distribution of one crystal axis. a) scatter plot of crystallographic axes of single grains; b) contoured plots with contour levels in normalized multiples of uniform distribution where relative high concentrations of axis orientation are reported in dark red. PfJ values indicate fabric strength of relative axis.

Crystallographic Preferred Orientation (CPO) data were plotted as pole figures, which show the orientation of each crystal axis relative to sample coordinates (Figure II.3a). CPO pole figures were generated as equal-area, lower hemisphere stereographic projection of the orientation of three principal crystallographic axes of all crystals for each phase individually. The average crystallographic orientation for each grain was preferred to the all-pixels data in order to avoid the overrepresentation of coarse grains. The CPO strength is quantified by the J index (Mainprice and Silver, 1993) as:

$$J = \int f(g)^2 dg$$

where 'g' is the crystal orientation and $f(g)$ is the orientation distribution function (ODF). The ODF represents the volume fraction of crystals with orientation 'g' calculated in a given orientation range (Michibayashi and Mainprice, 2004; Mainprice et al., 2014). The J-index varies from 1 for uniform crystallographic distributions, to infinitely large values for a single preferred orientation. Representative CPOs require at least 100 – 150 grains measured (Ben Ismaïl and Mainprice, 1998), which in this study was satisfied for olivine exclusively.

Fine scale microstructural heterogeneities in single samples and grains were investigated by quantitative analyses of misorientation angles and rotation axes. The distribution of misorientation angles was represented in misorientation histogram, where angles $< 2^\circ$ were considered as background noise. The preferred orientation of rotation axes was plotted in the crystal reference frame as Inverse pole figures (IPF) for each phase. IPF were produced for misorientations in the range 2° - 10° (i.e., above the noise threshold and below the grain boundary threshold). IPF and CPO were plotted as contoured diagrams with contour levels in normalized multiples of uniform distribution, which gives quantitative informations (Figure II.3b).

Selection of crystallographic axes for chemical analyses

Olivine grains for chemical analyses, and relative principal crystallographic axes, were identified using EBSD processed data.

Misorientation maps were produced to identify deformed and undeformed crystals. The Mis2Mean maps highlight domains with different orientations in single crystals, whereas KAM maps locate subgrain boundaries (Figure II.4). We considered as deformed crystals those grains characterized by misorientated bands separated by lines identified by KAM analyses.

EBSD crystallographic orientation maps of olivine were evaluated to select a subset of olivine crystals having at least one of the three principal crystallographic axes parallel to the sample surface.

The principal crystallographic axes of olivine ([100], [010], [001]) were identified from single grain analyses (Figure II.4). We reconstructed single grains of whole specimens by using MTEX MatLab® toolbox. This allowed us to automatically select single grains and plot their orientation on pole figures for each main crystallographic axis. Each principal crystallographic axis of a crystal is 90

defined by eigenvectors, vectors that represent the three principal components (Eigen vector 1, 2, 3 with relative eigenvalue E1, 2, 3) of the orientation tensor. The eigenvector corresponding to the biggest eigenvalue (Eigen vector 1 – E1) of each pole figure represents the orientation of the relative crystallographic axis in sample coordinates. E1 was calculated for [100], [010] and [001]. Generally one axis per olivine grain was found parallel to the sample surface. E1 plunge and azimuth of selected axis represent the preferred direction for geochemical profile analyses. All grains having axes plunge higher than 5° were discarded as considered not parallel to the sample surface. Only a few grains have two perpendicular axes parallel to the sample surface: when possible chemical profiles were analysed along both directions to investigate anisotropy of chemical composition profiles in olivine.

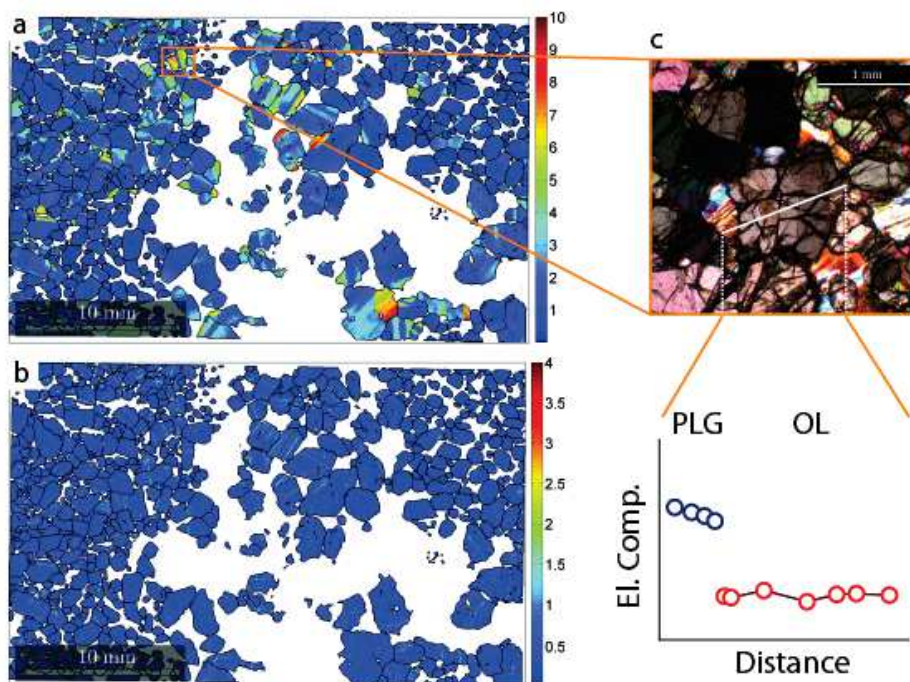


Figure II.4 – Example of EBSD processed maps used for grain selection protocol. a) Mis2Mean map: colours represent the misorientation angle of a pixel to the mean orientation of the relative grain; colour bands in single grain indicate kink bands. b) KAM map: colours represent the orientation angle of a pixel to the mean orientation of the neighbouring pixels; coloured lines indicate subgrain boundaries. c) Optical Microscope image of olivine in contact with interstitial plagioclase; the white line indicate the orientation of one crystallographic axis of olivine parallel to the sample surface. Along this preferred direction a geochemical profile is performed (red dots for olivine and blue for plagioclase).

3.2 Mineral major element analyses

Major element mapping, *in situ* and traverses major element analyses were performed by Electron Probe Micro Analyser (EPMA) CAMECA SX100 at Geosciences Montpellier (Université de Montpellier).

Electron Probe Micro Analyser

EPMA works by detecting the X-ray emitted by the interaction of incident electrons with atoms forming the analysed material. Electrons are produced by heated (2700°K) tungsten filament cathode located on top of the electron column (also referred to as “gun”) set vertically and perpendicular to the sample surface. A micro-volume of sample is bombarded by the accelerated and focused electron beam of 0.5-1 μm diameter. The collision of electrons produces interactions with atoms in the first μm thickness of sample surface. No material is removed from the sample surface. These atoms are excited and they release energy in terms of X-ray photons, which are characteristic to the elements being analysed. The energy released is quantified by X-ray wave length. Five Wavelength Dispersive Spectroscopy (WDS) spectrometers installed on CAMECA EPMA identify, analyse and quantify X-ray spectra specific of the analysed elements. The spectrometers analyses are based on the Bragg's law (Figure II.2) and use various moveable, shaped monocrystals as monochromators.

Data acquisition

In situ major element concentrations were measured as element oxides including SiO_2 , TiO_2 , Al_2O_3 , Cr_2O_3 , FeO , MnO , MgO , CaO , Na_2O , K_2O and NiO . Element oxides are analysed by specific WDS as following:

- Al, Si and Mg, Na by two Thallium Acid Phthalate (TAP);
- Ca, K by Large Pentaerythritol (LPET);
- Mn, Fe, Ni by Large Lithium Fluoride (LLIF);
- Cr, Ti by Pentaerythritol (PET).

Mapping of major element concentrations (Al, Ca, Fe, Mg, Ti) were performed within areas of ca. 50mm^2 . Areas of interest were selected after EBSD processed maps where heterogeneous textural relationships between phases were observed.

Natural minerals and synthetic oxides are monochromators used as standards for elements analysed. They include respectively silicates as Wollastonite, Albite, Forsterite, Orthoclase, and Al_2O_3 , TiO_2 , Fe_2O_3 , Cr_2O_3 oxides. For Ni and Mn pure metals were applied. Compositions of monochromator standards are reported in Table II.2a. The quality of measured data is verified each morning before sample analyses. Calibration of EPMA is operated on Si, Ca, Fe and results are also reported in Table II.2b (measured element intensity / reference element intensity). Measurements with total oxide percentage lower than 98% and exceeding 101% are related to surface damage such as surface roughness, alteration, or unexpected inclusions, and were excluded.

EPMA analyses were done with 20 kV accelerating potential, 10 nA beam current and 30 s counting times for all elements measured. A subset of selected olivines showing core-rim variations in Ca concentrations were further investigated with higher counting times up to 300 s applied only for Ca. Mapping of major element concentrations were done overnight for best time-to-resolution ratio.

Major element concentrations were determined along profiles across different phases. Profiles were performed along preferred directions selected according to (at least) one of the three principal crystallographic axis of olivine, as defined after EBSD analyses (see Chapter section II.3.1). Major elements chemical profiles were determined by a minimum of 8 analysed points, in grains smaller than 1 mm, and up to 15-18 analyses in coarse grained crystals. Zones for EPMA analyses were carefully selected to discard areas of intense alteration and fractures (Figure II.4). Sites were determined one-by-one optically on images of single grains, along the main crystallographic axis of olivine reported graphically (Figure II.4).

Table II.2a - Compositions of monochromator standards

Silicate Mineral	Si	Ti	Al	Cr	Fe	Mn	Mg	Ca	Na	K	Ni	O
Wollastonite	23.9							34.5				41.32
Albite	31.81		10.08		0.05		0.09	0.45	8.41	0.18		48.86
Forsterite	19.06				7.3	0.11	29.314				0.276	43.94
Orthoclase	30.41		8.99		1.33		0.02	0.02	0.24	14.01		45.75
Al_2O_3			52.92									47.08
TiO_2		59.95										40.05
Fe_2O_3					69.94							30.06
Cr_2O_3				68.42								31.58

Table II.2b - EPMA Calibration operated on Si, Ca, Fe: measured element intensity/reference element intensity per each day of analyses

Day of analyses	Si (SP1)	Ca (SP2)	Fe (SP3)	Ca (SP4)	Si (SP5)
18/08/2015	0.9938	0.9934	0.9988	1.0061	0.9903
18/08/2015	0.9944	0.9934	0.9919	1.0109	0.9905
18/08/2015	0.9949	0.9924	1.0008	1.0152	0.9914
18/08/2015	0.997	0.9927	0.9955	1.011	0.9842
19/08/2015	0.9916	0.9964	0.9956	1.0096	0.9894
19/08/2015	0.9952	0.9944	0.9861	1.0051	0.989
19/08/2015	0.9986	0.9959	0.9922	1.0091	0.9915
19/08/2015	0.9984	0.9939	1.0067	1.0133	0.9902
24/08/2015	0.995	0.9983	0.9974	1.0078	0.9876
24/08/2015	0.994	0.9928	0.9935	1.0118	0.9914
24/08/2015	0.9916	0.9924	0.9992	1.0058	0.9856
24/08/2015	0.996	0.9962	0.9955	1.0071	0.987
08/06/2016	0.9867	0.99	1.0007	0.9965	1.0058
08/06/2016	0.9925	0.9929	0.9982	0.9987	1.0055
08/06/2016	0.9905	0.999	1.0015	0.9958	1.0043
08/06/2016	0.9868	0.9899	0.9953	0.9992	1.009
10/06/2016	0.9868	0.991	1.0007	0.997	1.0086
10/06/2016	0.9921	0.9924	0.9945	0.9965	1.0005
10/06/2016	0.9889	0.9923	1.0005	0.9999	0.9987
10/06/2016	0.9904	0.9909	0.999	0.9971	1.0049
13/06/2016	0.9812	0.9892	0.9936	0.9911	0.9962
13/06/2016	0.9885	0.9899	0.9893	0.996	0.999
13/06/2016	0.9822	0.9885	0.9928	0.9946	0.9982
13/06/2016	0.9896	0.9902	0.9946	0.9998	1.0011
15/06/2016	0.9818	0.9999	1.0064	0.9963	0.996
15/06/2016	0.9795	0.9999	1.0086	0.9992	0.9995
15/06/2016	0.9882	0.9959	1.0005	0.996	0.9898
15/06/2016	0.9872	0.9999	1.0049	1.0039	0.9939
23/11/2016	1.0083	1.0102	0.9927	1.0062	0.9967
23/11/2016	1.0161	1.0009	0.9899	1.0035	0.989
23/11/2016	1.0116	1.0035	0.991	1.0046	0.9891
23/11/2016	1.0004	1.0065	0.9907	1.0144	0.9928
31/01/2017	1.0064	1.002	0.9987	1.0203	1.0131
31/01/2017	1	1.0013	0.999	1.0263	1.0071
31/01/2017	1.0067	1.0019	0.9996	1.0301	1.0063
03/02/2017	0.9937	0.9992	1.0054	1.0246	0.999
03/02/2017	0.9949	1.0081	0.9982	1.0236	1.0144
03/02/2017	0.9982	1.0034	1.0042	1.0312	1.0084
03/02/2017	0.9925	1.0016	1.0002	1.0242	0.997

4. Geochemistry

Concentrations of trace elements of bulk rock and in situ analyses were determined by Inductively Coupled Plasma Mass Spectrometry (ICP-MS). Three different facilities were used based on the material analysed.

Bulk rock analyses were performed with two ICP - quadrupole Mass Spectrometers, the Q-ICP-MS Agilent 7700x at Geosciences Montpellier and the Q-ICP-MS ICAP-Q, Thermo Scientific at HydroSciences Montpellier (Université de Montpellier).

In situ analyses were performed at Geosciences Montpellier (Université de Montpellier) using the Thermo Scientific Element 2XR (eXtended Range) High Resolution - ICP-MS (HR-ICP-MS), coupled with laser ablation (LA) system.

4.1 Inductively Coupled Plasma Mass Spectrometry

ICP-MS technique

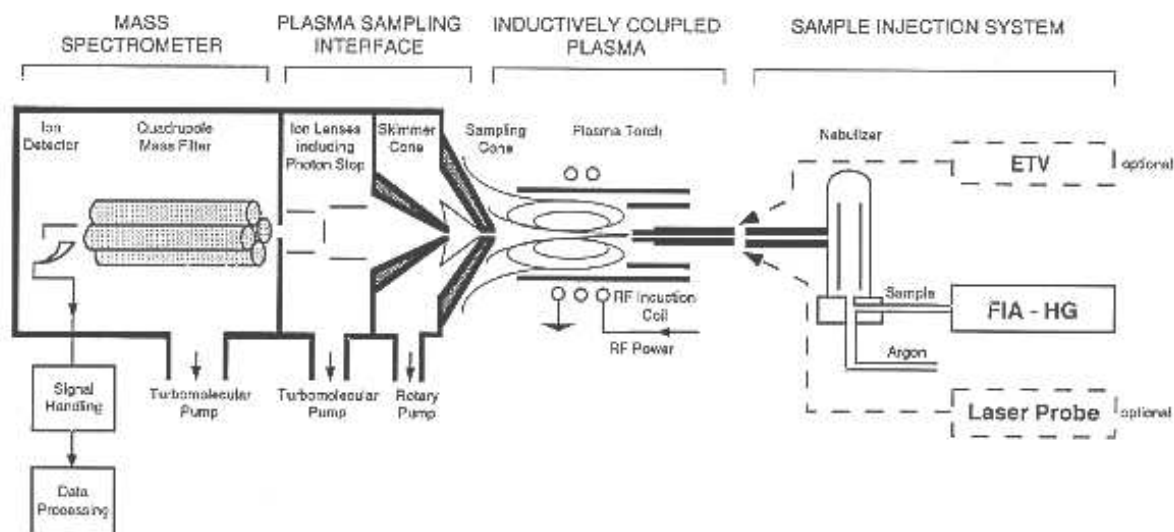


Figure II.5 – Simplified diagram of the ICP-MS instrument. See text for details.

In ICP-MS technique atoms in the sample are isolated by a high temperature plasma source and analysed by the combined mass spectrometer. The ICP-MS instrument is composed by four interconnected cells: the sample injection system, the Inductively Coupled Plasma (ICP), the plasma sampling interface and the mass spectrometer (Figure II.5).

Sample injection system and ICP

The sample is introduced into the ICP-MS instrument as an aerosol. The material is transferred through argon or helium (see Table.II.3 for detail on gas used) in a nebulizer chamber, where elements are converted into gaseous atoms. Drops of the produced aerosol condensate on the chamber wall, and only particles within 12 µm are transmitted to the plasma in order to obtain best ionization of the sample.

The ICP consists of plasma torch where Ar gas flows through a concentric quartz tube (torch). The plasma is produced by an intense electromagnetic field maintained by the high radio frequency (RF) generator. Temperatures in the centre of the plasma torch are maintained between 6000 °C and 8000°C for total ionization of atoms. The interaction with the plasma converts the gaseous atoms from the sample to positively charged ions.

Plasma sampling interface and mass spectrometer

The positively charged ions produced in the plasma are directed into the mass spectrometer via the plasma sampling interface (Figure II.5). This region consists of two metallic cones (usually made of nickel), called 'sampler' and 'skimmer cones'. The interface cones sample the centre portion of the ion beam coming from the ICP torch through small holes (~1mm, one per cone). This feature represents a limitation in terms of amount of total dissolved solids in the sample, which should not exceed 0.2% of total dissolved solids for best instrument performance and stability. In the interface region ions are transported from the plasma, which is at atmospheric pressure to the mass spectrometer analyser region at approximately 10^{-5} mbar. Positive ions are then extracted by the

Table II.3 – Measured elements and their masses in bulk rock and in situ analyses. For bulk analyses by Q-ICP-MS the gas used in the injection system is reported for each element.

Element mass	Bulk analyses		In situ analyses
	Q-ICP-MS		HR-ICP-MS
	Element	Gas flux	Element
7	Li	Ar	Li
11			B
29			Si
43			Ca
45	Sc	He	Sc
47	Ti	He	Ti
49	Ti	He	Ti
51	V	He	V
52	Cr	He	Cr
53	Cr	He	Cr
55	Mn	He	Mn
59	Co	He	Co
60	Ni	He	
62	Ni	He	Ni
63	Cu	He	Cu
65	Cu	He	
66	Zn	He	Zn
67	Zn	He	
68	Zn	He	
69	Ga	He	
71	Ga	He	
75	As	He	
85	Rb	Ar	Rb
86	Sr	Ar	
88	Sr	He	Sr
89	Y	Ar	Y
90	Zr	Ar	Zr
93	Nb	Ar	Nb
110	Cd	Ar	
112	Cd	Ar	
117	Sn	He	
118	Sn	He	
121	Sb	He	
123	Sb	He	Sb
133	Cs	Ar	Cs
137	Ba	Ar	Ba
138	Ba	Ar	
139	La	Ar	La
140	Ce	Ar	Ce
141	Pr	Ar	Pr
146	Nd	Ar	Nd
147	Sm	Ar	Sm
151	Eu	Ar	Eu
157	Gd	Ar	Gd
159	Tb	Ar	Tb
163	Dy	Ar	Dy
165	Ho	Ar	Ho
167	Er	Ar	Er
169	Tm	Ar	Tm
173	Yb	Ar	Yb
175	Lu	Ar	Lu
178	Hf	Ar	Hf
181	Ta	Ar	Ta
182	W	Ar	
183	W	Ar	
208	Pb	Ar	Pb
232	Th	Ar	Th
238	U	Ar	U

'extraction lens' that is at negative potential (- 8000 V), and conducted through the ion optics to focus and accelerate the ion beam.

Once the ions enter the mass spectrometer, they are separated by their mass-to-charge ratio. ICP-MS used for this study differ in the type of mass spectrometer installed, the quadrupole mass filter and magnetic sector.

Quadrupole ICP-MS

Trace element concentrations in bulk analyses were determined by Quadrupole ICP-MS (Q-ICP-MS). Quadrupole mass spectrometer consists of four cylindrical rods of the same length and diameter. The alternating voltages applied on the rods allows selection of ions by mass-to-charge ratio at a given instant in time, while the others are ejected from the quadrupole. This scanning process is then repeated for another analyte at a completely different mass-to-charge ratio until all the analytes in a multielement analysis have been detected. Both Q-ICP-MS used have mass resolution ($m/\Delta m$) of 1 u . The selected ions are detected by a discrete dynode detector (Secondary Electron Multiplier, SEM) and converted into an electrical signal. This signal is processed as number of counts per second and converted into element concentration using ICP-MS calibration standards.

High Resolution - ICP-MS

High Resolution - ICP-MS (HR-ICP-MS) Thermo Scientific Element 2XR was applied for *In situ* trace element analyses. The mass spectrometer of Thermo Scientific Element 2XR is based on double-focusing magnetic-sector mass technology. It consists of a magnetic sector that reduces the effect of interferences by mass overlap, and an electric multiplier detector.

The ion beam is first focused by the quadrupole and then transmitted to the magnetic sector where ions and molecules are first separated based on their mass ($m/\Delta m$). The selected ions are further separated by the electric multiplier based on their charge. This detector is a high count rates Faraday cup type detector (high sensibility extended to 10^9 cps) that can be used at different mass resolutions from low ($R=300$), to medium ($R=4000$) and high ($R=10000$), which allows

increasing the resolution of the instrument by reducing the size of the ion beam. The fact that Faraday cup exhibits no mass discrimination is an advantage in high precision measurements, as it is able to analyse ions of different masses in a single analytical run. A suppressor plate installed in the Faraday cup reduces error of measurements related to losses due to the incident ions. Finally, the selected ions are detected by the monocollector Secondary Electron Multiplier that measure elements in counts per second, which are function of the element concentration in the sample.

The HR-ICP-MS is coupled to a laser ablation (LA) system consisting of a Microlas (Geolas Q+) automated platform with a 193 nm Excimer Compex 102 laser from LambdaPhysik for *in situ* trace element composition analyses. The laser beam is focused on the sample surface to generate fine particles by ablation process. The Excimer Compex 102 laser has high quality ablation and form a vertical crater with a flat base. The ablated volume depend on the spot diameter: for spot size set at 77 μm , a volume of ca. $10^5 \mu\text{m}^3$ is ablated. Ablation analyses were performed using an in-house modified 30 cm³ ablation cell with a helium atmosphere to enhance sensitivity and reduce inter-element fractionation (Günther and Heinrich, 1999). The helium gas and ablated sample material are then mixed with argon gas in the sample injection system and nebulized before entering the plasma.

Interferences

The spectroscopic interferences are caused by the formation of poly-atomic ions (interfering species) having the same nominal mass as the isotope of interest (Evans and Giglio, 1993). Poly-atomic species having a difference of 0.1 amu mass-to-atomic charge with the isotope of interest cause an erroneously large concentration signal of the element analysed. Interfering species form in the ICP by interaction of plasma gas argon with certain elements, but also oxygen and hydrogen are involved. The sources of interfering elements can be the chemical composition of the introduced material to be analysed, the acid used for sample preparation and the plasma gas itself. Therefore, the formation of spectroscopic interferences strictly depends on the nature of the rock matrix or on the procedure of sample preparation where HCl and HNO₃ acids are used. The most common, and relevant for this study, spectroscopic interferences encountered in ICP-MS analyses are reported in Table II.4; we refer to May and Wiedmeyer (1998) for a complete list of interferences.

Table II.4 – Common spectroscopic interferences encountered during ICP-MS analyses. Sources of interfering elements refer to rock = rock matrix, acid = acid used during sample preparation, gas = plasma gas Ar.

Interfered isotope	Interference ions and molecules	Source
⁷⁵ As	⁴⁰ Ar ³⁵ Cl ⁺ , ⁵⁹ Co ¹⁶ O ⁺ , ³⁶ Ar ³⁸ Ar ¹ H ⁺ , ³⁸ Ar ³⁷ Cl ⁺ , ³⁶ Ar ³⁹ K, ⁴³ Ca ¹⁶ O ₂ , ²³ Na ¹² C ⁴⁰ Ar, ¹² C ³¹ P ¹⁶ O ₂ ⁺	Rock, gas
⁴⁰ Ca	⁴⁰ Ar ⁺	Gas
⁴² Ca	⁴⁰ Ar ¹ H ₂	Gas
⁴³ Ca	²⁷ Al ¹⁶ O ⁺	Rock
¹¹⁰ Cd	³⁹ K ₂ ¹⁶ O ⁺	Rock
¹¹¹ Cd	⁹⁵ Mo ¹⁶ O ⁺ , ⁹⁴ Zr ¹⁶ O ¹ H ⁺ , ³⁹ K ₂ ¹⁶ O ₂ ¹ H ⁺	Rock
¹¹² Cd	⁴⁰ Ca ₂ ¹⁶ O ₂ , ⁴⁰ Ar ₂ ¹⁶ O ₂ , ⁹⁶ Ru ¹⁶ O ⁺	Rock, gas
¹¹³ Cd	⁹⁶ Zr ¹⁶ O ¹ H ⁺ , ⁴⁰ Ca ₂ ¹⁶ O ₂ ¹ H ⁺ , ⁴⁰ Ar ₂ ¹⁶ O ₂ ¹ H ⁺ , ⁹⁶ Ru ¹⁷ O ⁺	Rock, gas
⁵² Cr	³⁵ Cl ¹⁶ O ¹ H ⁺ , ⁴⁰ Ar ¹² C ⁺ , ³⁶ Ar ¹⁶ O ⁺ , ³⁷ Cl ¹⁵ N ⁺ , ³⁴ S ¹⁸ O ⁺ , ³⁶ S ¹⁶ O ⁺ , ³⁸ Ar ¹⁴ N ⁺ , ³⁶ Ar ¹⁵ N ¹ H ⁺ , ³⁵ Cl ¹⁷ O ⁺	Rock, gas, acid
⁵³ Cr	³⁷ Cl ¹⁶ O ⁺ , ³⁸ Ar ¹⁵ N ⁺ , ³⁸ Ar ¹⁴ N ¹ H ⁺ , ³⁶ Ar ¹⁷ O ⁺ , ³⁶ Ar ¹⁶ O ¹ H ⁺ , ³⁵ Cl ¹⁷ O ¹ H ⁺ , ³⁵ Cl ¹⁸ O ⁺ , ³⁶ S ¹⁷ O ⁺ , ⁴⁰ Ar ¹³ C ⁺	Rock, gas, acid
⁶⁵ Cu	⁴⁹ Ti ¹⁶ O ⁺ , ³² S ¹⁶ O ₂ ¹ H ⁺ , ⁴⁰ Ar ²⁵ Mg ⁺ , ⁴⁰ Ca ¹⁶ O ¹ H ⁺ , ³⁶ Ar ¹⁴ N ₂ ¹ H ⁺	Rock, gas
⁶⁹ Ga	³⁵ Cl ¹⁶ O ¹⁸ O ⁺ , ³⁵ Cl ¹⁷ O ₂ ⁺ , ³⁷ Cl ¹⁶ O ₂ ⁺ , ³⁶ Ar ³³ S ⁺ , ³³ S ¹⁸ O ₂ ⁺	Rock, gas, acid
⁷¹ Ga	³⁵ Cl ¹⁸ O ₂ ⁺ , ³⁷ Cl ¹⁶ O ¹⁸ O ⁺ , ³⁷ Cl ¹⁷ O ₂ ⁺ , ³⁶ Ar ³⁵ Cl ⁺ , ³⁶ S ¹⁷ O ¹⁸ O ⁺ ,	Rock, gas, acid
¹⁷⁷ Hf	¹⁶¹ Dy ¹⁶ O ⁺	Rock
³⁹ K	³⁸ Ar ¹ H ⁺	Gas
⁴⁰ K	⁴⁰ Ar ⁺	Gas
⁴¹ K	⁴⁰ Ar ¹ H ⁺	Gas
⁵⁵ Mn	⁴⁰ Ar ¹⁴ N ¹ H ⁺ , ³⁹ K ¹⁶ O ⁺ , ³⁷ Cl ¹⁸ O ⁺ , ⁴⁰ Ar ¹⁵ N ⁺ , ³⁸ Ar ¹⁷ O ⁺ , ³⁶ Ar ¹⁸ O ¹ H ⁺ , ³⁸ Ar ¹⁶ O ¹ H ⁺ , ³⁷ Cl ¹⁷ O ¹ H ⁺ , ²³ Na ³² S ⁺ , ³⁶ Ar ¹⁹ F ⁺	Rock, gas, acid
⁵⁸ Ni	²³ Na ³⁵ Cl ⁺ , ⁴⁰ Ar ¹⁸ O ⁺ , ⁴⁰ Ca ¹⁸ O ⁺ , ⁴⁰ Ca ¹⁷ O ¹ H ⁺ , ⁴² Ca ¹⁶ O ⁺ , ²⁹ Si ₂ ⁺ , ⁴⁰ Ar ¹⁷ O ¹ H ⁺ , ²³ Na ³⁵ Cl ⁺	Rock, gas, acid
⁶⁰ Ni	⁴⁴ Ca ¹⁶ O ⁺ , ²³ Na ³⁷ Cl ⁺ , ⁴³ Ca ¹⁶ O ¹ H ⁺	Rock, acid
⁶¹ Ni	⁴⁴ Ca ¹⁶ O ¹ H ⁺ , ⁴⁵ Sc ¹⁶ O ⁺	Rock
⁶² Ni	⁴⁶ Ti ¹⁶ O ⁺ , ²³ Na ³⁹ K ⁺ , ⁴⁶ Ca ¹⁶ O ⁺	Rock
²⁰⁶ Pb	¹⁹⁰ Pt ¹⁶ O ⁺	Rock
²⁰⁸ Pb	¹⁹² Pt ¹⁶ O ⁺	Rock
¹²³ Sb	⁹⁴ Zr ¹⁶ O ₂	Rock
⁴⁵ Sc	¹² C ¹⁶ O ₂ ¹ H ⁺ , ²⁸ Si ¹⁶ O ¹ H ⁺ , ²⁹ Si ¹⁶ O ⁺ , ¹⁴ N ² ¹⁶ O ¹ H ⁺ , ¹³ C ¹⁶ O ₂ ⁺	Rock, acid
⁸⁴ Sr	³⁶ S ¹⁶ O ₃ ⁺	Rock
⁸⁶ Sr	⁸⁵ Rb ¹ H ⁺	Rock
¹⁸¹ Ta	¹⁶⁵ Ho ¹⁶ O ⁺	Rock
⁴⁷ Ti	³² S ¹⁴ N ¹ H ⁺ , ³⁰ Si ¹⁶ O ¹ H ⁺ , ³² S ¹⁵ N ⁺ , ³³ N ¹⁴ N ⁺ , ³³ S ¹⁴ N ⁺ , ¹⁵ N ¹⁶ O ₂ ⁺ , ¹⁴ N ¹⁶ O ₂ ¹ H ⁺ , ¹² C ³⁵ Cl ⁺ , ³¹ P ¹⁶ O ⁺	Rock, acid
⁴⁹ Ti	³² S ¹⁷ O ⁺ , ³² S ¹⁶ O ¹ H ⁺ , ³⁵ Cl ¹⁴ N ⁺ , ³⁴ S ¹⁵ N ⁺ , ³³ S ¹⁶ O ⁺ , ¹⁴ N ¹⁷ O ₂ ¹ H ⁺ , ¹⁴ N ³⁵ Cl ⁺ , ³⁶ Ar ¹³ C ⁺ , ³⁶ Ar ¹² C ¹ H ⁺ , ¹² C ³⁷ Cl ⁺ , ³¹ P ¹⁸ O ⁺	Rock, gas, acid
⁵⁰ V	³⁴ S ¹⁶ O ⁺ , ³⁶ Ar ¹⁴ N ⁺ , ³⁵ Cl ¹⁵ N ⁺ , ³⁶ S ¹⁴ N ⁺ , ³² S ¹⁸ O ⁺ , ³³ S ¹⁷ O ⁺	Rock, gas, acid
⁵¹ V	³⁴ S ¹⁶ O ¹ H ⁺ , ³⁵ Cl ¹⁶ O ⁺ , ³⁸ Ar ¹³ C ⁺ , ³⁶ Ar ¹⁵ N ⁺ , ³⁶ Ar ¹⁴ N ¹ H ⁺ , ³⁷ Cl ¹⁴ N ⁺ , ³⁶ S ¹⁵ N ⁺ , ³³ S ¹⁸ O ⁺ , ³⁴ S ¹⁷ O ⁺	Rock, gas, acid
¹⁸² W	¹⁶⁶ Er ¹⁶ O ⁺	Rock
⁶⁶ Zn	⁵⁰ Ti ¹⁶ O ⁺ , ³⁴ S ¹⁶ O ₂ ⁺ , ³³ S ¹⁶ O ₂ ¹ H ⁺ , ³² S ¹⁶ O ¹⁸ O ⁺ , ³² S ¹⁷ O ₂ ⁺ , ³³ S ¹⁶ O ¹⁷ O ⁺ , ³² S ³⁴ S ⁺ , ³³ S ₂ ⁺	Rock
⁶⁷ Zn	³⁵ Cl ¹⁶ O ₂ ⁺ , ³³ S ³⁴ S ⁺ , ³⁴ S ¹⁶ O ₂ ¹ H ⁺ , ³² S ¹⁶ O ¹⁸ O ¹ H ⁺ , ³³ S ³⁴ S ⁺ , ³⁴ S ¹⁶ O ¹⁷ O ⁺ , ³³ S ¹⁶ O ¹⁸ O ⁺ , ³² S ¹⁷ O ¹⁸ O ⁺ , ³³ S ¹⁷ O ₂ ⁺ , ³⁵ Cl ¹⁶ O ₂ ⁺	Rock, acid
⁶⁸ Zn	³⁶ S ¹⁶ O ₂ ⁺ , ³⁴ S ¹⁶ O ¹⁸ O ⁺ , ⁴⁰ Ar ¹⁴ N ₂ ⁺ , ³⁵ Cl ¹⁶ O ¹ O ⁺ , ^{S₂} , ³⁶ Ar ³² S ⁺ , ³⁴ S ¹⁷ O ₂ ⁺ , ³³ S ¹⁷ O ¹⁸ O ⁺ , ³² S ¹⁸ O ₂ ⁺ , ³² S ³⁶ S ⁺	Rock, gas, acid

Interfering species also concern Rare Earth Elements (REE). The REE spectroscopic interferences are well documented and often need specific corrections during the data processing (Table II.5).

Different methods can be applied to overcome the detection of spectroscopic interferences that can degrade the detection limits achieved. They include supplementary instrument equipment and post acquisitions corrections using elemental equations. In most ICP-MS, interferences are filtered in a collision cell, which is placed before the mass spectrometer. In the collision cell, the reaction with helium gas (inert gas that prevents the formation of new interferences) converts the interfering ions to neutral atoms, which are no longer stable in the mass spectrometer and rapidly ejected from the cell. However, the collision cell may not filter all interfering species that are then detected by the mass spectrometer. In order to overcome this problem, the HR-ICP-MS is also equipped with a magnetic sector. The latter discriminates ions based on their atomic mass and, therefore, it separates the isotopes of interest from their isobaric interferences having similar mass-to-atomic charge.

While most interferences are filtered by the instrument during analyses using HR-ICP-MS, analyses performed with Q-ICP-MS need further post-acquisition corrections for certain elements. REE concentrations were corrected in this study by a series of specific equation during data processing (Table II.5). Five calibration solutions were measured in parallel with mineral and rock sample solutions in order to correct after spectroscopic interferences on REE. These solutions include:

- two solutions of different element concentrations containing zirconium (Zr), hafnium (Hf), lead (Pb), thorium (Th), uranium (U), rubidium (Rb), barium (Ba), strontium (Sr), and the Light Rare Earth Elements (from La to Sm) and Heavy Rare Earth Elements (from Er to Lu);
- two solutions of different element concentrations containing the Medium Rare Earth Elements (from Eu to Ho);
- a solution containing praseodymium (Pr), Sm and Eu.

The equations used to correct the interferences for reliable concentration values are reported in Table II.5. Corrected concentrations for each REE are calculated after concentrations of interfering species and a correction factor (I). In turns, the correction factor is calculated after concentration of interfering elements in the calibration solutions as reported in Table II.5.

Table II.5 – Common spectroscopic interferences encountered on REE and Hf during ICP-MS analyses and relative correction equations.

Interfered isotope	Interfering oxide/hydroxide	Correction element	Correction equations	Correction Factor
¹⁵¹ Eu	BaO 135	Ba	$^{151}\text{Eu} = I(151) - ^{135}\text{BaOH} - ^{134}\text{BaOH}$	(Eu/Ba)
¹⁵⁷ Gd	CeOH 140	Ce	$^{157}\text{Gd} = I(157) - ^{141}\text{PrO} - ^{134}\text{CeOH}$	(Gd-Gd/Pr*Pr)/Ce
¹⁵⁷ Gd	PrO 141	Pr		(Gd/Pr)
¹⁵⁹ Tb	NdO 143	Nd	$^{159}\text{Tb} = I(159) - ^{143}\text{NdO} - ^{142}\text{NdOH}$	(Tb/Nd)
¹⁶³ Dy	NdOH 146	Nd	$^{163}\text{Dy} = I(163) - ^{147}\text{SmO} - ^{146}\text{NdOH}$	(Dy-Dy/Sm*Sm)/Nd
¹⁶³ Dy	NdOH 148	Sm		(Dy/Sm)
¹⁶⁵ Ho	SmO 147	Nd	$^{165}\text{Ho} = I(165) - ^{149}\text{SmO} - ^{148}\text{SmOH} - ^{148}\text{NdOH}$	(Ho-Ho/Sm*Sm)/Nd
¹⁶⁵ Ho	SmO149	Sm		(Ho/Sm)
¹⁶⁷ Er	EuO151	Eu corrected	$^{167}\text{Er} = I(167) - ^{151}\text{EuO}$	Er/(Eu-Eu/Ba*Ba)
¹⁶⁹ Tm	EuO153	Eu corrected	$^{169}\text{Tm} = I(169) - ^{153}\text{EuO}$	Tm/(Eu-Eu/Ba*Ba)
¹⁷⁴ Yb	GdO157	Gd corrected	$^{174}\text{Yb} = I(174) - ^{157}\text{GdO}$	Yb/(Gd-Gd/Pr*Pr-Gd/Ce*Ce)
¹⁷⁵ Lu	GdO158	Tb corrected	$^{175}\text{Lu} = I(175) - ^{159}\text{TbO}$	Lu/(Tb-Tb/Nd*Nd)
¹⁷⁸ Hf	TbO159	Dy corrected	$^{178}\text{Hf} = I(178) - ^{162}\text{DyO}$	Hf/(Dy-Dy/Sm*Sm-Dy/Nd*Nd)

4.2 Bulk analyses

Samples for ICP-MS analyses are introduced in a liquid form. Whole rock drill core were first dissolved by multi-acid digestion technique (Ionov et al., 1992; Godard et al., 2000). Screw-top Savillex® Teflon® beakers were used for multi-acid digestion. Digested samples were diluted in order to decrease element concentration to minimum 40 - 70 ppm (ug/mL) for best instrument performance and stability. Dilution factors were previously estimated based on material composition to reach appropriate element concentrations.

Analytical protocol: digestion and dilution procedure

Before digestion, the Savillex® Teflon® beakers were heated at 100°C with 0.25 ml of HClO₄ and 0.75 ml of HF 24 hours, and then rinsed three times with Milli-Q water.

Aliquots of 100 mg of rock powders were separated and placed in Savillex® Teflon® beakers.

Digestion was done by adding a 1:2.5 mixture of perchloric acid (HClO₄) and fluoridric acid (HF), followed by three evaporation steps to remove the remaining HF.

The protocol applied for 100 mg powder is:

- 1 ml HClO₄ + 2.5 ml HF heated at 120 °C for 24h then acids evaporation at 180 °C – 190 °C;
- 0.5 ml HClO₄ + 1 ml HF heated at 120 °C for 24h then acids evaporation at 180 °C – 190 °C;
- 0.5 ml HClO₄ evaporated at 190 °C;
- 0.25 ml HClO₄ evaporated at 190 °C, repeated twice (total acid evaporation is required).

The dry residues of dissolved samples were taken into solution in pure HNO₃ and Milli-Q water, and heated for 30 minutes at 100 °C. The resulting solution was diluted with Milli-Q water to 20.6 ml or 10.3 ml depending on dilution factor. This solution was further diluted for final dilution factors of about 4000 (gabbro bulk rocks).

In and Bi (10 ppb) were added in each sample solution during final dilution and used as internal standards to control instrument drift over the entire period of analyses.

Data acquisition

During ICP-MS measurements all samples were analysed for trace elements (Table II.3). Element concentrations were calculated as average of three runs per analyses.

The suite of samples, standards and calibration solutions was analysed following the procedure in order of analysis:

- multi-element standard solutions (Merck) for external calibration;
- blank 2% HNO₃ solutions to monitor for instrument background;
- chemical blanks undergone the same digestion process as dissolved powder samples, analysed to correct possible contamination during digestion procedure (one blank per five samples was prepared for each digestion protocol).
- digested samples, ca. 8 per analytical series;
- international standards to control the quality of data.

Elemental concentrations were calibrated by Merck solutions, except for Nb and Ta. These solutions were analysed before each series of analyses to optimize the signal and calibrate the mass spectrometer. Niobium (Nb) and Tantalum (Ta) are concentrated in the teflon that compose Savillex® beakers, and leaching of these two elements might occur during ICP-MS analyses. To avoid memory effects due to the introduction of concentrated Nb-Ta solutions in the instrument,

Nb and Ta concentrations were determined by using, respectively, Zr and Hf as internal standards. We used two equations based on the concentrations of Zr and Hf in a calibration solution. This technique is an adaptation to ICP-MS analysis of the method described by Jochum et al. (1990) for the determination of Nb by spark-source mass spectrometry.

For Nb we used the equation:

$$C_{Nb93} = \left(\frac{I_{Nb93}}{I_{Zr90}} \right) \left(\frac{M_{Nb93}}{M_{Zr90}} \right) (C_{Zr90}) \left(RSF_{\frac{Nb}{Zr}} \right)$$

where C_{Nb93} and C_{Zr90} are measured concentrations (ppb) of Nb and Zr in the sample, I_{Nb93} and I_{Zr90} are count per second measurements of masses 93 and 90, $\frac{M_{Nb93}}{M_{Zr90}}$ is the molar mass of ^{93}Nb and ^{90}Zr , and $RSF_{\frac{Nb}{Zr}}$ is the Relative Sensibility Factor. The RSF was calculated after the sensibility factor of Nb and Zr given by the instrument during analyses of calibration solutions.

For Ta we used the equation:

$$C_{Ta181} = \left(\frac{I_{Ta181}}{I_{Hf178}} \right) (C_{Hf178}) \left(RSF_{\frac{Ta}{Hf}} \right)$$

where C_{Ta181} and C_{Hf178} are measured concentrations (ppb) of Ta and Hf in the sample, I_{Ta181} and I_{Hf178} are count per second measurements of masses 181 and 178, and $RSF_{\frac{Ta}{Hf}}$ is the Relative Sensibility Factor for Ta and Hf.

4.3 In situ trace element analyses

In situ trace element LA-HR-ICP-MS analyses were performed on grains previously investigated for major element concentrations. The surface of each thin section was polished to remove carbon coating after EPMA analyses. Trace element concentrations were determined along profiles previously analysed for major element compositions. Sites were carefully selected optically to avoid alteration, fractures and surface defects.

Data acquisition

Olivine, plagioclase, clinopyroxene and orthopyroxene were analysed for trace elements (relative isotopes considered are reported in Table II.3). Ablation analyses were performed using an in-house modified 30 cm³ ablation cell with a helium atmosphere to enhance sensitivity and reduce inter-element fractionation (Günther and Heinrich, 1999). The laser energy density was set to 12-15 J cm² and repetition rate at 8 - 10 Hz. The laser spot size was set to 102-77 µm for olivine, and 77 µm for plagioclase and pyroxenes. A subset of olivines were analysed with a beam size of 51 µm and only compositions of selected trace elements of interest were determined: ⁴⁷Ti, ⁶²Ni, ⁸⁹Y, ⁹⁰Zr, ¹⁴⁶Nd, ¹⁶³Dy and ¹⁷³Yb. Data were collected in time resolved acquisition mode with the background signal collected for 2 min followed by 1 min (480 pulses for 8Hz, 600 pulses for 10Hz) of sample ablation. A second set of analyses were collected with 2.33 min and 40 sec of sample ablation. A reference basalt BIR-1G was used as standard to insure minimal matrix and analytical effects within single series and between runs. An in-house clinopyroxene (Inagli, Siberia) was also analysed as standard to correct for spectroscopic interferences of Heavy (H-) and Medium (M-) REE. Concentrations were calibrated against the NIST 612 rhyolitic glass using the values given in Pearce et al. (1997).

Data reduction

Data were reduced with the GLITTER software package (Van Achterbergh et al., 2001), using the linear fit to ratio method. ²⁹Si for olivine and ⁴³Ca for plagioclase and pyroxenes were used for internal standardization relative to EPMA data. Signals were carefully monitored and data were filtered for spikes on an element by element basis. Analyses with spikes for V, Cr, Cu, Rb, Sr, Ba were discarded as they may indicate the presence of cracks or inclusions. Values that were within 1σ of the detection limit were excluded during data reduction. Additional data treatment allowed removing any points that had more than 50% error in concentration. Elements ¹⁵¹Eu, ¹⁵⁷Gd, ¹⁵⁹Tb, ¹⁶³Dy, ¹⁶⁵Ho, ¹⁶⁷Er, ¹⁶⁹Tm, ¹⁷³Yb, ¹⁷⁵Lu were further corrected to account for the interferences between these elements occurring during measurements (Kalfoun et al, 2002). Correction factors were calculated from mean concentration of reference BIR or clinopyroxene in-house standard on a day bases of analyses.

5. Development of new standards adapted to high quality *in situ* geochemical data

Laser ablation ICP-MS is a powerful technique for the *in situ* analysis of trace element composition of minerals and other geological samples at a fine spatial resolution (tens of micrometres) in microgram per gram detection limits. The increased interest in this instrument and the various applications of the LA-ICP-MS technique lead to the need of standards of different compositions suitable for the diverse materials investigated. The complementary analysis of standards is essential in any LA-ICP-MS measurement to assess the quality instrument calibration and accuracy of analyses, and to assign values of element contents to the analysed material. Reference materials (RMs) are the most commonly used standards and are defined as material or substance sufficiently homogeneous, whose composition is well established (International Organization for Standardization, ISO Guide 33: 2015). Homogeneity of chemical composition is therefore a crucial and fundamental requirement for any material that may be analysed as standard.

Mineral element concentrations measured by LA-ICP-MS are calibrated against synthetic glass standard reference materials (SRMs) of the 600 series (SRM 610–617) of the National Institute of Standards and Technology (NIST). Their chemical composition values are certified and their major element compositions are very different from any geological matrix. NIST 610 and 612 are the most widely used SRMs and have similar concentrations of all trace elements of respectively *ca.* 400 µg/g and *ca.* 40 µg/g (Pearce et al., 1997; Rocholl et al., 1997; Eggins, 2003). On the other hand, the quality of the acquired LA-ICP-MS data is monitored by repeated analyses of secondary standards within single series of measurements. Commonly, geological reference glasses, provided by the United States Geological Survey (USGS), are used to control accuracy and reproducibility of element contents. More specifically, analyses of silicate minerals in this study were monitored with the reference Icelandic basalt BIR-1G, which compositions are well documented by many laboratories using different techniques (GeoRem database available at <http://georem.mpch-mainz.gwdg.de/>). In contrast to NIST glasses, BIR-1G (depleted basalt) and other USGS geological

standards are natural samples. However, the matrices of USGS secondary standards rarely match those of analyzed minerals.

The use of non-matrix matched secondary standards can introduce analytical problems and discrepancies in the quality control of LA-ICP-MS acquired data. This results from both laser- (during sample ablation) and plasma- induced fractionation that are often matrix dependent (e.g. Fryer et al. 1995; Guillonga and Günther 2002; Jackson and Günther 2003; Jochum et al. 2007). Therefore, matrix-matched secondary standards are necessary for accurate LA-ICP-MS quality monitoring. Natural minerals are rarely used as standards due to their inhomogeneous composition, often characterized by micro- or nano- scale inclusions. This makes it challenging to find appropriate homogeneous standards of various types of minerals as those investigated by *in situ* analyses. In-house olivine standards have been recently used by DeHoog et al. (2010). The olivine standard was prepared from one of the investigated samples and its composition was measured by ion probe and LA-ICP-MS.

Table II.6 – Mineral analysed and method used

Mineral	Type/Location	Short name	Analytical methods
Olivine	xenolith/San Carlos	<i>ol SC</i>	EPMA, LA-ICP-MS, ICP-MS
	magmatic	<i>ol M</i>	EPMA, LA-ICP-MS
Clinopyroxene	Inagli Massif (Siberia)	<i>cpx INA</i>	EPMA, LA-ICP-MS, ICP-MS
	diopside glass	<i>diop</i>	EPMA, LA-ICP-MS, ICP-MS
	Cr-diopside	<i>Cr-diop</i>	EPMA, LA-ICP-MS, ICP-MS
	augite/Oman	<i>aug</i>	EPMA, LA-ICP-MS
	diopside/Madagascar	<i>diop MAD</i>	ICP-MS
Chromite	Madagascar	<i>chr MAD</i>	EPMA, LA-ICP-MS, ICP-MS
	Cuba	<i>chr CU</i>	EPMA, LA-ICP-MS, ICP-MS

Here, we attempt to develop new secondary standards of natural minerals for high quality *in situ* geochemical data of olivine, clinopyroxene and chromite crystals. We selected two olivines, five clinopyroxenes of different compositions, and two chromites. Our aim is to verify the homogeneity of these crystals and to quantify their major and trace elements compositions. We performed a series of analyses including *in situ* major element EPMA and trace elements LA-ICP-MS, and solutions ICP-MS analyses. In Table II.6 we report a list of 9 analysed minerals and the relative analytical method used to determine their chemical compositions.

5.1 Sample selection and preparation

We analysed 9 minerals including:

- 2 olivines (ca. 140 mm³ each grain):
 - (i) two grains of San Carlos (*ol SC*), they were washed in dilute HNO₃ prior to analyses;
 - (ii) two grains of magmatic olivine (*ol M*; ca. 140 mm³), provided by O. Alard (Geosciences Montpellier).
- 4 clinopyroxenes (provided by O. Alard, Geosciences Montpellier):
 - (i) single-grain magmatic clinopyroxene (ca. 1.1 cm³) from Inagli Massif (Siberia, *cpx INA*), it was broken by hitting with a hammer to obtain various grains for different analyses;
 - (ii) grains (ca. 26.3 mm³ each grain) of synthetic diopside (*diop*);
 - (iii) grains (ca. 26 mm³ each grain) of Cr diopside (*Cr-diop*);
 - (iv) two grains ca. 62.5 mm³ each grain) of Ti-augite from Oman ophiolite (*aug*).
- 1 hydrothermal diopside from Madagascar (provided M. Godard, Geosciences Montpellier) of which exclusively mineral powder was analysed.
- 2 chromites:
 - (i) grains (ca. 203 mm³ each grain) from Madagascar (*chr MAD*), collected by O. Alard;
 - (ii) single-grain (ca. 1.05 cm³ each grain) and powder from Cuba (*chr CU*), provided by V. Colás (Universidad Nacional Autónoma de México)

Mineral grains were hand-picked after careful observations with a binocular microscope to discard those containing micro-inclusions. Two grains for each mineral were selected, one for *in situ* analyses and another to prepare mineral powders for solutions ICP-MS analyses. For *in situ* analyses grains were mounted in an epoxy puck from which a ca. 1 mm thick polished thin section was obtained. In order to reduce minerals to powder, grains were manually grinded with an Agate mortar. Grinding was done in three steps for each mineral. At each step, powder was removed from the mortar and mixed on weighing paper to avoid selected grinding of finer granulometry. The Agate mortar was cleaned three times with Ethanol and let dry before each grinding session.

5.2 Analytical procedure

In situ analyses

In situ analyses were performed first by EPMA and then by LA-ICP-MS. Mineral element compositions were determined for at least one rim and one core of each grain, following the same analytical procedure and data acquisition setup as reported in Chapter sections 3.2 and 4.3. LA-ICP-MS data for chromite crystals were obtained with laser spot size set to 77 μm and their concentrations were calibrated against the NIST 610 (Pearce et al., 1997). Si and Ca were used for internal standardization relative to EPMA data for olivine and clinopyroxenes, respectively, while Cr was used for chromite grains. The evaluation of the quality of acquired data was based on repeat measurements of BIR-1G (Appendix 6, Table A6.5). This resulted in reproducibility better than 3%, except for Ti, Cu, Zn, Rb, Eu, Hf, Ta and Th which is 6% or better; it is 9% for Ni and 29% for B. LA-ICP-MS data are corrected for isobaric interferences of Rare Earth Elements (REE) against multiple analyses of BIR-1G.

Solutions ICP-MS

Mineral solutions ICP-MS analyses were performed exclusively with the Q-ICP-MS Agilent 7700x (Geosciences Montpellier). We applied the same technique as reported in Chapter sections 4.1 and 4.2 for data acquisition and data processing. For sample digestion of silicate minerals the same multi-acid digestion technique (Ionov et al., 1992; Godard et al., 2000) was used; acid proportions were recalculated for 20 mg aliquot of sample powder. Distinct digestion and dilution protocols were adopted for chromites due to their characteristic resistance to acids. In the following we report the protocol adopted specifically for chromite powders.

Digestion and dilution of chromite powders

Aliquots of 20 mg of mineral separates were separated and placed in Savillex® Teflon® beakers. Samples for different protocols are distinguished by numbers (1, 2, 3, etc.).

A set of chromite powder was digested using the same protocol as silicates (chr MAD 4). Distinct chromite powder digestion was done by following four different protocols. For these we used first aqua regia (4 HCl : 1 HNO₃), then a mixture of HClO₄ and HF (1:2.5), to finish with HClO₄ and HNO₃.

Chromite digestion protocol I is (chr MAD 1):

- 800 µl HCl + 200 µl HNO₃ heating at 150 °C for 24h then acids evaporation at 180 °C – 190 °C;
- 400 µl HCl + 100 µl HNO₃ heating at 150 °C for 24h then acids evaporation at 180 °C – 190 °C, the procedure was repeated twice;
- 100µl HNO₃ evaporated at 190 °C;
- 400 µl HClO₄ evaporated at 190 °C, repeated twice;
- 100µl HNO₃ evaporated at 190 °C, repeated twice;
- 50µl HNO₃ evaporated at 190 °C (total acid evaporation is required).

Chromite digestion protocol II is (chr MAD 2 and 3):

- 800 µl HCl + 200 µl HNO₃ heating at 150 °C for 24h then acids evaporation at 180 °C – 190 °C;
- 400 µl HCl + 100 µl HNO₃ heating at 150 °C for 24h then acids evaporation at 180 °C – 190 °C, the procedure was repeated twice;
- 400 µl HClO₄ evaporated at 190 °C, repeated twice;
- 100µl HNO₃ evaporated at 190 °C, repeated twice;
- 50µl HNO₃ evaporated at 190 °C (total acid evaporation is required).

Chromite digestion protocol III is (chr CU 1 and 2):

- 800 µl HCl + 200 µl HNO₃ heating at 120 °C for 24h then acids evaporation at 180 °C – 190 °C;
- 400 µl HCl + 100 µl HNO₃ heating at 120 °C for 24h then acids evaporation at 180 °C – 190 °C, the procedure was repeated twice;
- 400 µl HClO₄ evaporated at 190 °C, repeated three times;
- 100µl HNO₃ evaporated at 190 °C, repeated three times (total acid evaporation is required).

Chromite digestion protocol IV is (chr CU 3 and 4):

- 800 µl HCl + 200 µl HNO₃ heating at 120 °C for 24h then acids evaporation at 180 °C – 190 °C;
- 400 µl HCl + 100 µl HNO₃ heating at 120 °C for 24h then acids evaporation at 180 °C – 190 °C, the procedure was repeated twice;
- 200 µl HClO₄ + 500 µl HF heating at 120 °C for 24h then acids evaporation at 180 °C – 190 °C;
- 400 µl HClO₄ evaporated at 190 °C, repeated three times;
- 100µl HNO₃ evaporated at 190 °C, repeated three times (total acid evaporation is required).

The dry residues of dissolved samples were taken into solution in pure HNO₃ and Milli-Q water, and heated for 30 minutes at 100 °C. The resulting solution was diluted with Milli-Q water to 20.6 ml. This solution was further diluted to final dilution factors of about 1600 for trace elements analyses. In order to take into account the possibly incomplete digestion of chromite, trace element concentrations were normalized to EPMA Cr values. Cr was analysed at dilution 10'000'000 for chr MAD and 6'600'000 for chr CU. Trace elements and Cr ICP-MS values are systematically low compared to *in situ* LA-ICP-MS and EMPA analyses (Appendix 6, Tables A6.1, A6.2, A6.3, A6.4) indicating incomplete digestion.

Table II.7 Comparison of Cr concentrations (ppm) in chromites between EPMA, LA-ICP-MS and solutions ICP-MS. EPMA and LA-ICP-MS Cr values are averages of all *in situ* analyses. Yield

Sample	<i>In situ</i> analyses		solutions ICP-MS			Yield (%)
	EPMA ppm	LA-ICP-MS ppm	Dilution protocol	Reference ICP-MS	ppm	
chr MAD	382568	383083	I	chr MAD 1	294231350	77
			II	chr MAD 2	265816301	69
			II	chr MAD 3	283472450	73
			Silicate	chr MAD 4	232584741	60
chr CU	263592	263545	III	chr CU 1	142774	54
			III	chr CU 2	188968	72
			IV	chr CU 3	n.d.	n.d.
			IV	chr CU 4	65613	25

Trace element analyses were corrected after the yield factor for chromites (Table II.7). The best digestion yield values were obtained for chr MAD 1 and 3 of respectively 77% and 73%, followed by chr CU 2 with 72% and chr MAD 2 with 67%. All other analyses lead to digestion of less than 60% of chromite powder. Digestion yield lower than 25% were calculated for chr CU 3 and 4 (Table II.7).

Quality of data was ensured by analyses and comparison of international standards during measurements and data reduction. We used three international standards: UB-N enriched serpentinite, BIR-1 basalt and DTS-1 dunite powder. Their compositions together with detection limits are reported in (Appendix 6 Table A6.6).

5.3 Results and discussion

Results of *in situ* major and trace elements compositions are reported in Appendix 6 Table A6.1 and Appendix 6 Table A6.2, and solutions ICP-MS trace elements contents are in Appendix 6 Table A6.3 and A6.4. Here, we first compare mineral element concentrations analysed with the different analytical techniques. Then, we evaluate the homogeneity of single samples in order select those suitable for LA-ICP-MS secondary standards.

5.3.1 Results

Comparison across analytical techniques

Olivines

In situ EPMA and LA-ICP-MS analyses (Figure II.6) plot overall on the 1:1 ratio line within error.

Geochemical LA-ICP-MS measurements and solutions ICP-MS analyses of ol SC overlap fairly well for HREE (Figure II.7a), whereas all other trace elements analysed by ICP-MS display higher absolute values than those from LA-ICP-MS (Figure II.7b). This may point to the contribution of trace-element rich micro-inclusions (e.g., Schiano et al., 1995; Bodinier et al., 1996; Ionov, 1996; Rosenbaum et al., 1996; Garrido et al., 2000) that were most likely included in solutions ICP-MS analyses and excluded during *in situ* LA-ICP-MS.

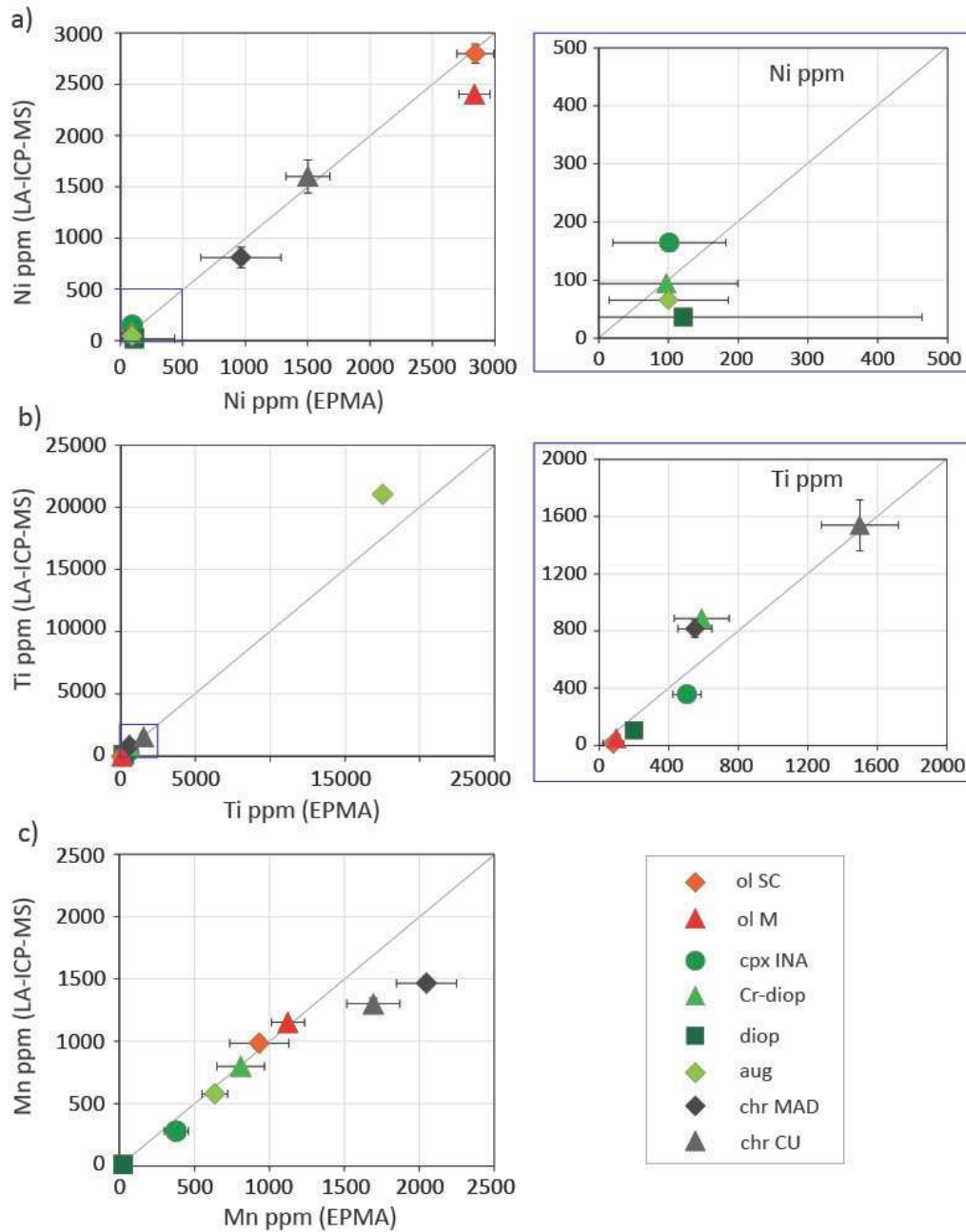


Figure II.6 – LA-ICP-MS vs EPMA analyses of minor elements concentrations in samples analysed: a) Ni (ppm), b) Ti (ppm), c) Mn (ppm). Plots on the right are zoom-in blue boxes reported in plots on the left. Compositions are average values of single-mineral *in situ* analyses.

Clinopyroxenes

In situ EPMA and LA-ICP-MS analyses (Figure II.6) plot overall on the 1:1 ratio line within error. It should be noted that *in situ* analyses of aug show Ti contents between 16545 and 18736 ppm

analysed by EPMA whereas those analysed by LA-ICP-MS are in the range 20001-22260 ppm (Figure II.6b), therefore indicating that results from the two methods are not perfectly equivalent.

Geochemical LA-ICP-MS measurements and solutions ICP-MS analyses of all clinopyroxenes analysed overlap fairly well (Figure II.7c-d-e-f), but some exceptions for certain elements are observed. More in detail, Cr-diop (Figure II.7e) and diop (Figure II.7c) display lower absolute values in Medium (M)- (Eu exclusively for Cr-diop) and Heavy (H)- REE from solutions ICP-MS compared to LA-ICP-MS, suggesting that corrections of *in situ* analyses may overestimate REE concentrations. This is possibly due to matrix effect related to the use of BIR-1G as secondary standard and, therefore, further illustrates the need of matrix-matched standards. Moreover, cpx INA (Figure II.7d) and Cr-diop (Figure II.7f) show higher contents of the most incompatible elements (i.e., Rb, Ba, Th, U, Nb) and Pb from ICP-MS data in comparison with *in situ* analyses. This could be related to the contribution of trace-element rich micro-inclusions that were most likely included in solutions ICP-MS analyses and excluded during *in situ* LA-ICP-MS, as similarly observed in olivine.

Chromites

In situ EPMA and LA-ICP-MS analyses (Figure II.6) plot overall on the 1:1 ratio line within error, except for Mn contents. Mn concentrations of Chr MAD plot in the range 1750 ppm for EPMA analyses, while LA-ICP-MS measurements give values of Mn in the range 1485-1510 ppm. Also, chr CU have Mn contents ranging between 1500 and 1988 ppm by EPMA corresponding respectively to 1247-1339 ppm by LA-ICP-MS, which do not plot along the 1:1 ratio line (Figure II.6c).

Geochemical data of chr CU overlap fairly across the two techniques (Figure II.7h). *In situ* analyses of chr CU show contents of Ni_{NChr} between 0.85 and 0.94 with one spike of 1.2, Zn_{NChr} , Co_{NChr} , Mn_{NChr} , V_{NChr} respectively in the ranges 0.91-0.93, 1.27-1.32, 1.36-1.66, and 1.3-1.35. These compositions are comparable to solutions ICP-MS analyses of chr CU 2, which showed the best digestion yield (72%), and slightly different than those of chr CU 1 and 4 (Figure II.7h). On the other hand, *in situ* analyses of chr MAD (Figure II.7g) display contents of Ni_{NChr} ($NChr$ = Normalized to chromite in MORB), Zn_{NChr} , Co_{NChr} , Mn_{NChr} , V_{NChr} respectively in the ranges 0.41-0.51, 0.86-0.88, 1.41-1.58, 1.59-1.7, 0.1-1.1, which are similar to compositions determined by solutions ICP-MS analyses of chr MAD 1 but different to those of chr MAD 2, 3 and 4 (average values of chr MAD 2-3-4: Ni_{NChr} = 0.6, Zn_{NChr} = 0.6, Co_{NChr} = 1.17, Mn_{NChr} = 1.25, V_{NChr} = 0.79).

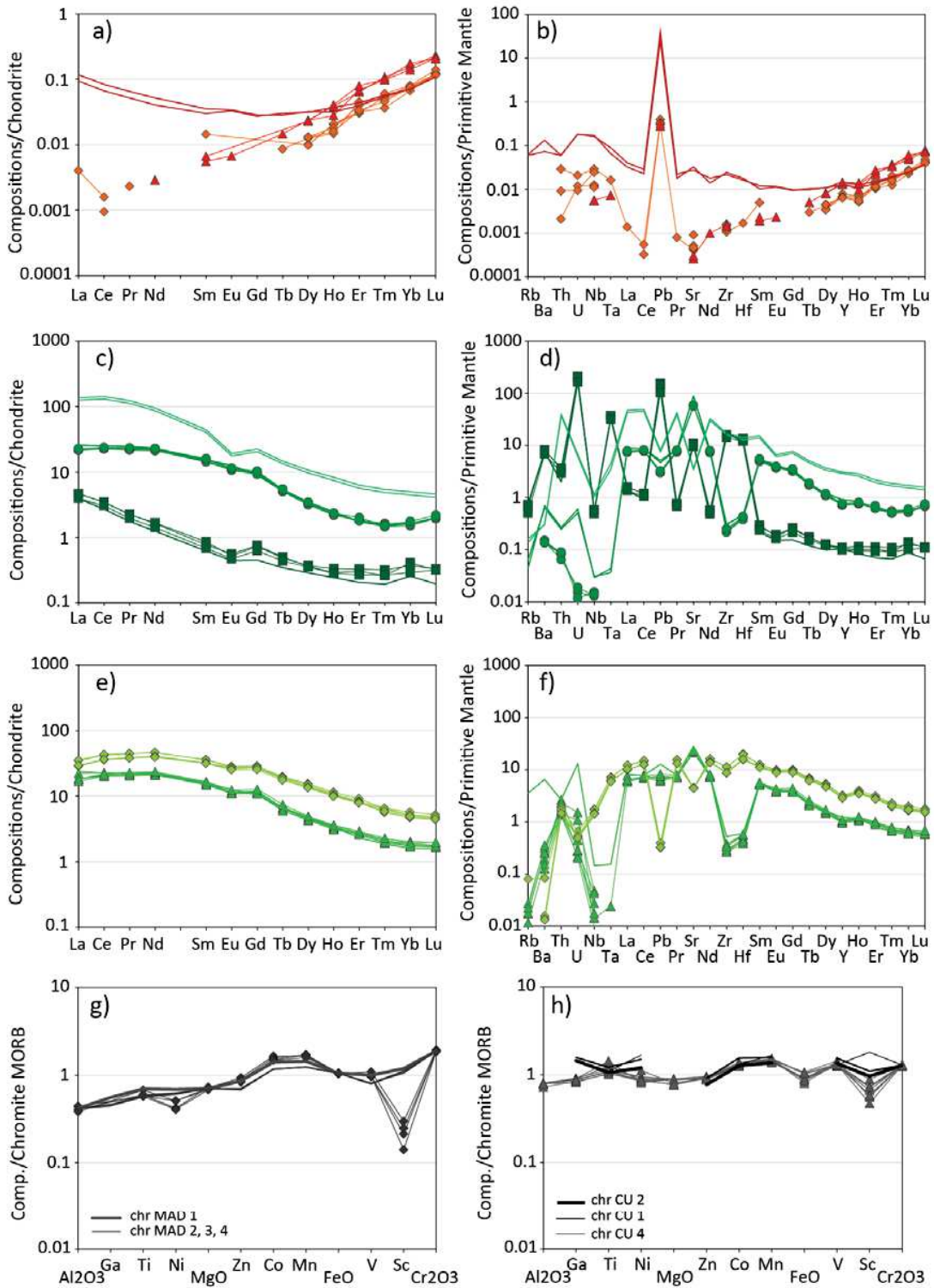


Figure 7 – Normalized trace elements compositions of samples analysed by LA-ICP-MS (symbols are as reported in Figure II.6) and solutions ICP-MS (lines without symbols). REE spider diagram for a) olivine, c) and e) clinopyroxenes. Extended trace elements spectra for b) olivine, d) and f) clinopyroxenes. Note that light green line in c) and d) are analyses of cpx MAD of which only solutions ICP-MS analyses were performed. Chromites compositions are reported in g) chr MAD, and h) chr CU.

Although all solutions ICP-MS data of chromites were corrected based on digestion yield, the discrepancies between results from the two analytical methods in some trace elements are related to digestion of samples. Digestion protocols I and III result as the most efficient.

Homogeneity of analysed minerals

Homogeneity was assessed by comparing multiple *in situ* analyses in single minerals.

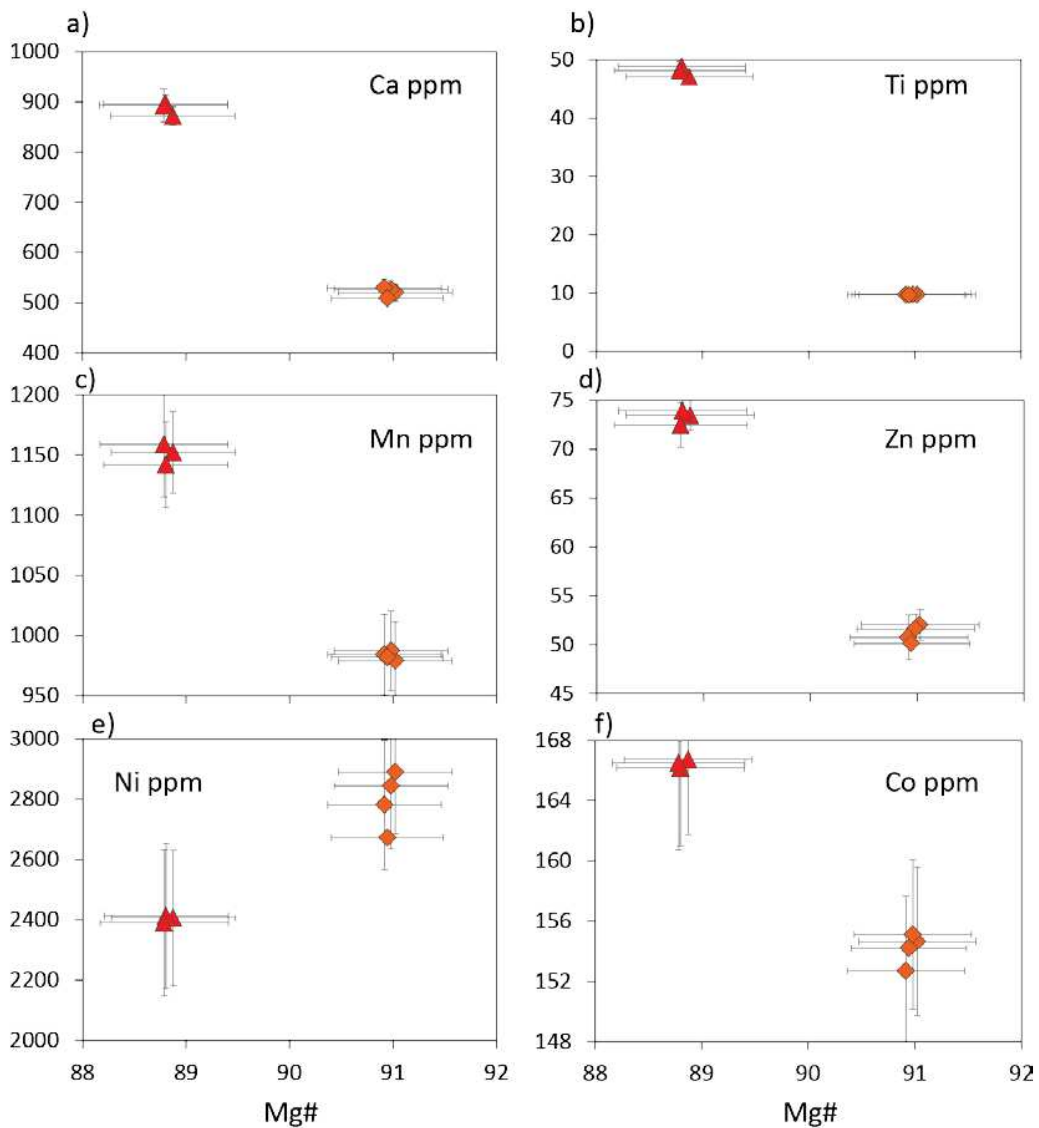


Figure 8 – Compositions of olivine: Mg# vs a) Ca (ppm), b) Ti (ppm), c) Mn (ppm), d) Zn (ppm), e) Ni (ppm), f) Co (ppm). Symbols are as in Figure II.6.

Olivines

The ol M has Mg# in the range 88.8-88.9, Ni between 2391 and 2414 ppm, and Mn, Ca, Co, Zn and Ti in the ranges 1142-1159 ppm, 872-896 ppm, 166.2-166.6 ppm, 73.5-73.9 ppm and 47.1-48.9 ppm, respectively (Figure II.8). The ol SC has Mg# between 90.9 and 91.0, Ni ranging from 2673 to 2845 ppm, and Mn, Ca, Co, Zn and Ti in the ranges 973-987 ppm, 509-537 ppm, 153-155 ppm, 50.1-52.1 ppm and 9.7-10.0 ppm, respectively (Figure II.8). Major and elements compositions of ol SC and ol M are relatively homogeneous. REE contents in both olivines show typical fractionated patterns from HREE to MREE with contents that are more variable in ol SC than ol M (Figure II.7a). LREE and the most incompatible elements are scattered in both analysed olivines (Figure II.7b), which is due to the fact that they generally fall close to or below detection limits and, therefore, they are difficult to analyse.

Clinopyroxenes

Among the analysed clinopyroxenes, cpx INA has the most homogeneous compositions with Mg# 96.5-96.6, CaO wt% between 25-25.5, NaO wt% in the range 0.2-0.3, and Ti, Mn, Zn and Y in the ranges 349-367 ppm, 272-282 ppm, 5-5.2 ppm, 3.2-3.5 ppm, respectively (Figure II.9). All trace element analyses of cpx INA overlap (Figure II.7c-d).

Cr-diop and aug display variable compositions in some major and minor elements (Figure II.9), while on average they show comparable trace elements contents between the multiple crystal sites analysed for each single mineral (Figure II.7e-f). Cr-diop has Mg# between 87.8-88.5, CaO wt% in the range from 24 to 24.9 and NaO wt% of 0.3-0.5, and Ti, Mn, Zn and Y in the ranges 772-952 ppm, 793-806 ppm, 14.7-15.9 ppm, 4.6-4.8 ppm, respectively (Figure II.9). Aug is characterized by Mg# of 75.9-76.6, CaO wt% of 23.1-23.4 and NaO wt% of 0.4-0.5, and Ti, Mn, Zn and Y in the ranges 20002-22260 ppm, 556-596 ppm, 17.3-18.4 ppm, 12.8-14.4 ppm, respectively (Figure II.9).

Homogeneity of diop could not be verified due to the lack of multiple *in situ* analyses.

Chromites

Both chromites are overall homogeneous showing, however, variations in Sc contents that are not correlated with the specific crystal site of analysis (i.e., core or rim) (Figure II.7). Moreover, chr

MAD displays slight variations in Ni_{Nchr} contents ranging from 0.4 to 0.5 (Figure II.7g), while chr CU show slight variations in Ti_{Nchr} with values between 1.0 and 1.4 (Figure II.7h).

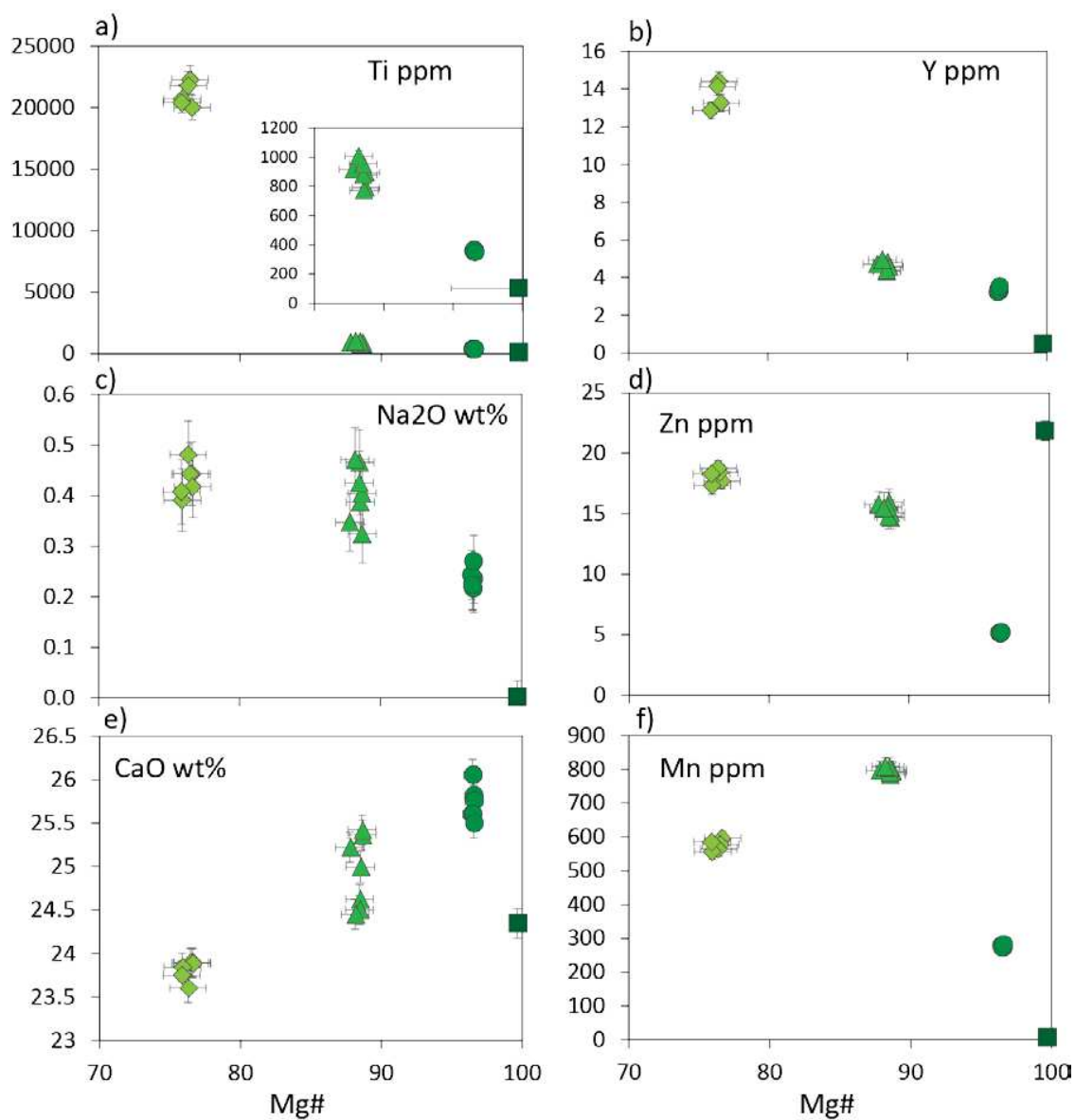


Figure II.9 - Compositions of clinopyroxenes: Mg# vs a) Ti (ppm), b) Y (ppm), c) Na_2O (wt%), d) Zn (ppm), e) Ca_2O (wt%), f) Mn (ppm). Symbols are as in Figure II.6.

5.3.2 Two standards for LA-ICP-MS analyses

Among all analysed minerals, cpx INA and chr CU better meet the requirements for LA-ICP-MS secondary standards. Compositions of cpx INA and chr CU are overall homogeneous. For cpx INA reproducibility across geochemical analytical methods are better than 10% for most elements

except for V, Mn, Co, Ni, Y, Zr (<20%) and Sc, Ti, Sr, Pb (<30%; Table II.8). The preferred values for cpx INA are reported in Table II.8. Further investigations are needed to better constrain the geochemical compositions of both minerals.

Table II.8 – Preferred values of major and trace elements of cpx INA. Reproducibility of analyses was calculated from the averages of in situ (EPMA and LA-ICP-MS) analyses and solutions ICP-MS.

cpx INA			
<i>(wt%)</i>	<i>Pref'd values</i>	σ	<i>Reproducibility (%)</i>
SiO ₂	54.92	0.25	
TiO ₂	0.08	0.02	
Al ₂ O ₃	0.18	0.02	
Cr ₂ O ₃	0.30	0.02	
FeO	1.11	0.02	
MnO	0.05	0.01	
MgO	17.55	0.05	
CaO	25.22	0.20	
Na ₂ O	0.24	0.02	
K ₂ O	0.00	0.00	
NiO	0.01	0.01	
Mg#	96.57	0.06	
<i>ppm</i>			
Li	0.42	0.28	67
B	15.3	0.5	-
Sc	51.3	12.2	24
Ti	437	115	26
V	5.26	0.71	14
Mn	311	49	16
Co	13.7	2.5	18
Ni	193	41	21
Cu	0.17	0.15	87
Zn	5.15	0.05	-
Sr	1547	466	30
Y	3.74	0.58	16
Zr	3.02	0.58	19
Nb	0.016	0.008	51
Ba	2.826	2.612	92
La	5.66	0.64	11
Ce	14.71	0.87	6
Pr	2.23	0.14	6
Nd	10.52	0.28	3
Sm	2.32	0.03	1.5
Eu	0.683	0.063	9
Gd	1.766	0.095	5
Tb	0.186	0.012	6
Dy	0.842	0.058	7
Ho	0.129	0.011	9
Er	0.283	0.004	1.6
Tm	0.038	0.001	1.4
Yb	0.274	0.003	1.1
Lu	0.049	0.001	1.5
Hf	0.135	0.012	8.8
Pb	0.740	0.245	33
Th	0.014	0.011	73

Chapter III

***Detailed microstructural and petro-geochemical
study of olivine-rich troctolites
from Atlantis Massif***

1. Introduction

In this Chapter I report the detailed microstructural and petro-geochemical study on olivine-rich troctolites from Atlantis Massif, coupled with geochemical modeling.

Chapter Section number 2 is the article intitled “Melt transport and mantle assimilation at Atlantis Massif (IODP Site U1309): Constraints from geochemical modeling” that I submitted, and was accepted for publication on the Special Issue ‘Reactive Geological Systems from the Mantle to the Abyssal sub-seafloor’ in *Lithos* (Ferrando et al., 2018). Authors of this article are:

Carlotta Ferrando^{a*}, Marguerite Godard^a, Benoit Ildefonse^a & Elisabetta Rampone^b

^a *Géosciences Montpellier, Univ. Montpellier, CNRS, 34095 Montpellier cedex 05, France*

^b *DISTAV, University of Genova, Corso Europa 26, I-16132 Genova, Italy*

**Corresponding author at: Géosciences Montpellier (UM 5243 - CNRS), Université de Montpellier, cc60, Place Eugene Bataillon, 34095 Montpellier cedex 5, France.*

Five tables were submitted as Supplementary Material and are reported in Appendix as follows:

- Appendix 2 : SupplementaryMaterial Table S1, average chemical compositions of rims and cores of olivine, plagioclase and clinopyroxene; SupplementaryMaterial Table S2, selected olivine-clinopyroxene geochemical profiles
- Appendix 4 : SupplementaryMaterial Table S3, quality of geochemical analyses
- Appendix 5 : SupplementaryMaterial Table S4, partition coefficients; Supplementary Material Table S5, diffusion coefficients; SupplementaryMaterial Table S6, compositions of starting materials used in geochemical modeling.

Chapter Section number 3 is dedicated to the characterization of the distribution of elements possibly affected by subsolidus re-equilibration (i.e., Ca, REE and Y) in olivine-rich troctolites from the Atlantis Massif. I am now elaborating the results of this preliminary work and performing cooling modeling.

2. Melt transport and mantle assimilation at Atlantis Massif (IODP Site U1309): Constraints from geochemical modeling

Abstract

Olivine-rich troctolites (>70% olivine) reveal that extensive melt impregnation of pre-existing olivine-rich lithologies participate to the building of slow spread oceanic crust. To constrain their origin and their impact on the structure and geochemistry of oceanic crust, we realized a multi-scale petro-structural, geochemical, and numerical modeling study of olivine-rich troctolites drilled at IODP Hole U1309D (Atlantis Massif, Mid-Atlantic Ridge 30°N). Discrete intervals of olivine-rich troctolites display sharp to diffuse contacts with neighboring troctolites or gabbros. Their texture is characterized by plastically deformed (high temperature imprint), corroded coarse-grained to undeformed fine-grained olivine embayed in poikilitic clinopyroxene and plagioclase. Olivine crystallographic preferred orientations show weak [001] clusters. Olivine has variable major and minor element compositions, but similar fractionated REE ($DyN/YbN = 0.04-0.11$). We distinguished three types of olivine-rich troctolites based on microstructure, texture and mineral composition. Olivine-rich troctolites 1 and 2 display sharp contacts with adjacent lithologies. Type 1 has modal olivine <75%, occurring mainly as single rounded grains with primitive compositions ($Mg\# = 85-86$), and associated with high $Mg\#$ clinopyroxene. Type 2 has higher olivine modes (>75%), dominantly forming aggregates, showing more evolved compositions ($Mg\# = 83-84$) and associated with slightly lower $Mg\#$ clinopyroxene. These variations of olivine modes and compositions are in contrast to common trends of magmatic crystallization that predicts decreasing modal olivine with melt differentiation towards evolved compositions. Type 3 has diffuse contacts with gabbroic veins and modal olivine overlapping those of types 1 and 2. Chemical traverses along principal crystallographic axes of olivine are flat, suggesting local equilibrium between olivine and neighboring phases. Mineral modes and compositions, together with textures and microstructures, suggest that olivine-rich troctolites formed after melt-rock interactions in a reactive porous flow process. Their compositions are best modeled by percolation of primitive MORBs into Hole U1309D impregnated and compositionally heterogeneous harzburgites, triggering orthopyroxene dissolution, followed by olivine assimilation and concomitant crystallization of clinopyroxene and plagioclase. Modeling shows that Ni variations in olivine at constant $Mg\#$ are mantle inherited.

Compositions of olivine-rich troctolite 1 are fitted assuming higher olivine assimilation (Ma = 0.06-0.13) in contrast to olivine-rich troctolites 2 and 3 (Ma = 0.01-0.02). Olivine-rich troctolite 3 was 'buffered' by crystallizing reacted melts, progressively more evolved as temperature decreased during a late stage process. We interpret olivine-rich troctolites from the Atlantis Massif as marking local assimilation of harzburgitic mantle into the gabbroic sequence during a period of enhanced magmatism at depth. Our study shows that the distribution and variable compositions of olivine-rich troctolites result from the incipient stages of this process when local spatial variations in mantle rock permeability, probably related to pyroxene distribution, controlled in turn melt transport and mantle-melt interactions.

2.1 Introduction

The formation of oceanic crust by partial melting of upwelling asthenosphere at mid-ocean ridges represents one of the main outcomes of mantle geodynamics at the surface of the Earth. The architecture of oceanic crust varies from "layered", characterized by a volcanic basaltic crust that overlies a lower crustal plutonic (gabbroic) sequence, to the "heterogeneous" formed by serpentinized peridotites intruded by gabbroic bodies and overlain by a thin or absent extrusive section (e.g., review in Coogan, 2014). Both architectures are observed along slow-spreading ridges while the former is dominant along fast-spreading centers (e.g., review in Coogan, 2014). The composition of the oceanic crust is commonly modeled as the product of fractional crystallization of primary mantle melts, forming the tholeiitic differentiation suite: dunite → troctolite (and wehrlite) → olivine gabbro → gabbro → basalt (e.g., Bowen, 1928; Gast, 1968). Accordingly, and based on early petrological studies that allowed to predict the effects of this fractional crystallization suite on the composition of basalts (e.g., O'Hara, 1965; Shaw, 1970), Mid-Ocean Ridge Basalts (MORB) have been used extensively to determine the composition of their mantle source as well as the conditions and extent of melting that led to their formation (e.g., Elthon, 1979; Grove et al., 1992; O'Neill and Jenner, 2012). Yet, petrographic observations and geochemical studies of oceanic plutonic sequences show that fractional crystallization may not uniquely account for the composition and textures of gabbroic series, thus challenging this simple differentiation model.

Textures of gabbroic rocks commonly show corroded grain boundaries of early crystallized minerals and the occurrence of interstitial phases (e.g., Holness et al., 2007), suggesting chemical reaction of the crystal mush with an interstitial melt. These textural features indicate disequilibrium among phases. On the other hand, chemical equilibrium between phases is observed for major elements, in particular for the most primitive end-members of gabbroic series (e.g., Langmuir, 1989; Lissenberg and Dick, 2008). Nevertheless, trace elements are in disequilibrium between coexisting phases (e.g., Drouin et al., 2009; Rampone et al., 2016) and display significant enrichments compared to those predicted by fractionation trends (e.g., Bédard, 1993; DePaolo, 1981; O'Hara, 1977). These observations have been interpreted as the result of 'open-system' processes including periodic melt injection and mineral assimilation. Chemical exchanges between a pre-existing crystal matrix and exotic melts (e.g., Bédard et al., 2000; Dick et al., 2000; Kvasnes and Grove, 2008; Lissenberg et al., 2013; Renna et al., 2016) or postcumulus reactions with late-stage interstitial melts (e.g., Borghini and Rampone, 2007) have been proposed as mechanisms able to modify the mineral chemistry of primary phases. Also, such reactions may in turn modify the composition of the reacting MORB-type melts (e.g., Lissenberg and Dick, 2008). Natural samples (e.g., Lissenberg et al., 2013; Lissenberg and Dick, 2008; Rampone et al., 2016; Sanfilippo et al., 2015, 2015) and experimental studies (e.g., Lambart et al., 2009; Van den Bleeken et al., 2011) point to a possibly important role of melt-rock interactions in the formation of the oceanic crust.

Olivine-rich troctolites represent the most primitive end-member of gabbroic rocks in the tholeiitic suite of the oceanic crust. They have >70% olivine modal contents, which approach that of dunites, but contain plagioclase and clinopyroxene. They were first described in intracontinental layered intrusions (e.g., 'feldspathic peridotite' and troctolite, Holness et al., 2007; O'Driscoll et al., 2007). Because their textures are distinguished by subhedral to rounded olivine grains embayed in large interstitial plagioclase and clinopyroxene crystals (e.g., Holness et al., 2007) and have rather primitive major element compositions (e.g., O'Driscoll et al., 2007), olivine-rich troctolites were interpreted first as products of magmatic crystallization and melt-rock reactions during replenishment of the magma chamber, or with melts from the host gabbros (e.g., Bédard, 2015 and references therein). Olivine-rich troctolites have also been observed at the mantle-crust transition zone of modern and paleo fast-spreading ridges (e.g., 'plagioclase-bearing dunite' and troctolite, Arai and Matsukage, 1996; Boudier and Nicolas, 1995). They contain olivines that display

microstructures consistent with high temperature deformation by dislocation creep, as commonly described in mantle peridotites (Boudier and Nicolas, 1995). They also show chemical variations inconsistent with fractionation trends (e.g., Arai et al., 1997). These olivine-rich troctolites are interpreted as mantle rocks, which composition and texture were modified as the result of extensive melt impregnation atop the upwelling mantle at the mantle-crust transition along spreading ridges (e.g., Boudier and Nicolas, 1995; Dijkstra et al., 2003; Higginson and Tommasi, 2012). More recently, intervals of olivine-rich troctolites have been extensively observed interlayered within the heterogeneous oceanic crust at modern slow-spreading ridges (e.g., Drouin et al., 2009, 2010; Sanfilippo et al., 2015; Suhr et al., 2008) and ophiolite analogues (e.g., Rampone et al., 2016; Renna et al., 2016; Sanfilippo et al., 2014, 2015). These olivine-rich troctolites present textures similar to the “feldspathic peridotite and troctolite” of large layered intrusions and of thick plutonic lenses, which formed after a cumulate protolith (e.g., O’Driscoll et al., 2007; Renna et al., 2016). However, they also show selective enrichments in the most incompatible elements generally interpreted as evidence of a melt-rock interaction (e.g., Basch et al., in this issue; Drouin et al., 2009; Rampone et al., 2016; Sanfilippo et al., 2014). Finally, some of these olivine-rich troctolites show textures and microstructures of high temperature deformation similar to those formed at the mantle-crust transition zone (Drouin et al., 2010), suggesting that the precursor material is of mantle origin (e.g., Basch et al., in this issue; Drouin et al., 2009, 2010; Sanfilippo et al., 2015, 2015; Sanfilippo and Tribuzio, 2013, 2011).

A reactive origin for the olivine-rich troctolites from modern slow-spread oceanic crust was first proposed following the studies of the heterogeneous gabbroic sequence exposed by detachment faulting at the Atlantis Massif (Drouin et al., 2009, 2010; Suhr et al., 2008). Discrete intervals of olivine-rich troctolites were recovered in IODP Hole U1309D (30°N, Mid-Atlantic Ridge (MAR), Expeditions 304/305; e.g., Blackman et al., 2011 and references therein). Because of their microstructural and textural similarities with impregnated peridotites, together with their mineral compositions inconsistent with a simple process of fractional crystallization, Drouin et al. (2009, 2010) and Suhr et al. (2008) inferred that olivine-rich troctolites from Hole U1309D could originally represent mantle relicts. Nevertheless, no unequivocal argument sustains this hypothesis, and the nature of the olivine-rich precursor remains to date unresolved (e.g., Drouin et al., 2009, 2010; Renna et al., 2016). In this contribution, we present a detailed multi-scale petro-structural and geochemical study of olivine-rich troctolites drilled at IODP Hole U1309D. Our purpose is to

investigate the mechanisms driving melt-rock interaction processes and ultimately identify the origin of these olivine-rich troctolites. For the first time, we reproduce the chemical compositions of olivines from olivine-rich troctolites using numerical modeling to simulate processes of melt-rock reactions combined with the effects of melt transport ('Plate Model' proposed by Vernières et al., 1997).

2.2 Geological setting

The Atlantis Massif is located at 30°N on the western flank of the slow spreading Mid-Atlantic Ridge (MAR), at the inside corner of the intersection with the Atlantis transform fault (Fig. 1). The corrugated core of the domal massif is a ~2 Ma old Oceanic Core Complex (OCC) that extends over an area approximately 8–10 km wide and 15 km long. Lower crust and upper mantle rocks are exposed via a long-lived and low-angle detachment fault (e.g., Blackman et al., 2002, 2011; Cann et al., 1997; Ildefonse et al., 2007) that spreads at an average (fault slip) rate of 26 mm/yr (Grimes et al., 2008).

IODP Hole U1309D, the deepest hole drilled at Atlantis Massif (Fig. 1), penetrated 1415.5 m below sea floor (mbsf). The recovered section is a highly heterogeneous gabbroic sequence (93.7% of oxide gabbro, gabbro, olivine-gabbro, and troctolite), with MORB-type diabase intrusions (2.9% of the recovered rocks) sampled dominantly in the upper 130 m (Blackman et al., 2011; Godard et al., 2009). Structural and geochemical investigations indicate that the crustal section at Site U1309 record a complex intrusive history, and was formed by multiple magmatic injections over a minimum accretion time of 200 (± 120) ka (Blackman et al., 2011; Grimes et al., 2008). Three major intrusive events were identified. For this study, we focus on the deepest crust interval that occurs below 600 mbsf. Constraints from $^{206}\text{Pb}/^{238}\text{U}$ zircon ages from oxide gabbros and leucocratic dykes indicate that the interval between 600 and 1235 mbsf represent the oldest intrusive event at ~1.24 Ma (Grimes et al., 2008). The vertical accretion of this section occurred by emplacement of multiple sills at ~7 km depth (Grimes et al., 2008).

The most primitive intervals have variable thicknesses and were recovered at different depths within the gabbroic sequence (Blackman et al., 2011). They comprise minor mantle peridotites ($\ll 1\%$ of total core) and 5.4% (total core) of olivine-rich troctolites observed in 22 discrete

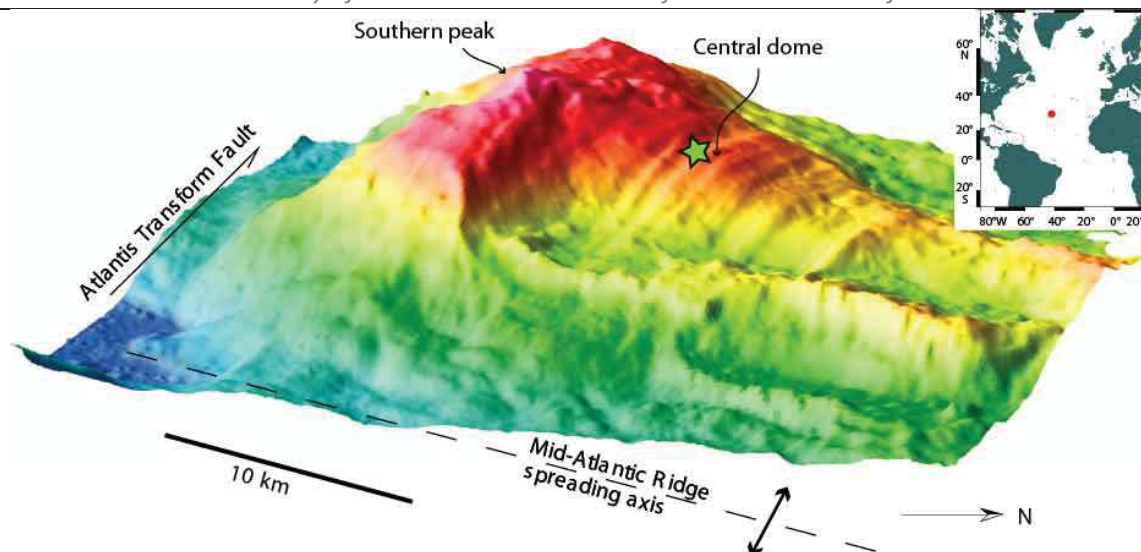


Fig. 1 - 3D reconstruction of Atlantis Massif OCC (looking W) modified after Blackman et al. (2002). The green star indicates the location of IODP Hole U1309D on the corrugated detachment fault surface of central dome. (For interpretation of the references to color in this figure legend, the reader is referred to the web version of this article.)

intervals throughout the core. The altered mantle relicts are impregnated residual harzburgite screens (Godard et al., 2009; Tamura et al., 2008) crosscut by gabbroic dikelets; they were recovered in the upper ~200 m at Holes U1309B and U1309D. Along slow spreading ridges, the formation of heterogeneous oceanic crust, made of serpentized mantle rocks intruded by discrete gabbroic bodies and exposed on the seafloor, is interpreted as related to low magma supply (e.g., Cannat et al., 1995; Dick, 1989).

Groundmass alteration at Hole U1309D is moderate and decreases downhole (Blackman et al., 2011). We selected for this study the interval between 1100 and 1300 mbsf where olivine-rich troctolite is the dominant lithology, and is locally very fresh with <1% serpentinization (Fig. 2 and 3). We collected a total of 15 olivine-rich troctolites: 1 sample at 1096 mbsf, 2 samples at 1125-1160 mbsf, 9 samples at 1190-1193 mbsf, and 3 samples at ~1195 mbsf. Three samples were collected in contact with gabbroic veins, at 1190.5 and 1193.5 mbsf. In order to compare the composition of olivine-rich troctolites with a magmatic end-member we also collected a troctolite at 1290 mbsf.

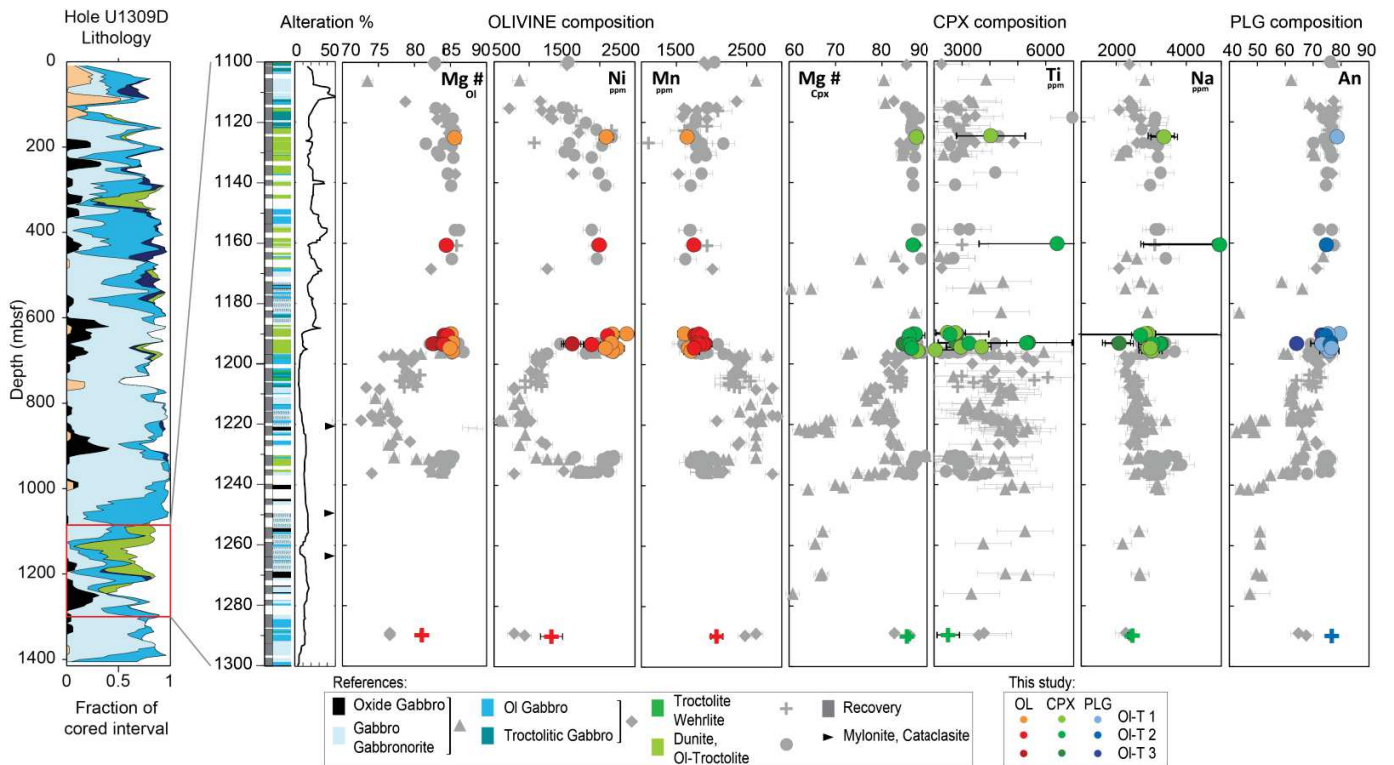


Fig. 2 - Olivine (Mg#, Ni, Mn), clinopyroxene (Mg#, Ti, Na) and plagioclase (An) compositions of analysed samples in the interval 1100-1300 mbsf. Recovery, lithology and alteration logs are reported after Blackman et al. (2006). Colored dots represent single samples analysed in this study. Grey symbols indicate data from previous studies (Drouin et al., 2009; Miller et al., 2009; Suhr et al., 2008).

2.3 Petrologic overview of U1309D olivine-rich troctolites

Shipboard data and previous on-shore petrologic and geochemical studies provide a first order characterization of the meter-scale downhole variability of the gabbroic sequence recovered at IODP Hole U1309D on the Atlantis Massif OCC (e.g., Blackman et al., 2011; Godard et al., 2009; Grimes et al., 2008; Miller et al., 2009). In contrast to what is described at Atlantis Bank, SW Indian Ridge (Dick et al., 2000), downhole chemical compositions show no significant crystallization trends throughout Hole U1309D (e.g., interval 1100-1300 mbsf in Fig. 2). Here, we summarize the principal characteristics of U1309D olivine-rich troctolites.

During IODP Expedition 304/305 olivine-rich troctolites (OI-T; >70% modal olivine, Blackman et al., 2006) were sampled in four main interfingered petrologic units within the gabbroic sequence, where they occur as ~40 cm to ~12 m thick discrete intervals crosscut by relatively more evolved

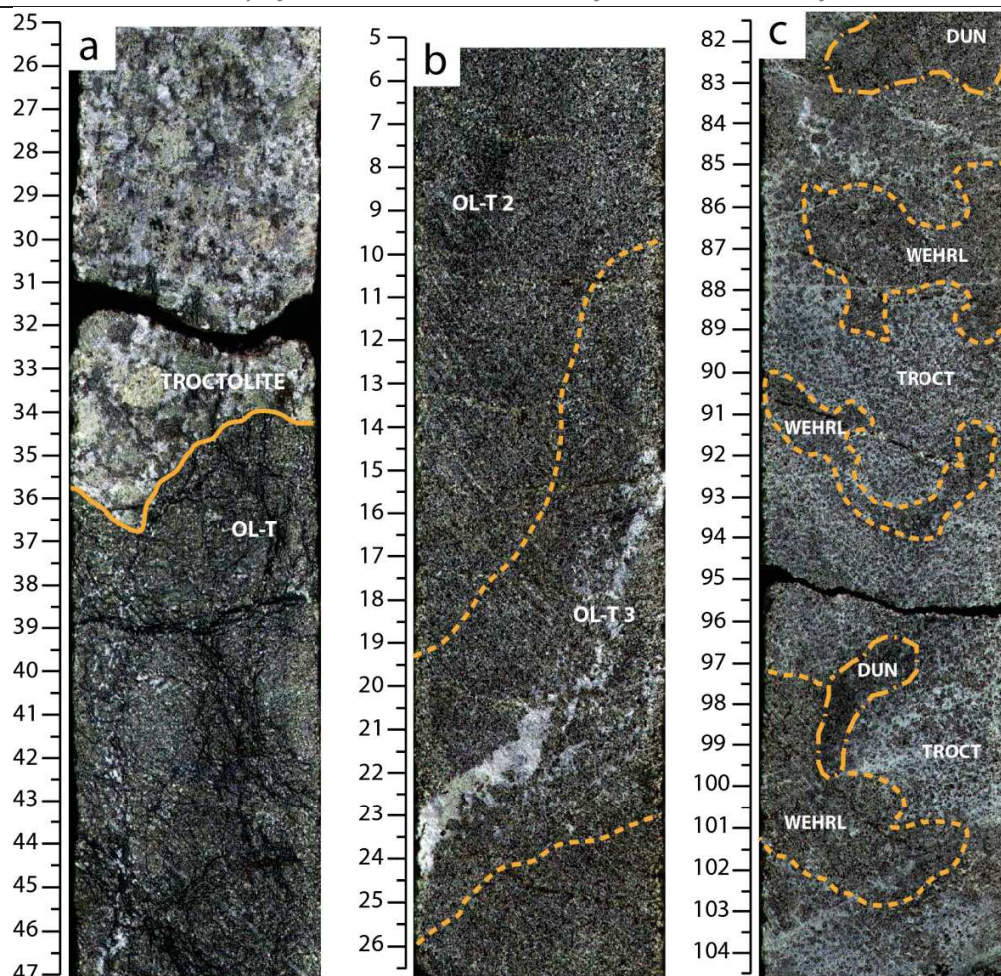


Fig. 3 - Examples of (a–b) recovered contacts between OL-T and gabbro, and (c) interval of heterogeneous OL-T. a) Core 227R-2, 25-47 cm shows sharp and irregular (in orientation) contact with troctolite. b) Core 248R-2, 5-26 cm shows OL-T2 (see text) cut by a gabbroic vein; contacts are diffuse and record an increase in modal plagioclase from the core of OL-T2 to the contact. This OL-T - gabbro boundary is an example of OL-T3. c) Core 248R-3, 82-104 cm is an example of OL-T1 composed of wehrlitic (WEHRL), troctolitic (TROCT) and minor dunitic (DUN) domains.

gabbroic rocks. Overall, the contacts between OL-T and troctolitic or gabbroic intervals are sharp, displaying no progressive modal variations. Throughout Hole U1309D, at the scale of few cm to a few dm, OL-T are heterogeneous in composition (Fig. 3c), varying from dunite (>90 vol% olivine at macroscopic to thin section scale and 10 vol% plagioclase, with <1 vol% clinopyroxene) to troctolite (~70 vol% olivine and ~30 vol% plagioclase) and wehrlite (~70 vol% olivine and ~30 vol% clinopyroxene).

OL-T display poikilitic textures that are characterized by rounded granular olivines embedded in large and interstitial plagioclase and/or clinopyroxene crystals, which resemble homogeneous

cumulate-like textures described in layered intrusions (e.g., Rum cumulate series; Holness et al., 2007). Nevertheless, olivine crystals display high-temperature dislocation creep, which is commonly described in mantle peridotites, while plagioclase and clinopyroxene show no deformation signature (Drouin et al., 2010). Yet, most Ol-T samples display crystallographic preferred orientation (CPO) of olivine with relatively stronger clustering of [001] crystallographic axes compared to the [100] and [010] axes (Drouin et al., 2010); this feature contrasts with the axial [100] fabrics typically observed for mantle olivine (e.g., Tommasi et al., 2000).

Bulk rock chemical data show that Ol-T are the most primitive crustal rock cored at Atlantis Massif with high bulk Mg# ($\text{Mg\#} = 100 \times \text{cationic Mg}/(\text{Mg} + \text{Fe}_{\text{TOT}})$ with all Fe (Fe_{TOT}) calculated as Fe^{2+}) of ~86 (in comparison with Mg# 81 of olivine gabbros; Godard et al., 2009). Olivine in Ol-T is characterized by relatively primitive compositions (Fo_{82} to Fo_{88} ; Drouin et al., 2009; Miller et al., 2009; Suhr et al., 2008) in contrast to gabbros and olivine gabbros that display lower forsterite contents (down to Fo_{72} ; Miller et al., 2009; Fig. 2). Plagioclase has anorthitic composition in most recovered rocks (An_{65} – An_{82} ; Miller et al., 2009; Drouin et al., 2009; Fig. 2), and clinopyroxene has generally high Mg# (75–90; Drouin et al., 2009; Miller et al., 2009; Suhr et al., 2008; Fig. 2). Trace elements (i.e., REE) in plagioclase and clinopyroxene from Ol-T are in equilibrium, whereas olivine is in chemical disequilibrium with both interstitial phases (Drouin et al., 2009). The absence of systematic modal variations between Ol-T and gabbro, together with the microstructures of Ol-T (Drouin et al., 2010), analyses of bulk rock compositions (Godard et al., 2009), and mineral chemical disequilibrium (Drouin et al., 2009), were interpreted as evidence that Ol-T at the Atlantis Massif are the result of a multi-stage melt impregnation process through an olivine-rich precursor (Drouin et al., 2009, 2010; Suhr et al., 2008).

2.4 Analytical methods

In order to document the scale of modal and chemical heterogeneities in Hole U1309D rocks, in particular Ol-T, the most relevant intervals were described in detail at the Bremen Core Repository. A first set of samples were selected from those used in Drouin et al. (2009), and a second set at the Bremen Core Repository.

Olivine, pyroxene and plagioclase CPO in most of the studied core intervals were provided by Drouin et al. (2010). We report complementary analyses of microstructures (morphological textures) and new data of in situ major and trace element compositions for olivine, plagioclase and clinopyroxene. Petro-geochemical profiles were done along preferred directions selected parallel to (at least) one of the three principal crystallographic axis of olivine, as defined by microstructural analysis. Plagioclase and clinopyroxene were analysed along the same profiles, in prolongation of the preferred direction in adjacent olivine crystals.

Microstructures were analytically characterized by indexation of Electron Backscattered Diffraction (EBSD) measurements using the SEM-EBSD facilities at Geosciences Montpellier (University of Montpellier). A set of 8 OI-T was analysed by a Scanning Electron Microscope (SEM) JEOL JSM 5600, and another set of 7 samples of OI-T and 1 troctolite were analysed by a Field Emission Gun (FEG) CamScan X500FE CrystalProbe. Operating conditions and data processing are given in the Supplementary Material - analytical methods and models.

Major element compositions of minerals were determined by Electron Probe Micro Analyser (EPMA) at Geosciences Montpellier (University of Montpellier), using a CAMECA SX100 equipped with five wavelength-dispersive X-ray spectrometers (WDS). Analyses were done with 20 kV accelerating potential, 10 nA beam current and 30 s counting times for all elements measured. Natural minerals and synthetic oxides are used as standards.

In situ trace element compositions were determined at Geosciences Montpellier, using a Thermo Scientific Element 2XR (eXtended Range) high resolution - Inductively Coupled Plasma Mass Spectrometry (ICP-MS). The ICP-MS is coupled with laser ablation (LA) system, a Microlas (Geolas Q+) automated platform with a 193 nm Excimer Compex 102 laser from LambdaPhysik. The laser energy density was set to 12-15 J cm² and repetition rate at 8-10 Hz. The laser spot size was set to 102-77 µm for olivine, and 77 µm for plagioclase and clinopyroxene. Data were reduced with the GLITTER software package (Van Achterbergh et al., 2001), using the linear fit to ratio method. Concentrations were calibrated against the NIST 612 rhyolitic glass using the values given in Pearce et al. (1997). ²⁹Si for olivine and ⁴³Ca for plagioclase and pyroxenes were used for internal standardization relative to EPMA data. The sample preparation and methods for data acquisition and reduction are detailed in the Supplementary Material - analytical methods and models -

together with the precision and accuracy of the LA-ICP-MS analyses and the values obtained for standard reference basalt BIR-1G (Supplementary Material Table S3).

Compositions of olivine, plagioclase and clinopyroxene are in Supplementary Material Tables S1 and S2.

2.5 Results

2.5.1 Downhole characteristics of Olivine-rich troctolites in the 1100-1300 mbsf interval

Ol-T is the dominant lithology between 1100 and 1300 mbsf of Hole U1309D. Contacts with neighbouring gabbros were recovered at different depths. Based on interval thickness and contact morphology, two main structural relationships are identified (Fig. 3a–b). A first feature is defined by dm to several m thick gabbroic intervals that cut Ol-T with sharp contacts (Fig. 3a). The >1 m thick gabbro intervals display regularly distributed modal composition and grain size variations, in contrast to cross-cut olivine-rich intervals that have either constant modal composition or irregularly distributed olivine modal contents. The second structural feature consists in 2 to 5 cm thick gabbroic veins (olivine <5 vol%) that show diffuse contacts with the Ol-T. These contacts display higher plagioclase modal contents progressively decreasing with increasing distance from the gabbroic vein, forming a plagioclase-rich halo of maximum 5 cm thickness within the Ol-T (Fig. 3b).

Ol-T in the top 90 m of 1100-1300 mbsf interval have ~70-80 vol% modal olivine and variable modal content of poikilitic interstitial phases, with clinopyroxene/plagioclase modal ratio between 0.4 and 1 (Table 1). Domains with >75 vol% modal olivine dominate between 1190 and 1193 mbsf, where local enrichments in plagioclase and minor clinopyroxene (up to ~25 vol% of plg) are shown. At 1193-1194 mbsf (Core U1309D-248R) olivine decreases downhole, while clinopyroxene content increases at the expense of olivine and plagioclase up to clinopyroxene/plagioclase ratio of 1 (Table 1). Except for this interval, no downhole correlations with depth are observed for compositional variations in Ol-T (Blackman et al., 2006).

In all studied Ol-T samples, two textural occurrences of olivine crystals are distinguished based on their morphology and deformation signature. The first type is formed by coarse to medium grained olivine crystals displaying well-defined and widely-spaced subgrain boundaries (Fig. 4d,f),

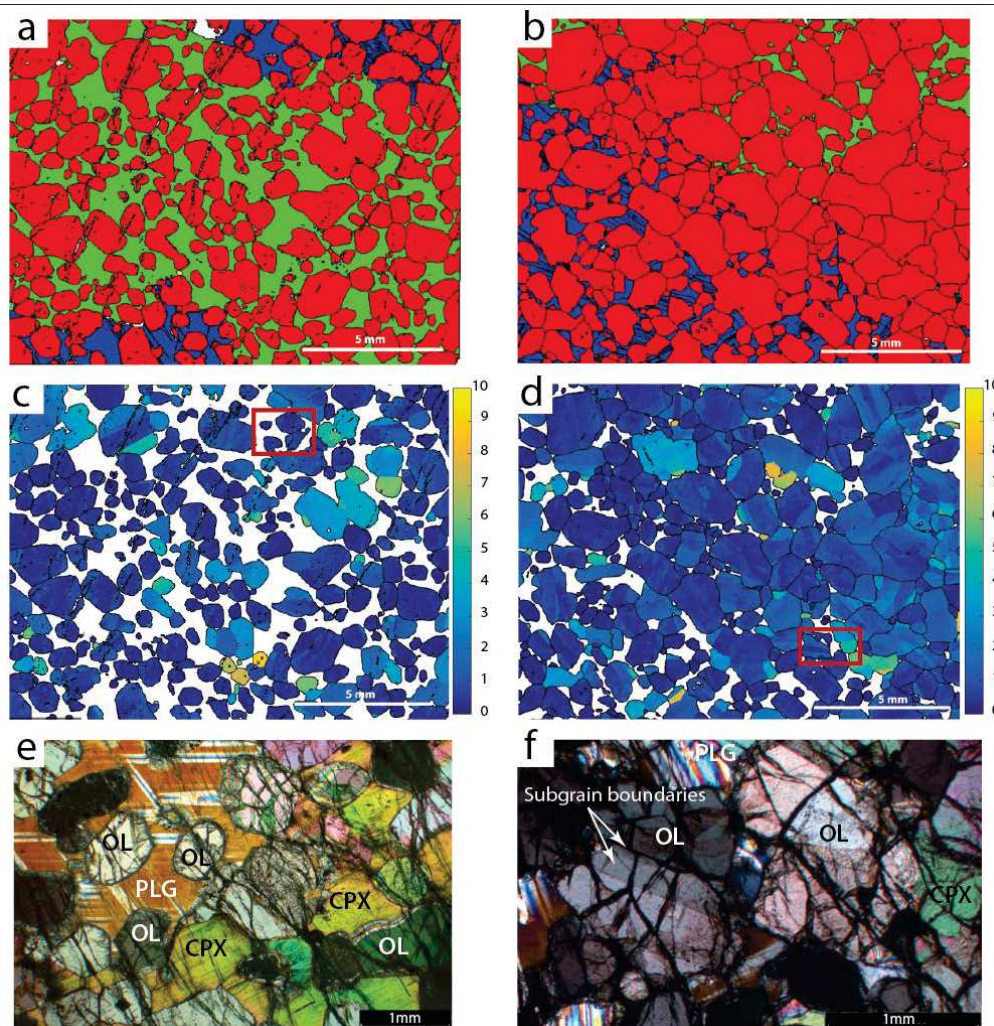


Fig. 4 - EBSD processed maps representative of a) and c) OL-T 1 sample 305-U1309D-247R-3W, 22-25 cm; b) and d) OL-T2 sample 305-U1309D-248R-2W, 43-48 cm. a)–b) EBSD phase maps where each color corresponds to a phase: red=olivine, blue=plagioclase, green=clinopyroxene. Note single grains embayed in poikilitic interstitial phases in a) OL-T1, and the abundance of olivine crystals (>75 vol%) forming aggregates in b) OL-T2. c)–d) Olivine EBSD maps of misorientation to the mean grain orientation, with threshold of misorientation angle for grain boundaries set at 10° . Red rectangles in c) and d) indicate the localization of photomicrographs reported in e) and f), respectively. Microscopic images (cross-polarized light) of e) fine-grained undeformed olivine embayed in poikilitic plagioclase and clinopyroxene (CPX) crystals, and f) medium-grained deformed olivine (OL) showing well defined subgrain boundaries, and corroded grain boundaries in contact with interstitial undeformed plagioclase (PLG). (For interpretation of the references to color in this figure legend, the reader is referred to the web version of this article.)

and partially corroded grain boundaries. Incipient olivine dissolution is often observed at intersections between grain and subgrain boundaries (Fig. 4f). This type of deformed olivine corresponds to the olivine described by Drouin et al. (2010) as recording high temperature

deformation signature. The second type comprises fine grained rounded olivine chadacrysts with no evidence of deformation (Fig. 4c,e) and, in few instances, forming chains of grains in near optical continuity. These undeformed olivines are interpreted as being formed after corrosion and disruption along grain and subgrain boundaries of pre-existing (deformed) coarse grained olivines (Drouin et al., 2010).

Table 1. List of samples and their principal textural characteristics and mineral chemical compositions. Ol = olivine, Cpx = clinopyroxene, Plg = plagioclase, Opx = orthopyroxene. Mg# = $100 \times \text{cationic (Mg)/(Mg + Fe)}$, with all Fe as Fe²⁺.

Sample IODP	Depth (mbsf)	Lithology	Core description		Thin section description							
			Tot Alteration %	Cpx/Plg	Mineral modes (% of EBSD indexed points)					Mineral Chemistry		
					Ol	Spl	Plg	Cpx	Opx	Mg# Ol	An Plg	Mg# Cpx
305-U1309D-227R-3W, 124-126	1096.17	Ol Troctolite 2	20	0.41	77	0	15	8	-	84.0	78.9	87.6
305-U1309D-234R-1W, 22-26	1124.97	Ol Troctolite 1	70	0.48	75	0	22	3	-	85.6	78.5	87.4
305-U1309D-241R-2W, 89-91	1160.66	Ol Troctolite 2	10	0.27	84	0	13	3	-	84.4	74.7	86.6
305-U1309D-247R-3W, 16-18	1190.05	Ol Troctolite 1	5	0.97	69	0	7	24	0	85.0	79.4	86.7
305-U1309D-247R-3W, 22-25	1190.11	Ol Troctolite 1	5	0.51	71	0	24	4	-	85.0	75.2	87.1
305-U1309D-247R-3W, 62-66	1190.51	Ol Troctolite 3	10	0.98	79	0	2	19	0	84.1	73.1	87.0
305-U1309D-247R-3W, 76-81	1190.65	Ol Troctolite 2	10	0.46	81	-	13	6	-	84.6	74.4	85.8
305-U1309D-248R-1W, 110-113	1193.00	Ol Troctolite 1	5	0.01	77	0	23	0	-	85.3	76.2	-
305-U1309D-248R-2W, 18-21	1193.32	Ol Troctolite 3	2	0.18	61	0	33	6	0	82.7	73.0	84.5
305-U1309D-248R-2W, 22-24	1193.36	Ol Troctolite 3	2	0.16	84	-	10	2	4	82.6	64.1	85.0
305-U1309D-248R-2W, 38-41	1193.52	Ol Troctolite 2	2	0.15	81	0	17	3	0	84.0	73.1	85.7
305-U1309D-248R-2W, 43-48	1193.57	Ol Troctolite 2	2	0.29	80	-	16	5	-	84.1	76.1	86.1
305-U1309D-248R-3W, 29-32	1194.78	Ol Troctolite 1	10	0.51	78	0	18	4	-	85.0	76.5	86.4
305-U1309D-248R-3W, 36-38	1194.85	Ol Troctolite 1	10	0.98	64	0	6	30	0	85.1	74.7	86.3
305-U1309D-248R-3W, 131-134	1195.80	Ol Troctolite 1	10	0.50	75	0	20	5	-	85.2	75.7	87.7
305-U1309D-268R-2W, 83-85	1290.06	Troctolite	10	0.85	34	-	35	30	1	81.0	76.6	85.3

Ol-Ts dominated by wehrlitic and troctolitic domains (cpx/plg ratio = 0.5-1, Table 1) contain 64-77 vol% modal olivine (Fig. 3c and 4a), whereas Ol-Ts with 77-84 vol% modal olivine show mainly dunitic domains and plagioclase is the dominant interstitial phase (cpx/plg = 0.15-0.46, Table 1; Fig. 3b and 4b). The former are characterized by olivines with Mg# ranging from 85 to 85.6 and the latter have olivines showing lower Mg# (84-84.6, Table 1). Ol-Ts with lower olivine modal contents predominantly show medium interstitial (in the range 0.3-1 mm) to large poikilitic (1-2 mm) grains of plagioclase and clinopyroxene (Fig. 4a) having An contents between 75 and 79.4, and Mg# ranging from 86.4 to 87.6, respectively (Supplementary Material Table S1). Plagioclase and clinopyroxene in Ol-Ts with higher modal olivine are mainly small (<300 μm) interstitial grains (Fig. 4b) that have An contents in the range 64-75, and Mg# between 85 and 86.6 (Supplementary Material Table S1), respectively.

Based on these structural and textural characteristics, and olivine chemical compositions, the studied Ol-Ts were classified in three types. Type 1 and 2 are portions of Ol-T sampled away from their sharp contacts against neighboring gabbros. Type 3 assembles Ol-T collected close to diffuse interfaces with gabbroic veins. Ol-T 1 contains <77 vol% modal olivine (except for one sample with olivine 78 vol%: 305-U1309D-248R-3W, 29-32) with the highest Mg# (Table 1; Fig. 4a,c and 5). Olivine is medium (2-3 mm) to fine (<1 mm) grained (Fig. 4a,c,e). Single olivine grains predominate and are embayed in large poikilitic oikocrysts of plagioclase and clinopyroxene (Fig. 4e). Ol-T 2 contains >77 vol% modal olivine with lower Mg# (Table 1; Fig. 4b,d and 5). Olivine is coarse (5-6 mm) to fine (<1 mm) grained, and forms aggregates of >15 grains (Fig. 4b,d,f). Coarse olivine crystals show lobate grain boundaries against adjacent small interstitial phases, which indicate partial dissolution of olivine by reaction with the melt that crystallized plagioclase and clinopyroxene. In Ol-T 2 plagioclase is the dominant interstitial phase. Ol-T 3 has variable amounts of olivine that overlap with those in Ol-T 1 and Ol-T 2, and the lowest olivine Mg# (82.6-84.1; Table 1). Its composition fills the gap between Ol-T and Troctolite (Fig.5). Plagioclase has the lowest measured An contents ($An_{64}-An_{73}$; Table 1) and clinopyroxene display the lowest Mg# (84.5-85 except in sample 305-U1309D-247R-3W, 62-66 with cpx Mg# 87; Table 1; Fig. 5). Note that orthopyroxene was found in one sample of Ol-T 3, occurring as fine-grained interstitial crystals with Mg# 84. Locally it appears as vermicular grains between olivine and plagioclase or clinopyroxene suggesting that orthopyroxene is not of mantle origin. Instead, it represents the product of late stage crystallization of an evolved melt (e.g., Borghini and Rampone, 2007). This melt concomitantly formed the cross-cutting gabbroic veins.

2.5.2 Mineral geochemistry

Two groups of elements are distinguished based on their behavior in olivines from Hole U1309D Ol-T. The first group is composed of elements (e.g., Mg, Fe, Ni, Mn, Zn and Li) that show distinct concentrations in olivines from the three groups of Ol-T. The second group is formed by lithophile trace elements that have similar concentrations in all analysed olivines, and minor variations in plagioclase and clinopyroxene.

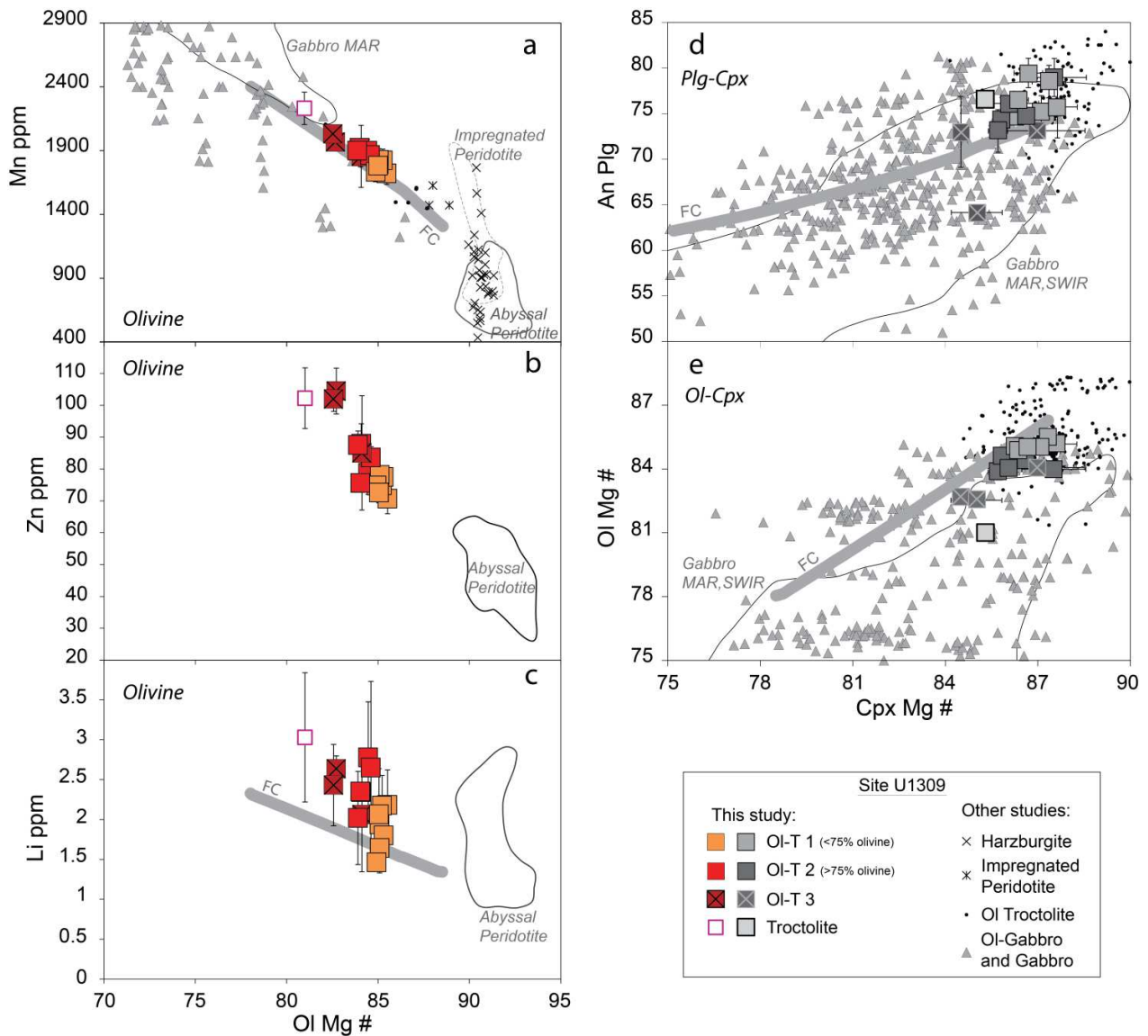


Fig. 5 - Olivine (Ol), plagioclase (Plg) and clinopyroxene (Cpx) compositions in Ol-T and troctolite selected from Hole U1309D. Values are reported as sample averages of crystal cores. Olivine Mg# ($Mg\# = 100 \times \text{cationic } (Mg/(Mg+Fe))$ with all Fe as Fe^{2+}) versus a) Mn (ppm), b) Zn (ppm), c) Li (ppm). Clinopyroxene Mg# versus d) Plagioclase An content (%), e) olivine Mg#. Data from previous studies are reported for comparison: harzburgite and impregnated peridotites from IODP Site U1309 (Miller et al., 2009; Tamura et al., 2008), Ol-T and gabbros from IODP Hole U1309D (Drouin et al., 2009; Miller et al., 2009; Suhr et al., 2008), abyssal peridotites (continuous black line, De Hoog et al., 2010; D'Errico et al., 2016), impregnated peridotites (dotted grey line, Seyler et al., 2007; Tartarotti et al., 2002), gabbros from Mid-Atlantic Ridge (MAR, continuous grey line, Hebert et al., 1991; Ross and Elthon, 1997) and from ODP Hole 735B (SWIR, Dick et al., 2002). The grey thick line in a), c), d), e) indicate major and minor element evolution of mineral element compositions during Fractional Crystallization (FC) of a Primitive MORB Mg# 71 (Presnall and Hoover, 1987). This trend was calculated at 2 kbar pressure using the integrated software Petrolog3 (Danyushevsky and Plechov, 2011). Partition coefficient values are in Supplementary Material Table S4. K_{Mn} was constant during simulation (no significant variations expected). Olivine K_{Li} is from Spandler and O'Neill (2010).

The composition of undeformed olivines overlaps that of deformed olivine within the same sample, or does not show systematic variations (Supplementary Material Table S1). Olivine rims display compositions similar to cores (Supplementary Material Table S1). In contrast, clinopyroxene and plagioclase show slight core-rim variations, similar to previously published data (Fig. 3b in Drouin et al., 2009). Such variations are most evident in small interstitial and isolated grains (or wedges) characterized by enrichments in incompatible elements, which are associated to lower An contents in plagioclase and lower Mg# in clinopyroxene (Supplementary Material Table S1). These variations were interpreted as resulting from late stage cooling of trapped melt (Drouin et al., 2009).

2.5.2.1 Minor transition elements and Li in olivine

Olivines have minor transition element compositions higher than those of olivines in abyssal peridotites (MAR 15°N, Seyler et al., 2007; peridotites from other oceanic locations, D'Errico et al., 2016; Tartarotti et al., 2002; Fig. 5a,b), but they are comparable with olivines in impregnated harzburgites (e.g., Site U1309, Miller et al., 2009; Tamura et al., 2008; Fig. 5a). Mn contents in olivine overlaps compositions of olivines in the most primitive gabbro end-members sampled along the Mid-Atlantic Ridge (IODP Hole U1309D, Drouin et al., 2009; Miller et al., 2009; Suhr et al., 2008; MARK area, Hebert et al., 1991; Lissenberg and Dick, 2008; Ross and Elthon, 1997; Fig.5a). Li contents are comparable with those of olivines in abyssal peridotites (Fig. 5c). Minor transition elements and Li contents are consistent with the compositional trend predicted for the earlier stages of fractional crystallization, from the most refractory troctolites to olivine depleted gabbros (Villiger et al., 2007): Ni, an element with a strong affinity for olivine (Supplementary Material Table S4), is enriched in high-Mg# olivine cores (Supplementary Material Table S1), while abundances in elements having moderately incompatible to compatible affinity, such as Mn, Zn and Co ($^{Ol/Melt}K_{Mn} = 1.15$, $^{Ol/Melt}K_{Zn} = 1.16$, $^{Ol/Melt}K_{Co} = 5.21$; Supplementary Material Table S4), display inverse negative correlation with olivine Mg# (Supplementary Material Table S1; Fig. 5).

Ol-T 1 (ol <75%) have olivine with Ni contents ranging from 1870 to 2820 ppm, Mn between 1670 and 1820 ppm, Zn and Li contents in the ranges 70.7-78.0 ppm and 1.5-2.2 ppm, respectively (values are averages per sample; Fig. 5). Olivine in Ol-T 2 (modal ol >75%) is distinguished by lower Ni contents (1790-2130 ppm), coupled with higher Mn (1800-2000 ppm), Zn (75.6-87.9 ppm) and Li

contents (2.1-2.9 ppm). Ol-T 3 displays olivine with the lowest Ni contents (1690-2080 ppm), and the highest Mn and Zn contents (Mn=1850-2030 ppm, Zn=85.0-104.4 ppm) of all investigated Ol-T (Fig. 5). Li contents of olivines in Ol-T 3 overlap with compositions of Ol-T 2 olivines (Li=2.06-2.65 ppm). Among all studied samples, troctolite is the most evolved end-member with olivine showing the lowest Ni contents (~1700 ppm), and the highest Mn (~2200 ppm), Zn (~102 ppm) and Li contents (~3 ppm).

These compositions apparently follow a trend of fractional crystallization as predicted at pressure conditions of 2 kbar (~7 km depth as predicted for emplacement of U1309 gabbroic sequence, Grimes et al., 2008; Fig. 5). However, the most primitive chemical compositions are observed in the Ol-T displaying less modal olivine (Ol-T 1; Fig. 5a-c). Extremely variable Ni abundances in olivine at constant Mg# were already highlighted in the previous study of Drouin et al. (2009). Our new geochemical dataset displays similar variations for Li (Fig. 5c), which are not expected after a simple process of fractional crystallization. Olivine is the major host of Li in mantle peridotites and, usually, does not show strong variations (e.g., De Hoog et al., 2010) in contrast to what observed in the studied olivine crystals.

2.5.2.2 Lithophile trace elements

Few trace element data are available for olivine in oceanic environments. Most studies focused on olivines from oceanic peridotites (e.g., Gakkel Ridge mantle, D'Errico et al., 2016) and orogenic massifs (e.g., in situ analyses and on separates from Ronda peridotite, Garrido et al., 2000; in situ analyses on Erro-Tobbio ophiolites, Rampone et al., 2016, and Internal Liguride and Pineto ophiolites, Sanfilippo et al., 2014), but gabbroic rocks have been little studied (Site U1309, Drouin et al., 2009; single primitive olivine gabbro from Hess Deep, Lissenberg et al., 2013; Erro-Tobbio olivine gabbros, Rampone et al., 2016).

Olivines from all our samples are on average depleted in lithophile trace elements and have similar trace element contents (Figs. 6a,b and 7a). In Hole U1309D Ol-T, they have Yb_N (N = values normalized to chondrites, after Sun and McDonough, 1989) ranging from 0.18 to 0.78, coupled to strong depletion in M - (medium) REE ($Dy_N = 0.005-0.064$) relative to HREE and scattered L - (light) REE ($La_N = 0.0003-0.006$). Their H - (heavy) REE content are higher than in mantle olivines from abyssal peridotites and mantle ophiolites (Gakkel Ridge, D'Errico et al., 2016; Erro-Tobbio ophiolite,

Rampone et al., 2016; Internal Ligurian and Pineto ophiolites, Sanfilippo et al., 2014). The strong normalized H-REE to M- (medium) REE fractionation ($Dy_N/Yb_N = 0.04-0.11$, Fig. 6a,b) that characterizes the studied olivines is similar to what observed in olivine from ophiolitic troctolites (e.g., Rampone et al., 2016; Sanfilippo et al., 2014), and oceanic olivine-rich gabbros (e.g. fast-spreading ridge at Hess Deep, Lissenberg et al., 2013). Within a same sample, olivines embayed in clinopyroxene have lower REE in comparison with olivines in contact with plagioclase.

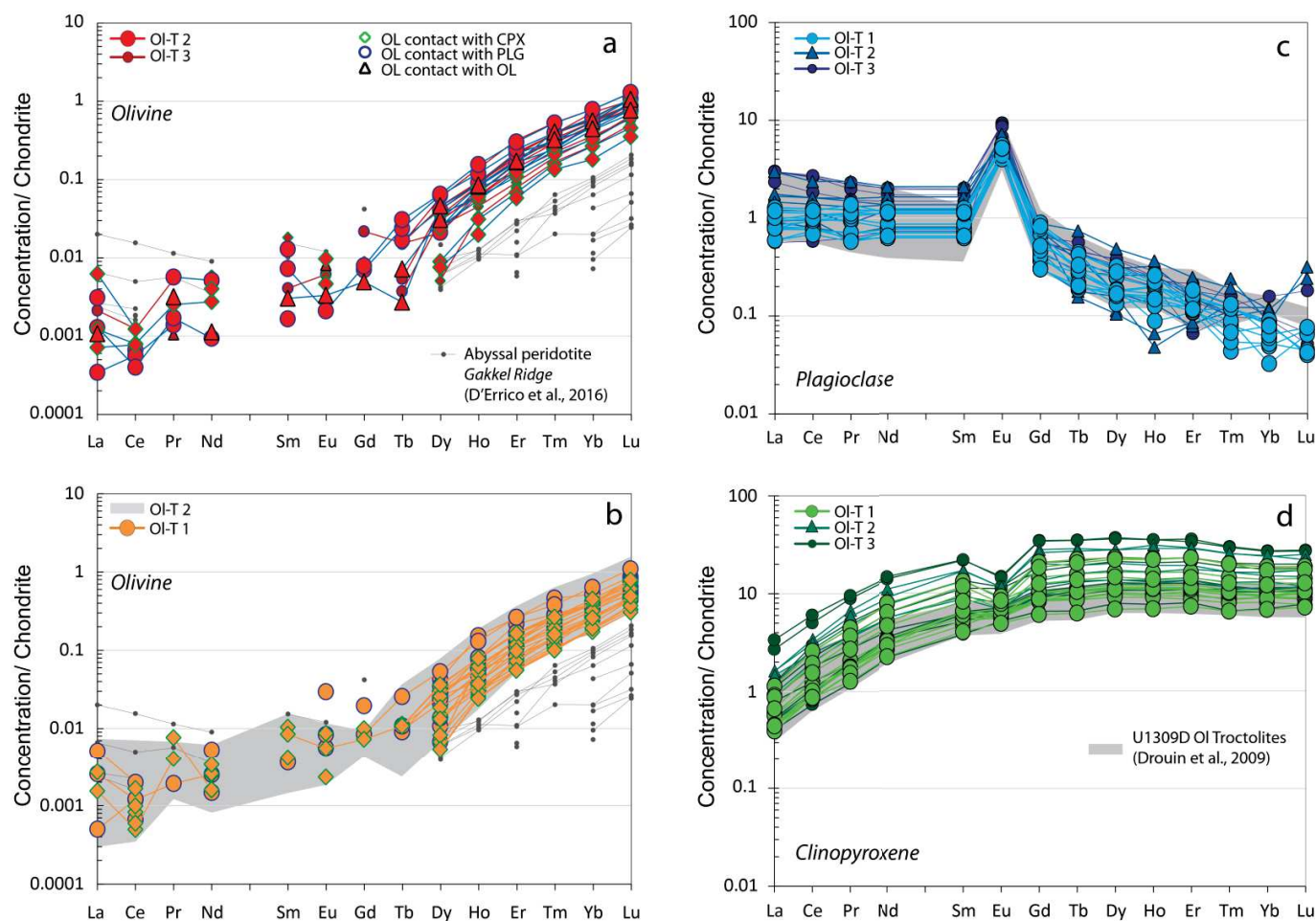


Fig. 6 - Chondrite-normalized Rare Earth Element (REE) concentrations of olivine from a) OI-T2 and OI-T3 and from b) OI-T1, and of c) plagioclase and d) clinopyroxene from OI-T of IODP Hole U1309D. REE abundances in olivines from abyssal peridotites of Gakkel Ridge (D'Errico et al., 2016) are shown for comparison in a) and b). REE abundance of OI-T2 olivine is also represented in b) for comparison. The dark grey fields in c) and d) are REE abundances of plagioclase and clinopyroxene cores in U1309D OI-T from previous study (Drouin et al., 2009). Symbols refer to phases in contact with analysed olivine (clinopyroxene=CPX, plagioclase=PLG, olivine=OL). Colors in each graph refer to the type of OI-T. Normalizing values after Sun and McDonough (1989). (For interpretation of the references to color in this figure legend, the reader is referred to the web version of this article.)

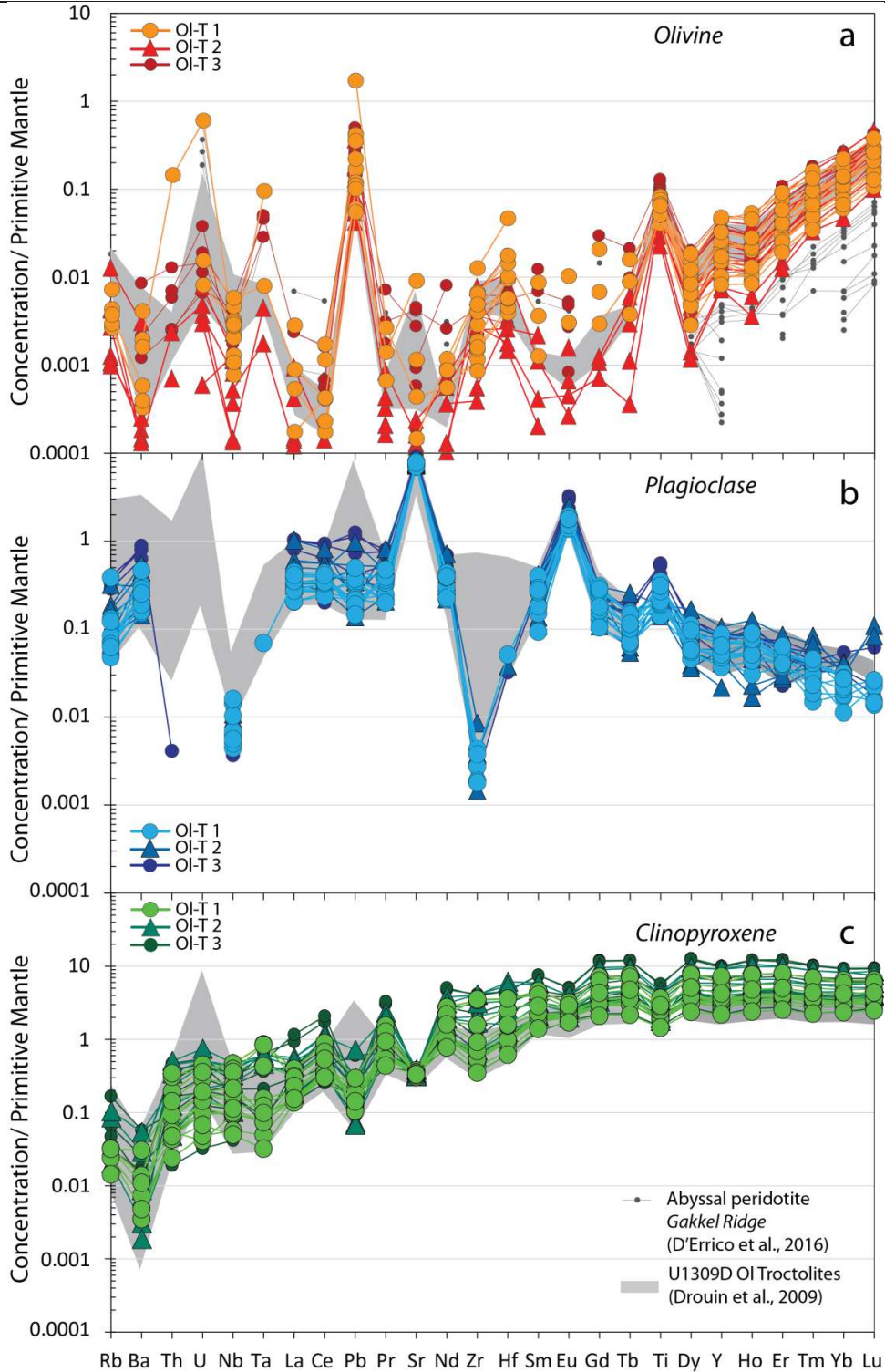


Fig. 7 - Primitive mantle-normalized trace element concentration diagrams for a) olivine, b) plagioclase and c) clinopyroxene from OI-T of IODP Hole U1309D. Symbols and colors refer to the type of OI-T. Olivines from abyssal peridotites of Gakkel Ridge (D'Errico et al., 2016) are shown for comparison. The grey fields are olivine, plagioclase and clinopyroxene cores in OI Troctolites of Atlantis Massif from Drouin et al. (2009). Normalizing values after Sun and McDonough (1989). (For interpretation of the references to color in this figure legend, the reader is referred to the web version of this article.)

Extended trace element patterns of olivines highlight positive anomalies in Ti (up to ~110 ppm in olivine-rich troctolites; $Ti/Dy = 4-12 \times$ Primitive Mantle-PM) and in the most incompatible High Field Strength Elements (HFSE), such as Zr-Hf and Th-U, relative to the neighboring trace elements (Fig. 7a).

All analysed samples have plagioclase displaying strong Eu positive anomalies ($Eu/Eu^* = 5-13$, except for an Ol-T 1 and an Ol-T 2 with $Eu/Eu^* = 3.5-5.5$). Drouin et al. (2009) showed that plagioclase from U1309D olivine-rich troctolites have comparable compositions to those of oceanic gabbros from the MARK area. All plagioclases have overall comparable REE patterns with La_N/Sm_N ranging between 0.7 and 2 (Fig. 6c). Note that the highest La_N/Sm_N ($La_N/Sm_N = 1-2$; Fig. 6c) are displayed by plagioclases in Ol-T 2, where they dominantly appear as isolated and small interstitial grains, and Ol-T 3 where they exhibit subhedral habit. Trace element patterns display positive anomalies in Sr and Ti relative to neighboring elements, and negative anomalies in Nb and Zr (Fig. 7b).

Clinopyroxenes from all investigated Ol-T have compositions similar to those of clinopyroxenes from gabbros sampled along the Mid-Atlantic Ridge (Drouin et al., 2009). They have flat patterns for MREE and HREE and depletion in LREE ($La_N/Sm_N = 0.07-0.16$, Fig. 6d). They have Yb_N concentrations ranging from 6.7 to 18.5 and Eu/Eu^* ratio between 0.7 and ~1 in Ol-T 1. It should be noted that small interstitial clinopyroxene grains in Ol-T 2 and large subhedral grains in Ol-T 3 display the highest REE concentrations associated with a slight deepening of the negative Eu anomaly (Ol-T 2, $Yb_N = 10.8-23.9$ and $Eu/Eu^* = 0.5-0.7$; Ol-T 3, up to $Yb_N = 26.6$ and $Eu/Eu^* = 0.6$; Fig. 6d). All clinopyroxenes are distinguished by moderate negative anomalies in Ti and slight depletion in Zr-Hf and Ta relative to neighbor trace elements (Fig. 7c; $Zr/Sm = 0.23-0.85 \times$ PM). Strong fractionation relative to neighboring elements is observed for Sr, Pb and Ba on extended trace element patterns (Fig. 7c; $Sr/Nd = 0.05-0.48 \times$ PM; $Pb/Ce = 0.06-3.7 \times$ PM).

2.5.3 Geochemical profiles

Rim-to-rim profiles across olivine and clinopyroxene crystals were performed to unravel possible mineral chemical zonation resulting from melt-rock interactions. We excluded small interstitial and isolated grains of clinopyroxene to avoid signature of late stage cooling of trapped melts; thus we selected the largest clinopyroxene grains adjacent to olivine. Results are reported in

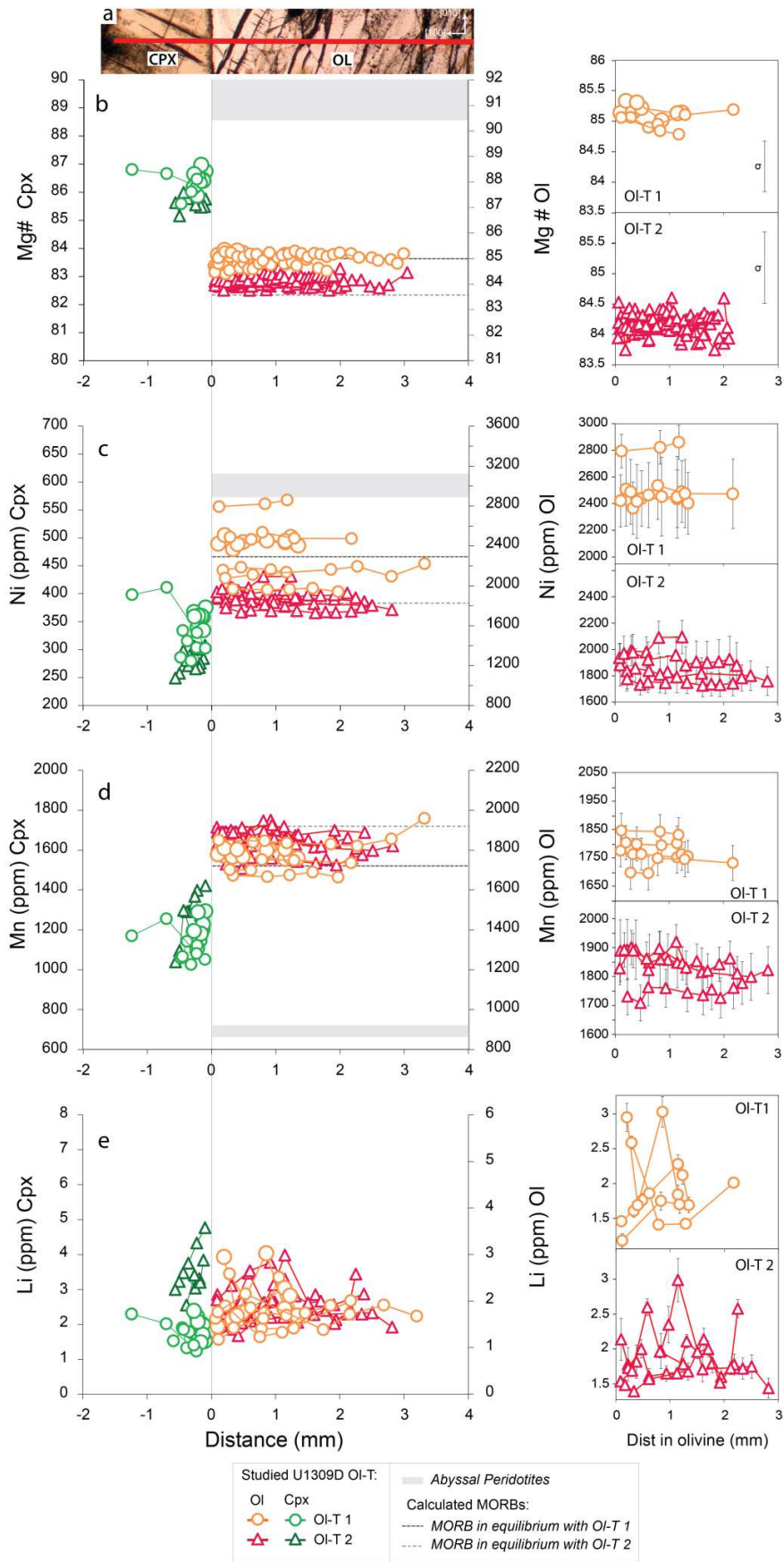


Fig. 8 - Chemical profiles across olivine and neighboring clinopyroxene. Profiles were performed along one of the principal axes of olivine ([100], [010], or [001]; see Analytical methods for further details) as illustrated in a) CPX=clinopyroxene, OL=olivine. Similar compositions were observed along different axes, and therefore no axis-distinction is made. We report a selection of two Ol-T1 (305-U1309D-248R-2W, 38-41; 305-U1309D-248R-2W, 43-48) and two samples of Ol-T2 (305-U1309D-247R-3W, 16-18; 305-U1309D-248R-3W, 36-38) for the following elements: b) Mg#, c) Ni (ppm), d) Mn (ppm), e) Li (ppm). Olivine profiles from single samples are enlarged on the right side of the figure. For comparison we report data of olivines from abyssal peridotites (De Hoog et al., 2010; D'Errico et al., 2016) and calculated olivine compositions in equilibrium with neighboring clinopyroxene (see text for details).

Fig. 8 for Mg# and trace elements having variable partitioning affinity in olivine (Ni, Mn and Li; Supplementary Material Table S4). For consistency, elements possibly affected by subsolidus re-equilibration were not included in the core-to-rim study as subsolidus re-equilibration takes place first at crystal rims (e.g., Ca and REE; Coogan et al., 2002; Sun and Liang, 2014). For the same reason, we considered only the Ca and REE compositions of cores.

Clinopyroxenes exhibit rather flat profiles in the studied samples, except for some grains that show scattered Mn and Li contents (Fig. 8d–e). This lack of zoning was interpreted as evidence of crystallization in an open system after constant input of undifferentiated melts by Drouin et al. (2009). Olivine also displays flat profiles for all elements considered, except some grains that display scattered Li contents. However, because of serpentinization along olivine edges, all geochemical analyses were performed at a minimum distance of 60 μm from olivine-clinopyroxene contact. As the actual mineral/mineral interface could not be measured, we cannot preclude possible local chemical variations at olivine rims. The possible impact of this gap in data on the shape of geochemical profiles is taken into account in the discussion.

Although element diffusion in olivine is anisotropic (e.g., Dohmen and Chakraborty, 2007), profile along distinct crystallographic axes display comparable compositions and shape in single olivine crystals (Supplementary Material Table S2). For this reason, in Fig. 8, we do not distinguish profiles along the fastest axis [001] from those along [100] and [010], and all analyzed profiles are reported for selected samples.

2.6 Discussion

2.6.1 Evidence of reactive Olivine-rich troctolites

Textural relationships in OI-T display deformed olivine grains embayed, sometimes dismembered and partly corroded, against clinopyroxene and/or plagioclase suggesting disequilibrium and reaction between olivine and interstitial phases. Conversely, clinopyroxene and plagioclase show no evidence of deformation and share sharp, relatively planar contacts indicative of equilibrium and crystallization from a common parent melt. Subgrain microstructures observed in olivines from studied OI-T are similar to those found in some oceanic gabbros, which are interpreted to form at subsolidus condition in lower oceanic crust cumulates (Yoshinobu and Hirth, 2002). However, the strong CPO characterizing these olivine gabbros are in contrast with the weak olivine CPO of OI-T from the Atlantis Massif (Drouin et al., 2010; this study).

Mineral chemistry and modal compositions provide complementary lines of evidence against the formation of OI-T by a simple process of fractional crystallization. The most primitive olivine compositions are found in OI-T 1 (<75 vol% of olivine), whereas OI-T 2 (>75 vol% of olivine) have olivine compositions similar to those of Hole U1309D olivine gabbros (Drouin et al., 2009, 2010; Miller et al., 2009) containing 5 to 45 vol% olivine, 40 vol% plagioclase and 15 to 55 vol% clinopyroxene. OI-T 3, which was sampled near gabbroic veins, displays the most evolved olivine compositions, although these compositions still overlap those of OI-T 1 and 2, independently of olivine contents. So, the chemical and modal variations of olivine are inversely correlated, in opposition to what is expected for a simple crystallization and magma differentiation trend (Villiger et al., 2007; Fig. 5). Also, olivines show a wide range of Ni and Li contents at a given olivine Mg# (Fig. 5); such trends are not predicted by models of magmatic crystallization. OI-T 1, which have the most primitive compositions, have also significantly more clinopyroxene (up to 25-30 vol%, Table 1) than the others OI-T and associated olivine gabbros, further suggesting an atypical differentiation trend. Clinopyroxene is characterized by high Mg#, which is classically interpreted as indicating high pressure crystallization (between 5 and 10 kbar; e.g., Grove et al., 1992), but this interpretation is however inconsistent with the low pressure conditions envisaged for the building of the gabbroic sequence at the Atlantis Massif OCC (Drouin et al., 2009; Grimes et al., 2008). Cores of large clinopyroxene crystals are characterized by a lack of (or small) Eu negative anomalies indicating early precipitation before or simultaneously with plagioclase, in contrast to the expected

fractional crystallization trends of MORB-type melt that predict early plagioclase crystallization (e.g., Grove et al., 1992; Villiger et al., 2007). Yet, in all Ol-T, trace element contents of clinopyroxene and plagioclase are in equilibrium with MORB-type melts (Drouin et al., 2009), indicating that they crystallized after a relatively evolved melt having compositions similar to those of basalts from Site U1309 (Mg# ~57, Godard et al., 2009; Fig. 6 in Drouin et al., 2009). In contrast, Mg# of melts calculated from clinopyroxene-olivine pairs show more primitive compositions (Mg# = 58-66; Fig. 9).

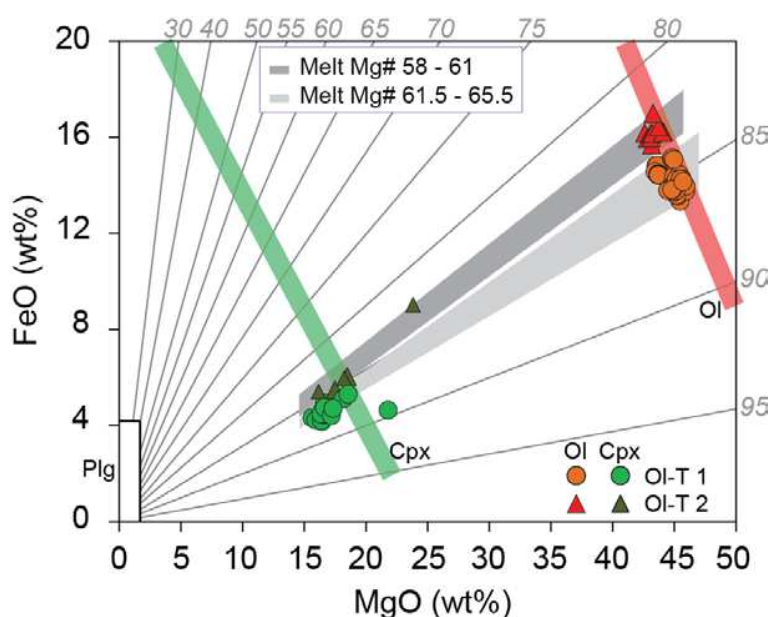


Fig. 9 - MgO (wt%) versus FeO (wt%) in olivine (red and orange symbols), and clinopyroxene (green symbols). Grey fields show the calculated range of compositions of olivine and clinopyroxene from melts in equilibrium with measured minerals. Calculations were performed using Petrolog3 (see Fig. 5 for details on the model) by selecting melts in equilibrium with measured clinopyroxene-olivine couples. Thin grey lines indicate iso-Mg# lines for Mg# ranging from 30 to 95. Variations of MgO and FeO are represented for olivine (Ol) in red line, clinopyroxene (Cpx) in green line and plagioclase (Plg) in white box. (For interpretation of the references to color in this figure legend, the reader is referred to the web version of this article.)

Finally, the enrichments in the most incompatible elements in olivines (i.e., U and HFSE) from Hole U1309D Ol-T seem to complement the strong depletion in selective elements (i.e., Zr-Hf) in plagioclase. This suggests re-equilibration of olivine with locally enriched MORB-type melts by the relatively ‘instantaneous’ crystallization of plagioclase and clinopyroxene. In contrast, disequilibrium signatures are observed for other incompatible elements (e.g., REE; Fig. 6 in Drouin et al., 2009) suggesting that re-equilibration may be not achieved for all elements. On the basis of Zr-Hf positive anomalies and enrichments in other incompatible elements in olivine, similar

conclusions have been reported by recent geochemical studies on OI-T from the Alpine ophiolites (Basch et al., in this issue; Rampone et al., 2016; Sanfilippo et al., 2014). Rampone et al. (2016) recently proposed that concomitant processes of olivine assimilation and plagioclase crystallization at decreasing melt mass are the mechanisms controlling HFSE anomalies in olivine and adjacent phases.

Combined textural, microstructural and chemical characteristics of U1309D OI-T indicate that they formed after a reactive process of olivine assimilation and concomitant crystallization of interstitial plagioclase and clinopyroxene. This melt-rock interaction progressively decreases olivine modal contents, and may account for an increase in MgO and Ni contents of the migrating melt (e.g., Collier and Kelemen, 2010; Lissenberg and Dick, 2008), while local crystallization of interstitial phases increases its contents in strongly incompatible elements. Modeling of the reactive process generally assumes that a MORB-type melt infiltrates and partially dissolves a pre-existing olivine matrix and recrystallizes new olivine, new plagioclase and additional clinopyroxene (e.g., Lissenberg and Dick, 2008; Rampone et al., 2016; Sanfilippo et al., 2014). Crystallization of clinopyroxene and plagioclase is generally thought to be preceded by formation of dunites with abundant crystallization of new crystals of olivine (e.g., Kelemen et al., 1997). Assimilation-Fractional Crystallization (AFC; DePaolo, 1981) is the most common and largely used model to reproduce chemical and modal variations at constant thermodynamic parameters. AFC models have been used to simulate the variations of major elements only (e.g., Lissenberg and Dick, 2008) or of minor and of some trace elements (i.e., Ti, Y, Zr, Hf; Rampone et al., 2016; Sanfilippo et al., 2014) during melt-rock interactions. The trends shown by other elements, in particular REE, were not reproduced successfully by this approach thus suggesting that element mineral-melt exchange is not the only control on OI-T and MORB compositions in a reactive system. These trends may be controlled also by element transport by migrating melts, which can play an important role in the re-distribution of the most incompatible elements (chromatographic effect, Navon and Stolper, 1987).

In the following sections, we first simulate melt-rock interactions by geochemical numerical modeling to quantify the effect of reactive transport through a porous media on the chemistry of reactive OI-T. Then, we investigate the equilibrium signature of mineral phases forming the U1309D OI-T.

2.6.2 Numerical simulations of compositional variations

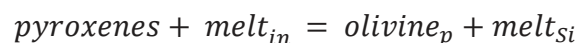
2.6.2.1 Model setup

The reaction process described above is triggered by a melt that infiltrates in an olivine-rich porous medium and thus controls element transport through the crystal matrix. In turn, melt flow through a solid matrix is governed by the 'percolation threshold' (fraction of melt produced > total porosity, Turcotte and Morgan, 1992). At constant melt viscosity, the percolation threshold is controlled by porosity (melt volume fraction), connected porosity and permeability (e.g., Kelemen et al., 1997; Turcotte and Morgan, 1992). Accordingly, the pre-existing porosity and permeability may be an important additional factor in determining melt composition and behavior during the reactive process. The formation of the most primitive OI-T 1, which display the highest clinopyroxene and plagioclase modes compared to OI-T 2 with <25 vol% of interstitial phases, could be related to a higher percolation threshold leading to higher melt/rock ratios.

The initial composition of the olivine-rich porous medium is set as that of a mantle harzburgite based on the following arguments. The heterogeneous plutonic section at the Atlantis Massif lacks the typical well-developed modal layering generally described in settings where cumulate-derived OI-Ts form (e.g., Bédard, 2015; Holness et al., 2007). The latter originate during the construction of a cumulate differentiation series in metres thick lenses ('intra-crustal origin', Renna et al., 2016) or in large magma chambers (e.g., Bédard et al., 2000; Bédard, 2015; O'Driscoll et al., 2007). In contrast, there is no structural evidence for magma chambers in Hole U1309D (e.g., Blackman et al., 2011; Grimes et al., 2008), and geochemical data does not indicate that the downhole gabbroic series formed by a continuous magma fractionation process (Fig. 2). Also, dunitic cumulates are not described in Hole U1309D. Dunitic cumulates would contain olivine with similar Mg# and REE contents compared to those of a mantle dunite, but higher Ni contents (see Supplementary Material - analytical methods and models). These features, together with the microstructural constrains from Drouin et al. (2010) lead us to discard the hypothesis of cumulate precursor of OI-T from the Atlantis Massif. The Ni concentrations in olivine from the studied OI-Ts are higher than those in associated troctolites and olivine gabbros, but are comparable to olivines from abyssal peridotites (Fig. 10c). We hypothesize that the impregnated harzburgites intruded by the plutonic sequence observed in the shallowest 200 m at Site U1309 (Tamura et al., 2008) preserved the first

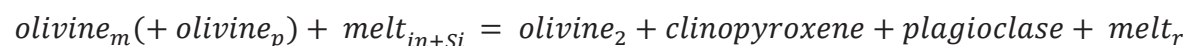
stages of melt impregnation of the shallow mantle prior to the extensive melt percolation that formed Ol-Ts.

We model the evolution of Ol-T from a harzburgitic matrix using a reactive porous flow numerical model, the 'Plate Model' proposed by Vernières et al., (1997) for REE contents and modified by Bedini et al. (2002) for Mg# contents, to explore the chemical effect on relict minerals and melt compositions. This model allows simulations in a rock-dominated system where the solid matrix buffers the melt composition. We simulate an open system and multi-stage process to reproduce the formation of compositional variations at centimeter scale observed in Hole U1309D Ol-T. Two main stages are modeled. *Stage 1* is the dunitization process that reproduces complete dissolution of pyroxenes in the starting harzburgite by an incoming melt assuming the following reaction:



where 'pyroxenes' are mantle orthopyroxenes and clinopyroxenes, 'melt_{in}' is the infiltrating (=incoming) Primary MORB, 'olivine_p' is the olivine precipitated at the rims of the mantle olivine (Saper and Liang, 2014), and 'melt_{Si}' is the Si-saturated melt resulting from the reaction.

Stage 2 simulates olivine assimilation (hereafter referred to as M_a = assimilated mass/infiltrating melt mass; see Supplementary Material) and progressive evolution of the infiltrating melt by crystallization of plagioclase and clinopyroxene following the reaction:



here, 'olivine_m' is the pre-existing mantle olivine partially modified by *Stage 1* (olivine_p); 'melt_{in+Si}' is the reacting melt composed of Si-rich melts after *Stage 1* and inputs of Primary MORB melt in an open system; 'olivine₂' represents the remaining olivine after reaction, re-equilibrated with the residual (= 'reacted') 'melt_r'. We applied this approach to simulate Fe-Mg exchanges (referred to as Mg# model in this study), chemical variations of Ni in olivine (Ni model), and REE contents in olivine (REE Plate model) during the formation of Ol-Ts. To evaluate the effect of simultaneous precipitation of plagioclase and clinopyroxene, we combined the results of the Mg# model with modal plagioclase variations during simple fractional crystallization (hereafter referred to as Combined model, Fig. 10).

Variations of Ni contents in olivine were calculated after the modified melt at each reaction increment from the Mg# model assuming:

$$C_{TOT}^{Ni} = \phi C_L^{Ni} + (1 - \phi) C_S^{Ni}$$

where the total concentration of nickel in the reactive cell, C_{TOT}^{Ni} , is expressed by Ni concentration in the interstitial melt, C_L^{Ni} , and in the solid material, C_S^{Ni} . Here, ϕ is the porosity and, for simplicity, we assume similar density for all phases. Knowing $C_S^{Ni} = D_G^{Ni} C_L^{Ni}$ (D_G^{Ni} = bulk partition coefficient of Ni), the equation of C_{TOT}^{Ni} can be solved for C_L^{Ni} at each reaction increment 'i':

$$C_{L_i}^{Ni} = (C_{TOT}^{Ni} - \phi_i C_{L_{i-1}}^{Ni}) / (1 - \phi_i) D_{G_i}$$

Based on the dependence of nickel partitioning on melt composition, we obtained equilibrium olivine using the Ni partition coefficient calculated at each reaction increment as function of MgO in the melt (equation after Hart and Davis, 1978).

We compared our models to the commonly used melt-dominated numerical models. We simulated the reaction of *Stage 2* with the AFC model for REE. Also, we reproduced trends of fractional and in situ crystallization to test the possible contribution of magmatic crystallization in the formation of chemical variations of Ol-T.

Following the calculated crystallization temperatures of plagioclase (~1230 °C; Drouin et al., 2009) and estimated pressure at which the gabbroic sequence at the Atlantis Massif formed (~7 km; Grimes et al., 2008), we used mineral/melt partition coefficients obtained at temperature in the range 1100-1200 °C and pressure of about 2 kbar. For *Stage 1* we used the whole rock composition of harzburgite from ODP Hole 1274A (Godard et al., 2008) as proxy for the mantle precursor of Hole U1309D Ol-T. Single phase compositions were taken from harzburgite collected at the Gakkel Ridge (D'Errico et al., 2016), which have mineral modal and calculated bulk rock compositions comparable to Hole 1274A harzburgite. Starting composition for *Stage 2* are the reacted and modified whole rock compositions after reaction in *Stage 1*. Due to the chemically heterogeneous feature of mantle relicts recovered at the Atlantis Massif (Miller et al., 2009; Tamura et al., 2008), two representative impregnated harzburgites were selected within IODP Hole U1309D for Ni simulations: from depths of 133 (H1; Tamura et al., 2008) and 173 mbsf (H2; Miller et al., 2009). For the Primary MORB magma ('melt_{in}') we used the estimated composition of melt formed by 6% aggregated fractional melting of a Depleted MORB Mantle (Workman and Hart,

2005). Only for simulations of REE we used a relatively more evolved melt (Gale et al., 2013) as a proxy of the last impregnation event recorded by Ol-T. Rock and melt starting compositions are reported in Supplementary Material Table S6, and partition coefficients used are in Supplementary Material Table S4. Further details on the Plate Model used in this study are given in the Supplementary Material - analytical methods and models.

2.6.2.2 Mg#-Ni simulations

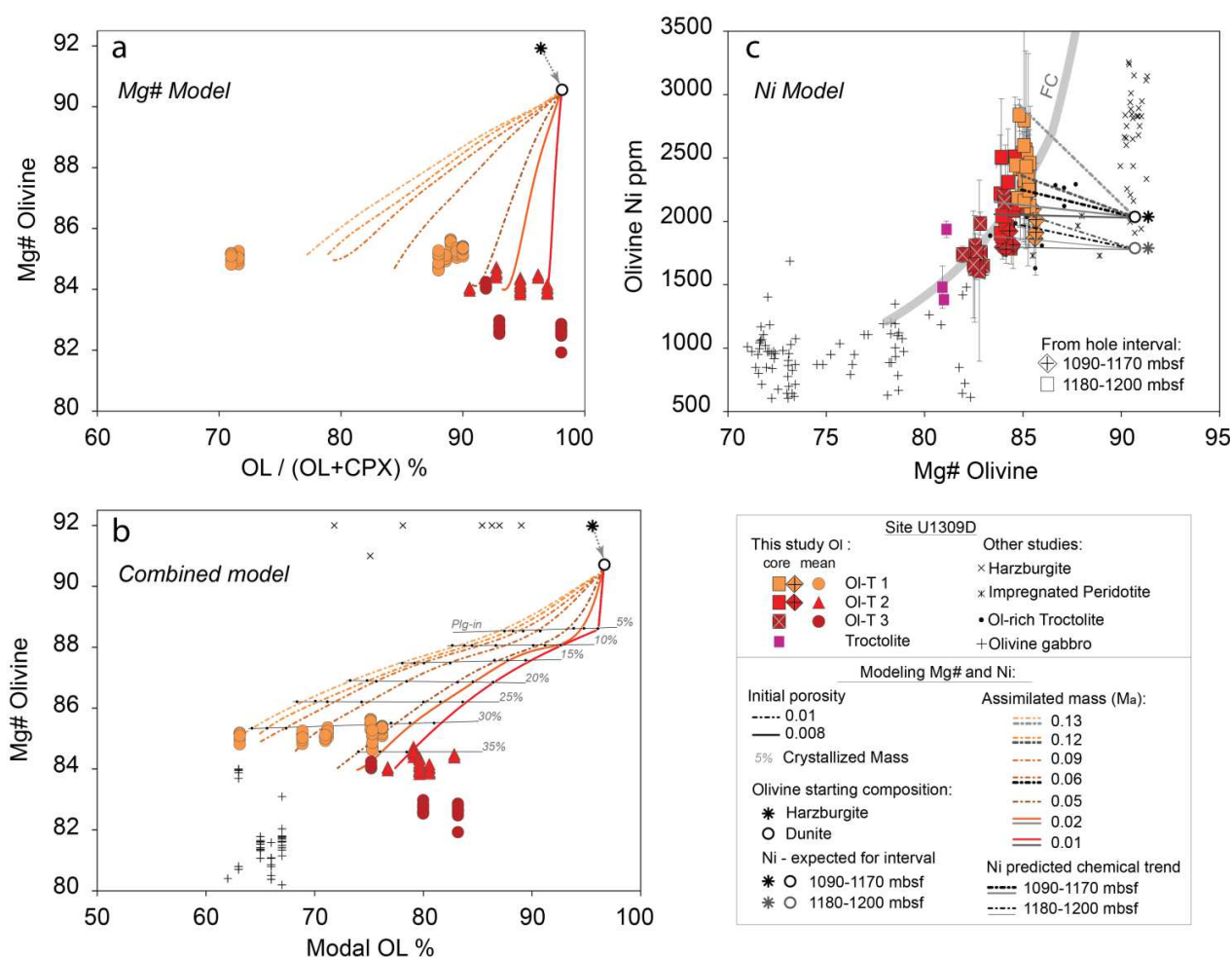


Fig. 10 - Mg# (=100 × Mg/(Mg + Fe)) versus a) modal olivine [ol/(ol + cpx)] and b) total modal olivine [ol/(ol+plg+cpx)] for Hole U1309D Ol-T. c) Mg# versus Ni contents in olivine. Olivines from abyssal harzburgite (D'Errico et al., 2016) and Hole U1309D olivine gabbro, olivine-rich troctolites, and impregnated harzburgites (Drouin et al., 2009; Miller et al., 2009; Suhr et al., 2008) are also reported for comparison. Data from this study are compared with reactive percolation modeling of a) Mg# model, b) Combined model, c) Ni model. Numerical experiments of melt-rock interactions were performed with the "Plate Model" of Vernières et al. (1997), initially designed for trace element applications (see text for details on the model). In

c) two compositions of olivine in impregnated harzburgite were used as expected starting material for formation of Ol-T from intervals 1090-1170 mbsf and 1180-1200 mbsf, respectively with the maximum Ni contents (U1309D-31R-2, 46-48 cm, 173 mbsf, Ni = 2000 ppm) and minimum Ni (U1309D-23R-2, 8-13 cm, 133 mbsf, Ni = 1750 ppm). Initial conditions of models and all other starting material compositions are reported in the text and in Supplementary Material Table S4 and S6. Two stages of melt-rock interactions are modeled (see text for details on reactions). Stage 1 (light grey arrow) form dunite that was used as starting material for Stage 2. Reaction in Stage 2 simulates percolation of an N-MORB sequentially more evolved at decreasing melt mass (% , reported in italic) by crystallization of clinopyroxene (and plagioclase). We used a simplified multi-stage approach whereby successively evolving melts infiltrated and reacted with the protolith. The latter is the resulting solid matrix from each previous reaction increment. The results of Stage 2 are shown in red to orange lines in a) and b), and black to grey lines in c) for different values of olivine mass assimilated (0.13 to 0.01, see legend). Fractional crystallization trend (FC, light grey line) was calculated with Petrolog3 (see Fig. 5 for details) and reported in c) for comparison; K_{Ni} vary during simulation following Beattie et al. (1991). (For interpretation of the references to color in this figure legend, the reader is referred to the web version of this article.)

The Mg# and Ni simulation of *Stage 1* produces only a slight decrease in olivine Mg# down to ~91 with invariable Ni contents (Fig. 10a), at relatively constant porosity. *Stage 2* produces significant decrease in olivine Mg# (down to 83.5) at variable extents of olivine dissolution (ol vol% = ol%/(cpx% + ol%)). At low M_a (0.01-0.02) the effect of the reaction is to decrease olivine Mg# at relatively constant modal contents, whereas higher M_a (between 0.06 and 0.13) accounts for a decrease in modal olivine at comparable but modest Mg# variations (Fig. 10a). The lowest olivine Mg# of the most olivine-rich Ol-T 2 (and Ol-T 3) are reproduced by low M_a in comparison with olivine in Ol-T 1 that is produced by higher olivine assimilation at higher proportion of interstitial melt. This confirms that pre-existing porosity and permeability, controlling the melt/rock ratio, play a fundamental role in the reactive process. However, this model does not reproduce the entire range of olivine modal contents of Ol-T 1, suggesting that other processes must be invoked, such as crystallization of the interstitial melt. The Combined model (Fig. 10b) reproduces all olivines in Ol-T 1 suggesting that their compositions result from melt-rock interactions at increasing melt mass and abundant precipitation of interstitial phases. We note, however, that the Combined model does not reproduce the modal content of Ol-T 2 and Ol-T 3. This is probably related to an over-estimation of plagioclase crystallization during the formation of Ol-T 2 and Ol-T 3 where dissolution and precipitation are minor processes.

Nickel simulations of *Stage 2* presented in Fig. 10c indicate that Ni contents of olivine in Ol-T from interval 1090-1170 mbsf (Ni = 1790-2018 ppm) may be accounted for by reactive melt

percolation through H1 (harzburgite at 133 mbsf in Hole U1309D). The same process may explain the origin of Ol-T collected between 1180 and 1200 mbsf from mantle protolith H2 (harzburgite at 173 mbsf in Hole U1309D). Thus olivine in the studied Ol-T inherits Ni concentrations from olivine in their mantle precursors. We note however that olivine has a wide range of Ni contents in the deeper interval of Ol-T (Fig. 10c). The highest Ni are obtained by models run at high M_a (up to 0.13), in contrast with low M_a (0.01-0.06) that produce no variation or solely a small increase in Ni contents. This suggests that the more reactive is the system (hence more Ni available in the percolating melt), the more variable are olivine compositions (e.g., Ol-T 1).

To summarize, Fe-Mg and Ni contents remain relatively constant during dunitization in *Stage 1* (e.g., Kelemen et al., 1997), and variable compositions at centimeter scale are formed after *Stage 2* of the reactive process. Ol-T 1 is the most reactive type of Ol-T, which is also affected by abundant crystallization of interstitial clinopyroxene and plagioclase in equal proportions (cpx/plg ~ 1). In contrast, the composition of olivine in Ol-T 2 and Ol-T 3 is 'buffered' by a slightly modified percolating melt. These local heterogeneities in Ol-T are likely inherited from the mineral modal distribution of the pre-existing harzburgitic matrix (i.e., orthopyroxene/olivine ratio), which in turn controls permeability and governs the melt/rock ratio of the system (e.g., Kelemen et al., 1997; von Bargen and Waff, 1986). Moreover, the measured and modeled strong variability of Ni contents in olivine demonstrate that not only reaction and crystallization have an effect on Ol-T formation, but locally olivine compositions also partially inherit those of the precursor mantle harzburgite.

2.6.2.3 REE models

In contrast to constraints from Mg# and Ni modeling, results of the REE Plate model show that *Stage 1* produces olivine with higher REE and less fractionated pattern ($Yb_N = 0.6$; $Dy_N/Yb_N = 0.18$) than the initial mantle olivine (Fig. 11). Olivine_p (see reaction *Stage 1* above) is in equilibrium with melt that is progressively saturated in silica and enriched in incompatible elements. Numerical simulations of *Stage 2* using the REE Plate model reproduce olivine with lower MREE to HREE fractionation at lower M_a (0.08-0.1) compared to models at greater M_a (0.19), but variations are small and negligible within the compositional interval of Ol-T from this study (Fig. 11). Curves reproduced for different clinopyroxene/plagioclase ratios also show negligible or little effect on REE contents in olivine.

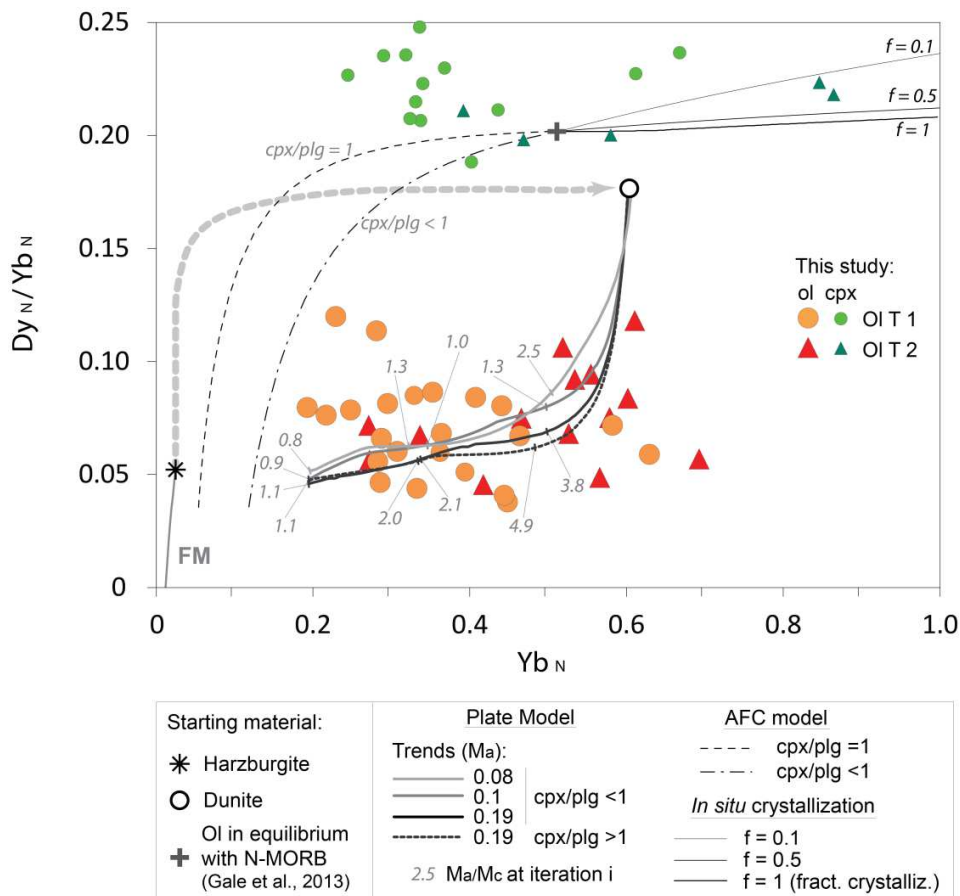


Fig. 11 - Ratio Dy_N/Yb_N versus Yb_N (N =normalized to Chondrites; Sun and McDonough, 1989) in olivine cores from OI-T 1 and OI-T 2. Data are compared with modeling of REE variations in olivine during fractional melting (FM), magmatic crystallization (in situ and fractional crystallization), Assimilation-Fractional Crystallization (AFC) and reactive percolation ('Plate Model', thick lines). Chemical trend of fractional melting was estimated with the equation proposed by Johnson et al. (1990) using the parameterization of Kinzler (1997). The starting material is a depleted harzburgite from ODP Hole 1272A (Godard et al., 2008). Magmatic crystallization was modeled using the equation proposed by Langmuir (1989) where ' f ' is the fraction of melt that returns to the magma chamber after its partial crystallization ($f=1$ simulates fractional crystallization). Curves were obtained for increments of crystallized mass of 2%. Olivine compositions were computed by AFC model (DePaolo, 1981) at decreasing melt mass ($F = 0.95-0.10$). The model assumes that initial melt assimilate olivine ($M_a = 100\%$ olivine) and crystallize plagioclase + clinopyroxene in different proportions ($cpx/plg = 1$ and $cpx/plg < 1$). REE variations were predicted using the 'Plate Model' of Vernières et al. (1997) in an open system (see text for details on reactions). Reaction Stage 1 (thick light grey arrow) form dunite that was used as starting material for Stage 2. Results from Stage 2 (thick curves) were performed at different olivine dissolution rates (M_a is the proportion of dissolved olivine in each simulation). Reported values in italic indicate the proportion of assimilated and crystallized fraction (M_a/M_c) at each reaction increment. K_d used for crystallization, melting and melt-rock interaction models are reported in Supplementary Material Table S4, and starting compositions in Supplementary Material Table S6.

AFC models of *Stage 2* can account for strong REE fractionations but the modeled REE abundances do not fall in the range of compositions of olivines from U1309D Ol-T (Fig. 11), suggesting that melt composition does not represent the principal factor controlling chemical variations in U1309D Ol-T. The simulated trends of fractional crystallization and in situ crystallization plot towards less fractionated REE and higher Yb_N , in contrast with depleted olivines in Ol-T (Fig. 11).

The olivine compositions simulated with the REE Plate model best reproduce those of U1309D Ol-T, in comparison with AFC and other melt-dominated models. However, measured and simulated Dy_N/Yb_N of olivines have similar, although scattered, REE contents in Ol-T 1, 2 and 3. This suggests that melt-rock reaction is not the unique control on chemical compositions and formation of Ol-T, and that dissolution of olivine has little effect on trace element composition of the migrating melt. Thus, REE Plate models demonstrate that melt transport is an additional factor driving element re-partitioning in a reactive percolation system. During melt transport and melt-rock interactions, MREE move faster and tend to be 'buffered' by percolating melts while the relatively slower HREE are governed by local changes in solid compositions and therefore decrease steadily (Godard et al., 1995; Navon and Stolper, 1987; Vernières et al., 1997); as a consequence, strongly fractionated REE patterns in olivine are produced (Fig. 11).

REE modeling, together with Mg# and Ni simulations, demonstrate that Ol-Ts inherit mantle Ni heterogeneities, and their formation is affected by mineral modal distribution of the harzburgitic matrix. In particular, modeling of Ni and REE Plate model indicates that the composition of pre-existing solid matrix exert a strong control on melt-rock reaction and compositional variations at the local scale between Ol-T 1 and 2, which points to a rock-dominated system.

2.6.3 Chemical equilibrium in U1309D olivine-rich troctolites

Chemical equilibrium between phases is described by element mineral/melt partition coefficients (e.g., Bédard, 2005). Partitioning depends on pressure, temperature and melt composition (e.g., Hart and Davis, 1978; see Supplementary Material Table S4) and, therefore, it may vary during melt-rock interactions (especially Ni, e.g., Hart and Davis, 1978). Experimental studies have shown that, upon melt-rock interactions, element abundances at rims of pre-existing minerals (such as olivine) are locally modified to reach instantaneous equilibrium with the

percolating melt (e.g., Lambart et al., 2009; Liang, 2003; Van den Bleeken et al., 2011). This effect results in core-to-rim compositional variations within crystals.

In contrast to these findings, clinopyroxene-to-olivine profiles in U1309D Ol-Ts show that for all analysed elements no core-to-rim variations are preserved. Element diffusion governs the intra-crystal composition after local rim modification (e.g., Chakraborty, 2008; Liang, 2003). Hence, slower element diffusion rates (Supplementary Material Table S5) compared to olivine dissolution rates (10^{-16} - 10^{-20} m²/s, Kvassnes and Grove, 2008) may prevent re-equilibration of olivine rim within a minimum distance from the melt-crystal boundary (i.e., compression of diffusion profile by dissolution, Liang, 2003). In this scenario, olivine would preserve its original core composition distinguished by high Mg# and low Mn contents similar to the associated harzburgite or common dunitic cumulates, which is not the case of olivines in Ol-T from Atlantis Massif (Figs. 5 and 8). Also, for some elements (i.e., Fe-Mg, Ni and Li, Supplementary Material Table S5) diffusion rates in olivine are slightly higher than dissolution rates, indicating that not all elements should present a flat profile in olivine.

An alternative hypothesis is that olivine flat profiles could represent the evidence of relatively fast element transport by intra-crystalline diffusion. At high temperatures, as those calculated for plagioclase crystallization in Hole U1309D Ol-Ts (~1230 °C; Drouin et al., 2009), element diffusion becomes more efficient (Chakraborty, 2008, and references therein), and olivine crystal composition may be completely modified. The lack of chemical variations between profiles along different preferred crystallographic directions in single olivine further suggests a compositional reset of olivine, operated by element diffusion. In this model, interstitial phases crystallized after the modified melt have to be in equilibrium with olivine. To test this hypothesis, we calculated melts in equilibrium with olivine and adjacent clinopyroxene for the most relevant elements.

We selected mineral-melt partition coefficients (Supplementary Material Table S4) experimentally determined at conditions that best match those predicted for the formation of the gabbroic sequence at the Atlantis Massif: T = 1100-1200 °C (Drouin et al., 2009) and P = 2 kbar (Grimes et al., 2008). In order to account for MgO-melt and mineral-stoichiometry control on partitioning of compatible and moderately incompatible elements in olivine (e.g., Hart and Davis, 1978), we used fractional crystallization modeling (in this study Petrolog3; Danyushevsky and Plechov, 2011) that calculate mineral and melt compositions as function of varying partition

coefficients (Fig. 9). Partitioning of incompatible elements is Si-melt dependent (e.g., Evans et al., 2008). Dissolution-precipitation processes at Site U1309 change mainly the melt MgO contents, whereas silica variations are negligible. Hence, the simple $C_L = C_s / f^{S-L} K_d$ (C=element content in L, melt and S, solid; K_d =element partition coefficient) was applied. For REE, we used mineral/melt partition coefficients derived from measured olivine and clinopyroxene compositions according to a recently developed lattice strain model (Sun and Liang, 2014), using the approach of Rampone et al. (2016).

Our calculations show that chemical equilibrium between olivine and clinopyroxene is observed for major and minor elements mainly hosted by olivine in primitive rocks (De Hoog et al., 2010), namely Fe-Mg, Ni and Mn (Figs. 8 and 9), and for Li, a trace element concentrated in olivine ($^{Ol/Melt}K_{Li} \geq ^{Plg/Melt}K_{Li} > ^{Cpx/Melt}K_{Li} > ^{Opx/Melt}K_{Li}$, Supplementary Material Table S4). In primitive rocks, other trace elements such as REE are hosted by clinopyroxene ($^{Cpx/Melt}K_{REE} \geq ^{Opx/Melt}K_{REE} > ^{Plg/Melt}K_{REE} > ^{Ol/Melt}K_{REE}$, Supplementary Material Table S4): the melts computed from the new dataset of REE contents display comparable HREE (Yb in particular) in all phases, whereas the strong MREE to LREE depletion in melts computed in equilibrium with olivine (Drouin et al., 2009) is still observed.

Finally, computed melts in equilibrium with clinopyroxene-olivine couples have higher Mg# of 62-66 for Ol-T 1 compared to melt Mg# of 58-61 found for Ol-T 2 (Fig. 9), which is consistent with the shift of MORB-type melts towards more primitive compositions after assimilation of olivine (Lissenberg and Dick, 2008). Re-equilibration times are evaluated, further in the discussion, to constrain the control of diffusion mechanism on mineral geochemical composition.

2.6.4 Genesis of Olivine-rich troctolites at Atlantis Massif

The results of analyses and modeling presented above are consistent with the formation of Ol-T recovered at the Atlantis Massif OCC after intensive melt impregnation of a depleted mantle harzburgite through a multi-stage reactive percolation process. Relicts of the pre-existing matrix can be recognized in the upper 200m of IODP Holes U1309B and U1309D (Blackman et al., 2011; Tamura et al., 2008). The migration of a primary olivine-saturated MORB-type melt lead to concomitant mantle pyroxenes dissolution and olivine precipitation around the original mantle olivine (Liang, 2003; Saper and Liang, 2014), thereby generating undersaturated olivine melts. The extent of melt-rock interactions is locally controlled by the orthopyroxene distribution in the

harzburgitic protolith. The crystallization of <8% of total melt (after modeling with Petrolog3) in new olivine crystals drove the percolating melt towards Si-rich compositions, thus suggesting that rather pervasive melt-mantle interactions (Collier and Kelemen, 2010) can account for the formation of Ol-T. If this is the case, melt migration through grain-scale porous flow, and the formation of Ol-T, took place in the transition from melting to crystallization region (e.g., Collier and Kelemen, 2010) beneath the Mid-Atlantic Ridge at the Atlantis Massif.

We propose the following scenario for the formation of Ol-Ts drilled at the Atlantis Massif (Fig.12).

- (i) The upwelling heterogeneous depleted mantle records partial melting episodes leaving behind harzburgites with variable compositions and (ortho)pyroxene modal contents (Fig. 12a), which constitute the lithospheric oceanic mantle. At shallow levels, primary MORB-type melts sporadically migrate upwards, forming gabbroic veins and dykes, and reactive porous flow locally occurs in the infiltrated mantle lithosphere. This event of melt impregnation occurs at low melt/rock ratios (Tamura et al., 2008).
- (ii) Further inputs of primitive MORBs trigger dissolution of orthopyroxene and melt influx becomes a dominant process. Simultaneously, new olivine crystallizes at the rims of mantle olivine (Fig. 12b) decreasing the melt MgO (e.g., Lambart et al., 2009; Saper and Liang, 2014). Orthopyroxene-rich zones of the mantle precursor have initially the lowest permeability (Toramaru and Fujii, 1986), and therefore form local permeability barriers where melt tend to accumulate. In turns, the significant volume of melt accumulated favors assimilation of mantle pyroxene (e.g., Pec et al., 2017), and locally enhances permeability. On the other hand, local orthopyroxene-poor zones have higher permeability that favors migration of the melt, leading to lower assimilation of mantle pyroxene. The progressive dissolution of orthopyroxene increases the Si contents of the percolating MORB, as well as its Cr concentrations (e.g., Arai et al., 1997). The pre-existing olivine fabric is disrupted and olivine CPO's with [001] cluster develop at high melt/rock ratios ($\geq 30\%$ melt, Drouin et al., 2010). The migrating melts become silica-saturated and the original harzburgite is transformed in an olivine + Si-melt system (e.g., Lambart et al., 2009).

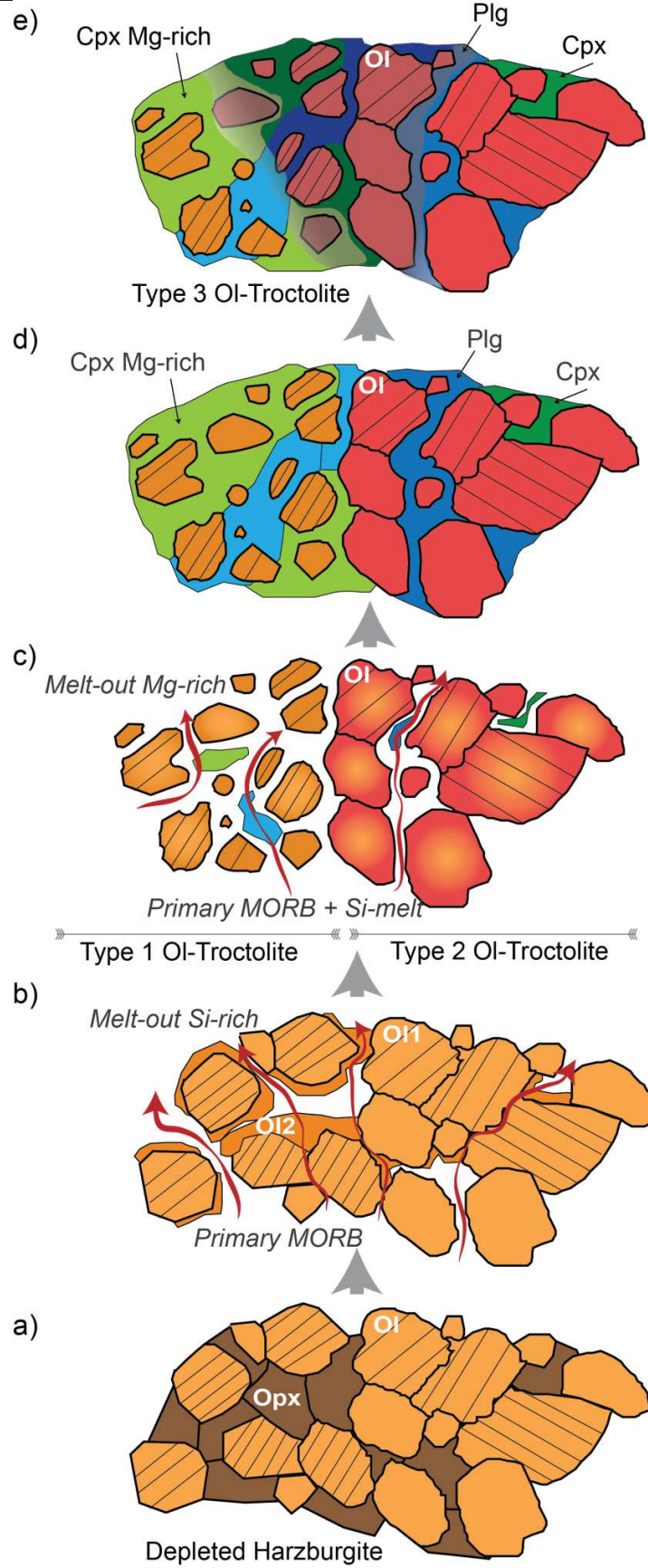


Fig. 12 - Schematic representation of sequential processes of melt impregnation forming Ol-T drilled at the Atlantis Massif. Percolation of primary MORBs through a heterogeneous residual harzburgite (from a) to b)) dissolve primary orthopyroxenes and crystallize olivine at rims of mantle olivine. Areas where higher proportions of orthopyroxene were originally present lead to higher porous flow and more production of Si-melt that dissolve olivine and form Ol-T 1 (from c) to d) on the left) with high Mg# clinopyroxene. Zones of higher initial permeability form Ol-T2 at less olivine assimilation extents (from c) to d) on the right). More evolved reacted melts crystallize at decreasing temperature in cross-cutting gabbroic veins forming Ol-T3 (e).

- (iii) At this stage, the silica-saturated melt and the dunitic matrix are in disequilibrium, and olivines tend to be partially dissolved (=assimilated). As reaction progress, local distinct Ol-Ts form. Higher dissolution of mantle orthopyroxene produces more Si-saturated melt leading to higher olivine assimilation (Fig. 12c). The latter accounts for the increase in MgO of the modified percolating melts and triggers the early crystallization of high Mg# poikilitic clinopyroxene in the most reactive Ol-T 1 (Fig. 12d). Zones with lower modal orthopyroxene lead to lower Si-melt production and record less olivine dissolution and minor crystallization of high Mg# clinopyroxene over plagioclase ($cpx/plg \ll 1$). Olivine re-equilibrates with a progressively evolved melt by crystallization of interstitial phases forming Ol-T 2 (Fig. 12d). Cr from the orthopyroxene-melt reaction is hosted in interstitial clinopyroxene, as evidenced by its high Cr contents (Cr_2O_3 is up to 1.5 wt% in Ol-T, Drouin et al., 2009 and this study; $Cr_2O_3 \sim 1.2$ wt% in primitive oceanic gabbros, e.g., Ross and Elthon, 1997).
- (iv) Relatively more evolved reacted MORB-type melts crystallize at decreasing temperature in cross-cutting gabbroic veins that 'buffer' the composition of pre-existing Ol-Ts and form Ol-T 3 (Fig. 12e).

2.6.5 The geodynamic context of Olivine-rich troctolites

The lower oceanic crust drilled at the Atlantis Massif was built by multiple injections of MORB-type melts in the absence of a steady-state magma chamber (Blackman et al., 2011; Godard et al., 2009; Ildefonse et al., 2014). The uppermost section of Hole U1309D is younger than underlying intrusive series, which implies that the intrusive activity occurred at different depths below the mid-ocean ridge during low angle rotation of the detachment fault (Grimes et al., 2008). Data from this study show that Ol-T formed after mantle rocks. Ol-Ts result from a period of enhanced magmatism at depth, as already proposed for the Atlantis Massif (Blackman et al., 2011; Ildefonse

et al., 2007) when melt migrated through a harzburgitic mantle by porous flow. This occurred probably during the early formation of the Atlantis Massif OCC (e.g., Blackman et al., 2011; Ildefonse et al., 2007, 2014). We posit that while the magmatic lower oceanic crust formed, shallower mantle screens were preserved due to the decrease in melt supply during exposure of the Atlantis Massif by long-lived detachment faulting. This is evidenced by the lack of mantle relicts downhole.

The model we propose is valid only if melt-rock interactions, which are found to modify the mantle units intercalated in the gabbroic sequence, occur within a reasonable time compared to emplacement of the gabbroic sequence. Mineral chemical profiles provide evidence of re-equilibration of the original olivine with the percolating and reacting melt by inter-crystal element diffusion. In order to test whether the diffusion mechanism in olivine is fast enough to reset the composition of precursor olivine, we compare the re-equilibration time of selected elements (Table 2) with the time of emplacement of the Atlantis Massif crustal section. We calculated minimum re-equilibration time (t_{eq}) with a simple but effective approach, using the equation $t_{eq} = r^2/\pi D_i$ (r = core-rim distance; D_i = element 'i' diffusion coefficient; Crank, 1975). Olivine was geometrically approximated to a sphere of radius 3mm, which corresponds to the core-rim length of the coarser analysed grain. We used diffusion rates experimentally obtained at lower oceanic crustal conditions (~1200 °C, quartz–fayalite–magnetite oxygen buffer, and Fo₉₀, Supplementary Material Table S5). Fast diffusion rates were calculated for Fe-Mg (e.g., Dohmen et al., 2007), followed at lower diffusivities by divalent cations Ni, Co and Mn (Jollands et al., 2016; Supplementary Material Table S5). Diffusion of Li occurs through two different site locations in olivine lattice, which favors its fast diffusion rates (Dohmen et al., 2010). To calculate minimum re-equilibration times, Mn was selected as slow diffuser between divalent cations ($D_{Mn} < D_{Ni} < D_{Co}$; e.g., Jollands et al., 2016; Petry et al., 2004). The minimum time required to re-equilibrate an olivine crystal is about 1.5 ka (D_{Mn} from Petry et al., 2004). Vast discrepancies exist between trace element (REE, Ti, Zr, Hf, etc.) diffusivities with rates that span over several orders of magnitude (see discussions in Jollands et al., 2016). Overall, trace elements diffusion rates are lower than (or very close to) Mn diffusivities. Minimum equilibration time of 105 ka was obtained for MREE (D_{Sm} from Remmert et al., 2008).

Table 2 - Re-equilibration times calculated for Fe-Mg, Mn and Sm. See text for references of reported diffusion coefficients (log D).

Elements	log D	Re-equilibration time
Fe-Mg	-16.6	210-300 yr
Mn	-17.2	1.5 ka
Sm	-19.2	105 ka

The smallest re-equilibration times were obtained for comparison based on Fe-Mg exchanges. The minimum time necessary to re-equilibrate Fe-Mg in olivine ($D_{\text{Fe-Mg}}$ from Dohmen et al., 2007) is 300 yr. We calculated Fe-Mg diffusivities as a function of Fo content in olivine (using the equation of Dohmen and Chakraborty, 2007) to test the validity of our simplistic method. Olivine initial composition was set at Fo₉₀ and its rim at Fo₈₄ to simulate re-equilibration in olivine from Ol-T 2. Following this method, Fe-Mg in olivine re-equilibrates in <210 yr showing our method is a relatively good approximation. The discrepancy may relate to differences in Fo content, inversely related to diffusion coefficients (the decrease in Fo increases element diffusion, Dohmen and Chakraborty, 2007) and was kept constant in the first equation.

The calculated melt-olivine re-equilibration times fall in a range below the 200 ka predicted for emplacement of the gabbroic sequence, thus supporting our model whereby Ol-T formed after enhanced melt impregnation of a mantle precursor before, or simultaneously, the building of the lower oceanic crust at the Atlantis Massif.

2.6.6 The effect of olivine assimilation on MORB compositions

Melt-rock interactions are found to modify MORB compositions by post-cumulus reactions (e.g., Ross and Elthon, 1997), or reactive crystallization through mantle matrix (Collier and Kelemen, 2010) and assimilation of a lower oceanic crust component (Lissenberg and Dick, 2008). The assimilation of a cumulate anorthitic and forsteritic assemblage can shift MORBs compositions towards apparent higher pressures (Lissenberg and Dick, 2008), as a consequence of the similarity with chemical trends typical of high pressure fractionations (e.g., Grove et al., 1992). In contrast, assimilation of a mantle component, as modeled by steady-state reactive crystallization process, leads to MORB fractionation characterized by constant Mg# at decreasing Ca# (Collier and Kelemen, 2010). Here, we calculate compositions of migrating MORBs after different magnitudes

of dissolved mantle olivine in order to quantify how much mantle was assimilated at the Atlantis Massif to form Ol-T.

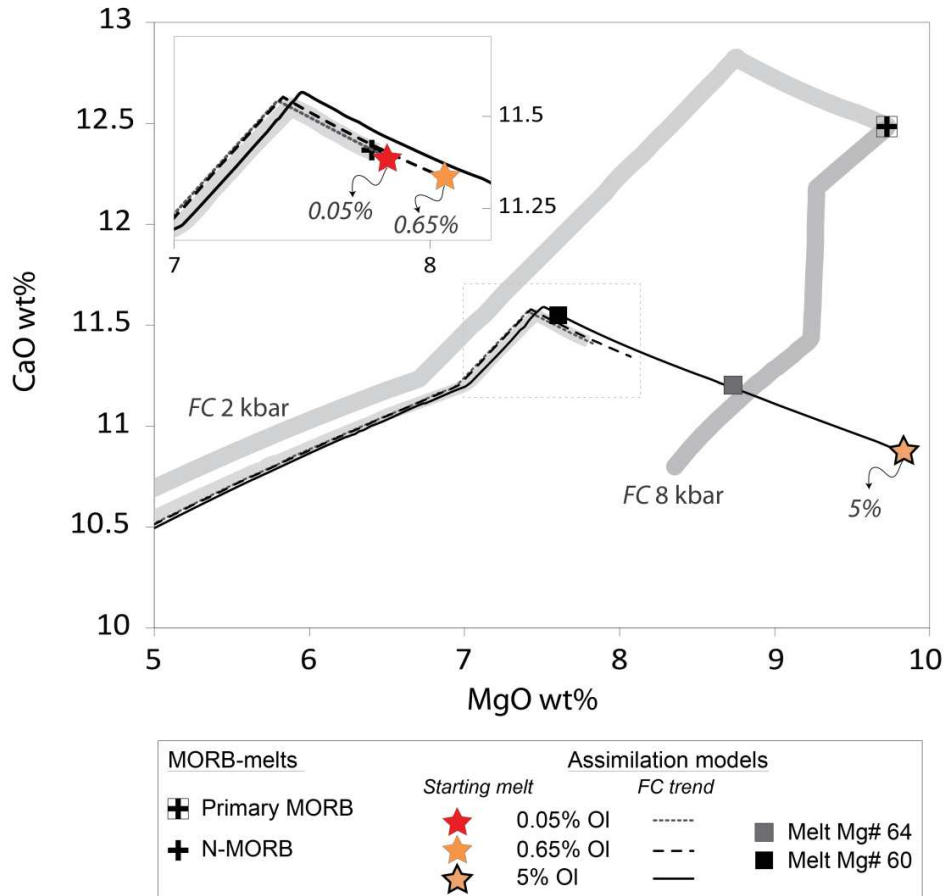


Fig. 13 - MgO (wt%) versus CaO (wt%) of melts calculated after fractional crystallization as predicted by Petrolog3 (see Fig. 5 for details on the model) at 2 kbar for (i) Primary MORB and N-MORB (thick light grey lines; Supplementary Material Table S6), (ii) melts after 0.05%, 0.65%, 5% of assimilated olivine, calculated using N-MORB as starting melt (Supplementary Material Table S6). Also shown is the liquid line of the primary MORB fractionating at pressures of 8 kbar.

We estimated that the contribution of mantle assimilation on the overall composition of the gabbroic sequence at the Atlantis Massif is between 0.05 and 0.65% (calculated considering that Ol-T constitute 5% of recovered rocks and using assimilation estimates from our reactive models). The latter was calculated for the most reactive Ol-T 1 (sample 305-U1309D-247R-3W, 16-18) and approaches estimations based on trace elements bulk compositions (<2%, Godard et al., 2009). Higher values of up to 5% assimilated mantle were deduced after major elements bulk compositions (Godard et al., 2009). In Fig. 13, we report calculated compositions of MORBs after

0.05%, 0.65% and 5% mantle olivine assimilation. Fractional crystallization trends of these melts are compared with evolution of a Primary MORB at low (2 kbar) and high (8 kbar) pressure crystallization. Overall, olivine dissolution increases MgO contents of the melt and decreases its CaO contents (Fig. 13) as expected from previous works (e.g., Lambart et al., 2009; Lissenberg and Dick, 2008). The highest assimilation percentage shifts MORB compositions towards much higher MgO than those predicted by low pressure fractional crystallization. Such MgO and CaO contents can otherwise be reached after crystallization at high pressures, and correspond to compositions predicted for the MORB-type melt in equilibrium with the mineral assemblage of OI-T 1 (Fig. 13). In contrast, the least reactive OI-T 2 is in equilibrium with a melt that records significant melt fractionation, again suggesting that olivine assimilation had a minor effect on the composition of this type of OI-T.

Estimations of mantle assimilation from this study seem to underestimate the extent of the reactive process compared to the Godard et al. (2009) estimates. This may be related to the fact that calculations were done at extremely local scale, and that our sampling may lack areas where olivine dissolution was much stronger, as predicted by bulk rock compositions. Our calculations provide a minimum estimate of the extent of mantle assimilation.

2.7 Conclusions

Major and trace element mineral compositions and reactive percolation modeling demonstrate that olivine from U1309D OI-T is of impregnated mantle origin. Textures and olivine compositions are locally inherited from the heterogeneous precursor. Chemical profiles reveal evidences of reaction and chemical equilibrium. On the other hand, trace elements indicate that element transport has a fundamental role on the re-distribution of the most incompatible elements (e.g., Godard et al., 1995; Vernières et al., 1997) thus controlling their composition in the mineral phases. Detailed analyses of modal and compositional variations of minerals, together with microstructural observations, appear to be suitable criteria to unravel the origin of olivine in OI-T.

Our results demonstrate that Primary MORB melt are modified during their upward migration by a complex history of interactions with the pre-existing deformed matrix in an open system. First, dissolution of mantle orthopyroxene coupled to minor olivine precipitation cause a shift of melt compositions towards silica saturation. The melt produced is progressively in chemical

disequilibrium with mantle material and the melt-rock reaction switches to dissolution of olivine (e.g., Lambart et al., 2009; Saper and Liang, 2014). As a result, the produced MORB melt is enriched in MgO similar to high pressure fractionated melts. It is saturated in olivine and, at decreasing temperature, forms the gabbroic suite surrounding mantle intervals that are preserved at the top of Hole U1309D.

The principle characteristics of reactive Ol-T, inferred from this study, and previous work (Drouin et al., 2009, 2010), are as following:

- (i) *Texture and microstructures.* Deformed (high temperature imprint) corroded coarse and medium grained to undeformed fine grained olivine are embayed in poikilitic clinopyroxene and plagioclase. Olivine crystallographic preferred orientations show relatively weak [001] clusters (Drouin et al., 2010) suggesting formation after melt impregnation at high melt/rock ratios (~30%).
- (ii) *Mineral modes and chemistry.* Olivine displays opposite correlation between modal contents and concentration of elements generally hosted in olivine (i.e., Mg#, Ni, Mn, Zn, Li), compared to trends predicted by MORB crystallization. Olivine is characterized by wide variations of Ni and Li at constant Mg#. Clinopyroxene and plagioclase have respectively high Mg# and high An, and both are in chemical equilibrium with olivine.
- (iii) *Geochemistry.* Similar mineral trace elements compositions characterize all types of Ol-T. Olivine displays strong fractionation of HREE to MREE with absolute values higher than associated mantle rocks and gabbros (Rampone et al., 2016). Olivine also shows enrichments in the most incompatible elements (i.e., HFSE) that seem to complement plagioclase compositions (Zr-Hf). Clinopyroxene cores do not display Eu negative anomalies. Calculated melts in equilibrium with clinopyroxene and plagioclase have trace elements comparable to Primary MORBs (Drouin et al., 2009) and are in equilibrium with olivine, except for MREE and LREE.

This work reveals that assimilation of mantle olivine accounts for local change of MORB compositions towards relatively primitive compositions. Up to 5% mantle component was assimilated at the Atlantis Massif. The high Mg# bulk Hole U1309D (Godard et al., 2009) indicate that the resulting reacted MORBs are likely those that formed the crustal sequence from troctolitic gabbro to olivine gabbro, gabbro and oxide gabbro recovered at Atlantis Massif. The downhole

bulk compositions point to low pressure crystallization (Godard et al., 2009), indicating that melt-rock interactions at Site U1309 did not shift MORB compositions towards apparent high pressure fractionation trends as, conversely, observed elsewhere (e.g., Lissenberg and Dick, 2008; Paquet et al., 2016). The complex reactive history that MORB melts record at Atlantis Massif might represent the missing link between mantle relicts, reactive OI-Ts and cumulate gabbros drilled at IODP Hole U1309D.

Acknowledgements

M.R. Renna and an anonymous reviewer are acknowledged for helpful comments and suggestions that improved the manuscript. We thank V. Basch, M.C. Jollands and J. Koepke for constructive discussions. The authors are grateful to Christophe Nevado and Doriane Delmas for providing high-quality thin sections and F. Barou for assistance and support on EBSD analyses. The authors thank B. Boyer and O. Bruguier for assistance on analytical instruments from the Microsonde Sud (Géosciences Montpellier, University of Montpellier) and AETE-ISO platform ("Analyses des Eléments en Trace dans l'Environnement et ISOtopes"; OREME observatory, University of Montpellier) respectively. This project has been supported by the People Programme (Marie Curie Actions) of the European Union's Seventh Framework Programme FP7/2007–2013/under REA-Grant Agreement No. 608001, 'ABYSS'. This research used samples and data provided by the Integrated Ocean Drilling Program (IODP).

Appendix A. Supplementary data

Supplementary data to this article can be found online at <https://doi.org/10.1016/j.lithos.2018.01.012>.

Supplementary Material - analytical methods and models

Analytical methods

Loss of sample for successive analyses was minimized by first analysing the microstructures, followed by measurements of major and then trace element concentrations. A single high-quality

polished thin section per sample was used for all analyses to avoid uncertainties on grains analysed related to 3D geometrical structure of crystals.

EBSD analyses

EBSD operates by detecting diffracted electrons produced by interaction of the primary electron beam with the crystal lattice. Each diffraction pattern is recorded by the EBSD Camera System, a Phototonic Science CoolView CCD, installed perpendicular to the incident electron beam, with an angular resolution of 0.3° . The image is then analysed by the Oxford Instruments AZtecHKL acquisition software. A set of 8 OI-T was analysed by a Scanning Electron Microscope (SEM) JEOL JSM 5600, and . The operating conditions were set at 17 kV accelerating voltage and 0.5 nA beam current. Another set of 7 samples of OI-T and 1 troctolite were analysed by a Field Emission Gun (FEG) CamScan X500FE CrystalProbe; operating conditions were a 15 kV accelerating voltage, and a 3.5 nA beam current. Areas of $\sim 30 \times 20$ mm were mapped for each sample at different sampling step sizes ranging between $13.5 \mu\text{m}$ for the most altered to $28 \mu\text{m}$ for the freshest samples (for evaluation of alteration degree see Table 1), as a function of the crystal fragments size in single, partially serpentinized grains. EBSD data were processed using the CHANNEL5 software from Oxford Instruments HKL to remove isolated single pixels and to increase the indexation rate by filling automatically the non-indexed pixel having up to 8 indexed neighbours. Indexation rates range from 64 % in most altered samples, to 95 % in the most preserved. Texture analyses of EBSD data were done using MTEX, an open-source MatLab[®] toolbox that provides quantitative microstructure analysis covering a wide range of properties (e.g., Mainprice et al., 2014). Single grains were reconstructed by automatically selecting adjacent pixels having misorientations $<10^\circ$ (misorientation angle of 10° define grain boundaries). Inter- granular misorientations were calculated, such as the misorientation of each pixel within single grain to the mean orientation of that same grain (Mis2Mean) and the Kernel Average Misorientation (KAM) that is the average angle of every pixel with its four neighbors. Modal compositions were determined by core observations and estimated at the scale of thin section by EBSD mapping.

LA-ICP-MS analyses

Thin sections were polished to remove carbon coating after EPMA analyses. Further surface cleaning was performed on the selected spot by pre-ablation in 5-6 pulse per second. LA-ICP-MS analyses were performed on grains previously investigated for major element concentrations,

using an in-house modified 30 cm³ ablation cell with a helium atmosphere to enhance sensitivity and reduce inter-element fractionation (Günther and Heinrich, 1999). Helium gas and ablated sample material were mixed with argon gas before entering the plasma. Data were collected in time resolved acquisition mode with the background signal collected for 2 min followed by 1 min of sample ablation, or with 2.33 min for the blank and 40 sec sampling. Concentrations were calibrated against the NIST 612 rhyolitic glass using the values given in Pearce et al. (1997). Data were reduced with the GLITTER software package (Van Achterbergh et al., 2001), using the linear fit to ratio method. Signals were carefully monitored and data were filtered for spikes on an element by element basis.

Instrument sensitivity related to analytical conditions was determined for each beam size from the average across all days of repeat measurements of NIST 612 (see SupplementaryMaterial Table S3). Detection limits were between 0.07 and 1 ppm for Li, B, Ti, Cr and Ni except for Ni in analyses performed with laser spot size of 51 (3 ppb); they were <55 ppb for Mn, Cu, Zn and <22 ppb for Sc, V, Co. Detection limits for the most incompatible elements were <5 ppb except for Zr, Ba (<15 ppb) and Sr, Gd (<10 ppb). Reference basalt BIR-1G was used as standard to monitor accuracy as well as reproducibility within single series and between runs. This resulted in reproducibility better than 5% for V, Co, Cu, Sr, Nb, Sb, Ba, REE and it is <12% for all other elements except B (30%), Pb (15%).

Numerical simulations

Reactive models

We used the Plate Model proposed by Vernières et al. (1997) for the simulation of trace-element fractionation during partial melting and reactive porous flow in the Earth's upper mantle. In this study, we consider porous flow independent of time and distance. Porous flow is simulated by the propagation of fluid batches through representative volumes of rock. Compared to a batch model (i.e., AFC), the advantage of the non-dimensional Plate Model is its ability to reproduce variations in parameters controlling the reaction, such as porosity, melt-rock ratio and crystallization in a porous media. Similarly, effects of melt transport on element redistribution during reaction are considered (i.e., chromatographic effect). Dissolution-precipitation processes are simulated by local-instantaneous equilibrium between phases after sequential partial melting and crystallization, at the scale of a representative volume. This allows control on phase

relationships (i.e., phase modal contents) and on their chemical variations upon reaction and melt percolation. In the Plate Model the infiltrated medium is considered as a column made of minerals forming the initial rock, and it is composed of chemical reactive cells. Based on initial porosity, a certain amount of infiltrating melt reacts with the given initial material from the bottom of the column to the top by creating new reactive cells at each reaction increment (Vernières et al., 1997).

The Plate Model was adapted to the simulation of Fe-Mg redistribution (Mg# model) in peridotite-melt systems by Bedini et al. (2002) using a total inverse method to avoid mineral stoichiometry violation. Details of the approach and procedure are reported by Bodinier et al. (2008). Mg and Fe mineral/melt partition coefficients were fixed after Ulmer (1989) for a pressure of 10 kbar and a temperature of 1200°C. They are allowed to vary during numerical experiments to account for Mg and Fe variations in the melt, based on experimental constraints (Ulmer, 1989).

Our model is not thermodynamically constrained. Temperature and pressure exert a fundamental control on element distribution between phases, thus changing the composition of the mineral phases (e.g., Villiger et al., 2007). However, variations in temperature and pressure during formation of the gabbroic sequence at Site U1309D are likely to be small, hence suggesting that they are unlikely the primary controlling parameters.

The formation of Ol-T may be accounted for by multiple combinations of porosity ϕ , dissolved (=‘assimilated’, M_a = assimilated mass/infiltrating melt mass) and crystallized (M_c = crystallized mass/infiltrating melt mass) masses in the reaction. We arbitrarily fixed initial porosity (ϕ_0) at 1%, whereas M_a and M_c were adjusted to allow variations of the ratio:

$$\frac{M_a}{M_c} = \frac{(1 - \phi_{i-1})F}{(1 - f)[\phi_{i-1} + F(1 - \phi_{i-1})]}$$

where F is the mass fraction of dissolved olivine (relative to the initial solid matrix), and f is the mass fraction of residual melt (relative to the initial porosity). The system is crystallization-dominated when the ratio is lower than 1, whereas it is (olivine-)assimilation-dominated if $M_a/M_c > 1$.

The olivine-rich protolith

Based on structural evidences and downhole bulk rock geochemical data of Hole U1309D (see Discussion for further details), the initial composition of the olivine-rich porous medium is set as that of a mantle harzburgite. The composition of the latter is that of mantle intervals recovered at Site U1309.

In order to test whether an ultramafic cumulate could represent the olivine-rich protolith of OI-T from the Atlantis Massif, we compared the compositions of olivines from harzburgitic mantle (used as starting material in the numerical simulations) with those from dunitic cumulate. While mantle relicts are preserved in the uppermost interval of IODP Holes U1309B and U1309D and, therefore, olivine compositions are measured, no dunitic cumulates are identified throughout these holes. Thus, we calculated the composition of cumulate olivine by simulating fractional crystallization ($P = 2$ kbar) after MORB-type melts used for the numerical models of reactive melt percolation: the primary MORB for Mg# and Ni, and the N-MORB for REE (compositions are reported in SupplementaryMaterial Table S6). We used Petrolog3 (Danyushevsky and Plechov, 2011) for Mg# and Ni concentrations, and the equation of Langmuir (1989) (with $f=1$; see Figure 11) for REE.

The calculated olivine Mg# of the dunitic cumulate ranges between 89 and 90, which is comparable to that of olivine in impregnated harzburgites from Site U1309 (Tamura et al., 2008). Olivine in the dunitic cumulate (referred to as 'olivine in equilibrium with N-MORB') have REE contents similar to those of a mantle dunite (Figure 11). As a consequence, variations of Mg# and REE contents in olivine simulated by reactive melt percolation modeling using an ultramafic cumulate protolith are comparable to those resulting from the mantle starting material. On the other hand, the calculated Ni contents of olivine in the dunitic cumulate range between 4000 and 4200 ppm, which are higher than those of U1309 impregnated harzburgites (Tamura et al., 2008; Figure 10c). Assimilation of olivine triggered by the reactive percolation process increases the Ni contents of olivine, as evidenced by the Ni model (see Discussion for further details). By using the composition of dunitic cumulate as starting material, Ni model would lead to high Ni contents (> 4200 ppm) of olivine, which would not reproduce those of olivines from the studied OI-T. The latter are otherwise reproduced using mantle harzburgite as starting material (see Discussion). This

indicates that the dunitic cumulate cannot represent the protolith of the studied heterogeneous Ol-T from the Atlantis Massif.

References

- Arai S. and Matsukage K., Petrology of gabbro-troctolite-peridotite complex from Hess Deep, equatorial Pacific: implications for mantle-melt interaction within the oceanic lithosphere, *Proc. Ocean Drill. Program Sci. Results* 147, 1996, 135–155, <http://dx.doi.org/10.2973/odp.proc.sr.147.008.1996>.
- Arai S., Matsukage K., Isobe E. and Vysotskiy S., Concentration of incompatible elements in oceanic mantle: effect of melt/wall interaction in stagnant or failed melt conduits within peridotite, *Geochim. Cosmochim. Acta* 61, 1997, 671–675.
- Basch V., Rampone E., Crispini L., Ferrando C., Ildefonse B. and Godard M., From mantle peridotites to hybrid troctolites: textural and chemical evolution during melt-rock interaction history (Mt. Maggiore, Corsica, France), *Lithos* 2018, (in this issue).
- Beattie, P., Ford, C., Russell, D., Partition coefficients for olivine-melt and orthopyroxene-melt systems. *Contrib. Mineral. Petrol.* 109, 1991, 212–224. doi:10.1007/BF00306480.
- Bédard J.H., Oceanic crust as a reactive filter: synkinematic intrusion, hybridization, and assimilation in an ophiolitic magma chamber, western Newfoundland, *Geology* 21, 1993, 77–80.
- Bédard J.H., Partitioning coefficients between olivine and silicate melts, *Lithos* 83, 2005, 394–419, <http://dx.doi.org/10.1016/j.lithos.2005.03.011>.
- Bédard J.H., Ophiolitic magma chamber processes, a perspective from the Canadian Appalachians, In: Charlier B., Namur O., Latypov R. and Tegner C., (Eds.), *Layered Intrusions*, 2015, Springer, Berlin, 693–732.
- Bédard J.H., Hebert R., Berclaz A. and Varfalvy V., Syntexis and the genesis of lower oceanic crust, In: Dilek Y., Moores E.M., Elthon D. and Nicolas A., (Eds.), *Ophiolites and Oceanic Crust: New Insights From Field Studies and the Ocean Drilling Program, Special Paper*, vol. 349, 2000, Geological Society of America, 105–119.
- Bedini R.M., Bodinier J.-L. and Vernières J., Numerical simulation of Fe-Mg partitioning during melting and melt-rock interactions in the upper mantle, In: *Extended Abstracts, Proceedings of 4th International Orogenic Lherzolites and Mantle Processes Conference*, 2002, Samani, Japan, (unpublished).
- Blackman D.K., Ildefonse B., John B.E., Ohara Y., Miller D.J., MacLeod C.J. and Expedition 304/305 Scientists, Expedition 304/305, In: *Proceedings of the Integrated Ocean Drilling Program 304/305, 2006* <http://dx.doi.org/10.2204/iodp.proc.304305.101.2006>.
- Blackman D.K., Ildefonse B., John B.E., et al., Drilling constraints on lithospheric accretion and evolution at Atlantis Massif, Mid-Atlantic Ridge 30N, *J. Geophys. Res. Solid Earth* 116, 2011, 1–25, <http://dx.doi.org/10.1029/2010JB007931>.
- Blackman D.K., Karson J.A., Kelley D.S., Cann J.R., Früh-Green G.L., Gee J.S., Hurst S.D., John B.E., Morgan J., Nooner S.L., Ross D.K., Schroeder T.J. and Williams E.A., Geology of the Atlantis Massif (Mid-Atlantic Ridge, 30° N): implications for the evolution of an ultramafic oceanic core complex, *Mar. Geophys. Res.* 23, 2002, 443–469, <http://dx.doi.org/10.1023/B:MARI.0000018232.14085.75>.
- Borghini G. and Rampone E., Postcumulus processes in oceanic-type olivine-rich cumulates: the role of trapped melt crystallization versus melt/rock interaction, *Contrib. Mineral. Petrol.* 154, 2007, 619–633, <http://dx.doi.org/10.1007/s00410-007-0217-5>.

- Boudier F. and Nicolas A., Nature of the Moho transition zone in the Oman Ophiolite, *J. Petrol.* 36, 1995, 777–796.
- Bodinier, J.L., Garrido, C.J., Chanefo, I., Bruguier, O., Gervilla, F., Origin of pyroxenite-peridotite veined mantle by refertilization reactions: Evidence from the Ronda peridotite (Southern Spain). *J. Petrol.* 49, 2008, 999–1025. doi:10.1093/petrology/egn014
- Bowen N.L., *The Evolution of the Igneous Rocks*, 1928, Dover, New York, N.Y., (332 pp.).
- Cann J.R., Blackman D.K., Smith D.K., McAllister E., Janssen B., Mello S., Avgerinos E., Pascoe A.R. and Escartin J., Corrugated slip surfaces formed at ridge–transform intersections on the Mid-Atlantic Ridge, *Nature*, 1997, <http://dx.doi.org/10.1038/385329a0>.
- Cannat M., Mével C., Maia M., Deplus C., Durand C., Gente P., Agrinier P., Belarouchi A., Dubuisson G., Humler E. and Reynolds J., Thin crust, ultramafic exposures, and rugged faulting patterns at the Mid-Atlantic Ridge (22°–24°N), *Geology* 23, 1995, 49–52, [http://dx.doi.org/10.1130/0091-7613\(1995\)023<0049:TCUEAR>2.3.CO;2](http://dx.doi.org/10.1130/0091-7613(1995)023<0049:TCUEAR>2.3.CO;2).
- Chakraborty S., Diffusion in solid silicates: a tool to track timescales of processes comes of age, *Annu. Rev. Earth Planet. Sci.* 36, 2008, 153–190, <http://dx.doi.org/10.1146/annurev.earth.36.031207.124125>.
- Collier M.L. and Kelemen P.B., The case for reactive crystallization at mid-ocean ridges, *J. Petrol.* 51, 2010, 1913–1940, <http://dx.doi.org/10.1093/petrology/egq043>.
- Coogan L.A., The lower oceanic crust, In: Turekian K.K. and Holland K.D., (Eds.), *Treatise on Geochemistry*, Second edition 4.14, 2014, Elsevier, Amsterdam, 497–541, <http://dx.doi.org/10.1016/B978-0-08-095975-7.00316-8>.
- Coogan L.A., Jenkin G.R.T. and Wilson R.N., Constraining the cooling rate of the lower oceanic crust: a new approach applied to the Oman ophiolite, *Earth Planet. Sci. Lett.* 199, 2002, 10.
- Crank J., *The Mathematics of Diffusion*, Second edition, 1975, Oxford University Press Ely House, London W.I.
- Danyushevsky, L. V., Plechov, P., *Petrolog3: Integrated software for modeling crystallization processes*, *Geochem. Geophys. Geosyst.*, 12, 2011, doi:10.1029/2011GC003516. 1
- De Hoog J.C.M., Gall L. and Cornell D.H., Trace-element geochemistry of mantle olivine and application to mantle petrogenesis and geothermobarometry, *Chem. Geol.* 270, 2010, 196–215, <http://dx.doi.org/10.1016/j.chemgeo.2009.11.017>.
- DePaolo D.J., Trace element and isotopic effects of combined wallrock assimilation and fractional crystallization, *Earth Planet. Sci. Lett.* 53, 1981, 189–202.
- D’Errico M.E., Warren J.M. and Godard M., Evidence for chemically heterogeneous Arctic mantle beneath the Gakkel Ridge, *Geochim. Cosmochim. Acta* 174, 2016, 291–312, <http://dx.doi.org/10.1016/j.gca.2015.11.017>.
- Dick H.J.B., Abyssal peridotites, very slow spreading ridges and ocean ridge magmatism, *Geol. Soc. Lond., Spec. Publ.* 42, 1989, 71–105, <http://dx.doi.org/10.1144/GSL.SP.1989.042.01.06>.
- Dick H.J.B., Tivey M.A. and Tucholke B.E., Plutonic foundation of a slow-spreading ridge segment: oceanic core complex at Kane Megamullion, 23°30’N, 45°20’W, *Geochem. Geophys. Geosyst.* 9, 2008, Q05014 <http://dx.doi.org/10.1029/2007GC001645>.
- Dick H.J.B., Natland, J.H., Alt, J.C., et al., A long in-situ section of the lower ocean crust: results of ODP Leg 176 drilling at the Southwest Indian Ridge, *Earth Planet. Sci. Lett.* 179, 2000, 31–51, [http://dx.doi.org/10.1016/S0012-821X\(00\)00102-3](http://dx.doi.org/10.1016/S0012-821X(00)00102-3).

- Dick, H.J.B., Ozawa, K., Meyer, P.S., Niu, Y., Robinson, P.T., Constantin, M., Hebert, R., Maeda, J., Natland, J.H., Hirth, J.G., Mackie, S.M., Primary silicate mineral chemistry of a 1.5-km section of very slow spreading lower ocean crust: ODP Hole 753B, Southwest Indian Ridge. *Proceedings of the Ocean Drilling Program 176*, 2002, 1–61.
- Dijkstra A.H., Barth M.G., Drury M.R., Mason P.R.D. and Vissers R.L.M., Diffuse porous melt flow and melt-rock reaction in the mantle lithosphere at a slow-spreading ridge: a structural petrology and LA-ICP-MS study of the Othris Peridotite Massif (Greece), *Geochem. Geophys. Geosyst.* 4, 2003, 8613, <http://dx.doi.org/10.1029/2001GC000278>.
- Dohmen R., Becker H.W. and Chakraborty S., Fe-Mg diffusion in olivine I: experimental determination between 700 and 1,200 °C as a function of composition, crystal orientation and oxygen fugacity, *Phys. Chem. Miner.* 34, 2007, 389–407, <http://dx.doi.org/10.1007/s00269-007-0157-7>.
- Dohmen R. and Chakraborty S., Fe-Mg diffusion in olivine II: point defect chemistry, change of diffusion mechanisms and a model for calculation of diffusion coefficients in natural olivine, *Phys. Chem. Miner.* 34, 2007, 409–430, <http://dx.doi.org/10.1007/s00269-007-0158-6>.
- Dohmen R., Kasemann S.A., Coogan L. and Chakraborty S., Diffusion of Li in olivine. Part I: experimental observations and a multi species diffusion model, *Geochim. Cosmochim. Acta* 74, 2010, 274–292, <http://dx.doi.org/10.1016/j.gca.2009.10.016>.
- Drouin M., Godard M., Ildefonse B., Bruguier O. and Garrido C.J., Geochemical and petrographic evidence for magmatic impregnation in the oceanic lithosphere at Atlantis Massif, Mid-Atlantic Ridge (IODP Hole U1309D, 30°N), *Chem. Geol.* 264, 2009, 71–88, <http://dx.doi.org/10.1016/j.chemgeo.2009.02.013>.
- Drouin M., Ildefonse B. and Godard M., A microstructural imprint of melt impregnation in slow spreading lithosphere: olivine-rich troctolites from the Atlantis Massif, Mid-Atlantic Ridge, 30°N, IODP Hole U1309D, *Geochem. Geophys. Geosyst.* 11, 2010, 1–21, <http://dx.doi.org/10.1029/2009GC002995>.
- Elthon D., High magnesia liquids as the parental magma for ocean floor basalts, *Nature* 278, 1979, 514–518, <http://dx.doi.org/10.1017/CBO9781107415324.004>.
- Evans T.M., Hugh H.S. and Tuff J., The influence of melt composition on the partitioning of REEs, Y, Sc, Zr and Al between forsterite and melt in the system CMAS, *Geochim. Cosmochim. Acta* 72, 2008, 5708–5721, <http://dx.doi.org/10.1016-6/j.gca.2008.09.017>.
- Gale A., Dalton C.A., Langmuir C.H., Su Y. and Schilling J.G., The mean composition of ocean ridge basalts, *Geochem. Geophys. Geosyst.* 14, 2013, 489–518, <http://dx.doi.org/10.1029/2012GC004334>.
- Garrido C.J., Bodinier J.L. and Alard O., Incompatible trace element partitioning and residence in anhydrous spinel peridotites and websterites from the Ronda orogenic peridotite, *Earth Planet. Sci. Lett.* 181, 2000, 341–358, [http://dx.doi.org/10.1016/S0012-821X\(00\)00201-6](http://dx.doi.org/10.1016/S0012-821X(00)00201-6).
- Gast P.W., Trace element fractionation and the origin of tholeiitic and alkaline magma types, *Geochim. Cosmochim. Acta* 32, 1968, 1057.
- Godard M., Awaji S., Hansen H., Hellebrand E., Brunelli D., Johnson K., Yamasaki T., Maeda J., Abratis M., Christie D., Kato Y., Mariet C. and Rosner M., Geochemistry of a long in-situ section of intrusive slow-spread oceanic lithosphere: results from IODP Site U1309 (Atlantis Massif, 30°N Mid-Atlantic-Ridge), *Earth Planet. Sci. Lett.* 279, 2009, 110–122, <http://dx.doi.org/10.1016/j.epsl.2008.12.034>.
- Godard M., Bodinier J.-L. and Vasseur G., Effects of mineralogical reactions on trace element redistributions in mantle rocks during percolation processes: a chromatographic approach, *Earth Planet. Sci. Lett.* 133, 1995, 449–461, [http://dx.doi.org/10.1016/0012-821X\(95\)00104-K](http://dx.doi.org/10.1016/0012-821X(95)00104-K).
- Godard M., Lagabrielle Y., Alard O. and Harvey J., Geochemistry of the highly depleted peridotites drilled at ODP Sites 1272 and 1274 (Fifteen-Twenty Fracture Zone, Mid-Atlantic Ridge): implications for mantle

- dynamics beneath a slow spreading ridge, *Earth Planet. Sci. Lett.* 267, 2008, 410–425, <http://dx.doi.org/10.1016/j.epsl.2007.11.058>.
- Grimes C.B., John B.E., Cheadle M.J. and Wooden J.L., Protracted construction of gabbroic crust at a slow spreading ridge: Constraints from $^{206}\text{Pb}/^{238}\text{U}$ zircon ages from Atlantis Massif and IODP Hole U1309D (30°N, MAR), *Geochem. Geophys. Geosyst.* 9, 2008, <http://dx.doi.org/10.1029/2008GC002063>.
- Grove T.L., Kinzler R.J. and Bryan W.B., Mantle flow and melt generation at mid-ocean ridges: fractionation of mid-ocean ridge basalt (MORB), In: Morgan J. P.J.P., Blackman D. B.D.B. and Sinton J. M.J.M., (Eds.), *Mantle Flow and Melt Generation at Mid-ocean Ridges*, Geophysical Monograph Series, vol. 71, 1992, AGU, Washington, D. C, 281–311, <http://dx.doi.org/10.1029/GM071p0281>.
- Günther, D., Heinrich, C.A., Enhanced sensitivity in laser ablation-ICP mass spectrometry using helium-argon mixtures as aerosol carrier — plenary lecture. *Journal of Analytical Atomic Spectrometry* 14 (9), 1999, 1363–1368.
- Hart S.R. and Davis K.E., Nickel partitioning between olivine and silicate melt, *Earth Planet. Sci. Lett.* 40, 1978, 203–219, <http://dx.doi.org/10.1016/j.pcad.2011.11.003>.
- Hebert R., Constantin M. and Robinson P.T., Primary mineralogy of Leg 118 gabbroic rocks and their place in the spectrum of oceanic mafic igneous rocks. *Proceeding of the ocean drilling program Leg 118*, *Sci. Results* 118, 1991, 3–20.
- Higgie K. and Tommasi A., Feedbacks between deformation and melt distribution in the crust–mantle transition zone of the Oman ophiolite, *Earth Planet. Sci. Lett.* 359–360, 2012, 61–72, <http://dx.doi.org/10.1016/j.epsl.2012.10.003>.
- Holness M.B., Anderson A.T., Martin V.M., MacLennan J., Passmore E. and Schwindinger K., Textures in partially solidified crystalline nodules: a window into the pore structure of slowly cooled mafic intrusions, *J. Petrol.* 48, 2007, 1243–1264, <http://dx.doi.org/10.1093/petrology/egm016>.
- Ildefonse B., Abe N., Godard M., Morris A., Teagle D.A.H. and Umino S., Formation and evolution of oceanic lithosphere: new insights on crustal structure and igneous geochemistry from ODP/IODP Sites 1256, U1309, and U1415, *Dev. Mar. Geol.* 2014, <http://dx.doi.org/10.1016/B978-0-444-62617-2.00017-7>.
- Ildefonse B., Blackman D.K., John B.E., et al., Oceanic core complexes and crustal accretion at slow-spreading ridges, *Geology* 35, 2007, 623–626, <http://dx.doi.org/10.1130/G23531A.1>.
- Johnson, K.T.M., Dick, H.J.B., Shimizu, N., Melting in the Oceanic Upper Mantle: an Ion Microprobe Study of Diopsides in Abyssal Peridotites. *J. Geophys. Res.* 95 (B3), 1990, 2661–2678.
- Jollands M.C., Hermann J., O'Neill H.S.C., Spandler C. and Padrón-Navarta J.A., Diffusion of Ti and some divalent cations in olivine as a function of temperature, oxygen fugacity, chemical potentials and crystal orientation, *J. Petrol.* 57, 2016, 1983–2010, <http://dx.doi.org/10.1093/petrology/egw067>.
- Kelemen P.B., Hirth G., Shimizu N., Spiegelman M. and Dick H.J., A review of melt migration processes in the adiabatically upwelling mantle beneath oceanic spreading ridges, *Philos. Trans. R. Soc. London, Ser. A* 355, 1997, 283–318, <http://dx.doi.org/10.1098/rsta.1997.0010>.
- Kinzler R.J., Melting of mantle peridotite at pressures approaching the spinel to garnet transition: application to mid-ocean ridge basalt petrogenesis, *J. Geophys. Res.*, 102, 1997, 853–874. [https://doi.org/10.1016/S0377-0273\(00\)00182-7](https://doi.org/10.1016/S0377-0273(00)00182-7).
- Kinzler R.J. and Grove T.L., Corrections and further discussion of the primary magmas of mid-ocean ridge basalts, 1 and 2, *J. Geophys. Res. Solid Earth* 98, 1993, 22339–22347, <http://dx.doi.org/10.1029/93JB02164>.
- Kvassnes A.J.S. and Grove T.L., How partial melts of mafic lower crust affect ascending magmas at oceanic ridges, *Contrib. Mineral. Petrol.* 156, 2008, 49–71, <http://dx.doi.org/10.1007/s00410-007-0273-x>.

- Lambart S., Laporte D. and Schiano P., An experimental study of focused magma transport and basalt-peridotite interactions beneath mid-ocean ridges: implications for the generation of primitive MORB compositions, *Contrib. Mineral. Petrol.* 157, 2009, 429–451, <http://dx.doi.org/10.1007/s00410-008-0344-7>.
- Langmuir C.H., Geochemical consequences of in situ crystallization, *Nature* 1989, <http://dx.doi.org/10.1038/340199a0>.
- Liang Y., Kinetics of crystal-melt reaction in partially molten silicates: 1. Grain scale processes, *Geochem. Geophys. Geosyst.* 4, 2003, <http://dx.doi.org/10.1029/2002GC000375>.
- Lissenberg C.J. and Dick H.J.B., Melt-rock reaction in the lower oceanic crust and its implications for the genesis of mid-ocean ridge basalt, *Earth Planet. Sci. Lett.* 271, 2008, 311–325, <http://dx.doi.org/10.1016/j.epsl.2008.04.023>.
- Lissenberg C.J., MacLeod C.J., Howard K.A. and Godard M., Pervasive reactive melt migration through fast-spreading lower oceanic crust (Hess Deep, equatorial Pacific Ocean), *Earth Planet. Sci. Lett.* 361, 2013, 436–447, <http://dx.doi.org/10.1016/j.epsl.2012.11.012>.
- Mainprice, D., Bachmann, F., Hielscher, R., Schaeben, H., Descriptive tools for the analysis of texture projects with large datasets using MTEX - strength, symmetry, and components. In: Faulkner, D.R., Meckenburgh, J., Mariani, E., (eds) *Rock Deformation from Field, Experiments and Theory: A Volume in Honour of Ernie Rutter*. Geological Society, London, Special Publications, 409, 2014. <http://dx.doi.org/10.1144/SP409.8>
- Miller D.J., Abratis M., Christie D., Drouin M., Godard M., Ildefonse B., Maeda J., Weinsteiger A., Yamasaki T., Suzuki Y., Niino A., Sato Y. and Takeda F., Data report: microprobe analyses of primary mineral phases from Site U1309, Atlantis Massif, IODP expedition 304/305, In: *Proceedings of the Integrated Ocean Drilling Program 304/305, 2009* <http://dx.doi.org/10.2204/iodp.proc.304305.202.2009>.
- Navon O. and Stolper E.M., Geochemical consequences of melt percolation – the upper mantle as a chromatographic column, *J. Geol.* 95, 1987, 285–307.
- O’Driscoll B., Donaldson C.H., Troll V.R., Jerram D.A. and Emeleus C.H., An origin for harrisitic and granular olivine in the Rum layered suite, NW Scotland: a crystal size distribution study, *J. Petrol.* 48, 2007, 253–270, <http://dx.doi.org/10.1093/petrology/egl059>.
- O’Hara M.J., Primary magmas and the origin of basalts, *Scott. J. Geol.* 1, 1965, 19–40, <http://dx.doi.org/10.1144/sjg01010019>.
- O’Hara M.J., Geochemical evolution during fractional crystallization of a periodically refilled magma chamber, *Nature* 266, 1977, 503.
- O’Neill H.S.C. and Jenner F.E., The global pattern of trace-element distributions in ocean floor basalts, *Nature* 491, 2012, 698–704, <http://dx.doi.org/10.1038/nature11678>.
- Paquet M., Cannat M., Brunelli D., Hamelin C. and Humler E., Effect of melt/mantle interactions on MORB chemistry at the easternmost Southwest Indian Ridge (61°–67°E), *Geochem. Geophys. Geosyst.* 17, 2016, <http://dx.doi.org/10.1002/2016GC006385>.
- Pearce N.J.G., Perkins W.T., Westgate J.A., Gorton M.P., Jackson S.E., Neal C.R., Chenery S.P., A compilation of new and published major and trace element data for NIST SRM 610 and NIST SRM 612 glass reference materials. *Geostandards Newsletter. The Journal of Geostandards and Geoanalysis* 21 (1), 1997, 115–144.
- Pec M., Holtzman B., Zimmerman M., Kohlstedt D., Reaction infiltration instabilities in mantle rocks: An experimental investigation. *J. Petrol.* 58(5), 2017, 979–1003, <https://doi.org/10.1093/petrology/egx043>.

- Petry C., Chakraborty S. and Palme H., Experimental determination of Ni diffusion coefficients in olivine and their dependence on temperature, composition, oxygen fugacity, and crystallographic orientation, *Geochim. Cosmochim. Acta* 68, 2004, 4179–4188, <http://dx.doi.org/10.1016/j.gca.2004.02.024>.
- Presnall D. and Hoover J.D., High pressure phase equilibrium constraints on the origin of mid-ocean ridge basalts, In: Mysen B.O., (Ed), *Magmatic Processes: Physicochemical Principles*, 1987, Special Publication-Geochemical Society, 75–89.
- Remmert P., Dohmen R., Chakraborty, S., Diffusion of REE, Hf and Sr in Olivine, *EOS Tans. Am. Geophys. Union*, 2008 (Fall Meeting Supplementary, Abstract MR33A-1844). doi:10.1029/2001GC000205.
- Rampone E., Borghini G., Godard M., Ildefonse B., Crispini L. and Fumagalli P., Melt/rock reaction at oceanic peridotite/gabbro transition as revealed by trace element chemistry of olivine, *Geochim. Cosmochim. Acta* 190, 2016, 309–331, <http://dx.doi.org/10.1016/j.gca.2016.06.029>.
- Renna M.R. and Tribuzio R., Olivine-rich troctolites from Ligurian ophiolites (Italy): evidence for impregnation of replacive mantle conduits by MORB-type melts, *J. Petrol.* 52, 2011, 1763–1790, <http://dx.doi.org/10.1093/petrology/egr029>.
- Renna M.R., Tribuzio R. and Ottolini L., New perspectives on the origin of olivine-rich troctolites and associated harrisites from the Ligurian ophiolites (Italy), *J. Geol. Soc. Lond.* 173, 2016, 916–932, <http://dx.doi.org/10.1144/jgs2015-135>.
- Ross D.K. and Elthon D., Cumulus and postcumulus crystallization in the oceanic crust: major- and trace-element geochemistry of Leg 153 gabbroic rocks, *Proc. Ocean Drill. Program Sci. Results* 153, 1997, 333–353, <http://dx.doi.org/10.2973/odp.proc.sr.153.023.1997>.
- Sanfilippo A., Morishita T., Kumagai H., Nakamura K., Okino K., Hara K., Tamura A. and Arai S., Hybrid troctolites from mid-ocean ridges: inherited mantle in the lower crust, *Lithos* 232, 2015, 124–130, <http://dx.doi.org/10.1016/j.lithos.2015.06.025>.
- Sanfilippo A., Tribuzio R., Melt transport and deformation history in a nonvolcanic ophiolitic section, northern Apennines, Italy: Implications for crustal accretion at slow spreading settings. *Geochem. Geophys. Geosyst.* 12, 2011, 1–34. doi:10.1029/2010GC003429.
- Sanfilippo A. and Tribuzio R., Building of the deepest crust at a fossil slow-spreading centre (Pineto gabbroic sequence, Alpine Jurassic ophiolites), *Contrib. Mineral. Petrol.* 165, 2013, 705–721, <http://dx.doi.org/10.1007/s00410-012-0831-8>.
- Sanfilippo A., Tribuzio R. and Tiepolo M., Mantle-crust interactions in the oceanic lithosphere: constraints from minor and trace elements in olivine, *Geochim. Cosmochim. Acta* 141, 2014, 423–439, <http://dx.doi.org/10.1016/j.gca.2014.06.012>.
- Sanfilippo A., Tribuzio R., Tiepolo M. and Berno D., Reactive flow as dominant evolution process in the lowermost oceanic crust: evidence from olivine of the Pineto ophiolite (Corsica), *Contrib. Mineral. Petrol.* 170, 2015, <http://dx.doi.org/10.1007/s00410-015-1194-8>.
- Saper L. and Liang Y., Formation of plagioclase-bearing peridotite and plagioclase-bearing wehrlite and gabbro suite through reactive crystallization: an experimental study, *Contrib. Mineral. Petrol.* 167, 2014, 1–16, <http://dx.doi.org/10.1007/s00410-014-0985-7>.
- Seyler M., Lorand J.P., Dick H.J.B. and Drouin M., Pervasive melt percolation reactions in ultra-depleted refractory harzburgites at the Mid-Atlantic Ridge, 15° 20'N: ODP Hole 1274A, *Contrib. Mineral. Petrol.* 153, 2007, 303–319, <http://dx.doi.org/10.1007/s00410-006-0148-6>.
- Shaw D.M., Trace element fractionation during anatexis, *Geochim. Cosmochim. Acta* 40, 1970, 73.

- Spandler, C., O'Neill, H.S.C., Diffusion and partition coefficients of minor and trace elements in San Carlos olivine at 1,300°C with some geochemical implications. *Contrib. Mineral. Petrol.* 159, 2010, 1–28. doi:10.1007/s00410-009-0456-8.
- Suhr G., Hellebrand E., Johnson K. and Brunelli D., Stacked gabbro units and intervening mantle: a detailed look at a section of IODP leg 305, hole U1309D, *Geochem. Geophys. Geosyst.* 9, 2008, <http://dx.doi.org/10.1029/2008GC002012>.
- Sun C. and Liang Y., An assessment of subsolidus re-equilibration on REE distribution among mantle minerals olivine, orthopyroxene, clinopyroxene, and garnet in peridotites, *Chem. Geol.* 372, 2014, 80–91, <http://dx.doi.org/10.1016/j.chemgeo.2014.02.014>.
- Sun S.-s. and McDonough W.F., Chemical and isotopic systematics of oceanic basalts: implications for mantle composition and processes, *Geol. Soc. Lond., Spec. Publ.* 42, 1989, 313–345, <http://dx.doi.org/10.1144/GSL.SP.1989.042.01.19>.
- Tamura A., Arai S., Ishimaru S. and Andal E.S., Petrology and geochemistry of peridotites from IODP Site U1309 at Atlantis Massif, MAR 30° N: micro- and macro-scale melt penetrations into peridotites, *Contrib. Mineral. Petrol.* 155, 2008, 491–509, <http://dx.doi.org/10.1007/s00410-007-0254-0>.
- Tartarotti P., Susini S., Nimis P. and Ottolini L., Melt migration in the upper mantle along the Romanche Fracture Zone (Equatorial Atlantic), *Lithos* 63, 2002, 125–149, [http://dx.doi.org/10.1016/S0024-4937\(02\)00116-0](http://dx.doi.org/10.1016/S0024-4937(02)00116-0).
- Tommasi A., Mainprice D., Gilles C. and Yvan C., Viscoplastic self-consistent and equilibrium-based modeling of olivine lattice preferred orientations: implications for the upper mantle seismic anisotropy, *J. Geophys. Res.* 105, 2000, 7893–7908, <http://dx.doi.org/10.1029/1999JB900411>.
- Toramaru A. and Fujii N., Connectivity of melt phase in a partially molten peridotite, *J. Geophys. Res.* 91, 1986, 9239–9252.
- Turcotte D.L. and Morgan J.P., The physics of magma migration and mantle flow beneath a mid-ocean ridge, In: Morgan J.P., Blackman D.B. and Sinton J.M., (Eds.), *Mantle Flow and Melt Generation at Mid-Ocean Ridges*, Geophysical Monograph Series, vol. 71, 1992, AGU, Washington, D. C, 155–182, <http://dx.doi.org/10.1029/GM071p0155>.
- Ulmer, P., The dependence of the Fe²⁺-Mg cation-partitioning between olivine and basaltic liquid on pressure, temperature and composition - An experimental study to 30 kbars. *Contributions to Mineralogy and Petrology* 101, 1989, 261–273. doi:10.1007/BF00375311
- Van Achterbergh, E., Ryan, C.G., Jackson, S.E., Griffin, W., Data reduction software for LA-ICP-MS. In: Sylvester, P. (Eds.), *Laser ablation ICP-MS in the Earth Science*. Mineralogical Association of Canada 2001, pp. 239–243.
- Van den Bleeken G., Müntener O. and Ulmer P., Melt variability in percolated peridotite: an experimental study applied to reactive migration of tholeiitic basalt in the upper mantle, *Contrib. Mineral. Petrol.* 161, 2011, 921–945, <http://dx.doi.org/10.1007/s00410-010-0572-5>.
- Vernières J., Godard M. and Bodinier J.-L., A plate model for the simulation of trace element fractionation during partial melting and magma transport in the Earth's upper mantle, *J. Geophys. Res. Solid Earth* 102, 1997, 24771–24784.
- Villiger S., Ulmer P. and Müntener O., Equilibrium and fractional crystallization experiments at 0.7 GPa; the effect of pressure on phase relations and liquid compositions of tholeiitic magmas, *J. Petrol.* 48, 2007, 159–184, <http://dx.doi.org/10.1093/petrology/egl058>.

- von Bargen N. and Waff H.S., Permeabilities, interfacial areas and curvatures of partially molten systems: results of numerical computations of equilibrium microstructures, *J. Geophys. Res.* 91, 1986, 9261–9276.
- Workman R.K. and Hart S.R., Major and trace element composition of the depleted MORB mantle (DMM), *Earth Planet. Sci. Lett.* 231, 2005, 53–72, <http://dx.doi.org/10.1016/j.epsl.2004.12.005>.
- Yoshinobu A. S., Hirth G., Microstructural and experimental constraints on the rheology of partially molten gabbro beneath oceanic spreading centers, *J. Struct. Geol.*, 24, 2002, 1101–1107. doi:10.1016/S0191-8141(01)00094-3.

3. Ca and REE chemical profiles: a record of subsolidus re-equilibration in Olivine-rich troctolites from Hole U1309D?

3.1 Introduction

The detailed microstructural and petro-geochemical study on the reactive olivine-rich troctolites recovered at IODP Hole U1309D have demonstrated that they formed after significant melt impregnation of a heterogeneous harzburgitic mantle. They are characterized by local variations in mineral major and minor element compositions that were interpreted as resulting from melt-rock chemical disequilibrium that locally enhanced reaction. The multiple melt-rock interactions ultimately consisted in dissolution of olivine and precipitation of plagioclase and clinopyroxene.

On the other hand, trace element compositions of olivines are comparable among all studied samples. They display characteristic strong normalized H- to M-REE fractionations compared to mantle olivines. Melt transport was invoked to explain such trace element signature of olivine. The discrepancy between higher velocities of M-REE compared to those of H-REE during melt transport, as described by the chromatographic effect (e.g., Navon and Stolper, 1987), lead to the observed depletion in more incompatible (M-) REE (Chapter section III.2; Ferrando et al., 2018). Similar REE fractionations have been observed elsewhere in reactive olivine-rich troctolites from Alpine ophiolite (Erro-Tobbio Unit, Rampone et al., 2016; Internal Ligurian and Pineto ophiolites, Sanfilippo et al., 2014), and seem to be a common characteristic of these lithologies.

REE fractionations in olivine crystals have been also observed in eclogite and peridotite xenoliths (e.g., Witt-Eickschen and O'Neill, 2005; Sun and Liang, 2013). Textural and chemical features of these rocks show no evidence of melt-rock interactions, and compositions were alternatively interpreted as resulting from subsolidus re-equilibration during cooling (Sun and Liang, 2013; Sun and Liang, 2014). Because clinopyroxene has high affinity for incompatible elements (e.g., Johnson *et al.*, 1990; Wood and Blundy, 2003), while their solubility in olivine decreases with decreasing temperature, upon cooling ($T < 1000^{\circ}\text{C}$; Coogan *et al.*, 2002, Sun and Liang, 2014) REE and Y are re-distributed between the two phases leading to a progressive decrease of REE concentrations in olivine. Sun and Liang (2014) developed parameterized lattice

strain models for REE and Y partitioning among mantle minerals in a wide range of temperature conditions to investigate the effect of cooling on REE partitioning. They used mineral-melt partitioning models that were calibrated against experimentally determined high quality mineral/melt REE and Y partition coefficients (Sun and Liang, 2012, 2013). The lattice strain models are based on the temperature-dependence of partition coefficients (see Chapter sections I.3.1 and I.3.3), and allow to quantitatively determine the (re-)equilibration temperatures between two minerals.

Sun and Liang (2014) observed that as temperature decreases from 1300°C to 700°C REE abundances in clinopyroxene increase by within a factor of 1.5, while those in olivine decrease systematically. Olivine/clinopyroxene REE partition coefficients decrease by 1.5 to 3 orders of magnitude from H- to L-REE, thus they decrease with increasing ionic radius (Sun and Liang, 2014; Figure I.42 in Chapter section I.3.3). Hence cooling can account for REE fractionations in olivine. These findings challenge our interpretation of REE fractionations of olivines in reactive olivine-rich troctolites questioning their magmatic origin.

The effect of cooling, similarly to that observed on REE and Y, is also recorded by Ca concentrations in olivine and clinopyroxene (Coogan *et al.*, 2002; VanTongeren *et al.*, 2008). During cooling Ca moves out of olivine to enter into clinopyroxene. As for REE and Y, subsolidus re-equilibration takes place at the rim where the Ca content of olivine decreases with decreasing temperature. A Ca diffusion flux is produced from the core of the olivine crystal toward its rim (e.g., Chakraborty, 2008; Lasaga, 1983).

In this section, I describe the measured Ca, REE and Y contents along clinopyroxene-to-olivine profiles in olivine-rich troctolites from the Atlantis Massif, IODP Hole U1309D. The aim of this preliminary study is to investigate whether REE fractionations in olivine are due to melt transport as earlier proposed (Chapter section III.2; Ferrando *et al.*, submitted), or they are an effect of subsolidus re-equilibration. Ca profiles are equally considered to further evaluate cooling of the oceanic crustal section at the Atlantis Massif. Timing of subsolidus re-equilibration has not been modeled in this preliminary study. It will be the topic of a 'short' publication that is now in preparation.

3.2 Results

Clinopyroxene-to-olivine geochemical profiles were performed in a total of 15 samples of olivine-rich troctolites, which are those selected by Ferrando et al. (2018). Ca, Y and REE traverses were performed along principal crystallographic axes of olivine and across adjacent clinopyroxene crystals following the procedure illustrated in Ferrando et al. (2018) and in Chapter II. All results are reported in Appendix 2.

Olivine-rich troctolites (OI-T) were distinguished in three types based on microstructure, texture and mineral compositions by Ferrando et al. (2018). OI-T 1 (modal olivine <75%) is the most reactive end-member, while OI-T2 (> 75% of olivine) and OI-T3 formed locally after lower extents of melt-rock interactions.

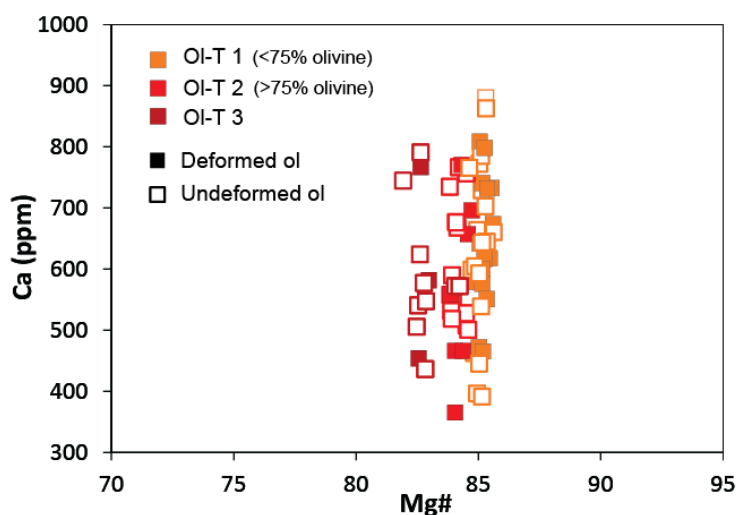


Figure III.1 – Ca (ppm) vs Mg# of olivines in olivine-rich troctolites from Hole U1309D.

Olivines in all OI-Ts from Hole U1309D have on average comparable REE contents (Ferrando et al., 2018) characterized by strong normalized H-REE to M- (medium) REE fractionation ($Dy_N/Yb_N = 0.04 - 0.11$). Despite this, in-sample variations are observed between olivines in contact with plagioclase and those embayed in clinopyroxene (Figure 6 in Ferrando et al., 2018). The latter have Yb_N ranging between 0.17 and 0.4 that are lower than, but partially overlapping with those in the former ($Yb_N = 0.25-0.64$). These in-sample variations of olivine REE compositions might suggest re-distribution of REE between olivine and clinopyroxene during cooling of the lower oceanic crust at

the Atlantis Massif. Ca contents in olivine spam within the same range for all analysed samples, from 365 to 880 ppm (Figure III.1).

Rim-to-rim Ca, Y and REE profiles across olivine and clinopyroxene crystals show no variations regarding the different crystallographic direction considered, as previously observed for other elements (i.e., Mg#, Ni, Mn and Li; Ferrando et al., 2018). Clinopyroxene profiles were difficult to analyse due to their fine-grained size and interstitial habit, but at least two points (or more) were measured corresponding to core and rim. Most Ca profiles in clinopyroxene are scattered with some rims showing higher Ca contents compared to relative cores (Figure III.2a), while relative profiles of Y and REE are flat (Figure III.2b). Ca, REE and Y profiles in olivine are described in detail per type of olivine-rich troctolite.

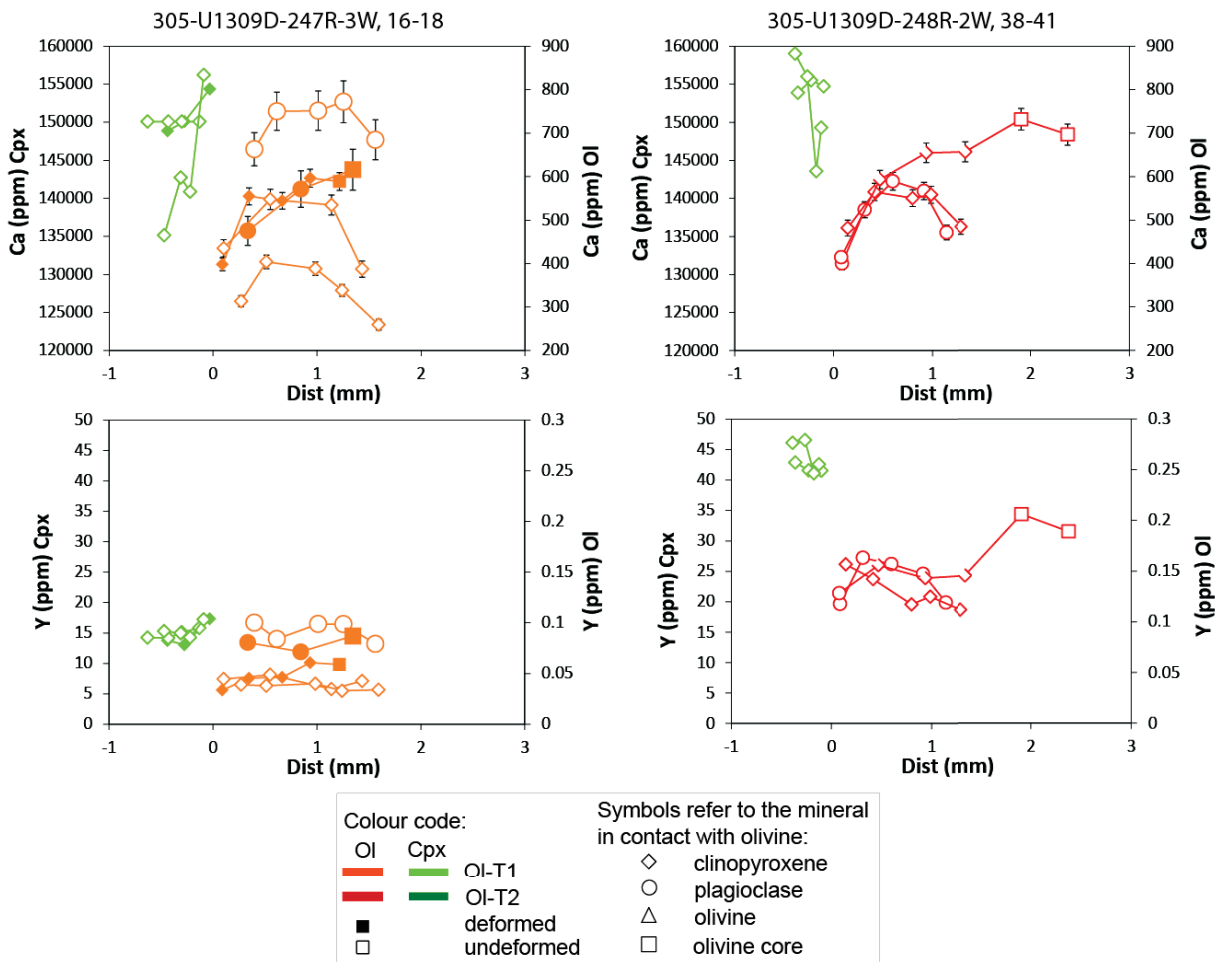


Figure III.2 – Clinopyroxene-to-olivine profiles in OI-T1 (left) and OI-T2 (right). Sample reference is reported on top.

Note that olivine geochemical profiles were performed in grains in contact with clinopyroxene and plagioclase. No remarkable differences are observed between the two textural occurrences of olivine in terms of core-to-rim profiles: both share the same characteristic illustrated here.

Ol-T1

Olivines in O-T1 occur mostly as fine-grained of, overall, less than 2 mm diameter, embayed in large poikilitic plagioclase and clinopyroxene. These fine-grained olivines display Ca contents ranging between 300 and 550 ppm at rims, and from 400 to 620 ppm at cores, except for one olivine grain in sample 305-U1309D-247R-3W, 16-18 that have 660 ppm of Ca at rim and 770 ppm at core (Figure III.3). Ca contents in olivine are systematically lower at rims and higher at cores of crystals. Y contents show no core-to-rim variations, except for two olivine grains in sample 305-U1309D-248R-3W, 131-134 that show 0.07-0.1 Y contents at rim and 0.12-0.14 at core.

Some coarser-grained olivines are also observed in Ol-T1, particularly in sample 305-U1309D-234R-1W, 22-26. It should be noted that this sample was recovered in the borehole at 1124 mbsf, where alteration is relatively higher compared to deeper samples (Figure 2 in Ferrando et al., 2018). The coarse-grained olivines reach 4 mm of diameter, and show Ca contents ranging from 600 to 760 ppm with no core-to-rim variations. Their Ca compositions overlap with those of fine-grained olivine cores. Y contents display no core-to-rim variations.

All olivine grains show rather flat or scattered profiles in H- (Yb) and M- (Dy) REE (Figure III.3).

Ol-T2

Olivines in Ol-T2 are coarser-grained compared to those in Ol-T1, with diameters between 2 and 4.5 mm. All grains have Ca contents at rims (300-590 ppm) lower than those at cores (480-758 ppm; Figure III.4). Some olivines also show core-to-rim variations in Y contents, but others have rather constant Y contents.

M- and H-REE do not vary systematically within single-olivine grains, resulting in flat or scattered profiles (Figure III.4).

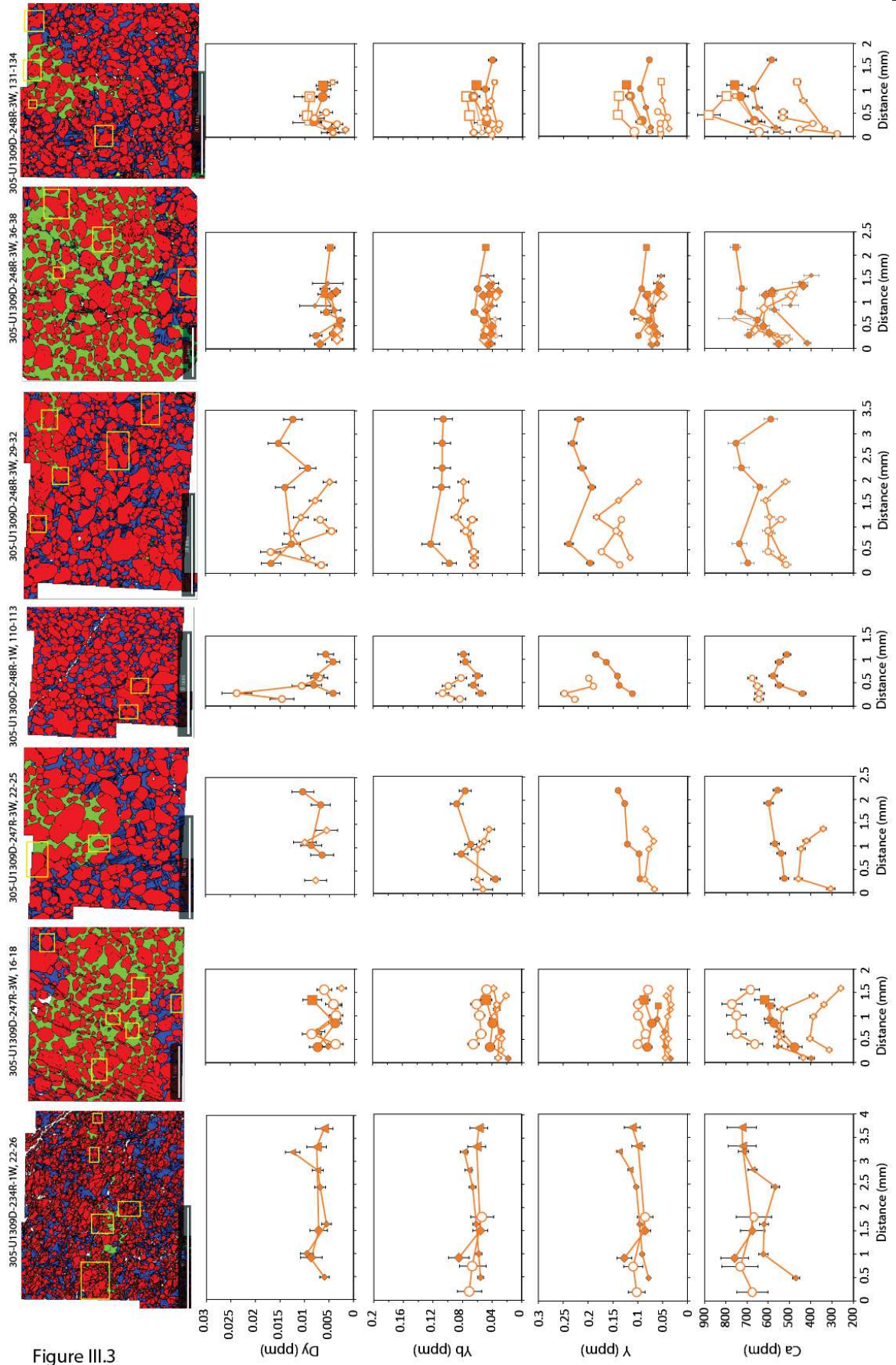


Figure III.3

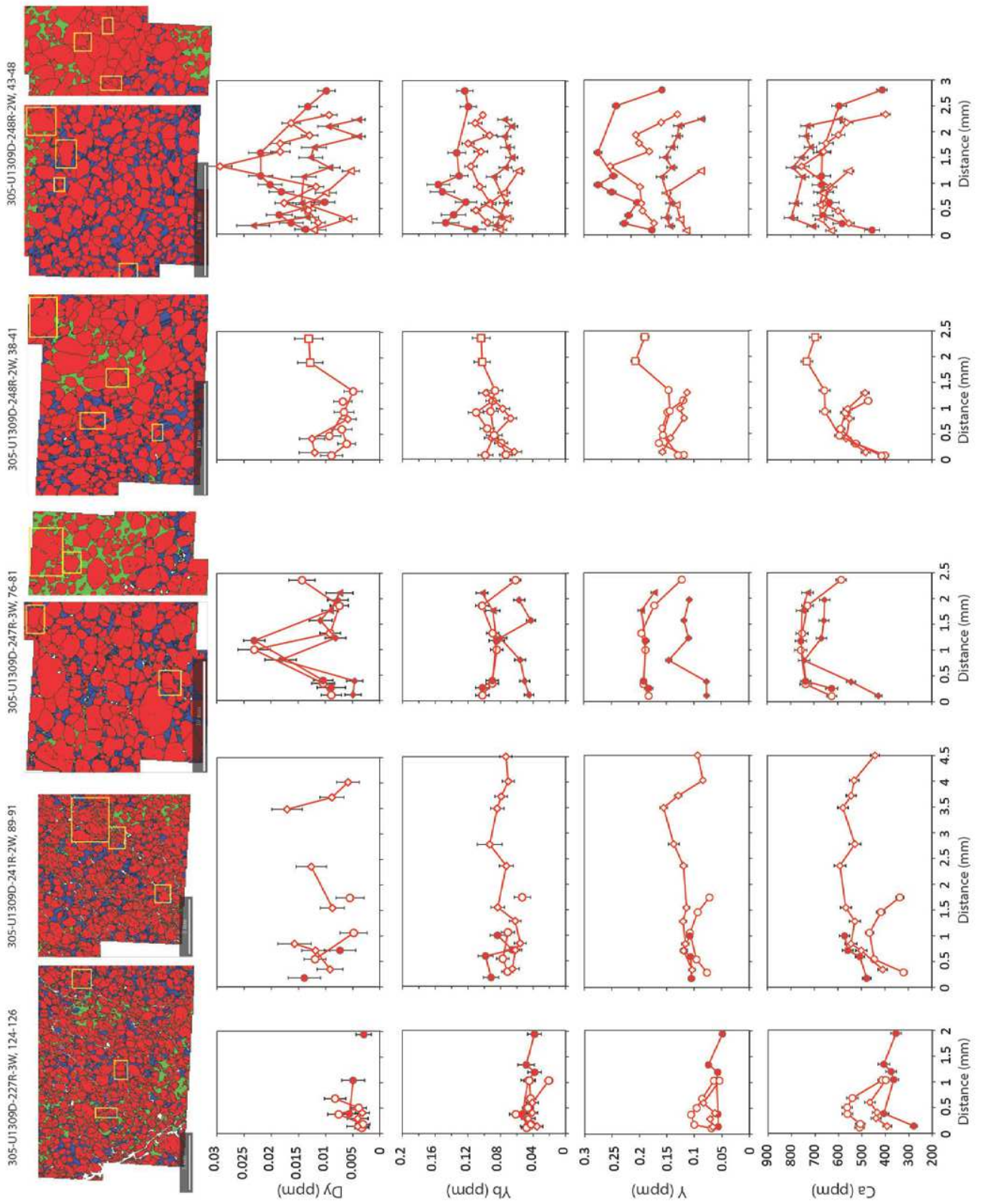


Figure III.4

Figure III.3 – Rim-to-rim and rim-to-core (core is square symbol) profiles in olivines from OI-T1. Distance is in mm and 0 is the contact with adjacent phase. Colour and symbol coding is reported in Figure III.2. On top the EBSD phase map: red = olivine, blue = plagioclase,

Figure III.4 – Rim-to-rim and rim-to-core (core is square symbol) profiles in olivines from OI-T2. Distance, colour and symbol coding as in Figure III.3.

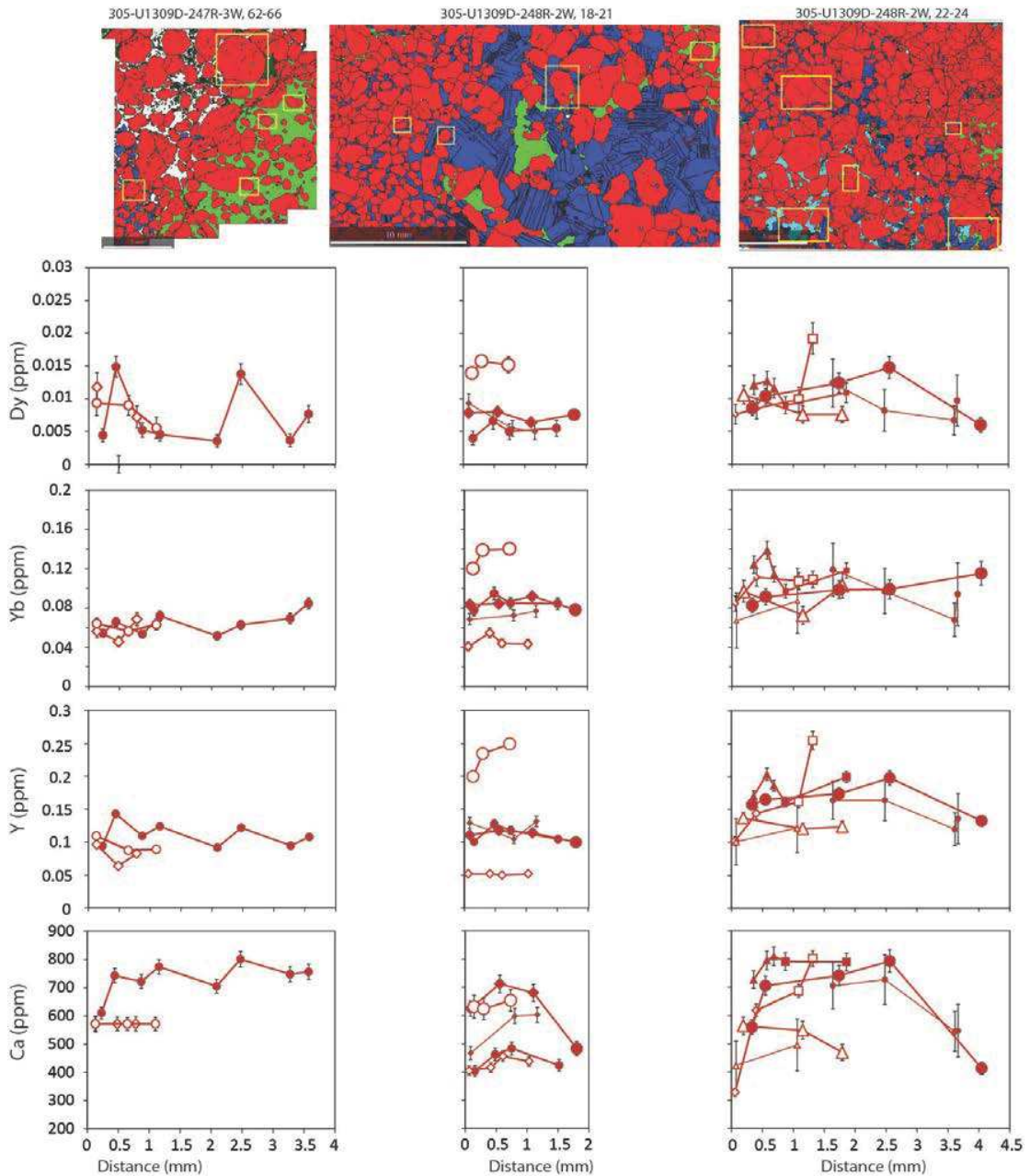


Figure III.5 – Rim-to-rim and rim-to-core (core is square symbol) profiles in olivines from OI-T3. Distance, colour and symbol coding as in Figure III.3.

Ol-T3

Olivine in Ol-T3 has textural characteristics that overlap with both Ol-T1 and Ol-T2 (Ferrando et al., 2018). Two samples of Ol-T3, notably 305-U1309D-248R-2W, 18-21 and 305-U1309D-248R-2W, 22-24, show that both coarser- and finer- grained olivines display lower Ca contents at their rims, ranging between 310 and 480 ppm, and higher at cores (490-810 ppm). Core-to-rim variations in Y contents are observed in two grains only, while other olivines have flat Y profiles.

In contrast, sample 305-U1309D-247R-3W, 62-66 has olivines with flat Ca and Y profiles. This sample is distinguished by intense seawater alteration compared to the other olivine-rich troctolites. Plagioclase is completely altered, while clinopyroxene and olivine are partially preserved (Phase map in Figure III.5).

H-REE and M-REE show flat profiles or scattered values as in olivines from Ol-T1 and Ol-T2.

3.3 Discussion and conclusions

Chemical re-equilibration under subsolidus conditions occurs at the mineral-mineral interface producing a compositional gradient between core and rim of the olivine crystal. If subsolidus re-equilibration is 'faster' than Ca, REE and Y diffusion in olivine, the latter would preserve lower Ca, REE and Y contents at the rim and higher at the core leading to 'bell-shape' core-to-rim profiles.

All analysed olivines in U1309D olivine-rich troctolites have REE flat profiles. On the other hand, all fine-grained and some coarser-grained olivines are characterized by Ca and Y 'bell-shape' profiles, similar to those described and obtained by modeling of cooling at subsolidus conditions (e.g., Coogan *et al.*, 2002, 2007). The lack of core-to-rim variations in certain coarse-grained olivine grains does not correlate with either the mineral phase in contact with olivine, or the type of Ol-T. Instead, it seems to be related to the degree of alteration. Regardless the type of Ol-T considered, those samples displaying relative higher degrees of serpentinization (first column-sample from the left in Figures III.3, III.4 and III.5) have olivines showing flat geochemical profiles. The Ca, REE and Y contents were measured by LA-ICP-MS, which requires analytical spot sizes over 77µm. Also, serpentinization affects grain boundaries and develops in cracks. Hence, it is possible that, in partially serpentinized grains, the olivine rim in contact with clinopyroxene (or plagioclase) was not

analysed. The analysed olivine rims may, therefore, represent 'apparent' rims. In contrast, finer-grained olivines are embayed in poikilitic interstitial phases that prevent circulation of fluids and serpentinization. These olivine grains thus may preserve the cooling signature.

In order to assess the effect of subsolidus re-equilibration on REE fractionations in U1309D olivine-rich troctolites, I calculated the re-equilibration temperature between clinopyroxene and olivine by using the lattice strain model of Sun and Liang (2014). This approach could provide a first indication of the closure temperature of the system that is the temperature at which coexisting phases reach equilibrium. When the equilibrium temperature is $<1000^{\circ}\text{C}$, REE concentrations in olivine are most likely affected by subsolidus re-equilibration (Sun and Liang, 2014). First, I calculate partition coefficients between olivine and clinopyroxene from U1309D olivine-rich troctolites. Generally, they regularly decrease from HREE to MREE (e.g., Spandler and O'Neill, 2010), whereas LREE partition coefficients are poorly constrained (Figure III.6). Second, I compared these calculated partition coefficients to computed olivine/clinopyroxene partition coefficients at temperatures of 900°C , 1000°C , 1050°C and 1200°C using mineral compositions of U1309D olivine-rich troctolites. Overall, equilibrium temperatures for all olivine-rich troctolites range between 1000°C and 1100°C (Figure III.6), except for few olivine grains in Ol-T1 showing $\sim 1200^{\circ}\text{C}$ (Figure III.6). In single olivine grains, re-equilibration temperatures seem decreasing from HREE to MREE, which is probably related to the strong REE fractionation recorded in Ol-Ts from the Atlantis Massif (Drouin *et al.*, 2009; Ferrando *et al.*, 2018).

Calculated equilibrium temperatures are equal to or higher than 1000°C , suggesting that the strong REE fractionation in olivine is not related to subsolidus re-equilibration. Yet, we cannot preclude that olivines showing low REE contents might be slightly chemically modified after cooling, having equilibrium temperatures close to 1000°C . Further investigations and comparison between different models are the key to better understand the effect of cooling.

Ca profiles in olivine from U1309D olivine-rich troctolites show core-to-rim variations typical of cooling. The discrepancy between Ca and REE could be related to the difference in diffusion rates. Ca diffusion coefficients are higher than those of REE (Figure I.47 in Chapter I.3.4), thus Ca ions would move faster from the core to the rim compared to REE. This ultimately would lead to 'bell-shape' diffusion profiles observed in olivine. If this hypothesis is true, the closure time (e.g., Chakraborty, 2008) recorded by Ca would be lower (because the process is faster) than that

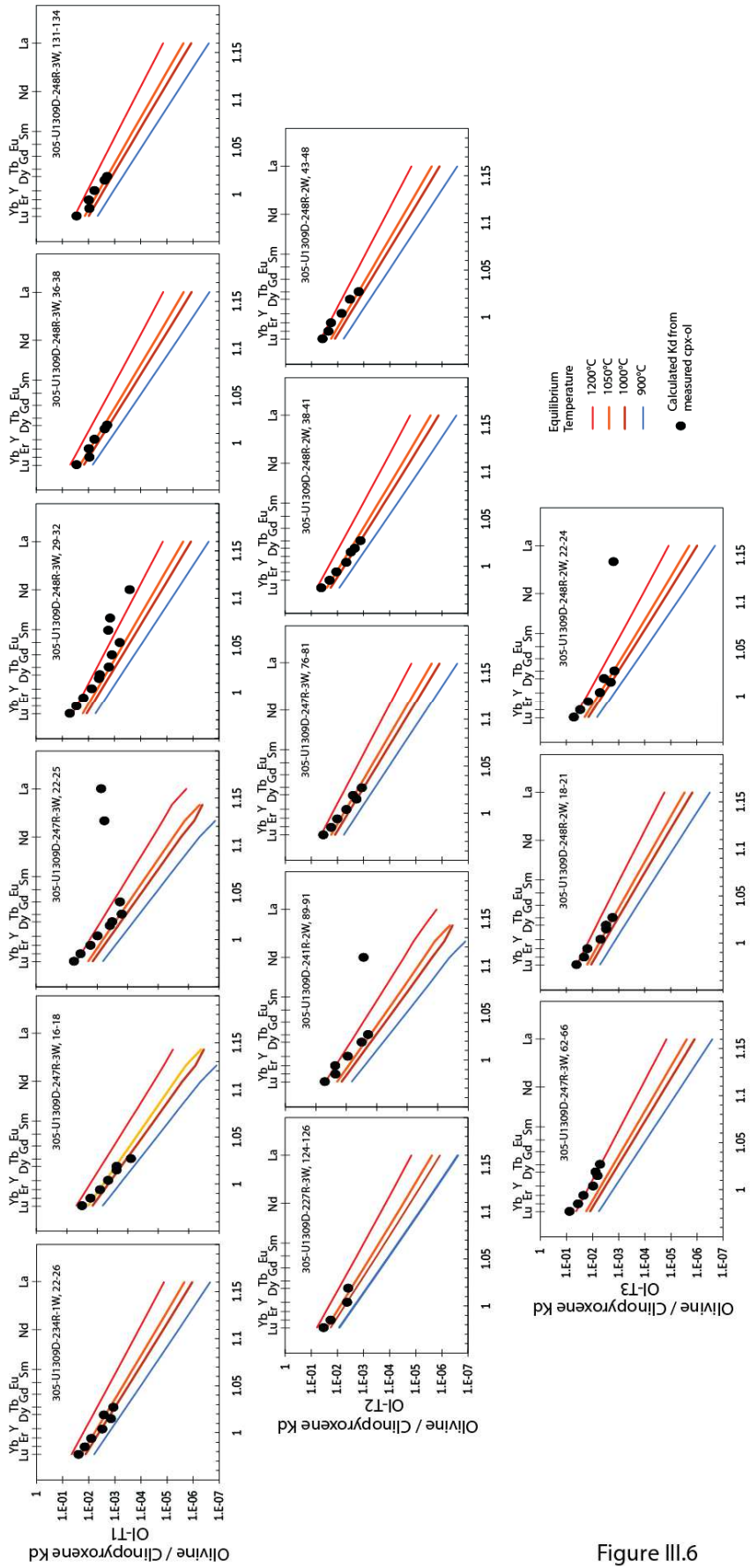


Figure III.6

recorded by REE. Closure time (or time of re-equilibration, t_{eq}) can be calculated by the simple relation $t_{eq} = r^2/\pi D_i$ (r = core-rim distance; D_i = element 'i' diffusion coefficient; Crank, 1975).

Alternatively, Ca-in-olivine geospeedometer (Coogan *et al.*, 2002) provide more precise information on equilibration temperature. It would unravel the cooling history of olivine-rich troctolites from the Atlantis Massif by quantifying the cooling rate and the closure temperature. The use of Ca-in-olivine-geospeedometer, together with a detailed observation of crosscutting relationships between gabbros, olivine-rich troctolites and alteration veins, would help understanding the interplay between magma injection associated with melt-rock interactions, cooling and exhumation. It would shed light on the temporal sequence of these three events from the formation of the lower crustal sequence to exhumation on the seafloor. Cooling time from REE and Ca, together with cooling rates and closure temperatures of the gabbroic sequence at Atlantis Massif, will be estimated and are the subject of my next publication.

Chapter IV

Olivine gabbros from Atlantis Bank

(SouthWest Indian Ridge, 32°S):

insights from IODP Expedition 360

1. Introduction

International Ocean Discovery Program (IODP) Expedition 360 drilled Hole U1473A on the summit of Atlantis Bank, in a two-months period between December 2015 and January 2016. The objective of Expedition 360 was to explore the three dimensional architecture and composition of the lower oceanic crust formed at slow-spreading ridges. This falls within the framework of my thesis, which was determinant for my participation to IODP Expedition 360. My research proposal focused on the study of the most primitive lithologies that, from the outcome of previously drilled Holes at Atlantis Bank (Robinson *et al.*, 1989; Dick *et al.*, 2000), were likely represented by troctolite and olivine gabbro. By studying such rocks I aimed to provide new constraints on the relative contributions of fractional crystallization and reactive porous melt flow processes upon the formation of the lower oceanic crust.

I was in the shipboard science party during Expedition 360 as member of the structural group. My task was to describe and measure structures related to magmatic fabric and igneous layering. The outcomes of this Expedition are reported in the Proceedings of IODP Expedition 360, in MacLeod *et al.* (2017) available at <http://publications.iodp.org/proceedings/360/360title.html>. This Chapter summarizes the main results of IODP Expedition 360, with particular detail on my contribution off-shore, and describes the first outcome of my on-shore study. I first provide an overview of the geological setting (Section II.2) and briefly explain the rationale and objectives of IODP Expedition 360 (Sections II.3.1 and II.3.2; MacLeod *et al.*, 2017). Finally, I summarize the structural features of recovered rocks that we described off-shore, and I report the results of my geochemical study on-shore. The latter comprises a set of whole rock analyses of olivine gabbros sampled at different depths throughout IODP Hole U1473A. These results will be published in a comprehensive study of *in situ* characterization of rocks from Hole U1473A involving 10 participants of Expedition 360 from different laboratories worldwide, coordinated by L. France.

2. Geological setting

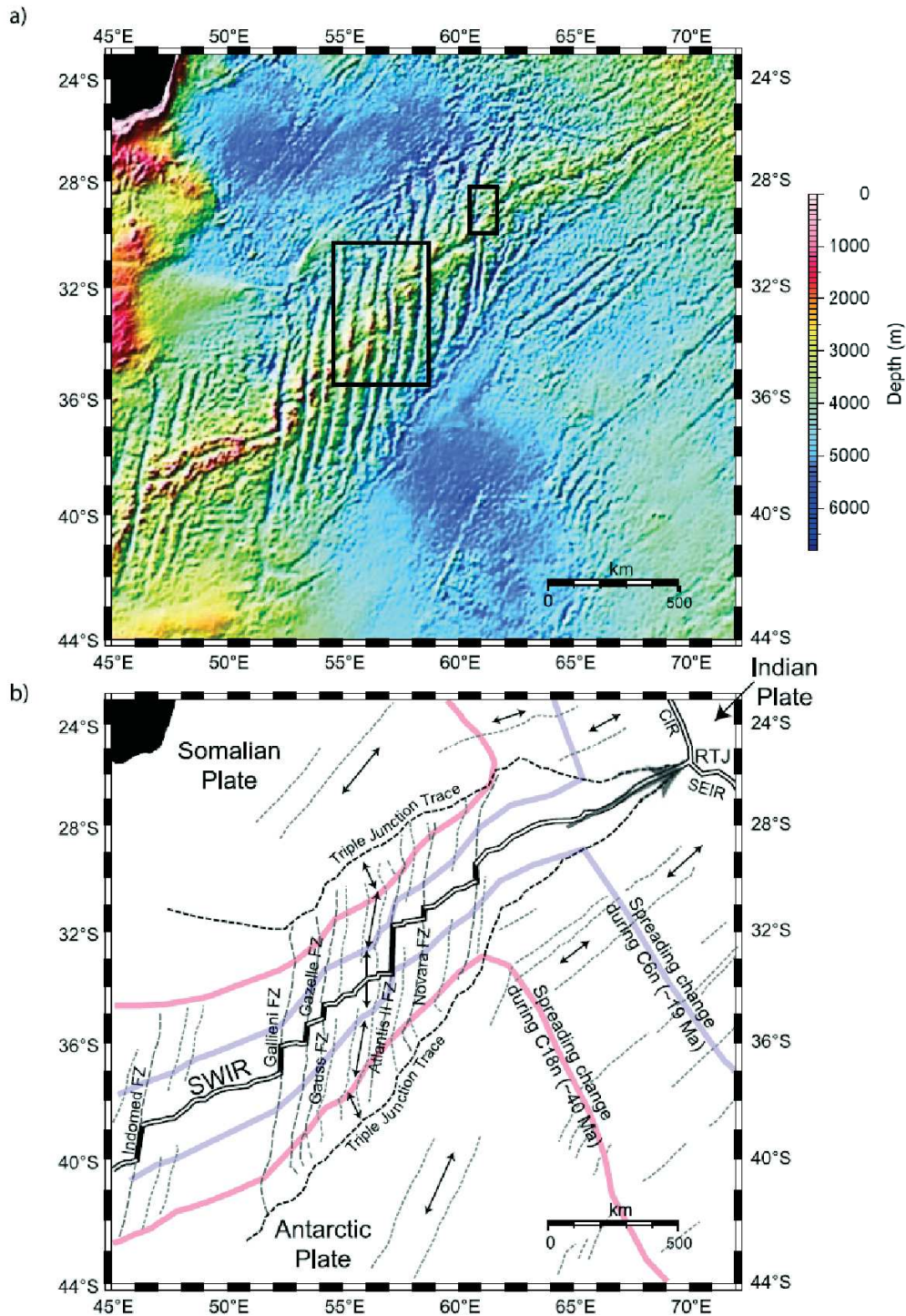


Figure IV.1 – Overview of the SWIR after Baines et al. (2007). a) bathymetry from satellite gravity data, and b) interpretation of the bathymetry showing triple junction traces (black dashed lines), the current ridge axis (double black line), transform faults (thick black lines), and the trends of fracture zones (gray dashed lines), isochrons of 40 Ma (red line) and 19 Ma (blue line). RTJ = Rodriguez Triple Junction; SEIR = Southeast Indian Ridge; CIR = Central Indian Ridge.

The SWIR extends 7700 km from the Bouvet Triple Junction (BTJ) in the South Atlantic to the Rodrigues Triple Junction (RTJ) in the central Indian Ocean, and marks the boundary between the Nubian and Somalian plates in the north and the Antarctic plate in the south (e.g., Sauter and Cannat, 2010; Figure IV.1). SWIR spreads at a rate of 14 mm/yr (full-spreading rate) varying only slightly along the ridge axis (e.g., Chu and Gordon, 1999; Patriat *et al.*, 1997, 2008). Investigations along the SWIR by high-resolution mapping (e.g., Munsch and Schlich, 1990; Wang and Cochran, 1995; Mendel *et al.*, 1997; Patriat *et al.*, 1997; Cannat *et al.*, 1999; Muller *et al.*, 1999; Sauter *et al.*, 2001, 2002, 2013; Zhao *et al.*, 2013) and sampling (e.g., Le Roex *et al.*, 1983, 1992; Dick *et al.*, 1991a, 2003; Cannat, 1993; Mével *et al.*, 1997; MacLeod *et al.*, 1998; Cannat *et al.*, 2003; Standish *et al.*, 2008; Paquet *et al.*, 2016) have shown an apparent absence of volcanic activity on long axial sections of the ridge where large portions of mantle peridotites are exposed directly to the seafloor. In addition to amagmatic ridge segments, spreading along the SWIR spans a wide range of melt production from nearly zero, where the seismically defined oceanic crust is anomalously thin (Minshull and White, 1996; Muller *et al.*, 1999; Minshull *et al.*, 2006), to increasing magma supply that form some of the thickest ocean crust ever measured away from a mantle hot spot (e.g., Muller *et al.*, 2000; Minshull *et al.*, 2006).

The SWIR strikes approximately southwest–northeast for most of its length (Figure IV.1). Between 52°E and 60°E the SWIR is segmented by a series of closely spaced large-offset transform faults (e.g., Sauter and Cannat, 2010), of which the Atlantis II Transform at 57°E (Figure IV.1) offsets the ridge by 200 km (Engel and Fisher, 1975; Dick *et al.*, 1991b). The ridge segment on the west side of this transform fault spreads to the north at 8.5 mm/yr and to the south at 5.5 mm/yr, which is in contrast with faster spreading to the south of the eastern SWIR segment (AN-1) from the Atlantis II Transform (Dick *et al.*, 1991b; Mendel *et al.*, 1997; Hosford *et al.*, 2003; Baines *et al.*, 2007). This asymmetric spreading lengthened the transform fault of 3 mm/yr for at least the past 20 Myr (Baines *et al.*, 2007), and accounted for the uplift of a series of blocks. These blocks extend parallel to the Atlantis II Transform fault and along a line south of, and perpendicular to, spreading segment AN-1 (Figure IV.2). The shallower and northernmost portion of these 5 km high blocks is the Atlantis Bank (Dick *et al.*, 1991b).

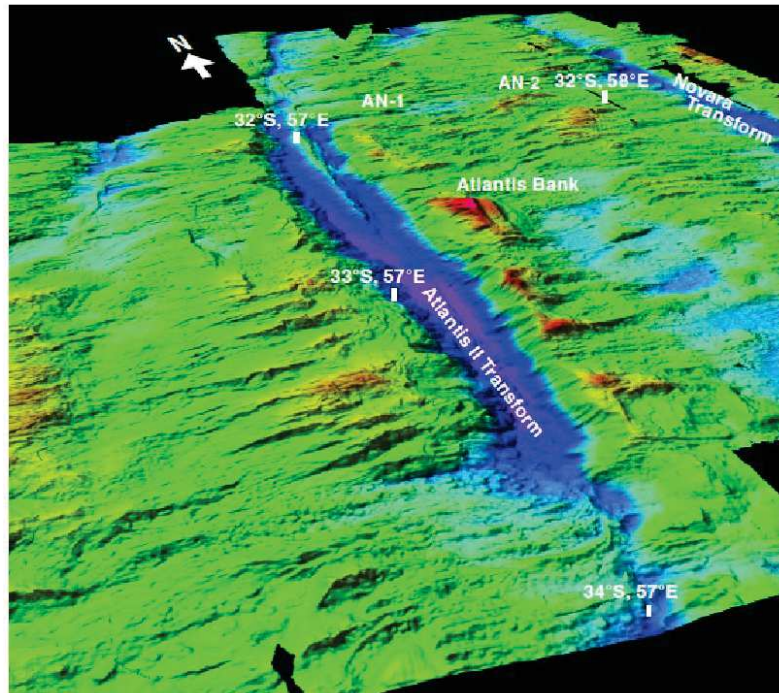


Figure IV.2 - 3-D perspective view of the Atlantis II Transform, looking north-northeast, and location of the elevated transverse ridge where Atlantis Bank is located (MacLeod *et al.*, 2017).

2.1 The Atlantis Bank

The Atlantis Bank is located at $32^{\circ}43'S$, $57^{\circ}17'E$, 95 km south of the SWIR axis and 18 km east of the transform fault (Figure IV.2). The dome of Atlantis Bank is ~ 40 km long by ~ 30 km wide (Figure IV.3), rising from 5700 mbsl at the base of the transform wall to 700 mbsl (Dick *et al.*, 1991b; Baines *et al.*, 2003; Hosford *et al.*, 2003; Figure IV.2-3a). The summit region is a ~ 25 km² broadly flat pavement ranging from ~ 750 to 689 mbsf (Dick *et al.*, 1999).

From 1991 to 2002 Atlantis Bank was explored by several site surveys including high-resolution bathymetric mapping, multibeam, magnetic, and gravity surveys and rock sampling using seabed rock coring, remotely operated vehicle (ROV), submersible dives, and dredging (Dick *et al.*, 1991b, 1999; MacLeod *et al.*, 1998; Arai *et al.*, 2000; Kinoshita *et al.*, 1999, 2001; Matsumoto *et al.*, 2002). The central flat surface of Atlantis Bank exposes bare rock locally constituted of igneous rocks (mostly gabbro) surrounded by beach gravel and limestone pavement (MacLeod *et al.*, 1998; Kinoshita *et al.*, 2001; Matsumoto *et al.*, 2002). Shallow drilling on this central region during RRS James Clark Ross Cruise JR31 (MacLeod *et al.*, 1998) and sample dredging (Dick *et al.*, 1991a) reveal

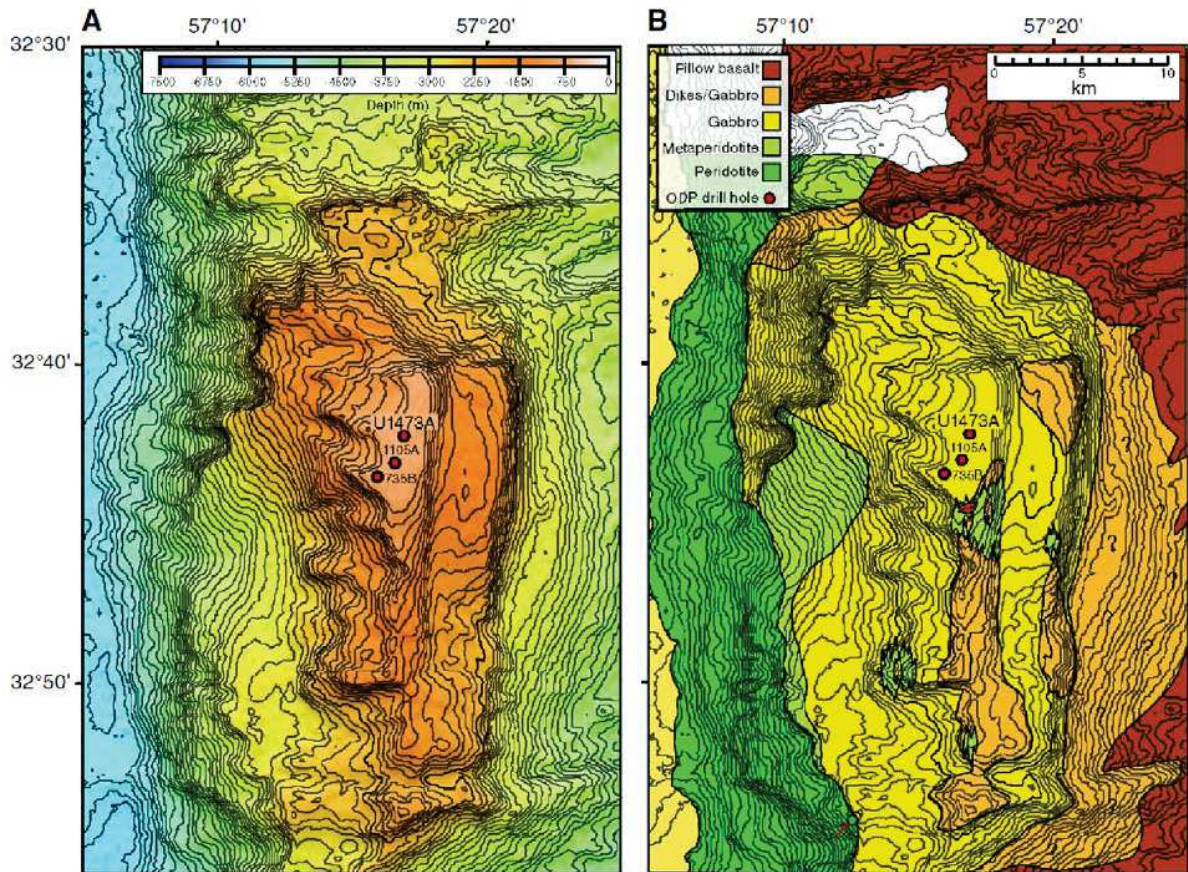


Figure IV.3 – a) Bathymetry of Atlantis Bank area, with ODP/IODP drill sites marked. b) Summary of mapping of the same area (MacLeod *et al.*, 2017).

that the dome comprises an unusual abundance of gabbro relative to peridotites for SWIR traverse ridges, while serpentinized peridotite and minor pillow basalts were collected at the southern tip of the bank (Figure IV.3b).

Deeper investigations were conducted by scientific drilling during three ODP Legs from 1987 to 1999. The deepest hole, ODP Hole 735B, with the best recovery ever in hard rock drilling, was started during ODP Leg 118 and deepened in ODP Leg 176 to a total of 1508 mbsf with 87% core recovery (Robinson *et al.*, 1989; Dick *et al.*, 2000). Hole 735B is located at the southwest corner of the relatively flat surface of the Atlantis Bank platform (32°43.395'S, 57°15.959'E, 731 m water depth). Olivine-bearing gabbro to troctolite are the main lithologies recovered, making up about 78% of the section, while the other 22% of Hole 735B are minor microgabbros, and ferrogabbros consisting of oxide-bearing gabbros and gabbronorites (Dick *et al.*, 2000). Subsequently, the 158 m

Olivine gabbros from Atlantis Bank

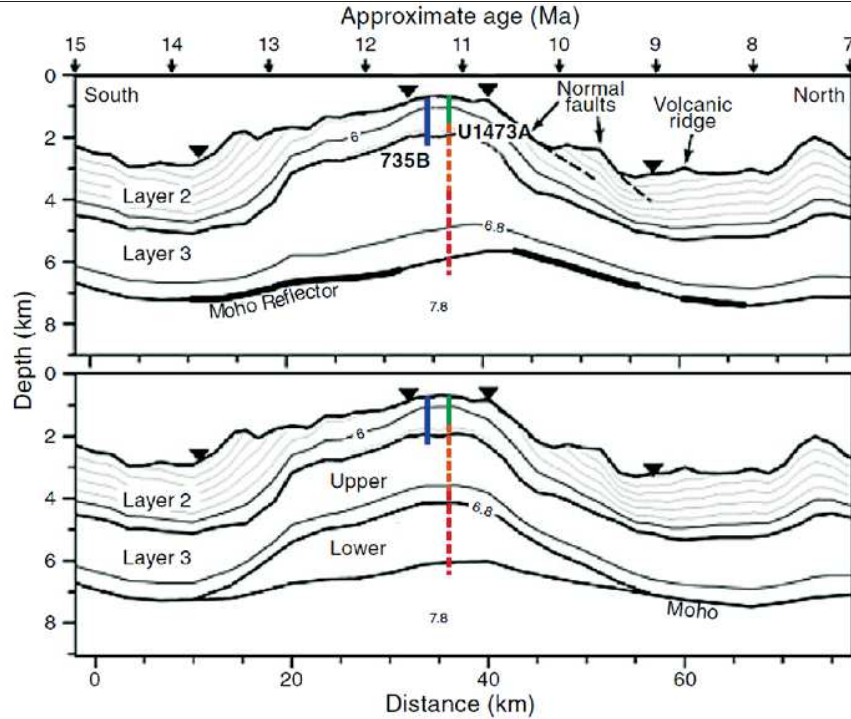


Figure IV.4 – North–south seismic velocity models over Atlantis Bank (MacLeod *et al.*, 2017; after Muller *et al.*, 2000), together with principal drill sites. Green line = depth of Hole U1473A drilled during Expedition 360; orange line = projected penetration during the remainder of SloMo Phase I, red line = projected penetration during SloMo Phase II (riser drilling); triangles = ocean-bottom hydrophones.

deep ODP Hole 1105A was drilled in 1998 during engineering ODP Leg 179 in the center of the platform (32°43.13'S, 57°16.65'E; Pettigrew *et al.*, 1999), also in gabbro and with similar overall core recovery. Video survey (Dick *et al.*, 1991b) and drilling of shallow cores (MacLeod *et al.*, 1998) showed that the exposed rocks frequently appeared foliated, which indicated intense crystal-plastic deformation. Where this foliation was clearly observed its orientation was east-west, parallel to the ridge axis and orthogonal to the adjacent Atlantis II Transform fault (Dick *et al.*, 1991a). Strong crystal-plastic deformation was also found in oxide gabbro and olivine gabbro of the uppermost 500 m of Hole 735B, but diminished markedly down-section (e.g., Robinson and Von Herzen, 1989; Cannat *et al.*, 1991; Dick *et al.*, 1991a, 2000). These deformation signatures were interpreted as representing a detachment fault zone that is preserved over large regions in the deeper waters on both sides of the platform (Kinoshita *et al.*, 1999a; Matsumoto *et al.*, 2002). Based on site surveys and deep drilling, the domal structure of Atlantis Bank was interpreted as an OCC that was unroofed by a low-angle long-lived detachment faulting, which exposed the lower

portion of the 11-12 Myr old oceanic crust directly on the seafloor (Dick *et al.*, 1991a, 2000; MacLeod *et al.*, 2000; Baines *et al.*, 2008; Rioux *et al.*, 2016). The downhole progressively younger ages suggest that newly formed crust moved to shallower depths and away from the axial region, while new enhanced magmatism intruded to the lower oceanic crust (Baines *et al.*, 2008; Rioux *et al.*, 2016). The development of faulting was triggered by an increase of full-spreading rate up to 17 km/Myr, over which Atlantis Bank lower oceanic crust was built for a period of ~2.3 Myr (Baines *et al.*, 2008; Rioux *et al.*, 2016).

A wide-angle seismic refraction survey in the vicinity of Hole 735B reveals a crustal structure that is highly heterogeneous (Muller *et al.*, 2000). The crust consists of a 2-2.5 km thick high-velocity-gradient oceanic layer 2 and a 1-2 km thick low-velocity-gradient layer 3 (Minshull *et al.*, 1998; Muller *et al.*, 2000; Figure IV.4). The olivine gabbros recovered by deep drilling evidence two principal and many secondary intrusive events forming the lower oceanic crust at the Atlantis Bank, in absence of a steady-state magma chamber (Dick *et al.*, 2000). Based on shipboard whole rock compositions of Hole 735B, five chemical trends can be distinguished, each characterized by an upward trend of decreasing Mg#, with a sharp increase in Mg# at the beginning of each overlying unit (Dick *et al.*, 2000). The two chemical units in the upper 600 m of the borehole have more primitive compositions in comparison with the lower three chemical trends (Dick *et al.*, 2000; Figure IV.5). The occurrence of ferrograbbros at different depths in the borehole was attributed to reaction and crystallization of migrating late silicic melts by permeable flow (Dick *et al.*, 2000). These melts are thought to be compacted out of the crystallizing gabbro and redistributed throughout the lower oceanic crust at the Atlantis Bank (Dick *et al.*, 2000).

The strong crystal-plastic deformation in Hole 735B suggests that such melt transport was driven by deformation at the early initiation stages of the detachment fault and during its development in a still partially molten body. Deformation-controlled melt transport also occurred during the later stages of faulting in cooler and brittle oceanic crust where felsic veins and their oxide-rich reaction zones formed (Dick *et al.*, 2000).

A striking feature of the lower oceanic crust recovered at the Atlantis Bank is the absence of primitive cumulates such as dunites or wherlites. They could be present out of the section or beneath the hole at the contact with the underlying mantle, but this would only be revealed by a lateral and deeper Hole (Dick *et al.*, 2000; MacLeod *et al.*, 2017). The seismically defined Moho

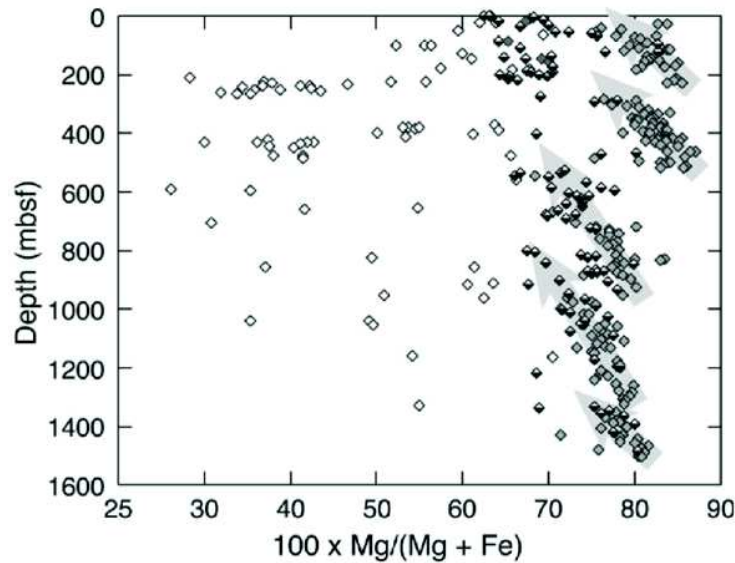


Figure IV.5 –Leg 176, shipboard XRF whole rock gabbro from ODP Hole 735B (Dick *et al.*, 2000). Filled, half-filled to open symbols represent recovered gabbros respectively from the most primitive ($TiO_2 < 0.4 \text{ wt}\%$), medium ($TiO_2 0.4-1.0 \text{ wt}\%$), and most evolved ($TiO_2 > 1.0 \text{ wt}\%$).

discontinuity was found at $\sim 5 \text{ km}$ beneath Atlantis Bank (Muller *et al.*, 2000; Figure IV.4). However, the overlap in P-wave seismic velocity between gabbro and $\sim 20\%$ – 40% partially serpentinized peridotite (e.g., Miller and Christensen, 1997) make it difficult to define the nature of the discontinuity, whether it represent the boundary between igneous crust and underlying mantle or a serpentinization front (e.g., Minshull *et al.*, 1998).

3. IODP Expedition 360

The principal aim of Expedition 360 was to establish a legacy hole (now Hole U1473A), suitable for deep penetration, at the Atlantis Bank and then to drill as deep as possible into the lower crustal gabbro layer. The ultimate goal was to leave a hole open and ready to be deepened during subsequent expeditions. Although the target depth of $\sim 1300 \text{ m}$ was not achieved, and although five roller cones were lost in the hole, Expedition 360 successfully obtained 59% recovery over the entire interval (63% of the cored interval; MacLeod *et al.*, 2017) as illustrated by the 2.85 m long piece of rock recovered on core 66R at 603 mbsf (Figure IV.6). We achieved the deepest igneous rock penetration from the seafloor on a single R/V JOIDES Resolution expedition to date (789.7

mbsf) and recovered 469.4 m of crustal magmatic rocks. The 89 cores from Hole U1473A comprise gabbros, diabase dikes and felsic veins (MacLeod *et al.*, 2017). Leg 1 of SloMo project achieved its principal goal by leaving the hole in good condition overall, and, after minor remediation operations carried out during IODP Expedition 362T (July 2016), it can be reoccupied for further drilling to reach deeper the Moho discontinuity.



Figure IV.6 - Longest piece (2.85 m) of rock recovered in core 66R at 603 mbsf during Expedition 360 at the Atlantis Bank (MacLeod *et al.*, 2017b).

3.1 The rationale behind IODP Expedition 360

IODP Expedition 360 was the first stage (Leg 1) of Phase I of the multi-leg drilling project "Nature of the Lower Crust and Moho at Slower Spreading Ridges" (SloMo), which falls under the scope of the IODP Science Plan 2013-2023. The SloMo project addresses questions on the composition, diversity, and architecture of the lower ocean crust and mantle, with the scope of understanding the deep and shallow processes involved in the formation of the oceanic crust at slow-spreading ridges (MacLeod *et al.*, 2017). The Moho has generally been regarded as the seismically boundary between crust and mantle, typically identified at ~6 to 7 km beneath the oceans. However, the discovery of abundant partially serpentized peridotite on the seafloor and on the walls of fracture zones (e.g., Cannat, 1993; Cannat *et al.*, 1995,2006; Blackman *et al.*, 2002; MacLeod *et al.*, 2002; Escartín *et al.*, 2003; Früh-green *et al.*, 2016) supported early models whereby Moho was considered a hydration front in the mantle (Hess, 1962). One of the scopes of SloMo is to resolve

the controversy as to whether the Moho at slow spreading ridges can be a serpentinization front (MacLeod *et al.*, 2017). To accomplish these challenges SloMo principally aims to drill as deeply as possible into the oceanic in order to encounter the mantle-crust boundary. Phase I of SloMo plans to drill 3 km through lower crustal gabbros, and to penetrate the inferred crust-mantle boundary. The subsequent Phase II proposes using the Japanese riser drill ship Chikyu to drill to 6 km through the Moho itself and into the mantle (Figure IV.7).

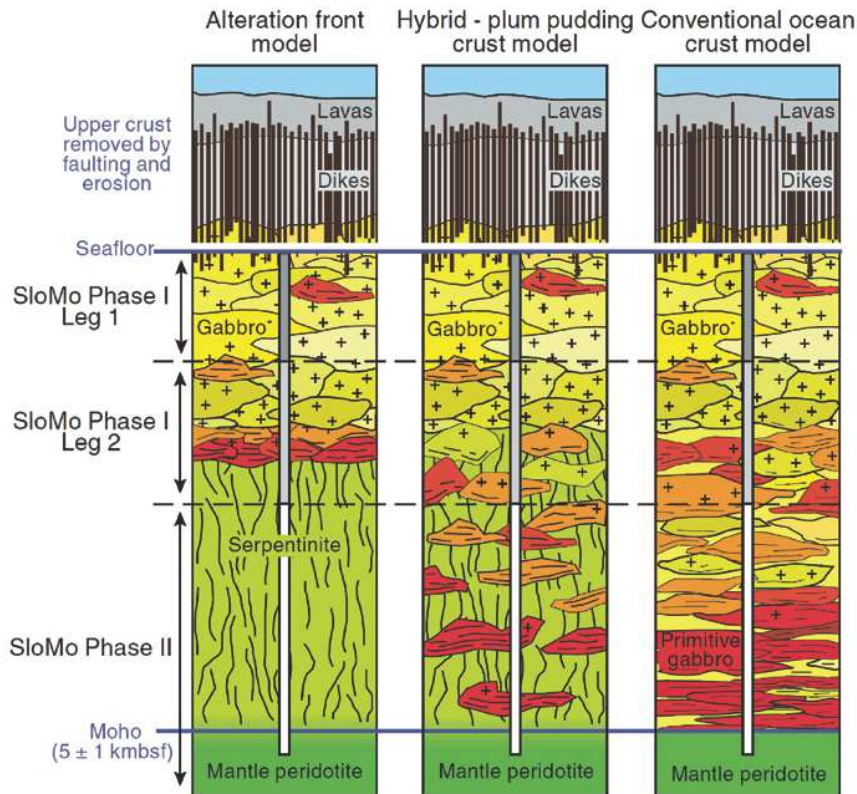


Figure IV.7 - Alternative models for the lower crust and mantle as modified from Dick *et al.* (2006), showing the depth of the seismic Moho discontinuity detected at Atlantis Bank (Muller *et al.*, 2000). From to left to the right: 'alteration front model' proposed by Muller *et al.* (1997) and 'hybrid-plum pudding crust model' from Cannat (1996) better reflect structure of the oceanic crust at slow-spreading ridges, while 'conventional ocean crust model' is the Penrose model generally accepted for fast-spreading ocean crust. On the very left are reported the expected drilling depths for each Phase of SloMo project (MacLeod *et al.*, 2017).

Formation of seafloor along slow and ultraslow mid-ocean-ridges, such as the SouthWest Indian Ridge (SWIR), is accommodated by faulting and ductile deformation (e.g., Cannat, 1993; Cannat, *et al.*, 1995; Dick *et al.*, 2000; Ildefonse *et al.*, 2014 and references therein; and see Chapter I.1). At Atlantis Bank (SWIR, 32°S, 57°E) lower portions of the oceanic crust are exhumed by long lived

detachment faulting, thus representing a direct access to lower oceanic gabbros and, possibly, to the crust-mantle boundary. Insights from two existing ODP Holes provide a unique opportunity to examine lower crustal stratigraphy in three dimensions and the petro-geochemical heterogeneity of the gabbroic body at Atlantis Bank (MacLeod *et al.*, 2017). For these reasons, in 2012, H. Dick and 32 co-proponents submitted the drilling Proposal 800-Full (available at http://iodp.tamu.edu/scienceops/expeditions/indian_ridge_moho.html) to IODP, where they presented the principal objective of the SloMo Project. Deep drilling at the ultraslow spreading SWIR was able to recover a portion of lower crust that directly reflect the interplay between magmatic and tectonic processes, and where mantle flow, melt inputs and melt migration can be investigated (MacLeod *et al.*, 2017).

Leg 1 of SloMo project achieved its principal goal by leaving the hole in good condition overall, and, after minor remediation operations carried out during IODP Expedition 362T (July 2016), it can be reoccupied for further drilling to reach deeper the Moho discontinuity.

3.2 Scientific objectives

The availability of downhole data from other two locations at the Atlantis Bank was a unique opportunity to examine for the first time the lateral continuity of igneous, metamorphic and structural stratigraphy on a ~kilometer scale, and hence to study the three dimensional characteristic of lower oceanic crust formed at an ultraslow spreading centre. By comparing the results from Hole U1473A with those from prior ODP drilling on Atlantis Bank (Holes 735B and 1105A), we could assess the spatial and temporal scales of magmatic accretion of the plutonic lower crust, the accretion processes, and the mechanisms by which the lower crust is exhumed.

The first objective of Expedition 360 was to determine the extent to which the igneous, metamorphic, and structural stratigraphy found in Holes 735B and 1105A is laterally continuous across the wave-cut platform on Atlantis Bank. The second objective was based on the findings of mantle screens incorporated within the gabbro section at Atlantis Massif on the Mid Atlantic Ridge (Blackman *et al.*, 2006, 2011, Drouin *et al.*, 2009, 2010; Ferrando *et al.*, 2018), as documented and discussed in Chapter III of this work. Comparable mantle relicts were not found in other ODP Holes at the Atlantis Bank, thus raising the question of whether this is simply related to undersampling of

the most primitive end-members or it reflects a profound difference between the two different mid-ocean ridges.

The third and fourth objectives of Expedition 360 were to investigate the modes of melt delivery, transport and reaction with the lower oceanic crust. These modes include small intrusive cumulate bodies, larger intrusive units on the scale of hundreds of meters, anastomosing channels produced by focused flow and melt-rock reaction, and compaction of late iron titanium-rich melts into shear zones where they hybridized olivine gabbro to iron titanium oxide-rich gabbro and gabbronorite (Dick *et al.*, 2000). The three dimensional continuity of these features can further document the extent and proportion of such reactive processes and provide new constraints on their role in modifying MORB melts compositions (e.g., Lissenberg *et al.*, 2013; Lissenberg and Dick, 2008; Lissenberg and MacLeod, 2017).

The fifth objective was to study the lateral distribution of deformation features by comparison of previous drilling results with IODP Hole U1473A. The three-dimensional study of deformation characteristics can provide important insights on how magmatism and tectonism interact, and hence how lower crustal is accreted in ultraslow spreading environments.

3.3 IODP Hole U1473A

The suitable location for Hole U1473A was found at 32°42.3622'S, 057°16.6880'E in 710 m water depth, 2.2 km north-northeast of Hole 735B and 1.4 km north of Hole 1105A (Figure IV.3). IODP Hole U1473A was drilled to a total depth of 789.7 mbsf, recovering 469.4 m of core with over 96% recovery within the lower 200 m of the hole. A target depth of 1300 mbsf was originally estimated, derived from prior experience of drilling conditions at Atlantis Bank and assuming a nominal 4 days contingency time for weather and operational issues. However, this depth was not achieved largely because the number of days available on site for coring was substantially less than planned due in particular to a medical evacuation (Figure IV.10). IODP Hole U1473A cores are composed of a variety of gabbroic lithologies, from primitive olivine gabbros to evolved oxide-rich gabbros cut by felsic veins (~1.5% of the total) and rare diabase dikes (Figure IV.11). This crustal section has undergone static hydrothermal alteration, extensive recrystallization associated with crystal-plastic

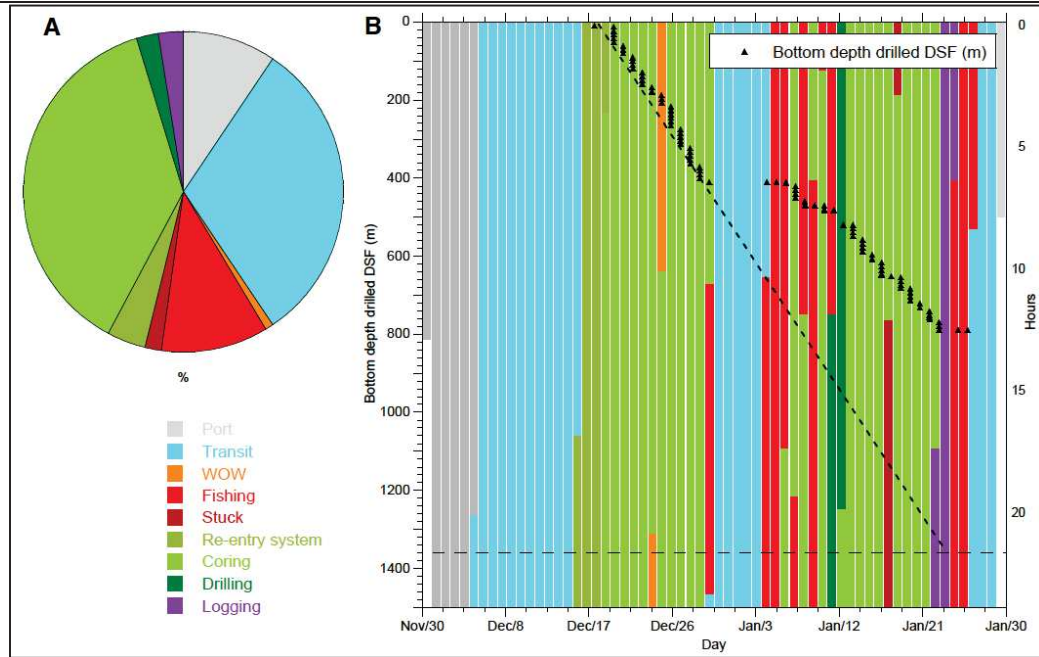


Figure IV.10 - Expedition 360 operational time distribution (MacLeod *et al.*, 2017). a) Proportional time by major operational categories. b) Operational categories in a) are shown on a timeline, with each vertical bar representing one day. Advancement in Hole U1473A is shown with black triangles, which represent the bottom of drilled or cored intervals.

deformation, and alteration associated with veining and late cataclastic deformation (Figure IV.11). Static alteration occurs throughout the hole, ranging from <3% to 90%, with locally intense veining and characterized by colorless amphibole, talc, serpentine, and clay minerals after olivine; however, away from fault zones, much of the section is very fresh (78% with <30% replacement minerals). The proportion and overall intensity of crystal-plastic deformation in the core decreases downhole; however, ultramylonites are present throughout the core (Figure IV.11). Crystal-plastic fabrics are always defined by elongated and recrystallized plagioclase together with recrystallized olivine (if present). In samples with higher deformation intensities also pyroxene is deformed and elongated.

In the following I summarize the primary igneous characteristics of cores recovered at IODP Hole U1473A, from their structural to petrologic features, described in MacLeod *et al.* (2017).

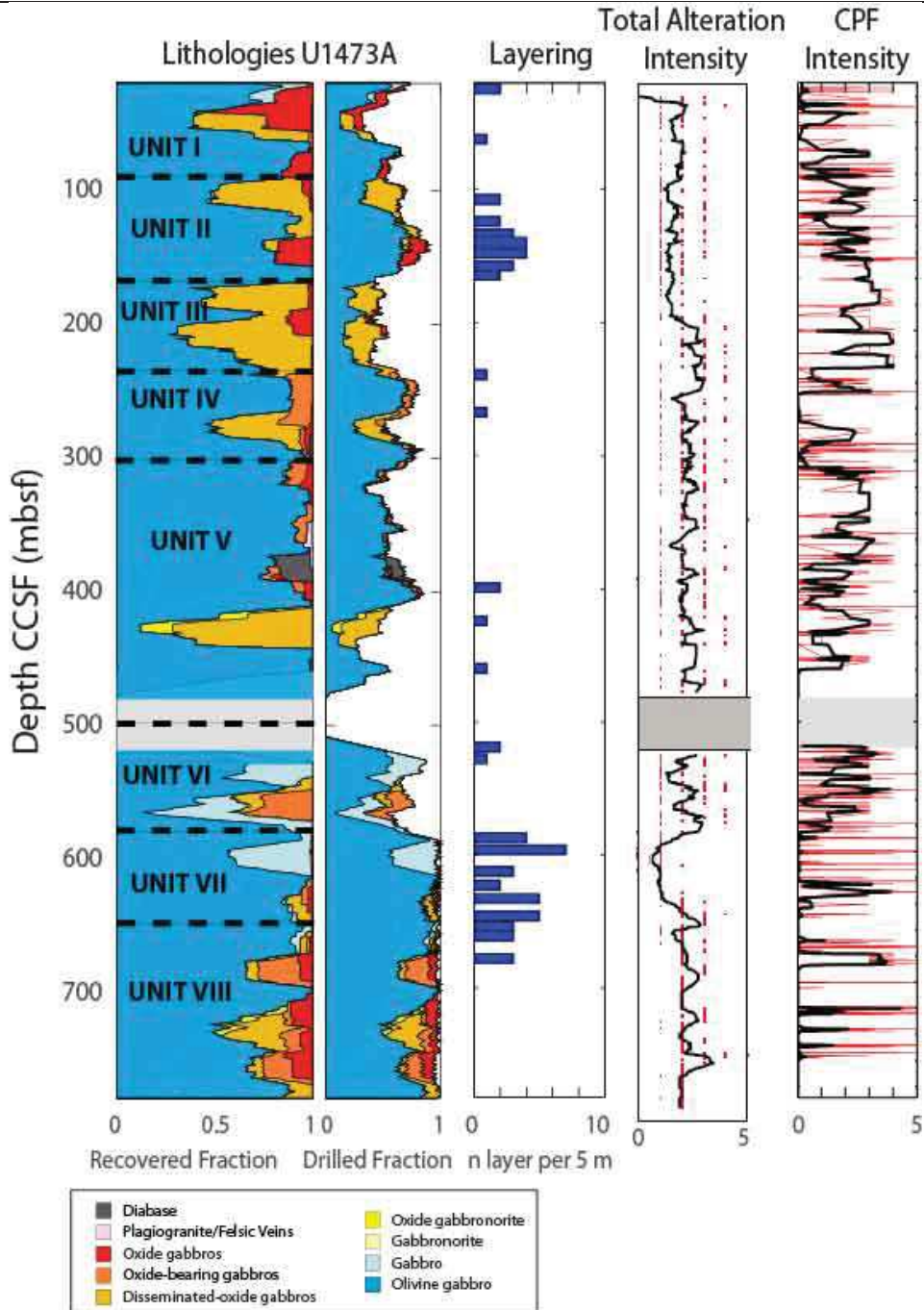


Figure IV.11 – IODP Hole U1473A downhole variations and distribution of, from the left to right, lithologies, igneous layering, static alteration intensity and crystal-plastic fabric (CPF) intensity (MacLeod et al., 2017).

Relative abundances of rocks are averaged over 20 m, reported as recovered fraction and total drilled fraction. Igneous layering is identified as number of layers every 5 m. Running averages over 10 m are reported for intensities of static alteration and crystal-plastic deformation. Alteration intensity: 0 = <3%, 1 = 3%–9%, 2 = 10%–29%, 3 = 30%–59%, 4 = 60%–90%, 5 = >90%. CPF intensity: 0 = undeformed, 1 = foliated, 2 = porphyroclastic, 3 = protomylonitic, 4 = mylonitic, 5 = ultramylonitic.

3.3.1 Igneous petrology

Eight main lithologic units were identified based on changes in mineral modes, grain size, texture, and the occurrence of other igneous features such as layering and the presence of felsic material (Figure IV.11). The main lithology is dominated by olivine gabbro (<1% oxide; 76.5%), followed in abundance by disseminated-oxide gabbro (containing 1%–2% oxide; 9.5% abundance), gabbro (*sensu stricto*; <1% oxide; 5.1%), oxide gabbro (>5% oxide; 3.7%), oxide-bearing gabbro (2%–5% oxide; 3.7%), and felsic veins (1.5%). Units I, IV and VI consist mostly of coarse grained subophitic olivine gabbros, while local enrichments in oxide distinguish Units III and VIII. Units II and VII are characterized by interlayered series of coarse-grained subophitic gabbros and medium-grained subophitic gabbros.

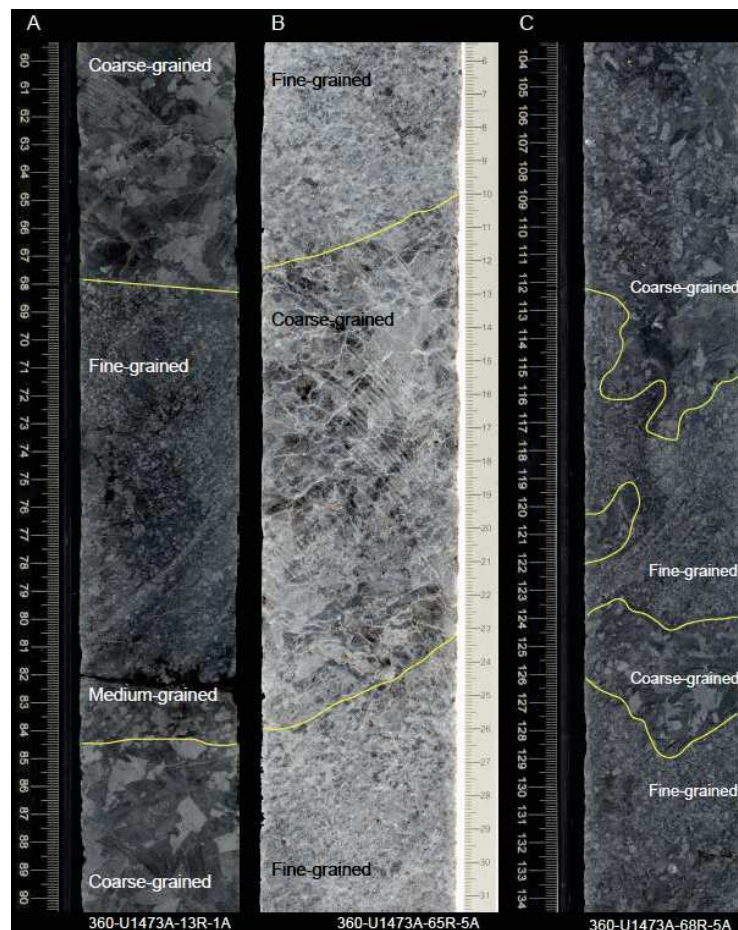


Figure IV.12- Grain size variations in olivine gabbro from IODP Hole U1473A. a) Grain size igneous layering showing planar and sharp contact between coarse and fine grained olivine gabbro. Sample 360-U1473A-13R-1A. b) Parallel, sharp and relatively planar grain size layering in sample 360-U1473A-65R-5A. c) Irregular to patchy igneous layering with fine- to coarse-grain variations in sample 360-U1473A-68R-5A.

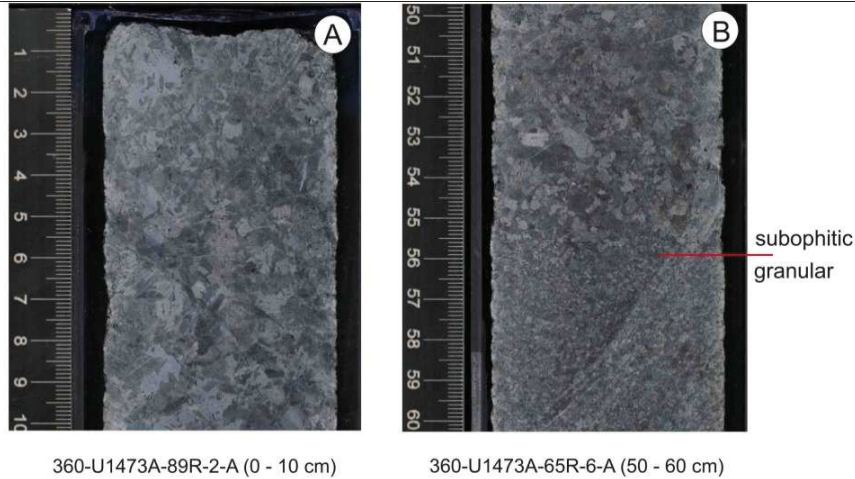


Figure IV.13 – Examples of gabbros from Hole U1473A (MacLeod et al., 2017): a) subophitic texture in coarse-grained olivine gabbro; b) contact between subophitic and granular texture in olivine gabbro.

Olivine gabbros are on average coarse-grained, but are locally medium- to fine-grained in layers or patchy domains (defining the igneous layering, Figure IV.12). The texture of coarse-grained rocks is generally subophitic, except gabbros in Unit III that show granular textures (Figure IV.13). Medium-grained rocks are mostly characterized by a granular texture in hand specimen, although they often show local subophitic textures under the microscope. Olivine crystals are generally subhedral, equant to subequant, and occur either as an early cumulus phase locally occluded in plagioclase or as an interstitial to poikilitic phase (mostly in olivine gabbros from Unit VIII). Clinopyroxene is commonly subhedral to anhedral, with subequant to poikilitic habit, and generally encloses tabular plagioclase (totally or partially) and rarely olivine (Figure IV.14b). Plagioclase occurs as euhedral to subhedral tabular minerals partly or totally embayed by large clinopyroxenes (Figure IV.14). In the latter textural occurrence plagioclase sometimes show lobate contacts against poikilitic clinopyroxene (Figure IV.14b-c).



Figure IV.14 – Characteristic textures of gabbros from Hole U1473A: a) euhedral randomly oriented elongated and tabular plagioclase (Pl) showing igneous and tapered twins (3R-2, 89–98 cm; XPL). Clinopyroxene (Cpx) is subophitic and undeformed; b) weakly developed preferred dimensional orientation of tabular elongated Pl showing igneous twinning with undeformed Cpx oikocryst including Pl chadacrysts (80R-5, 68–71 cm; XPL). c) preserved and slightly bent igneous twins and tapered twins in Pl (9R-2, 141–145 cm; XPL); d) deformed olivine (Ol) grain displaying straight subgrain boundaries (3R-4, 40–42 cm; XPL)

3.3.2 Downhole magmatic fabric and igneous layering

Magmatic fabric

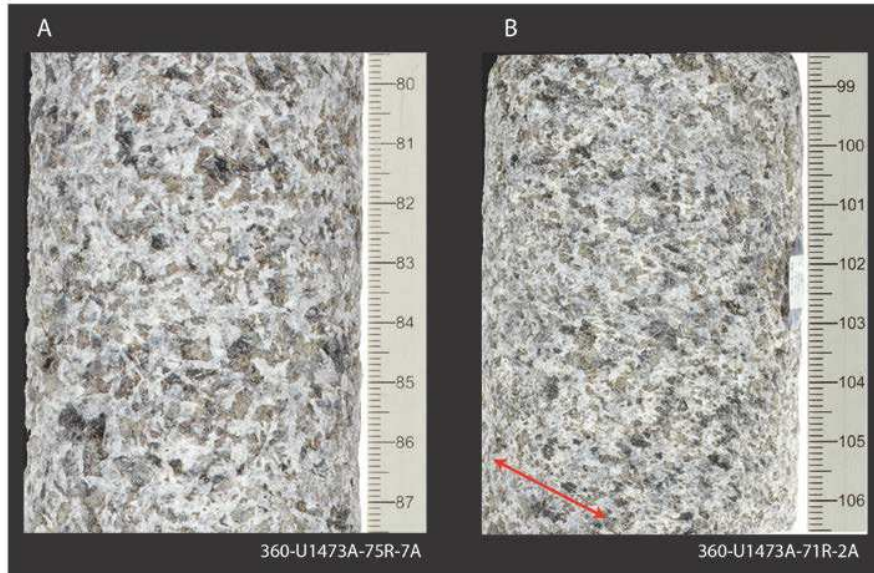


Figure IV.15 – Examples of mineral orientations in gabbros from Hole U1473A: a) random orientation of minerals indicate an isotropic fabric (75R-7); b) elongated laths of euhedral to subhedral tabular plagioclase showing shape-preferred orientation in a medium grained gabbro are evidence of magmatic fabric (71R-2). Red arrow indicate the orientation.

Identifiable magmatic textures are preserved in 42% of Hole U1473A gabbros, including olivine gabbro, disseminated oxide to oxide gabbro and minor gabbro. They have relatively well-preserved magmatic textures that appear undeformed in the core, or show local evidence for crystal-plastic deformation. The majority of the gabbros display random orientation of subhedral (e.g., plagioclase) to anhedral (e.g., poikilitic clinopyroxene) primary igneous minerals (Figure IV.14a and Figure IV.15a) that range from fine- to coarse-grained subophitic and granular textures. Weakly to moderately-developed magmatic fabrics, defined by elongated laths of euhedral to subhedral tabular plagioclase and minor pyroxene showing shape-preferred orientation (Figure IV.15b), were observed in discrete intervals of about 80 cm maximum thickness. Throughout the first 400 mbsf of IODP Hole U1473A, magmatic fabrics are present in medium- to coarse-grained intervals. Interlayered fine-grained intervals are overprinted by crystal-plastic deformation and do not retain their presumed original magmatic fabric (Figure IV.16), or have isotropic fabrics. Below 500 mbsf magmatic fabrics are better preserved because of the lesser abundance of crystal-plastic and

brittle deformation (Figure IV.12). No systematic variation of magmatic fabric intensity is observed with depth. Generally, magmatic fabrics are shallow- to moderately dipping, ranging between 10° and 50°. No systematic variation in dip is observed with depth.

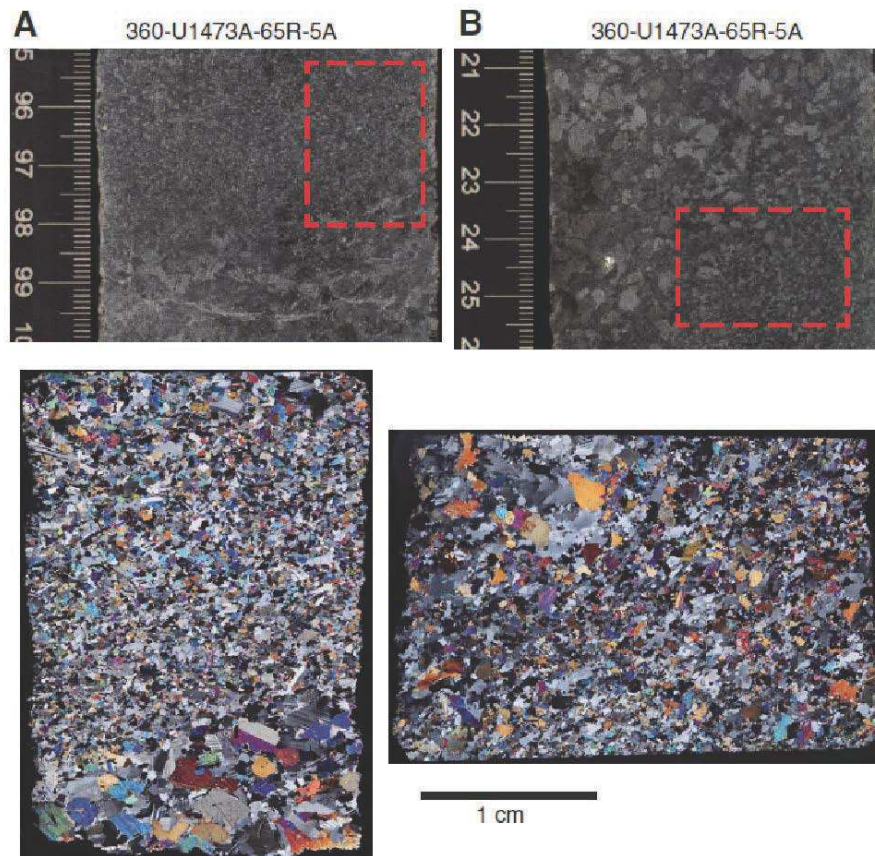


Figure IV.16 A. Examples of magmatic textures vs crystal plastic overprint in gabbros from U1473A (MacLeod et al., 2017): a) undeformed primary grain size variation with euhedral and elongated plagioclase defining a weak magmatic fabric parallel to boundary between fine- and medium-grained olivine gabbro. Contact is planar and relatively sharp (65R-5, 95–99 cm; bottom: XPL); b) fine-grained layer grading to coarse-grained material, overprinted by weak crystal-plastic deformation (65R-5, 22–26 cm; bottom: XPL). Plagioclase in fine-grained olivine gabbro is weakly recrystallized and defines the foliation.

The mineral phases that define magmatic textures in a particular interval were confirmed by thin section observations. Magmatic textures completely free of any crystal plastic overprint represent 10% of samples observed in the thin section suite. Overall, the primary igneous minerals are generally randomly oriented. However, few fine-grained olivine gabbros display weak magmatic fabrics mainly defined by the shape-preferred orientation of tabular elongated plagioclase (Figure IV.16).

Igneous layering

Igneous layering was observed throughout IODP Hole U1473A, characterized by variations in grain size between two (or more) intervals, either patchy or with planar contacts (Figure IV.12). A total of 67 series of igneous layering were identified downhole with particular intervals exhibiting intense igneous layering at 105-165 and 580-680 mbsf (Figure IV.11). These intervals correspond to lithologic Units II and overlap Units VII and VIII (Figure IV.11), respectively. Grain size layering is generally characterized by sharp changes in grain size between fine- and medium-grained or medium- and coarse-grained gabbros (Figure IV.12a-b). About 50% of these layered series show planar and sub-parallel boundaries between layers of 5-10 to 15-20 cm thickness (Figure IV.12a). Other intervals that display grain size variations are often limited to centimeter-scale patches with irregular boundaries (Figure IV.12c). The most irregular contacts are displayed in fine-grained layers that are also variable in orientation from sub-horizontal to sub-vertical in the core reference frame. Although crystal-plastic deformation when present largely overprints primary magmatic structures, some undeformed alternating grain size layers are nevertheless observed, and attest to their magmatic origin. Among these, a few display contacts characterized by sub-parallel magmatic fabrics, while grain size layers are commonly isotropic.

3.3.3 Are there evidences of melt-rock interactions?

The preliminary observations of textural features of olivine gabbros from Hole U1473A suggest that they formed by fractional crystallization from of a primary melt with a relatively primitive composition saturated in olivine. They show a typical order of crystallization with first subhedral to interstitial olivine, followed by the formation of subhedral plagioclase and poikilitic clinopyroxene. The subophitic texture and olivine habit ranging from rounded to interstitial may also suggest the early synchronous crystallization of the three primary phases. However, olivine gabbros locally display plagioclase chadacrysts having irregular shape and resorbed grain boundaries against enclosing clinopyroxene oikocrysts. This feature is commonly documented in olivine gabbros from other gabbroic occurrences in modern oceanic crust (e.g., Blackman et al., 2006; Lissenberg and Dick, 2008, Sanfilippo et al., 2013), and is interpreted as an evidence for assimilation of plagioclase by an invading melt crystallizing clinopyroxene. Furthermore, olivine-rich gabbroic rocks collected in fast- (e.g., Lissenberg et al., 2013; Gillis et al., 2014) and slow- spreading ridges (e.g., Dick et al.,

2000; Blackman *et al.*, 2006; Lissenberg and Dick, 2008; Godard *et al.*, 2009; Drouin *et al.*, 2009, 2010, Ferrando *et al.*, 2018), as well as in ophiolites (e.g., Renna and Tribuzio, 2011; Rampone *et al.*, 2016; Sanfilippo *et al.*, 2014), reveal microstructural and chemical variations demonstrating that the simple fractional crystallization process is not applicable to all cases of crustal accretion.

The irregular and local (cm to dm scale) textural and compositional variations are generally interpreted as the result of intensive melt impregnation through a pre-existing crustal or mantle matrix, in contrast with the systematic layered series commonly described in magmatic intrusions, classically interpreted as cumulates (e.g., Holness, 2005). One of the most striking features of IODP Hole U1473A is the textural variability, characterized by grain size variations at a cm to dm scale that are either organized in parallel layers (igneous layering, Figure IV.12a-b), or randomly arranged in patches ('irregular layering', Figure IV.12c). Similar irregular domains of variable mineral modal composition and grain size have been already described in previously drilled ODP Hole 735B (Dick *et al.*, 1991a, 1999) and ODP Hole 1105A (Pettigrew *et al.*, 1999), and in dredge hauls at Atlantis Bank (e.g., Casey *et al.*, 2007; Dick *et al.*, 2000). By comparison with studies of oceanic crust formed at other locations, the observed textural characteristic may suggest that melt-rock reaction processes occurred during the first phases of crystallization of olivine gabbros in Hole U1473A (MacLeod *et al.*, 2017b). Yet, further structural, microstructural and petro-geochemical studies are needed to test this hypothesis.

4. Whole rock geochemistry of olivine gabbros from IODP Hole U1473A:

Data report

Post-cruise trace elements geochemical analyses were performed at Geosciences Montpellier on representative samples of olivine gabbros from IODP Hole U1473A. For a set of these samples, major element whole rock compositions and contents of 10 trace elements (Ni, Cr, Co, Sc, Sr, V, Y, Zr, Zn and Cu) were determined during IODP Expedition 360. More in detail, shipboard analyses include compositions of 113 fresh olivine gabbros (MacLeod *et al.*, 2017), of which 14 are samples from the same lithological intervals as those I collected for post-cruise geochemical analyses (lithological intervals 4, 24, 43, 99, 125, 175, 203, 204, 205, 228, 243, 248 and 264, see Appendix 3). In the following, I summarize the whole rock compositions from MacLeod *et al.* (2017) and I report

data of whole rock trace elements compositions. Finally, a comparison with bulk rock data of Atlantis Massif is discussed.

4.1 Shipboard geochemical analyses

Shipboard geochemical analyses of representative lithologies (olivine gabbros, gabbros, disseminated-oxide gabbros, oxide gabbros, diabase dikes, and felsic veins) were performed by inductively coupled plasma–atomic emission spectroscopy (ICP-AES).

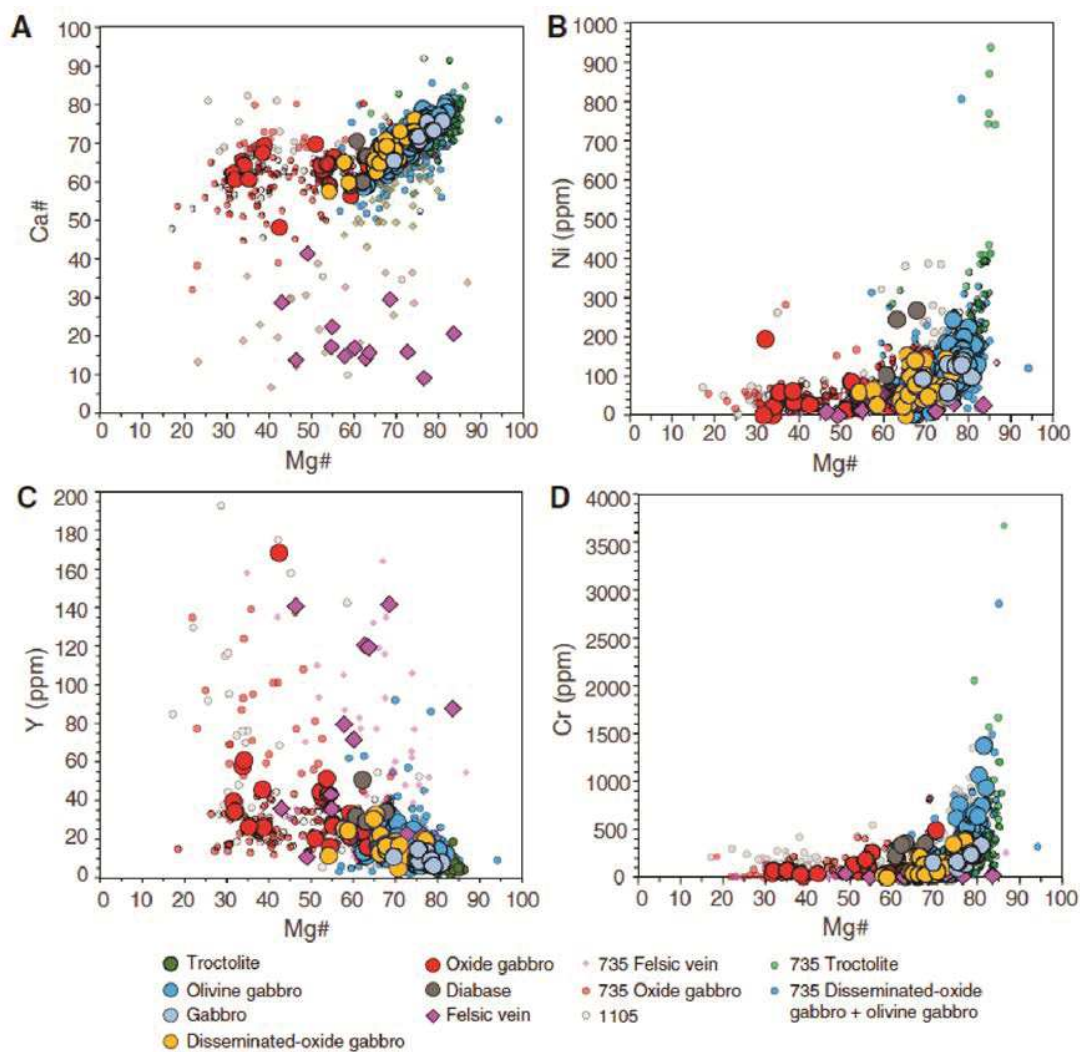


Figure IV.17 – Compositions of rocks recovered in Hole U1473A in terms of Mg# vs a) Ca#, b) Ni (ppm), c) Y (ppm), d) Cr (ppm) (MacLeod et al., 2017). The most primitive rocks, olivine gabbro and minor troctolite, have the highest Mg#, Ca#, and Ni, Cr content and the lowest Y. Chemical data for rocks recovered from Holes 735B and 1105A are shown for comparison.

Olivine gabbros from Atlantis Bank

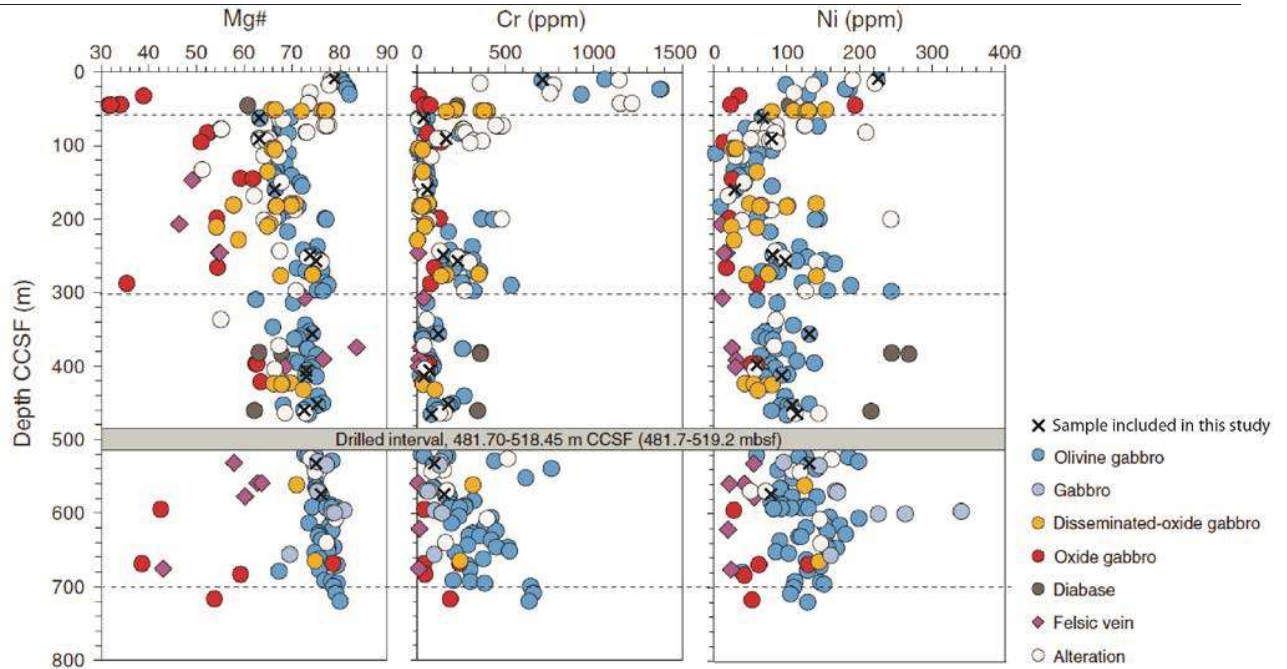


Figure IV.18 – Downhole chemical variations of Mg#, Cr (ppm) and Ni (ppm) in Hole U1473A (MacLeod et al., 2017). Also highlighte (x) are the samples adjacent, in the core, to those of this study (see text for further details).

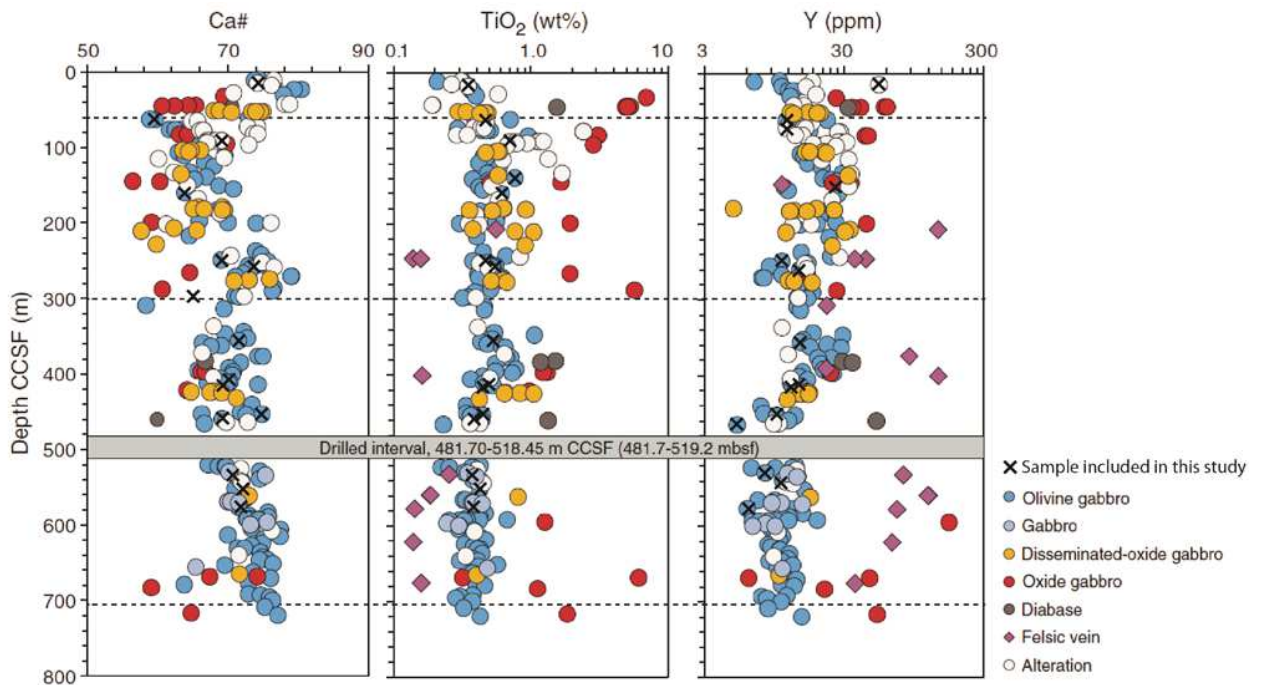


Figure IV.19 - Downhole chemical variations of Ca#, TiO_2 (wt%) and Ni (ppm) in Hole U1473A (MacLeod et al., 2017). Also highlighte (x) are the samples adjacent, in the core, to those of this study (see text for further details).

Olivine gabbros have Mg# ranging from 62 to 82, Ca# between 58 and 81, and contain up to 1380 ppm Cr and 244 ppm Ni, with 0.2–1.1 wt% TiO₂ (average = 0.5 wt%) and 5–29 ppm Y (Figure IV.17; MacLeod *et al.*, 2017). In comparison, disseminated oxide gabbros and oxide gabbros have lower Mg# ranging between 32 and 77, Ca# between 48 and 76; they contain lower Cr (<316 ppm) and Ni (<194 ppm), and higher TiO₂ (average = 0.6-7 wt%) and Y up to 168 ppm (Figure IV.17; MacLeod *et al.*, 2017). Olivine gabbros represent the most primitive lithology recovered from IODP Hole U1473A.

The Mg#, Ca# and contents of Cr, Ni and Y display overall correlated systematic variations (Figures IV.18 and IV.19), while TiO₂ contents are more scattered (Figure IV.19). Three trends of fractional crystallization are identified and discontinuities are placed at 60-90 mbsf, 300 mbsf, and 700 mbsf with maxima in Mg#, Ca#, and Cr and Ni concentrations occurring at the base of each crystallization interval, which indicate that compositions evolve upward. The 200-400 m thick intervals are interpreted as intrusion of individual magma batches, and the most primitive compositions encountered at the base of each cycle represent the first lithology that crystallized

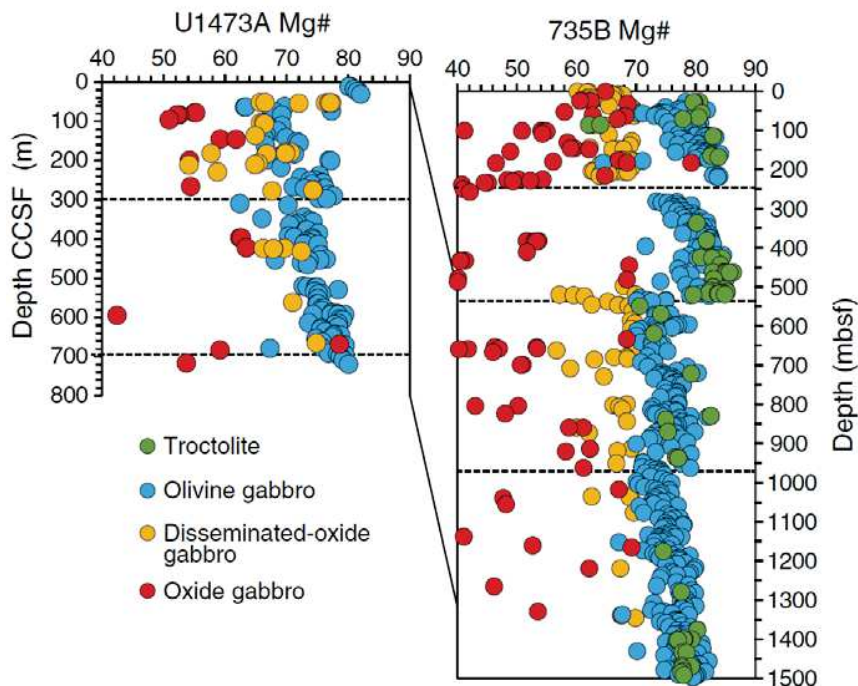


Figure IV.20 – Comparison of downhole variations in Mg# between the gabbros sequences from Holes U1473A and 735B (MacLeod *et al.*, 2017).

(MacLeod *et al.*, 2017). Comparable geochemical cycles were identified in downhole bulk rock chemical compositions of olivine gabbros from ODP Hole 735B previously drilled at Atlantis Bank and was interpreted in a similar way (Dick *et al.*, 2000). A broad correlation may be identified between the unit at the top of Hole U1473A and 450 mbsf in Hole 735B (Figure IV.20), thus might indicating lateral continuity although chemical variations are complex (MacLeod *et al.*, 2017). The comparison between chemical compositions of the two Hole drilled at Atlantis Bank suggest similar process of igneous accretion driven by multiple magma intrusions (Dick *et al.*, 2000).

4.2 Post-cruise geochemical analyses

4.2.1 Sampling strategy and analytical method

A total of 28 samples of olivine gabbros, 2 olivine-bearing gabbros and 2 disseminated-oxide gabbros were selected at different depths for representative compositions throughout Hole U1473A (see Appendix 3). I collected the most fresh intervals showing total alteration <15%, except for one olivine gabbro having 18% alteration (MacLeod *et al.*, 2017). To ensure accuracy and reproducibility between analyses from different laboratories two internal standards were distributed comprising one olivine gabbro and one olivine-bearing oxide gabbro from Hole U1473A (see Appendix 3), which were analysed together with rock samples.

The analytical procedure used for whole rock trace element analyses is presented in Chapter II. Limits of detection, procedural blank contributions and average compositions obtained for international rock standards UBN, BIR-1, PM-S, BHVO and BE-N are reported in Appendix 4.

Whole rock compositions are reported in Appendix 3.

4.2.2 Results

Hole U1473A olivine gabbros, olivine-bearing gabbros and disseminated-oxide gabbros have compositions that overlap those of the most enriched olivine gabbros recovered at Hole U1309D (Atlantis Massif, Figure IV.22).

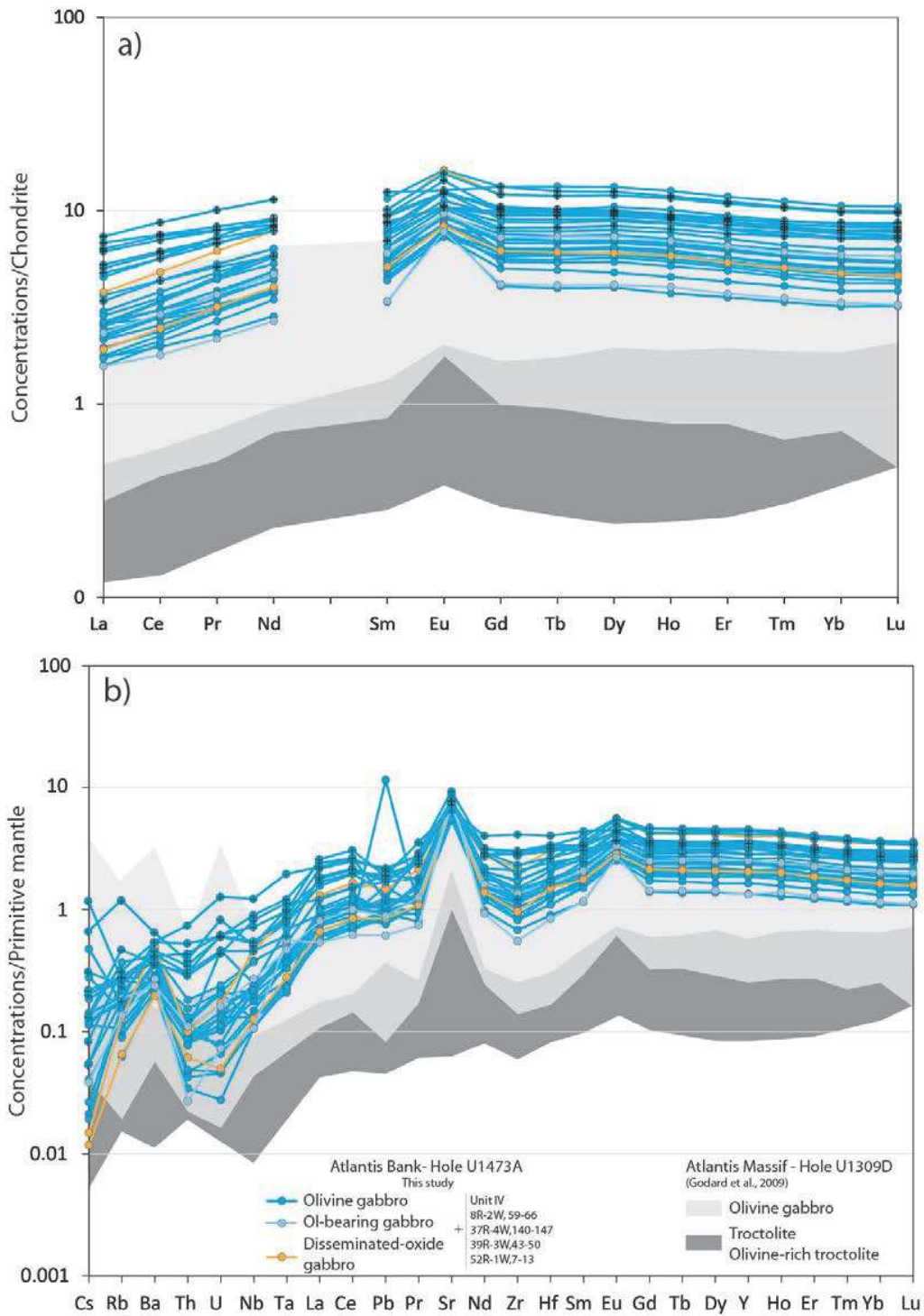


Figure IV.22- Whole rock trace element compositions of olivine gabbro, olivine-bearing gabbro and disseminated-oxide gabbro from Hole U1473A: a) REE compositions normalized to CI Chondrite; b) extended trace element spider normalized to primitive mantle. Normalizing values are from Sun and McDonough (1989). Whole rock compositions of olivine gabbro, troctolite and olivine-rich troctolite from Hole U1309D (Godard et al., 2009) are shown for comparison.

All studied samples have relatively flat MREE-HREE segment on chondrite normalized patterns (average Dy/Yb $\sim 1.2 \times$ C1-chondrite). Olivine gabbros have HREE contents that vary in a relative wide compositional range (Yb = 3.2-10.6 \times C1-chondrite; Figure IV.22a) and slightly depleted to depleted LREE patterns (La/Yb ~ 0.4 -0.9 \times C1-chondrite). The lowest HREE contents overlaps compositions of olivine-bearing gabbros (Yb = 3.3-6 \times C1-chondrite), while the highest HREE contents are comparable to those of disseminated-oxide gabbros (Yb = 4.7-10.1 \times C1-chondrite; Figure IV.22a). Olivine-bearing gabbros and disseminated-oxide gabbros have similar depleted LREE patterns (La/Yb ~ 0.4 -0.5 \times C1-chondrite). Overall Hole U1473A gabbroic rocks display a positive anomaly in Eu (average Eu/Eu* ~ 1.4). The highest Eu/Eu* values are found in olivine-bearing gabbros (Eu/Eu* = 1.5-2) and the lowest in olivine gabbros (Eu/Eu* = 1-1.7), with intermediate Eu anomalies in disseminated-oxide gabbros (Eu/Eu* = 1.5).

Extended trace element patterns (Figure IV.22b) show that analysed samples are overall depleted in the most incompatible lithophile elements (i.e., Th, U, Nb, Ta) except for Cs, Rb, Ba, which are elements affected by hydrothermal alteration. Olivine gabbros display the most variable depletion signature (Th = 0.08-0.7 \times Primitive Mantle, PM; U = 0.03-1.25 \times PM; Th/Ce = 0.04-0.3 \times PM; Nb/Zr ~ 0.01 -0.04), whereas olivine-bearing gabbros and disseminated-oxide gabbros have similar rather constant depletions (Th = 0.06-0.1 \times Primitive Mantle, PM; U = 0.07-0.17 \times PM; Th/Ce = 0.04-0.1 \times PM; Nb/Zr ~ 0.01). Slight depletion in Zr and Hf relative to REE (Zr/Sm ~ 12 -24) is also observed overall. Slightly negative Pb anomalies are displayed by all samples (Pb/Ce ~ 0.06 -0.14 \times PM=0.1), except for one olivine gabbro from the top of the borehole showing a positive Pb anomaly (Pb/Ce ~ 1.5 ; Figure IV.22b). They have Sr positive anomalies (Figure IV.22b), which are higher in olivine-bearing gabbros (Sr/Sr* ~ 5 -10) compared to olivine gabbros (Sr/Sr* ~ 2 -7), while disseminated-oxide gabbros are intermediate (Sr/Sr* ~ 3 -6).

Sr and Eu signature is consistent with higher modal content of plagioclase in olivine-bearing gabbros than olivine gabbros. Noteworthy, olivine gabbros have variable compositions. The highest trace element concentrations (Yb ~ 7 -10 \times C1-chondrite; Figure IV.22a), coupled with less depleted signatures in LREE (La/Yb ~ 0.5 -0.9 \times C1-chondrite) and other incompatible elements (Th = 0.3-0.7 \times Primitive Mantle, PM; U = 0.4-1.25 \times PM; Th/Ce = 0.14-0.3 \times PM), are found in olivine gabbros from the lithological Unit IV and other discrete samples in Units I and V. These intervals do not correspond to the evolved end-member of differentiation trends defined by shipboard data (i.e.,

Mg#, Figure IV.18), and show no distinct alteration compared to other analysed olivine gabbros. Further investigations and a complete geochemical study of U1473A rocks are needed to identify the origin of such chemical variations.

5. Comparison with Atlantis Massif (30°N, Mid-Atlantic Ridge)

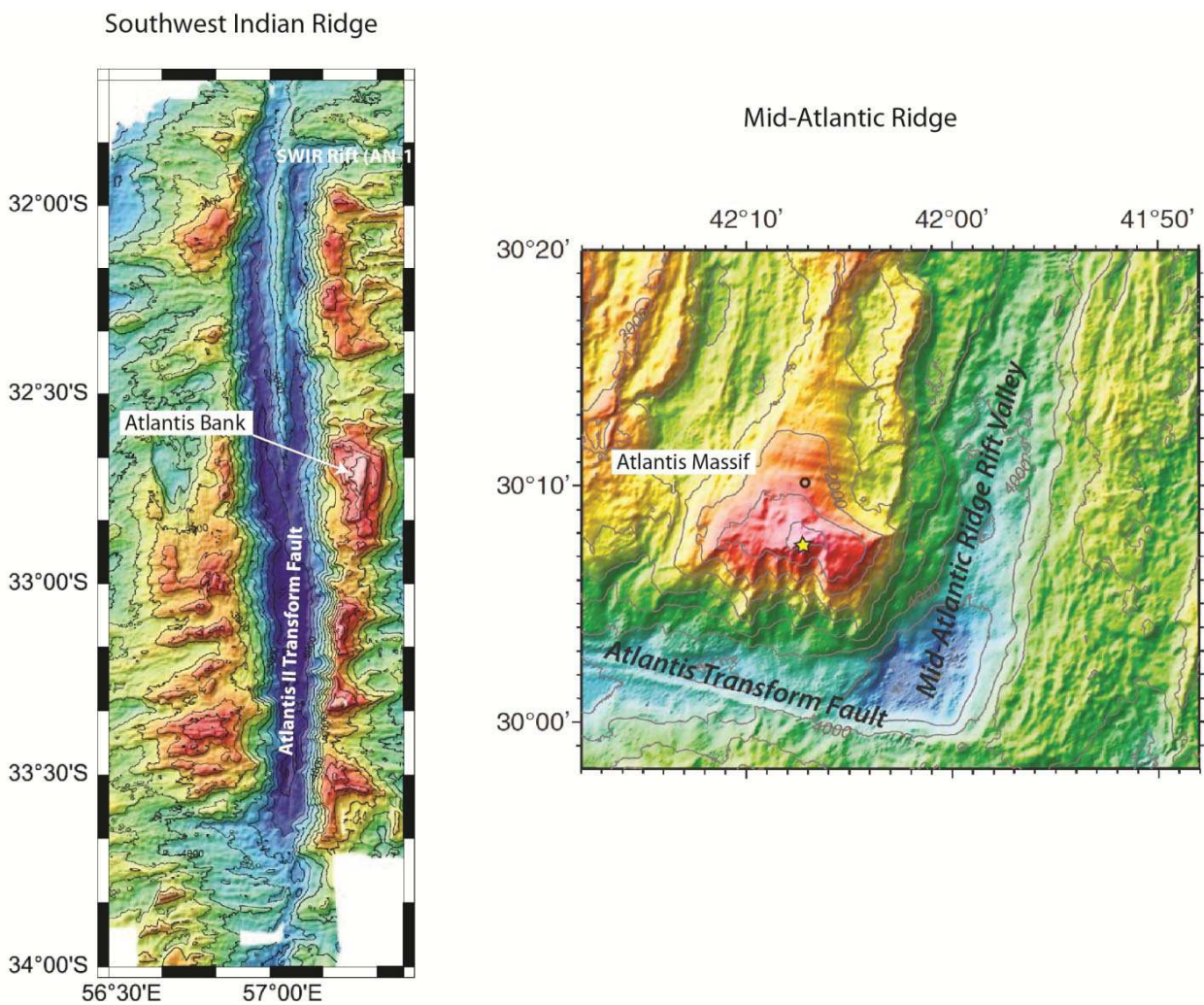


Figure IV.23 – Comparison of bathymetric data between the Atlantis Bank OCC at SWIR (Baines et al., 2007) and the Atlantis Massif OCC at MAR (Blackman et al., 2014). Note that Atlantis Massif is located at the intersaction MAR-transform fault, while Atlantis Bank is farther with respect to the intersaction SWIR-transform fault.

Atlantis Bank extends parallel to the Atlantis II Transform fault and 95 km south of the SWIR axis (Figure IV.23). The Atlantis Bank OCC formed by long-lived detachment faulting, which developed perpendicular to the ridge axis during a period of enhanced spreading rate at the northern inside corner of the paleo-SWIR (e.g., Dick *et al.*, 1991a; Baines *et al.*, 2003, 2007, 2008). On the other hand, the lower oceanic crust composing the dome of Atlantis Massif is currently exposed at the inside corner of the eastern intersection of the Mid-Atlantic Ridge with the Atlantis Transform Fault (Figure IV.23). Corrugations on the detachment surface show that Atlantis Massif OCC also formed by faulting perpendicular to the ridge axis (e.g., Blackman *et al.*, 2002; MacLeod *et al.*, 2009). Ages of the gabbroic sequences are in agreement with the location of the two OCC, where older crust is found at the, farther from rift, Atlantis Bank (~13 Myr) and younger at the Atlantis Massif (~2 Myr).

The lithologic proportions and the igneous stratigraphy of the three Holes (735B, 1105A, U1473A) recovered at Atlantis Bank are comparable and characterized by abundance of olivine gabbro as main lithology (Figure IV.24); they also share variable occurrences of oxide-bearing to oxide-rich intervals. The gabbroic section has overall evolved chemical signature, and is sporadically distinguished by troctolitic intervals in Hole 735B that represent the most primitive rock recovered at Atlantis Bank. In contrast, the lower oceanic crust recovered in Hole U1309D at the Atlantis Massif shows overall more primitive compositions (Figure IV.24) with noteworthy abundance of olivine-rich intervals of troctolitic and wherlitic compositions throughout the section (Blackman *et al.*, 2011, and references therein). Yet, the most abundant lithology at Site U1309 is gabbro (Figure IV.24). Another important difference is the presence of mantle relicts in the upper meters of the Atlantis Massif OCC (200 m of Hole U1309D), a feature that has not been observed at Atlantis Bank (MacLeod *et al.*, 2017).

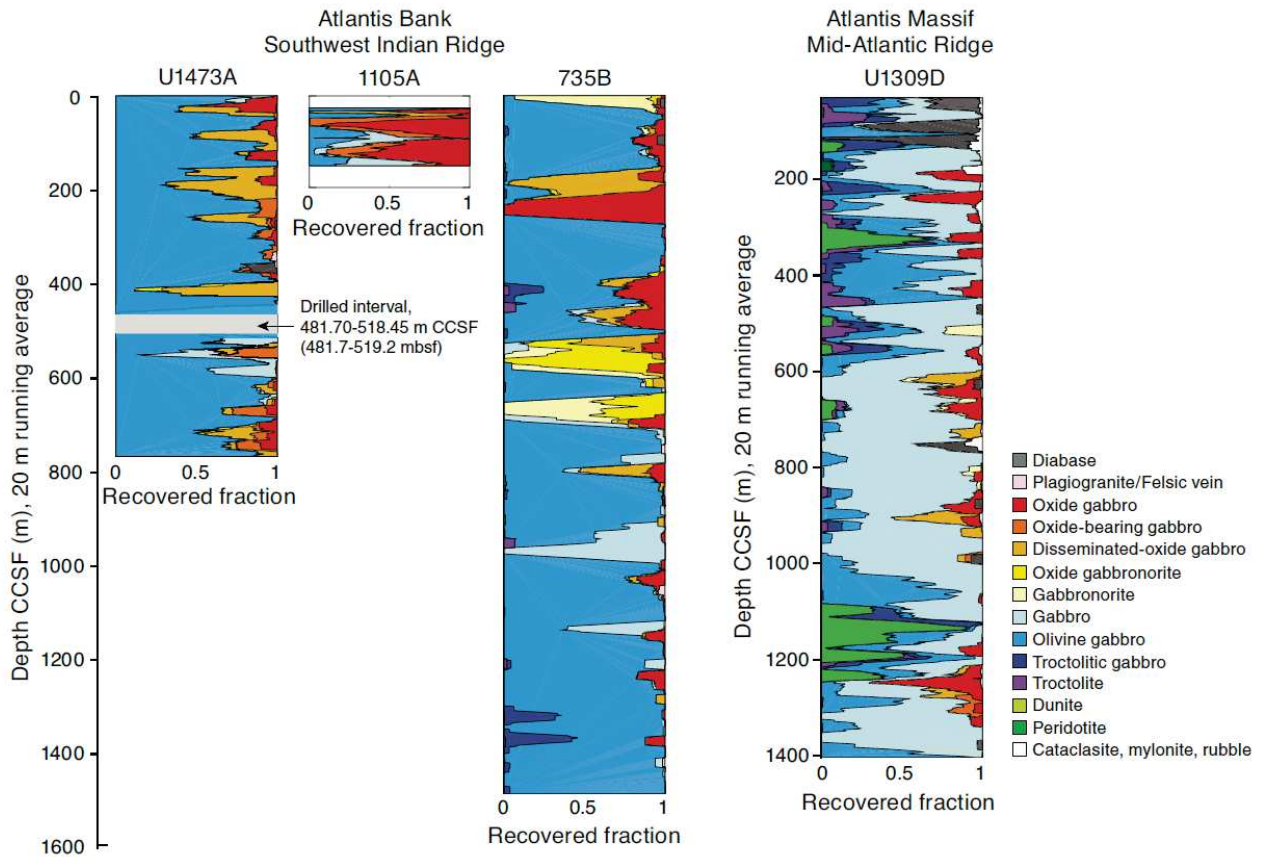


Figure IV.24 – Comparison of lithostratigraphic variations (MacLeod *et al.*, 2017) between holes drilled at Atlantis Bank (U1473A, 1105A, 735B) and at Atlantis Massif (U1309D).

Computed bulk Hole major element compositions and measured geochemistry agree with lithological observations. Indeed, Atlantis Massif has more primitive composition in comparison with the relatively evolved signature of Atlantis Bank (MacLeod *et al.*, 2017). However, by subtracting the contribution of olivine-rich troctolites in the gabbroic section of Hole U1309D, the gabbroic rocks from the two locations have similar compositions (Figure IV.25). This further suggests that assimilation of a primitive rock does change the geochemical budget of the oceanic crust, as reported in Chapter III. There is no petrological and chemical evidence of such assimilation process in the exposed oceanic crust at Atlantis Bank.

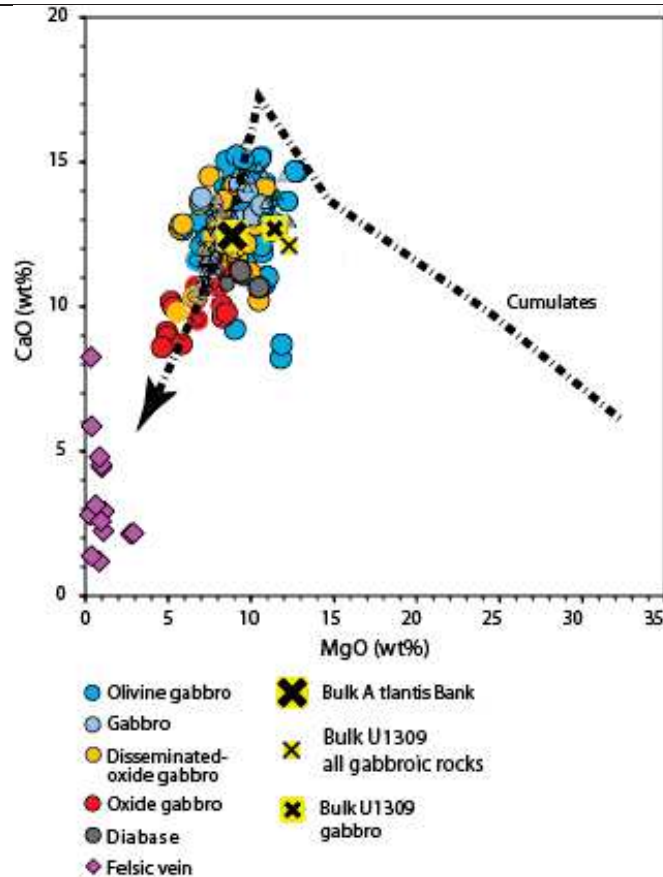


Figure IV.25 – CaO (wt%) vs MgO (wt%) for lithologies recovered from Hole U1473A and bulk composition of Atlantis Bank (MacLeod *et al.*, 2017). Bulk Hole compositions of Hole U1309D are also shown for comparison: ‘bulk U1309 all gabbroic rocks’ are calculated considering olivine-rich troctolites, while for ‘bulk U1309 gabbro’ olivine-rich troctolites were discarded (Godard *et al.*, 2009).

Trace element whole rock analyses show that Atlantis Bank olivine gabbros have patterns similar to those of gabbroic rocks from Atlantis Massif (Figure IV.22). IODP Hole U1473A have overall higher trace element concentrations and less REE fractionated patterns compared to Hole U1309D ($\text{La/Yb} \sim 0.3\text{--}0.4 \times \text{C1-chondrite}$ in olivine gabbros from Hole U1309D, and $\text{La/Yb} \sim 0.4\text{--}0.9 \times \text{C1-chondrite}$ in olivine gabbros from Hole U1473A). This supports a more evolved signature of Atlantis Bank gabbroic sequence compared to Atlantis Massif (Figure IV.22).

Downhole whole rock chemical compositions show that the gabbroic section at Atlantis Bank was built by individual magmatic events that formed 200 to 400 m thick units, each one of which presents upward chemical differentiation trends (Dick *et al.*, 2000; MacLeod *et al.*, 2017). Such evidence is not displayed by the complex chemical distribution throughout IODP Hole U1309D

(Godard *et al.*, 2009). Accretion of the lower oceanic crust at the Atlantis Massif was conversely interpreted as the result of short-lived multiple episodic magma injections intruding a relatively depleted lithospheric mantle at different depths (Godard *et al.*, 2009; Grimes *et al.*, 2008). It should be noted that while younger ages are found at the bottom of the 1.5 km thick crustal section at the Atlantis Bank (Rioux *et al.*, 2016), the gabbroic sequence at Atlantis Massif is constituted by two intervals of which the younger is on top though showing complex and locally heterogeneous age distribution (Grimes *et al.*, 2008).

Although both Atlantis Bank and Atlantis Massif are the result of long-lived low-angle detachment faulting, they have different structural features and compositions. The distinct downhole age distribution in Hole U1473A and Hole U1309D is evidence of an extremely heterogeneous oceanic crust formed at slow- and ultraslow-spreading ridges. Magmatic intrusions may occur beneath the ridge axis or laterally during faulting and development of OCCs, leading to heterogeneous emplacement of gabbroic rocks at different depths over an overall similar time frame (~2 Myr for Atlantis Bank and Atlantis Massif). MacLeod *et al.* (2017) highlight that at Atlantis Bank the lower crustal sequence records higher degrees of crystal-plastic deformation compared to gabbroic rocks at the Atlantis Massif, possibly suggesting a distinct thermal regime and different complex interplay between magma supply and tectonic extension. At slow-spreading ridges extension may be primarily accommodated by ductile deformation of upwelling mantle and short-lived episodes of magmatic injections (e.g., Godard *et al.*, 2009; Grimes *et al.*, 2008). This could be demonstrated by the presence of mantle laths within the younger gabbroic sequence recovered at the Atlantis Massif (e.g., Blackman *et al.*, 2006, 2011). During episodes of enhanced magma supply, detachment fault may root in a zone of magmatic accretion in the lower–middle crust exhuming shallower gabbroic sequence, such as the one recovered at Atlantis Bank (e.g., Ildfonse *et al.*, 2007; Baines *et al.*, 2008). Peridotite outcrops have been identified on flanks of the Atlantis Bank OCC (Figure IV.3; Dick *et al.*, 1991a; MacLeod *et al.*, 1998) suggesting that the oceanic crust is rather heterogeneous. Whether extension is accommodated by early ductile or brittle deformation is currently investigated by the Expedition 360 Shipboard Party and colleagues. Similar spreading-perpendicular lithological variations have been documented elsewhere, for example, along the Mid-Atlantic Ridge (e.g., Kane megamullion, Dick *et al.*, 2008). This suggests that upper mantle relicts could be early preserved in the top section of an OCC (as at the Atlantis Massif). Their absence in Holes 735B, 1105A and U1473A (Atlantis Bank) can be due to significant crustal

denudation and erosion of estimated 2.5-3 km of the upper section (John *et al.*, 2004). Alternatively, the crustal section analogous to Atlantis Massif may be found below Holes 735B and U1473A at Atlantis Bank and it has not yet been drilled.

These observations underline the heterogeneous nature of lower oceanic crust formed at slow- and ultraslow-spreading ridges. Differences between Atlantis Bank and Atlantis Massif demonstrate that mechanisms of crustal accretion may vary between different ridge segments or along the same rift.

Discussion

The accretion of oceanic crust at spreading centers is primarily controlled by the cooling and chemical differentiation of primary MORB-type melts. Basalts constitute the upper section of the oceanic crust and, therefore, its most accessible portion. For this reason, they have been by far the most studied lithotype collected *in situ*. They are interpreted as the result of melt generation by mantle upwelling, and subsequent processes of fractional (and equilibrium) or *in situ* crystallization at variable depths (e.g., Langmuir *et al.*, 1992; Coogan, 2014). On this basis, their compositions have been used to interpret the compositions of the lower oceanic crust and the mantle source, and to understand the formation of oceanic crust, but also to investigate melting processes and melt extraction mechanisms (e.g., O'Neill and Jenner, 2012).

The lower oceanic crust is composed of plutonic, gabbroic rocks. At slow-spreading ridges, they have extremely heterogeneous textures and compositions, which make it difficult to collect a representative portion of such gabbroic sequences. Furthermore, at fast-spreading ridges, *in situ* sampling of plutonic rocks is challenged by their presence at depths in the oceanic crust. Consequently, ocean gabbros have been little studied for many years, before advances in modern marine geology permitted the recovery of a significant number of samples. Our early understanding of processes forming the lower oceanic crust comes from studies of ophiolite complexes where gabbroic sequences outcrop on land (e.g., Alpine and Apennine ophiolites). Petrographic and geochemical investigations of gabbroic bodies from ophiolite massifs analogous to modern slow-spreading crust have documented that there are migrating melts that not only crystallize but may also interact with the host rock (e.g., see discussions in Rampone *et al.*, 2016; Sanfilippo *et al.*, 2015b). This suggests that fractional crystallization is not the only process controlling the formation and geochemical composition of the oceanic crust. Lower oceanic crustal rocks represent a transition between mantle and upper oceanic crust. The characterization of this 'missing link' is crucial for our understanding of the formation of the oceanic crust.

At slow-spreading ridges, long-lived detachment faults exhume gabbroic rocks and ultramafic sections on the seafloor, thus providing a unique window of *in situ* deeper sections of oceanic crust. Deep drilling and seafloor dredging have provided scientists with increasing proportions of lower oceanic crustal rocks from active spreading centres. Among drilling expeditions at these uplifted domal structures, the OCC, the deepest hole (~1500 m) was recovered at Atlantis Bank (ODP Hole 735B, SWIR), followed by IODP Hole U1309D at Atlantis Massif (MAR), and recently

IODP Hole U1473A about 2 km far from ODP Hole 735B at the Atlantis Bank. Studies of recovered gabbroic rocks have shed light on the heterogeneous architecture of the lower oceanic crust, composed of serpentinized mantle rocks intruded by multiple magmatic bodies. The structural and chemical features of *in situ* gabbroic rocks record reactive and crystallization processes (e.g., Lissenberg and Dick, 2008; Drouin *et al.*, 2009, 2010; Lissenberg and MacLeod, 2017) similar to those observed in ophiolite complexes. These melt-rock interactions are expected to also modify the primary composition of host rocks and that of migrating melts (e.g., Collier and Kelemen, 2010; Lissenberg and Dick, 2008). Whether this process affects only locally the chemistry of lower oceanic crust or has an impact on the global geochemical budget of oceanic crust is still matter of debate (Lissenberg and Dick, 2008; O'Neill and Jenner, 2012).

My thesis focused on sections of heterogeneous lower oceanic crust exposed at the Atlantis Massif OCC (30°N) at the slow-spreading Mid-Atlantic Ridge, and at the Atlantis Bank OCC (32°S, 57°E) at the ultraslow-spreading Southwest Indian Ridge. The detailed microstructural and petro-geochemical work on olivine-rich primitive rocks from Atlantis Massif and the preliminary results on gabbroic rocks from Atlantis Bank presented herein aimed at understanding the processes involved in the formation of the lower oceanic crust at slower-spreading ridge segments. I have showed that melt migration and mineral assimilation occur locally at different depths in the lower oceanic crust, and in the mantle. These reactive processes contribute significantly to shaping the architecture of heterogeneous lower oceanic crust and have a local control on its composition.

The gabbroic sequence of Atlantis Bank

IODP Expedition 360 drilled Hole U1473A on the Atlantis Bank (MacLeod *et al.*, 2017), where previous drilling expeditions drilled ODP Holes 735B and 1105A (Dick *et al.*, 2000; Pettigrew *et al.*, 1999). Shipboard studies of recovered gabbroic rocks have documented textures of plagioclase assimilation, as evidenced by resorbed grain boundaries, by an invading melt crystallizing clinopyroxene. Previous geochemical studies on olivine gabbros from Atlantis Bank have demonstrated that melt-rock interactions through reactive porous flow take place in an earlier crystallized matrix at crustal conditions (Lissenberg and MacLeod, 2017). Whole rock compositions of these olivine gabbros cover a wide range of trace element contents up to relatively evolved signature ($Yb = 3-10 \times C1\text{-chondrite}$; MORB $Yb = 19$). These new trace element data presented in

this manuscript, together with geochemical profiles in clinopyroxene from ODP Hole 735B olivine gabbro (Lissenberg and MacLeod, 2017), suggest that assimilation of oceanic crustal rocks at Atlantis Bank is triggered by trace element enriched melts.

The gabbroic sequence of Atlantis Massif

The gabbroic sequence recovered on the Atlantis Massif (IODP Site U1309) is characterized by slivers of mantle rocks, within the shallowest levels of the borehole, and olivine-rich troctolites occurring as intervals interfingering with gabbroic lithologies at different depths. Mineral composition and reactive percolation modeling allowed me to demonstrate that olivine-rich troctolites formed after impregnation of a mantle precursor. I showed that the extent of melt-rock interactions at Atlantis Massif is locally controlled by mineral modal heterogeneities, most likely in terms of orthopyroxene distribution in the pre-existing harzburgite. The latter governs the permeability of the system and thus, in turn, controlling the flow and volume of percolating melts. At Site U1309 reactions between olivine-saturated melts and orthopyroxene generate undersaturated olivine melts by concomitant pyroxene dissolution and olivine precipitation. Permeability is enhanced locally after orthopyroxene dissolution, which increases porosity and volume of the percolating melt. The modified melt becomes progressively in chemical disequilibrium with the host matrix. These reactions lead to the increase of MgO in the melt, which becomes progressively saturated in clinopyroxene. When saturation is attained clinopyroxene and plagioclase precipitate from the melt. Zones of the mantle precursor rich in orthopyroxene have initially the lowest permeability, and therefore form local permeability barriers where melt tends to accumulate. The significant volume of melt favors the reactive process in local orthopyroxene-rich areas (e.g., Pec *et al.*, 2017), in comparison with orthopyroxene-poor zones, and leads to the formation of the most reactive olivine-rich troctolites.

Reactive olivine-rich troctolites have also been observed in Alpine and Apennine ophiolite complexes analogous to the Atlantis Massif OCC (Renna and Tribuzio, 2011; Sanfilippo and Tribuzio, 2011, 2013; Sanfilippo *et al.*, 2014, 2015b; Rampone *et al.*, 2016). Assimilation of mantle olivine was also invoked to explain their origin. The strong fractionation of Rare Earth Elements in olivine ($Dy_N/Yb_N = 0.04 - 0.11$) suggests that melt transport has a major control on the trace element distribution among minerals and melt during reactive percolation processes.

My study shows that melt-rock interactions occur locally at the Atlantis Massif. Successive melt injections can lead to the entrapment of mantle portions leading to the in situ formation of reactive olivine-rich troctolites, within more evolved gabbros, thereby changing the architecture of the lower oceanic crust at slow-spreading ridges. Mantle laths are thereby incorporated in the oceanic crust, thus leading to the over-estimation of the thickness of the magmatic oceanic crust.

The reacted melts

Percolating melts are generally modeled as having compositions of primary MORBs. Lissenberg and Dick (2008) demonstrated that assimilation of oceanic crustal component, assuming it contains olivine, can increase the MgO and Al_2O_3 contents of melt while decreasing its CaO content (Figure D.1). By simulating melt percolation and assimilation of up to 5% of mantle component, I was also able to predict the local increase in MgO contents of the infiltrating melt, thereby leading to a shift toward apparent high pressure fractionations within the intervals of olivine-rich troctolites. Comparable MgO enrichments through mantle olivine dissolution have been documented in MORBs from the easternmost part of the SWIR (61° - 67°E) (Figure D.2), where impregnated peridotites are exposed on the seafloor (Paquet *et al.*, 2016).

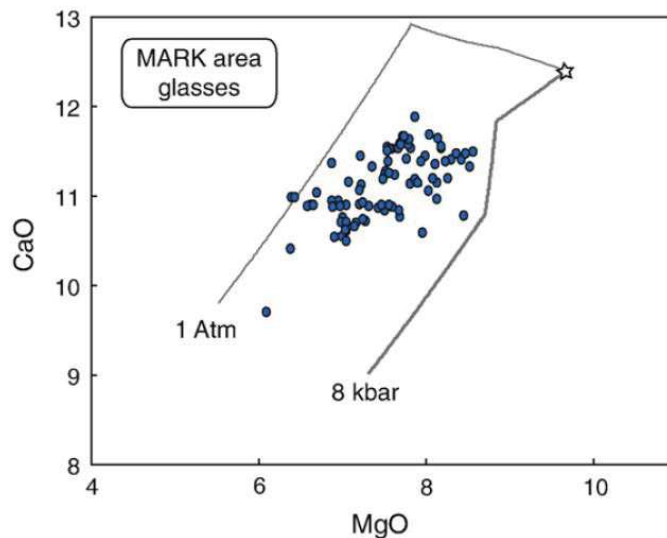


Figure D.1 – MgO (wt%) vs CaO (wt%) concentrations of MORB glasses from the Mid-Atlantic Ridge Kane (MARK) area (Lissenberg and Dick, 2008). Chemical trends of fractional crystallization at 1 atm (light grey) and 8 kbar (dark grey) are reported.

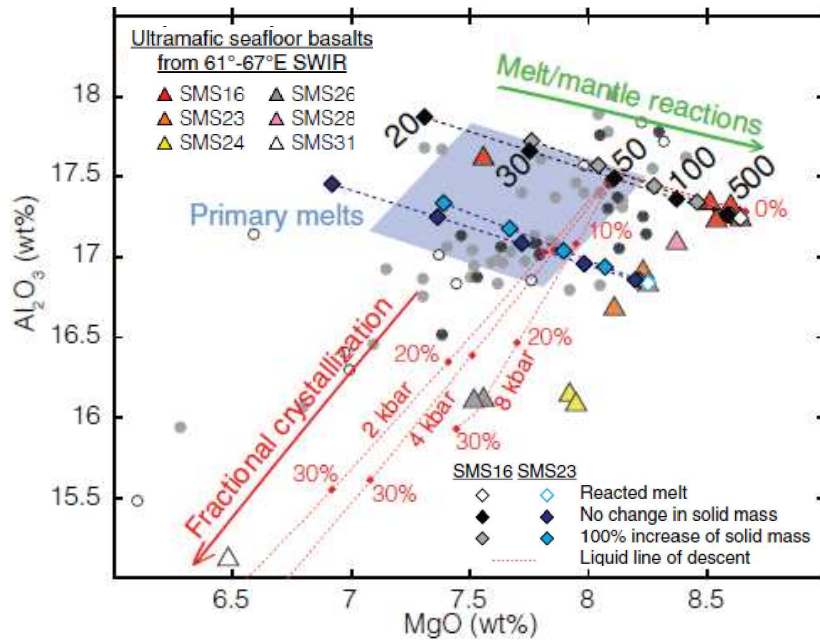


Figure D.2 – MgO (wt%) vs Al_2O_3 (wt%) concentrations of MORB from the easternmost Southwest Indian Ridge (61° - 67° E) (Paquet *et al.*, 2016). Rombus symbols represent mass balance models and red dotted lines are fractional crystallization trends calculated at different pressures as noted.

The studies of gabbroic rocks from the oceanic crust provide a consistent body of evidence suggesting that melt-rock interactions and mineral assimilation can change, at least locally, the composition of migrating MORB-type melts. Nevertheless, it should be noted that no high pressure chemical signature is observed in MORBs from the Atlantis Massif. There, the fate of reacted melts is restricted to *in situ* precipitation of interstitial high Mg# (86-88) clinopyroxene and plagioclase ($An=74-81$), and the formation of gabbroic veins, thereby further modifying the composition of olivine-rich troctolites (olivine-rich troctolite type 3), while the lower oceanic crust cooled. Similar evidence of melt flow and mineral precipitation are observed elsewhere in the oceanic gabbroic crust. At the Kane Megamullion, channel-like gabbroic veins occur through the lower oceanic crustal rocks (Lissenberg and Dick, 2008). The occurrence of subpoikilitic clinopyroxene in olivine gabbros from Atlantis Bank, coupled with the poorly correlated mineral compositions throughout Hole 735B (Dick *et al.*, 2002), suggests *in situ* precipitation of a clinopyroxene-saturated melt. This melt was locally modified after melt-rock interactions and plagioclase assimilation.

Heterogeneous lower oceanic crust at Atlantis Massif, Kane Megamullion and Atlantis Bank formed at ridge segments where extension is tectonically accommodated (OCC) and during

episodes of enhanced magma supply (e.g., Ildefonse *et al.*, 2007a; Tucholke *et al.*, 2008). At these ridge systems melt-rock interactions appear to change locally the compositions of percolating melt and pre-existing material; thus they affect the geochemical budget of the oceanic crust. At Kane Megamullion and Atlantis Bank, the assimilation of crustal component is found to affect the composition of basalts that erupt at seafloor. Their composition is shifted toward apparent high pressure fractionations (e.g., Lissenberg and Dick, 2008) (Figure D.1).

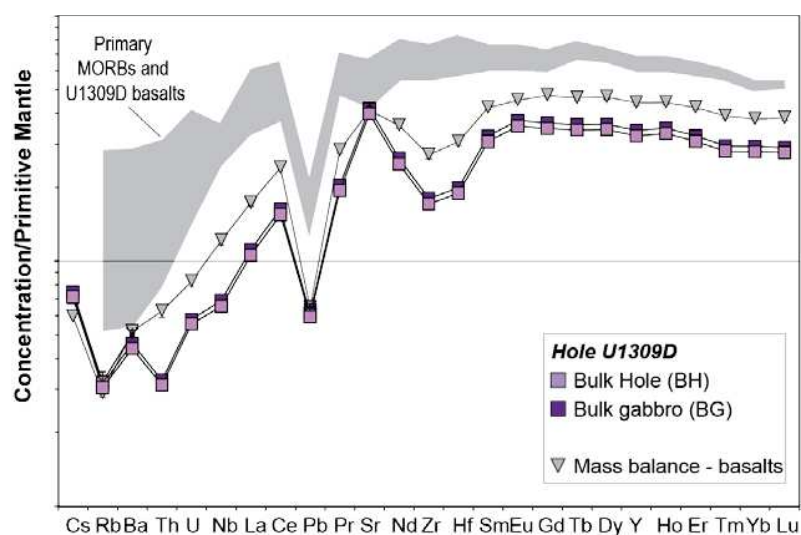


Figure D.3 – Trace elements compositions of U1309D basalts and Primary MORBs (Godard *et al.*, 2009). Calculated Bulk compositions of Hole U1309D are also reported.

On the other hand, at the Atlantis Massif we document assimilation of mantle component (Drouin *et al.*, 2009, 2010; Ferrando *et al.*, 2018), which change compositions of percolating melt locally. Basalts collected at the Atlantis Massif have compositions comparable with Primary MORBs (Figure D.3), suggesting that the composition of erupted basalts was not affected by the reactive process. In contrast, at the nearly amagmatic region of the SWIR, between 61°E and 67°E, MORBs record a geochemical signature inherited from mantle-melt interactions (Figure D.2). This suggests that the contribution of the reactive processes is greater at amagmatic regions compared to rather magmatic segments (Figure D.4). My study, together with studies elsewhere, suggests that the effect of melt percolation and mineral assimilation on the MORB plumbing system is negligible at more magmatically robust ridge segments. In contrast, it could affect nearly amagmatic spreading centers. This thereby suggests that their effect on MORBs is likely controlled by melt productivity in the upwelling mantle.

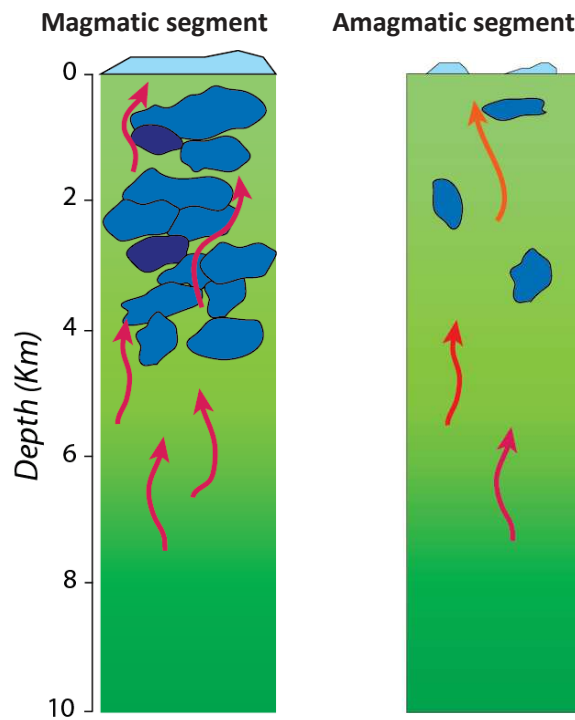


Figure D.4 – Schematic representation of the effect of mantle-melt interaction processes at magmatic vs amagmatic segments. Red to orange colors of arrows indicate the compositional change of percolating MORBs.

Timing of processes

The results presented in this study support a model whereby the heterogeneous lower oceanic crust is formed by multiple processes, including melt percolation and mineral assimilation after melt-rock interactions, magmatic crystallization, and cooling. In order to investigate the chemical effect and timing of these different processes, I measured geochemical profiles across adjacent minerals. Melt-rock interactions are found to modify the composition of pre-existing crystals. Timing of re-equilibration was determined in this work by major and trace element compositions in olivine and clinopyroxene. The results show that melt-rock reactions occur within the time predicted for emplacement of gabbroic sequences (~200 kyr at Atlantis Massif, MAR, and Atlantis Bank, SWIR). However, for precise estimates of re-equilibration time, elements with very slow diffusion rates in pre-existing minerals must be taken into account. Specifically, in olivine crystals the slow diffusion rates of phosphorous, in comparison with diffusion of other elements (e.g., Watson *et al.*, 2015), may preserve the primary composition of olivine core (e.g., Welsch *et al.*,

2014) thus providing insights on the time and conditions at which melt-rock interactions took place.

Mineral chemical compositions may not exclusively record magmatic processes, but they can also provide insights on the cooling stage of crustal accretion. At subsolidus conditions some elements can be re-distributed among rock forming minerals, leading to chemical variations in single crystals (Lasaga, 1983; Chakraborty, 2008). For example, at decreasing temperature Ca is no longer stable in olivine and it tends to diffuse into adjacent phases, mainly clinopyroxene, to reach chemical equilibrium. The diffuse fluxes of Ca induce core-to-rim chemical variations (e.g., Coogan *et al.*, 2002; VanTongeren *et al.*, 2008). Olivines in olivine-rich troctolites from the Atlantis Massif show core-to-rim variations of Ca (and Y-REE), suggesting chemical re-equilibration under subsolidus conditions. From Ca-in-olivine profiles, the temperature, timing and rate of cooling can be quantitatively determined using geospeedometry (Lasaga, 1983). The Ca-in-olivine geospeedometer proposed by Coogan *et al.* (2002) can be applied to lower oceanic crustal rocks in order to better understand the history of oceanic crustal accretion. To date, the cooling history of lower oceanic crust recovered at the Atlantis Massif remains an open question.

During cooling, heat is removed from the lower oceanic crust by conduction, and by advection via hydrothermal convection (e.g., Morgan and Chen, 1993; Quick and Denlinger, 1993; MacLennan *et al.*, 2005). Fluid circulation at high-temperatures (up to 365°C; e.g., Seyfried *et al.*, 2011; Rouméjon and Cannat, 2014) and alteration at depth (up to 8 km; e.g., Andreani *et al.*, 2007) is documented at slow-spreading ridges where detachment faults promote infiltration of seawater (e.g., Schroeder and John, 2004; Boschi *et al.*, 2006; Andreani *et al.*, 2007; Früh-Green *et al.*, 2017). At the Atlantis Massif a complex history of hydrothermal alteration has been observed, where locally gabbros appear to crosscut serpentized mantle peridotites (Früh-Green *et al.*, 2017). Furthermore, the occurrence of gabbro-norites in the lower part of the gabbroic sequence suggests that some water must have been present at depths (e.g., Koepke *et al.*, 2007; Nonnotte *et al.*, 2005). Godard *et al.* (2009) proposed that water may come from assimilation of hydrated lithospheric material; yet this hypothesis has never been tested. The interplay between magmatic processes and hydrothermal cooling, which is no longer confined to the shallower depths of oceanic crust, seems to play an important role in the construction of the oceanic crust.

The aforementioned considerations leave three main open questions:

- If melt-rock interactions occur also at fast-spreading ridges, how fast are they and chemical re-equilibration?
- Are later melt injections heating and reacting with a cooled and previously serpentinized lithospheric mantle?
- How fast is, and at which temperature conditions occurs cooling of the lower oceanic crust at a slow-spreading ridge?

Conclusions and perspectives

Conclusions

My study of gabbroic rocks from Atlantis Massif and Atlantis Bank, together with studies elsewhere along slower-spreading segments at MAR (Kane Megamullion) and SWIR (61°- 67°E) and in analogous ophiolite complexes (Appennine and Alpine ophiolites) showed that melt transport and associated mineral assimilation processes are probably ubiquitous. They likely contribute significantly to shaping the slow-spread lower oceanic crust. At the Atlantis Bank assimilation of an oceanic crustal component is invoked, while at the Atlantis Massif the precursor material is harzburgitic mantle.

The reactive percolation process recorded in olivine-rich troctolites from the Atlantis Massif is controlled by the distribution of orthopyroxene in the mantle precursor. Modified melts after melt-rock interactions seem to cool in the lower oceanic crust without affecting the MORB compositions. The example of Atlantis Massif suggests that although melt-rock interactions occur at depths, they do not necessarily play a major role overall in the geochemical budget of the oceanic crust. The fact that they contrarily affect MORB compositions at amagmatic regions (61°- 67°E, SWIR) points to extremely heterogeneous and variable mechanisms of formation of the oceanic crust at slow-spreading ridges. In turns this reflects its heterogeneous architecture and composition. It should be noted that my results comprise exclusively regions where faulting, and locally magmatism, mainly governs ocean spreading. Local variations in spreading processes along ridge segments can play a role in magma production, percolation and reaction beneath spreading centers, thus may rule the contribution of melt-rock interactions on the MORB plumbing system. At present-day, the effect of the interplay between magmatism and tectonic spreading along slow-spreading ridges on oceanic crust composition and architecture remains debated, and needs to be further documented.

Melt-rock interaction processes have been also documented at Hess Deep along the fast-spreading East-Pacific Rise. There, the assimilation of a gabbroic component plays a complex and significant role in modifying the trace element composition of MORBs, which is conventionally interpreted as being directly related to mantle source heterogeneity. Studies worldwide have shown that melt transport and associated mineral assimilation processes likely play a major role in the building of the oceanic crust overall, but further studies are needed to better understand the various extents of such reactive processes.

Perspectives

Fluid- and melt-rock interactions are found to play a fundamental role in the formation of the lower oceanic crust by affecting its chemical composition and architecture. Among the diverse unresolved questions, three are of main interest:

- (i) the timing of chemical re-equilibration in reacted crustal rocks at fast-spreading ridges;
- (ii) the evidence of serpentinized mantle prior to melt-rock interactions at active slow-spreading ridges, as for example at the Atlantis Massif or Kane Megamullion, compared to analogous ophiolite complexes;
- (iii) the chemical constraints of melt-rock interactions at Atlantis Bank.

Understanding the formation of the lower oceanic crust at the global scale requires comparison between data from both slow- and fast-spreading mid-ocean ridges. Melt-rock interactions in the lower oceanic crust are now well-documented at slow-spreading ridges, while at fast-spreading centers they are little constrained (Lissenberg *et al.*, 2013). Geochemical profiles in minerals from troctolites and olivine gabbros from fast-spreading lower oceanic crust at Hess Deep (Gillis *et al.*, 2014) should be performed to extrapolate timing of chemical re-equilibration after melt-rock interactions. These results would provide further constraints on the extent of chemical reactions and on their role on faster crustal accretion.

Stable isotopes (e.g., Sr, B, Li) are used as tracers of seawater-rock interactions (e.g., Vils *et al.*, 2009, and references therein). Because Sr does not fractionate during fluid-rock interactions (e.g., Banner and Hanson, 1990), $^{87}\text{Sr}/^{86}\text{Sr}$ of seawater is imprinted upon hydrothermal processes of mantle rocks. If hydrothermal alteration takes place prior to melt-rock interactions, the seawater signature should be inherited by crystallizing phases after the reacted melt, such as interstitial plagioclase and clinopyroxene in olivine-rich troctolites from the Atlantis Massif. In order to investigate the interplay between magmatic processes and seawater circulation at Atlantis Massif OCC, I propose to perform *in situ* analyses of Sr isotopes in plagioclase, as this mineral contains essentially the entire Sr budget of rocks in basaltic systems (Sr >100 ppm). *In situ* analyses of Sr isotopes are a powerful tool to shed light on processes occurring within a crystal–liquid–vapor mush system, otherwise hidden in whole rock isotopic analyses (e.g., Chutas *et al.*, 2012). Compared to common leaching analytical techniques on mineral separates for isotope measurements, *in situ* analyses allow for avoidance of any alteration or inclusions. Moreover,

specific sites in single minerals can be analyzed and inter-crystal isotopic compositions may be recorded. Sr isotopes analyses on plagioclase from U1309D olivine-rich troctolites should be performed on powders obtained after *in situ* microdrilling. Different microstructural sites should be analyzed in order to identify, eventually, variations of the Sr isotopic signature between core and rim in plagioclase crystals, and interstitial fine-grained plagioclase, which may result from fluid- and melt-rock interactions.

During Expedition 360 at the Atlantis Bank (IODP Hole U1473A) I sampled olivine gabbros displaying grain size and, locally, modal variations with irregular contacts. Generally, planar and sutured contacts are, instead, expected in layered gabbros (e.g., Holness, 2005; Gillis *et al.*, 2014) indicating that the grain size variations in olivine gabbros from Hole U1473A may not simply reflect processes of fractional crystallization. As previously discussed, textural and chemical features of olivine gabbros from previous deep drilling expeditions at Atlantis Bank have highlighted melt-rock interaction processes occurring in the lower oceanic crust. Fine-grained and irregular layers might reflect channelized and/or more distributed permeable flow through Atlantis Bank OCC. The lateral continuity of such reactive processes has never been investigated. With the whole sample collection from Atlantis Bank (i.e., from three boreholes) we are able to provide insights on the three-dimensional occurrence of melt-rock interactions throughout an OCC. A detailed microstructural and petro-geochemical study, similar to that presented in this thesis, should be done across the irregular contacts. Mineral geochemical profiles will help to understand the timing of such processes at an ultraslow-spreading ridge, and to estimate the composition of percolating melts at the Atlantis Bank.

Conclusions

Mon étude des roches gabbroïques de l'Atlantis Massif et de l'Atlantis Bank, ainsi que d'autres études effectuées le long de segments à extension plus lente tels que MAR (Kane Megamullion) et SWIR (61 ° - 67 ° E) et dans des complexes ophiolitiques analogues (Apennins et ophiolites alpines), montrent que le transport de magma et les processus associés d'assimilation de minéraux sont probablement omniprésents lors de la formation de la croûte océanique. Ils contribuent vraisemblablement à façonner de manière significative la croûte océanique inférieure en contexte d'extension lente. A l'Atlantis Bank, l'assimilation d'un composant océanique crustal est impliquée, alors qu'à l'Atlantis Massif, le protolithe est un manteau harzburgitique.

Le processus de percolation réactive observé dans les troctolites riches en olivine à l'Atlantis Massif est contrôlé par la distribution de l'orthopyroxène dans le manteau d'origine. Le magma modifié après interaction magma-roche semble se refroidir dans la croûte océanique inférieure sans affecter la composition des MORBs. L'exemple de l'Atlantis Massif suggère que, bien que les interactions magma-roche se produisent en profondeur, elles ne jouent pas nécessairement un rôle majeur dans le bilan géochimique de la croûte océanique. Le fait qu'elles affectent les compositions de MORBs dans des régions amagmatiques (61-67 ° E, SWIR) indique des mécanismes extrêmement hétérogènes et variables de formation de la croûte océanique aux dorsales lentes. Ceci reflète l'hétérogénéité de l'architecture et de la composition de la croûte océanique en contexte d'extension lente. Il est important de noter que mes résultats se concentrent sur des régions où l'expansion océanique est principalement contrôlée par les failles extensives, et par endroits le magmatisme. Les variations locales de processus d'expansion le long de segments de dorsale lente peuvent influencer dans la production de magma, sa percolation et les réactions magma-roche au niveau des dorsales. Elles contrôlent donc la contribution des interactions magma-roche dans la composition des MORBs. Actuellement, l'effet de l'action conjuguée du magmatisme et des processus tectoniques le long des dorsales à propagation lente, sur la composition et l'architecture de la croûte océanique reste controversé et doit être étudié davantage.

Les interactions magma-roche ont également été étudiées le long de la dorsale rapide Est-Pacifique, à Hess Deep. L'assimilation d'un composant gabbroïque joue un rôle complexe mais significatif dans la modification de la composition en éléments en traces des MORBs, généralement

interprétés comme étant directement liée à l'hétérogénéité de la source mantellique. A travers le monde, de nombreuses études ont montré que le transport réactif de magma et les processus d'assimilation de minéraux jouent un rôle majeur dans la formation de la croûte océanique, mais des études supplémentaires sont nécessaires pour comprendre toutes les implications de ces processus réactifs.

Perspectives

Les interactions fluide-roche et magma-roche jouent un rôle fondamental dans la formation de la croûte océanique inférieure, en affectant sa composition chimique et son architecture. Parmi les divers problèmes non résolus, les trois suivants méritent tout particulièrement considération :

- (i) Le timing de rééquilibrage chimique dans les roches crustales réagies aux dorsales rapides;
- (ii) La présence d'un manteau déjà serpentinisé avant les interactions magma-roche aux dorsales lentes, comme par exemple au niveau d'Atlantis Massif ou de Kane Megamullion, mis en parallèle avec des complexes ophiolitiques analogues;
- (iii) Les contraintes géochimiques des interactions magma-roche à l'Atlantis Bank.

Pour comprendre la formation de la croûte océanique inférieure à l'échelle globale, il faut comparer les données provenant des dorsales lentes et rapides. Les interactions magma-roche dans la croûte océanique inférieure sont maintenant bien documentées aux dorsales lentes, mais restent moins bien contraintes au niveau des dorsales rapides (Lissenberg *et al.*, 2013). Afin de préciser le timing du rééquilibrage chimique après interaction magma-roche, il serait nécessaire d'effectuer des profils géochimiques dans les minéraux provenant des troctolites et des gabbros à olivines provenant de la croûte océanique inférieure issue de la dorsale rapide à Hess Deep (Gillis *et al.*, 2014). Ces résultats fourniraient des contraintes supplémentaires sur l'étendue des réactions chimiques et sur leur rôle en milieu d'accrétion crustale rapide.

Des isotopes stables (par exemple Sr, B, Li) sont utilisés comme traceurs d'interactions entre l'eau de mer et la roche (voir Vils *et al.*, 2009, et références incluses). Le Sr ne fractionnant pas pendant les interactions fluide-roche (voir Banner *et Hanson*, 1990), le manteau acquiert

l'empreinte isotopique du $^{87}\text{Sr}/^{86}\text{Sr}$ de l'eau de mer durant les processus hydrothermaux. De plus, si l'altération hydrothermale a lieu avant les interactions magma-roche, la signature de l'eau de mer devrait être héritée dans les phases cristallisées par le magma, telles que le plagioclase interstitiel ou le clinopyroxène des troctolites riches en olivine de l'Atlantis Massif. Afin de mieux comprendre les interactions entre les processus magmatiques et la circulation de l'eau de mer à l'Atlantis Massif OCC, je propose d'effectuer des analyses *in situ* des isotopes du Sr dans le plagioclase. En effet, ce minéral contient la majorité du Sr total de la roche dans les systèmes basaltiques ($\text{Sr} > 100$ ppm). Les analyses *in situ* des isotopes du Sr sont un puissant outil pour étudier les processus se produisant dans un système solide-liquide-vapeur. En effet, les analyses isotopiques de roches totales ne permettent pas une analyse détaillée *in situ* des différents composants du système (Chutas *et al.*, 2012). Ainsi, les analyses *in situ* permettent d'éviter les altérations de surface ou éventuelles inclusions présentes dans les minéraux, contrairement aux attaques acides généralement utilisées lors de la séparation des minéraux pour les mesures isotopiques. De plus, les analyses *in situ* permettent de comprendre si une zonation de composition isotopique est observée du cœur aux bordures des minéraux étudiés. Les analyses isotopiques du Sr devraient donc idéalement être effectuées sur des poudres obtenues après micro-forage *in situ* des plagioclases des troctolites riches en olivine du site U1309D. Différents sites microstructuraux devraient être analysés pour identifier les variations potentielles de la signature isotopique du Sr entre le cœur et la bordure des cristaux de plagioclase, ainsi les films de plagioclases interstitiels. Ces variations pourraient être indicatives de processus d'interactions fluide-roche et magma-roche.

Durant l'expédition 360 à l'Atlantis Bank (IODP Hole U1473A), j'ai échantillonné des portions de gabbros à olivines caractérisés par des variations de tailles de grains et de compositions modales, et montrant des contacts irréguliers. Les contacts planaires et suturés sont courants dans les gabbros lités (Holness, 2005; Gillis *et al.*, 2014), ils indiquent que les variations de taille des grains dans les gabbros à olivines au site U1473A ne témoignent pas simplement de processus de cristallisation fractionnée.

Comme discuté précédemment, les caractéristiques texturales et chimiques des gabbros à olivine provenant des précédentes campagnes de forage profond à l'Atlantis Bank ont mis en évidence des processus d'interaction magma-roche se produisant dans la croûte océanique

inférieure. Les litages à grains fins et irréguliers pourraient refléter une percolation plus ou moins canalisée à travers l'OCC d'Atlantis Bank. La continuité latérale de ces processus réactifs n'a encore jamais été étudiée. En utilisant l'ensemble des échantillons collectés à l'Atlantis Bank (c'est-à-dire des trois forages), nous sommes en mesure de fournir des informations sur l'organisation tridimensionnelle des interactions magma-roche dans un OCC. Une étude microstructurale et pétrogéochimique détaillée, similaire à celle présentée dans cette thèse, devrait être réalisée à travers les contacts irréguliers. Les profils géochimiques à l'échelle minérale aideront à comprendre le timing de ces processus en environnement de dorsale ultra-lente, et à estimer la composition des magmas impliqués dans la formation de la croûte océanique à l'Atlantis Bank.

References

- Aigner-Torres, M., Blundy, J., Ulmer, P. & Pettke, T. (2007). Laser Ablation ICPMS study of trace element partitioning between plagioclase and basaltic melts: An experimental approach. *Contributions to Mineralogy and Petrology* 153, 647–667. doi:10.1007/s00410-006-0168-2
- Agranier, A. & Lee, C. T. A. (2007). Quantifying trace element disequilibria in mantle xenoliths and abyssal peridotites. *Earth and Planetary Science Letters* 257, 290–298. doi:10.1016/j.epsl.2007.02.041
- Aharonov, E., Whitehead, J. A., Kelemen, P. B. & Spiegelman, M. (1995). Channeling instability of upwelling melt in the mantle. *Journal of Geophysical Research* 100, 20433–20450. doi:10.1029/95JB01307
- Albarede, F. & Bottinga, Y. (1972). Kinetic disequilibrium in trace element partitioning between phenocrysts and host lava. *Geochimica et Cosmochimica Acta* 36, 141–156. doi:10.1016/0016-7037(72)90003-8
- Andreani, M., Escartín, J., Delacour, A., Ildefonse, B., Godard, M., Dymant, J., Fallick, A. E. & Fouquet, Y. (2014). Tectonic structure, lithology, and hydrothermal signature of the Rainbow massif (Mid-Atlantic Ridge 36°14'N). *Geochemistry, Geophysics, Geosystems* 15, 3543–3571. doi:10.1002/2014GC005269
- Andreani, M., Mével, C., Boullier, A. M. & Escartín, J. (2007). Dynamic control on serpentine crystallization in veins: Constraints on hydration processes in oceanic peridotites. *Geochemistry, Geophysics, Geosystems* 8.
- Arai, S., Dick, H.J.B., and Scientific Party, 2000. Cruise Report, Mode 2000 (Kairei/Kaiko KR00-06): Yokosuka, Japan (Japanese Agency for Marine-Earth Science and Technology).
- Asimow, P. D. (1999). A model that reconciles major- and trace-element data from abyssal peridotites. *Earth and Planetary Science Letters* 169, 303–319. doi:10.1016/S0012-821X(99)00084-9
- Aumento, F., Melson, W. G., & DSDP Leg 37 Scientific Party (1977). Initial Reports of the deep sea drilling project (Vol. 37) Washington: U.S. Government Printing Office. doi:10.2973/dsdp.proc.37.1977.
- Baines, A. G., Cheadle, M. J., Dick, H. J. B., Scheirer, A. H., John, B. E., Kuszniir, N. J. & Matsumoto, T. (2003). Mechanism for generating the anomalous uplift of oceanic core complexes: Atlantis Bank, southwest Indian Ridge. *Geology* 31, 1105–1108.
- Baines, G.A., Cheadle, M. J., Dick, H. J. B., Scheirer, A. H., John, B. E., Kuszniir, N. J. & Matsumoto, T. (2007). Evolution of the Southwest Indian ridge from 55°45'E to 62°E: Changes in plate-boundary geometry since 26 Ma. *Geochemistry, Geophysics, Geosystems* 8.
- Baines, A. G., Cheadle, M. J., John, B. E. & Schwartz, J. J. (2008). The rate of oceanic detachment faulting at Atlantis Bank, SW Indian Ridge. *Earth and Planetary Science Letters* 273, 105–114.
- Banner, J. L. & Hanson, G. N. (1990). Calculation of simultaneous isotopic and trace element variations during water-biomineral interaction with application to carbonate diagenesis. *Geochimica et Cosmochimica Acta* 54, 3123–3137.
- Barclay, A. H., Toomey, D. R. & Solomon, S. C. (1998). Seismic structure and crustal magmatism at the Mid-Atlantic Ridge, 35°N. *Journal of Geophysical Research* 103, 17827–17844. doi:10.1029/98JB01275

- Barclay, A. H., Toomey, D. R. & Solomon, S. C. (2001). Microearthquake characteristics and crustal Vp/Vs structure at the Mid-Atlantic Ridge, 35°N. *Journal of Geophysical Research* 106, 2017–2034. doi:10.1029/2000JB900371
- Beattie, P. (1994). Systematics and energetics of trace-element partitioning between olivine and silicate melts: Implications for the nature of mineral/melt partitioning. *Chemical Geology* 117, 57–71. doi:10.1016/0009-2541(94)90121-X
- Beattie, P., Ford, C. & Russell, D. (1991). Partition coefficients for olivine-melt and orthopyroxene-melt systems. *Contributions to Mineralogy and Petrology* 109, 212–224. doi:10.1007/BF00306480
- Bédard, J.H. (2001). Parental magmas of the Nain Plutonic Suite anorthosites and mafic cumulates: a trace element modelling approach. *Contributions to Mineralogy and Petrology* 141, 747–771. doi:10.1007/s004100100268
- Bédard, J. H. (2005). Partitioning coefficients between olivine and silicate melts. *Lithos* 83, 394–419. doi:10.1016/j.lithos.2005.03.011
- Bedard, J. H., Hebert, R., Berclaz, A. & Varfalvy, V. (2000). Syntexis and the genesis of lower oceanic crust. In: *Ophiolites and oceanic crust: new insights from field studies and the Ocean Drilling Program*, Dilek, Y., Moores, E.M., Elthon, D., Nicolas, A. (Eds), Special Paper. Geological Society of America, 349, 105–119.
- Bedini, R.M., Bodinier, J.-L. & Vernières, J. (2002). Numerical simulation of Fe-Mg partitioning during melting and melt-rock interactions in the upper mantle. Extended Abstracts, Proceedings of 4th International Orogenic Lherzolites and Mantle Processes Conference. Japan: Samani (unpublished).
- Ben Ismail, W. & Mainprice, D. (1998) A statistical view of the strength of seismic anisotropy in the upper mantle based on petrofabric studies of Ophiolite and xenolith samples. *Tectonophysics*, 296, 145 – 157.
- Bird, P. (2003). An updated digital model of plate boundaries. *Geochemistry, Geophysics, Geosystems* 4. doi:10.1029/2001GC000252
- Blackman, D.K. & Collins, J.A. (2010). Lower crustal variability and the crust/mantle transition at the Atlantis Massif oceanic core complex. *Geophysical Research Letters* 37, 1–5. doi:10.1029/2010GL045165
- Blackman, D.K., Karson, J.A., Kelley, D.S., Cann, J.R., Früh-Green, G.L., Gee, J.S., Hurst, S.D., John, B.E., Morgan, J., Nooner, S.L., Ross, D.K., Schroeder, T.J. & Williams, E.A. (2002). Geology of the Atlantis Massif (Mid-Atlantic Ridge, 30° N): Implications for the evolution of an ultramafic oceanic core complex. *Marine Geophysical Researches* 23, 443–469. doi:10.1023/B:MARI.0000018232.14085.75
- Blackman, D. K., Canales, J. P. & Harding, A. (2009). Geophysical signatures of oceanic core complexes. *Geophysical Journal International* 178, 593–613. doi:10.1111/j.1365-246X.2009.04184.x
- Blackman, D. K. & Forsyth, D. W. (1989). Axial topographic relief associated with ridge-transform intersections. *Earth and Planetary Science Letters* 95, 115–129. doi:10.1016/0012-821X(89)90171-4

- Blackman, D. K., Ildefonse, B., John, B. E., Ohara, Y., Miller, D. J., Macleod, C. J. & Expedition 304/305 Scientists (2006). Proceedings of the Integrated Ocean Drilling Program 304/305. doi:10.2204/iodp.proc.304305.101.2006
- Blackman, D.K., Ildefonse, B., John, B.E., Ohara, Y., Miller, D.J., Abe, N., Abratis, M., Andal, E.S., Andreani, M., Awaji, S., Beard, J.S., Brunelli, D., Charney, A.B., Christie, D.M., Collins, J., Delacour, A.G., Delius, H., Drouin, M., Einaudi, F., Escartín, J., Frost, B.R., Früh-Green, G., Fryer, P.B., Gee, J.S., Godard, M., Grimes, C.B., Halfpenny, A., Hansen, H.E., Harris, A.C., Tamura, A., Hayman, N.W., Hellebrand, E., Hirose, T., Hirth, J.G., Ishimaru, S., Johnson, K.T.M., Karner, G.D., Linek, M., MacLeod, C.J., Maeda, J., Mason, O.U., McCaig, A.M., Michibayashi, K., Morris, A., Nakagawa, T., Nozaka, T., Rosner, M., Searle, R.C., Suhr, G., Tominaga, M., Von Der Handt, A., Yamasaki, T. & Zhao, X., (2011). Drilling constraints on lithospheric accretion and evolution at Atlantis Massif, Mid-Atlantic Ridge 30N. *Journal of Geophysical Research: Solid Earth* 116, 1–25. doi:10.1029/2010JB007931
- Blundy, J. & Wood, B. (1994). Prediction of crystal-melt partition coefficients from elastic moduli. *Nature*, 452–454. doi:10.1038/372452a0
- Blundy, J. & Wood, B. (2003). Partitioning of trace elements between crystals and melts. *Earth and Planetary Science Letters* 210, 383–397. doi:10.1016/S0012-821X(03)00129-8
- Bodinier, J. L., Garrido, C. J., Chanefo, I., Bruguier, O. & Gervilla, F. (2008). Origin of pyroxenite-peridotite veined mantle by refertilization reactions: Evidence from the Ronda peridotite (Southern Spain). *Journal of Petrology* 49, 999–1025. doi:10.1093/petrology/egn014
- Bodinier, J. & Godard, M. (2003). Orogenic, Ophiolitic, and Abyssal Peridotites. In: *Treatise on Geochemistry* 2.04, 1–73, Carlson, R.W. (eds.), Amsterdam., 103–170.
- Bodinier, J. L. & Godard, M. (2014). Orogenic, Ophiolitic, and Abyssal Peridotites. In: *Treatise on Geochemistry* 3.4, 103-170, Second Edition. H. D. Holland, K.K. Turekian (eds.), Amsterdam. 10.1016/B0-08-043751-6/02004-1
- Bodinier, J.-L., Merlet, C., Bedini, R.M., Simien, F., Remaïdi, M., Garrido, C.J. (1996). Distribution of Nb, Ta and other highly incompatible trace elements in the lithospheric mantle: the spinel paradox. *Geochimica et Cosmochimica Acta* 60 (3), 545–550.
- Bonatti, E., Honnorez, J. & Ferrara G. (1971). A Discussion on the Petrology of Igneous and Metamorphic Rocks from the ocean floor - I. Ultramafic rocks - Peridotite—gabbro—basalt complex from the equatorial Mid-Atlantic Ridge. *Philosophical Transactions of the Royal Society of London A: Mathematical, Physical and Engineering Sciences* 268, 385-402.
- Borghini, G. & Rampone, E. (2007). Postcumulus processes in oceanic-type olivine-rich cumulates: The role of trapped melt crystallization versus melt/rock interaction. *Contributions to Mineralogy and Petrology* 154, 619–633. doi:10.1007/s00410-007-0217-5
- Borghini, G., Rampone, E., Crispini, L., De Ferrari, R. & Godard, M. (2007). Origin and emplacement of ultramafic-mafic intrusions in the Erro-Tobbio mantle peridotite (Ligurian Alps, Italy). *Lithos* 94, 210–229. doi:10.1016/j.lithos.2006.06.014
- Boschi, C., Früh-Green, G.L., Delacour, A., Karson, J.A. & Kelley, D.S. (2006). Mass transfer and fluid flow during detachment faulting and development of an oceanic core complex, Atlantis Massif (MAR 30°N). *Geochemistry, Geophysics, Geosystems* 7. doi:10.1029/2005GC001074

- Boudier, F., Bouchez, J. L., Nicolas, A., Cannat, M., Ceuleneer, G., Misseri, M. & Montigny, R. (1985). Kinematics of oceanic thrusting in the Oman ophiolite: model of plate convergence. *Earth and Planetary Science Letters* 75, 215–222. doi:10.1016/0012-821X(85)90103-7
- Boudier, F. & Nicolas, A. (1985). Harzburgite and lherzolite subtypes in ophiolitic and oceanic environments. *Earth and Planetary Science Letters* 76, 84–92. doi:10.1016/0012-821X(85)90150-5
- Boudier, F. & Nicolas, A. (1995). Nature of the moho transition zone in the Oman ophiolite. *Journal of Petrology* 36, 777–796. doi:10.1093/petrology/36.3.777
- Boudier, F., Nicolas, A. & Ildefonse, B. (1996). Magma chambers in the Oman ophiolite: fed from the top and the bottom. *Earth and Planetary Science Letters* 144, 239–250. doi:10.1016/0012-821X(96)00167-7
- Bowen, N. L. (1928). *The evolution of the igneous rocks*. Princeton, New Jersey, Princeton University Press, New York, Dover.
- Bozkurt, E. & Park, L. R. G. (1994). Southern Menderes Massif: an incipient metamorphic core complex in western Anatolia, Turkey. *Journal of the Geological Society* of 151, 213–216.
- Brady, J. B. & Cherniak, D. J. (2010). Diffusion in Minerals: An Overview of Published Experimental Diffusion Data. *Reviews in Mineralogy and Geochemistry* 72, 899–920. doi:10.2138/rmg.2010.72.20
- Brenan, J. M., Neroda, E., Lundstrom, C. C., Shaw, H. F., Rverson, F. J. & Phinney, D. L. (1998). Behaviour of boron, beryllium, and lithium during melting and crystallization: constraints from mineral-melt partitioning experiments. *Geochimica et Cosmochimica Acta* 62, 2129–2141. doi:10.1016/S0016-7037(98)00131-8
- Brice, J. C. (1975). Some thermodynamic aspects of the growth of strained crystals. *Journal of Crystal Growth* 28, 249–253. doi:10.1016/0022-0248(75)90241-9
- Buck, W. R., Lavier, L. L. & Poliakov, A. N. B. (2005). Modes of faulting at mid-ocean ridges. *Nature* 434, 719–723. doi:10.1038/nature03358
- Buck, W. R. & Su, W. (1989). Focused mantle upwelling below mid-ocean ridges due to feedback between viscosity and melting. *Geophysical Research Letters* 16, 641–644. doi:10.1029/GL016i007p00641
- Bunge, H. J. (1982). *Texture Analysis in Materials Science: Mathematical Models*. Butterworths, London.
- Burgess, K. D. & Cooper, R. F. (2013). Extended planar defects and the rapid incorporation of Ti⁴⁺ into olivine. *Contributions to Mineralogy and Petrology* 166, 1223–1233. doi:10.1007/s00410-013-0918-x
- Canales, J. P., Detrick, R. S., Lin, J., Collins, J. A. & Toomey, D. R. (2000). Crustal and upper mantle seismic structure beneath the rift mountains and across a nontransform offset at the Mid-Atlantic Ridge (35° N). *Journal of Geophysical Research* 105, 2699–2719.
- Canales, J. P., Nedimović, M. R., Kent, G. M., Carbotte, S. M. & Detrick, R. S. (2009). Seismic reflection images of a near-axis melt sill within the lower crust at the Juan de Fuca ridge. *Nature* 460, 89–93. doi:10.1038/nature08095

- Canales, J. P., Tucholke, B. E., Xu, M., Collins, J. A. & DuBois, D. L. (2008). Seismic evidence for large-scale compositional heterogeneity of oceanic core complexes. *Geochemistry, Geophysics, Geosystems* 9. doi:10.1029/2008GC002009
- Cann, J.R., Blackman, D.K., Smith, D.K., McAllister, E., Janssen, B., Mello, S., Avgerinos, E., Pascoe, A.R., and Escartin, J. (1997). Corrugated slip surfaces formed at ridge–transform intersections on the Mid-Atlantic Ridge. *Nature* 385, 329–332. doi:10.1038/385329a0
- Cann, J. R. (1974). A model for mid oceanic crustal structure developed. *Geophysical Journal of the Royal Astronomical Society* 39, 169–187. doi:10.1111/j.1365-246X.1974.tb05446.x
- Cannat, M., Mével, C., Maia, M., Deplus, C., Durand, C., Gente, P., Agrinier, P., Belarouchi, A., Dubuisson, G, Humler, E. & Reynolds, J. (1995). Thin crust, ultramafic exposures, and rugged faulting patterns at the Mid-Atlantic Ridge (22°–24°N). *Geology* 23, 49–52. 10.1130/0091-7613(1995)023<0049:TCUEAR>2.3.CO;2
- Cannat, M. (1993). Emplacement of mantle rocks in the seafloor at mid-ocean ridges. *Journal of Geophysical Research: Solid Earth* 98, 4163–4172. doi:10.1029/92JB02221
- Cannat, M. (1996). How thick is the magmatic crust at slow spreading oceanic ridges? *Journal of Geophysical Research* 101, 2847–2857. doi: 10.1029/95JB03116
- Cannat, M., Céline, R. J. & Fujimoto, H. (2003). Melt supply variations to a magma-poor ultra-slow spreading ridge (Southwest Indian Ridge 61° to 69°E). *Geochemistry, Geophysics, Geosystems* 4, 1–21.
- Cannat, M., Lagabriele, Y., Bougault, H., Casey, J., De Coutures, N., Dmitriev, L. & Fouquet, Y. (1997). Ultramafic and gabbroic exposures at the Mid-Atlantic Ridge: Geologic mapping in the 15°N region. *Tectonophysics* 279, 193–213. 10.1016/S0040-1951(97)00113-3
- Cannat, M., Mével, C. & Stakes, D. (1991). Normal ductile shear zones at an oceanic spreading ridge: tectonic evolution of Site 735 gabbros (Southwest Indian Ocean). *Proc. ODP Sci. Results* 118, 415–429.
- Cannat, M., Sauter, D., Escartín, J., Lavier, L. & Picazo, S. (2009). Oceanic corrugated surfaces and the strength of the axial lithosphere at slow spreading ridges. *Earth and Planetary Science Letters* 288, 174–183. doi:10.1016/j.epsl.2009.09.020
- Cannat, M., Sauter, D., Mendel, V., Ruellan, E., Okino, K., Escartin, J., Combiér, V. & Baala, M. (2006). Modes of seafloor generation at a melt-poor ultraslow-spreading ridge. *Geology* 34, 605–608. doi:10.1130/G22486.1
- Carbotte, S. M., Detrick, R. S., Harding, A., Canales, J. P., Babcock, J., Kent, G., Van Ark, E., Nedimovic, M. & Diebold, J. (2006). Rift topography linked to magmatism at the intermediate spreading Juan de Fuca Ridge. *Geology* 34, 209–212. doi:10.1130/G21969.1
- Carbotte, S. & Scheirer, D. S. (2004). Variability of ocean crustal structure created along the global mid ocean ridge. In: *Hydrogeology of the Oceanic Lithosphere*, Davis EE and Elderfield H (ed.). Cambridge: Cambridge University Press., 59–107.
- Casey, J.F., Banerji, D., & Zarian, P. (2007). Leg 179 synthesis: geochemistry, stratigraphy, and structure of gabbroic rocks drilled in ODP Hole 1105A, Southwest Indian Ridge. In Casey, J.F., and Miller, D.J. (Eds.), *Proceedings of the Ocean Drilling Program, Scientific Results*, 179: College Station, TX (Ocean Drilling Program), 1–125.

- Ceuleneer, G. & Rabinowicz, M. (1992). Mantle Flow and Melt Migration Beneath Oceanic Ridges: Models Derived from Observations in Ophiolites. In: *Mantle Flow and Melt Migration Beneath Oceanic Ridges*, Phipps Morgan, J., Blackman, D. K. & Sinton, J. M. (eds), American Geophysical Union, Geophysical Monograph 71, 123–154. doi:10.1029/GM071p0123
- Chakraborty, S. (1997). Rates and mechanisms of Fe-Mg interdiffusion in olivine at 980°-1300°C. *Journal of Geophysical Research: Solid Earth* 102, 12317–12331. doi:10.1029/97JB00208
- Chakraborty, S. (2008). Diffusion in Solid Silicates: A Tool to Track Timescales of Processes Comes of Age. *Annual Review of Earth and Planetary Sciences* 36, 153–190. doi:10.1146/annurev.earth.36.031207.124125
- Chakraborty, S. (2010). Diffusion Coefficients in Olivine, Wadsleyite and Ringwoodite. *Reviews in Mineralogy and Geochemistry* 72, 603–639. doi:10.2138/rmg.2010.72.13
- Chen, Y.J. (2001) Thermal effects of gabbros accretion from a deeper second melt lens at the fast spreading East Pacific Rise. *Journal of Geophysical Research* 106(B5), 8581–8588. doi:10.1029/2000JB900420
- Chen, Y. & Zhang, Y. (2008). Olivine dissolution in basaltic melt. *Geochimica et Cosmochimica Acta* 72, 4756–4777. doi:10.1016/j.gca.2008.07.014
- Cherniak, D. J. (1995). Diffusion of lead in plagioclase and K-feldspar: an investigation using Rutherford Backscattering and Resonant Nuclear Reaction Analysis. *Contributions to Mineralogy and Petrology* 120, 358–371. doi:10.1007/BF00306513
- Cherniak, D. J. (1998). Pb diffusion in clinopyroxene. *Chemical Geology* 150, 105–117. doi:10.1016/S0009-2541(98)00056-4
- Cherniak, D. J. (2001). Pb diffusion in Cr diopside, augite, and enstatite, and consideration of the dependence of cation diffusion in pyroxene on oxygen fugacity. *Chemical Geology* 177, 381–397. doi:10.1016/S0009-2541(00)00421-6
- Cherniak, D. J. (2002). Ba diffusion in feldspar. *Geochimica et Cosmochimica Acta* 66, 1641–1650.
- Cherniak, D. J. (2003). REE diffusion in feldspar. *Chemical Geology* 193, 25–41.
- Cherniak, D. J. (2010a). REE diffusion in olivine. *American Mineralogist* 95, 362–368. doi:10.2138/am.2010.3345
- Cherniak, D. J. (2010b). Cation Diffusion in Feldspars. *Reviews in Mineralogy and Geochemistry* 72, 691–733. doi:10.2138/rmg.2010.72.15
- Cherniak, D. J. & Dimanov, A. (2010). Diffusion in Pyroxene, Mica and Amphibole. *Reviews in Mineralogy and Geochemistry* 72, 641–690. doi:10.2138/rmg.2010.72.14
- Cherniak, D.J. & Liang, Y. (2012). Ti diffusion in natural pyroxene. *Geochimica et Cosmochimica Acta* 98, 31–47. doi:10.1016/j.gca.2012.09.021
- Cherniak, D.J. & Liang, Y. (2014). Titanium diffusion in olivine. *Geochimica et Cosmochimica Acta* 147, 43–57. doi:10.1016/j.gca.2014.10.016
- Cherniak, D. J. & Van Orman, J. A. (2014). Tungsten diffusion in olivine. *Geochimica et Cosmochimica Acta*. Elsevier Ltd 129, 1–12. doi:10.1016/j.gca.2014.10.016

- Cherniak, D. J. & Watson, E. B. (1994). A study of strontium diffusion in plagioclase using Rutherford backscattering spectroscopy. *Geochimica et Cosmochimica Acta* 58, 5179–5190. doi:10.1016/0016-7037(94)90303-4
- Christensen, N. I. (1970). Composition and evolution of the oceanic crust. *Marine Geology* 8, 139–154.
- Christensen, N. I. & Salisbury, M. H. (1975). Structure and constitution of the lower oceanic crust. *Reviews of Geophysics* 13, 57–86. doi:10.1029/RG013i001p00057
- Christensen, N. I. & Shaw, G. H. (1970). Elasticity of Mafic Rocks from the Mid-Atlantic Ridge. *Geophysical Journal of the Royal Astronomical Society* 20, 271–284. doi:10.1111/j.1365-246X.1970.tb06070.x
- Chu, D. H. & Gordon, R. G. (1999). Evidence for motion between Nubia and Somalia along the Southwest Indian Ridge. *Nature* 398, 64–67.
- Chutas, N. I., Bates, E., Prevec, S. A., Coleman, D. S. & Boudreau, A. E. (2012). Sr and Pb isotopic disequilibrium between coexisting plagioclase and orthopyroxene in the Bushveld Complex, South Africa: Microdrilling and progressive leaching evidence for sub-liquidus contamination within a crystal mush. *Contributions to Mineralogy and Petrology* 163, 653–668.
- Collier, J. S. & Singh, S. C. (1998). A seismic inversion study of the axial magma chamber reflector beneath the East Pacific Rise near 10°N. *Geological Society of Special Publication* 148, 17–28. doi:10.1144/GSL.SP.1998.148.01.02
- Collier, M. L. & Kelemen, P. B. (2010). The case for reactive crystallization at mid-ocean ridges. *Journal of Petrology* 51, 1913–1940. doi:10.1093/petrology/egq043
- Conference Participants. 1972. Penrose field conference on ophiolites. *Geotimes* 17:24–25.
- Connolly, J. A. D., Schmidt, M. W., Solferino, G. & Bagdassarov, N. (2009). Permeability of asthenospheric mantle and melt extraction rates at mid-ocean ridges. *Nature* 462, 209–212. doi:10.1038/nature08517
- Coogan, L.A., (2014). The Lower Oceanic Crust. In: Turekian, K.K., Holland, K.D. (Eds.), *Treatise on Geochemistry, Second Edition* 4.14. Elsevier, Amsterdam, pp. 497–541. doi:http://dx.doi.org/10.1016/B978-0-08-095975-7.00316-8
- Coogan, L. A., Hain, A., Stahl, S. & Chakraborty, S. (2005). Experimental determination of the diffusion coefficient for calcium in olivine between 900°C and 1500°C. *Geochimica et Cosmochimica Acta* 69, 3683–3694. doi:10.1016/j.gca.2005.03.002
- Coogan, L. A., Jenkin, G. R. T. & Wilson, R. N. (2002). Constraining the cooling rate of the lower oceanic crust: a new approach applied to the Oman ophiolite. *Earth and Planetary Science Letters* 199, 127–146. doi:10.1016/S0012-821X(02)00554-X
- Coogan, L. A., Saunders, A. D., Kempton, P. D. & Norry, M. J. (2000). Evidence from oceanic gabbros for porous melt migration within a crystal mush beneath the Mid-Atlantic Ridge. *Geochemistry, Geophysics, Geosystems* 1. doi:10.1029/2000GC000072
- Daines, M. J. & Kohlstedt, D. L. (1994). The transition from porous to channelized flow due to melt/rock reaction during melt migration. *Geophysical Research Letters* 21, 145–148. doi:10.1029/93GL03052

- Dasgupta, R., Hirschmann, M. M. & Smith, N. D. (2007). Water follows carbon: CO₂ incites deep silicate melting and dehydration beneath mid-ocean ridges. *Geology* 35, 135–138. doi:10.1130/G22856A.1
- Dasgupta, R., Mallik, A., Tsuno, K., Withers, A. C., Hirth, G. & Hirschmann, M. M. (2013). Carbon-dioxide-rich silicate melt in the Earth's upper mantle. *Nature* 493, 211–215. doi:10.1038/nature11731
- De Hoog, J.C.M., Gall, L. & Cornell, D.H. (2010). Trace-element geochemistry of mantle olivine and application to mantle petrogenesis and geothermobarometry. *Chemical Geology* 270, 196–215. doi:10.1016/j.chemgeo.2009.11.017
- D'Errico, M.E., Warren, J.M. & Godard, M. (2016). Evidence for chemically heterogeneous Arctic mantle beneath the Gakkel Ridge. *Geochimica et Cosmochimica Acta* 174, 291–312. doi:10.1016/j.gca.2015.11.017
- DePaolo, D. J. (1981). Trace element and isotopic effects of combined wallrock assimilation and fractional crystallization. *Earth and Planetary Science Letters* 53, 189–202.
- Detrick, R. S. (1987). Multichannel seismic imaging of a crustal magma chamber along the EPR. *Nature* 330, 533–537. doi:10.1038/326035a0
- Dick, H. J. B. (1989). Abyssal peridotites, very slow spreading ridges and ocean ridge magmatism. *Geological Society of London, Special Publications* 42, 71–105. doi:10.1144/GSL.SP.1989.042.01.06
- Dick, H. J. B. & Bullen, T. (1984). Chromian spinel as a petrogenetic indicator in abyssal and alpine-type peridotites and spatially associated lavas. *Contributions to Mineralogy and Petrology* 86, 54–76. doi:10.1007/BF00373711
- Dick, H. J. B., Fisher, R. L. & Bryan, W. B. (1984). Mineralogical variability of the uppermost mantle along mid-ocean ridges. *Earth and Planetary Science Letters* 69, 88–106.
- Dick, H. J. B., Lin, J. & Schouten, H. (2003). An ultraslow-spreading class of ocean ridge. *Nature* 426, 405–412. doi:10.1038/nature02128
- Dick, H.J.B., Lissenberg, J. & Warren, J.M. (2010). Mantle melting, melt transport, and delivery beneath a slow-spreading ridge: The paleo-MAR from 23°15'N to 23°45'N. *Journal of Petrology* 51, 425–467. doi:10.1093/petrology/egp088
- Dick, H. J. B., Meyer, P. S., Bloomer, S., Kirby, S., Stakes, D. & Mawer, C. (1991b). Lithostratigraphic evolution of an in-situ section of oceanic Layer 3. In Von Herzen, R.P., Robinson, P.T., et al., *Proceedings of the Ocean Drilling Program, Scientific Results*, 118: College Station, TX (Ocean Drilling Program) 439–538.
- Dick, H. J. B. & Natland, J. H. (1996). Late-stage melt evolution and transport in the shallow mantle beneath the East Pacific Rise. *Proceedings of the Ocean Drilling Program* 147, 103–134. doi:doi:10.2973/odp.proc.sr.147.007.1996
- Dick, H.J.B., Natland, J.H., Alt, J.C., Bach, W., Bideau, D., Gee, J.S., Haggas, S., Hertogen, J.G.H., Hirth, G., Holm, P.M., Ildefonse, B., Iturrino, G.J., John, B.E., Kelley, D.S., Kikawa, E., Kingdon, A., LeRoux, P.J., Maeda, J., Meyer, P.S., Miller, D.J., Naslund, H.R., Niu, Y.-L., Robinson, P.T., Snow, J., Stephen, R.A., Trimby, P.W., Worm, H.-U. & Yoshinobu, A., (2000). A long in situ

- section of the lower ocean crust: results of ODP Leg 176 drilling at the Southwest Indian Ridge. *Earth and Planetary Science Letters* 179, 31–51. doi:10.1016/S0012-821X(00)00102-3
- Dick, H.J.B., Natland, J.H., Miller, D.J., & Science Party Leg 176 (1999). *Proceedings of the Ocean Drilling Program, Initial Reports, 176*: College Station, TX (Ocean Drilling Program).
- Dick, H.J.B., Ozawa, K., Meyer, P.S., Niu, Y., Robinson, P.T., Constantin, M., Hebert, R., Maeda, J., Natland, J.H., Hirth, J.G. & Mackie, S.M. (2002). Primary silicate mineral chemistry of a 1.5-km section of very slow spreading lower ocean crust: ODP Hole 753B, Southwest Indian Ridge. *Proceedings of the Ocean Drilling Program 176*, 1–61.
- Dick, H.J.B., Schouten, H., Meyer, P.S., Gallo, D.G., Bergh, H., Tyce, R., Patriat, P., Johnson, K.T.M., Snow, J. & Fischer, A., (1991a). Tectonic evolution of the Atlantis II Fracture Zone. *Proceedings of the Ocean Drilling Program 118*, 359–398.
- Dick, H.J.B., Tivey, M.A. & Tucholke, B.E. (2008). Plutonic foundation of a slow-spreading ridge segment: Oceanic core complex at Kane Megamullion, 23°30'N, 45°20'W. *Geochemistry, Geophysics, Geosystems* 9, Q05014. doi:10.1029/2007GC001645
- Dijkstra, A. H., Drury, M. R. & Vissers, R. L. M. (2001). Structural petrology of plagioclase peridotites in the West Othris Mountains (Greece): Melt impregnation in mantle lithosphere. *Journal of Petrology* 42, 5–24. doi:10.1093/petrology/42.1.5
- Dimanov, A., Jaoul, O. & Sautter, V. (1996). Calcium self-diffusion in natural diopside single crystals. *Geochimica et Cosmochimica Acta* 60, 4095–4106. doi:10.1016/S0016-7037(96)00250-5
- Dimanov, A., Wiedenbeck, M., 2006. (Fe,Mn)-Mg interdiffusion in natural diopside: effect of pO₂. *European Journal of Mineralogy* 18, 705–718. doi:10.1127/0935-1221/2006/0018-0705
- Dinter, D. A. & Royden, L. (1993). Late Cenozoic extension in northeastern Greece: Strymon Valley detachment system and Rhodope metamorphic core complex. *Geology* 21, 45–48. doi:10.1130/0091-7613(1993)021<0045:LCEING>2.3.CO;2
- Dodson, M. H. (1973). Closure temperature in cooling geochronological and petrological systems. *Contributions to Mineralogy and Petrology* 40, 259–274. doi:10.1007/BF00373790
- Dohmen, R., Becker, H. W. & Chakraborty, S. (2007). Fe-Mg diffusion in olivine I: Experimental determination between 700 and 1,200°C as a function of composition, crystal orientation and oxygen fugacity. *Physics and Chemistry of Minerals* 34, 389–407. doi:10.1007/s00269-007-0157-7
- Dohmen, R. & Chakraborty, S. (2007). Fe-Mg diffusion in olivine II: Point defect chemistry, change of diffusion mechanisms and a model for calculation of diffusion coefficients in natural olivine. *Physics and Chemistry of Minerals* 34, 409–430. doi:10.1007/s00269-007-0158-6
- Dohmen, R., Chakraborty, S., Palme, H. & Rammensee, W. (2003). Role of element solubility on the kinetics of element partitioning: In situ observations and a thermodynamic kinetic model. *Journal of Geophysical Research* 108. doi:10.1029/2001JB000587
- Dohmen, R., Kasemann, S. A., Coogan, L. & Chakraborty, S. (2010). Diffusion of Li in olivine. Part I: Experimental observations and a multi species diffusion model. *Geochimica et Cosmochimica Acta* 74, 274–292. doi:10.1016/j.gca.2009.10.016
- Donaldson, C. H. (1976). An experimental investigation of olivine morphology. *Contributions to Mineralogy and Petrology* 57, 187–213. doi:10.1007/BF00405225

- Donaldson, C. H. (1977). Laboratory Duplication of Comb Layering in Rhum Pluton. *Mineralogical Magazine* 41, 323–336. doi:10.1180/minmag.1977.041.319.03
- Donaldson, C. H. (1985). The Rates of Dissolution of Olivine, Plagioclase, and Quartz in a Basalt Melt. *Mineralogical Magazine* 49, 683–693. doi:10.1180/minmag.1985.049.354.07
- Drouin, M., Godard, M., Ildefonse, B., Bruguier & O., Garrido, C.J. (2009). Geochemical and petrographic evidence for magmatic impregnation in the oceanic lithosphere at Atlantis Massif, Mid-Atlantic Ridge (IODP Hole U1309D, 30°N). *Chemical Geology* 264, 71–88. doi:10.1016/j.chemgeo.2009.02.013
- Drouin, M., Ildefonse, B. & Godard, M. (2010). A microstructural imprint of melt impregnation in slow spreading lithosphere: Olivine-rich troctolites from the Atlantis Massif, Mid-Atlantic Ridge, 30°N, IODP Hole U1309D. *Geochemistry, Geophysics, Geosystems* 11, 1–21. doi:10.1029/2009GC002995
- Dunn, R. A. (2015). Crust and lithospheric structure - Seismic structure of Mid-ocean ridges. *Treatise on Geophysics, Second Edition*, 419–451. doi.org/10.1016/B978-0-444-53802-4.00011-7
- Dunn, R. A., Lekić, V., Detrick, R. S. & Toomey, D. R. (2005). Three-dimensional seismic structure of the Mid-Atlantic Ridge (35°N): Evidence for focused melt supply and lower crustal dike injection. *Journal of Geophysical Research B: Solid Earth* 110, 1–17. doi:10.1029/2004JB003473
- Dunn, R. A., Toomey, D. R. & Solomon, S. C. (2000). Three-dimensional seismic structure and physical properties of the crust and shallow mantle beneath the East Pacific Rise at 9°30'N. *Journal of Geophysical Research: Solid Earth* 105, 23537–23555. doi:10.1029/2000JB900210
- Dygert, N., Liang, Y., Sun, C. & Hess, P. (2014). An experimental study of trace element partitioning between augite and Fe-rich basalts between augite and Fe-rich basalts. *Geochimica et Cosmochimica Acta* 132, 170–186. doi:10.1016/j.gca.2014.01.042
- Eggin S.M. (2003). Laser Ablation ICP-MS Analysis of Geological Materials Prepared as Lithium Borate Glasses. *Geostandards Newsletter* 27, 147–162. doi:10.1111/j.1751-908X.2003.tb00642.x
- Elthon, D. (1979). High magnesia liquids as the parental magma for ocean floor basalts. *Nature* 278, 514–518. doi:10.1017/CBO9781107415324.004
- Elthon, D., Stewart, M. & Ross, D. K. (1992). Compositional trends of minerals in oceanic cumulates. *Journal of Geophysical Research* 97, 15189–15199. doi:10.1029/92JB01187
- Engel, A. E. J., Engel, C. G. & Havens, R. G. (1965). Chemical Characteristics of Oceanic Basalts and the Upper Mantle. *Geological Society of America Bulletin* 76, 719–734.
- Engel, C. G. & Fisher, R. L. (1975). Granitic to ultramafic rock complexes of the Indian Ocean ridge system, western Indian Ocean. *Bulletin of the Geological Society of America* 86, 1553–1578.
- Escartín, J., Mével, C., MacLeod, C. J. & McCaig, A. M. (2003) Constraints on deformation conditions and the origin of oceanic detachments: The Mid-Atlantic Ridge core complex at 15°45'N. *Geochemistry, Geophysics, Geosystems* 4(8), 1067. doi:10.1029/2002GC000472
- Escartin, J., Mével, C., Petersen, S., Bonnemains, D., Cannat, M., Andreani, M., Augustin, N., Bezos, A., Chavagnac, V., Choi, Y., Godard, M., Haaga, K., Hamelin, C., Ildefonse, B., Jamieson, J.,

- John, B., Leleu, T., MacLeod, C.J., Massot-Campos, M., Nomikou, P., Olive, J.A., Paquet, M., Rommevaux, C., Rothenbeck, M., Steinfuhrer, A., Tominaga, M., Triebe, L., Campos, R., Gracias, N. & Garcia, R. (2017). Tectonic structure, evolution, and the nature of oceanic core complexes and their detachment fault zones (13° 20'N and 13° 30'N, Mid-Atlantic Ridge). *Geochemistry, Geophysics, Geosystems* 18, 1451–1482. doi:10.1002/2016GC006775.
- Escartín, J., Smith, D. K., Cann, J., Schouten, H., Langmuir, C. H. & Escrig, S. (2008). Central role of detachment faults in accretion of slow-spreading oceanic lithosphere. *Nature* 455, 790–794. doi:10.1002/2014GC005269
- Evans, E.H. & Giglio, J.J. (1993) Interferences in inductively coupled plasma mass spectrometry. A review. *Journal of Analytical Atomic Spectrometry* 8, 1-18. 10.1039/JA9930800001
- Evans, T.M., Hugh, H.S. & Tuff, J. (2008). The influence of melt composition on the partitioning of REEs, Y, Sc, Zr and Al between forsterite and melt in the system CMAS. *Geochimica et Cosmochimica Acta* 72, 5708–5721. doi:10.1016/j.gca.2008.09.017
- Faak, K., Chakraborty, S. & Coogan, L. A. (2013). Mg in plagioclase: Experimental calibration of a new geothermometer and diffusion coefficients. *Geochimica et Cosmochimica Acta* 123, 195–217. doi:10.1016/j.gca.2013.05.009
- Faak, K., Coogan, L. A. & Chakraborty, S. (2014). A new Mg-in-plagioclase geospeedometer for the determination of cooling rates of mafic rocks. *Geochimica et Cosmochimica Acta* 140, 691–707. doi:10.1016/j.gca.2014.06.005
- Faul, U. H. (1997). Permeability of partially molten upper mantle rocks from experiments and percolation theory. *Journal of Geophysical Research* 102, 10299–10311. doi:10.1029/96JB03460
- Ferrando C., Godard M., Ildefonse B., Rampone E. (2018, in press). Melt transport and mantle assimilation at Atlantis massif (IODP site U1309): Constraints from geochemical modeling. *Lithos*. doi:10.1016/j.lithos.2018.01.012
- Fynn, G. W. & Powell, W. J. A., 1979. *The Cutting and Polishing of Electro-optic Materials*. Adam Hilger, London, 216 pp.
- Foley, S. F., Prelevic, D., Rehfeldt, T. & Jacob, D. E. (2013). Minor and trace elements in olivines as probes into early igneous and mantle melting processes. *Earth and Planetary Science Letters* 363, 181–191. doi:10.1016/j.epsl.2012.11.025
- Fornari, D. J. et al. (1988). Geochemical and structural studies of the Lamont seamounts: seamounts as indicators of mantle processes. *Earth and Planetary Science Letters* 89, 63–83. doi:10.1016/0012-821X(88)90033-7
- Früh-Green, G.L., Orcutt, B.N., Green, S., Cotterill, C., and Expedition 357 Scientists, 2016. Expedition 357 Preliminary Report: Atlantis Massif Serpentinization and Life. doi:10.14379/iodp.pr.357.2016
- Fryer, B.J., Jackson, S.E. & Longerich, H.P. (1995). The design, operation and role of the Laser-Ablation microprobe coupled with an Inductively Coupled Plasma-Mass Spectrometer (LAM-ICP-MS) in the Earth Sciences. *The Canadian Mineralogist* 33, 303-312.

- Fujiwara, T., Lin, J., Matsumoto, T., Kelemen, P. B., Tucholke, B. E. & Casey, J. F. (2003). Crustal evolution of the mid-atlantic ridge near the fifteen-twenty fracture zone in the last 5 Ma. *Geochemistry, Geophysics, Geosystems* 4 (3). doi:10.1029/2002GC000364
- Gaetani, G. A. (2004). The influence of melt structure on trace element partitioning near the peridotite solidus. *Contributions to Mineralogy and Petrology* 147, 511–527. doi:10.1007/s00410-004-0575-1
- Gale, A., Dalton, C. A., Langmuir, C. H., Su, Y. & Schilling, J. G. (2013). The mean composition of ocean ridge basalts. *Geochemistry, Geophysics, Geosystems* 14, 489–518. doi:10.1029/2012GC004334
- Gale, A., Langmuir, C. H. & Dalton, C. A. (2014). The global systematics of ocean ridge basalts and their origin. *Journal of Petrology* 55, 1051–1082. doi:10.1093/petrology/egu017
- Garrido, C.J., Bodinier, J.L. & Alard, O. (2000). Incompatible trace element partitioning and residence in anhydrous spinel peridotites and websterites from the Ronda orogenic peridotite. *Earth and Planetary Science Letters* 181, 341–358. doi:10.1016/S0012-821X(00)00201-6
- Gillis, K. M. et al. (2014). Primitive layered gabbros from fast-spreading lower oceanic crust. *Nature* 505, 204–207.
- Godard, M., Awaji, S., Hansen, H., Hellebrand, E., Brunelli, D., Johnson, K., Yamasaki, T., Maeda, J., Abratis, M., Christie, D., Kato, Y., Mariet, C. & Rosner, M. (2009). Geochemistry of a long in-situ section of intrusive slow-spread oceanic lithosphere: Results from IODP Site U1309 (Atlantis Massif, 30°N Mid-Atlantic-Ridge). *Earth and Planetary Science Letters* 279, 110–122. doi:10.1016/j.epsl.2008.12.034
- Godard, M., Bodinier, J.-L. & Vasseur, G. (1995). Effects of mineralogical reactions on trace element redistributions in mantle rocks during percolation processes: A chromatographic approach. *Earth and Planetary Science Letters* 133, 449–461. doi:10.1016/0012-821X(95)00104-K
- Godard, M., Jousset, D. & Bodinier, J. L. (2000). Relationships between geochemistry and structure beneath a palaeo-spreading centre: A study of the mantle section in the Oman ophiolite. *Earth and Planetary Science Letters* 180, 133–148. doi:10.1016/S0012-821X(00)00149-7
- Godard, M., Lagabrielle, Y., Alard, O. & Harvey, J. (2008). Geochemistry of the highly depleted peridotites drilled at ODP Sites 1272 and 1274 (Fifteen-Twenty Fracture Zone, Mid-Atlantic Ridge): Implications for mantle dynamics beneath a slow spreading ridge. *Earth and Planetary Science Letters* 267, 410–425. doi:10.1016/j.epsl.2007.11.058
- Goldschmidt, V.M. (1937). The principles of distribution of chemical elements in minerals and rocks. The seventh Hugo Müller Lecture, delivered before the Chemical Society on March 17th, 1937. *Journal of the Chemical Society* 1937, 655-673. 10.1039/JR9370000655
- Goss, A. R., Perfit, M. R., Ridley, W. I., Rubin, K. H., Kamenov, G. D., Soule, S. A., Fundis, A. & Fornari, D. J. (2010). Geochemistry of lavas from the 2005-2006 eruption at the East Pacific Rise, 9°46'N-9°56'N: Implications for ridge crest plumbing and decadal changes in magma chamber compositions. *Geochemistry, Geophysics, Geosystems* 11, 1–35. doi:10.1029/2009GC002977

References

- Gracia, E., Bideau, D., Hekinian, R. & Lagabriele, Y. (1999). Detailed geological mapping of two contrasting second-order segments of the Mid-Atlantic Ridge between Oceanographer and Hayes fracture zones (33° 30'N-35° N). *Journal of Geophysical Research-Solid Earth* 104, 22903–22921. doi:10.1029/1999JB900161
- Green, D.H. & Falloon, T.J. (2005) Primary magmas at mid-ocean ridges, “hotspots,” and other intraplate settings: Constraints on mantle potential temperature. In: *Plates, plumes, and paradigms*, Foulger, G.R., Natland, J.H., Presnall, D.C., and Anderson, D.L., (eds.). Geological Society of America Special Paper 388, 217–247.
- Green, T. H., Blundy, J. D., Adam, J. & Yaxley, G. M. (2000). SIMS determination of trace element partition coefficients between garnet, clinopyroxene and hydrous basaltic liquids at 2-7.5 GPa and 1080-1200°C. *Lithos* 53, 165–187. doi:10.1016/S0024-4937(00)00023-2
- Grimes, C.B., John, B.E., Cheadle, M.J. & Wooden, J.L. (2008). Protracted construction of gabbroic crust at a slow spreading ridge: Constraints from 206Pb/238U zircon ages from Atlantis Massif and IODP Hole U1309D (30°N, MAR). *Geochemistry, Geophysics, Geosystems* 9. doi:10.1029/2008GC002063
- Grove, T. L., Kinzler, R. J. & Bryan, W. B. (1992). Mantle Flow and Melt Generation at Mid- Ocean Ridges: Fractionation of Mid-Ocean Ridge Basalt (MORB). In: *Mantle Flow and Melt Generation*, Phipps Morgan, J., Blackman, D. K. & Sinton, J. M. (eds), American Geophysical Union, Geophysical Monograph 71, 281–311.
- Gudfinnsson, G. H. & Presnall, D. C. (2000). Melting behaviour of model lherzolite in the system CaO-MgO-Al₂O₃-SiO₂-FeO at 0.7-2.8 GPa. *Journal of Petrology* 41, 1241-1269.
- Guillonga, M., & Günther, D. (2002). Effect of particle size distribution on ICP-induced elemental fractionation in laser ablation-inductively coupled plasma-mass spectrometry. *Journal of Analytical Atomic Spectrometry* 17, 831-837. doi: 10.1039/B202988J
- Günther, D. & Heinrich, C.A. (1999) Comparison of ablation behaviour of 266 nm ND:YAG and 193 nm ArF excimer lasers for LA-ICP-MS analysis. *Journal of Analytical Atomic Spectrometry* 14, 1396-1374
- Harrison, T. M. & Watson, E. B. (1983). Kinetics of zircon dissolution and zirconium diffusion in granitic melts of variable water content. *Contributions to Mineralogy and Petrology* 84, 66–72. doi:10.1007/BF01132331
- Harrison, T. M. & Watson, E. B. (1984). The behavior of apatite during crustal anatexis: Equilibrium and kinetic considerations. *Geochimica et Cosmochimica Acta* 48, 1467–1477. doi:10.1016/0016-7037(84)90403-4
- Hart, S. R. (1993). Equilibration during mantle melting: a fractal tree model. *Proceedings of the National Academy of Sciences of the United States of America* 90 (24), 11914–11918.
- Hart, S.R. & Davis, K.E. (1978). Nickel partitioning between olivine and silicate melt. *Earth and Planetary Science Letters* 40, 203–219. doi:10.1016/j.pcad.2011.11.003
- Hauri, E. H., Wagner, T. P. & Grove, T. L. (1994). Experimental and natural partitioning of Th, U, Pb and other trace elements between garnet, clinopyroxene and basaltic melts. *Chem. Geol.* 117, 149–166.

- Hebert, R., Constantin, M. & Robinson, P.T. (1991). Primary mineralogy of Leg 118 gabbroic rocks and their place in the spectrum of oceanic mafic igneous rocks. *Proceedings of the Ocean Drilling Program Leg 118, Sci. Results* 118, 3–20.
- Hebert, L. B. & Montési, L. G. J. (2010). Generation of permeability barriers during melt extraction at mid-ocean ridges. *Geochemistry, Geophysics, Geosystems* 11, 1–17.
doi:10.1029/2010GC003270
- Hellebrand, E., Suhr, G. & Scientific Parties Expeditions 304/305 (2007). Evolved Melt Migration in Primitive Lower Crustal Gabbros at IODP Site U1309, 30N, Mid- Atlantic Ridge. *Eos Trans. AGU*, 88(52), Fall Meet. Suppl., Abstract T53B-1299.
- Henstock, T. J., Woods, A. W. & White, R. S. (1993). The accretion of oceanic crust by episodic sill intrusion. *Journal of Geophysical Research* 98, 4143–4161. doi:10.1029/92JB02661
- Herd, C. D. K. (2008). Basalts as Probes of Planetary Interior Redox State. *Reviews in Mineralogy and Geochemistry* 68, 527–553. doi:10.2138/rmg.2008.68.19
- Herzberg, C. (2004). Partial crystallization of mid-ocean ridge basalts in the crust and mantle. *Journal of Petrology* 45, 2389–2405. doi:10.1093/petrology/egh040
- Herzberg, C., Asimow, P. D., Arndt, N., Niu, Y., Leshner, C. M., Fitton, J. G., Cheadle, M. J. & Saunders, A. D. (2007). Temperatures in ambient mantle and plumes: Constraints from basalts, picrites, and komatiites. *Geochemistry, Geophysics, Geosystems* 8. doi:10.1029/2006GC001390
- Hess, H.H. 1962. The history of the ocean basins, 599–620. In: *Petrologic Studies: A Volume in Honor of A.F. Buddington, A.E.J. Engel, H.L. James, and B.F. Leonard*, eds. Geological Society of America, Boulder, CO.
- Higgie, K. & Tommasi, A. (2012). Feedbacks between deformation and melt distribution in the crust-mantle transition zone of the Oman ophiolite. *Earth and Planetary Science Letters* 359–360, 61–72. doi:10.1016/j.epsl.2012.10.003
- Holness, M. B. (2005). Spatial constraints on magma chamber replenishment events from textural observations of cumulates: The Rum Layered Intrusion, Scotland. *Journal of Petrology* 46, 1585–1601.
- Holness, M.B., Anderson, A.T., Martin, V.M., MacLennan, J., Passmore, E. & Schwindinger, K. (2007). Textures in partially solidified crystalline nodules: A window into the pore structure of slowly cooled mafic intrusions. *Journal of Petrology* 48, 1243–1264. doi:10.1093/petrology/egm016
- Holness, M. B., Namur, O. & Cawthorn, R. G. (2013). Disequilibrium dihedral angles in layered intrusions: A microstructural record of fractionation. *Journal of Petrology* 54, 2067–2093. doi:10.1093/petrology/egt041
- Holness, M. B., Sides, R., Prior, D. J., Cheadle, M. J. & Upton, B. G. J. (2012). The peridotite plugs of Rum: Crystal settling and fabric development in magma conduits. *Lithos* 134–135, 23–40. doi:10.1016/j.lithos.2011.11.024
- Hosford, A., Tivey, M., Matsumoto, T., Dick, H., Schouten, H. & Kinoshita, H. (2003). Crustal magnetization and accretion at the Southwest Indian Ridge near the Atlantis II fracture zone, 0–25 Ma. *Journal of Geophysical Research: Solid Earth* 108, 1–23.
- Hunter, R. H. (1996). Texture Development in Cumulate Rocks. *Developments in Petrology* 15, 77–101. doi:10.1016/S0167-2894(96)80005-4

- Ildefonse, B. (2014a). Crustal Accretion. In : Encyclopedia of Marine Geosciences (Eds : J. Harff, M. Meschede, S. Petersen, J. Thiede). SpringerReference, Earth Sciences Series. 6pp. doi:10.1007/978-94-007-6644-0_8-1
- Ildefonse, B., Abe, N., Godard, M., Morris, A., Teagle, D.A.H. & Umino, S. (2014). Formation and Evolution of Oceanic Lithosphere: New Insights on Crustal Structure and Igneous Geochemistry from ODP/IODP Sites 1256, U1309, and U1415, *Developments in Marine Geology*. doi:10.1016/B978-0-444-62617-2.00017-7
- Ildefonse, B., Blackman, D.K., John, B.E., Ohara, Y., Miller, D.J., MacLeod, C.J., Abe, N., Abratis, M., Andal, E.S., Andréani, M., Awaji, S., Beard, J.S., Brunelli, D., Charney, A.B., Christie, D.M., Delacour, A.G., Delius, H., Drouin, M., Einaudi, F., Escartin, J., Frost, B.R., Fryer, P.B., Gee, J.S., Godard, M., Grimes, C.B., Halfpenny, A., Hansen, H.E., Harris, A.C., Hayman, N.W., Hellebrand, E., Hirose, T., Hirth, J.G., Ishimaru, S., Johnson, K.T.M., Karner, G.D., Linek, M., Maeda, J., Mason, O.U., McCaig, A.M., Michibayashi, K., Morris, A., Nakagawa, T., Nozaka, T., Rosner, M., Searle, R.C., Suhr, G., Tamura, A., Tominaga, M., von der Handt, A., Yamasaki, T. & Zhao, X. (2007a). Oceanic core complexes and crustal accretion at slow-spreading ridges. *Geology* 35, 623–626. doi:10.1130/G23531A.1
- Ildefonse, B., Christie, D.M., Abe, N., Arai, S., Bach, W., Blackman, D., Duncan, R., Hooft, E., Humphris, S. & Miller, J. (2007b). Mission Moho Workshop: Drilling through the oceanic crust to the mantle. *Scientific Drilling* 11–18. doi:10.2204/iodp.sd.4.02.2007
- Ionov, D., 1996. Distribution and residence of lithophile trace elements in minerals of garnet and spinel peridotites: an ICP-MS study. *Journal of Conference Abstracts* 1, 278.
- Ionov, D. A., Chanefo, I. & Bodinier, J. L. (2005). Origin of Fe-rich Iherzolites and wehrlites from Tok, SE Siberia by reactive melt percolation in refractory mantle peridotites. *Contributions to Mineralogy and Petrology* 150, 335–353. doi:10.1007/s00410-005-0026-7
- Ionov, D. A., Savoyant, L., Dupuy, C. (1992) Application of the ICP-MS technique to trace element analysis of peridotites and their minerals, *Geostandards Newsletter* 16, 311-315.
- Irvine, T. N. (1982). Terminology for layered intrusions. *Journal of Petrology* 23, 127–162. doi:10.1093/petrology/23.2.127-a
- Jackson, S.E., Günther, D. (2003). The nature and sources of laser induced isotopic fractionation in laser ablation-multicollector-inductively coupled plasma-mass spectrometry. *Journal of Analytical Atomic Spectrometry* 18, 205-212.
- Jaques, A. L. & Green, D. H. (1980). Anhydrous melting of peridotite at 0-15 Kb pressure and the genesis of tholeiitic basalts. *Contributions to Mineralogy and Petrology* 73, 287–310. doi:10.1007/BF00381447
- Jochum, M., Cronin, M.F., Kessler, W.S. & Shea, D. (2007). Observed horizontal temperature advection by tropical instability waves. *Geophysical Research Letters* 34. doi: 10.1029/2007GL029416.
- Jochum, K.P., Seufert, H.M. & Thirlwall, M.F. (1990). High-sensitivity Nb analysis by spark-source mass spectrometry (SSMS) and calibration of XRF Nb and Zr. *Chemical Geology* 81, 1-16.

- John, B. E. (1987). Geometry and evolution of a mid-crustal extensional fault system: Chemehuevi Mountains, southeastern California. Geological Society of London, Special Publications 28, 313–335.
- John, B. E., Foster, D. A., Murphy, J. M., Cheadle, M. J., Baines, A. G., Fanning, C. M. & Copeland, P. (2004). Determining the cooling history of in situ lower oceanic crust-Atlantis Bank, SW Indian Ridge. *Earth and Planetary Science Letters* 222, 145–160.
- Johnson, K. T. M., Dick, H. J. B. & Shimizu, N. (1990). Melting in the Oceanic Upper Mantle: an Ion Microprobe Study of Diopsides in Abyssal Peridotites. *Journal of Geophysical Research* 95 (B3), 2661–2678.
- Jollands, M.C., Hermann, J., O'Neill, H.S.C., Spandler, C. & Padrón-Navarta, J.A. (2016). Diffusion of Ti and some Divalent Cations in Olivine as a Function of Temperature, Oxygen Fugacity, Chemical Potentials and Crystal Orientation. *Journal of Petrology* 57, 1983–2010. doi:10.1093/petrology/egw067
- Jollands, M.C., O'Neill, H.S.C. & Hermann, J. (2014). The importance of defining chemical potentials, substitution mechanisms and solubility in trace element diffusion studies: the case of Zr and Hf in olivine. *Contributions to Mineralogy and Petrology* 168. doi:10.1007/s00410-014-1055-x
- Karson, J. A. & Elthon, D. (1987). Evidence for variations in magma production along oceanic spreading centers: a critical appraisal. *Geology* 15, 127–131. doi:10.1130/0091-7613(1987)15<127:EFVIMP>2.0.CO
- Karson, J.A., Früh-Green, G.L., Kelley, D.S., Williams, E.A., Yoerger, D.R. & Jakuba, M. (2006). Detachment shear zone of the Atlantis Massif core complex, Mid-Atlantic Ridge, 30°N. *Geochemistry, Geophysics, Geosystems* 7. doi:10.1029/2005GC001109
- Kalfoun, F., Ionov, D., Merlet, C. (2002). HFSE residence and Nb/Ta ratios in metasomatised, rutile-bearing mantle peridotites. *Earth and Planetary Science Letters* 199, 49–65.
- Kelemen, P. (1986). Assimilation of Ultramafic Rock in Subduction-Related Magmatic Arcs. *The Journal of Geology* 94, 829–843. doi:10.1086/629090
- Kelemen, P. B. (1990). Reaction between ultramafic rock and fractionating basaltic magma I. phase relations, the origin of calc-alkaline magma series, and the formation of discordant dunite. *Journal of Petrology* 31, 51–98. doi:10.1093/petrology/31.1.51
- Kelemen, P. B. and Aharonov, E. (1998) Periodic Formation of Magma Fractures and Generation of Layered Gabbros in the Lower Crust Beneath Oceanic Spreading Ridges, in *Faulting and Magmatism at Mid-Ocean Ridges*, W. Roger Buck, P. T. Delaney, J. A. Karson and Y. Lagabrielle (eds), American Geophysical Union, Washington, D. C. doi: 10.1029/GM106p0267
- Kelemen, P. B., Braun, M. & Hirth, G. (2000). Spatial distribution of melt conduits in the mantle beneath oceanic spreading ridges: Observations from the Ingalls and Oman ophiolites. *Geochemistry, Geophysics, Geosystems* 1. doi:10.1029/1999GC000012
- Kelemen, P. B., Dick, H. J. B. & Quick, J. E. (1992). Formation of harzburgite by pervasive melt/rock reaction in the upper mantle. *Nature* 358, 635–641. doi:10.1038/358635a0
- Kelemen, P. B., Hirth, G., Shimizu, N., Spiegelman, M. & Dick, H. J. (1997a). A review of melt migration processes in the adiabatically upwelling mantle beneath oceanic spreading ridges.

- Philosophical Transactions of the Royal Society of London. Series A: Mathematical, Physical and Engineering Sciences 355, 283–318. doi:10.1098/rsta.1997.0010
- Kelemen, P. B., Kikawa, E. & Miller, D. J. (2007b). Processes in a 20-km-Thick Conductive Boundary Layer beneath the Mid-Atlantic Ridge, 14°–16°N. *Proceedings of the Ocean Drilling Program 209*, 1–38. doi:10.2973/odp.proc.sr.209.001.2007
- Kelemen, P. B., Kikawa, E., Miller, D. J. & Expedition 209 Scientist (2004). *Proceedings of the Ocean Drilling Program, Initial Reports*. Texas A&M University, Ocean Drilling Program, College Station, TX. 209. doi:10.2973/odp.proc.ir.209.2004.
- Kelemen, P. B., Koga, K. & Shimizu, N. (1997c). Geochemistry of gabbro sills in the crust–mantle transition zone of the Oman ophiolite: implications for the origin of the oceanic lower crust. *Earth and Planetary Science Letters* 146, 475–488.
- Kelemen, P. B., Shimizu, N. & Salters, V. J. M. (1995). Extraction of mid-ocean-ridge basalt from the upwelling mantle by focused flow of melt in dunite channels. *Nature* 375, 747–753.
- Kelley, D.S., Karson, J.A., Blackman, D.K., Fruh-Green, G.L., Butterfield, D.A., Lilley, M.D., Olson, E.J., Schrenk, M.O., Roe, K.K., Lebon, G.T. & Rivizzigno, P. (2001). An off-axis hydrothermal vent field near the Mid-Atlantic Ridge at 30 degrees N. *Nature* 412, 145–149. doi:10.1038/35084000
- Kent, M., Harding, J. & Orcutt, A. (1993). Distribution of Magma Beneath the East Pacific Rise Between the Clipperton Transform and the 9°17'N Deval From Forward Modeling of Common Depth Point Data. *Journal of Geophysical Research* 98, 13,945-13,969.
- Kerr, R. C. (1995). Convective crystal dissolution. *Contributions to Mineralogy and Petrology* 121, 237–246. doi:10.1007/BF02688239
- Kinoshita, H., Dick, H.J.B. & Shipboard Scientific Party (2001). *Atlantis II Fracture Zone: MODE'98 Preliminary Report: Yokosuka, Japan (JAMSTEC Deep Sea Research)*.
- Kinoshita, J., Dick, H. & Shipboard Party JAMSTEC/WHOI (1999). Deep sea diving expedition in SW Indian Ridge (paper presented in honor of Don Heinrichs for his dedication in Marine Geosciences of NSF), *Eos, Transactions of the American Geophysical Union*, 80(46):F526.
- Kinzler, R. J. & Grove, T. L. (1992). Primary magmas of mid-ocean ridge basalts 2. Applications. *Journal of Geophysical Research* 97, 6907–6926. 10.1029/91JB02841
- Kinzler, R. J. & Grove, T. L. (1993). Corrections and further discussion of the primary magmas of mid-ocean ridge basalts, 1 and 2. *Journal of Geophysical Research: Solid Earth* 98, 22339–22347. doi:10.1029/93JB02164
- Klein, E. M. & Langmuir, C. H. (1987). Global correlations of ocean ridge basalt chemistry with axial depth and crustal thickness. *Journal of Geophysical Research* 92, 8089–8115. 10.1029/JB092iB08p08089
- Kloe, R., Drury, M. R. & van Roermund, H. L. M. (2000). Evidence for stable grain boundary melt films in experimentally deformed olivine-orthopyroxene rocks. *Physics and Chemistry of Minerals* 27, 480–494. doi:10.1007/s002690000090
- Koepke, J., Berndt, J., Feig, S. T. & Holtz, F. (2007). The formation of SiO₂-rich melts within the deep oceanic crust by hydrous partial melting of gabbros. *Contributions to Mineralogy and Petrology* 153, 67–84.

- Köhler, T. P. & Brey, G. P. (1990). Calcium exchange between olivine and clinopyroxene calibrated as a geothermobarometer for natural peridotites from 2 to 60 kb with applications. *Geochimica et Cosmochimica Acta* 54, 2375–2388. doi:10.1016/0016-7037(90)90226-B
- Kohlstedt, D. L. & Holtzman, B. K. (2009). Shearing Melt Out of the Earth: An Experimentalist's Perspective on the Influence of Deformation on Melt Extraction. *Annual Review of Earth and Planetary Sciences* 37, 561–593. doi:10.1146/annurev.earth.031208.100104
- Kohn, S. C. & Schofield, P. F. (1994). The importance of melt composition in controlling trace-element behaviour: an experimental study of Mn and Zn partitioning between forsterite and silicate melts. *Chemical Geology* 117, 73–87. doi:10.1016/0009-2541(94)90122-8
- Korenaga, J. & Kelemen, P. B. (1997). Origin of gabbro sills in the Moho transition zone of the Oman ophiolite: Implications for magma transport in the oceanic lower crust. *Journal of Geophysical Research: Solid Earth* 102, 27729–27749. doi:10.1029/97JB02604
- Kvassnes, A. J. S. & Grove, T. L. (2008). How partial melts of mafic lower crust affect ascending magmas at oceanic ridges. *Contributions to Mineralogy and Petrology* 156, 49–71. doi:10.1007/s00410-007-0273-x
- Lagabriele, Y. & Cannat, M. (1990). Alpine Jurassic ophiolites resemble the modern Central Atlantic basement. *Geology* 18, 319–322.
- Lagabriele, Y., Vitale Brovarone, A. & Ildefonse, B. (2015). Fossil oceanic core complexes recognized in the blueschist metaophiolites of Western Alps and Corsica. *Earth-Science Reviews*. 141, 1–26. doi:10.1016/j.earscirev.2014.11.004
- Lambart, S., Laporte, D. & Schiano, P. (2009). An experimental study of focused magma transport and basalt-peridotite interactions beneath mid-ocean ridges: Implications for the generation of primitive MORB compositions. *Contribution to Mineralogy and Petrology* 157, 429–451. doi:10.1007/s00410-008-0344-7
- Langmuir, C. H. (1989). Geochemical consequences of in situ crystallization. *Nature*, 199–205. doi:10.1038/340199a0
- Langmuir, C. H. & Hanson, G. N. (1980). An evaluation of major element heterogeneity in the mantle sources of basalts. *Philosophical Transactions of the Royal Society A: Mathematical, Physical and Engineering Sciences* 297, 383–407.
- Langmuir, C. H., Klein, E. M. & Plank, T. (1992). Petrological systematics of mid-ocean ridge basalts: Constraints on melt generation beneath ocean ridges. In: *Mantle Flow and Melt Generation at Mid-Ocean Ridges*, J. P. Morgan, D. K. Blackman and J. M. Sinton (eds), *Geophys. Monogr.* 71, 183–280, American Geophysical Union, Washington, D. C.. doi: 10.1029/GM071p0183
- Langmuir, C.H. & Forsyth., D.W. (2007). Mantle melting beneath mid-ocean ridges. *Oceanography* 20, 78-89.
- Lasaga, A. C. (1983). *Geospeedometry: An Extension of Geothermometry*. Saxena S.K (Ed.) *Kinetics and Equilibrium in Mineral Reactions*. Springer, New York, NY, 81–114. doi:10.1007/978-1-4612-5587-1_3
- Latourrette, T. & Wasserburg, G. J. (1998). Mg diffusion in anorthite implications for the formation of early solar system planetesimal.pdf. *Earth and Planetary Science Letters* 158, 91–108.

- Laubier, M., Grove, T.L., Langmuir, C.H., 2014. Trace element mineral/melt partitioning for basaltic and basaltic andesitic melts: An experimental and laser ICP-MS study with application to the oxidation state of mantle source regions. *Earth and Planetary Science Letters* 392, 265–278. doi:10.1016/j.epsl.2014.01.053
- le Roex, A. P., Dick, H. J. B., Erlank, A., Reid, A. M., Frey, F. A. & Hart, S. R. (1983). Geochemistry, mineralogy and petrogenesis of lavas erupted along the Southwest Indian Ridge between the Bouvet Triple Junction and 11°E. *Journal of Petrology* 24, 267–318.
- le Roex, A. P., Dick, H. J. B. & Watkins, R. T. (1992). Petrogenesis of anomalous K-enriched MORB from the Southwest Indian Ridge: 11°53'E to 14°38'E. *Contributions to Mineralogy and Petrology* 110, 253–268.
- Le Roux, V., Dasgupta, R., Lee, C.T.A., 2011. Mineralogical heterogeneities in the Earth's mantle: Constraints from Mn, Co, Ni and Zn partitioning during partial melting. *Earth and Planetary Science Letters* 307, 395–408. doi:10.1016/j.epsl.2011.05.014
- Lee, C. T. A., Harbert, A. & Leeman, W. P. (2007). Extension of lattice strain theory to mineral/mineral rare-earth element partitioning: An approach for assessing disequilibrium and developing internally consistent partition coefficients between olivine, orthopyroxene, clinopyroxene and basaltic melt. *Geochimica et Cosmochimica Acta* 71, 481–496. doi:10.1016/j.gca.2006.09.014
- Li, C. & Ripley, E. M. (2010). The relative effects of composition and temperature on olivine-liquid Ni partitioning: Statistical deconvolution and implications for petrologic modeling. *Chemical Geology*. Elsevier B.V. 275, 99–104. doi:10.1016/j.chemgeo.2010.05.001
- Liang, Y. (1999). Diffusive dissolution in ternary systems: analysis with applications to quartz and quartzite dissolution in molten silicates. *Geochimica et Cosmochimica Acta* 63, 3983–3995. doi:10.1016/S0016-7037(99)00203-3
- Liang, Y. (2000). Dissolution in molten silicates: Effects of solid solution. *Geochimica et Cosmochimica Acta* 64, 1617–1627. doi:10.1016/S0016-7037(00)00331-8
- Liang, Y. (2003). Kinetics of crystal-melt reaction in partially molten silicates: 1. Grain scale processes. *Geochemistry, Geophysics, Geosystems* 4. doi:10.1029/2002GC000375
- Lissenberg, C. J. & Dick, H. J. B. (2008). Melt-rock reaction in the lower oceanic crust and its implications for the genesis of mid-ocean ridge basalt. *Earth and Planetary Science Letters* 271, 311–325. doi:10.1016/j.epsl.2008.04.023
- Lissenberg, C. J. & MacLeod, C. J. (2017). A reactive porous flow control on mid-ocean ridge magmatic evolution. *Journal of Petrology* 57, 2195–2220. doi:10.1093/petrology/egw074
- Lissenberg, C. J., MacLeod, C. J., Howard, K. A. & Godard, M. (2013). Pervasive reactive melt migration through fast-spreading lower oceanic crust (Hess Deep, equatorial Pacific Ocean). *Earth and Planetary Science Letters*. Elsevier 361, 436–447. doi:10.1016/j.epsl.2012.11.012
- Liu, X., Xiong, X., Audétat, A., Li, Y., Song, M., Li, L., Sun, W. & Ding, X. (2014). Partitioning of copper between olivine, orthopyroxene, clinopyroxene, spinel, garnet and silicate melts at upper mantle conditions. *Geochimica et Cosmochimica Acta* 125, 1–22. doi:10.1016/j.gca.2013.09.039

- Loocke, M., Snow, J. E. & Ohara, Y. (2013). Melt stagnation in peridotites from the Godzilla Megamullion Oceanic Core Complex, Parece Vela Basin, Philippine Sea. *Lithos*. 182–183, 1–10. doi:10.1016/j.lithos.2013.09.005
- Lundstrom, C.C., Shaw, H.F., Ryerson, F.J., Williams, Q. & Gill, J. (1998). Crystal chemical control of clinopyroxene-melt partitioning in the Di-Ab-An system: Implications for elemental fractionations in the depleted mantle. *Geochimica et Cosmochimica Acta* 62, 2849–2862. doi:10.1016/S0016-7037(98)00197-5
- Macdonald, K. C. (1982). Mid-Ocean Ridges: Fine Scale Tectonic, Volcanic and Hydrothermal Processes Within the Plate Boundary Zone. *Annual Review of Earth and Planetary Sciences* 10, 155–190. doi:10.1146/annurev.ea.10.050182.001103
- Macdonald, K. C., Scheirer, D. S., Carbotte, S. & Fox, P. J. (1993a). It's only topography: Part 1. *GSAToday* 3, 1–35.
- Macdonald, K. C., Scheirer, D. S., Carbotte, S. & Fox, P. J. (1993b). It's only topography: Part 2. *GSAToday* 3, 1–35.
- Maclennan, J., Hulme, T. & Singh, S. C. (2005). Cooling of the lower oceanic crust. *Geology* 33, 357–360. doi:10.1130/G21207.1
- MacLeod, C.J., Dick, H.J.B., Allerton, S., Robinson, P.T., Coogan, L.A., Edwards, S.J., Galley, A., Gillis, K.M., Hirth, G., Hunter, A.G., Hutchinson, D., Kvassnes, A.J., Natland, J.H., Salisbury, M., Schandl, E.S., Stakes, D.S., Thompson, G.M. & Tivey, M.A. (1998). Geological mapping of slow-spread lower ocean crust: a deep-towed video and wireline rock drilling survey of Atlantis Bank (ODP Site 735, SW Indian Ridge). *InterRidge News* 7(2), 39–43.
- MacLeod, C.J., Dick, H.J.B., Blum, P., Abe, N., Blackman, D.K., Bowles, J.A., Cheadle, M.J., Cho, K., Ciazela, J., Deans, J.R., Edgcomb, V.P., Ferrando, C., France, L., Ghosh, B., Ildefonse, B.M., Kendrick, M.A., Koepke, J.H., Leong, J.A.M., Liu, C., Ma, Q., Morishita, T., Morris, A., Natland, J.H., Nozaka, T., Pluemper, O., Sanfilippo, A., Sylvan, J.B., Tivey, M.A., Tribuzio, R. & Viegas, L.G.F. (2017). *Proceedings of the International Ocean Discovery Program* 360. doi:10.14379/iodp.proc.360.103.2017
- MacLeod, C.J., Escartin, J., Banerji, D., Banks, G.J., Gleeson, M., Irving, D.H.B., Lilly, R.M., McCaig, A.M., Niu, Y., Allerton, S. & Smith, D.K. (2002). Direct geological evidence for oceanic detachment faulting: The Mid-Atlantic Ridge, 15°45'N. *Geology* 30, 879–882. doi:10.1130/0091-7613(2002)030<0879:DGEFOD>2.0.CO;2
- MacLeod, C. J., Searle, R. C., Murton, B. J., Casey, J. F., Mallows, C., Unsworth, S. C., Achenbach, K. L. & Harris, M. (2009). Life cycle of oceanic core complexes. *Earth and Planetary Science Letters* 287, 333–344. doi:10.1016/j.epsl.2009.08.016
- MacLeod, C. J., Wright, W. P., Perry, C. T. & Dick, H. J. B. (2000). Tectonic evolution and uplift/subsidence history of Atlantis Bank, a Transverse Ridge near the Atlantis II Fracture Zone, SW Indian Ridge. *Eos, Transactions of the American Geophysical Union* 81:1129.
- Mainprice, D., Bachmann, F., Hielscher, R. & Schaeben, H. (2014) Descriptive tools for the analysis of texture projects with large datasets using MTEX - strength, symmetry, and components. In: *Rock Deformation from Field, Experiments and Theory: A Volume in Honour of Ernie Rutter*, Faulkner, D.R., Meckenburgh, J., Mariani, E., (eds). Geological Society, London, Special Publications, 409, <http://dx.doi.org/10.1144/SP409.8>

- Mainprice, D. & Silver, P. G. (1993). Interpretation of SKS-waves using samples from the subcontinental lithosphere. *Physics of the Earth and Planetary Interiors*, 78, 257–280.
- Marjanović, M., Carbotte, S. M., Carton, H., Nedimović, M. R., Mutter, J. C. & Canales, J. P. (2014). A multi-sill magma plumbing system beneath the axis of the East Pacific Rise. *Nature Geoscience* 7, 825–829. doi:10.1038/ngeo2272
- Matsumoto, T., Dick, H.J.B. & Scientific Party (2002). Investigation of Atlantis Bank and the SW Indian Ridge from 568E to 588E: Preliminary Report: Tokyo (Japanese Agency for Marine-Earth Science and Technology).
- Matzen, A. K., Baker, M. B., Beckett, J. R. & Stolper, E. M. (2013). The temperature and pressure dependence of nickel partitioning between olivine and silicate melt. *Journal of Petrology* 54, 2521–2545. doi:10.1093/petrology/egt055
- May T.W. & Wiedmeyer, R.H. (1998) A table of polyatomic interferences in ICP-MS. *Atomic Spectroscopy*, 19, 150-155.
- McDade, P., Blundy, J. D. & Wood, B. J. (2003). Trace element partitioning on the Tinaquillo solidus at 1.5 GPa. *Physics of the Earth and Planetary Interiors* 139, 129–147. doi:10.1016/S0031-9201(03)00149-3
- McKenzie, D. P. (1984). The generation and compaction of partial melts. *Journal of Petrology* 25, 713–765. doi:10.1093/petrology/25.3.713
- McKenzie, D.P. & Bickle, M. J. (1988). The volume and composition of melt generated by extension of the lithosphere. *Journal of Petrology* 29, 625–679. doi:10.1093/petrology/29.3.625
- Melson, W.G., Rabinowitz, P.D., Bougault, H., Fujii, T., Graham, A.L., Johnson, H.P., Lawrence, J.R., Natland, J.H., Prosser, E., Rhodes, J.M. & Zolotarev B.P. (1979). Deep Sea Drilling Project 45. doi:10.2973/dsdp.proc.45.1979
- Mendel, V., Sauter, D., Parson, L. & Vanney, J. (1997). Segmentation and Morphotectonic Variations Along a Super Slow-Spreading Center The Southwest Indian Ridge (57°E-70°E). *Marine Geophysical Researches* 19(6), 505–533.
- Mével, C. (2003). Serpentinization of abyssal peridotites at mid-ocean ridges. *Comptes Rendus Geoscience* 335, 825–852. doi:10.1016/j.crte.2003.08.006
- Mével, C., Agrinier, P., Cannat, M., Decitre, S., Dappoigny, A., Humler, E., Jendrzewski, N., Kienast, J.R., Ludden, J., Murton, B., Oufi, O., Seyler, M.R. & Tamura, Y. (1997). Sampling the South West Indian Ridge: first results of the EDUL cruise (R/V Marion Dufresne II, August 1997). *InterRidge News* 6(2), 25–26.
- Meyer, P., Dick, H. J. B. & Thompson, G. (1989). Cumulate gabbros from the Southwest Indian Ridge, 54°S – 7°16'E: implications for magmatic processes at a slow spreading ridge. *Contributions to Mineralogy and Petrology* 103, 44–63.
- Michael, P. J. & Cornell, W. C. (1998). Influence of spreading rate and magma supply on crystallization and assimilation beneath mid-ocean ridges: Evidence from chlorine and major element chemistry of mid-ocean ridge basalts. *Journal of Geophysical Research* 103, 18325. doi:10.1029/98JB00791

- Michibayashi, K. & Mainprice, D. (2004) The role of pre-existing mechanical anisotropy on shear zone development within oceanic mantle lithosphere: an example from the Oman omphiolite. *Journal of Petrology* 45, 405-414.
- Miller, D.J., Abratis, M., Christie, D., Drouin, M., Godard, M., Ildefonse, B., Maeda, J., Weinsteiger, A., Yamasaki, T., Suzuki, Y., Niino, A., Sato, Y. & Takeda, F. (2009). Data report: microprobe analyses of primary mineral phases from Site U1309, Atlantis Massif, IODP Expedition 304/305, in: *Proceedings of the Integrated Ocean Drilling Program 304/305*. doi:10.2204/iodp.proc.304305.202.2009
- Miller, D. J. & Christensen, N. I. (1997). Seismic velocities of lower crustal and upper mantle rocks from the slow-spreading Mid-Atlantic Ridge, south of the Kane Fracture Transform Zone (MARK). In: Karson, J.A., Cannat, M., Miller, D.J., and Elthon, D. (Eds.), *Proceedings of the Ocean Drilling Program, Scientific Results 153*, 437–454.
- Miller, K. J., Zhu, W.I., Montési, L. G. J. & Gaetani, G. A. (2014). Experimental quantification of permeability of partially molten mantle rock. *Earth and Planetary Science Letters*. 388, 273–282. doi:10.1016/j.epsl.2013.12.003
- Minshull, T. A., Muller, M. R., Robinson, C. J., White, R. S. & Bickle, M. J. (1998). Is the oceanic Moho a serpentinization front? In Mills, R.A., and Harrison, K. (Eds.), *Modern Ocean Floor Processes and the Geological Record*. Geological Society Special Publications 148, 71–80.
- Minshull, T. A., Muller, M. R. & White, R. S. (2006). Crustal structure of the Southwest Indian Ridge at 66°E: Seismic constraints. *Geophysical Journal International* 166, 135–147.
- Minshull, T. A. & White, R. S. (1996). Thin crust on the flanks of the slow-spreading Southwest Indian ridge. *Geophysical Journal International* 125, 139–148.
- Miranda, E. A. & John, B. E. (2010). Strain localization along the Atlantis Bank oceanic detachment fault system, Southwest Indian Ridge. *Geochemistry, Geophysics, Geosystems* 11.
- Muller, M. R., Minshull, T. A. & White, R. S. (1999). Segmentation and melt supply at the Southwest Indian Ridge. *Geology* 27, 867–870.
- Muller, M. R., Minshull, T. A. & White, R. S. (2000). Crustal structure of the Southwest Indian Ridge. *Journal of Geophysical Research* 105, 25809 – 25828.
- Moll, M., Paulick, H., Suhr, G. & Bach, W. (2007). Data Report: Microprobe Analyses of Primary Phases (Olivine, Pyroxene, and Spinel) and Alteration Products (Serpentine, Iowite, Talc, Magnetite, and Sulfides) in Holes 1268A, 1272A, and 1274A. In: *Proceedings of the Ocean Drilling Program 209 Sci. Results 209*. doi:10.2973/odp.proc.sr.209.003.2007
- Morgan, J. P. (1987). Melt migration beneath mid-ocean spreading centers. *Geophysical Research Letters* 14, 1238–1241. doi:10.1029/GL014i012p01238
- Morgan, J. P. & Chen, Y. J. (1993). The genesis of oceanic crust: Magma injection, hydrothermal circulation, and crustal flow. *Journal of Geophysical Research: Solid Earth* 98, 6283–6297. doi:10.1029/92JB02650
- Morgan, Z. & Liang, Y. (2005). An experimental study of the kinetics of Iherzolite reactive dissolution with applications to melt channel formation. *Contributions to Mineralogy and Petrology* 150, 369–385. doi:10.1007/s00410-005-0033-8

- Müller, R. D., Sdrolias, M., Gaina, C. & Roest, W. R. (2008). Age, spreading rates, and spreading asymmetry of the world's ocean crust. *Geochemistry, Geophysics, Geosystems* 9, 1–19. doi:10.1029/2007GC001743
- Müntener, O., Manatschal, G., Desmurs, L. & Pettke, T. (2010). Plagioclase peridotites in ocean-continent transitions: Refertilized mantle domains generated by melt stagnation in the shallow mantle lithosphere. *Journal of Petrology* 51, 255–294. doi:10.1093/petrology/egp087
- Munsch, M. & Schlich, R. (1990). Etude géophysique détaillée du point triple de Rodriguez et de la zone axiale des trois dorsales associées (Océan Indien). *Oceanologica Acta* 10.
- Mysen, B. O. (1995). Experimental, in situ, high-temperature studies of properties and structure of silicate melts relevant to magmatic processes. *European Journal of Mineralogy* 7, 745–766.
- Mysen, B. O. (2007). Olivine/melt transition metal partitioning, melt composition, and melt structure-Influence of Al³⁺ for Si⁴⁺ substitution in the tetrahedral network of silicate melts. *Geochimica et Cosmochimica Acta* 71, 5500–5513. doi:10.1016/j.gca.2007.09.021
- Mysen, B. O. (2008). Olivine/melt transition metal partitioning, melt composition, and melt structure-Melt polymerization and Qn-speciation in alkaline earth silicate systems. *Geochimica et Cosmochimica Acta* 72, 4796–4812. doi:10.1016/j.gca.2008.07.010
- Mysen, B. O. & Dubinsky, E. V. (2004). Melt structural control on olivine/melt element partitioning of Ca and Mn. *Geochimica et Cosmochimica Acta* 68, 1617–1633. doi:10.1016/j.gca.2003.09.010
- Mysen, B. O. & Shang, J. (2005). Evidence from olivine/melt element partitioning that nonbridging oxygen in silicate melts are not equivalent. *Geochimica et Cosmochimica Acta* 69, 2861–2875. doi:10.1016/j.gca.2004.12.028
- Mysen, B. & Richet, P. (2005). *Silicate glasses and melts*. Elsevier Science
- Nagasawa, H. (1966). Trace Element Partition Coefficient in Ionic Crystals. *Science* 152, 767–769. doi:10.1126/science.152.3723.767
- Natland, J. H. & Dick, H. J. B. (2001). Formation of the lower ocean crust and the crystallization of gabbroic cumulates at a very slowly spreading ridge. *Journal of Volcanology and Geothermal Research* 110, 191–233. doi:10.1016/S0377-0273(01)00211-6
- Navon, O. & Stolper, E. M. (1987). Geochemical consequences of melt percolation - the Upper Mantle as a chromatographic column. *Journal of Geology* 95, 285–307.
- Nicolas, A. (1986). A melt extraction model based on structural studies in mantle peridotites. *Journal of Petrology* 27, 999–1022. doi:10.1093/petrology/27.4.999
- Nicolas, A., Reuber, I. & Benn, K. (1988). A new magma chamber model based on structural studies in the Oman ophiolite. *Tectonophysics* 151, 87–105. doi:10.1016/0040-1951(88)90242-9
- Nicolas, A., Boudier, F., Ildefonse, B. & Ball, E. (2000). Accretion of Oman and United Arab Emirates ophiolite – Discussion of a new structural map. *Marine Geophysical Researches* 21, 147–180. doi:10.1023/A:1026769727917
- Niu, Y. (1997). Mantle Melting and Melt Extraction Processes beneath Ocean Ridges: Evidence from Abyssal Peridotites. *Journal of Petrology* 38, 1047–1074. doi:10.1093/petrology/38.8.1047

- Niu, Y. (2004). Bulk-rock major and trace element compositions of abyssal peridotites: Implications for mantle melting, melt extraction and post-melting processes beneath Mid-Ocean ridges. *Journal of Petrology* 45, 2423–2458. doi:10.1093/petrology/egh068
- Niu, Y. & O'Hara, M. J. (2008). Global correlations of ocean ridge basalt chemistry with axial depth: A new perspective. *Journal of Petrology* 49, 633–664. doi:10.1093/petrology/egm051
- Nonnotte, P., Ceuleneer, G. & Benoit, M. (2005). Genesis of andesitic-boninitic magmas at mid-ocean ridges by melting of hydrated peridotites: Geochemical evidence from DSDP Site 334 gabbro-norites. *Earth and Planetary Science Letters* 236, 632–653.
- O'Driscoll, B., Donaldson, C. H., Troll, V. R., Jerram, D. A. & Emeleus, C. H. (2007). An origin for harrisitic and granular olivine in the rum layered suite, NW Scotland: A crystal size distribution study. *Journal of Petrology* 48, 253–270. doi:10.1093/petrology/egl059
- O'Hara, M. J. (1965). Primary magmas and the origin of basalts. *Scottish Journal of Geology* 1, 19–40. doi:10.1144/sjg01010019
- O'Hara, M. J. & Fry, N. (1996). The Highly Compatible Trace Element Paradox — Fractional Crystallization Revisited. *Journal of Petr* 37, 859–890. doi:10.1093/petrology/37.4.859
- O'Hara, M. J. & Herzberg, C. (2002). Interpretation of trace element and isotope features of basalts: Relevance of field relations, petrology, major element data, phase equilibria, and magma chamber modeling in basalt petrogenesis. *Geochimica et Cosmochimica Acta* 66, 2167–2191. doi:10.1016/S0016-7037(02)00852-9
- O'Neill, H. & Jenner, F. E. (2012). The global pattern of trace-element distributions in ocean floor basalts. *Nature* 491, 698–704. doi:10.1038/nature11678
- Onsager, L. (1945). Theories and Problems of Liquid Diffusion. *Annals of the New York Academy of Sciences* 46, 241–265. doi:10.1111/j.1749-6632.1945.tb36170.x
- Oxburgh, E. R. (1980). Heat flow and magma genesis. In: Hargraves, R. B. (ed.) *Physics of magmatic processes*. Princeton University Press, Princeton, NJ, 161–199.
- Pallister, J. S. & Hopson, C. a. (1981). Samail Ophiolite plutonic suite: Field relations, phase variation, cryptic variation and layering, and a model of a spreading ridge magma chamber. *Journal of Geophysical Research* 86, 2593–2644. doi:10.1029/JB086iB04p02593
- Paquet, M., Cannat, M., Brunelli, D., Hamelin, C. & Hulmer, E. (2016). Effect of melt/mantle interactions on MORB chemistry at the easternmost Southwest Indian Ridge (61°–67°E). *Geochemistry Geophysics Geosystems* 17, 2825–2834.
- Patriat, P., Sauter, D., Munsch, M. & Parson, L. (1997). A Survey of the Southwest Indian Ridge Axis Between Atlantis II Fracture Zone and the Indian Ocean Triple Junction: Regional Setting and Large Scale Segmentation. *Marine Geophysical Researches* 19, 457–480.
- Patriat, P., Sloan, H. & Sauter, D. (2008). From slow to ultraslow: A previously undetected event at the Southwest Indian Ridge at ca. 24 Ma. *Geology* 36, 207–210.
- Paulick, H., Bach, W., Godard, M., De Hoog, J.C.M., Suhr, G. & Harvey, J. (2006). Geochemistry of abyssal peridotites (Mid-Atlantic Ridge, 15°20'N, ODP Leg 209): Implications for fluid/rock interaction in slow spreading environments. *Chemical Geology* 234, 179–210. doi:10.1016/j.chemgeo.2006.04.011

- Pearce, N.J.G., Perkins, W.T., Westgate, J.A., Gorton, M.P., Jackson, S.E., Neal, C.R. & Chenery S.P. (1997). A compilation of new and published major and trace element data for NIST SRM 610 and NIST SRM 612 glass reference materials. *Geostandards Newsletter: The Journal of Geostandards and Analysis* 21, 115 – 144.
- Pec, M., Holtzman, B. K., Zimmerman, M. & Kohlstedt, D. L. (2017). Reaction infiltration instabilities in mantle rocks: an experimental investigation. *Journal of Petrology* 58, 979–1004. doi:10.1130/G36611.1
- Perfit, M. R. and Chadwick, W. W. (1998) Magmatism at Mid-Ocean Ridges: Constraints from Volcanological and Geochemical Investigations, in *Faulting and Magmatism at Mid-Ocean Ridges* (eds W. Roger Buck, P. T. Delaney, J. A. Karson and Y. Lagabriele), American Geophysical Union, Washington, D. C.. doi: 10.1029/GM106p0059
- Petry, C., Chakraborty, S. & Palme, H. (2004). Experimental determination of Ni diffusion coefficients in olivine and their dependence on temperature, composition, oxygen fugacity, and crystallographic orientation. *Geochimica et Cosmochimica Acta* 68, 4179–4188. doi:10.1016/j.gca.2004.02.024
- Pettigrew, T.J., Casey, J.F., Miller, D.J., Araki, E., Boissonnas, R., Busby, R., Einaudi, F., Gerdomb, M., Guo, Z.P., Hoskins, H., Myers, G., Rao, D.G., Shibata, T., Thy P. (1999). *Proceedings of the Ocean Drilling Program, Initial Reports, 179*: College Station, TX (Ocean Drilling Program). doi:10.2973/odp.proc.ir.179.1999
- Peuble, S., 2014. *Caractérisation expérimentale des processus d’hydratation et de carbonatation des roches basiques et ultrabasiques*, PhD – University of Montpellier.
- Presnall, D. & Hoover, J. D. (1987). High pressure phase equilibrium constraints on the origin of mid-ocean ridge basalts. In: *Magmatic Processes: Physicochemical Principles*, B.O. Mysen (eds.). *Geochemical Society, Special Publication* 75–89.
- Presnall, D. C., Dixon, S. A., Dixon, J. R., O’Donnell, T. H., Brenner, N. L., Schrock, R. L. & Dycus, D. W. (1978). Liquidus phase relations on the join diopside-forsterite-anorthite from 1 atm to 20 kbar: Their bearing on the generation and crystallization of basaltic magma. *Contributions to Mineralogy and Petrology* 66, 203–220. doi:10.1007/BF00372159
- Presnall, D. C., Gudfinnsson, G. H. & Walter, M. J. (2002). Generation of mid-ocean ridge basalts at pressures from 1 to 7 GPa. *Geochimica et Cosmochimica Acta* 66, 2073–2090. doi:10.1016/S0016-7037(02)00890-6
- Prodehl, C., Kennett, B., Artemieva, I. M. & Thybo, H. (2013). 100 years of seismic research on the Moho. *Tectonophysics* 609, 9–44. doi:10.1016/j.tecto.2013.05.036
- Quick, J. E. & Denlinger, R. P. (1993). Ductile deformation and the origin of layered gabbro in ophiolites. *Journal of Geophysical Research* 98, 14015–14027. doi:10.1029/93JB00698
- Rabinowicz, M. & Ceuleneer, G. (2005). The effect of sloped isotherms on melt migration in the shallow mantle: A physical and numerical model based on observations in the Oman ophiolite. *Earth and Planetary Science Letters* 229, 231–246. doi:10.1016/j.epsl.2004.09.039
- Rabinowicz, M., Nicolas, A. & Vigneresse, J. L. (1984). A rolling mill effect in asthenosphere beneath oceanic spreading centers. *Earth and Planetary Science Letters* 67, 97–108. doi:10.1016/0012-821X(84)90042-6

- Raith, R. W. (1963). The crustal rocks. In: Hill M.N. (edit), *The Sea*, vol. 3, Wiley Interscience, New York, 85-102.
- Rampone, E. & Borghini, G. (2008). Melt migration and intrusion in the Erro-Tobbio peridotites (Ligurian Alps, Italy): Insights on magmatic processes in extending lithospheric mantle. *European Journal of Mineralogy* 20, 573–585. doi:10.1127/0935-1221/2008/0020-1807
- Rampone, E., Borghini, G., Godard, M., Ildefonse, B., Crispini, L. & Fumagalli, P. (2016). Melt/rock reaction at oceanic peridotite/gabbro transition as revealed by trace element chemistry of olivine. *Geochimica et Cosmochimica Acta* 190, 309–331. doi:10.1016/j.gca.2016.06.029
- Rampone, E., Piccardo, G. B., Vannucci, R. & Bottazzi, P. (1997). Chemistry and origin of trapped melts in ophiolitic peridotites. *Geochimica et Cosmochimica Acta* 61, 4557–4569. doi:10.1016/s0016-7037(97)00260-3
- Renna, M. R. & Tribuzio, R. (2011). Olivine-rich troctolites from Ligurian ophiolites (Italy): Evidence for impregnation of replacive mantle conduits by MORB-type melts. *Journal of Petrology* 52, 1763–1790. doi:10.1093/petrology/egr029
- Riley, G. N. & Kohlstedt, D. L. (1991). Kinetics of melt migration in upper-mantle type rocks. *Earth and Planetary Science Letters* 105, 500–521.
- Rioux, M., Cheadle, M. J., John, B. E. & Bowring, S. A. (2016). The temporal and spatial distribution of magmatism during lower crustal accretion at an ultraslow-spreading ridge: High-precision U–Pb zircon dating of ODP Holes 735B and 1105A, Atlantis Bank, Southwest Indian Ridge. *Earth and Planetary Science Letters* 449, 395–406. doi:10.1016/j.epsl.2016.05.047
- Robinson, P.T., Von Herzen, R., et al., 1989. *Proceedings of the Ocean Drilling Program, Initial Reports*, 118: College Station, TX (Ocean Drilling Program).
- Rocholl, A.B.E., Simon K., Jochum K.P., Bruhn F., Gehann R., Kramar U., Luecke W., Molzahn M., Pernicka E., Seufert M., Spettel B. & Stummeier J. (1997). Chemical characterisation of NIST silicate glass certified reference material SRM 610 by ICP-MS, TIMS, LIMS, SSMS, INAA, AAS and PIXE. *Geostandards Newsletter: The Journal of Geostandards and Geoanalysis* 21, 101–114.
- Rollinson, H. R., Searle, M. P., Abbasi, I. A., Al-Lazki, A. I. & Al Kindi, M. H. (2014). Tectonic Evolution of the Oman Mountains. *Geological Society of London, Special Publications* 392, 1-7. doi:10.1144/sp392
- Rosenbaum, J.M., Zindler, A., Rubenstone, J.L., 1996. Mantle fluids: evidence from fluid inclusions. *Geochimica et Cosmochimica Acta* 60, 3229–3252.
- Ross, D.K. & Elthon, D. (1997). Cumulus and postcumulus crystallization in the oceanic crust: major- and trace-element geochemistry of Leg 153 gabbroic rocks. In: *Proceedings of the Ocean Drilling Program 153, Sci. Results*, 333–353. doi:10.2973/odp.proc.sr.153.023.1997
- Rouméjon, S. & Cannat, M. (2014). Serpentinization of mantle derived peridotites at mid ocean ridges: mesh texture in the context of tectonic exhumation. 2354–2379.
- Salters, V.J.M., Longhi, J.E. & Bizimis, M. (2002). Near mantle solidus trace element partitioning at pressures up to 3.4 GPa. *Geochemistry, Geophysics, Geosystems* 3, 1–23. doi:10.1029/2001GC000148

- Sanfilippo, A., Dick, H. J. B. & Ohara, Y. (2013). Melt-rock reaction in the mantle: Mantle troctolites from the parecevela ancient back-arc spreading center. *Journal of Petrology* 54, 861–885. doi:10.1093/petrology/egs089
- Sanfilippo, A., Morishita, T., Kumagai, H., Nakamura, K., Okino, K., Hara, K., Tamura, A. & Arai, S. (2015a). Hybrid troctolites from mid-ocean ridges: Inherited mantle in the lower crust. *Lithos* 232, 124–130. doi:10.1016/j.lithos.2015.06.025
- Sanfilippo, A., Tribuzio, R., Ottolini, L. & Hamada, M. (2017). Water, lithium and trace element compositions of olivine from Lanzo South replacive mantle dunites (Western Alps): New constraints into melt migration processes at cold thermal regimes. *Geochimica et Cosmochimica Acta* 214, 51–72. doi:10.1016/j.gca.2017.07.034
- Sanfilippo, A., Tribuzio, R. & Tiepolo, M. (2014). Mantle-crust interactions in the oceanic lithosphere: Constraints from minor and trace elements in olivine. *Geochimica et Cosmochimica Acta* 141, 423–439. doi:10.1016/j.gca.2014.06.012
- Sanfilippo, A., Tribuzio, R., Tiepolo, M. & Berno, D. (2015b). Reactive flow as dominant evolution process in the lowermost oceanic crust: evidence from olivine of the Pineto ophiolite (Corsica). *Contributions to Mineralogy and Petrology* 170, 38. doi:10.1007/s00410-015-1194-8
- Sanfilippo, A. & Tribuzio, R. (2011). Melt transport and deformation history in a nonvolcanic ophiolitic section, northern Apennines, Italy: Implications for crustal accretion at slow spreading settings. *Geochemistry, Geophysics, Geosystems* 12, 1–34. doi:10.1029/2010GC003429
- Sanfilippo, A. & Tribuzio, R. (2013). Building of the deepest crust at a fossil slow-spreading centre (Pineto gabbroic sequence, Alpine Jurassic ophiolites). *Contribution to Mineralogy and Petrology* 165, 705–721. doi:10.1007/s00410-012-0831-8
- Saper, L. & Liang, Y. (2014). Formation of plagioclase-bearing peridotite and plagioclase-bearing wehrlite and gabbro suite through reactive crystallization: An experimental study. *Contributions to Mineralogy and Petrology* 167, 1–16. doi:10.1007/s00410-014-0985-7
- Sauter, D. & Cannat, M. (2010). Diversity of Hydrothermal Systems on Slow Spreading Ocean Ridges: The Ultraslow Spreading Southwest Indian Ridge. *Geophysical Monograph Series* 188 153–173.
- Sauter, D., Parson, L., Mendel, V., Rommevaux-Jestin, C., Gomez, O., Briaes, A., Mével, C. & Tamaki, K. (2002). TOBI sidescan sonar imagery of the very slow-spreading Southwest Indian Ridge: Evidence for along-axis magma distribution. *Earth and Planetary Science Letters* 199, 81–95.
- Sauter, D., Patriat, P., Rommevaux-Jestin, C., Cannat, M., Briaes, A. & Gallieni Shipboard Scientific Party (2001). The Southwest Indian Ridge between 49°15'E and 57°E: focused accretion and magma redistribution. *Earth and Planetary Science Letters* 192, 303–317.
- Sauter, D., Cannat, M., Rouméjon, S., Andreani, M., Birot, D., Bronner, A., Brunelli, D., Carlut, J., Delacour, A., Guyader, V., MacLeod, C.J., Manatschal, G., Mendel, V., Ménez, B., Pasini, V., Ruellan, E. & Searle, R. (2013). Continuous exhumation of mantle-derived rocks at the Southwest Indian Ridge for 11 million years. *Nature Geosciences* 6, 314–320. doi:10.1038/ngeo1771

- Schiano, P., Clocchiatti, R., Shimizu, N., Maury, R.C., Jochum, K.P. & Hofmann, A.W. (1995). Hydrous, silica-rich melts in the sub-arc mantle and their relationship with erupted arc lavas. *Nature* 377, 595–600.
- Schilling, J.-G. (1973). Iceland Mantle Plume: Geochemical Study of Reykjanes Ridge. *Nature* 242, 565–571. doi:10.1038/242565a0
- Schroeder, T. & John, B.E. (2004). Strain localization on an oceanic detachment fault system, Atlantis Massif, 30°N, Mid-Atlantic Ridge. *Geochemistry, Geophysics Geosystems* 5. doi:10.1029/2004GC000728
- Schwarzer R.A. (1997) Automated crystal lattice orientation mapping using a computer-controlled SEM. *Micron* 28, 249–265.
- Sempéré, J.-C., Lin, J., Brown, H. S., Schouten, H. & Purdy, G. M. (1993). Segmentation and morphotectonic variations along a slow-spreading center: the Mid-Atlantic Ridge (24°N–30°40'N). *Marine Geophysical Researches* 15, 153–200.
- Seyfried, W. E., Pester, N. J., Ding, K. & Rough, M. (2011). Vent fluid chemistry of the Rainbow hydrothermal system (36°N, MAR): Phase equilibria and in situ pH controls on seafloor alteration processes. *Geochimica et Cosmochimica Acta*. Elsevier Ltd 75, 1574–1593.
- Seyfried, W.E., Pester, N.J., Tutolo, B.M. & Ding, K. (2015). The Lost City hydrothermal system: Constraints imposed by vent fluid chemistry and reaction path models on seafloor heat and mass transfer processes. *Geochimica et Cosmochimica Acta* 163, 59–79. doi:10.1016/j.gca.2015.04.040
- Seyler, M., Lorand, J. P., Dick, H. J. B. & Drouin, M. (2007). Pervasive melt percolation reactions in ultra-depleted refractory harzburgites at the Mid-Atlantic Ridge, 15° 20'N: ODP Hole 1274A. *Contributions to Mineralogy and Petrology* 153, 303–319. doi:10.1007/s00410-006-0148-6
- Shaw, D. M. (1970). Trace element fractionation during anatexis. *Geochimica et Cosmochimica Acta* 34, 237–243.
- Shen, Y. & Forsyth, D. W. (1995). Geochemical constraints on initial and final depths of melting beneath mid-ocean ridges. *Journal of Geophysical Research: Solid Earth* 100, 2211–2237. doi:10.1029/94JB02768
- Singh, S.C., Crawford, W.C., Carton, H., Seher, T., Combiér, V., Cannat, M., Pablo Canales, J., Düsünür, D., Escartin, J. & Miranda, J.M. (2006). Discovery of a magma chamber and faults beneath a Mid-Atlantic Ridge hydrothermal field. *Nature* 442, 1029–1032. doi:10.1038/nature05105
- Sleep, N. H. (1975). Formation of oceanic crust: Some thermal constraints. *Journal of Geophysical Research* 80, 4037–4042.
- Smith, D. K., Cann, J. R. & Escartín, J. (2006). Widespread active detachment faulting and core complex formation near 13° N on the Mid-Atlantic Ridge. *Nature* 442, 4037–4042. doi:10.1029/JB080i029p04037
- Smith, D. K., Escartín, J., Schouten, H. & Cann, J. R. (2008). Fault rotation and core complex formation: Significant processes in seafloor formation at slow-spreading mid-ocean ridges (Mid-Atlantic Ridge, 13°-15°N). *Geochemistry, Geophysics, Geosystems* 9. doi:10.1029/2007GC001699

- Solomon, S. C. & Toomey, D. R. (1992). The structure of Mid-ocean ridges. *Annual Reviews Earth Planetary Sciences* 20, 329–64.
- Soule, S. A., Fornari, D. J., Perfit, M. R. & Rubin, K. H. (2007). New insights into mid-ocean ridge volcanic processes from the 2005-2006 eruption of the East Pacific Rise, 9°46'N-9°56'N. *Geology* 35, 1079–1082. doi:10.1130/G23924A.1
- Spandler, C., O'Neill, H.S.C., 2010. Diffusion and partition coefficients of minor and trace elements in San Carlos olivine at 1,300°C with some geochemical implications. *Contributions to Mineralogy and Petrology* 159, 1–28. doi:10.1007/s00410-009-0456-8
- Spandler, C., O'Neill, H.S.C., Kamenetsky, V.S., 2007. Survival times of anomalous melt inclusions from element diffusion in olivine and chromite. *Nature* 447, 303–306. doi:10.1038/nature05759
- Sparks, D. W. & Parmentier, E. M. (1991). Melt extraction from the mantle beneath spreading centers. *Earth and Planetary Science Letters* 105, 368–377. doi:10.1016/0012-821X(91)90178-K
- Spiegelman, M. (1993). Physics of Melt Extraction: Theory, Implications and Applications. *Philosophical Transactions of the Royal Society A: Mathematical, Physical and Engineering Sciences* 342, 23–41. doi:10.1098/rsta.1993.0002
- Spiegelman, M., Kelemen, P. B. & Aharonov, E. (2001). Causes and consequences of flow organization during melt transport: the reaction infiltration instability in compactible media. *Journal of Geophysical Research* 106, 2061–2077. doi:10.1029/2000JB900240
- Spiegelman, M. & Kenyon, P. (1992). The requirements for chemical disequilibrium during magma migration. *Earth and Planetary Science Letters* 109, 611–620. doi:10.1016/0012-821X(92)90119-G
- Spiegelman, M. & McKenzie, D. (1987). Simple 2-D models for melt extraction at mid-ocean ridges and island arcs. *Earth and Planetary Science Letters* 83, 137–152. doi:10.1016/0012-821X(87)90057-4
- Stakes, D. S., Perfit, M. R., Tivey, M. A., Caress, D. W., Ramirez, T. M. & Maher, N. (2006). The Cleft revealed: Geologic, magnetic, and morphologic evidence for construction of upper oceanic crust along the southern Juan de Fuca Ridge. *Geochemistry, Geophysics, Geosystems* 7. doi:10.1029/2005GC001038
- Standish, J. J., Dick, H. J. B., Michael, P. J., Melson, W. G. & O'Hearn, T. (2008). MORB generation beneath the ultraslow spreading Southwest Indian Ridge (9°-25°E): Major element chemistry and the importance of process versus source. *Geochemistry, Geophysics, Geosystems* 9.
- Stevenson, D. J. (1989). Spontaneous small-scale melt segregation in partial melts undergoing deformation. *Geophysical Research Letters* 16, 1067–1070. doi:10.1029/GL016i009p01067
- Stolper, E. M. (1980). A phase diagram for Mid-Ocean Ridge basalts: preliminary results and implications for petrogenesis. *Contributions to Mineralogy and Petrology* 74, 13–27.
- Sun, C., Graff, M. & Liang, Y. (2017). Trace element partitioning between plagioclase and silicate melt: The importance of temperature and plagioclase composition, with implications for terrestrial and lunar magmatism. *Geochimica et Cosmochimica Acta* 206, 273–295. doi:10.1016/j.gca.2017.03.003

- Sun, C. & Liang, Y. (2012). Distribution of REE between clinopyroxene and basaltic melt along a mantle adiabat: Effects of major element composition, water, and temperature. *Contributions to Mineralogy and Petrology* 163, 807–823. doi:10.1007/s00410-011-0700-x
- Sun, C. & Liang, Y. (2014). An assessment of subsolidus re-equilibration on REE distribution among mantle minerals olivine, orthopyroxene, clinopyroxene, and garnet in peridotites. *Chemical Geology*. Elsevier B.V. 372, 80–91. doi:10.1016/j.chemgeo.2014.02.014
- Suhr, G., Hellebrand, E., Johnson, K. & Brunelli, D. (2008). Stacked gabbro units and intervening mantle: A detailed look at a section of IODP Leg 305, Hole U1309D. *Geochemistry, Geophysics, Geosystems* 9. doi:10.1029/2008GC002012
- Sun, S. -s. & McDonough, W.F. (1989). Chemical and isotopic systematics of oceanic basalts: implications for mantle composition and processes. *Geological Society of London, Special Publications* 42, 313–345. doi:10.1144/GSL.SP.1989.042.01.19
- Takahashi, E. (1986). Melting of a dry peridotite KLB-1 up to 14 GPa: Implications on the Origin of peridotitic upper mantle. *Journal of Geophysical Research* 91, 9367–9382. doi:10.1029/JB091iB09p09367
- Takahashi, E. & Kushiro, I. (1983). Melting of a dry peridotite at high pressures and basalt magma genesis. *American Mineralogist* 68, 859–879. doi:10.1144/gsjgs.139.6.0771
- Takahashi, E., Shimazaki, T., Tsuzaki, Y. & Yoshida, H. (1993). Melting Study of a Peridotite KLB-1 to 6.5 GPa, and the Origin of Basaltic Magmas. *Philosophical Transactions of the Royal Society A: Mathematical, Physical and Engineering Sciences* 342, 105–120. doi:10.1098/rsta.1993.0008
- Tamura, A., Arai, S., Ishimaru, S. & Andal, E. S. (2008). Petrology and geochemistry of peridotites from IODP Site U1309 at Atlantis Massif, MAR 30°N: Micro- and macro-scale melt penetrations into peridotites. *Contributions to Mineralogy and Petrology* 155, 491–509. doi:10.1007/s00410-007-0254-0
- Tartarotti, P., Susini, S., Nimis, P. & Ottolini, L. (2002). Melt migration in the upper mantle along the Romanche Fracture Zone (Equatorial Atlantic). *Lithos* 63, 125–149. doi:10.1016/S0024-4937(02)00116-0
- Taura, H., Yurimoto, H., Kurita, K. & Sueno, S. (1998). Pressure dependence on partition coefficients for trace elements between olivine and the coexisting melts. *Physics and Chemistry of Minerals* 25, 469–484. doi:10.1007/s002690050138
- Teagle, D. A. H., Alt, J. C., Umino, S., Miyashita, S., Banerjee, N. R., Wilson, D. S., & the Expedition 309/312 Scientists. (2006). *Proc. IODP, 309/312*. Washington, DC: Integrated Ocean Drilling Program Management International, Inc. doi:10.2204/iodp.proc.309312.2006.
- Teagle, D.A.H., Ildefonse, B., Blum, P., & the Expedition 335 Scientists (2012). *Proceedings IODP, 335*. Tokyo: Integrated Ocean Drilling Program Management International, Inc. doi:10.2204/iodp.proc.335.2012.
- Tolstoy, M., Bohnenstiehl, D. R., Edwards, M. H. & Kurras, G. J. (2001). Seismic character of volcanic activity at the ultraslow-spreading Gakkel Ridge. *Geology* 29, 1139–1142. doi:10.1130/0091-7613(2001)029<1139:SCOVAA>2.0.CO;2

References

- Toomey, D., Solomon, S. & Purdy, G. (1988). Microearthquakes beneath Median Valley of Mid-Atlantic Ridge near 23°N: Tomography and tectonics. *Journal of Geophysical Research* 93, 9093–9112. doi:10.1029/JB093iB08p09093
- Toramaru, A. & Fujii, N. (1986). Connectivity of melt phase in a partially molten peridotite. *Journal of Geophysical Research: Solid Earth* 91, 9239–9252. doi:10.1029/JB091iB09p09239
- Tormey, D. R., Grove, T. L. & Bryan, W. B. (1987). Experimental petrology of N-MORB near the Kane Fracture Zone: 22-25°N, mid-Atlantic ridge. *Contributions to Mineralogy and Petrology* 96, 121–139.
- Tsai, T. L. & Dieckmann, R. (2002). Variation of the oxygen content and point defects in olivines, (Fex Mg_{1-x})₂SiO₄, 0.2 ≤ x ≤ 1.0. *Physics and Chemistry of Minerals* 29, 680–694. doi:10.1007/s00269-002-0283-1
- Tucholke, B. E., Behn, M. D., Buck, W. R. & Lin, J. (2008). Role of melt supply in oceanic detachment faulting and formation of megamullions. *Geology* 36, 455–458. doi:10.1130/G24639A.1
- Tucholke, B. E., Fujioka, K., Ishihara, T., Hirth, G. & Kinoshita, M. (2001). Submersible study of an oceanic megamullion in the central North Atlantic. *Journal of Geophysical Research* 106, 16,145–16,161. doi:10.1029/2001JB000373
- Tucholke, B. E. & Lin, J. (1994). A geological model for the structure of ridge segments in slow spreading ocean crust. *Journal of Geophysical Research* 99, 11,937–11,958. doi:10.1029/94JB00338.
- Tucholke, B. E., Lin, J. & Kleinrock, M. C. (1998). Megamullions and mullion structure defining oceanic metamorphic core complexes on the Mid-Atlantic Ridge. *Journal of Geophysical Research* 103, 9857–9866. doi:10.1029/98JB00167
- Tucholke, B. E., Lin, J., Kleinrock, M. C., Tivey, M. A., Reed, T. B., Goff, J. & Jaroslow, G. E. (1997). Segmentation and crustal structure of the western Mid-Atlantic Ridge flank, 25°25'–27°10'N and 0–29 m.y. *Journal of Geophysical Research* 102, 10203–10223.
- Tuff, J. & O'Neill, H. S. C. (2010). The effect of sulfur on the partitioning of Ni and other first-row transition elements between olivine and silicate melt. *Geochimica et Cosmochimica Acta* 74, 6180–6205. doi:10.1016/j.gca.2010.08.014
- Turcotte, D.L. & Morgan, J.P. (1992). The Physics of Magma Migration and Mantle Flow Beneath a Mid-Ocean Ridge. In: *Mantle Flow and Melt Generation at Mid-Ocean Ridges*, J. P. Morgan, D. B. Blackman, and J. M. Sinton (eds.), *Geophys. Monogr.* 71, 155–182, AGU, Washington, D. C. doi:10.1029/GM071p0155
- Tursack, E. & Liang, Y. (2012). A comparative study of melt-rock reactions in the mantle: Laboratory dissolution experiments and geological field observations. *Contributions to Mineralogy and Petrology* 163, 861–876. doi:10.1007/s00410-011-0703-7
- Ulmer, P. (1989). The dependence of the Fe²⁺-Mg cation-partitioning between olivine and basaltic liquid on pressure, temperature and composition - An experimental study to 30 kbars. *Contributions to Mineralogy and Petrology* 101, 261–273. doi:10.1007/BF00375311
- Umino, S., Miyashita, S., Hotta, F. & Adachi, Y. (2003). Along-strike variation of the sheeted dike complex in the Oman Ophiolite: Insights into subaxial ridge segment structures and the

- magma plumbing system. *Geochemistry, Geophysics, Geosystems* 4.
doi:10.1029/2001GC000233
- Van Achterbergh, E., Ryan, C.G., Jackson, S.E. & Griffin, W.L. (2001). Data reduction software for LA-ICP-MS: appendix; In Sylvester, P.J. (ed.), *Laser Ablation –ICP-Mass Spectrometry in the Earth Sciences: Principles and Applications*, Mineralogical Association of Canada Short Course Series, Ottawa, Ontario, Canada 29, 239-243.
- Van Ark, E. M. et al. (2007). Seismic structure of the endeavour segment, Juan de Fuca Ridge: Correlations with seismicity and hydrothermal activity. *Journal of Geophysical Research: Solid Earth* 112, 1–22. doi:10.1029/2005JB004210
- Van den Bleeken, G., Müntener, O. & Ulmer, P. (2011). Melt variability in percolated peridotite: An experimental study applied to reactive migration of tholeiitic basalt in the upper mantle. *Contrib. to Mineral. Petrol.* 161, 921–945. doi:10.1007/s00410-010-0572-5
- Van den Bleeken, G., Müntener, O. & Ulmer, P. (2010). Reaction processes between tholeiitic melt and residual peridotite in the uppermost mantle: An experimental study at 0.8 GPa. *Journal of Petrology* 51, 153–183. doi:10.1093/petrology/egp066
- Van Orman, J. A., Cherniak, D. J. & Kita, N. T. (2014). Magnesium diffusion in plagioclase: Dependence on composition, and implications for thermal resetting of the ²⁶Al-²⁶Mg early solar system chronometer. *Earth and Planetary Science Letters*. Elsevier B.V. 385, 79–88. doi:10.1016/j.epsl.2013.10.026
- Van Orman, J. A., Grove, T. L. & Shimizu, N. (1998). Uranium and thorium diffusion in diopside. *Earth and Planetary Science Letters* 160, 505–519. doi:10.1016/S0012-821X(98)00107-1
- Van Orman, J. A., Grove, T. L. & Shimizu, N. (2001). Rare earth element diffusion: influence of temperature, pressure, and ionic radius, and an elastic model for diffusion in silicates. *Contribution Mineralogy Petrology* 141, 687–703.
- VanTongeren, J. A., Kelemen, P. B. & Hanghøj, K. (2008). Cooling rates in the lower crust of the Oman ophiolite: Ca in olivine, revisited. *Earth and Planetary Science Letters* 267, 69–82.
- Vernières, J., Godard, M. & Bodinier, J.-L. (1997). A plate model for the simulation of trace element fractionation during partial melting and magma transport in the Earth's upper mantle. *Journal of Geophysical Research-Solid Earth* 102, 24771–24784.
- Vils, F., Tonarini, S., Kalt, A. & Seitz, H. M. (2009). Boron, lithium and strontium isotopes as tracers of seawater-serpentinite interaction at Mid-Atlantic ridge, ODP Leg 209. *Earth and Planetary Science Letters* 286, 414–425.
- Villiger, S., Müntener, O. & Ulmer, P. (2007a). Crystallization pressures of mid-ocean ridge basalts derived from major element variations of glasses from equilibrium and fractional crystallization experiments. *Journal of Geophysical Research: Solid Earth* 112, 1–18. doi:10.1029/2006JB004342
- Villiger, S., Ulmer, P. & Müntener, O. (2007b). Equilibrium and fractional crystallization experiments at 0.7 GPa; the effect of pressure on phase relations and liquid compositions of tholeiitic magmas. *Journal of Petrology* 48, 159–184. doi:10.1093/petrology/egl058
- Villiger, S., Ulmer, P., Müntener, O. & Thompson, A. B. (2004). The liquid line of descent of anhydrous, mantle-derived, tholeiitic liquids by fractional and equilibrium crystallization - An

- experimental study at 1.0 GPa. *Journal of Petrology* 45, 2369–2388. doi:10.1093/petrology/egh042
- von Barga, N. & Waff, H. S. (1986). Permeabilities, interfacial areas and curvatures of partially molten systems: results of numerical computations of equilibrium microstructures. *Journal of Geophysical Research* 91, 9261–9276.
- Walter, M. J. (2014). Melt Extraction and Compositional Variability in Mantle Lithosphere. In: *Treatise on Geochemistry* 3.10, 393-419, Second Edition. H. D. Holland, K.K. Turekian (eds.), Amsterdam.
- Walter, M. J. & Presnall, D. C. (1994). Melting Behavior of Simplified Lherzolite in the System CaO-MgO-Al₂O₃-SiO₂-Na₂O from 7 to 35 kbar. *Journal of Petrology* 35, 329–359.
- Wang, C., Liang, Y., Xu, W. & Dygert, N. (2013). Effect of melt composition on basalt and peridotite interaction: Laboratory dissolution experiments with applications to mineral compositional variations in mantle xenoliths from the North China Craton. *Contribution to Mineralogy and Petrology* 166, 1469–1488. doi:10.1007/s00410-013-0938-6
- Wark, D. A. & Watson, E. B. (1998). Grain-scale permeabilities of texturally equilibrated, monomineralic rocks. *Earth and Planetary Science Letters* 164, 591–605. doi:10.1016/S0012-821X(98)00252-0
- Watson, E.B. & Brenan, J. M. (1987). Fluids in the lithosphere, 1. Experimentally-determined wetting characteristics of CO₂H₂O fluids and their implications for fluid transport, host-rock physical properties, and fluid inclusion formation. *Earth and Planetary Science Letters* 85, 497–515. doi:10.1016/0012-821X(87)90144-0
- Watson, E. B., Cherniak, D. J. & Holycross, M. E. (2015). Diffusion of phosphorus in olivine and molten basalt. *American Mineralogist* 100, 2053–2065.
- Welsch, B., Hammer, J. & Hellebrand, E. (2014). Phosphorus zoning reveals dendritic architecture of olivine. *Geology* 42, 867–870.
- White, S. M., Haymon, R. M., Fornari, D. J., Perfit, M. R. & Macdonald, K. C. (2002). Correlation between volcanic and tectonic segmentation of fast-spreading ridges: Evidence from volcanic structures and lava flow morphology on the East Pacific Rise at 9°-10°N. *Journal of Geophysical Research-Solid Earth* 107 (B8), EPM 7-1–EPM 7-20. doi:10.1029/2001JB000571
- White, S. M., Mason, J. L., Macdonald, K. C., Perfit, M. R., Wanless, V. D. & Klein, E. M. (2009). Significance of widespread low effusion rate eruptions over the past two million years for delivery of magma to the overlapping spreading centers at 9°N East Pacific Rise. *Earth and Planetary Science Letters* 280, 175–184. doi:10.1016/j.epsl.2009.01.030
- White, W. M. (2013). *Geochemistry*, John Wiley and Sons, UK
- White, W. M. & Klein, E. M. (2014). Composition of the Oceanic Crust. In: *Treatise on Geochemistry* 4.13, 457 - 496, Second Edition. H. D. Holland, K.K. Turekian (eds.), Amsterdam. doi:10.1016/B978-0-08-095975-7.00315-6
- Wilson, D. S., Teagle, D. A. H., Acton, G. D., & ODP Leg 206 Scientific Party. (2003). *Proc. ODP, Init. Repts.*, 206. College Station: TX (Ocean Drilling Program). doi:10.2973/odp.proc.ir.206.2003.
- Witt-Eickschen, G. & O'Neill, H. S. C. (2005). The effect of temperature on the equilibrium distribution of trace elements between clinopyroxene, orthopyroxene, olivine and spinel in

- upper mantle peridotite. *Chemical Geology* 221, 65–101.
doi:10.1016/j.chemgeo.2005.04.005
- Wood, B. J. & Blundy, J. D. (2001). The effect of cation charge on crystal–melt partitioning of trace elements. *Earth and Planetary Science Letters* 188, 59–71. doi:10.1016/S0012-821X(01)00294-1
- Wood, B. J. & Blundy, J. D. (2003). Trace Element Partitioning under Crustal and Uppermost Mantle Conditions: The Influences of Ionic Radius, Cation Charge, Pressure, and Temperature. In: *Treatise on Geochemistry* 2.09, 395–424, Carlson, R.W. (eds.), Amsterdam.
- Wood, B. J. & Blundy, J. D. (2014). Trace Element Partitioning: The Influences of Ionic Radius, Cation Charge, Pressure, and Temperature. In: *Treatise on Geochemistry* 3.11, 421–448, Second Edition. H. D. Holland, K.K. Turekian (eds.), Amsterdam. 10.1016/B978-0-08-095975-7.00209-6
- Workman, R.K., Hart, S.R., 2005. Major and trace element composition of the depleted MORB mantle (DMM). *Earth and Planetary Science Letters* 231, 53–72.
doi:10.1016/j.epsl.2004.12.005
- Xuejin Wang & Cochran, J. R. (1995). Along-axis gravity gradients at mid-ocean ridges: implications for mantle flow and axial morphology. *Geology* 23, 29–32.
- Yang, H.-J., Kinzler, R. J. & Grove, T. L. (1996). Experiments and models of anhydrous, basaltic olivine-plagioclase-augite saturated melts from 0.001 to 10 kbar. *Contributions to Mineralogy and Petrology* 124, 1–18. doi:10.1007/s004100050169
- Zhang, J. & Herzberg, C. (1994). Melting experiments on anhydrous peridotite KLB-1 from 5.0 to 22.5 GPa. *Journal of Geophysical Research* 99, 17,729–17,742. 10.1029/94JB01406
- Zhang, X., Ganguly, J. & Ito, M. (2010). Ca-Mg diffusion in diopside: Tracer and chemical inter-diffusion coefficients. *Contributions to Mineralogy and Petrology* 159, 175–186.
doi:10.1007/s00410-009-0422-5
- Zhang, Y. & Cherniak, D. J. (2010). Diffusion in Minerals and Melts. *Reviews in Mineralogy and Geochemistry*. doi:10.2138/rmg.2010.72.2
- Zhang, Y., Walker, D. & Leshner, C. E. (1989). Diffusive crystal dissolution. *Contributions to Mineralogy and Petrology* 102, 492–513. doi:10.1007/BF00371090

Appendix

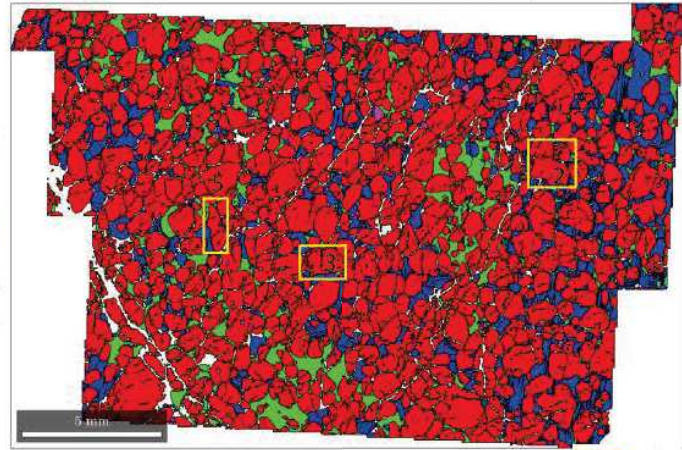
Appendix 1

Appendix 1 contains a summary of microstructures of olivine-rich troctolites from IODP Hole U1309D (Atlantis Massif). Each page is one sample. The location of samples in the core section is shown together with the thin section image. Modal abundances reported on the side of the core image (O = olivine, C = clinopyroxene, P = plagioclase) were calculated using the code Image J. EBSD maps presented include: phase map, Misorientation to the mean orientation (Mis2Mean) map of olivines and the Kernel Average Misorientation (KAM) map of olivines. Olivines pole figures are also reported for each sample.

305-U1309D-227R-3W (1095 mbsf)

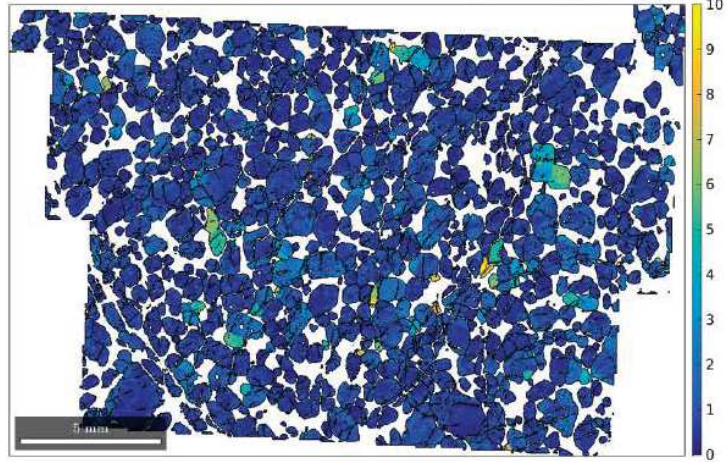
305-U1309D-227R-3W, 124-126

Phase map

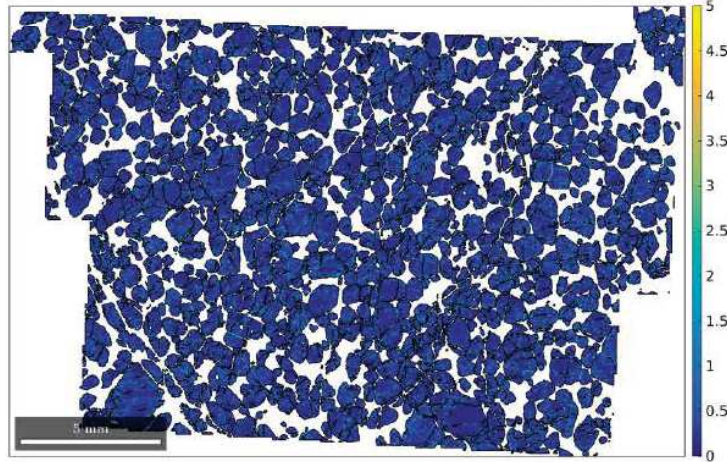


spl
ol
plg
cpx

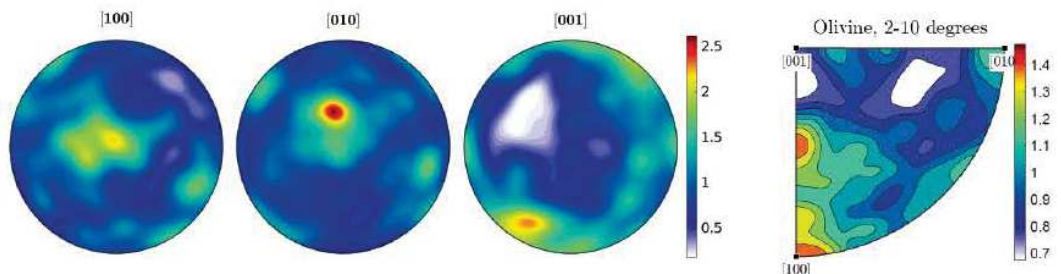
Olivine Mis2Mean



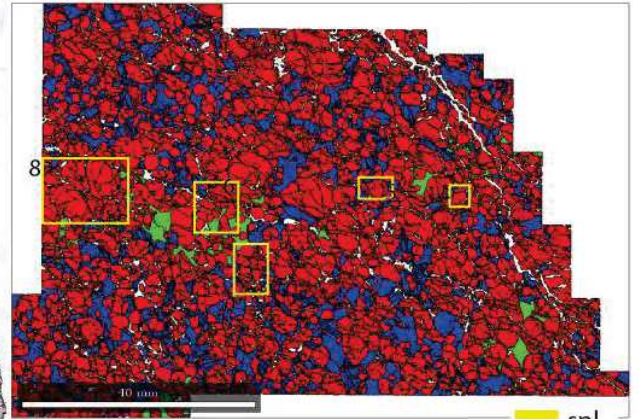
Olivine KAM



Olivine

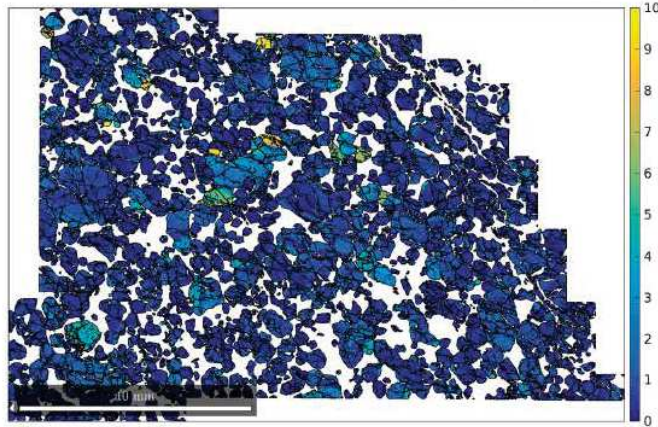


305-U1309D-234R-1W (1124 mbsf)

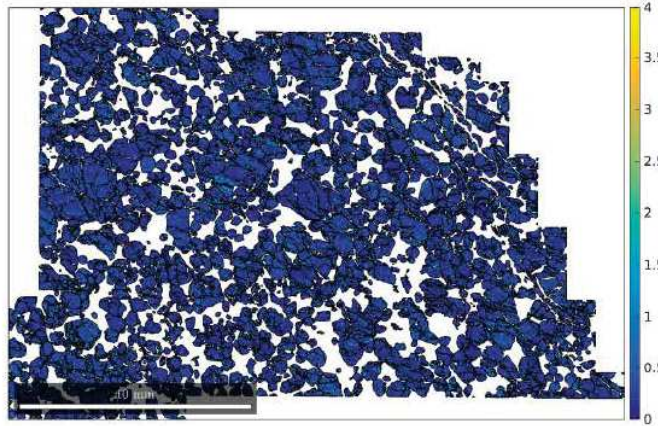


- spl
- ol
- plg
- cpx

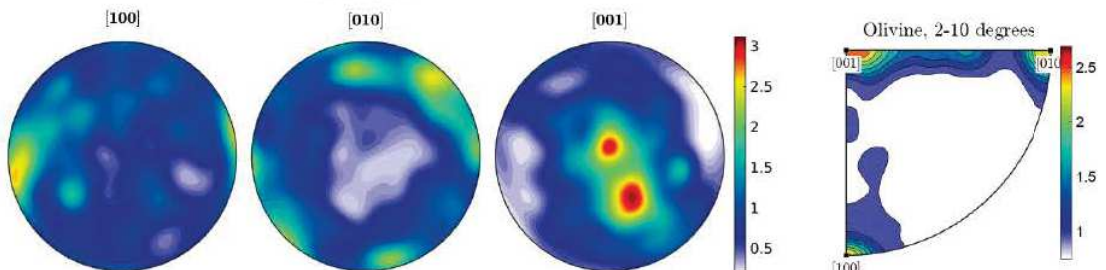
Olivine Mis2Mean



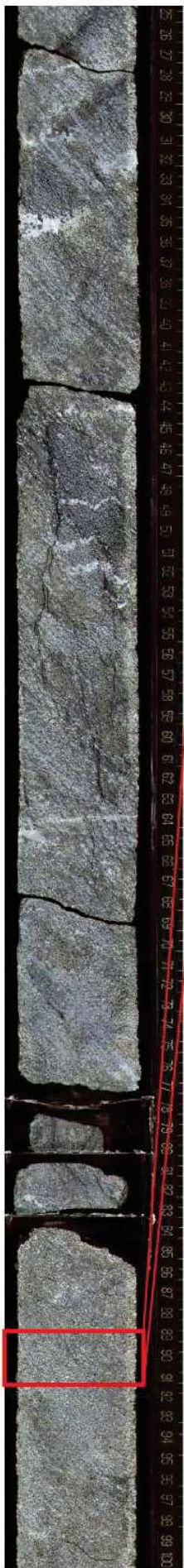
Olivine KAM



Olivine



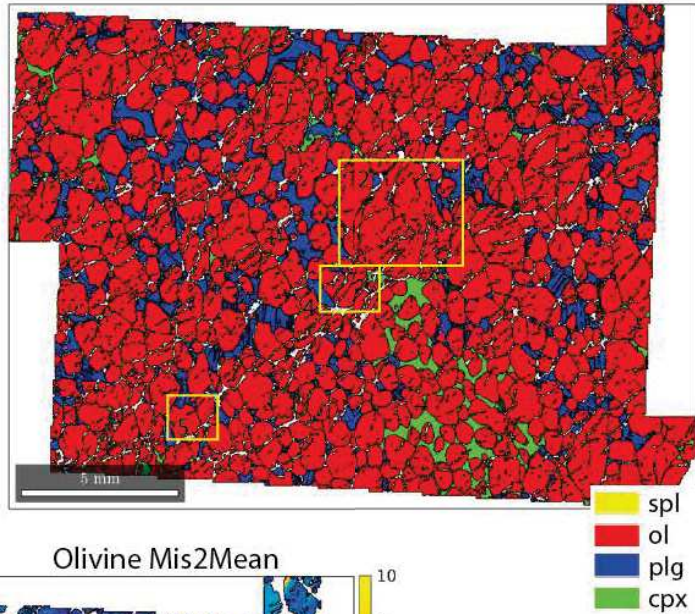
305-U1309D-241R-2W (1160 mbsf)



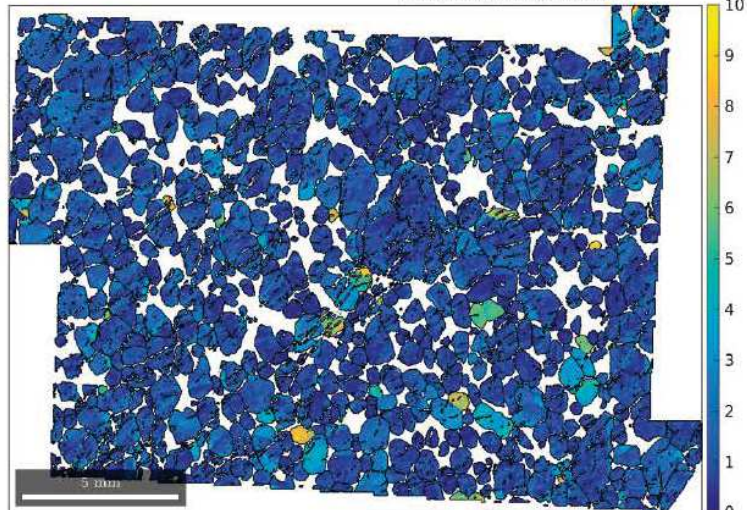
305-U1309D-241R-2W, 89-91



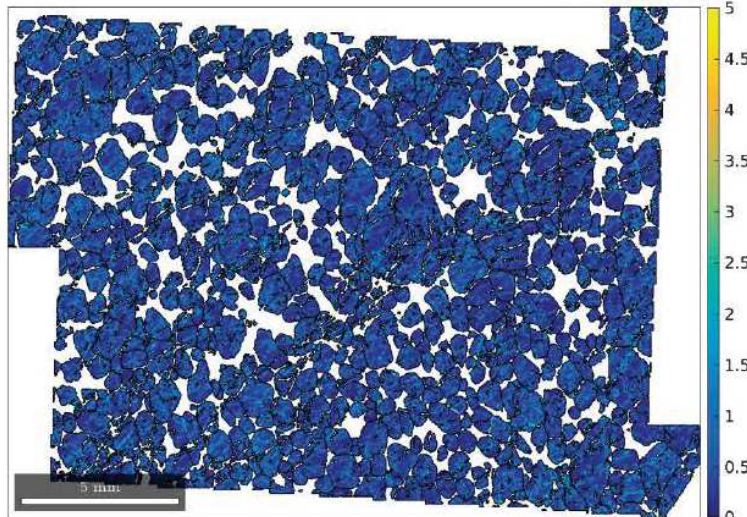
Phase map



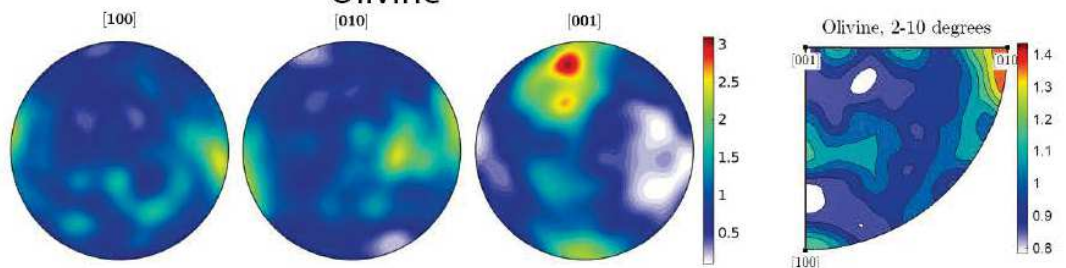
Olivine Mis2Mean



Olivine KAM



Olivine



305-U1309D-247R-3W (1190 mbsf)

305-U1309D-247R-3W, 16-18

Phase map

O 77%
C+P 23%

O 77%
C+P 82%

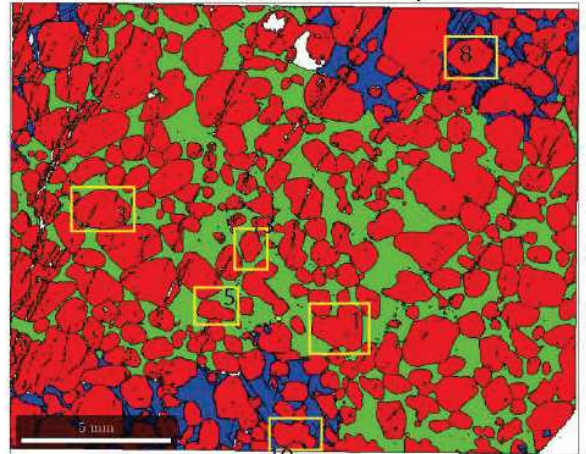
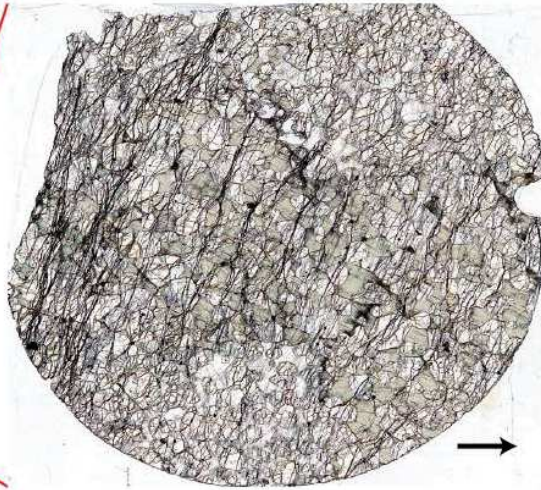
O 90%
C+P 10%

O 81%
C+P 19%

O 71%
C+P 29%

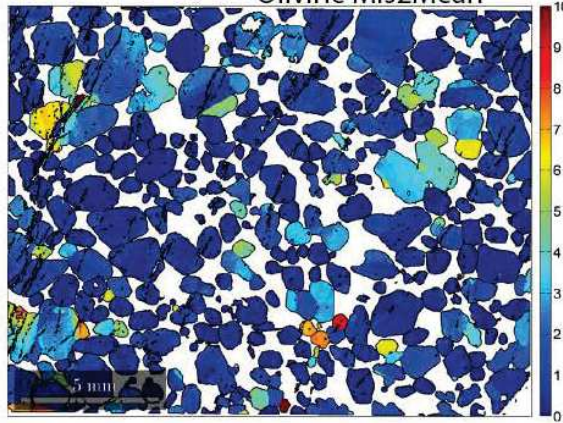
O 80%
C+P 20%

TOT
O 82%
C+P 18%



■ spl
■ ol
■ plg
■ cpx

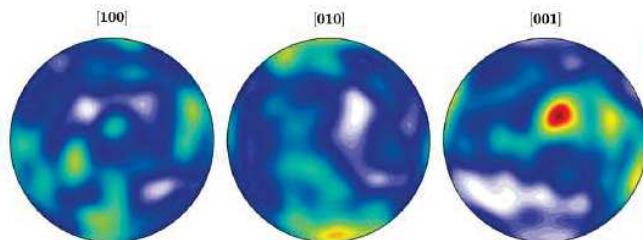
Olivine Mis2Mean



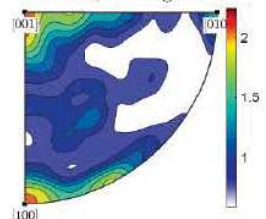
Olivine KAM



Olivine



Olivine, 2-10 degrees



305-U1309D-247R-3W (1190 mbsf)

305-U1309D-247R-3W, 22-25



O 77%
C+P 23%

O 77%
C+P 82%

O 90%
C+P 10%

O 81%
C+P 19%

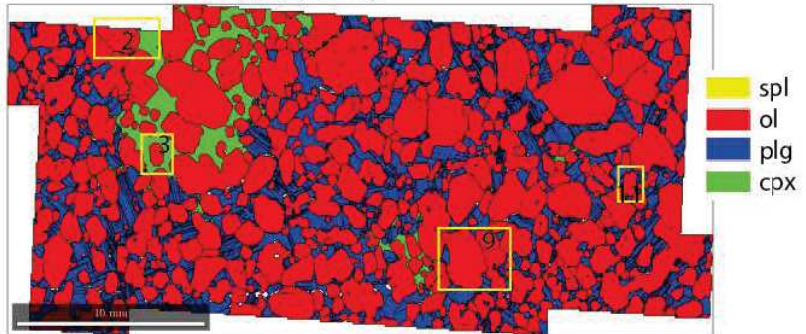
O 71%
C+P 29%

O 80%
C+P 20%

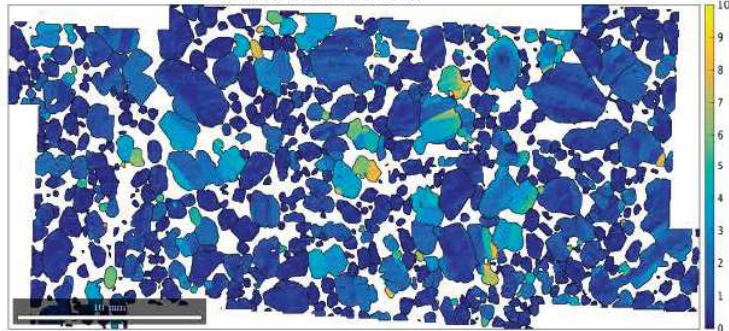
TOT
O 82%
C+P 18%



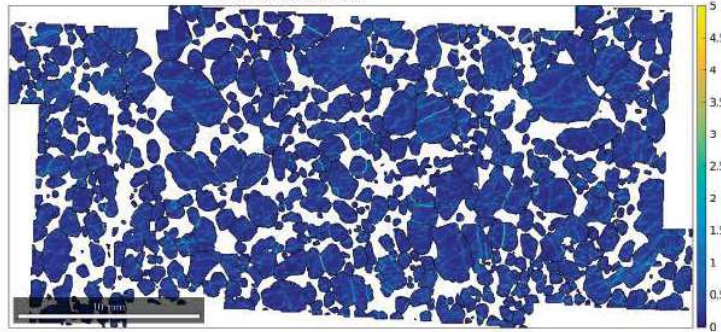
Phase map



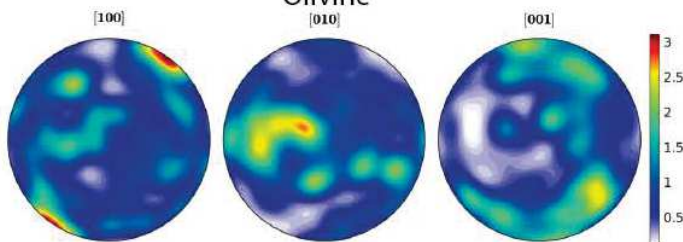
Olivine Mis2Mean



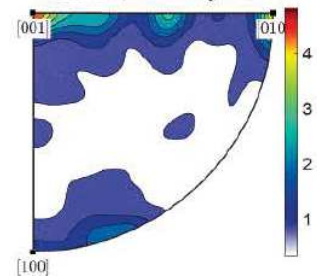
Olivine KAM



Olivine



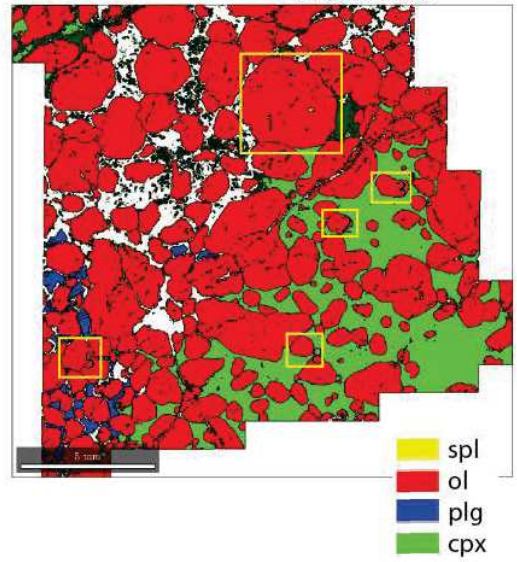
Olivine, 2-10 degrees



305-U1309D-247R-3W (1190 mbsf)

305-U1309D-247R-3W, 62-66

Phase map



O 77%
C+P 23%

O 77%
C+P 82%

O 90%
C+P 10%

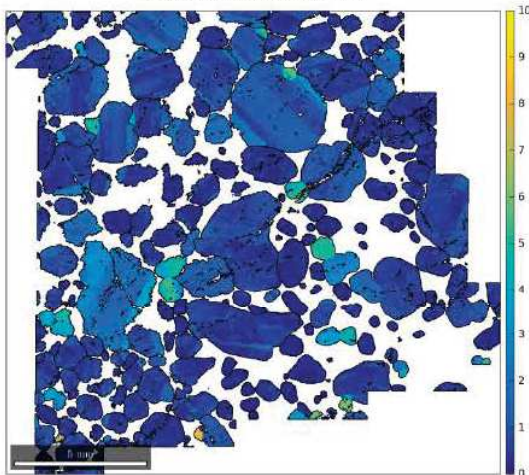
O 81%
C+P 19%

O 71%
C+P 29%

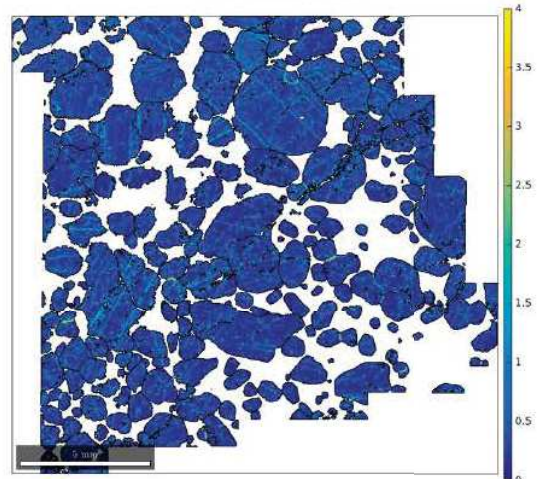
O 80%
C+P 20%

TOT
O 82%
C+P 18%

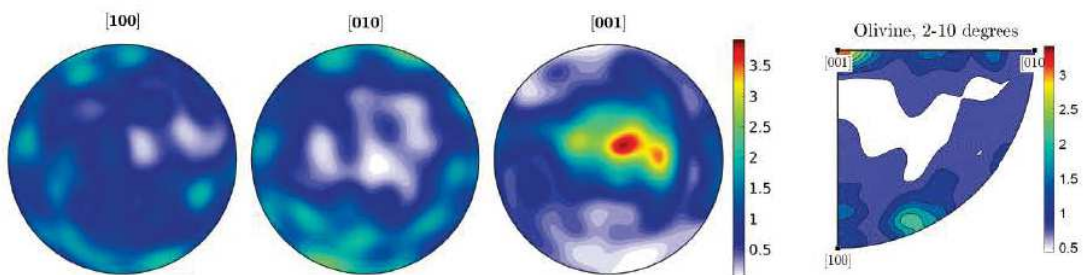
Olivine Mis2Mean



Olivine KAM

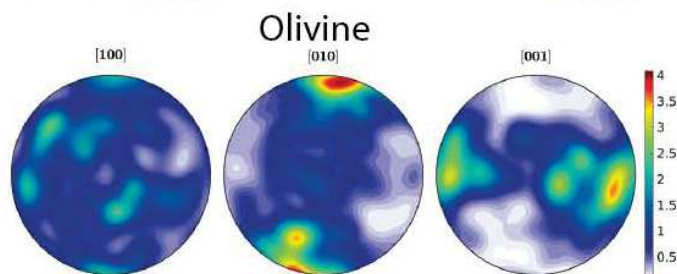
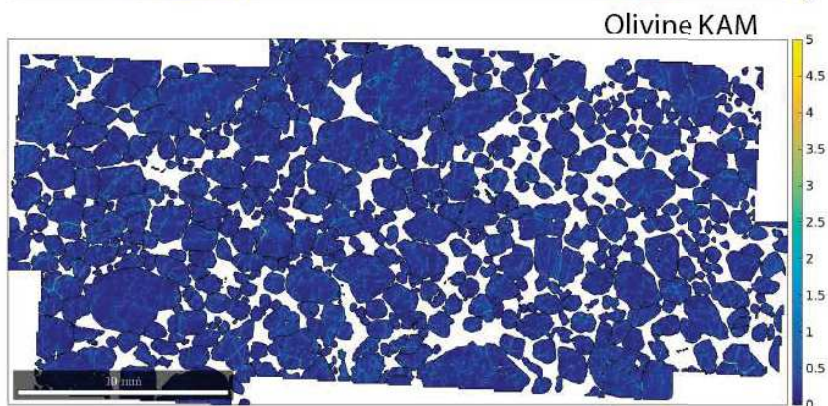
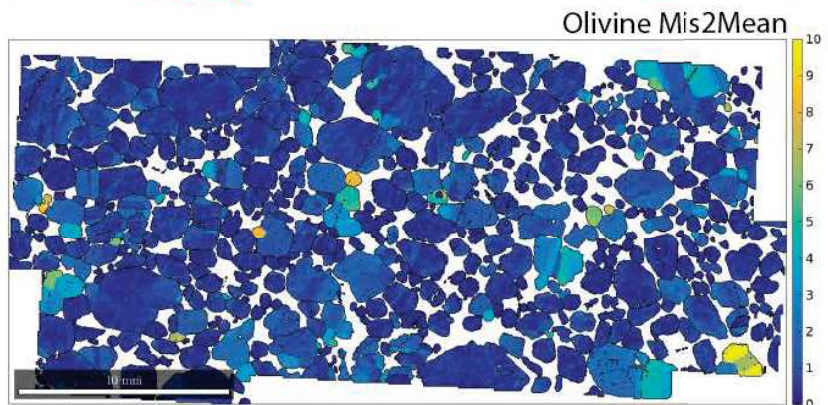
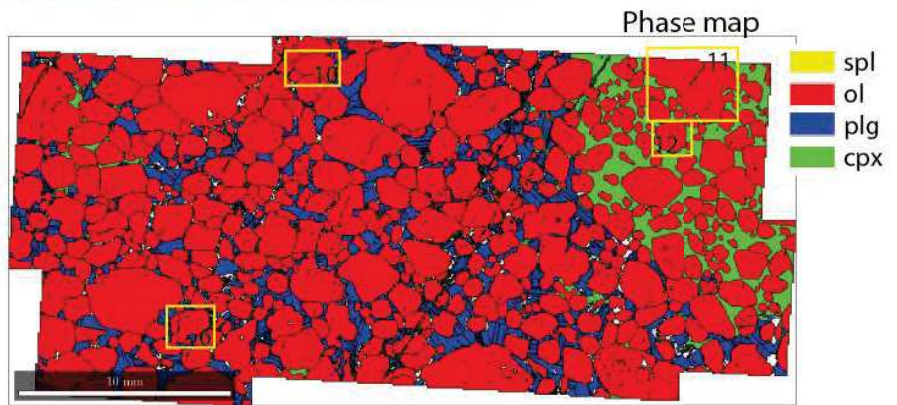
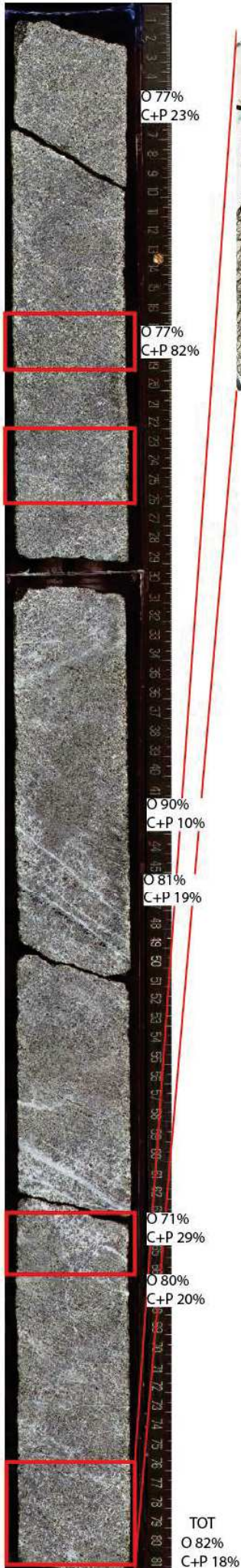


Olivine



305-U1309D-247R-3W (1190 mbsf)

305-U1309D-247R-3W, 76-81

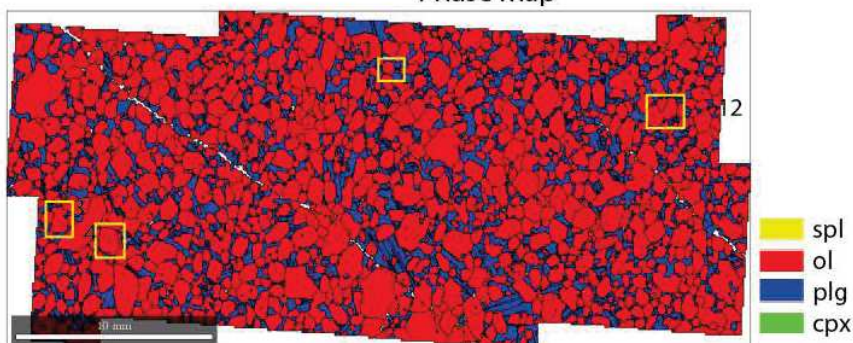


305-U1309D-248R-1W (1193 mbsf)

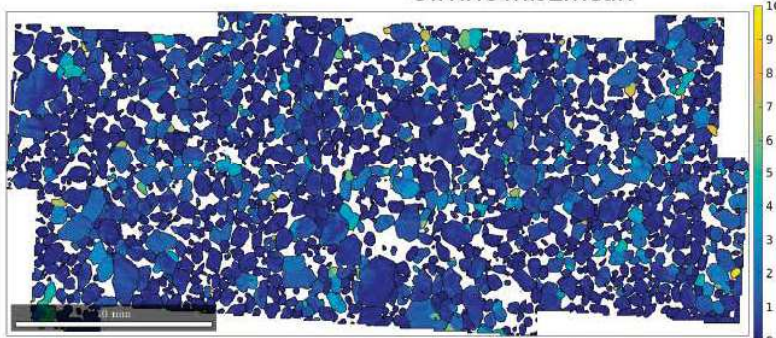
305-U1309D-248R-1W, 110-113



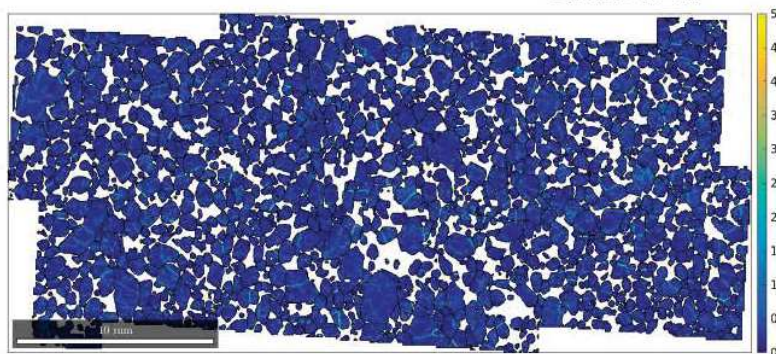
Phase map



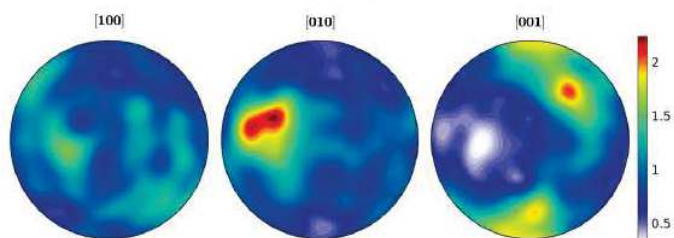
Olivine Mis2Mean



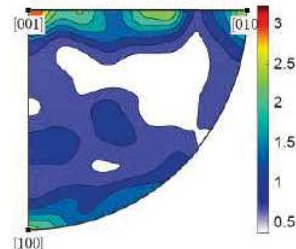
Olivine KAM



Olivine

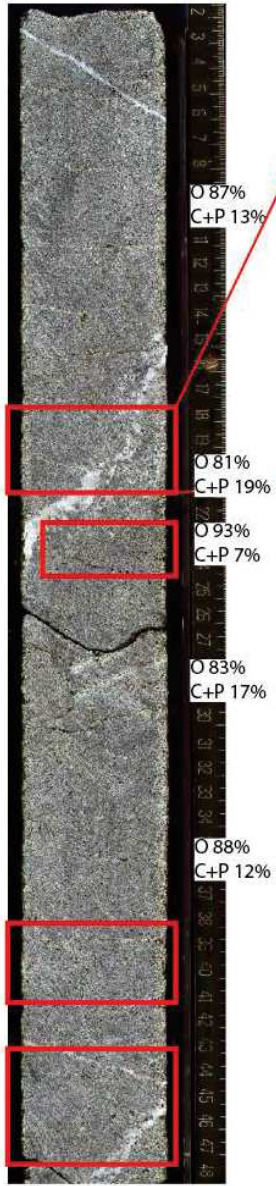


Olivine, 2-10 degrees

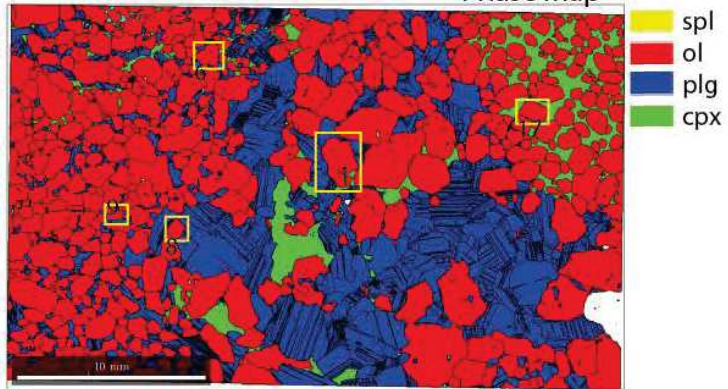


305-U1309D-248R-2W (1193 mbsf)

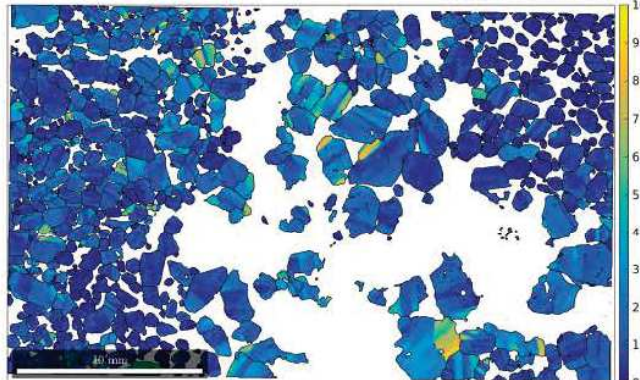
305-U1309D-248R-2W, 18-21



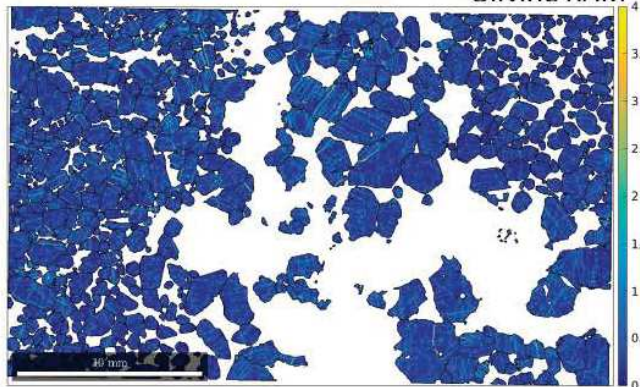
Phase map



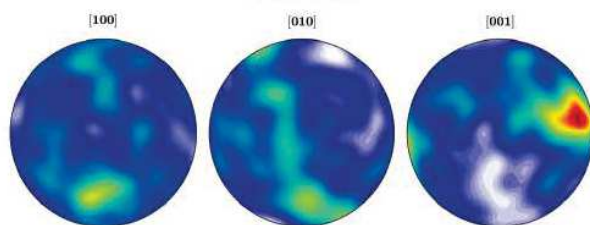
Olivine Mis2Mean



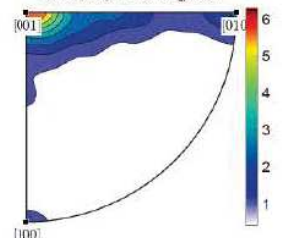
Olivine KAM



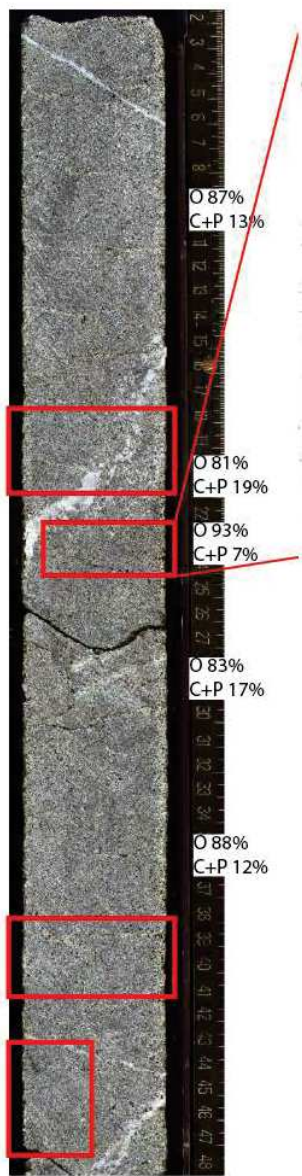
Olivine



Olivine, 2-10 degrees

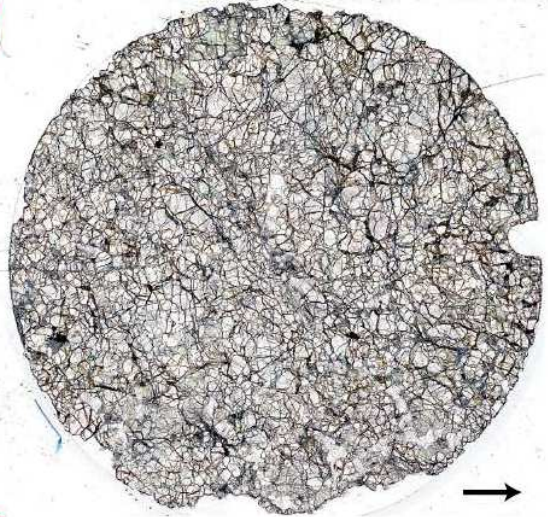


305-U1309D-248R-2W (1193 mbsf)

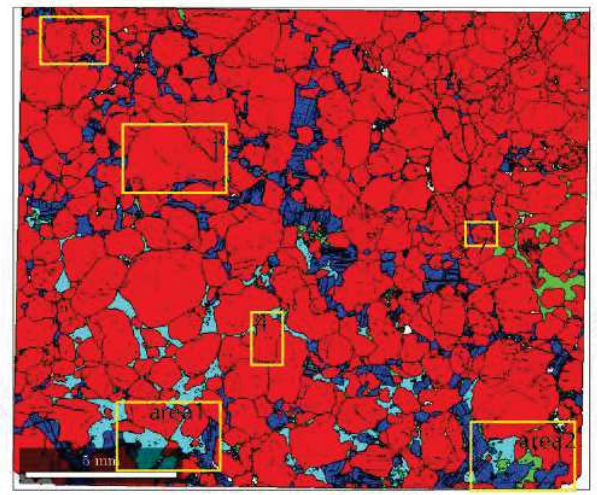


TOT O 86%
C+P 14%

305-U1309D-248R-2W, 22-24

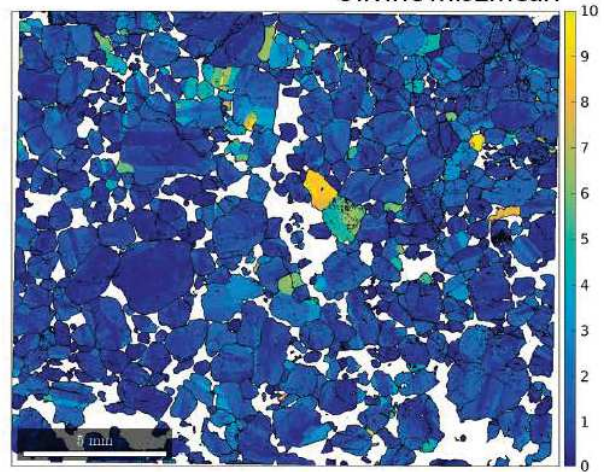


Phase map

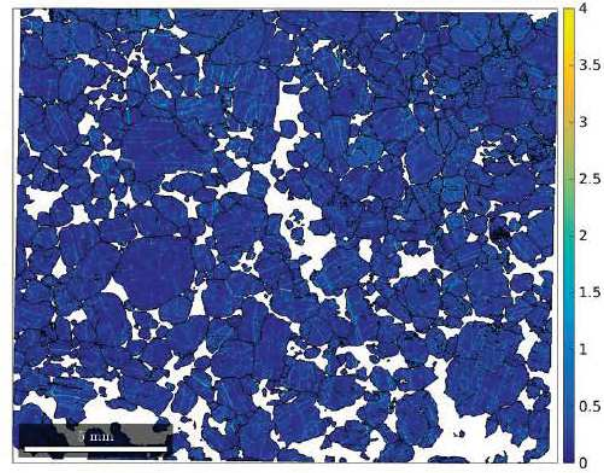


spl
 ol
 plg
 cpx
 opx

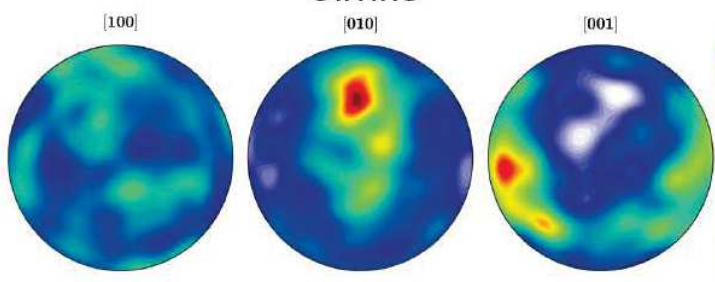
Olivine Mis2Mean



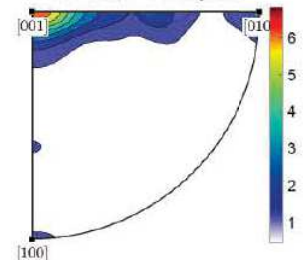
Olivine KAM



Olivine

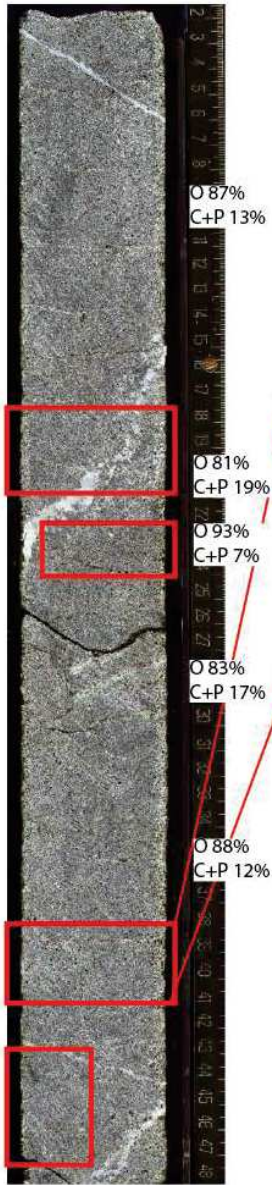


Olivine, 2-10 degrees



305-U1309D-248R-2W (1193 mbsf)

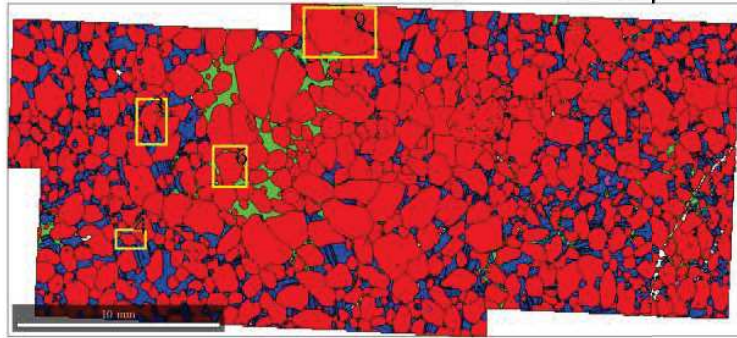
305-U1309D-248R-2W, 38-41



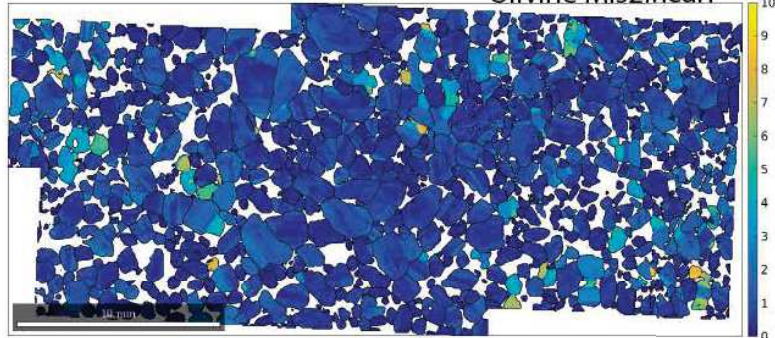
TOT O 86%
C+P 14%



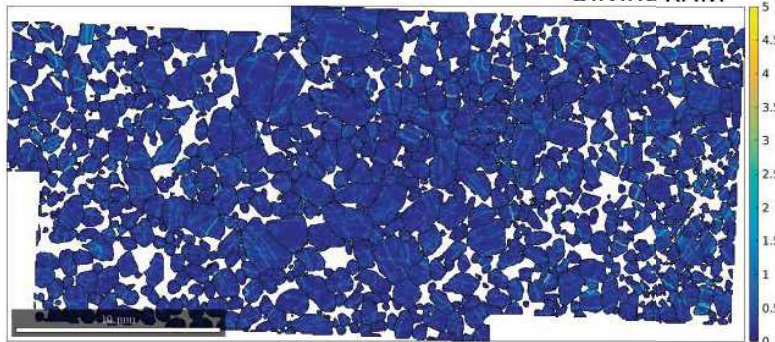
Phase map



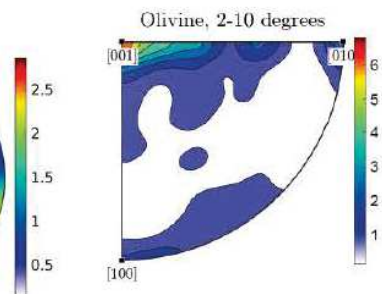
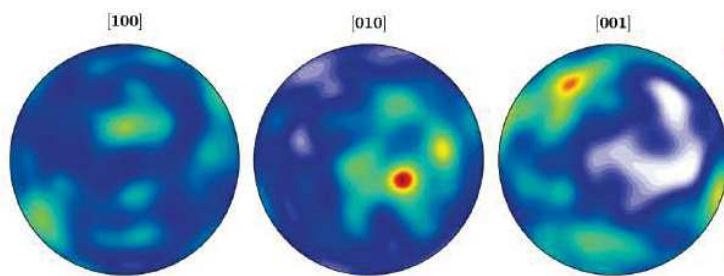
Olivine Mis2Mean



Olivine KAM

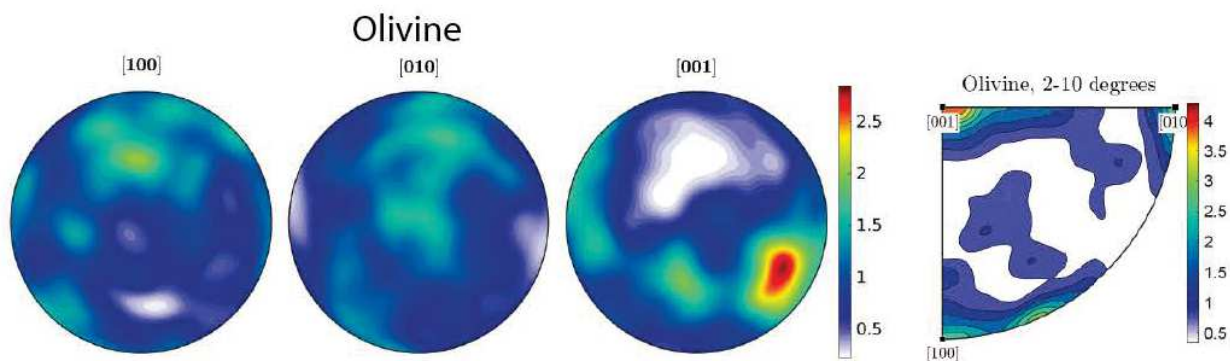
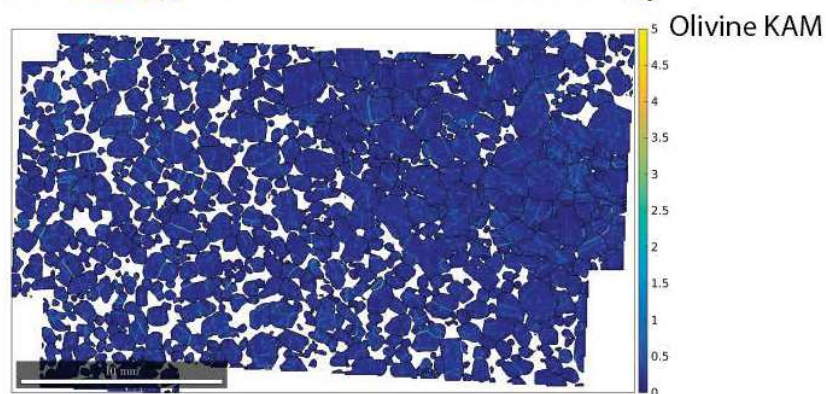
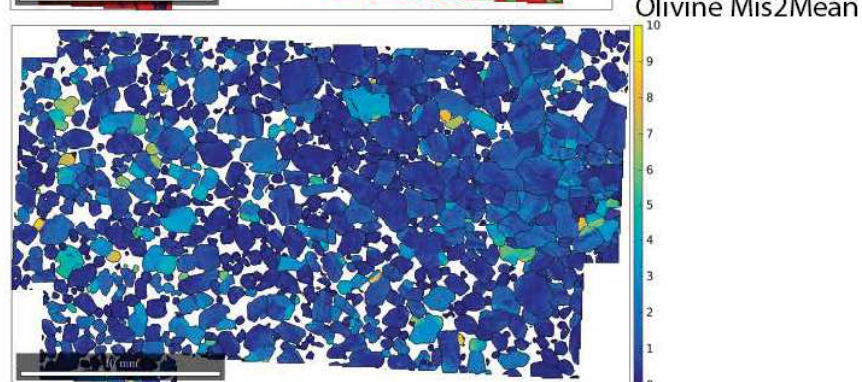
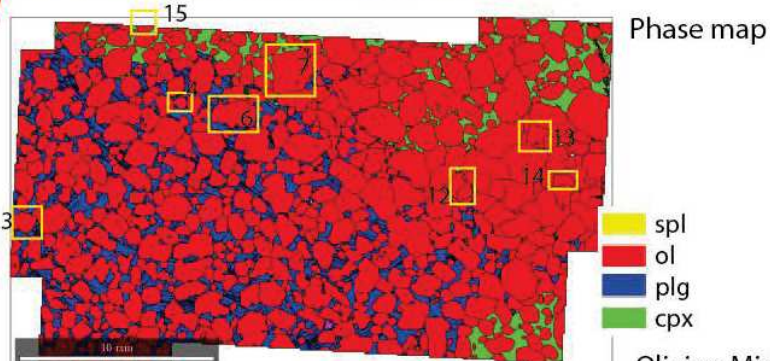
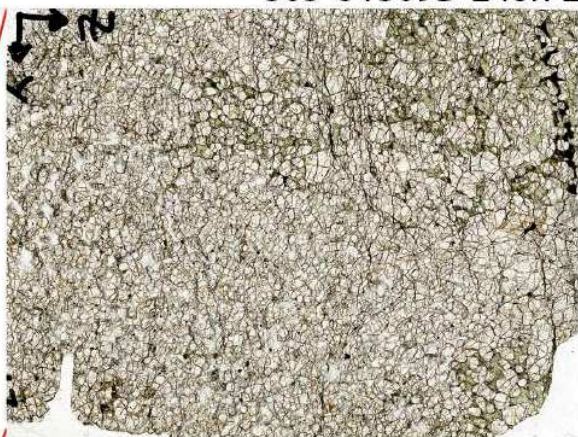
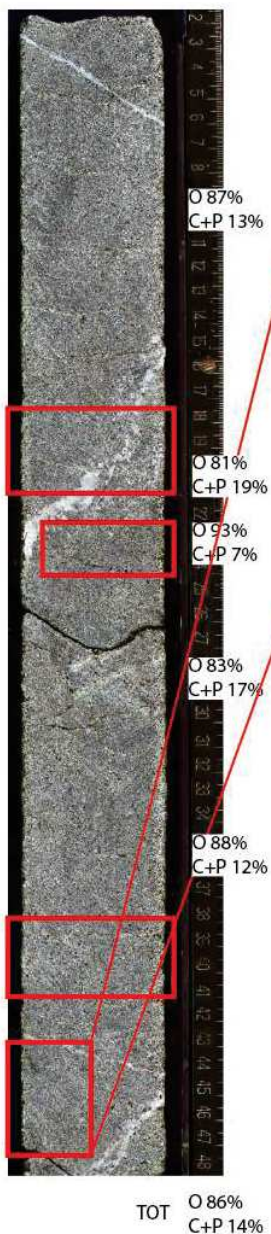


Olivine



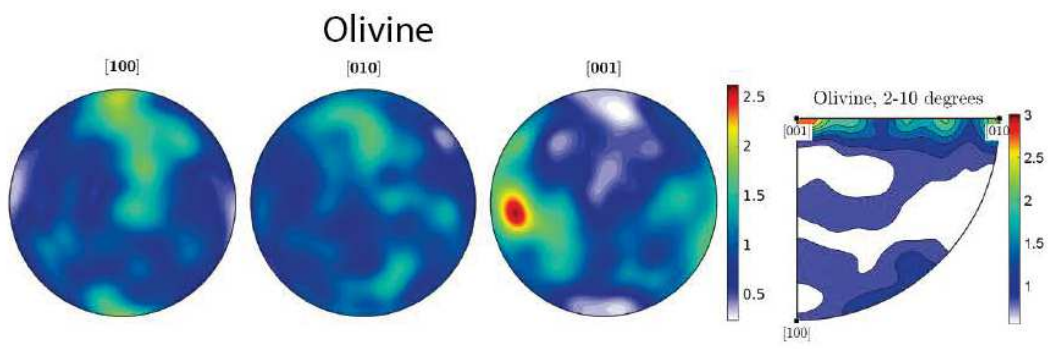
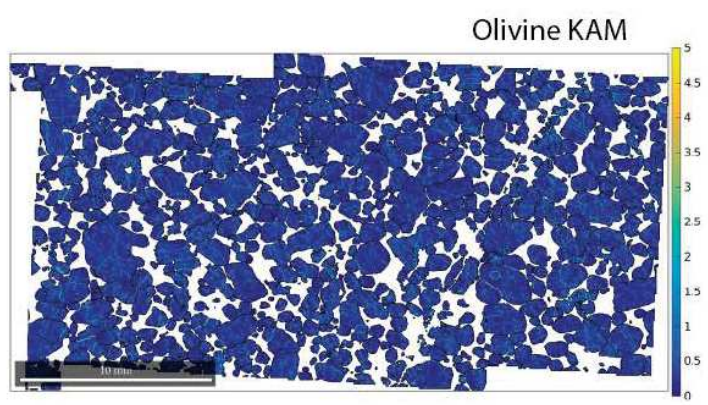
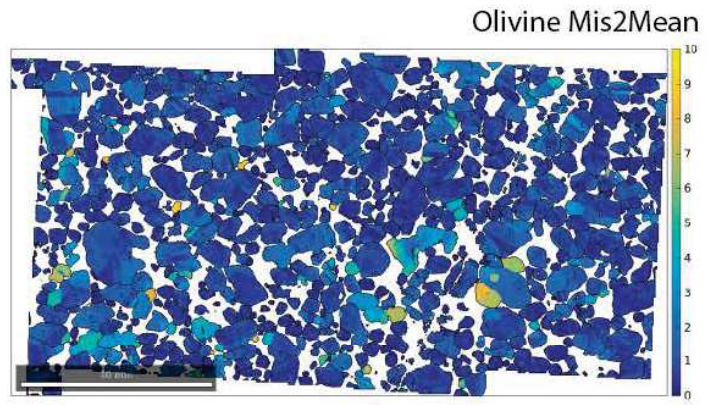
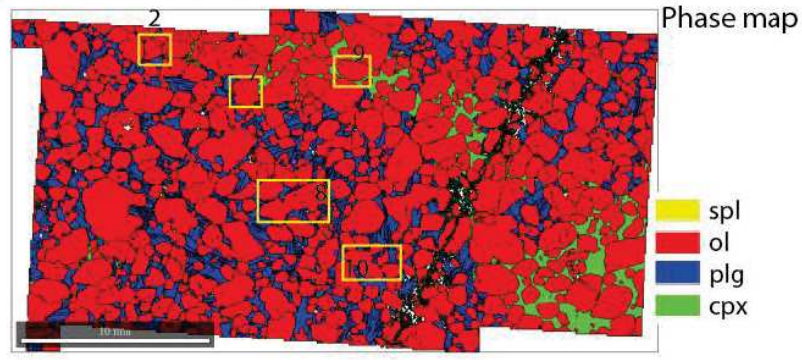
305-U1309D-248R-2W (1193 mbsf)

305-U1309D-248R-2W, 43-48



305-U1309D-248R-3W (1194 mbsf)

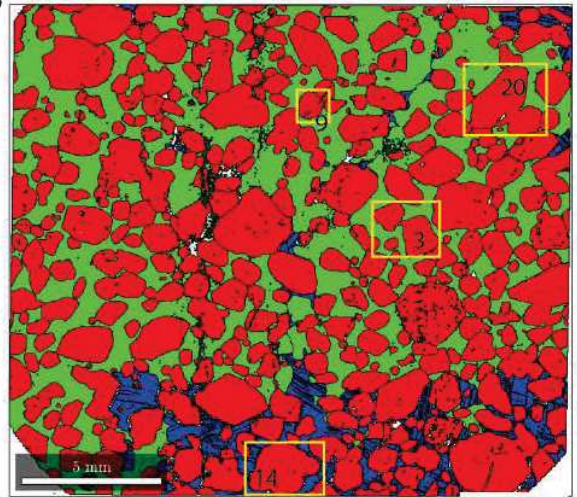
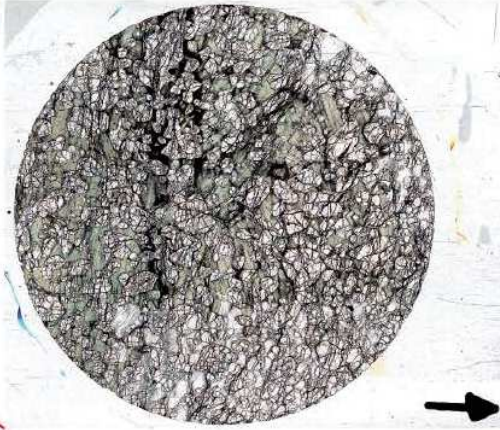
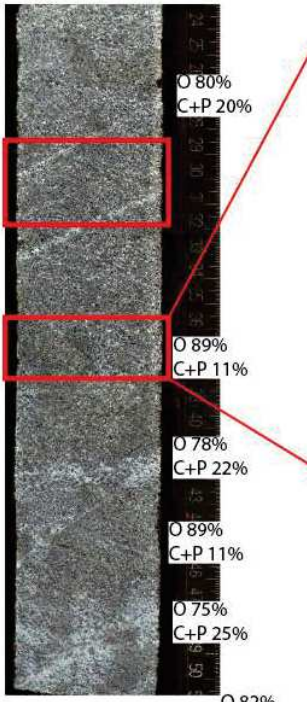
305-U1309D-248R-3W, 29-32



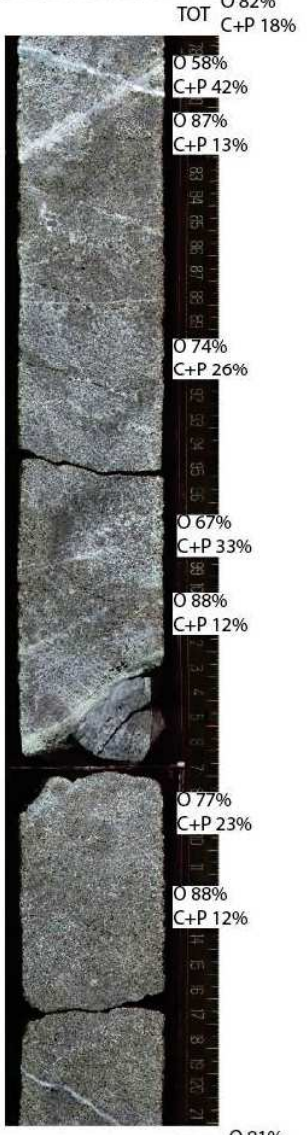
305-U1309D-248R-3W (1194 mbsf)

305-U1309D-248R-3W, 36-38

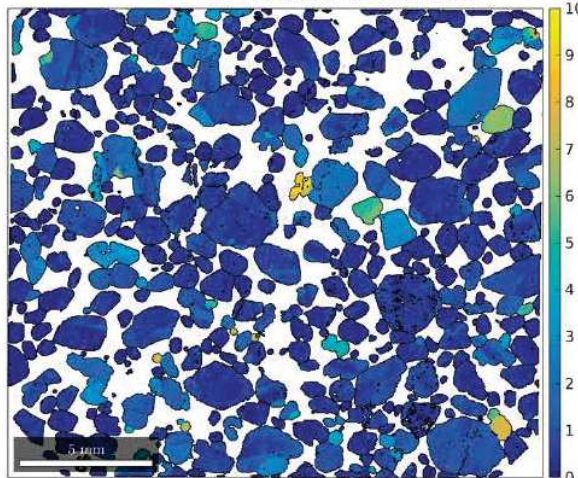
Phase map



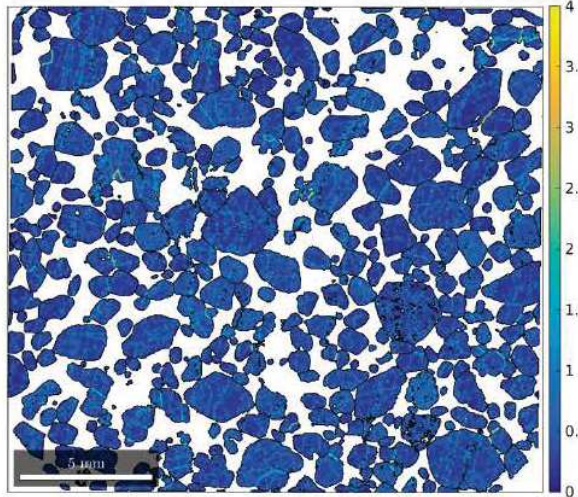
■ spl
■ ol
■ plg
■ cpx



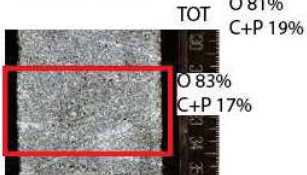
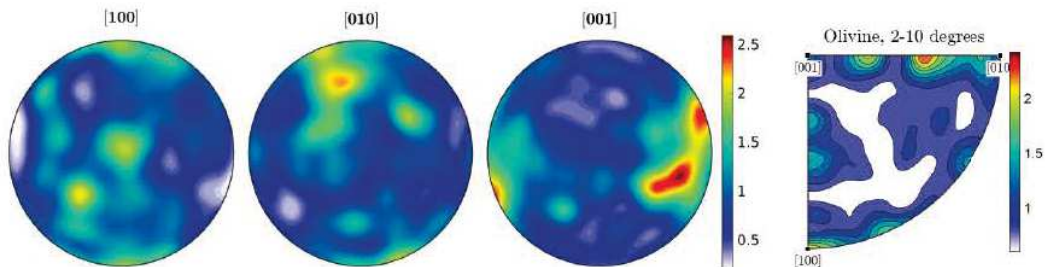
Olivine Mis2Mean



Olivine KAM



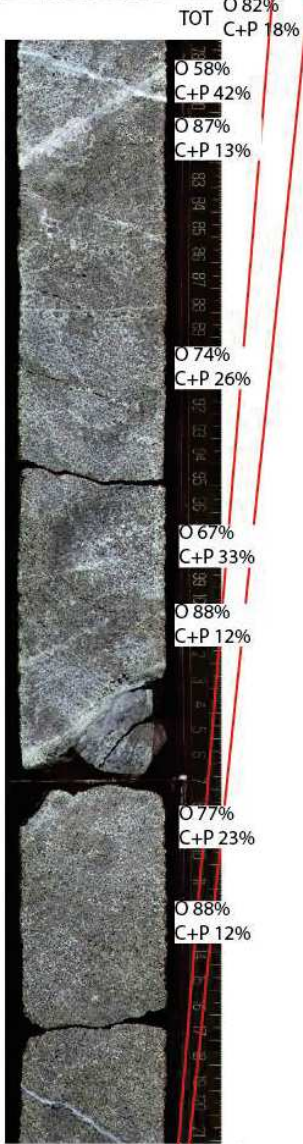
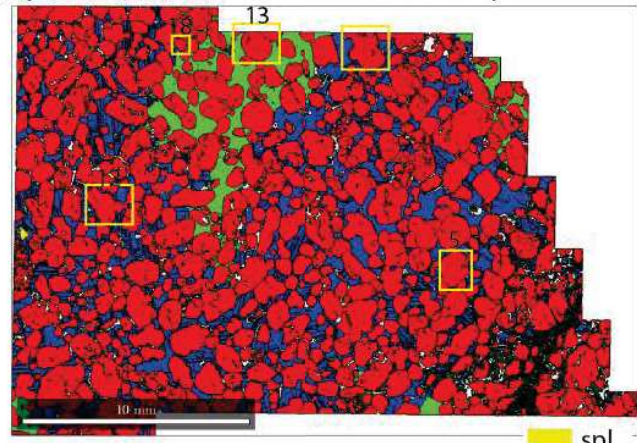
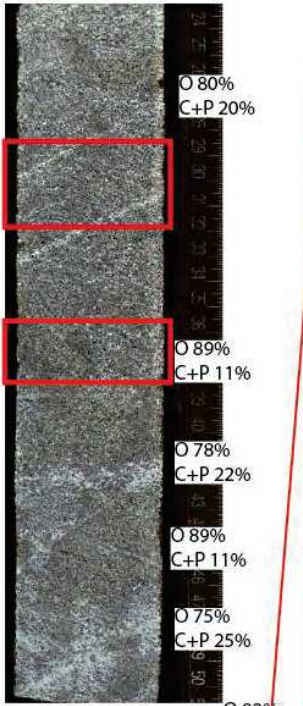
Olivine



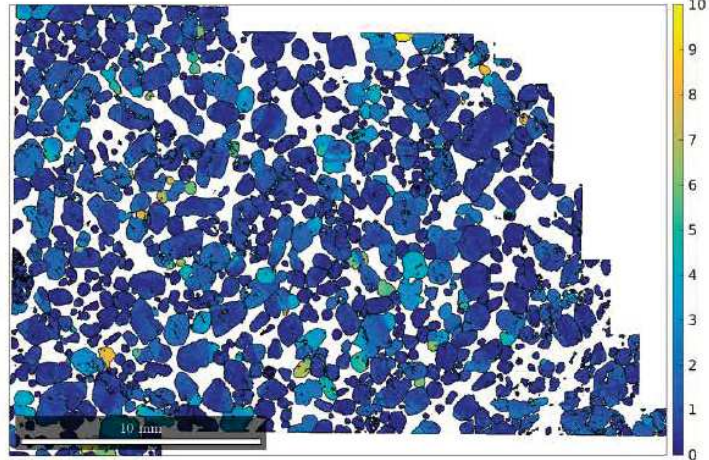
305-U1309D-248R-3W (1194 mbsf)

305-U1309D-248R-3W, 131-134

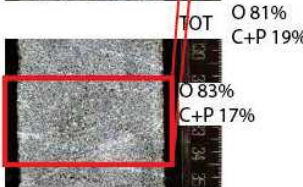
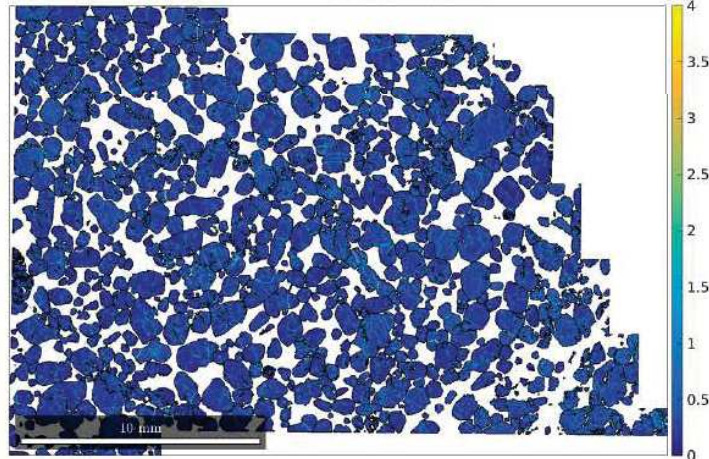
Phase map



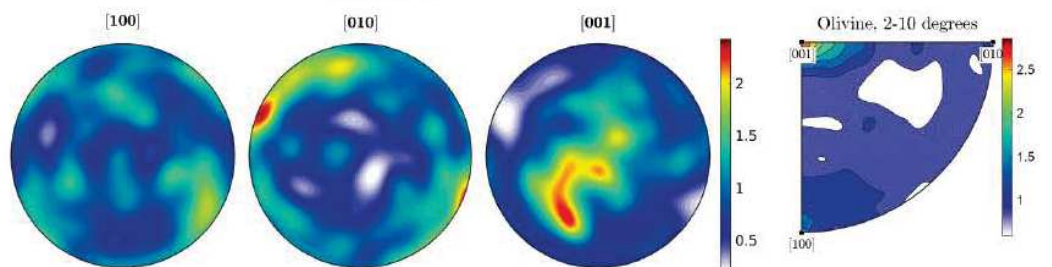
Olivine Mis2Mean



Olivine KAM



Olivine



Appendix 2

Appendix 2 contains major and trace elements geochemical data of minerals in olivine-rich troctolites and troctolite from IODP Hole U1309D. These data are the Supplementary Material of Ferrando et al. (2018). Finally, olivine, plagioclase and clinopyroxene rim-to-rim and/or core-to-rim geochemical profiles are reported following the classification in three types of olivine-rich troctolites (OI-T1, OI-T2, OI-T3).

Table S1 - Major and trace element average compositions of olivines in OI-Ts from IODP Hole U1309D

Expedition/Hole Sample Depth (mbsf)	305-U1309D 227R-3W, 124-126 1096.17														305-U1309D 234R-1W, 22-26 1124.97														305-U1309D 241R-2W, 89-91 1160.66														305-U1309D 247R-3W, 16-18 1190.05														305-U1309D 247R-3W, 22-25 1190.11													
	OI-T 2 Shape Deformation							anhdral undeformed							OI-T1 corroded deformed							anhdral/rounded undeformed							OI-T1 corroded deformed							anhdral/rounded undeformed							OI-T deformed							rounded undeformed																				
	n.	4		4		5		3		4		4		6		5		3		2		5		5		6		5		7		4		4		3		2		1																														
Location	rim	α	core	α	rim	α	core	α	rim	α	core	α	rim	α	core	α	rim	α	core	α	rim	α	core	α	rim	α	core	α	rim	α	core	α	rim	α	core	α	rim	α	core	α																														
SiO ₂	40.37	0.15	40.47	0.19	40.56	0.01	40.37	0.07	40.30	0.12	40.22	0.08	40.24	0.23	40.36	0.28	40.45	0.13	40.42	0.12	40.62	0.07	40.43	0.09	40.23	0.05	40.42	0.10	40.06	0.35	40.22	0.30	39.73	0.09	39.72	0.08	39.84	0.04	39.55	-																														
TiO ₂	0.02	0.01	0.01	0.01	0.02	0.01	0.00	0.00	0.03	0.01	0.02	0.01	0.01	0.00	0.01	0.01	0.01	0.01	0.02	0.02	0.01	0.02	0.01	0.02	0.01	0.01	0.01	0.01	0.02	0.01	0.02	0.01	0.01	0.01	0.01	0.01	0.01	0.01	0.01	0.03	-																													
Al ₂ O ₃	0.00	0.01	0.01	0.01	0.01	0.00	0.00	0.00	0.00	0.00	0.01	0.01	0.01	0.01	0.01	0.01	0.01	0.00	0.01	0.01	0.00	0.00	0.01	0.01	0.00	0.00	0.00	0.01	0.01	0.02	0.01	0.00	0.01	0.01	0.01	0.01	0.01	0.01	0.02	0.01	0.03	-																												
Cr ₂ O ₃	0.01	0.01	0.00	0.00	0.00	0.00	0.02	0.00	0.00	0.01	0.00	0.01	0.01	0.01	0.02	0.01	0.02	0.01	0.02	0.02	0.01	0.01	0.01	0.00	0.01	0.01	0.01	0.01	0.03	0.03	0.03	0.02	0.02	0.02	0.02	0.03	0.02	0.02	0.01	0.02	-																													
FeO	14.81	0.14	14.73	0.03	14.69	0.18	14.77	0.08	13.66	0.13	13.74	0.18	13.62	0.32	13.72	0.28	14.43	0.12	14.34	0.12	14.44	0.02	14.41	0.05	14.13	0.25	14.04	0.04	14.18	0.39	14.23	0.32	14.25	0.10	14.12	0.11	14.21	0.09	14.06	-																														
MnO	0.22	0.01	0.22	0.01	0.23	0.01	0.22	0.00	0.22	0.01	0.22	0.00	0.21	0.01	0.22	0.01	0.23	0.01	0.22	0.01	0.22	0.00	0.22	0.00	0.20	0.01	0.20	0.02	0.21	0.01	0.21	0.01	0.22	0.02	0.23	0.03	0.23	0.01	0.21	-																														
MgO	43.52	0.16	43.56	0.25	43.53	0.12	43.54	0.01	45.57	0.53	45.55	0.26	45.58	0.35	45.34	0.28	43.69	0.22	43.81	0.09	43.80	0.14	43.86	0.10	44.95	0.20	44.87	0.05	45.13	0.25	45.27	0.32	45.22	0.22	45.28	0.41	45.23	0.22	44.64	-																														
CaO	0.07	0.01	0.08	0.00	0.07	0.01	0.09	0.01	0.09	0.01	0.09	0.02	0.08	0.01	0.10	0.00	0.08	0.00	0.08	0.01	0.06	0.01	0.09	0.02	0.07	0.02	0.09	0.01	0.06	0.02	0.07	0.01	0.08	0.01	0.07	0.06	0.06	0.00	0.08	-																														
Na ₂ O	0.02	0.02	0.01	0.02	0.01	0.01	0.01	0.01	0.00	0.01	0.00	0.01	0.01	0.01	0.00	0.00	0.01	0.00	0.00	0.00	0.01	0.01	0.01	0.00	0.00	0.00	0.00	0.00	0.00	0.00	0.00	0.00	0.00	0.00	0.00	0.00	0.01	0.01	0.01	-																														
K ₂ O	0.00	0.00	0.00	0.00	0.00	0.00	0.00	0.00	0.00	0.00	0.00	0.00	0.00	0.00	0.00	0.00	0.00	0.00	0.00	0.00	0.00	0.00	0.00	0.00	0.00	0.00	0.00	0.00	0.00	0.00	0.00	0.00	0.00	0.00	0.00	0.00	0.00	0.00	0.01	-																														
NiO	0.26	0.02	0.25	0.03	0.25	0.00	0.26	0.03	0.26	0.01	0.27	0.01	0.26	0.01	0.27	0.02	0.25	0.01	0.25	0.03	0.25	0.01	0.26	0.01	0.30	0.01	0.30	0.01	0.31	0.02	0.31	0.02	0.32	0.01	0.30	0.01	0.29	0.05	0.30	-																														
Total	99.30	0.07	99.35	0.46	99.37	0.32	99.28	0.07	100.16	0.52	100.12	0.36	100.04	0.44	100.04	0.29	99.17	0.26	99.17	0.26	99.17	0.35	99.45	0.08	99.33	0.20	99.93	0.41	99.94	0.12	100.00	0.70	100.37	0.42	99.87	0.10	99.77	0.45	99.91	0.10	99.15	-																												
Mg#	83.97	0.17	84.06	0.05	84.08	0.13	84.01	0.07	85.60	0.03	85.53	0.09	85.65	0.22	85.49	0.18	84.37	0.11	84.49	0.09	84.40	0.06	84.44	0.08	85.01	0.17	85.07	0.05	85.02	0.32	85.01	0.22	84.98	0.15	85.11	0.10	85.01	0.15	85.04	-																														
ppm																																																																						
Li	2.26	0.99	2.01	0.14	2.66	0.48	2.52	0.17	2.54	0.37	2.09	0.57	3.37	1.05	2.38	-	3.62	0.17	3.57	0.15	2.67	0.40	2.38	0.19	2.69	0.40	2.29	0.44	1.81	0.83	1.73	0.75	1.71	0.20	1.42	0.07	1.36	0.73	1.86	-																														
B	8.43	0.64	7.89	1.99	10.12	1.44	9.84	1.36	10.72	1.90	10.36	3.39	9.28	661.07	8.85	-	5.79	0.22	5.47	0.20	6.40	0.87	6.84	1.62	13.05	4.88	12.03	5.57	8.50	1.56	8.54	1.19	6.03	0.25	6.69	0.29	5.81	0.88	5.45	-																														
Ca	3.17	53	365	20	436	58	509	61	667	105	645	40	671	0	732	-	571	23	506	19	393	44	497	44	589	167	698	94	405	168	506	156	576	30	539	20	324	24	445	-																														
Sc	7.21	0.39	7.31	0.43	7.91	0.45	8.55	0.57	8.64	0.08	8.50	0.72	7.57	1.51	8.88	-	9.44	0.38	9.57	0.36	8.23	0.02	9.07	0.13	6.83	0.81	7.52	0.29	7.53	0.18	7.23	0.05	7.13	0.39	6.73	0.21	6.82	0.33	5.79	-																														
Ti	55.1	14.3	51.8	3.2	48.2	0.9	58.2	2.5	91.9	26.0	81.4	23.2	87.3	19.5	103.1	-	71.3	3.4	83.3	3.6	64.3	2.2	78.0	6.8	67.1	4.3	81.8	1.6	72.8	6.1	67.7	6.0	92.2	12.7	88.2	3.0	112.4	11.3	84.1	-																														
V	2.94	0.24	3.29	0.14	2.84	0.19	3.64	0.14	5.88	0.11	5.12	0.59	4.99	0.88	6.28	-	3.96	0.14	4.43	0.15	3.63	0.40	4.12	1.9	5.07	0.32	6.09	0.16	5.02	0.04	5.20	0.35	5.67	0.26	5.54	0.17	6.55	0.39	4.67	-																														
Cr	58.7	2.1	67.4	8.1	63.5	5.8	81.9	4.5	89.0	10.8	27.0	38.2	n.d.	-	n.d.	-	63.1	3.9	81.1	4.3	67.2	7.4	71.8	1.0	n.d.	-	n.d.	-	63.0	40.0	33.5	47.4	91.3	20.6	100.5	3.1	131.8	8.1	101.1	-																														
Mn	2053	47	1986	148	1830	5	1882	46	1742	66	1667	2	1803	5	1816	-	2036	76	1890	66	1922	9	1897	129	1784	26	1783	48	1763	8	1767	36	1837	12	1885	58	1805	30	1759	-																														
Co	167	6	164	15	157	1	162	3	162	2	149	16	163	11	165	-	164	6	157	5	162	1	155	6	171	8	164	10	158	12	161	7	154.2	0.3	153	5	154	2	150	-																														
Ni	1905	51	1882	158	1862	68	1842	59	2151	135	2010	133	1901	128	1868	-	1891	206	1789	160	1850	46	1800	13	2821	120	2657	128	2554	47	2514	35	2224	17	2220	81	2166	21	2114	-																														
Cu	0.073	0.045	0.081	0.019	0.149	0.049	0.133	0.049	0.360	0.294	0.204	0.041	0.169	1.188	0.148	-	0.000	0.021	0.154	0.015	0.336	0.104	1.254	1.593	0.068	0.062	0.122	0.016	n.d.	-	0.028	0.039	0.128	0.024	0.533	0.030	0.076	0.107	0.000	-																														
Zn	74.7	9.8	76.7	6.5	71.1	2.1	75.1	3.1	73.4	7.5	68.8	4.8	76.2	2.7	74.5	-	84.5	2.8	81.7	2.6	79.8	2.9	77.2	8.7	76.4	0.7	78.8	2.9	69.3	2.1	70.7	3.5	11.4	1.2	78.5	2.7	78.6	0.2	77.0	-																														
Rb	b.d.l.	-	0.015	0.036	n.d.	-	n.d.	-	n.d.	-	n.d.	-	n.d.	-	b.d.l.	-	0.0404	0.0046	b.d.l.	-	0.0050	0.0003	b.d.l.	-	b.d.l.	-	b.d.l.	-	b.d.l.	-	b.d.l.	-	b.d.l.	-	b.d.l.	-	0.0083	0.028	b.d.l.	-																														
Sr	b.d.l.	-	0.0231	0.0657	0.0024	0.0034	0.0000	0.0000	0.0268	0.0279	0.0045	0.0064	b.d.l.	-	b.d.l.	-	b.d.l.	-	b.d.l.	-	0.0473	0.0087	b.d.l.	-	b.d.l.	-	b.d.l.	-	b.d.l.	-	b.d.l.	-	b.d.l.	-	0.4715	0.6668	b.d.l.	-	0.0075	0.0106	b.d.l.	-																												
Y	0.0526	0.0053	0.0597	0.0043	0.0690	0.0124	0.0872	0.0053	0.1133	0.0081	0.0905	0.0078	0.0935	0.0085	0.1090	-	0.1079	0.0061	0.1062	0.0056	0.0868	0.0061	0.1223	0.0208	0.0754	0.0363	0.0825	0.0202	0.0563	0.0279	0.1022	0.0071	0.0750	0.0045	0.0580	0.0096	0.0600	-	0.0075	0.0106	b.d.l.	-																												
Zr	0.0094	0.0133	0.0128	0.0038	0.0132	0.0095	0.0233	0.0050	0.0443	0.0095	0.0412	0.0088	0.0315	#DIV/0!	0.0320	-	0.0492	0.0069	0.0711	0.0069	0.0442	0.0048	0.0696	0.0289	0.0159	0.0225	b.d.l.	-	0.0156	0.0000	0.0070	0.0099	0.0464	0.0021	0.0450	0.0045	0.0562	0.0098	0.0413	-																														
Nb	0.0027	0.0000	0.0011	0.0005	0.0008	0.0007	0.0015	0.0001	0.0037	0.0010	0.0049	0.0011	0.0020	0.0009	0.0026	-	0.0025	0.0008	b.d.l.	-	0.0021	0.0017	0.0022	0.0030	0.0018	0.0000	0.0010	0.0009	0.0010	0.0000	0.0014	0.0031	0.0013	0.0019	0.0008	0.0016	0.0022	b.d.l.	-																															
Sb	b.d.l.	-	b.d.l.	-	b.d.l.	-	b.d.l.	-	b.d.l.	-	b.d.l.	-	b.d.l.	-	b.d.l.	-	b.d.l.	-	b.d.l.	-	b.d.l.	-	b.d.l.	-	b.d.l.	-	b.d.l.	-	b.d.l.	-	0.0066	0.0000	b.d.l.	-	b.d.l.	-	b.d.l.	-	b.d.l.	-	b.d.l.																													

Table S1 (continued olivine)

Expedition/Hole Sample Depth (mbsf)	305-U1309D 247R-3W, 62-66 1190.51										305-U1309D 247R-3W, 76-81 1190.65										305-U1309D 248R-1W, 110-113 1193										305-U1309D 248R-2W, 18-21 1193.32										305-U1309D 248R-2W, 22-24 1193.36																																																																																																																																																																																																																																																																																																																																																																																																																																																																																																																																																																																																																																																																																																																																																																																																																																																																																																																																																																																													
	OH-T3 Shape anhydral/deformed					anhydral/rounded undeformed					OH-T2 corroded deformed					anhydral undeformed					OH-T1 corroded deformed					rounded undeformed					OH-T3 corroded deformed					rounded undeformed					OH-T3 corroded deformed					anhydral undeformed																																																																																																																																																																																																																																																																																																																																																																																																																																																																																																																																																																																																																																																																																																																																																																																																																																																																																																																																																																																								
	n.	3	4	5	6	7	8	9	10	11	12	13	14	15	16	17	18	19	20	21	22	23	24	25	26	27	28	29	30	31	32	33	34	35	36	37	38	39	40	41	42	43	44	45	46	47	48	49	50	51	52	53	54	55	56	57	58	59	60	61	62	63	64	65	66	67	68	69	70	71	72	73	74	75	76	77	78	79	80	81	82	83	84	85	86	87	88	89	90	91	92	93	94	95	96	97	98	99	100	101	102	103	104	105	106	107	108	109	110	111	112	113	114	115	116	117	118	119	120	121	122	123	124	125	126	127	128	129	130	131	132	133	134	135	136	137	138	139	140	141	142	143	144	145	146	147	148	149	150	151	152	153	154	155	156	157	158	159	160	161	162	163	164	165	166	167	168	169	170	171	172	173	174	175	176	177	178	179	180	181	182	183	184	185	186	187	188	189	190	191	192	193	194	195	196	197	198	199	200	201	202	203	204	205	206	207	208	209	210	211	212	213	214	215	216	217	218	219	220	221	222	223	224	225	226	227	228	229	230	231	232	233	234	235	236	237	238	239	240	241	242	243	244	245	246	247	248	249	250	251	252	253	254	255	256	257	258	259	260	261	262	263	264	265	266	267	268	269	270	271	272	273	274	275	276	277	278	279	280	281	282	283	284	285	286	287	288	289	290	291	292	293	294	295	296	297	298	299	300	301	302	303	304	305	306	307	308	309	310	311	312	313	314	315	316	317	318	319	320	321	322	323	324	325	326	327	328	329	330	331	332	333	334	335	336	337	338	339	340	341	342	343	344	345	346	347	348	349	350	351	352	353	354	355	356	357	358	359	360	361	362	363	364	365	366	367	368	369	370	371	372	373	374	375	376	377	378	379	380	381	382	383	384	385	386	387	388	389	390	391	392	393	394	395	396	397	398	399	400	401	402	403	404	405	406	407	408	409	410	411	412	413	414	415	416	417	418	419	420	421	422	423	424	425	426	427	428	429	430	431	432	433	434	435	436	437	438	439	440	441	442	443	444	445	446	447	448	449	450	451	452	453	454	455	456	457	458	459	460	461	462	463	464	465	466	467	468	469	470	471	472	473	474	475	476	477	478	479	480	481	482	483	484	485	486	487	488	489	490	491	492	493	494	495	496	497	498	499	500	501	502	503	504	505	506	507	508	509	510	511	512	513	514	515	516	517	518	519	520	521	522	523	524	525	526	527	528	529	530	531	532	533	534	535	536	537	538	539	540	541	542	543	544	545	546	547	548	549	550	551	552	553	554	555	556	557	558	559	560	561	562	563	564	565	566	567	568	569	570	571	572	573	574	575	576	577	578	579	580	581	582	583	584	585	586	587	588	589	590	591	592	593	594	595	596	597	598	599	600	601	602	603	604	605	606	607	608	609	610	611	612	613	614	615	616	617	618	619	620	621	622	623	624	625	626	627	628	629	630	631	632	633	634	635	636	637	638	639	640	641	642	643	644	645	646	647	648	649	650	651	652	653	654	655	656	657	658	659	660	661	662	663	664	665	666	667	668	669	670	671	672	673	674	675	676	677	678	679	680	681	682	683	684	685	686	687	688	689	690	691	692	693	694	695	696	697	698	699	700	701	702	703	704	705	706	707	708	709	710	711	712	713	714	715	716	717	718	719	720	721	722	723	724	725	726	727	728	729	730	731	732	733	734	735	736	737	738	739	740	741	742	743	744	745	746	747	748	749	750	751	752	753	754	755	756	757	758	759	760	761	762	763	764	765	766	767	768	769	770	771	772	773	774	775	776	777	778	779	780	781	782	783	784	785	786	787	788	789	790	791	792	793	794	795	796	797	798	799	800	801	802	803	804	805	806	807	808	809	810	811	812	813	814	815	816	817	818	819	820	821	822	823	824	825	826	827	828	829	830	831	832	833	834	835	836	837	838	839	840	841	842	843	844	845	846	847	848	849	850	851	852	853	854	855	856	857	858	859	860	861	862	863	864	865	866	867	868	869	870	871	872	873	874	875	876	877	878	879	880	881	882	883	884	885	886	887	888	889	890	891	892	893	894	895	896	897	898	899	900	901	902	903	904	905	906	907	908	909	910	911	912	913	914	915	916	917	918	919	920	921	922	923	924	925	926	927	928	929	930	931	932	933	934	935	936	937	938	939	940	941	942	943	944	945	946	947	948	949	950	951	952	953	954	955	956	957	958	959	960	961	962	963	964	965	966	967	968	969	970	971	972	973	974	975	976	977	978	979	980	981	982	983	984	985	986	987	988	989	990	991	992	993	994	995	996	997	998	999
SiO ₂	39.87	0.24	39.85	0.05	39.99	0.17	39.83	0.32	39.93	0.09	39.98	0.02	39.94	0.10	39.95	-	39.88	0.20	39.71	0.13	39.73	0.06	39.71	0.16	40.03	0.23	39.99	0.05	39.73	0.03	39.89	0.05	39.77	0.05	39.80	0.13	39.77	0.27	39.85	0.22																																																																																																																																																																																																																																																																																																																																																																																																																																																																																																																																																																																																																																																																																																																																																																																																																																																																																																																																																																																														
TiO ₂	0.01	0.01	0.01	0.01	0.02	0.00	0.00	0.01	0.01	0.01	0.02	0.01	0.02	0.00	0.01	-	0.03	0.03	0.01	0.01	0.02	0.01	0.02	0.02	0.02	0.01	0.01	0.01	0.01	0.03	0.01	0.03	0.03	0.02	0.03	0.02	0.00	0.01	0.01	0.02	0.01																																																																																																																																																																																																																																																																																																																																																																																																																																																																																																																																																																																																																																																																																																																																																																																																																																																																																																																																																																																													
Al ₂ O ₃	0.01	0.01	0.01	0.01	0.01	0.00	0.01	0.00	0.01	0.01	0.01	0.01	0.00	0.01	0.00	0.02	-	0.01	0.01	0.01	0.01	0.01	0.02	0.01	0.01	0.01	0.01	0.00	0.01	0.01	0.01	0.01	0.00	0.00	0.01	0.00	0.01	0.01	0.01	0.01	0.00																																																																																																																																																																																																																																																																																																																																																																																																																																																																																																																																																																																																																																																																																																																																																																																																																																																																																																																																																																																													
Cr ₂ O ₃	0.01	0.01	0.00	0.00	0.00	0.00	0.00	0.00	0.01	0.00	0.02	0.02	0.02	0.01	0.00	-	0.02	0.02	0.00	0.01	0.02	0.02	0.01	0.01	0.01	0.01	0.01	0.01	0.01	0.01	0.02	0.01	0.01	0.00	0.02	0.00	0.01	0.01	0.01	0.01																																																																																																																																																																																																																																																																																																																																																																																																																																																																																																																																																																																																																																																																																																																																																																																																																																																																																																																																																																																														
FeO	15.10	0.01	15.15	0.07	15.10	0.05	15.08	0.08	14.50	0.07	14.61	0.05	14.52	-	14.00	0.40	14.03	0.15	13.81	0.09	13.90	0.12	15.94	0.35	15.94	0.18	16.05	0.15	16.20	0.07	16.15	0.02	16.16	0.06	16.40	0.44	16.43	0.41																																																																																																																																																																																																																																																																																																																																																																																																																																																																																																																																																																																																																																																																																																																																																																																																																																																																																																																																																																																																
MnO	0.23	0.01	0.23	0.03	0.23	0.00	0.22	0.01	0.23	0.01	0.22	0.01	0.23	-	0.21	0.02	0.22	0.00	0.21	0.02	0.21	0.00	0.25	0.00	0.24	0.02	0.24	0.01	0.26	0.02	0.24	0.00	0.24	0.01	0.26	0.02	0.24	0.01	0.25	0.01																																																																																																																																																																																																																																																																																																																																																																																																																																																																																																																																																																																																																																																																																																																																																																																																																																																																																																																																																																																														
MgO	44.80	0.18	44.70	0.04	44.91	0.10	44.89	0.19	44.83	0.04	44.87	0.18	44.66	0.22	44.44	-	44.78	0.69	45.18	0.08	45.29	0.11	45.40	0.09	42.89	0.40	42.96	0.39	43.31	0.72	43.32	0.64	43.15	0.10	43.18	0.14	43.54	0.42	43.49	0.28																																																																																																																																																																																																																																																																																																																																																																																																																																																																																																																																																																																																																																																																																																																																																																																																																																																																																																																																																																																														
CaO	0.09	0.00	0.11	0.01	0.07	0.03	0.08	0.02	0.08	0.02	0.10	0.01	0.10	0.00	0.12	-	0.09	0.01	0.10	0.02	0.10	0.01	0.10	0.00	0.07	0.02	0.07	0.02	0.07	0.01	0.08	0.01	0.08	0.01	0.10	0.01	0.06	0.01	0.08	0.01																																																																																																																																																																																																																																																																																																																																																																																																																																																																																																																																																																																																																																																																																																																																																																																																																																																																																																																																																																																														
Na ₂ O	0.00	0.00	0.00	0.00	0.00	0.00	0.00	0.01	0.00	0.01	0.01	0.00	0.00	0.00	-	0.00	0.00	0.01	0.01	0.00	0.01	0.01	0.01	0.01	0.00	0.01	0.00	0.00	0.00	0.00	0.00	0.00	0.00	0.01	0.00	0.00	0.01	0.01	0.00	0.00																																																																																																																																																																																																																																																																																																																																																																																																																																																																																																																																																																																																																																																																																																																																																																																																																																																																																																																																																																																														
K ₂ O	0.00	0.00	0.00	0.00	0.00	0.00	0.00	0.00	0.00	0.00	0.00	0.00	0.00	0.00	-	0.00	0.00	0.00	0.00	0.00	0.00	0.00	0.00	0.00	0.00	0.00	0.00	0.00	0.00	0.00	0.00	0.00	0.00	0.00	0.00	0.00	0.00	0.00	0.00	0.00	0.00																																																																																																																																																																																																																																																																																																																																																																																																																																																																																																																																																																																																																																																																																																																																																																																																																																																																																																																																																																																													
NiO	0.30	0.02	0.26	0.00	0.28	0.01	0.27	0.01	0.29	0.01	0.29	0.01	0.31	0.00	0.29	-	0.29	0.04	0.31	0.02	0.29	0.02	0.33	0.																																																																																																																																																																																																																																																																																																																																																																																																																																																																																																																																																																																																																																																																																																																																																																																																																																																																																																																																																																																																														

Table S1 - Major and trace element average compositions of clinopyroxenes in OI-Ts from IODP Hole U1309D

Expedition/Hole	305-U1309D								305-U1309D								305-U1309D								305-U1309D								305-U1309D																							
	227R-3W, 124-126								234R-1W, 22-26								241R-2W, 89-91								247R-3W, 16-18								247R-3W, 22-25								247R-3W, 62-66								247R-3W, 76-81							
Sample	1096.2								1125.0								1160.7								1190.1								1190.1								1190.5								1190.7							
Depth (mbsf)	interstitial								interstitial								small interstitial								poikilitic								large poikilitic								interstitial								small interstitial							
n.	1		6		6		3		3		2		3		3		4		5		6		2		2		6		8																											
Location	core	σ	core	σ	rim	σ	wedge	σ	core	σ	rim	σ	core	σ	rim	σ	core	σ	rim	σ	core	σ	rim	σ	wedge	σ	core	σ	rim	σ																										
SiO ₂	52.20	0.24	51.53	0.29	51.63	0.21	51.65	0.11	51.45	0.35	52.14	1.06	51.47	0.18	51.69	0.27	51.21	0.25	51.13	0.34	51.57	0.14	51.99	0.14	50.55	1.40	51.36	0.09	51.45	0.17																										
TiO ₂	0.57	0.05	0.67	0.20	0.56	0.14	0.80	0.14	0.79	0.07	0.61	0.15	0.41	0.07	0.46	0.06	0.46	0.06	0.46	0.07	0.47	0.19	0.38	0.06	0.83	0.06	0.43	0.03	0.45	0.03																										
Al ₂ O ₃	3.24	0.06	3.29	0.17	3.34	0.18	3.20	0.18	3.63	0.48	3.13	0.46	3.62	0.08	3.50	0.14	3.63	0.09	3.65	0.20	4.31	1.20	3.46	0.05	3.15	0.19	3.67	0.08	3.63	0.11																										
Cr ₂ O ₃	1.18	0.07	1.27	0.13	1.32	0.06	1.17	0.12	1.30	0.04	1.00	0.38	1.35	0.07	1.28	0.05	1.34	0.09	1.34	0.13	1.03	0.21	1.16	0.16	1.04	0.05	1.39	0.05	1.38	0.06																										
FeO	3.92	0.11	4.20	0.24	4.28	0.22	4.28	0.10	4.39	0.20	4.46	0.95	4.61	0.34	4.61	0.45	4.36	0.17	4.61	0.54	4.63	0.32	5.35	0.85	4.91	0.02	5.02	0.16	4.87	0.45																										
MnO	0.11	0.03	0.13	0.02	0.14	0.02	0.14	0.01	0.13	0.01	0.15	0.01	0.15	0.02	0.14	0.02	0.13	0.02	0.14	0.02	0.12	0.02	0.16	0.01	0.15	0.03	0.16	0.01	0.16	0.01																										
MgO	15.48	0.17	16.31	0.29	16.43	0.35	16.55	0.20	15.95	0.06	16.92	1.04	16.85	0.62	17.07	0.84	16.56	0.43	17.13	0.69	17.55	2.22	17.79	1.45	16.43	0.34	17.05	0.42	17.12	0.86																										
CaO	22.83	0.40	21.95	0.35	21.75	0.55	21.90	0.29	21.20	0.68	20.67	2.06	20.89	0.95	20.94	0.90	21.32	0.61	20.75	1.13	18.25	5.27	19.53	2.71	20.18	0.60	20.01	0.60	20.28	1.26																										
Na ₂ O	0.42	0.07	0.45	0.05	0.46	0.05	0.46	0.05	0.56	0.13	0.43	0.07	0.39	0.03	0.40	0.01	0.38	0.04	0.38	0.05	0.72	0.60	0.36	0.04	1.12	1.06	0.36	0.03	0.36	0.04																										
K ₂ O	0.00	0.01	0.00	0.00	0.00	0.00	0.00	0.00	0.00	0.00	0.00	0.00	0.00	0.00	0.00	0.00	0.00	0.00	0.00	0.00	0.01	0.02	0.00	0.00	0.17	0.23	0.00	0.00	0.00	0.00																										
NiO	0.01	0.04	0.03	0.01	0.04	0.02	0.02	0.02	0.05	0.01	0.04	0.01	0.05	0.01	0.05	0.02	0.04	0.01	0.04	0.02	0.06	0.05	0.05	0.01	0.06	0.03	0.05	0.01	0.04	0.01																										
Total	99.97	0.53	99.83	0.40	99.97	0.12	100.18	0.25	99.45	0.16	99.56	0.57	99.82	0.12	100.15	0.46	99.46	0.51	99.63	0.43	98.73	1.16	100.23	0.43	98.59	1.18	99.50	0.33	99.75	0.17																										
Mg#	87.55	1.04	87.38	0.55	87.26	0.46	87.32	0.19	86.63	0.58	87.16	2.10	86.71	0.46	86.88	0.56	87.13	0.40	86.90	0.99	87.01	1.55	85.61	0.96	85.65	0.20	85.84	0.14	86.25	0.63																										
ppm																																																								
Li	4.15	0.18	4.19	0.37	4.23	0.16	4.50	0.18	2.00	0.55	4.69	0.21	2.64	0.16	2.91	0.16	2.78	0.48	2.60	0.32	2.40	0.42	2.27	0.13	2.41	0.38	1.98	0.43	2.16	0.26																										
B	6.38	0.40	7.16	1.10	6.93	1.27	7.29	0.16	5.87	0.18	5.13	0.37	12.69	5.93	9.67	0.11	9.24	0.12	8.35	0.36	14.04	2.60	11.69	0.66	15.54	0.62	8.12	0.36	7.87	0.57																										
Sc	132.0	4.4	125.0	7.9	117.3	4.5	129.2	7.4	111.7	6.0	123.7	4.1	106.1	1.0	111.1	10.0	100.6	0.2	97.7	6.7	101.5	4.8	100.4	3.3	113.0	4.2	106.7	4.3	109.4	6.6																										
Ti	3609	170	4475	1597	3147	785	5389	1249	4232	311	4549	243	2448	60	2687	309	2780	484	2938	629	2352	546	1940	63	4429	1041	2527	237	2678	282																										
V	344	12	389	43	345	21	420	13	351	20	375	12	328	3	349	33	365	1	356	32	321	22	302	10	407	33	324	22	343	31																										
Cr	7761	784	5690	647	6204	232	5258	415	7914	463	8367	465	6234	457	6636	618	8181	792	7809	639	6849	356	7266	240	6533	41	8609	386	8576	248																										
Mn	1060	35	1113	69	1176	21	1103	90	1306	112	1503	50	1121	86	1188	84	1120	100	1107	108	1121	76	1102	36	1233	32	1280	101	1264	112																										
Co	26.92	0.87	29.56	3.27	30.33	1.44	29.43	1.37	31.81	1.99	33.56	1.07	32.41	0.32	32.31	0.71	31.84	1.48	30.42	2.64	31.88	1.67	28.35	0.91	32.27	1.56	31.76	1.45	31.80	1.02																										
Ni	247	14	293	38	310	26	293	6	274	10	287	11	373	12	375	16	346	9	342	55	354	34	351	12	320	15	334	14	335	6																										
Cu	0.13	0.02	0.42	0.23	5.37	8.92	0.47	0.24	1.56	0.40	0.86	0.06	0.19	0.14	n.d.	-	0.74	0.88	0.63	0.57	2.90	3.85	0.37	0.04	0.63	0.74	0.24	0.12	0.51	0.51																										
Zn	15.31	0.70	16.87	2.29	17.28	0.59	16.96	2.28	24.39	0.17	25.81	0.93	18.98	1.56	19.38	0.68	21.52	0.98	20.69	1.03	22.61	5.03	20.45	0.71	22.34	1.00	23.04	1.58	22.23	2.16																										
Rb	b.d.l.	-	0.020	0.010	b.d.l.	-	b.d.l.	-	0.060	0.008	b.d.l.	-	b.d.l.	-	b.d.l.	-	0.020	0.000	0.021	0.006	0.110	0.005	0.025	0.005	0.071	0.005	0.010	0.000	0.011	0.000																										
Sr	6.67	0.23	7.12	0.15	6.94	0.11	7.02	0.08	7.30	0.06	8.18	0.27	6.85	0.21	6.82	0.74	7.64	0.29	7.28	0.46	7.96	0.41	7.80	0.24	7.35	0.02	7.02	0.25	6.97	0.42																										
Y	20.60	0.68	22.26	7.16	19.80	6.42	25.51	1.38	27.13	2.23	29.36	0.97	14.38	0.86	15.76	2.09	19.99	4.70	23.13	5.43	11.95	2.66	12.49	0.39	23.77	4.26	18.97	1.53	20.83	2.66																										
Zr	23.04	0.77	31.81	20.38	21.29	13.60	42.16	15.96	31.14	5.10	36.92	1.25	6.21	0.42	6.62	1.89	12.58	6.94	22.01	10.57	5.49	2.10	5.74	0.18	22.82	8.46	8.44	1.30	10.08	2.81																										
Nb	0.180	0.010	0.270	0.070	0.263	0.044	0.295	0.020	0.280	0.030	0.234	0.013	0.070	0.010	0.087	0.035	0.160	0.170	0.225	0.077	0.090	0.040	0.104	0.005	0.193	0.041	0.080	0.010	0.073	0.026																										
Sb	b.d.l.	-	0.010	0.010	b.d.l.	-	b.d.l.	-	b.d.l.	-	b.d.l.	-	b.d.l.	-	b.d.l.	-	b.d.l.	-	b.d.l.	-	b.d.l.	-	b.d.l.	-	b.d.l.	-	b.d.l.	-	b.d.l.	-	b.d.l.	-																								
Ba	b.d.l.	-	0.060	0.030	0.042	0.044	0.045	0.019	0.150	0.130	0.182	0.028	0.030	0.010	b.d.l.	-	0.050	0.030	0.070	0.043	0.220	0.260	0.150	0.012	0.214	0.275	0.050	0.020	0.043	0.009																										
La	0.230	0.010	0.210	0.080	0.192	0.054	0.244	0.028	0.260	0.040	0.242	0.013	0.110	0.000	0.125	0.040	0.150	0.090	0.179	0.049	0.140	0.060	0.190	0.007	0.359	0.095	0.140	0.030	0.160	0.047																										
Ce	1.230	0.040	1.280	0.530	1.122	0.402	1.511	0.271	1.480	0.240	1.590	0.059	0.620	0.010	0.669	0.183	0.790	0.370	0.959	0.350	0.610	0.220	0.756	0.025	1.893	0.524	0.660	0.130	0.790	0.209																										
Pr	0.340	0.010	0.360	0.150	0.312	0.116	0.438	0.076	0.400	0.070	0.414	0.019	0.170	0.000	0.180	0.046	0.220	0.110	0.272	0.111	0.150	0.050	0.164	0.006	0.455	0.153	0.200	0.030	0.224	0.045																										
Nd	2.590	0.100	3.070	1.270	2.525	1.031	3.670	0.651	3.260	0.390	3.420	0.150	1.370	0.030	1.536	0.353	1.870	0.730	2.335	0.863	1.310	0.400	1.215	0.045	3.365	0.870	1.660	0.250	1.843	0.350																										
Sm	1.410	0.070	1.730	0.700	1.407	0.551	2.103	0.284	1.920	0.180	2.190	0.140	0.870	0.060	0.971	0.182	1.250	0.340	1.442	0.479	0.680	0.150	0.715	0.031	1.706	0.322	1.050	0.130	1.148	0.225																										
Eu	0.450	0.020	0.490	0.080	0.480	0.073	0.522	0.008	0.460	0.060	0.508	0.026	0.340	0.010	0.391	0.044	0.380	0.030	0.400	0.067	0.340	0.050	0.298	0.012	0.568	0.094	0.380	0.050	0.409	0.025																										
Gd	2.470	0.090	3.680	1.300	2.981	1.124	4.379	0.322	3.790	0.400	3.998	0.150	1.910	0.300	2.201	0.195	2.380	0.830	2.608	0.779	1.610	0.380	1.475	0.048	3.258	0.665	2.170	0.210	2.361	0.123																										
Tb	0.490	0.020	0.690	0.240	0.590	0.205	0.801	0.050	0.670	0.050	0.751	0.030	0.360	0.050	0.412	0.053	0.490	0.140	0.556	0.156	0.300	0.080	0.176	0.010	0.643	0.109	0.44																													

Table S1 (continued clinopyroxene)

Expedition/Hole	305-U1309D				305-U1309D				305-U1309D				305-U1309D				305-U1309D				305-U1309D				305-U1309D							
Sample	248R-2W, 18-21				248R-2W, 22-24				248R-2W, 38-41				248R-2W, 43-48				248R-3W, 29-32				248R-3W, 36-38				248R-3W, 131-134				268R-2W, 83-85			
Depth (mbsf)	1193.3				1193.4				1193.5				1194.8				1194.8				1195.8				1290.1							
Shape	large poikilitic to subhedral				small interstitial				small interstitial				small interstitial				interstitial				poikilitic				large poikilitic				subhedral			
n.	2		2		2		3		4		3		3		3		4		4		5		3		2		3					
Location	core	σ	rim	σ	core	σ	wedge	σ	core	σ	rim	σ	core	σ	wedge	σ	core	σ	rim	σ	core	σ	rim	σ	core	σ	rim	σ				
SiO ₂	53.03	0.02	52.53	0.01	51.92	0.02	52.30	1.85	50.78	0.16	50.57	0.25	51.03	0.39	51.03	0.28	51.03	0.25	50.95	0.21	51.97	0.04	51.92	0.29	51.28	0.97	51.32	0.78	51.25	0.20	52.02	0.53
TiO ₂	0.46	0.11	0.47	0.05	0.90	0.26	0.92	0.40	0.88	0.03	0.95	0.07	0.54	0.23	0.69	0.16	0.62	0.06	0.62	0.03	0.49	0.09	0.50	0.06	0.34	0.13	0.46	0.18	0.42	0.02	0.56	0.28
Al ₂ O ₃	2.73	0.21	2.82	0.01	2.80	0.06	2.70	0.46	3.26	0.08	3.24	0.08	3.46	0.11	3.36	0.13	3.44	0.01	3.40	0.09	3.41	0.08	3.40	0.19	3.55	0.20	3.93	1.02	3.45	0.07	3.02	0.15
Cr ₂ O ₃	0.57	0.08	0.59	0.08	0.60	0.05	0.57	0.18	0.98	0.07	1.10	0.04	1.30	0.11	1.29	0.09	1.29	0.05	1.27	0.05	1.26	0.03	1.25	0.05	1.39	0.12	1.23	0.05	0.79	0.04	0.56	0.11
FeO	6.55	0.12	5.75	0.40	5.19	0.32	6.80	1.95	4.85	0.19	4.79	0.26	4.88	0.67	4.73	0.23	4.84	0.25	4.84	0.38	5.06	0.27	4.96	0.35	4.25	0.12	4.58	0.16	5.08	0.15	5.38	0.11
MnO	0.19	0.01	0.15	0.02	0.15	0.02	0.20	0.03	0.14	0.01	0.16	0.01	0.16	0.02	0.14	0.00	0.13	0.02	0.15	0.01	0.13	0.02	0.15	0.02	0.14	0.00	0.14	0.02	0.15	0.01	0.17	0.02
MgO	20.04	0.01	17.99	0.71	16.54	0.07	19.41	3.96	16.33	0.55	16.27	0.68	16.88	1.04	16.38	0.39	17.19	0.44	16.85	0.51	17.85	0.41	17.53	0.95	16.92	0.54	17.40	0.21	16.56	0.34	16.67	0.41
CaO	16.64	0.18	19.42	1.06	21.98	0.15	16.79	6.36	20.95	0.69	21.40	0.88	20.76	1.83	21.20	0.74	20.63	0.70	20.53	0.98	19.98	0.59	20.21	1.04	21.23	0.40	19.80	0.57	21.55	0.50	21.01	0.74
Na ₂ O	0.28	0.05	0.34	0.07	0.44	0.00	0.32	0.10	0.44	0.03	0.45	0.04	0.41	0.05	0.40	0.05	0.40	0.03	0.40	0.06	0.39	0.01	0.37	0.06	0.41	0.04	0.67	0.49	0.33	0.01	0.30	0.05
K ₂ O	0.00	0.00	0.00	0.00	0.00	0.00	0.00	0.01	0.00	0.00	0.00	0.00	0.00	0.00	0.00	0.00	0.00	0.00	0.00	0.00	0.00	0.00	0.00	0.00	0.00	0.00	0.01	0.01	0.00	0.00	0.00	0.01
NiO	0.04	0.01	0.05	0.01	0.04	0.01	0.04	0.01	0.03	0.02	0.03	0.01	0.04	0.01	0.03	0.01	0.04	0.01	0.03	0.02	0.05	0.00	0.04	0.01	0.03	0.03	0.04	0.01	0.02	0.03	0.01	0.01
Total	100.52	0.34	100.12	0.17	100.55	0.23	100.04	0.59	98.64	0.36	98.97	0.66	99.46	0.11	99.26	0.05	99.60	0.19	99.05	0.48	100.60	0.33	100.35	0.60	99.53	0.43	99.58	0.51	99.61	0.12	99.71	0.17
Mg#	84.51	0.22	84.80	0.38	85.03	0.83	83.73	1.10	85.72	0.31	85.82	0.20	86.08	0.96	86.07	0.39	86.38	0.33	86.13	0.64	86.29	0.45	86.30	0.29	87.65	0.65	87.13	0.53	85.32	0.12	84.66	0.58
ppm																																
Li	2.67	0.15	2.59	0.17	3.45	1.03	3.08	0.16	3.79	0.57	3.69	1.11	3.36	0.18	3.16	0.22	1.84	0.05	1.54	0.09	1.90	0.17	1.49	0.24	1.23	0.43	1.66	0.33	3.61	0.20	3.48	0.48
B	13.24	0.30	12.44	0.33	5.56	0.64	10.32	8.26	5.62	0.45	5.87	0.83	8.47	0.62	8.46	0.11	9.61	0.22	8.99	0.59	6.01	1.07	8.90	5.63	9.59	5.01	10.09	4.66	8.11	5.54	8	6
Sc	99.4	1.1	101.1	1.9	122.3	18.3	119.4	20.5	110.5	4.1	121.2	11.6	99.8	9.2	110.7	0.5	108.0	6.7	101.5	3.3	103.2	4.1	107.5	10.8	100.2	1.5	96.5	7.9	102.0	2.5	102.5	4.6
Ti	2675	48	2659	37	6277	1208	6737	1699	5511	325	6212	485	2514	13	3236	466	3279	403	2786	107	3427	461	3523	649	2378	724	2529	725	2808	102	3941	1659
V	366	1	372	6	447	8	477	34	440	27	482	28	332	23	376	10	343	40	305	10	353	18	354	31	329	11	320	35	342	37	378	36
Cr	n.d.	-	n.d.	-	2683	81	2579	41	6082	65	6361	537	8115	1121	7651	611	7171	428	6712	296	5770	79	5453	826	7657	1792	7092	1163	3569	130	3262	403
Mn	1341	40	1281	18	1477	6	1351	67	1313	72	1333	75	1198	143	1108	96	1081	79	1057	35	1224	44	1171	110	1205	34	1153	54	1325	106	1408	112
Co	35.78	0.60	35.59	1.15	38.00	3.02	34.07	3.48	32.55	1.96	32.17	3.32	31.25	3.66	28.41	1.62	28.45	1.61	27.95	0.89	34.19	0.25	29.91	2.83	33.05	3.17	30.49	2.00	39.57	1.15	39.05	1.17
Ni	248	4	243	1	311	15	274	39	287	13	286	19	278	29	258	13	291	17	286	12	389	31	338	34	370	40	344	27	219	9	206	12
Cu	0.06	0.04	0.09	0.02	0.56	0.02	0.11	0.02	0.17	0.10	0.85	0.71	0.09	0.01	0.14	0.07	0.07	0.04	0.78	0.03	n.d.	-	0.29	0.30	0.56	0.58	0.52	0.35	3.13	4.32	0.17	0.03
Zn	24.85	0.63	24.73	1.08	27.74	1.58	23.68	2.61	24.05	1.24	25.48	1.24	21.83	2.11	19.52	2.13	17.43	0.95	17.88	0.61	19.83	0.86	17.36	1.20	21.26	4.58	20.01	1.95	26.40	2.37	25.95	3.74
Rb	b.d.l.	-	b.d.l.	-	0.041	0.012	0.009	0.002	0.050	0.030	0.049	0.037	0.010	0.009	0.018	0.008	0.010	0.000	0.023	0.002	b.d.l.	-	b.d.l.	-	0.020	0.000	0.044	0.000	b.d.l.	-	b.d.l.	-
Sr	6.48	0.10	6.32	0.16	6.99	0.57	6.23	0.22	7.88	0.27	7.98	0.68	6.19	0.49	6.08	0.42	6.47	0.29	6.77	0.22	6.78	0.59	6.66	0.61	6.82	0.17	6.76	0.51	6.57	0.16	6.62	0.35
Y	16.08	0.23	16.13	1.36	35.97	13.92	39.06	10.99	41.76	0.77	43.52	2.35	26.76	0.50	44.23	8.49	31.21	2.06	26.80	0.66	17.58	2.29	18.97	2.71	12.30	3.31	14.70	3.67	14.29	0.22	19.78	4.66
Zr	7.78	0.02	7.84	1.24	28.74	25.20	34.00	18.52	46.41	1.83	48.65	6.46	21.07	3.08	65.26	29.47	36.35	4.17	27.81	0.70	8.75	2.09	13.13	5.06	4.71	1.14	11.25	7.08	6.53	0.92	17.72	12.19
Nb	0.140	0.020	0.120	0.025	0.147	0.080	0.173	0.019	0.240	0.030	0.268	0.014	0.320	0.010	0.407	0.017	0.240	0.020	0.200	0.008	0.080	0.000	0.097	0.024	0.130	0.020	0.158	0.025	0.070	0.033	0.158	0.057
Sb	b.d.l.	-	b.d.l.	-	b.d.l.	-	b.d.l.	-	b.d.l.	-	b.d.l.	-	b.d.l.	-	b.d.l.	-	b.d.l.	-	b.d.l.	-	b.d.l.	-	b.d.l.	-	0.006	0.000	b.d.l.	-	b.d.l.	-	b.d.l.	-
Ba	0.030	0.008	b.d.l.	-	0.178	0.120	0.034	0.000	0.220	0.140	0.219	0.170	0.010	0.000	0.020	0.000	b.d.l.	-	0.074	0.008	b.d.l.	-	0.051	0.009	0.130	0.110	0.119	0.105	b.d.l.	-	0.017	0.029
La	0.190	0.030	0.169	0.020	0.426	0.300	0.533	0.123	0.380	0.000	0.363	0.021	0.370	0.030	0.530	0.071	0.190	0.020	0.193	0.007	0.150	0.010	0.172	0.034	0.110	0.000	0.173	0.052	0.139	0.013	0.259	0.119
Ce	1.000	0.140	0.918	0.057	2.109	1.370	2.749	0.721	1.970	0.100	2.071	0.089	1.610	0.150	2.801	0.492	1.140	0.060	1.018	0.033	0.850	0.140	0.998	0.217	0.550	0.030	0.932	0.341	0.693	0.143	1.285	0.578
Pr	0.240	0.020	0.216	0.001	0.578	0.380	0.684	0.217	0.590	0.040	0.625	0.001	0.390	0.060	0.753	0.215	0.340	0.020	0.307	0.010	0.230	0.040	0.255	0.070	0.140	0.030	0.237	0.088	0.185	0.023	0.328	0.162
Nd	1.880	0.110	1.776	0.047	4.560	2.740	5.280	1.739	4.630	0.460	4.847	0.265	2.890	0.390	6.152	1.957	2.850	0.150	2.502	0.085	1.860	0.410	2.148	0.377	1.270	0.320	1.814	0.662	1.548	0.122	2.562	1.178
Sm	0.960	0.040	1.012	0.027	2.464	1.210	2.645	0.841	2.560	0.040	2.664	0.132	1.480	0.210	3.043	0.914	1.690	0.160	1.529	0.050	1.120	0.200	1.244	0.151	0.790	0.240	0.980	0.353	0.927	0.055	1.416	0.557
Eu	0.390	0.000	0.391	0.018	0.734	0.180	0.777	0.143	0.670	0.020	0.696	0.061	0.380	0.010	0.494	0.049	0.420	0.040	0.394	0.013	0.420	0.090	0.443	0.053	0.340	0.080	0.360	0.085	0.356	0.016	0.408	0.086
Gd	1.950	0.080	2.001	0.058	5.201	2.680	5.494	2.086	5.470	0.190	5.746	0.24																				

Table S2 (continued OI-T1)

Sample Phase	105-011090-248R_3W_38																																																																																																																																																																																																																																																																																																																																																																																																																																																																																																																																																																																																																																																																																																																																																																																																
	CLINOPIROXENE interstitial undeformed										OLIVINE corroded deformed																																																																																																																																																																																																																																																																																																																																																																																																																																																																																																																																																																																																																																																																																																																																																																																						
Shape Deformation																																																																																																																																																																																																																																																																																																																																																																																																																																																																																																																																																																																																																																																																																																																																																																																																	
n-grain																																																																																																																																																																																																																																																																																																																																																																																																																																																																																																																																																																																																																																																																																																																																																																																																	
Axis																																																																																																																																																																																																																																																																																																																																																																																																																																																																																																																																																																																																																																																																																																																																																																																																	
Location																																																																																																																																																																																																																																																																																																																																																																																																																																																																																																																																																																																																																																																																																																																																																																																																	
Dist. (mm)																																																																																																																																																																																																																																																																																																																																																																																																																																																																																																																																																																																																																																																																																																																																																																																																	
SiO2	0.07 0.16 0.16	0.16	0.23 0.23	0.32 0.32	0.40 0.40	0.48 0.48	0.56 0.56	0.64 0.64	0.72 0.72	0.80 0.80	0.88 0.88	0.96 0.96	1.04 1.04	1.12 1.12	1.20 1.20	1.28 1.28	1.36 1.36	1.44 1.44	1.52 1.52	1.60 1.60	1.68 1.68	1.76 1.76	1.84 1.84	1.92 1.92	2.00 2.00	2.08 2.08	2.16 2.16	2.24 2.24	2.32 2.32	2.40 2.40	2.48 2.48	2.56 2.56	2.64 2.64	2.72 2.72	2.80 2.80	2.88 2.88	2.96 2.96	3.04 3.04	3.12 3.12	3.20 3.20	3.28 3.28	3.36 3.36	3.44 3.44	3.52 3.52	3.60 3.60	3.68 3.68	3.76 3.76	3.84 3.84	3.92 3.92	4.00 4.00	4.08 4.08	4.16 4.16	4.24 4.24	4.32 4.32	4.40 4.40	4.48 4.48	4.56 4.56	4.64 4.64	4.72 4.72	4.80 4.80	4.88 4.88	4.96 4.96	5.04 5.04	5.12 5.12	5.20 5.20	5.28 5.28	5.36 5.36	5.44 5.44	5.52 5.52	5.60 5.60	5.68 5.68	5.76 5.76	5.84 5.84	5.92 5.92	6.00 6.00	6.08 6.08	6.16 6.16	6.24 6.24	6.32 6.32	6.40 6.40	6.48 6.48	6.56 6.56	6.64 6.64	6.72 6.72	6.80 6.80	6.88 6.88	6.96 6.96	7.04 7.04	7.12 7.12	7.20 7.20	7.28 7.28	7.36 7.36	7.44 7.44	7.52 7.52	7.60 7.60	7.68 7.68	7.76 7.76	7.84 7.84	7.92 7.92	8.00 8.00	8.08 8.08	8.16 8.16	8.24 8.24	8.32 8.32	8.40 8.40	8.48 8.48	8.56 8.56	8.64 8.64	8.72 8.72	8.80 8.80	8.88 8.88	8.96 8.96	9.04 9.04	9.12 9.12	9.20 9.20	9.28 9.28	9.36 9.36	9.44 9.44	9.52 9.52	9.60 9.60	9.68 9.68	9.76 9.76	9.84 9.84	9.92 9.92	10.00 10.00	10.08 10.08	10.16 10.16	10.24 10.24	10.32 10.32	10.40 10.40	10.48 10.48	10.56 10.56	10.64 10.64	10.72 10.72	10.80 10.80	10.88 10.88	10.96 10.96	11.04 11.04	11.12 11.12	11.20 11.20	11.28 11.28	11.36 11.36	11.44 11.44	11.52 11.52	11.60 11.60	11.68 11.68	11.76 11.76	11.84 11.84	11.92 11.92	12.00 12.00	12.08 12.08	12.16 12.16	12.24 12.24	12.32 12.32	12.40 12.40	12.48 12.48	12.56 12.56	12.64 12.64	12.72 12.72	12.80 12.80	12.88 12.88	12.96 12.96	13.04 13.04	13.12 13.12	13.20 13.20	13.28 13.28	13.36 13.36	13.44 13.44	13.52 13.52	13.60 13.60	13.68 13.68	13.76 13.76	13.84 13.84	13.92 13.92	14.00 14.00	14.08 14.08	14.16 14.16	14.24 14.24	14.32 14.32	14.40 14.40	14.48 14.48	14.56 14.56	14.64 14.64	14.72 14.72	14.80 14.80	14.88 14.88	14.96 14.96	15.04 15.04	15.12 15.12	15.20 15.20	15.28 15.28	15.36 15.36	15.44 15.44	15.52 15.52	15.60 15.60	15.68 15.68	15.76 15.76	15.84 15.84	15.92 15.92	16.00 16.00	16.08 16.08	16.16 16.16	16.24 16.24	16.32 16.32	16.40 16.40	16.48 16.48	16.56 16.56	16.64 16.64	16.72 16.72	16.80 16.80	16.88 16.88	16.96 16.96	17.04 17.04	17.12 17.12	17.20 17.20	17.28 17.28	17.36 17.36	17.44 17.44	17.52 17.52	17.60 17.60	17.68 17.68	17.76 17.76	17.84 17.84	17.92 17.92	18.00 18.00	18.08 18.08	18.16 18.16	18.24 18.24	18.32 18.32	18.40 18.40	18.48 18.48	18.56 18.56	18.64 18.64	18.72 18.72	18.80 18.80	18.88 18.88	18.96 18.96	19.04 19.04	19.12 19.12	19.20 19.20	19.28 19.28	19.36 19.36	19.44 19.44	19.52 19.52	19.60 19.60	19.68 19.68	19.76 19.76	19.84 19.84	19.92 19.92	20.00 20.00	20.08 20.08	20.16 20.16	20.24 20.24	20.32 20.32	20.40 20.40	20.48 20.48	20.56 20.56	20.64 20.64	20.72 20.72	20.80 20.80	20.88 20.88	20.96 20.96	21.04 21.04	21.12 21.12	21.20 21.20	21.28 21.28	21.36 21.36	21.44 21.44	21.52 21.52	21.60 21.60	21.68 21.68	21.76 21.76	21.84 21.84	21.92 21.92	22.00 22.00	22.08 22.08	22.16 22.16	22.24 22.24	22.32 22.32	22.40 22.40	22.48 22.48	22.56 22.56	22.64 22.64	22.72 22.72	22.80 22.80	22.88 22.88	22.96 22.96	23.04 23.04	23.12 23.12	23.20 23.20	23.28 23.28	23.36 23.36	23.44 23.44	23.52 23.52	23.60 23.60	23.68 23.68	23.76 23.76	23.84 23.84	23.92 23.92	24.00 24.00	24.08 24.08	24.16 24.16	24.24 24.24	24.32 24.32	24.40 24.40	24.48 24.48	24.56 24.56	24.64 24.64	24.72 24.72	24.80 24.80	24.88 24.88	24.96 24.96	25.04 25.04	25.12 25.12	25.20 25.20	25.28 25.28	25.36 25.36	25.44 25.44	25.52 25.52	25.60 25.60	25.68 25.68	25.76 25.76	25.84 25.84	25.92 25.92	26.00 26.00	26.08 26.08	26.16 26.16	26.24 26.24	26.32 26.32	26.40 26.40	26.48 26.48	26.56 26.56	26.64 26.64	26.72 26.72	26.80 26.80	26.88 26.88	26.96 26.96	27.04 27.04	27.12 27.12	27.20 27.20	27.28 27.28	27.36 27.36	27.44 27.44	27.52 27.52	27.60 27.60	27.68 27.68	27.76 27.76	27.84 27.84	27.92 27.92	28.00 28.00	28.08 28.08	28.16 28.16	28.24 28.24	28.32 28.32	28.40 28.40	28.48 28.48	28.56 28.56	28.64 28.64	28.72 28.72	28.80 28.80	28.88 28.88	28.96 28.96	29.04 29.04	29.12 29.12	29.20 29.20	29.28 29.28	29.36 29.36	29.44 29.44	29.52 29.52	29.60 29.60	29.68 29.68	29.76 29.76	29.84 29.84	29.92 29.92	30.00 30.00	30.08 30.08	30.16 30.16	30.24 30.24	30.32 30.32	30.40 30.40	30.48 30.48	30.56 30.56	30.64 30.64	30.72 30.72	30.80 30.80	30.88 30.88	30.96 30.96	31.04 31.04	31.12 31.12	31.20 31.20	31.28 31.28	31.36 31.36	31.44 31.44	31.52 31.52	31.60 31.60	31.68 31.68	31.76 31.76	31.84 31.84	31.92 31.92	32.00 32.00	32.08 32.08	32.16 32.16	32.24 32.24	32.32 32.32	32.40 32.40	32.48 32.48	32.56 32.56	32.64 32.64	32.72 32.72	32.80 32.80	32.88 32.88	32.96 32.96	33.04 33.04	33.12 33.12	33.20 33.20	33.28 33.28	33.36 33.36	33.44 33.44	33.52 33.52	33.60 33.60	33.68 33.68	33.76 33.76	33.84 33.84	33.92 33.92	34.00 34.00	34.08 34.08	34.16 34.16	34.24 34.24	34.32 34.32	34.40 34.40	34.48 34.48	34.56 34.56	34.64 34.64	34.72 34.72	34.80 34.80	34.88 34.88	34.96 34.96	35.04 35.04	35.12 35.12	35.20 35.20	35.28 35.28	35.36 35.36	35.44 35.44	35.52 35.52	35.60 35.60	35.68 35.68	35.76 35.76	35.84 35.84	35.92 35.92	36.00 36.00	36.08 36.08	36.16 36.16	36.24 36.24	36.32 36.32	36.40 36.40	36.48 36.48	36.56 36.56	36.64 36.64	36.72 36.72	36.80 36.80	36.88 36.88	36.96 36.96	37.04 37.04	37.12 37.12	37.20 37.20	37.28 37.28	37.36 37.36	37.44 37.44	37.52 37.52	37.60 37.60	37.68 37.68	37.76 37.76	37.84 37.84	37.92 37.92	38.00 38.00	38.08 38.08	38.16 38.16	38.24 38.24	38.32 38.32	38.40 38.40	38.48 38.48	38.56 38.56	38.64 38.64	38.72 38.72	38.80 38.80	38.88 38.88	38.96 38.96	39.04 39.04	39.12 39.12	39.20 39.20	39.28 39.28	39.36 39.36	39.44 39.44	39.52 39.52	39.60 39.60	39.68 39.68	39.76 39.76	39.84 39.84	39.92 39.92	40.00 40.00	40.08 40.08	40.16 40.16	40.24 40.24	40.32 40.32	40.40 40.40	40.48 40.48	40.56 40.56	40.64 40.64	40.72 40.72	40.80 40.80	40.88 40.88	40.96 40.96	41.04 41.04	41.12 41.12	41.20 41.20	41.28 41.28	41.36 41.36	41.44 41.44	41.52 41.52	41.60 41.60	41.68 41.68	41.76 41.76	41.84 41.84	41.92 41.92	42.00 42.00	42.08 42.08	42.16 42.16	42.24 42.24	42.32 42.32	42.40 42.40	42.48 42.48	42.56 42.56	42.64 42.64	42.72 42.72	42.80 42.80	42.88 42.88	42.96 42.96	43.04 43.04	43.12 43.12	43.20 43.20	43.28 43.28	43.36 43.36	43.44 43.44	43.52 43.52	43.60 43.60	43.68 43.68	43.76 43.76	43.84 43.84	43.92 43.92	44.00 44.00	44.08 44.08	44.16 44.16	44.24 44.24	44.32 44.32	44.40 44.40	44.48 44.48	44.56 44.56	44.64 44.64	44.72 44.72	44.80 44.80	44.88 44.88	44.96 44.96	45.04 45.04	45.12 45.12	45.20 45.20	45.28 45.28	45.36 45.36	45.44 45.44	45.52 45.52	45.60 45.60	45.68 45.68	45.76 45.76	45.84 45.84	45.92 45.92	46.00 46.00	46.08 46.08	46.16 46.16	46.24 46.24	46.32 46.32	46.40 46.40	46.48 46.48	46.56 46.56	46.64 46.64	46.72 46.72	46.80 46.80	46.88 46.88	46.96 46.96	47.04 47.04	47.12 47.12	47.20 47.20	47.28 47.28	47.36 47.36	47.44 47.44	47.52 47.52	47.60 47.60	47.68 47.68	47.76 47.76	47.84 47.84	47.92 47.92	48.00 48.00	48.08 48.08	48.16 48.16	48.24 48.24	48.32 48.32	48.40 48.40	48.48 48.48	48.56 48.56	48.64 48.64	48.72 48.72	48.80 48.80	48.88 48.88	48.96 48.96	49.04 49.04	49.12 49.12	49.20 49.20	49.28 49.28	49.36 49.36	49.44 49.44	49.52 49.52	49.60 49.60	49.68 49.68	49.76 49.76	49.84 49.84	49.92 49.92	50.00 50.00	50.08 50.08	50.16 50.16	50.24 50.24	50.32 50.32	50.40 50.40	50.48 50.48	50.56 50.56	50.64 50.64	50.72 50.72	50.80 50.80	50.88 50.88	50.96 50.96	51.04 51.04	51.12 51.12	51.20 51.20	51.28 51.28	51.36 51.36	51.44 51.44	51.52 51.52	51.60 51.60	51.68 51.68	51.76 51.76	51.84 51.84	51.92 51.92	52.00 52.00	52.08 52.08	52.16 52.16	52.24 52.24	52.32 52.32	52.40 52.40	52.48 52.48	52.56 52.56	52.64 52.64	52.72 52.72	52.80 52.80	52.88 52.88	52.96 52.96	53.04 53.04	53.12 53.12	53.20 53.20	53.28 53.28	53.36 53.36	53.44 53.44	53.52 53.52	53.60 53.60	53.68 53.68	53.76 53.76	53.84 53.84	53.92 53.92	54.00 54.00	54.08 54.08	54.16 54.16	54.24 54.24	54.32 54.32	54.40 54.40	54.48 54.48	54.56 54.56	54.64 54.64	54.72 54.72	54.80 54.80	54.88 54.88	54.96 54.96	55.04 55.04	55.12 55.12	55.20 55.20	55.28 55.28	55.36 55.36	55.44 55.44	55.52 55.52	55.60 55.60	55.68 55.68	55.76 55.76	55.84 55.84	55.92 55.92	56.00 56.00	56.08 56.08	56.16 56.16	56.24 56.24	56.32 56.32	56.40 56.40	56.48 56.48	56.56 56.56	56.64 56.64	56.72 56.72	56.80 56.80	56.88 56.88	56.96 56.96	57.04 57.04	57.12 57.12	57.20 57.20	57.28 57.28	57.36 57.36	57.44 57.44	57.52 57.52	57.60 57.60	57.68 57.68	57.76 57.76	57.84 57.84	57.92 57.92	58.00 58.00	58.08 58.08	58.16 58.16	58.24 58.24	58.32 58.32	58.40 58.40	58.48 58.48	58.56 58.56	58.64 58.64	58.72 58.72	58.80 58.80	58.88 58.88	58.96 58.96	59.04 59.04	59.12 59.12	59.20 59.20	59.28 59.28	59.36 59.36	59.44 59.44	59.52 59.52	59.60 59.60	59.68 59.68	59.76 59.76	59.84 59.84	59.92 59.92	60.00 60.00	60.08 60.08	60.16 60.16	60.24 60.24	60.32 60.32	60.40 60.40	60.48 60.48	60.56 60.56	60.64 60.64	60.72 60.72	60.80 60.80	60.88 60.88	60.96 60.96	61.04 61.04	61.12 61.12	61.20 61.20	61.28 61.28	61.36 61.36	61.44 61.44	61.52 61.52

Table S2 - Olivine-clinopyroxene major and trace element profiles in OI-T type 2 from IODP Hole U1309D

Sample	[905-U1309D-248R-2W, 38-41																																																	
	OLIVINE anhydral			CLINOPYROXENE interstitial											OLIVINE corroded																																			
Phase	undeformed																																																	
Shape	undeformed																																																	
Deformation	undeformed																																																	
n. grain	6								9																																									
Axis	[100]																																																	
Location	rim								rim																																									
Dist. (mm)	0.06 σ		0.14 σ		0.22 σ		0.29 σ		0.58 σ		0.71 σ		0.97 σ		1.17 σ		0.23 σ		0.30 σ		0.36 σ		0.00 σ		0.15 σ		0.44 σ		0.58 σ		0.73 σ		0.87 σ		1.02 σ		1.16 σ		1.31 σ		1.45 σ		1.60 σ		1.75 σ		1.89 σ			
SiO ₂	39.28	0.35	39.52	0.35	39.67	0.35	39.68	0.35	39.40	0.35	39.44	0.35	39.78	0.35	50.89	0.43	50.75	0.43	50.73	0.43	51.01	0.43	50.57	0.42	39.42	0.35	39.62	0.35	39.36	0.35	39.37	0.35	39.52	0.35	39.52	0.35	39.28	0.35	39.56	0.35	39.52	0.35	39.60	0.35	39.46	0.35	39.59	0.35		
TiO ₂	0.02	0.03	0.00	0.00	0.01	0.03	0.00	0.03	0.04	0.03	0.03	0.03	0.05	0.03	0.96	0.06	0.86	0.05	0.86	0.06	0.89	0.06	1.01	0.06	0.02	0.03	0.01	0.03	0.03	0.03	0.00	0.03	0.00	0.03	0.03	0.03	0.00	0.02	0.03	0.00	0.00	0.04	0.03	0.03	0.03	0.03				
Al ₂ O ₃	0.01	0.02	0.03	0.02	0.00	0.00	0.04	0.02	0.07	0.02	0.01	0.02	0.01	0.02	3.28	0.07	3.20	0.06	3.28	0.07	3.15	0.06	3.29	0.07	0.01	0.02	0.01	0.02	0.02	0.02	0.02	0.02	0.02	0.02	0.00	0.02	0.00	0.02	0.01	0.02	0.03	0.02	0.02	0.00	0.02	0.00	0.02			
Cr ₂ O ₃	0.03	0.04	0.01	0.04	0.01	0.03	0.00	0.00	0.18	0.04	0.01	0.04	0.03	0.04	1.15	0.07	0.95	0.06	0.92	0.06	0.94	0.06	1.10	0.07	0.01	0.04	0.01	0.04	0.02	0.04	0.01	0.04	0.02	0.04	0.02	0.04	0.02	0.04	0.00	0.04	0.00	0.00	0.03	0.04	0.04	0.04	0.03	0.04		
FeO	15.07	0.23	15.07	0.23	15.16	0.23	15.22	0.23	15.32	0.23	15.04	0.23	15.14	0.23	4.87	0.13	5.00	0.13	4.68	0.13	4.77	0.13	4.60	0.13	15.00	0.23	15.01	0.23	15.08	0.23	14.89	0.23	15.18	0.23	15.19	0.23	15.08	0.23	15.05	0.23	15.08	0.23	15.34	0.23	15.17	0.23	15.28	0.23		
MnO	0.21	0.04	0.25	0.04	0.21	0.04	0.23	0.04	0.23	0.04	0.25	0.04	0.19	0.04	0.15	0.04	0.18	0.04	0.14	0.04	0.13	0.04	0.15	0.04	0.20	0.04	0.22	0.04	0.23	0.04	0.21	0.04	0.22	0.04	0.22	0.04	0.25	0.04	0.19	0.04	0.21	0.04	0.24	0.04	0.24	0.04	0.23	0.04		
MgO	44.66	0.89	44.45	0.89	44.39	0.89	44.64	0.89	44.34	0.89	44.75	0.89	44.90	0.90	16.45	0.42	17.13	0.43	15.73	0.40	16.66	0.42	15.97	0.41	44.54	0.89	44.62	0.89	44.92	0.90	44.58	0.89	44.65	0.89	44.70	0.89	45.16	0.90	44.55	0.89	44.48	0.89	44.47	0.89	44.68	0.89	44.66	0.89		
CaO	0.07	0.01	0.09	0.01	0.09	0.01	0.09	0.01	0.07	0.01	0.07	0.01	0.07	0.01	21.65	0.40	20.60	0.38	21.76	0.40	21.06	0.39	21.53	0.40	0.06	0.01	0.08	0.01	0.11	0.01	0.09	0.01	0.09	0.01	0.09	0.01	0.10	0.01	0.10	0.01	0.11	0.01	0.10	0.01	0.11	0.01	0.11	0.01		
Na ₂ O	0.03	0.04	0.01	0.03	0.00	0.04	0.03	0.04	0.03	0.04	0.00	0.00	0.00	0.00	0.52	0.08	0.50	0.08	0.41	0.08	0.42	0.07	0.43	0.08	0.01	0.04	0.01	0.04	0.03	0.04	0.00	0.00	0.02	0.04	0.02	0.04	0.02	0.04	0.00	0.02	0.00	0.00	0.02	0.04	0.04	0.04	0.04			
K ₂ O	0.00	0.01	0.00	0.00	0.00	0.00	0.00	0.01	0.00	0.00	0.00	0.00	0.00	0.00	0.01	0.01	0.00	0.01	0.01	0.01	0.00	0.00	0.01	0.01	0.00	0.00	0.01	0.01	0.01	0.01	0.00	0.00	0.01	0.01	0.00	0.00	0.01	0.00	0.00	0.01	0.00	0.01	0.01	0.00	0.01	0.00	0.00			
NiO	0.23	0.05	0.25	0.05	0.23	0.04	0.26	0.05	0.28	0.05	0.27	0.05	0.22	0.05	0.03	0.04	0.04	0.04	0.03	0.04	0.04	0.04	0.03	0.04	0.31	0.05	0.26	0.04	0.29	0.05	0.30	0.05	0.27	0.05	0.31	0.05	0.26	0.04	0.27	0.05	0.27	0.05	0.24	0.04	0.29	0.05	0.26	0.05	0.28	0.05
Total	99.60	0.99	99.68	0.98	99.77	0.98	100.18	0.98	99.96	0.99	99.87	0.99	100.38	0.99	99.93	0.74	99.21	0.74	98.54	0.73	99.06	0.74	98.67	0.73	99.59	0.99	99.85	0.99	100.09	0.99	99.47	0.99	100.01	0.99	100.10	0.99	100.15	0.99	99.77	0.99	99.74	0.99	100.13	0.99	99.94	0.99	100.08	0.99		
Mg#	84.08	0.84	84.02	0.84	83.92	0.84	83.95	0.85	83.76	0.85	84.13	0.84	84.09	0.84	85.76	1.19	85.93	1.16	85.70	1.20	86.17	1.17	86.10	1.18	84.11	0.84	84.12	0.84	84.15	0.84	84.22	0.83	83.98	0.84	83.99	0.84	84.23	0.83	84.07	0.84	84.02	0.84	83.86	0.85	83.94	0.84	83.91	0.84	84.06	0.84

Spot size	77																	77																																						
	rim																	rim																																						
Li	1.84	0.09	1.25	0.06	1.74	0.08	1.98	0.09	1.59	0.08	4.77	0.27	4.33	0.25	3.75	0.22	1.24	0.07	1.52	0.08	7.22	0.22	7.07	0.22	1.24	0.07	1.52	0.08	7.22	0.22	7.07	0.22	1.24	0.07	1.52	0.08	7.22	0.22	7.07	0.22	1.24	0.07	1.52	0.08	7.22	0.22	7.07	0.22	1.24	0.07	1.52	0.08				
B	5.94	0.35	6.46	0.38	5.95	0.36	6.12	0.38	5.45	0.34	6.54	0.52	6.52	0.43	4.94	0.42	5.76	0.39	4.74	0.33	5.91	0.41	6.22	0.46	6.22	0.46	6.22	0.46	6.22	0.46	6.22	0.46	6.22	0.46	6.22	0.46	6.22	0.46	6.22	0.46	6.22	0.46	6.22	0.46	6.22	0.46	6.22	0.46	6.22	0.46	6.22	0.46	6.22	0.46		
Ca	482	18	565	20	551	20	558	20	485	17	154733	4899	155519	4923	153875	4873	415	15	593	21	655	22	657	23	732	25	732	25	732	25	732	25	732	25	732	25	732	25	732	25	732	25	732	25	732	25	732	25	732	25	732	25	732	25		
Sc	6.87	0.24	7.03	0.24	6.01	0.21	6.09	0.21	6.31	0.22	110	4	114	4	120	4	7.24	0.26	7.19	0.26	6.63	0.25	7.61	0.29	7.61	0.29	7.61	0.29	7.61	0.29	7.61	0.29	7.61	0.29	7.61	0.29	7.61	0.29	7.61	0.29	7.61	0.29	7.61	0.29	7.61	0.29	7.61	0.29	7.61	0.29	7.61	0.29	7.61	0.29		
Ti	101.56	3.24	108.29	3.44	79.37	2.55	75.9	2.44	88.04	2.82	5664	242	5832	255	6387	302	114	4	110	4	91	3	104	3	104	3	104	3	104	3	104	3	104	3	104	3	104	3	104	3	104	3	104	3	104	3	104	3	104	3	104	3	104	3	104	3
V	5.2	0.2	6.1	0.2	4.9	0.2	4.5	0.1	4.5	0.1	4.52	15	4.69	15	4.85	16	5.6	0.2	6.3	0.2	5.9	0.2	6.3	0.2	6.3	0.2	6.3	0.2	6.3	0.2	6.3	0.2	6.3	0.2	6.3	0.2	6.3	0.2	6.3	0.2	6.3	0.2	6.3	0.2	6.3	0.2	6.3	0.2	6.3	0.2	6.3	0.2	6.3	0.2		
Cr	52.14	2.28	73.37	3.27	56.76	2.58	57.86	2.68	50.7	2.4	5857	315	6108	340	6298	393	66.86	3.39	83.41	4.33	86.43	4.6	80.18	4.37	77.77	4.34	79.78	4.57	79.78	4.57	79.78	4.57	79.78	4.57	79.78	4.57	79.78	4.57	79.78	4.57	79.78	4.57	79.78	4.57	79.78	4.57	79.78	4.57	79.78	4.57	79.78	4.57	79.78	4.57		
Mn	1848	60	1858	60	1945	63	1898	62	1871	62	1419	50	1396	49	1292	47	1913	64	1910	65	1925	66	1875	64	1897	66	1897	66	1897	66	1897	66	1897	66	1897	66	1897	66	1897	66	1897	66	1897	66	1897	66	1897	66	1897	66	1897	66	1897	66	1897	66
Co	151	5	155	5	157	5	158	5	156	5	36	1	35	1	31	1	158	5	156	5	157	5	157	5	157	5	157	5	157	5	157	5	157	5	157	5	157	5	157	5	157	5	157	5	157	5	157	5	157	5	157	5	157	5		
Ni	1918	76	1952	78	1861	76	1869	77	1861	78	308	12	301	11	27																																									

Table S2 (continued OI-T2)

Phase		CLINOPYROXENE																																																			
Shape		interstitial																																																			
Deformation		undeformed																																																			
n. grain																																																					
Axis																																																					
Location																																																					
Dist. (mm)		core														rim		core										rim																									
		0.88 σ	0.94 σ	1.00 σ	1.06 σ	1.13 σ	1.19 σ	1.25 σ	1.31 σ	1.38 σ	1.44 σ	1.50 σ	1.56 σ	1.63 σ	1.69 σ	1.75 σ	1.81 σ	1.94 σ	2.00 σ	2.06 σ	2.13 σ	2.19 σ	2.19 σ	2.38 σ	2.44 σ	2.50 σ	2.50 σ	2.50 σ	2.50 σ																								
SiO ₂	39.44	0.35	39.35	0.35	39.49	0.35	39.56	0.35	39.72	0.35	39.57	0.35	39.64	0.35	39.46	0.35	39.59	0.35	39.46	0.35	39.26	0.35	39.62	0.35	39.78	0.35	39.55	0.35	39.72	0.35	39.60	0.35	50.93	0.43	39.56	0.35	39.40	0.35	51.21	0.43	51.21	0.43	50.92	0.43	51.47	0.43	51.18	0.43					
TiO ₂	0.00	0.00	0.00	0.03	0.00	0.03	0.00	0.03	0.01	0.03	0.02	0.03	0.02	0.03	0.02	0.03	0.03	0.03	0.03	0.01	0.03	0.05	0.03	0.04	0.03	0.00	0.00	0.00	0.00	0.06	0.03	0.01	0.03	0.66	0.05	0.02	0.03	0.02	0.03	0.69	0.05	0.47	0.04	0.40	0.04	0.42	0.04	0.53	0.05				
Al ₂ O ₃	0.01	0.02	0.01	0.02	0.02	0.02	0.02	0.02	0.01	0.02	0.03	0.02	0.00	0.02	0.00	0.02	0.00	0.00	0.03	0.02	0.03	0.02	0.01	0.02	0.00	0.00	0.00	0.02	0.01	0.02	0.02	0.03	0.36	0.06	0.00	0.00	0.04	0.02	3.25	0.06	3.56	0.07	3.57	0.07	3.45	0.07	3.51	0.07					
Cr ₂ O ₃	0.02	0.04	0.05	0.04	0.04	0.04	0.01	0.04	0.02	0.04	0.02	0.04	0.01	0.04	0.03	0.04	0.03	0.04	0.02	0.04	0.00	0.04	0.01	0.04	0.00	0.00	0.04	0.04	0.04	0.00	0.00	1.26	0.07	0.00	0.00	0.02	0.04	1.22	0.07	1.38	0.07	1.40	0.07	1.31	0.07	1.40	0.07						
FeO	14.87	0.25	14.95	0.25	14.96	0.25	14.86	0.25	14.81	0.25	15.08	0.25	15.03	0.25	15.08	0.25	15.04	0.25	14.99	0.25	15.14	0.25	15.15	0.25	15.08	0.25	14.96	0.25	14.86	0.25	14.84	0.25	4.61	0.13	14.56	0.24	14.89	0.25	4.67	0.13	5.30	0.14	4.73	0.13	5.62	0.14	4.98	0.13					
MnO	0.24	0.04	0.25	0.04	0.22	0.04	0.25	0.04	0.21	0.04	0.23	0.04	0.23	0.04	0.24	0.04	0.28	0.04	0.21	0.04	0.24	0.04	0.24	0.04	0.24	0.04	0.24	0.04	0.20	0.04	0.20	0.04	0.14	0.04	0.22	0.04	0.25	0.04	0.14	0.04	0.18	0.04	0.16	0.04	0.17	0.04	0.14	0.04					
MgO	44.35	0.89	44.31	0.89	44.28	0.89	44.29	0.89	44.02	0.88	44.14	0.89	44.48	0.89	44.35	0.89	44.80	0.90	44.76	0.90	44.08	0.88	44.19	0.89	44.38	0.89	44.90	0.90	44.32	0.89	44.66	0.89	16.05	0.41	44.85	0.90	44.22	0.89	16.58	0.42	17.61	0.44	16.28	0.41	18.08	0.45	16.63	0.42					
CaO	0.11	0.01	0.04	0.02	0.11	0.01	0.11	0.01	0.11	0.01	0.11	0.01	0.11	0.01	0.09	0.01	0.10	0.01	0.09	0.01	0.10	0.01	0.10	0.01	0.10	0.01	0.10	0.01	0.10	0.01	0.08	0.01	0.06	0.01	21.78	0.40	0.10	0.01	0.06	0.01	21.12	0.39	19.45	0.36	21.47	0.39	18.68	0.35	20.50	0.38			
Na ₂ O	0.01	0.04	0.01	0.04	0.00	0.00	0.00	0.04	0.04	0.04	0.01	0.04	0.00	0.00	0.00	0.00	0.00	0.00	0.00	0.00	0.00	0.04	0.00	0.00	0.03	0.04	0.00	0.00	0.01	0.04	0.01	0.04	0.46	0.08	0.01	0.04	0.00	0.00	0.36	0.07	0.36	0.07	0.45	0.07	0.35	0.07	0.39	0.07					
K ₂ O	0.00	0.00	0.01	0.01	0.00	0.01	0.00	0.00	0.00	0.01	0.01	0.00	0.00	0.00	0.00	0.00	0.00	0.00	0.00	0.00	0.01	0.01	0.00	0.00	0.00	0.00	0.00	0.00	0.00	0.00	0.00	0.00	0.00	0.00	0.00	0.00	0.00	0.00	0.00	0.00	0.00	0.00	0.00	0.00	0.00	0.00	0.00	0.00	0.00				
NiO	0.27	0.05	0.26	0.04	0.23	0.05	0.27	0.05	0.25	0.05	0.26	0.05	0.26	0.04	0.27	0.05	0.23	0.05	0.26	0.05	0.28	0.05	0.28	0.05	0.29	0.05	0.28	0.05	0.27	0.05	0.25	0.05	0.25	0.05	0.25	0.05	0.25	0.05	0.24	0.04	0.21	0.04	0.27	0.05	0.03	0.04	0.04	0.04	0.03	0.04	0.04	0.04	0.05
Total	99.31	0.99	99.25	0.99	99.35	0.99	99.37	0.99	99.21	0.99	99.48	0.99	99.78	0.99	99.55	0.99	100.11	1.00	99.83	1.00	99.20	0.99	99.61	0.99	99.92	0.99	100.07	1.00	99.55	0.99	99.66	0.99	99.23	0.74	99.51	1.00	99.16	0.99	99.27	0.74	99.57	0.74	99.42	0.74	99.59	0.74	99.30	0.74					
Mg#	84.17	0.89	84.08	0.89	84.06	0.89	84.16	0.89	84.12	0.89	83.91	0.89	84.07	0.89	83.98	0.89	84.15	0.89	84.19	0.89	83.85	0.89	83.86	0.90	83.99	0.89	84.25	0.89	84.17	0.89	84.29	0.88	86.12	1.21	84.60	0.87	84.11	0.89	86.36	1.19	85.55	1.19	85.99	1.21	85.16	1.19	85.63	1.22					
Spot size	77		77		77		77		77		77		77		77		77		77		77		77		77		77		77		77		77		77		77		77		77		77		77		77		77				
Li	1.68	0.12			2.14	0.16			1.80	0.14			1.60	0.13			1.78	0.15			1.72	0.15			3.31	0.19	3.04	0.18	3.48	0.20	3.23	0.19	3.00	0.18			8.38	0.58	9.33	0.64	8.91	0.62	8.03	0.56	8.54	0.59							
B	13.77	2.05			11.36	1.97			11.24	2.04			12.00	2.27			11.83	2.34			10.60	2.19			10.60	2.19							8.38	0.58	9.33	0.64	8.91	0.62	8.03	0.56	8.54	0.59											
Ca	753	32			659	30			649	30			597	28			562	27			567	28			150873	4774	139009	4399	153375	4854	132934	4207	146514	4636																			
Sc	7.45	0.29			7.06	0.28			7.68	0.31			7.52	0.31			7.28	0.31			7.28	0.31			111	4	98	3	106	4	93	3	110	4																			
Ti	74	2			76	3			88	3			82	3			80	3			84	3			2906	119	2246	94	2523	107	2505	108	3565	157																			
V	8.9	0.3			5.5	0.2			6.4	0.2			6.4	0.2			6.0	0.2			5.7	0.2			369	12	302	10	348	11	316	10	383	13																			
Cr	199.05	8.3			90.67	4			98.37	4.41			97.06	4.42			93.53	4.34			82.27	3.89			8083	608	7931	611	8907	707	7322	602	7219	616																			
Mn	1744	65			1755	68			1761	70			1726	69			1778	72			1778	74			1176	39	1115	38	1298	44	1097	37	1040	35																			
Co	166	8			152	8			156	8			156	8			159	9			154	9			30	1	30	1	34	1	29	1	27	1																			
Ni	1748	82			1727	87			1736	89			1731	91			1743	94			1783	99			267	12	265	12	298	13	257	12	248	12																			
Cu	0.198	0.011			0.234	0.014			0.236	0.014			0.242	0.014			0.182	0.012			0.083	0.010			0.185	0.016	0.076	0.014	0.092	0.016	0.079	0.014	0.090	0.013																			
Zn	84.88	2.87			83.54	2.89			85.29	2.97			83.87	2.94			83.38	2.94			84.73	3.01			21.02	0.72	21.38	0.74	23.32	0.80	20.33	0.70	18.01	0.62																			
Rb	b.d.l.	-			0.0046	0.0014			0.0053	0.0013			b.d.l.	-			0.0042	0.0014			b.d.l.	-			0.023	0.003	0.009	0.003	b.d.l.	-	0.011	0.002	0.013																				

Table A2.P - Major and trace element profiles of olivine in OI-T 1 from IODP Hole U1309D

Sample Shape Deformation n. grain Axis Location Dist. (mm)	305-U1309D-234R-1W, 22-26																																											
	anhedral undeformed 5										corroded deformed 6										corroded deformed 8																							
[010]	rim					core					rim					core					rim					core					core													
[100]	rim					core					rim					core					rim					core					core													
	σ	σ	σ	σ	σ	σ	σ	σ	σ	σ	σ	σ	σ	σ	σ	σ	σ	σ	σ	σ	σ	σ	σ	σ	σ	σ	σ	σ	σ	σ	σ	σ	σ	σ	σ	σ	σ	σ	σ	σ				
SiO2	40.19	0.22	40.60	0.22	40.49	0.22	40.48	0.22	40.49	0.22	40.29	0.22	40.35	0.22	40.31	0.22	40.34	0.22	40.21	0.81	40.17	0.81	40.19	0.81	40.29	0.81	40.00	0.81	40.17	0.81	40.23	0.81	40.54	0.22	40.39	0.22	40.28	0.22	40.42	0.22	40.53	0.22		
TiO2	0.00	0.02	0.03	0.03	0.02	0.02	0.03	0.02	0.02	0.03	0.01	0.02	0.00	0.02	0.01	0.02	0.01	0.02	0.01	0.03	0.00	0.03	0.00	0.03	0.03	0.03	0.04	0.03	0.02	0.03	0.04	0.03	0.00	0.00	0.02	0.03	0.02	0.02	0.01	0.02	0.01	0.02	0.00	0.03
Al2O3	0.02	0.02	0.04	0.02	0.01	0.02	0.00	0.02	0.00	0.00	0.00	0.02	0.02	0.02	0.00	0.00	0.01	0.02	0.00	0.02	0.01	0.02	0.00	0.00	0.03	0.02	0.00	0.00	0.01	0.02	0.00	0.02	0.02	0.02	0.02	0.02	0.00	0.02	0.00	0.00	0.00	0.00	0.00	0.00
Cr2O3	0.00	0.00	0.06	0.03	0.01	0.03	0.03	0.03	0.00	0.00	0.02	0.03	0.00	0.03	0.03	0.03	0.01	0.03	0.00	0.00	0.00	0.00	0.00	0.01	0.03	0.02	0.00	0.00	0.02	0.03	0.00	0.02	0.01	0.03	0.03	0.03	0.00	0.00	0.00	0.00	0.00	0.00	0.00	0.00
FeO	13.40	0.20	13.47	0.21	13.56	0.21	13.27	0.20	13.54	0.21	13.60	0.21	13.61	0.21	13.60	0.21	13.44	0.20	13.55	0.21	13.66	0.22	13.76	0.22	13.94	0.22	13.67	0.22	13.98	0.22	14.07	0.22	13.84	0.22	13.48	0.21	13.59	0.21	13.61	0.21	13.55	0.21	13.54	0.21
MnO	0.22	0.04	0.19	0.04	0.26	0.04	0.22	0.04	0.19	0.04	0.20	0.04	0.19	0.04	0.23	0.04	0.20	0.04	0.21	0.04	0.22	0.04	0.21	0.04	0.22	0.04	0.21	0.04	0.17	0.04	0.23	0.04	0.21	0.04	0.21	0.04	0.22	0.04	0.21	0.04	0.21	0.04	0.23	0.04
MgO	45.53	0.40	45.17	0.40	45.20	0.40	45.45	0.40	45.39	0.40	45.17	0.40	45.34	0.40	45.69	0.40	45.59	0.40	45.19	0.40	46.06	0.41	45.92	0.41	45.77	0.41	45.54	0.41	45.88	0.41	45.82	0.41	45.84	0.41	45.39	0.40	45.03	0.40	45.37	0.40	45.49	0.40	45.51	0.40
CaO	0.06	0.01	0.09	0.01	0.09	0.01	0.08	0.01	0.09	0.01	0.10	0.01	0.09	0.01	0.09	0.01	0.09	0.01	0.09	0.01	0.07	0.01	0.07	0.01	0.07	0.01	0.08	0.01	0.09	0.01	0.10	0.01	0.09	0.01	0.11	0.01	0.11	0.01	0.11	0.01	0.11	0.01	0.11	0.01
Na2O	0.00	0.00	0.01	0.03	0.00	0.00	0.01	0.03	0.03	0.03	0.00	0.01	0.03	0.00	0.00	0.01	0.03	0.00	0.00	0.00	0.03	0.03	0.01	0.03	0.00	0.00	0.01	0.03	0.00	0.00	0.00	0.00	0.00	0.00	0.02	0.03	0.00	0.00	0.01	0.03	0.00	0.00	0.01	0.03
K2O	0.00	0.01	0.00	0.00	0.00	0.00	0.00	0.01	0.00	0.00	0.00	0.00	0.00	0.00	0.01	0.00	0.00	0.00	0.00	0.00	0.00	0.01	0.00	0.00	0.00	0.01	0.00	0.00	0.00	0.00	0.00	0.00	0.00	0.01	0.00	0.01	0.00	0.00	0.00	0.00	0.00	0.00	0.00	0.00
NiO	0.28	0.04	0.27	0.04	0.25	0.04	0.22	0.04	0.27	0.04	0.26	0.04	0.24	0.04	0.24	0.04	0.28	0.04	0.24	0.04	0.28	0.05	0.27	0.05	0.29	0.05	0.27	0.05	0.28	0.05	0.26	0.05	0.27	0.05	0.29	0.04	0.26	0.04	0.27	0.04	0.25	0.04	0.25	0.04
Total	99.71	0.51	99.92	0.51	99.89	0.50	99.79	0.51	100.02	0.51	99.85	0.50	99.81	0.51	100.27	0.51	99.94	0.51	99.63	0.50	100.51	0.94	100.45	0.94	100.49	0.94	100.13	0.94	100.52	0.93	100.64	0.94	100.55	0.94	100.04	0.50	99.68	0.50	99.87	0.50	100.06	0.51	100.22	0.51
Mg#	85.83	0.65	85.67	0.66	85.60	0.66	85.92	0.65	85.67	0.66	85.55	0.66	85.59	0.66	85.69	0.66	85.81	0.65	85.60	0.66	85.73	0.69	85.61	0.69	85.40	0.69	85.59	0.69	85.41	0.69	85.31	0.70	85.51	0.69	85.72	0.66	85.52	0.66	85.60	0.66	85.69	0.66	85.70	0.66
Spot size									102		102								102		77		77		77		77		77		77		102		102									
Li									3.71	0.60	2.38	0.41							3.02	0.56	2.32	0.14	3.57	0.21	2.49	0.16	2.91	0.18	3.36	0.21	3.28	0.22	2.72	0.33	1.68	0.22								
B									10.02	0.67	8.85	0.63							8.54	0.64	13.71	1.30	13.25	1.32	12.75	1.35	13.20	1.48	12.80	1.54	10.41	1.54	10.01	0.55	7.96	0.45								
Ca									674	75	732	87							667	85	469	16	621	21	617	21	565	19	673	22	717	24	759	65	673	59								
Sc									7.53	0.42	8.88	0.52							7.60	0.47	8.38	0.27	8.43	0.28	9.01	0.30	9.37	0.31	9.47	0.32	9.01	0.31	9.00	0.41	7.99	0.38								
Ti									86	6	103	8							88	7	64	13	57	12	65	14	71	16	77	19	83	24	116	7	98	6								
V									5.2	0.3	6.3	0.4							4.8	0.3	4.7	0.2	3.9	0.1	4.7	0.2	4.3	0.1	5.2	0.2	7.2	0.2	5.8	0.3	5.5	0.3								
Cr																					55	5	44	4	54	5	43	4	57	6	123	16												
Mn									1797	68	1816	70							1809	72	1687	52	1659	52	1668	52	1718	54	1696	54	1704	55	1809	62	1666	58								
Co									160	27	165	30							167	33	161	5	159	5	161	5	163	5	162	5	160	5	175	22	138	18								
Ni									1893	110	1868	113							1909	119	2024	109	2079	117	2104	124	2127	133	2082	138	2086	166	2505	131	1916	101								
Cu									<0.00	0.025	0.148	0.031							0.169	0.035	0.120	0.012	0.181	0.013	0.233	0.014	0.153	0.013	0.218	0.014	0.183	0.015	0.866	0.081	0.175	0.027								
Zn									75.38	9.16	74.48	9.68							77.06	10.71	64.51	5.37	63.66	5.56	65.42	6.04	68.07	6.68	69.39	7.27	71.62	9.22	82.58	7.62	72.17	6.93								
Rb									<0.00	0.0032	<0.00	0.0032							<0.00	0.0034	<0.00	0.0024	<0.00	0.0025	<0.00	0.0025	<0.00	0.0025	<0.00	0.0023	<0.00	0.0026	<0.00	0.0038	<0.00	0.0024								
Sr									<0.00	0.0036	<0.00	0.0038							0.0070	0.0023	<0.00	0.0023	<0.00	0.0023	0.0090	0.0023	0.0070	0.0022	<0.00	0.0020	<0.00	0.0022	<0.00	0.0046	<0.00	0.0032								
Y									0.1020	0.0170	0.1090	0.0190							0.0850	0.0160	0.0780	0.0035	0.0910	0.0040	0.0960	0.0041	0.1030	0.0043	0.1150	0.0047	0.1370	0.0054	0.1270	0.0150	0.0850	0.0110								
Zr									0.0375	0.0100	0.0320	0.0100							0.0255	0.0096	0.0310	0.0035	0.0570	0.0044	0.0350	0.0037	0.0370	0.0036	0.0390	0.0037	0.0440	0.0041	0.0580	0.0120	0.0474	0.0091								
Nb									<0.00	0.0006	0.0026	0.0009							0.0020	0.0008	0.0020	0.0006	0.0080	0.0010	<0.00	0.0006	0.0030	0.0006	<0.00	0.0004	0.0040	0.0007	0.0067	0.0014	0.0049	0.0010								
Sb									<0.00	0.0032	<0.00	0.0034							<0.00	0.0033	<0.00	0.0016	<0.00	0.0016	<0.00	0.0014	<0.00	0.0016	<0.00	0.0016	<0.00	0.0015	<0.00	0.0035	<0.00	0.0026								
Ba									<0.00	0.0075	<0.00	0.0067							<0.00	0.0072	<0.00	0.0027	<0.00	0.0033	0.0100	0.0031	<0.00	0.0026	<0.00	0.0026	<0.00	0.0031	<0.00	0.0065	<0.00	0.0053								
La									<0.00	0.0006	<0.00	0.0007							<0.00	0.0																								

Table A2.P (continued olivine in OI-T1)

Sample Shape Deformation n. grain Axis Location Dist. (mm)	305-U1309D-247R-3W, 16-18																																																	
	corroded undeformed 14 [100]							corroded deformed 1 [010]							anhedral - rounded deformed 8 [001]							anhedral - rounded deformed 8 (bis) [001]																												
	σ	rim	σ	rim	σ	0.28	1.03	σ	rim	σ	0.69	core	σ	rim	σ	0.06	0.38	core	σ	1.06	σ	1.25	rim	σ	0.00	σ	0.06	σ	0.38	core	σ	1.06																		
TiO2	40.36	0.22	40.37	0.22	40.37	0.22	39.94	0.80	39.99	0.80	40.09	0.81	40.01	0.80	40.21	0.22	40.34	0.22	40.34	0.22	40.42	0.22	40.29	0.22	40.30	0.22	40.40	0.22	40.38	0.22	40.69	0.22	40.17	0.22	40.32	0.22	40.11	0.81	40.26	0.81	39.75	0.80	39.88	0.80	40.04	0.81				
TiO2	0.03	0.02	0.05	0.02	0.01	0.02	0.00	0.03	0.00	0.00	0.02	0.03	0.01	0.03	0.01	0.03	0.02	0.03	0.01	0.03	0.02	0.03	0.01	0.02	0.03	0.03	0.03	0.02	0.00	0.00	0.00	0.02	0.03	0.03	0.03	0.03	0.00	0.03	0.01	0.03	0.05	0.03	0.02	0.03	0.00	0.03				
Al2O3	0.02	0.02	0.02	0.02	0.01	0.02	0.01	0.02	0.00	0.00	0.02	0.02	0.02	0.02	0.00	0.02	0.02	0.02	0.03	0.02	0.03	0.02	0.00	0.02	0.01	0.02	0.02	0.02	0.00	0.00	0.00	0.02	0.00	0.00	0.00	0.02	0.00	0.00	0.00	0.00	0.00	0.00	0.00	0.00	0.00	0.02	0.02	0.00	0.02	
Cr2O3	0.01	0.03	0.00	0.00	0.00	0.03	0.05	0.03	0.00	0.00	0.02	0.03	0.01	0.03	0.00	0.00	0.03	0.03	0.02	0.03	0.00	0.00	0.00	0.00	0.00	0.03	0.03	0.00	0.00	0.03	0.00	0.03	0.06	0.03	0.04	0.03	0.00	0.00	0.02	0.03	0.01	0.03	0.04	0.03	0.04	0.03	0.00	0.00		
FeO	13.60	0.21	13.55	0.21	13.32	0.20	14.00	0.21	14.10	0.21	13.97	0.21	13.93	0.21	14.07	0.22	14.10	0.22	14.03	0.22	14.25	0.22	13.82	0.22	14.01	0.22	13.77	0.22	14.05	0.22	13.92	0.22	13.76	0.22	13.91	0.22	14.24	0.22	14.73	0.23	14.52	0.22	14.26	0.22	14.52	0.22				
MnO	0.18	0.04	0.22	0.04	0.21	0.04	0.20	0.04	0.23	0.04	0.21	0.04	0.20	0.04	0.22	0.04	0.21	0.04	0.19	0.04	0.21	0.04	0.19	0.04	0.24	0.04	0.22	0.04	0.19	0.04	0.23	0.04	0.24	0.04	0.22	0.04	0.22	0.04	0.19	0.04	0.20	0.04	0.21	0.04	0.21	0.04				
MgO	45.24	0.40	45.36	0.40	45.22	0.40	45.85	0.40	45.70	0.40	45.62	0.40	46.09	0.41	44.86	0.40	44.74	0.40	44.93	0.40	44.72	0.40	44.53	0.40	45.06	0.40	44.86	0.40	44.85	0.40	45.02	0.40	44.57	0.40	44.93	0.40	45.15	0.41	45.24	0.41	45.11	0.41	45.11	0.41	45.11	0.41	45.40	0.40		
CaO	0.11	0.01	0.08	0.01	0.06	0.01	0.09	0.01	0.09	0.01	0.10	0.01	0.09	0.01	0.05	0.01	0.08	0.01	0.08	0.01	0.06	0.01	0.09	0.01	0.07	0.01	0.10	0.01	0.09	0.01	0.09	0.01	0.08	0.01	0.08	0.01	0.08	0.01	0.10	0.01	0.10	0.01	0.10	0.01	0.10	0.01				
Na2O	0.01	0.03	0.00	0.00	0.00	0.00	0.00	0.00	0.01	0.03	0.00	0.03	0.03	0.03	0.00	0.00	0.01	0.03	0.00	0.00	0.00	0.00	0.00	0.00	0.00	0.00	0.00	0.00	0.00	0.00	0.00	0.00	0.00	0.00	0.00	0.00	0.00	0.00	0.00	0.00	0.00	0.00	0.00	0.00	0.00	0.00	0.00	0.00		
K2O	0.01	0.01	0.00	0.00	0.00	0.00	0.00	0.00	0.00	0.00	0.00	0.01	0.01	0.01	0.00	0.01	0.00	0.01	0.00	0.00	0.00	0.00	0.01	0.01	0.00	0.00	0.00	0.01	0.00	0.01	0.00	0.00	0.01	0.00	0.00	0.00	0.01	0.00	0.00	0.00	0.00	-23.10	0.00	0.00	0.00	0.00	0.01			
NiO	0.24	0.04	0.25	0.04	0.24	0.04	0.30	0.04	0.27	0.04	0.30	0.04	0.26	0.04	0.29	0.05	0.30	0.05	0.28	0.05	0.30	0.05	0.30	0.05	0.30	0.05	0.31	0.05	0.29	0.05	0.34	0.05	0.29	0.05	0.31	0.05	0.33	0.05	0.28	0.05	0.29	0.05	0.31	0.05	0.28	0.04	0.01	0.01		
Total	99.80	0.51	99.91	0.50	99.45	0.50	100.43	0.93	100.40	0.93	100.34	0.93	100.66	0.93	99.74	0.52	99.83	0.52	99.91	0.52	100.01	0.52	99.24	0.51	100.06	0.52	99.71	0.51	99.87	0.51	100.28	0.52	99.21	0.51	99.86	0.52	100.14	0.93	100.80	0.94	100.03	0.93	99.94	0.93	100.54	0.93				
Mg#	85.57	0.66	85.65	0.66	85.82	0.65	85.38	0.66	85.24	0.67	85.34	0.67	85.50	0.66	85.04	0.69	84.98	0.69	85.09	0.69	84.83	0.70	85.18	0.69	85.14	0.69	85.31	0.69	85.05	0.69	85.22	0.69	85.24	0.69	85.20	0.69	84.97	0.70	84.55	0.71	84.71	0.70	84.94	0.70	84.79	0.68	0.68	0.68		
Spot size	102		102				77		77		77		77		102		102		102		102		102		102		102		102		102		102		102		102		102		102		102		102		102		102	
Li	1.84	0.25	1.83	0.26			2.23	0.10	1.58	0.08	2.08	0.09			2.87	0.21	3.08	0.24	2.59	0.21	2.70	0.22	1.98	0.18			2.87	0.21	3.08	0.24	2.59	0.21	2.70	0.22	1.98	0.18			2.87	0.21	3.08	0.24	2.59	0.21	2.70	0.22	1.98	0.18		
B	9.54	0.56	8.74	0.54			18.68	1.04	17.86	0.99	19.03	1.06			10.27	0.50	10.11	0.50	9.46	0.48	9.28	0.48	7.45	0.42			10.27	0.50	10.11	0.50	9.46	0.48	9.28	0.48	7.45	0.42			10.27	0.50	10.11	0.50	9.46	0.48	9.28	0.48	7.45	0.42		
Ca	722	67	724	71			398	15	596	21	589	20			663	38	750	44	752	45	772	48	685	46			663	38	750	44	752	45	772	48	685	46			663	38	750	44	752	45	772	48	685	46		
Sc	8.20	0.40	8.15	0.41			5.90	0.19	7.22	0.23	7.16	0.23			7.27	0.41	7.37	0.42	7.48	0.44	7.63	0.46	7.84	0.51			7.27	0.41	7.37	0.42	7.48	0.44	7.63	0.46	7.84	0.51			7.27	0.41	7.37	0.42	7.48	0.44	7.63	0.46	7.84	0.51		
Ti	110	7	105	7			62	2	83	3	78	2			68	5	74	6	73	6	84	7	79	7			68	5	74	6	73	6	84	7	79	7			68	5	74	6	73	6	84	7	79	7		
V	5.9	0.3	5.8	0.3			4.7	0.2	5.9	0.2	6.7	0.2			5.1	0.2	5.7	0.2	5.3	0.2	6.1	0.2	5.8	0.2			5.1	0.2	5.7	0.2	5.3	0.2	5.8	0.2			5.1	0.2	5.7	0.2	5.3	0.2	6.1	0.2	5.8	0.2	5.8	0.2		
Cr																																																		
Mn	1764	62	1768	64			1809	62	1735	59	1758	60			1756	84	1818	89	1811	91	1838	95	1694	94			1756	84	1818	89	1811	91	1838	95	1694	94			1756	84	1818	89	1811	91	1838	95	1694	94		
Co	145	20	153	23			180	6	173	6	172	6			166	9	167	9	166	9	167	9	139	8			166	9	167	9	166	9	167	9	139	8			166	9	167	9	139	8			166	9	139	8
Ni	1908	103	1988	109			2683	257	2637	253	2566	246			2886	728	2904	751	2819	755	2804	782	2331	715			2886	728	2904	751	2819	755	2804	782	2331	715			2886	728	2904	751	2819	755	2804	782	2331	715		
Cu	0.304	0.037	0.269	0.036			0.122	0.018	0.063	0.017	0.217	0.019			<0.00	0.020	0.083	0.021	0.090	0.022	0.113	0.023	0.018			<0.00	0.020	0.083	0.021	0.090	0.022	0.113	0.023			0.020	0.083	0.021	0.090	0.022	0.113	0.023			0.020	0.083				
Zn	72.82	7.35	74.79	8.00			77.07	3.13	75.62	3.07	76.74	3.11			75.73	3.07	76.83	3.15	74.67	3.11	74.70	3.17	66.29	2.95			75.73	3.07	76.83	3.15	74.67	3.11	74.70	3.17	66.29	2.95			75.73	3.07	76.83	3.15	74.67	3.11	74.70	3.17	66.29	2.95		
Rb	<0.00	0.0028	<0.00	0.0029			<0.00	0.0035	<0.00	0.0033	<0.00	0.0033			<0.00	0.0035	<0.00	0.0033	<0.00	0.0033	<0.00	0.0033	<0.00	0.0033			<0.00	0.0035	<0.00	0.0033	<0.00	0.0033	<0.00	0.0033	<0.00	0.0033	<0.00	0.0033	<0.00	0.0033	<0.00	0.0033	<0.00	0.0033	<0.00	0.0033	<0.00	0.0033	<0.00	
Sr	0.0485	0.0076	0.0465	0.0078			<0.00	0.0044	<0.00	0.0043	<0.00	0.0043			<0.00	0.0036	<0.00	0.0037	<0.00	0.0037	<0.00	0.0037	<0.00	0.0029			<0.00	0.0036	<0.00	0.0037	<0.00	0.0037	<0.00	0.0037	<0.00	0.0029			<0.00	0.0036	<0.00	0.0037	<0.00	0.0037	<0.00	0.0029				
Y	0.0990	0.0130	0.1110	0.0160			0.0337	0.0022	0.0607	0.0031	0.0589	0.0031			0.1002	0.0086	0.0841	0.0075	0.0989	0.0090	0.0987	0.0094	0.0793	0.0082			0.1002	0.0086	0.0841	0.0075	0.0989	0.0090	0.0987	0.0094	0.0793	0.0082			0.1002	0.0086	0.0841	0.0075	0.0989	0.0090	0.0987	0.009				

Table A2.P (continued olivine in OI-T1)

Sample																				305-U1309D-247R-3W, 22-25																												
Shape		corroded undeformed						rounded undeformed						anhedral undeformed						anhedral/rounded deformed																												
Deformation		10						13						5						2																												
n. grain		[100]						rim						rim						rim																												
Axis		rim						rim						rim						rim																												
Location		rim						rim						rim						rim																												
Dist. (mm)		1.25						1.63						0.63						1.19																												
		σ						σ						σ						σ																												
		σ						σ						σ						σ																												
SiO2	40.17	0.81	40.20	0.81	40.21	0.81	40.35	0.22	40.09	0.22	40.53	0.22	40.30	0.22	39.65	0.80	40.19	0.81	39.94	0.80	40.34	0.81	40.45	0.81	40.18	0.81	40.25	0.81	40.13	0.81	40.11	0.81	40.34	0.81	40.08	0.81	39.66	0.35	39.64	0.35	39.60	0.35	39.67	0.35	39.87	0.35		
TiO2	0.02	0.03	0.00	0.00	0.01	0.03	0.02	0.02	0.00	0.00	0.02	0.02	0.00	0.02	0.03	0.03	0.03	0.03	0.01	0.03	0.02	0.03	0.03	0.03	0.00	0.00	0.02	0.03	0.02	0.03	0.00	0.03	0.00	0.03	0.02	0.03	0.03	0.03	0.02	0.03	0.01	0.03	0.02	0.03	0.01	0.03		
Al2O3	0.03	0.02	0.02	0.02	0.00	0.02	0.02	0.02	0.00	0.00	0.00	0.00	0.02	0.02	0.01	0.02	0.01	0.02	0.01	0.02	0.02	0.02	0.03	0.02	0.00	0.02	0.00	0.00	0.01	0.02	0.01	0.02	0.00	0.00	0.04	0.02	0.00	0.00	0.00	0.00	0.00	0.00	0.00	0.02	0.00	0.02	0.07	0.02
Cr2O3	0.02	0.03	0.00	0.03	0.01	0.03	0.01	0.03	0.00	0.03	0.03	0.03	0.02	0.03	0.05	0.03	0.00	0.00	0.05	0.03	0.02	0.03	0.03	0.03	0.01	0.03	0.01	0.03	0.00	0.00	0.00	0.00	0.03	0.01	0.03	0.01	0.04	0.03	0.04	0.02	0.04	0.03	0.04	0.05	0.03			
FeO	14.47	0.22	14.53	0.22	14.25	0.21	13.67	0.21	13.78	0.21	13.87	0.21	13.81	0.21	14.37	0.22	14.34	0.22	14.43	0.22	14.50	0.22	14.45	0.21	14.50	0.22	14.40	0.21	14.39	0.21	14.38	0.21	14.37	0.21	14.44	0.21	14.17	0.23	14.16	0.23	14.06	0.23	14.07	0.23	14.09	0.23		
MnO	0.23	0.04	0.22	0.04	0.24	0.04	0.17	0.04	0.19	0.04	0.22	0.04	0.22	0.04	0.21	0.04	0.23	0.04	0.21	0.04	0.22	0.04	0.21	0.04	0.24	0.04	0.19	0.04	0.22	0.04	0.21	0.04	0.23	0.04	0.23	0.04	0.19	0.04	0.23	0.04	0.21	0.04	0.22	0.04	0.23	0.04		
MgO	45.24	0.40	45.30	0.40	45.15	0.40	45.02	0.40	44.96	0.40	44.96	0.40	44.82	0.40	44.98	0.40	45.20	0.41	45.24	0.41	45.47	0.40	45.41	0.40	45.54	0.40	45.66	0.40	45.54	0.40	45.47	0.40	45.40	0.40	45.40	0.40	45.36	0.89	45.46	0.89	44.97	0.88	44.97	0.88	44.60	0.88		
CaO	0.10	0.01	0.10	0.01	0.08	0.01	0.07	0.01	0.09	0.01	0.09	0.01	0.08	0.01	0.05	0.01	0.07	0.01	0.06	0.01	0.05	0.01	0.06	0.01	0.05	0.01	0.06	0.01	0.06	0.01	0.06	0.01	0.06	0.01	0.04	0.01	0.09	0.01	0.08	0.01	0.09	0.01	0.00	0.00	0.11	0.02		
Na2O	0.00	0.00	0.00	0.00	0.00	0.03	0.00	0.00	0.02	0.03	0.00	0.03	0.01	0.03	0.00	0.00	0.03	0.03	0.00	0.00	0.02	0.03	0.00	0.00	0.01	0.03	0.01	0.03	0.01	0.03	0.01	0.03	0.00	0.00	0.00	0.00	0.00	0.00	0.00	0.00	0.01	0.04	0.03	0.03	0.00	0.00	0.02	0.04
K2O	0.01	0.01	0.00	-3.28	0.01	0.01	0.00	0.00	0.00	0.01	0.00	0.00	0.00	0.00	0.01	0.01	0.00	0.00	0.00	-5.51	0.00	0.00	0.00	0.00	0.00	0.00	0.00	0.01	0.00	0.01	0.00	0.00	0.00	0.00	0.00	0.00	0.00	0.00	0.00	0.01	0.01	0.01	0.01	0.00	0.01	0.00	0.01	
NiO	0.29	0.05	0.30	0.04	0.32	0.05	0.24	0.04	0.33	0.05	0.30	0.04	0.27	0.04	0.32	0.05	0.27	0.05	0.31	0.05	0.30	0.04	0.30	0.04	0.31	0.05	0.32	0.04	0.34	0.04	0.35	0.05	0.32	0.04	0.32	0.05	0.32	0.05	0.31	0.05	0.32	0.05	0.32	0.05	0.30	0.04		
Total	100.57	0.93	100.66	0.93	100.28	0.93	99.59	0.50	99.45	0.50	100.02	0.50	99.56	0.50	99.68	0.93	100.37	0.94	100.26	0.93	100.96	0.93	100.96	0.93	100.83	0.93	100.92	0.93	100.73	0.93	100.61	0.93	100.73	0.93	100.58	0.93	99.83	0.99	99.93	0.99	99.32	0.98	99.30	0.98	99.35	0.98		
Mg#	84.79	0.68	84.75	0.68	84.96	0.68	85.44	0.66	85.33	0.66	85.25	0.67	85.26	0.66	84.80	0.70	84.89	0.70	84.82	0.70	84.83	0.68	84.86	0.68	84.85	0.68	84.96	0.68	84.94	0.68	84.93	0.67	84.92	0.68	84.86	0.68	85.09	0.84	85.13	0.84	85.07	0.83	84.94	0.84				
Spot size		102						102						77						77						77																						
Li		2.96	0.28	1.84	0.18	1.20	0.13								0.93	0.07	1.61	0.10	2.90	0.16	1.46	0.10	1.52	0.11													1.57	0.08	1.85	0.09	1.77	0.08						
B		7.55	0.44	7.24	0.44	7.70	0.49								9.32	0.49	9.52	0.51	9.24	0.51	9.66	0.55	9.87	0.59													5.85	0.26	6.21	0.27	5.45	0.24						
Ca		475	34	571	42	616	47								313	13	404	16	388	15	338	14	259	13												555	20	597	22	568	21							
Sc		8.11	0.55	7.19	0.51	7.26	0.54								7.44	0.23	7.25	0.23	7.14	0.22	6.74	0.21	7.36	0.23													7.40	0.23	6.85	0.21	6.36	0.20						
Ti		85	8	69	7	72	8								65	2	62	2	65	2	63	2	72	3													101	4	83	3	75	3						
V		5.3	0.2	4.6	0.2	5.5	0.2								4.4	0.1	4.9	0.2	5.0	0.2	4.9	0.2	5.7	0.2													5.5	0.2	5.9	0.2	5.1	0.2						
Cr															48	5	67	7	67	7	67	7	78	9												76.71	2.41	105.85	3.31	87.76	2.74							
Mn		1772	102	1742	105	1793	112								1766	65	1744	65	1740	66	1760	68	1771	70													1845	57	1829	57	1860	57						
Co		152	10	148	10	155	11								166	8	166	8	166	8	165	8	167	9												154	5	154	5	153	5							
Ni		2575	831	2467	838	2489	891								2557	210	2540	215	2538	224	2547	236	2618	256													2212	85	2236	84	2233	83						
Cu															<0.00	0.014	0.055	0.015	<0.00	0.015	0.095	0.016	<0.00	0.018												0.111	0.019	0.145	0.020	0.125	0.021							
Zn															65.28	3.48	72.81	3.99	73.49	4.16	74.17	4.37	76.31	4.71													80.56	2.91	82.19	2.93	82.34	2.91						
Rb															<0.00	0.0029	<0.00	0.0027	<0.00	0.0028	<0.00	0.0026	<0.00	0.0031											<0.00	0.0026	<0.00	0.0025	<0.00	0.0028								
Sr															<0.00	0.0027	<0.00	0.0026	<0.00	0.0026	<0.00	0.0026	<0.00	0.0028												0.9430	0.0290	<0.00	0.0037	<0.00	0.0039							
Y															0.0390	0.0023	0.0380	0.0023	0.0400	0.0025	0.0330	0.0022	0.0340	0.0025													0.1072	0.0054	0.0972	0.0050	0.0930	0.0050						
Zr															<0.00	0.0028	<0.00	0.0033	<0.00	0.0032	<0.00	0.0033	<0.00	0.0035												0.0478	0.0042	0.0449	0.0041	0.0286	0.0034							
Nb															<0.00	0.0005	0.0020	0.0006	<0.00	0.0007	<0.00	0.0005	0.0010	0.0006												0.0021	0.0007	0.0040	0.0009	0.0017	0.0007							
Sb															<0.00	0.0013	<0.00	0.0013	<0.00	0.0017	<0.00	0.0018	<0.00	0.0018												<0.00	0.0018	<0.00	0.0018	<0.00	0.0018							
Ba															<0.00	0.0033	0.0110	0.0037	<0.00	0.0029	<0.00	0.0031	<0.00	0.0034												<0.00	0.0035	<0.00	0.0038	0.0113	0.0035							
La															<0.00	0.0007	<0.00	0.0005	<0.00	0.0008	<0.00	0.0007	<0.00	0.0009												<0.00	0.0004	<0.00	0.0004	<0.00	0.0004							
Ce															<0.00	0.0009	0.0030	0.0008	<0.00	0.0006	<0.00	0.0007	<0.00	0.0009												<0.00	0.0006	<0.00	0.0004	<0.00	0.0004							

Table A2.P (continued olivine in OI-T1)

Sample Shape Deformation n. grain Location	core			rounded undeformed 3												corroded deformed 9 (profile) [100]										
Dist. (mm)	0.86 σ	0.94 σ	1.00 σ	0.35	0.35	0.35	0.35	0.35	0.35	0.35	0.35	0.35	0.35	0.35	0.35	0.35	0.35	0.35	0.35	0.35	0.35	0.35	0.35	0.35	0.35	
	39.77	39.62	39.77	39.77	39.72	39.67	39.75	39.75	39.75	39.82	39.82	39.79	39.87	39.59	39.59	39.81	39.57	39.57	39.49	39.55	39.56	39.80	39.65	39.68	39.81	39.81
	0.03	0.03	0.01	0.03	0.00	0.01	0.03	0.03	0.03	0.01	0.03	0.02	0.03	0.02	0.03	0.02	0.03	0.03	0.00	0.00	0.03	0.03	0.00	0.00	0.00	0.03
	0.00	0.00	0.00	0.02	0.03	0.02	0.02	0.01	0.02	0.00	0.02	0.00	0.02	0.00	0.02	0.01	0.02	0.01	0.02	0.02	0.02	0.03	0.02	0.01	0.02	0.00
	0.04	0.03	0.05	0.03	0.01	0.03	0.01	0.03	0.02	0.03	0.02	0.04	0.04	0.03	0.03	0.04	0.03	0.04	0.03	0.04	0.02	0.03	0.00	0.00	0.04	0.04
	14.19	14.23	14.17	14.23	13.99	14.17	14.23	14.04	14.23	14.23	14.23	13.98	14.34	14.28	14.14	14.23	14.19	14.23	14.16	14.23	14.11	14.23	14.06	14.23	14.28	14.23
	0.23	0.04	0.26	0.04	0.20	0.04	0.22	0.04	0.23	0.04	0.24	0.04	0.22	0.04	0.22	0.04	0.23	0.04	0.24	0.04	0.21	0.04	0.25	0.04	0.24	0.04
	45.10	0.89	45.76	0.90	44.99	0.88	45.34	0.89	45.71	0.90	45.26	0.89	44.99	0.88	45.07	0.89	45.19	0.89	44.91	0.88	45.17	0.89	45.04	0.89	44.84	0.88
	0.00	0.00	0.09	0.01	0.11	0.01	0.09	0.01	0.08	0.01	0.07	0.01	0.08	0.01	0.09	0.01	0.07	0.01	0.07	0.01	0.07	0.01	0.08	0.01	0.07	0.01
	0.00	0.00	0.00	0.03	0.00	0.00	0.00	0.00	0.03	0.04	0.00	0.00	0.00	0.00	0.01	0.04	0.04	0.03	0.01	0.04	0.00	0.00	0.01	0.03	0.01	0.04
	0.01	0.01	0.00	0.00	0.00	0.00	0.00	0.00	0.00	0.00	0.00	0.01	0.00	0.01	0.00	0.01	0.00	0.00	0.00	0.00	0.01	0.00	0.00	0.01	0.00	0.01
	0.31	0.04	0.30	0.04	0.28	0.04	0.30	0.04	0.31	0.05	0.33	0.05	0.31	0.04	0.32	0.05	0.32	0.04	0.30	0.04	0.30	0.04	0.29	0.05	0.30	0.04
	99.66	0.98	100.27	0.99	99.38	0.98	99.88	0.99	100.14	0.99	99.91	0.99	99.85	0.99	99.98	0.98	99.75	0.98	99.59	0.98	99.15	0.98	99.48	0.98	99.57	0.98
	85.00	0.84	85.20	0.83	85.14	0.83	85.08	0.84	85.30	0.83	85.01	0.84	85.29	0.83	84.85	0.84	84.83	0.84	84.91	0.84	85.07	0.84	84.94	0.84	85.05	0.84
	1.61 σ	0.50 σ	rim	(cont.cpx)	rim	[001]	core	rim	5.75 σ	6.50 σ	7.25 σ	8.25 σ	9.25 σ	0.00 σ	0.11 σ	0.23 σ	0.34 σ									
SpO2	0.03	0.03	0.01	0.03	0.00	0.00	0.01	0.03	0.03	0.03	0.01	0.03	0.02	0.03	0.02	0.03	0.00	0.00	0.03	0.03	0.00	0.00	0.00	0.03	0.02	0.03
TiO2	0.00	0.00	0.00	0.02	0.03	0.02	0.02	0.02	0.01	0.02	0.00	0.02	0.00	0.02	0.03	0.02	0.00	0.00	0.00	0.03	0.02	0.01	0.00	0.00	0.02	0.02
Al2O3	0.04	0.03	0.05	0.03	0.01	0.03	0.01	0.03	0.02	0.03	0.02	0.04	0.04	0.03	0.03	0.03	0.00	0.00	0.02	0.03	0.00	0.00	0.04	0.04	0.02	0.03
Cr2O3	0.04	0.03	0.05	0.03	0.01	0.03	0.01	0.03	0.02	0.03	0.02	0.04	0.04	0.03	0.03	0.03	0.00	0.00	0.02	0.03	0.00	0.00	0.04	0.04	0.02	0.03
FeO	14.19	14.23	14.17	14.23	13.99	14.17	14.23	14.04	14.23	14.23	14.23	13.98	14.34	14.28	14.14	14.23	14.19	14.23	14.16	14.23	14.11	14.23	14.06	14.23	14.28	14.23
MnO	0.23	0.04	0.26	0.04	0.20	0.04	0.22	0.04	0.23	0.04	0.24	0.04	0.22	0.04	0.22	0.04	0.23	0.04	0.24	0.04	0.21	0.04	0.25	0.04	0.24	0.04
MgO	45.10	0.89	45.76	0.90	44.99	0.88	45.34	0.89	45.71	0.90	45.26	0.89	44.99	0.88	45.07	0.89	45.19	0.89	44.91	0.88	45.17	0.89	45.04	0.89	44.84	0.88
CaO	0.00	0.00	0.09	0.01	0.11	0.01	0.09	0.01	0.08	0.01	0.07	0.01	0.08	0.01	0.09	0.01	0.07	0.01	0.07	0.01	0.07	0.01	0.08	0.01	0.07	0.01
Na2O	0.00	0.00	0.00	0.03	0.00	0.00	0.00	0.00	0.03	0.04	0.00	0.00	0.00	0.00	0.01	0.04	0.04	0.03	0.01	0.04	0.00	0.00	0.01	0.03	0.01	0.04
K2O	0.01	0.01	0.00	0.00	0.00	0.00	0.00	0.00	0.00	0.00	0.00	0.01	0.00	0.01	0.00	0.00	0.00	0.00	0.00	0.00	0.00	0.00	0.00	0.01	0.00	0.01
NiO	0.31	0.04	0.30	0.04	0.28	0.04	0.30	0.04	0.31	0.05	0.33	0.05	0.31	0.04	0.32	0.05	0.32	0.04	0.30	0.04	0.30	0.04	0.29	0.05	0.30	0.04
Total	99.66	0.98	100.27	0.99	99.38	0.98	99.88	0.99	100.14	0.99	99.91	0.99	99.85	0.99	99.98	0.98	99.75	0.98	99.59	0.98	99.15	0.98	99.48	0.98	99.57	0.98
Mg#	85.00	0.84	85.20	0.83	85.14	0.83	85.08	0.84	85.30	0.83	85.01	0.84	85.29	0.83	84.85	0.84	84.83	0.84	84.91	0.84	85.07	0.84	84.94	0.84	85.05	0.84

Table A2.P (continued olivine in OI-T1)

Sample Shape Deformation n. grain Axis Location	anhedral undeformed 9																								corroded deformed 10																													
	[001]															core									[001]																													
	rim (cont. plg)																								rim																													
	rim																								rim																													
Dist. (mm)	2.30 σ	2.50 σ	2.60 σ	2.80 σ	2.90 σ	3.00 σ	0.03 σ	0.07 σ	0.13 σ	0.19 σ	0.40 σ	0.47 σ	0.55 σ	0.75 σ	0.92 σ	1.03 σ	1.13 σ	1.25 σ	1.33 σ	1.48 σ	1.67 σ	1.80 σ	0.07 σ	0.49 σ	0.64 σ																													
SiO2	39.87	0.35	39.77	0.35	39.68	0.35	39.82	0.35	40.02	0.35	40.02	0.35	39.60	0.35	39.61	0.35	39.27	0.35	39.49	0.35	39.57	0.35	39.55	0.35	39.62	0.35	39.51	0.35	39.43	0.35	39.47	0.35	39.54	0.35	39.40	0.35	39.32	0.35	39.57	0.35	39.44	0.35	39.74	0.35	40.10	0.35	39.96	0.35						
TiO2	0.01	0.03	0.00	0.03	0.00	0.03	0.03	0.03	0.00	0.00	0.00	0.03	0.03	0.04	0.03	0.02	0.03	0.00	0.00	0.01	0.03	0.00	0.00	0.01	0.03	0.00	0.00	0.03	0.03	0.00	0.03	0.04	0.03	0.03	0.03	0.03	0.03	0.02	0.03	0.01	0.03	0.00	0.00	0.01	0.03	0.03	0.03	0.01	0.03					
Al2O3	0.02	0.02	0.00	0.00	0.03	0.02	0.00	0.02	0.03	0.02	0.00	0.02	0.02	0.02	0.00	0.02	0.00	0.02	0.00	0.00	0.01	0.02	0.02	0.02	0.03	0.02	0.00	0.00	0.03	0.02	0.02	0.02	0.01	0.02	0.00	0.00	0.01	0.02	0.01	0.02	0.01	0.02	0.02	0.02	0.00	0.00	0.00	0.00	0.03	0.02	0.00	0.02		
Cr2O3	0.03	0.04	0.03	0.04	0.02	0.04	0.02	0.04	0.00	0.00	0.01	0.04	0.03	0.04	0.02	0.04	0.00	0.00	0.00	0.02	0.04	0.01	0.04	0.03	0.04	0.01	0.04	0.01	0.04	0.03	0.03	0.00	0.00	0.01	0.04	0.00	0.00	0.00	0.04	0.01	0.04	0.03	0.04	0.00	0.00	0.03	0.04	0.02	0.04					
FeO	14.14	0.24	14.28	0.24	14.16	0.24	14.27	0.24	14.28	0.24	14.08	0.24	14.42	0.23	14.46	0.23	14.44	0.23	14.48	0.23	14.39	0.23	14.30	0.23	14.36	0.23	14.34	0.23	14.51	0.23	14.32	0.23	14.46	0.23	14.42	0.23	14.46	0.23	14.39	0.23	14.55	0.23	14.70	0.23	14.00	0.24	13.94	0.24	14.01	0.24				
MnO	0.23	0.04	0.23	0.04	0.23	0.04	0.22	0.04	0.23	0.04	0.23	0.04	0.21	0.04	0.23	0.04	0.21	0.04	0.25	0.04	0.24	0.04	0.20	0.04	0.19	0.04	0.24	0.04	0.23	0.04	0.24	0.04	0.24	0.04	0.21	0.04	0.19	0.04	0.23	0.04	0.22	0.04	0.21	0.04	0.23	0.04	0.21	0.04	0.20	0.04				
MgO	45.11	0.90	45.53	0.91	44.74	0.89	45.25	0.90	44.72	0.89	45.45	0.90	44.83	0.89	44.79	0.89	44.54	0.89	44.98	0.90	44.91	0.90	45.38	0.90	45.38	0.90	44.85	0.89	45.25	0.90	45.66	0.91	45.26	0.90	45.33	0.90	45.01	0.90	45.59	0.91	44.94	0.90	44.99	0.90	45.09	0.90	45.65	0.91	45.44	0.90				
CaO	0.11	0.01	0.10	0.01	0.11	0.01	0.10	0.01	0.09	0.01	0.10	0.01	0.08	0.01	0.07	0.01	0.09	0.01	0.08	0.01	0.10	0.01	0.10	0.01	0.10	0.01	0.08	0.01	0.11	0.01	0.09	0.01	0.09	0.01	0.08	0.01	0.09	0.01	0.08	0.01	0.07	0.01	0.07	0.01	0.10	0.01	0.09	0.01	0.10	0.01				
Na2O	0.03	0.04	0.04	0.04	0.00	0.00	0.00	0.00	0.01	0.04	0.01	0.04	0.00	0.03	0.02	0.03	0.00	0.00	0.00	0.00	0.02	0.04	0.00	0.00	0.02	0.04	0.00	0.00	0.01	0.04	0.00	0.00	0.01	0.04	0.00	0.00	0.01	0.04	0.00	0.00	0.02	0.04	0.00	0.00	0.00	0.00	0.00	0.00	0.00	0.00				
K2O	0.00	0.01	0.00	0.01	0.00	0.00	0.00	0.00	0.00	0.00	0.00	0.00	0.00	0.00	0.01	0.01	0.00	0.00	0.01	0.01	0.00	0.00	0.01	0.01	0.01	0.01	0.00	0.00	0.00	0.00	0.00	0.01	0.00	0.01	0.00	0.01	0.00	0.00	0.00	0.00	0.01	0.00	0.00	0.00	0.01	0.00	0.00	0.00	0.00	0.00				
NiO	0.27	0.05	0.28	0.05	0.28	0.05	0.28	0.05	0.29	0.05	0.29	0.05	0.32	0.05	0.32	0.05	0.25	0.05	0.29	0.05	0.30	0.05	0.30	0.05	0.30	0.05	0.29	0.05	0.29	0.05	0.27	0.05	0.31	0.05	0.28	0.05	0.27	0.05	0.31	0.05	0.27	0.05	0.30	0.05	0.29	0.05	0.29	0.05	0.26	0.05				
Total	99.83	1.00	100.27	1.00	99.25	0.99	100.00	1.00	99.67	0.99	100.20	1.00	99.53	0.99	99.55	0.99	98.82	0.98	99.59	0.99	99.55	0.99	99.88	1.00	100.02	1.00	99.44	0.99	99.98	1.00	100.07	1.00	99.90	1.00	99.92	1.00	99.47	0.99	99.94	1.00	99.65	0.99	99.76	0.99	99.47	1.00	100.35	1.01	100.01	1.00				
Mg#	85.04	0.86	85.04	0.86	84.92	0.86	84.97	0.86	84.81	0.87	85.19	0.86	84.72	0.83	84.67	0.83	84.61	0.83	84.70	0.83	84.77	0.83	84.98	0.82	84.92	0.83	84.79	0.83	84.75	0.83	85.04	0.82	84.80	0.83	84.85	0.83	84.73	0.83	84.96	0.82	84.63	0.83	84.51	0.83	85.16	0.85	85.38	0.85	85.26	0.86				
Spot size	77				77				77				77				77		77						77		77																											
Li	1.93	0.24			1.69	0.22			1.91	0.12			1.25	0.08			1.34	0.09	1.76	0.12					1.92	0.13																												
B	10.83	3.53			12.40	4.30			13.36	1.68			13.65	1.78			12.32	1.68	11.98	1.71					11.62	1.74																												
Ca	753	38			589	31			533	20			592	22			595	23	614	23					520	21																												
Sc	8.77	0.40			8.74	0.41			7.93	0.28			8.61	0.30			8.54	0.30	8.45	0.30					7.57	0.27																												
Ti	82.36	2.56			107.46	3.34			64.91	2			80	2.46			82.13	2.53	79.19	2.44					72.56	2.26																												
V	3.6	0.2			4.2	0.2			4.6	0.2			5.5	0.2			5.5	0.2	5.4	0.2					4.5	0.2																												
Cr	53.83	7.81			65.4	9.93			70.16	4.9			88.25	6.33			87.18	6.45	89.19	6.83					80.04	6.37																												
Mn	1854	168			1958	185			1671	81			1665	83			1673	85	1688	88					1663	89																												
Co	154	17			166	19			149	8			151	9			148	9	150	9					140	9																												
Ni	2093	222			2220	246			1966	106			1959	108			1965	112	1974	116					1939	118																												
Cu	0.085	0.013			0.067	0.012			0.073	0.007			0.050	0.006			0.146	0.011	0.397	0.025					0.483	0.033																												
Zn	72.81	6.31			73.97	6.66			70.89	3.49			71.68	3.59			71.65	3.67	71.81	3.77					64.65	3.49																												
Rb	<0.00	0.0014			<0.00	0.0017			0.0045	0.0012			0.0038	0.0011			<0.00	0.0013	0.0094	0.0016					<0.00	0.0018																												
Sr	<0.00	0.0022			<0.00	0.0024			0.0086	0.0019			<0.00	0.0018			0.0859	0.0046	0.3430	0.0150					0.1245	0.0068																												
Y	0.1729	0.0088			0.1629	0.0086			0.0862	0.0040			0.1018	0.0047			0.1367	0.0060	0.1035	0.0048					0.0734	0.0043																												
Zr	0.0468	0.0041			0.0367	0.0036			0.0317	0.0028			0.0462	0.0035			0.0475	0.0037	0.0407	0.0032					0.0448	0.0043																												
Nb	<0.00	0.0003			<0.00	0.0005			0.0007	0.0003			0.0020	0.0005			<0.00	0.0003	<0.00	0.0003					0.0043	0.0009																												
Sb																																																						
Ba	<0.00	0.0029			<0.00	0.0024			<0.00	0.0022																																												

Table A2.P (continued olivine in OI-T1)

Sample	corroded deformed 13												rounded deformed 17						rounded undeformed 18											
Shape	[010]												[010]						[001]											
Deformation	rim												rim			core			rim			rim			core			rim		
n. grain	[010]												rim			core			rim			rim			core			rim		
Axis	[010]												rim			core			rim			rim			core			rim		
Location	rim												rim			core			rim			rim			core			rim		
Dist. (mm)	1.38	σ	0.00	σ	0.38	σ	0.78	σ	1.34	σ	0.00	σ	0.31	σ	0.66	σ	0.06	σ	0.16	σ	0.28	σ	0.41	σ	0.53	σ				
SiO2	40.19	0.22	40.30	0.22	39.58	0.23	40.33	0.22	40.43	0.22	40.46	0.22	40.48	0.22	40.42	0.22	40.41	0.81	40.11	0.81	40.28	0.81	40.33	0.81	40.34	0.81				
TiO2	0.02	0.03	0.02	0.02	0.00	0.02	0.04	0.02	0.00	0.00	0.01	0.03	0.00	0.00	0.01	0.02	0.01	0.03	0.01	0.03	0.00	0.00	0.00	0.03	0.02	0.03				
Al2O3	0.02	0.02	0.03	0.02	0.04	0.02	0.01	0.02	0.00	0.02	0.02	0.02	0.00	0.00	0.02	0.02	0.03	0.02	0.02	0.03	0.02	0.00	0.00	0.00	0.00	0.00				
Cr2O3	0.01	0.03	0.02	0.03	0.02	0.03	0.03	0.03	0.02	0.03	0.02	0.03	0.02	0.03	0.01	0.03	0.00	0.00	0.01	0.03	0.01	0.03	0.03	0.03	0.04	0.03				
FeO	13.87	0.21	13.71	0.21	13.97	0.21	13.85	0.21	13.67	0.21	13.74	0.21	14.04	0.21	13.88	0.21	14.31	0.21	14.16	0.21	14.28	0.21	13.92	0.21	14.19	0.21				
MnO	0.23	0.04	0.23	0.04	0.20	0.04	0.23	0.04	0.19	0.04	0.22	0.04	0.25	0.04	0.21	0.04	0.20	0.04	0.23	0.04	0.22	0.04	0.22	0.04	0.23	0.04				
MgO	44.75	0.40	44.88	0.40	44.95	0.40	44.69	0.40	44.93	0.40	44.95	0.40	44.76	0.40	44.68	0.40	45.76	0.40	45.65	0.40	45.95	0.41	45.80	0.40	45.58	0.40				
CaO	0.10	0.01	0.06	0.01	0.09	0.01	0.09	0.01	0.05	0.01	0.05	0.01	0.07	0.01	0.06	0.01	0.05	0.01	0.06	0.01	0.07	0.01	0.03	0.01	0.08	0.01				
Na2O	0.00	0.00	0.01	0.03	0.00	0.00	0.00	0.00	0.00	0.00	0.00	0.03	0.02	0.03	0.02	0.03	0.00	0.00	0.02	0.03	0.00	0.00	0.00	0.00	0.00	0.00				
K2O	0.00	0.01	0.00	0.00	0.00	0.00	0.00	0.00	0.00	0.00	0.00	0.00	0.00	0.01	0.00	0.00	0.00	0.01	0.00	0.00	0.00	-2.23	0.00	0.00	0.00	0.00				
NiO	0.27	0.04	0.26	0.04	0.27	0.04	0.26	0.04	0.28	0.04	0.32	0.04	0.29	0.04	0.27	0.04	0.25	0.04	0.29	0.04	0.27	0.05	0.28	0.04	0.30	0.04				
Total	99.45	0.50	99.52	0.50	99.12	0.51	99.52	0.50	99.56	0.50	99.81	0.50	99.93	0.50	99.57	0.50	101.02	0.93	100.56	0.93	101.11	0.93	100.61	0.93	100.77	0.93				
Mg#	85.19	0.66	85.37	0.66	85.15	0.66	85.19	0.66	85.42	0.66	85.36	0.66	85.04	0.67	85.16	0.67	85.08	0.67	85.18	0.67	85.16	0.67	85.43	0.67	85.13	0.67				

Spot size	77			77			77			77			77			
Li	2.14	0.08	2.01	0.08	1.81	0.07	2.49	0.29	1.87	0.22	2.55	0.29	4.50	0.49	3.28	0.35
B	5.59	0.23	5.28	0.22	6.22	0.24	15.06	0.75	13.47	0.69	14.08	0.74	13.24	0.74	13.51	0.77
Ca	334	13	435	16	465	17	275	14	451	17	391	16	533	22	530	20
Sc	6.61	0.21	6.99	0.22	8.11	0.25	7.25	0.23	6.84	0.21	6.63	0.21	6.21	0.20	7.37	0.23
Ti	45	2	50	2	62	3	99	5	80	4	83	5	94	6	87	5
V	4.4	0.1	4.9	0.2	5.9	0.2	6.0	0.2	4.9	0.2	4.7	0.2	26.8	0.9	7.8	0.3
Cr	56	7	69	8	67	7	106	10	87	9	87	9	1844	210	173	21
Mn	1922	61	1929	61	1890	59	1724	62	1726	63	1748	65	1778	67	1768	68
Co	168	5	165	5	165	5	168	5	165	5	165	5	167	5	165	5
Ni	2499	321	2486	311	2537	312	2498	101	2427	99	2446	102	2514	107	2555	111
Cu	<0.00	0.018	0.120	0.019	<0.00	0.018	<0.00	0.021	0.187	0.022	0.948	0.073	0.777	0.066	0.792	0.067
Zn	77.35	2.35	76.90	2.34	75.89	2.30	75.54	2.32	76.89	2.36	75.69	2.33	100.33	3.09	81.82	2.51
Rb	<0.00	0.0025	<0.00	0.0026	<0.00	0.0026	<0.00	0.0053	<0.00	0.0045	<0.00	0.0046	0.0240	0.0064	0.0400	0.0054
Sr	<0.00	0.0028	<0.00	0.0030	<0.00	0.0029	0.0200	0.0051	0.0190	0.0041	0.0370	0.0044	0.9760	0.0330	0.6760	0.0230
Y	0.0361	0.0024	0.0496	0.0029	0.0521	0.0029	0.0530	0.0034	0.0540	0.0031	0.0540	0.0032	0.0390	0.0033	0.0590	0.0034
Zr	<0.00	0.0075	<0.00	0.0074	<0.00	0.0076	<0.00	0.0071	0.0180	0.0059	<0.00	0.0059	0.0510	0.0089	0.0470	0.0067
Nb	<0.00	0.0005	0.0019	0.0007	<0.00	0.0006	<0.00	0.0008	<0.00	0.0008	<0.00	0.0007	0.0140	0.0020	0.0050	0.0010
Sb	<0.00	0.0019	<0.00	0.0019	<0.00	0.0019	<0.00	0.0028	<0.00	0.0021	<0.00	0.0024	<0.00	0.0028	<0.00	0.0025
Ba	<0.00	0.0032	<0.00	0.0036	<0.00	0.0039	<0.00	0.0063	0.0130	0.0049	<0.00	0.0058	0.2640	0.0200	0.2610	0.0160
La	0.0019	0.0006	<0.00	0.0005	<0.00	0.0003	<0.00	0.0013	<0.00	0.0011	<0.00	0.0013	0.0060	0.0018	<0.00	0.0013
Ce	<0.00	0.0004	<0.00	0.0004	<0.00	0.0004	<0.00	0.0019	0.0060	0.0017	<0.00	0.0017	<0.00	0.0023	<0.00	0.0018
Pr	<0.00	0.0002	<0.00	0.0002	<0.00	0.0002	<0.00	0.0007	<0.00	0.0006	<0.00	0.0006	<0.00	0.0008	<0.00	0.0006
Nd	<0.00	0.0016	<0.00	0.0017	<0.00	0.0013	<0.00	0.0025	<0.00	0.0021	<0.00	0.0024	<0.00	0.0027	<0.00	0.0029
Sm	<0.00	0.0009	<0.00	0.0009	<0.00	0.0010	<0.00	0.0007	<0.00	0.0011	<0.00	0.0019	<0.00	0.0022	<0.00	0.0013
Eu	<0.00	0.0003	<0.00	0.0004	<0.00	0.0003	<0.00	0.0007	<0.00	0.0005	<0.00	0.0005	<0.00	0.0009	0.0024	0.0008
Gd	<0.00	0.0021	<0.00	0.0024	<0.00	0.0017	<0.00	0.0063	<0.00	0.0053	<0.00	0.0054	<0.00	0.0067	<0.00	0.0057
Tb	<0.00	0.0003	<0.00	0.0003	<0.00	0.0003	<0.00	0.0006	<0.00	0.0005	<0.00	0.0007	<0.00	0.0009	<0.00	0.0007
Dy	0.0018	0.0006	<0.00	0.0009	0.0044	0.0010	<0.00	0.0013	<0.00	0.0011	0.0035	0.0011	0.0081	0.0020	0.0057	0.0013
Ho	0.0011	0.0002	0.0020	0.0003	0.0019	0.0003	0.0015	0.0004	0.0023	0.0004	0.0013	0.0003	0.0015	0.0005	0.0018	0.0004
Er	0.0104	0.0014	0.0120	0.0016	0.0134	0.0017	0.0087	0.0019	0.0108	0.0018	0.0131	0.0019	0.0074	0.0020	0.0124	0.0020
Tm	0.0027	0.0004	0.0038	0.0005	0.0043	0.0005	0.0030	0.0005	0.0035	0.0005	0.0027	0.0004	0.0035	0.0007	0.0028	0.0005
Yb	0.0324	0.0033	0.0422	0.0039	0.0375	0.0035	0.0414	0.0051	0.0454	0.0046	0.0312	0.0039	0.0478	0.0065	0.0513	0.0053
Lu	0.0104	0.0007	0.0112	0.0008	0.0120	0.0008	0.0122	0.0012	0.0104	0.0009	0.0115	0.0010	0.0110	0.0013	0.0113	0.0010
HF	<0.00	0.0006	<0.00	0.0008	<0.00	0.0006	<0.00	0.0004	0.0020	0.0009	<0.00	0.0006	<0.00	0.0017	<0.00	0.0003
Ta	<0.00	0.0004	<0.00	0.0005	<0.00	0.0005	<0.00	0.0006	<0.00	0.0006	<0.00	0.0006	<0.00	0.0007	<0.00	0.0006
Pb	0.0205	0.0017	0.0186	0.0016	0.0263	0.0019	0.0500	0.0045	0.0440	0.0038	0.0570	0.0047	0.0840	0.0075	0.0680	0.0058
Th	<0.00	0.0001	<0.00	0.0001	<0.00	0.0000	<0.00	0.0001	<0.00	0.0001	<0.00	0.0000	<0.00	0.0001	<0.00	0.0001
U	<0.00	0.0000	<0.00	0.0000	<0.00	0.0000	<0.00	0.0002	<0.00	0.0000	<0.00	0.0001	<0.00	0.0002	<0.00	0.0001

Table A2.P (continued olivine in OI-T2)

Sample Shape Deformation n. grain Axis Location	rounded undeformed												anhedral undeformed												corroded undeformed											
	4												6												9											
	rim				core				rim				core				rim				rim															
	[001]				[100]				[100]				[100]				[100]																			
Dist. (mm)	0.04 σ	0.11 σ	0.18 σ	0.27 σ	0.46 σ	0.60 σ	0.65 σ	0.75 σ	0.14 σ	0.22 σ	0.29 σ	0.58 σ	0.71 σ	0.97 σ	0.00 σ	0.15 σ	0.44 σ	0.58 σ	0.73 σ	0.87 σ	1.02 σ	1.16 σ	1.31 σ	1.45 σ												
SiO2	39.46	0.35	39.17	0.35	39.45	0.34	39.34	0.35	39.08	0.35	39.35	0.35	39.00	0.35	39.31	0.35	39.28	0.35	39.52	0.35	39.52	0.35	39.28	0.35	39.56	0.35	39.52	0.35	39.42	0.35						
TiO2	0.01	0.03	0.03	0.03	0.03	0.03	0.02	0.03	0.03	0.03	0.01	0.03	0.01	0.03	0.03	0.03	0.02	0.03	0.00	0.00	0.01	0.03	0.00	0.00	0.02	0.03	0.00	0.03	0.00	0.03						
Al2O3	0.01	0.02	0.02	0.02	0.02	0.02	0.00	0.00	0.02	0.02	0.00	0.02	0.02	0.02	0.01	0.02	0.03	0.02	0.00	0.00	0.04	0.02	0.01	0.02	0.01	0.02	0.01	0.02	0.01	0.02						
Cr2O3	0.00	0.00	0.00	0.04	0.06	0.03	0.03	0.04	0.01	0.04	0.00	0.00	0.02	0.04	0.03	0.04	0.01	0.04	0.01	0.04	0.01	0.04	0.01	0.04	0.02	0.04	0.01	0.04	0.01	0.04						
FeO	15.21	0.23	15.13	0.23	15.35	0.22	15.16	0.23	15.16	0.23	15.07	0.23	14.96	0.23	15.07	0.23	15.16	0.23	15.22	0.23	15.32	0.23	15.04	0.23	15.14	0.23	15.00	0.23	15.01	0.23						
MnO	0.24	0.04	0.22	0.04	0.24	0.04	0.23	0.04	0.24	0.04	0.23	0.04	0.22	0.04	0.21	0.04	0.25	0.04	0.21	0.04	0.23	0.04	0.23	0.04	0.20	0.04	0.22	0.04	0.22	0.04						
MgO	44.73	0.89	44.98	0.90	44.78	0.88	45.02	0.90	44.28	0.89	44.50	0.89	44.36	0.89	44.77	0.89	44.66	0.89	44.45	0.89	44.39	0.89	44.64	0.89	44.75	0.89	44.90	0.90	44.54	0.89						
CaO	0.08	0.01	0.07	0.01	0.07	0.01	0.08	0.01	0.07	0.01	0.08	0.01	0.07	0.01	0.07	0.01	0.09	0.01	0.09	0.01	0.09	0.01	0.08	0.01	0.11	0.01	0.09	0.01	0.09	0.01						
Na2O	0.00	0.00	0.01	0.04	0.00	0.04	0.00	0.00	0.02	0.04	0.01	0.04	0.00	0.00	0.03	0.04	0.01	0.03	0.00	0.04	0.03	0.04	0.03	0.04	0.00	0.00	0.02	0.04	0.02	0.04						
K2O	0.00	0.00	0.00	0.00	0.00	0.01	0.01	0.01	0.00	0.00	0.00	0.00	0.00	0.00	0.00	0.01	0.00	0.00	0.00	0.00	0.00	0.00	0.00	0.00	0.00	0.00	0.01	0.01	0.01	0.01						
NiO	0.26	0.05	0.26	0.04	0.25	0.04	0.24	0.04	0.32	0.05	0.20	0.04	0.25	0.04	0.24	0.05	0.25	0.05	0.26	0.05	0.28	0.05	0.27	0.05	0.22	0.05	0.31	0.05	0.26	0.04						
Total	99.99	0.99	99.87	0.99	100.25	0.98	100.14	0.99	99.26	0.98	99.56	0.99	99.00	0.98	99.63	0.99	99.60	0.99	99.68	0.98	99.77	0.98	100.18	0.99	99.96	0.99	99.87	0.99	99.85	0.99						
Mg#	83.98	0.84	84.13	0.83	83.87	0.82	84.11	0.84	83.89	0.84	83.96	0.84	84.00	0.83	84.21	0.83	84.08	0.84	84.02	0.84	83.92	0.84	83.95	0.85	83.76	0.85	84.13	0.84	84.09	0.84	84.11	0.84				
Spot size	77												77												77											
Li	1.84												1.25												1.98											
B	5.94												6.46												5.76											
Ca	482												565												415											
Sc	6.87												7.03												7.19											
Ti	101.56												108.29												113.55											
V	5.2												6.1												6.3											
Cr	52.14												73.37												66.86											
Mn	1848												1858												1913											
Co	151												155												156											
Ni	1918												1952												1873											
Cu	0.056												0.064												0.000											
Zn	86.19												82.85												85.27											
Rb	0.0152												<0.00												<0.00											
Sr	0.0194												0.0181												<0.00											
Y	0.1110												0.1008												0.0909											
Zr	0.0372												0.0327												0.0254											
Nb	0.0034												0.0047												<0.00											
Sb	<0.00												<0.00												<0.00											
Ba	0.0038												0.0025												<0.00											
La	0.0036												<0.00												<0.00											
Ce	<0.00												<0.00												<0.00											
Pr	<0.00												<0.00												<0.00											
Nd	<0.00												<0.00												<0.00											
Sm	<0.00												<0.00												<0.00											
Eu	<0.00												<0.00												<0.00											
Gd	<0.00												<0.00												<0.00											
Tb	<0.00												<0.00												<0.00											
Dy	0.0120												0.0125												<0.00											
Ho	0.0056												0.0064												0.0036											
Er	0.0143												0.0210												0.0210											
Tm	0.0063												0.0073												0.0076											
Yb	0.0628												0.0908												0.0984											
Lu	0.0247												0.0277												0.0236											
Hf	<0.00												<0.00												<0.00											
Ta	<0.00												<0.00												<0.00											
Pb	0.0159												0.0178												0.0179											
Th	<0.00												<0.00												<0.00											
U	<0.00												<0.00												<0.00											

Table A2.P (continued olivine in OI-T2)

Sample Shape Deformation n. grain Axis Location	rounded undeformed 4																	corroded deformed 6																																				
	[001]																	[100]																																				
	rim (cont. plg)																	rim																																				
Dist. (mm)	core																	core																																				
	0.27 σ	0.31 σ	0.35 σ	0.39 σ	0.43 σ	0.05 σ	0.09 σ	0.14 σ	0.18 σ	0.23 σ	0.27 σ	0.32 σ	0.36 σ	0.45 σ	0.09 σ	0.17 σ	0.26 σ	0.35 σ	0.52 σ	0.61 σ	0.78 σ	0.87 σ	0.96 σ	1.05 σ	1.13 σ	1.22 σ	1.31 σ																											
SiO ₂	39.46	0.34	39.36	0.34	39.45	0.34	39.56	0.35	39.68	0.35	39.25	0.34	39.22	0.34	39.48	0.34	39.68	0.35	39.58	0.35	39.47	0.34	39.51	0.35	39.67	0.35	39.53	0.35	39.79	0.35	39.68	0.35	39.37	0.34	39.77	0.35	39.54	0.35	39.43	0.34	39.68	0.35	39.69	0.35	39.70	0.35	39.57	0.35	39.48	0.34	39.55	0.35	39.75	0.35
TiO ₂	0.00	0.00	0.01	0.03	0.02	0.03	0.00	0.03	0.03	0.03	0.04	0.03	0.00	0.00	0.03	0.03	0.00	0.00	0.03	0.03	0.00	0.00	0.03	0.03	0.00	0.00	0.03	0.03	0.00	0.00	0.02	0.02	0.00	0.00	0.03	0.03	0.01	0.02	0.02	0.03	0.02	0.03	0.02	0.03	0.02	0.01	0.02	0.11	0.02	0.00	0.02	0.01	0.03	
Al ₂ O ₃	0.04	0.02	0.00	0.02	0.01	0.02	0.00	0.00	0.01	0.02	0.01	0.02	0.01	0.02	0.01	0.02	0.00	0.00	0.02	0.02	0.00	0.00	0.03	0.02	0.01	0.02	0.01	0.02	0.00	0.00	0.03	0.03	0.00	0.00	0.03	0.03	0.01	0.02	0.02	0.03	0.01	0.03	0.02	0.03	0.02	0.01	0.02	0.11	0.02	0.00	0.02	0.01	0.03	
Cr ₂ O ₃	0.03	0.03	0.01	0.04	0.03	0.04	0.03	0.04	0.01	0.03	0.00	0.00	0.03	0.04	0.01	0.03	0.00	0.00	0.02	0.04	0.00	0.00	0.00	0.00	0.00	0.00	0.00	0.00	0.03	0.00	0.03	0.00	0.00	0.01	0.03	0.01	0.04	0.01	0.03	0.02	0.03	0.01	0.03	0.02	0.03	0.02	0.03	0.02	0.03	0.00	0.00	0.02	0.03	
FeO	14.93	0.24	15.01	0.24	14.77	0.24	14.68	0.24	14.46	0.23	14.99	0.24	14.72	0.24	15.12	0.24	14.86	0.24	15.20	0.24	15.14	0.24	15.10	0.24	15.19	0.24	15.01	0.24	15.05	0.24	15.22	0.24	15.02	0.24	15.19	0.24	14.96	0.24	15.00	0.24	15.05	0.24	14.78	0.24	14.84	0.24	14.83	0.24	14.92	0.24	14.93	0.24	14.83	0.24
MnO	0.25	0.04	0.23	0.04	0.22	0.04	0.21	0.04	0.21	0.04	0.25	0.04	0.24	0.04	0.24	0.04	0.23	0.04	0.23	0.04	0.23	0.04	0.25	0.04	0.21	0.04	0.26	0.04	0.23	0.04	0.23	0.04	0.25	0.04	0.24	0.04	0.24	0.04	0.24	0.04	0.24	0.04	0.25	0.04	0.25	0.04	0.22	0.04	0.21	0.04	0.24	0.04		
MgO	44.22	0.87	44.25	0.87	43.89	0.87	44.27	0.87	44.31	0.87	43.95	0.87	43.97	0.87	44.33	0.87	44.21	0.87	44.47	0.88	43.93	0.87	44.64	0.88	44.42	0.88	44.49	0.88	44.69	0.88	44.73	0.88	44.50	0.88	44.75	0.88	44.83	0.88	43.85	0.87	44.76	0.88	44.31	0.87	44.08	0.87	43.96	0.87	44.65	0.88	43.46	0.86	44.48	0.88
CaO	0.10	0.01	0.10	0.01	0.10	0.01	0.07	0.01	0.09	0.01	0.09	0.01	0.09	0.01	0.08	0.01	0.09	0.01	0.09	0.01	0.08	0.01	0.08	0.01	0.08	0.01	0.08	0.01	0.05	0.01	0.06	0.01	0.08	0.01	0.06	0.01	0.09	0.01	0.09	0.01	0.09	0.01	0.09	0.01	0.11	0.01	0.09	0.01	0.21	0.02	0.10	0.01		
Na ₂ O	0.01	0.04	0.00	0.00	0.00	0.00	0.04	0.04	0.00	0.00	0.00	0.00	0.00	0.00	0.01	0.04	0.00	0.00	0.00	0.00	0.02	0.04	0.01	0.04	0.01	0.04	0.00	0.00	0.01	0.03	0.00	0.00	0.00	0.00	0.00	0.04	0.04	0.00	0.00	0.00	0.04	0.03	0.03	0.01	0.03	0.00	0.00	0.03	0.04	0.00	0.00			
K ₂ O	0.00	0.00	0.00	0.00	0.00	0.01	0.00	0.00	0.00	0.01	0.00	0.01	0.01	0.01	0.00	0.01	0.00	0.01	0.00	0.00	0.00	0.01	0.01	0.01	0.00	0.00	0.00	0.00	0.00	0.00	0.00	0.01	0.00	0.01	0.00	0.00	0.00	0.00	0.00	0.00	0.01	0.01	0.01	0.00	0.01	0.00	0.00	0.00	0.00	0.00	0.00	0.00		
NiO	0.28	0.04	0.26	0.04	0.28	0.04	0.24	0.04	0.25	0.04	0.22	0.04	0.26	0.04	0.27	0.04	0.28	0.04	0.24	0.04	0.29	0.04	0.27	0.04	0.26	0.04	0.26	0.04	0.27	0.04	0.25	0.04	0.21	0.04	0.27	0.04	0.27	0.04	0.25	0.04	0.26	0.04	0.26	0.04	0.26	0.04	0.25	0.04	0.23	0.04	0.23	0.04		
Total	99.32	0.97	99.22	0.97	98.76	0.97	99.11	0.97	99.05	0.97	98.80	0.97	98.55	0.97	99.58	0.97	99.35	0.97	99.87	0.98	99.20	0.97	99.89	0.98	99.85	0.97	99.66	0.98	100.12	0.98	100.21	0.98	99.44	0.97	100.29	0.98	99.96	0.98	98.93	0.97	100.11	0.98	99.43	0.97	99.25	0.97	99.07	0.97	99.64	0.98	98.76	0.96	99.67	0.98
Mg#	84.08	0.86	84.01	0.86	84.12	0.86	84.31	0.86	84.53	0.85	83.94	0.86	84.19	0.85	83.94	0.87	84.13	0.86	83.91	0.87	83.79	0.87	84.05	0.87	83.90	0.87	84.08	0.86	84.11	0.87	83.97	0.87	84.08	0.86	84.00	0.86	84.00	0.87	84.00	0.86	84.00	0.87	84.00	0.86	84.12	0.86	84.09	0.86	84.21	0.86	83.84	0.87	84.25	0.86
Spot size	77																	77																																				
Li	1.44																	1.75																																				
B	10.31																	10.83																																				
Ca	411																	594																																				
Sc	6.74																	7.38																																				
Ti	79.69																	87.99																																				
V	3.6																	4.9																																				
Cr	46.83																	80.1																																				
Mn	1822																	1799																																				
Co	154																	156																																				
Ni	1759																	1801																																				
Cu	0.035																	0.064																																				
Zn	81.74																	86.35																																				
Rb	0.0047																	0.0070																																				
Sr	<0.00																	<0.00																																				
Y	0.1188																	0.1816																																				
Zr	0.0291																	0.0838																																				
Nb	0.0023																	0.0100																																				
Sb																																																						
Ba	<0.00																	<0.00																																				
La	<0.00																	<0.00																																				
Ce	<0.00																	<0.00																																				
Pr	<0.00																	0.0004																																				
Nd	<0.00																	<0.00																																				
Sm	0.0082																	<0.00																																				
Eu	<0.00																	<0.00																																				
Gd	<0.00																	<0.00																																				
Tb	0.0009																	0.0008																																				
Dy	0.0084																	0.0113																																				
Ho	0.0048																	0.0072																																				
Er	0.0340																	0.0363																																				
Tm	0.0109																	0.0095																																				
Yb	0.1033																	0.0998																																				
Lu	0.0250																	0.0255																																				
Hf	<0.00																	0.0057																																				
Ta	<0.00																	<0.00																																				
Pb	0.0197																	0.0171																																				
Th	<0.00																	<0.00																																				
U	<0.00																	<0.00																																				

Table A2.P (continued olivine in OI-T2)

Sample Shape Deformation n. grain Axis Location	anhedral undeformed 12																				anhedral undeformed 13																																							
	rim (cont. cpx)										rim										core						rim																																	
	[010]					core					rim					[010]					rim																																							
	1.19 σ		1.25 σ		1.31 σ		1.38 σ		1.44 σ		1.50 σ		1.56 σ		1.63 σ		1.69 σ		1.75 σ		1.81 σ		1.94 σ		2.00 σ		2.06 σ		0.05 σ		0.11 σ		0.16 σ		0.21 σ		0.27 σ		0.32 σ		0.43 σ		0.54 σ		0.05 σ		0.10 σ		0.16 σ		0.21 σ		0.26 σ							
Dist. (mm)																																																												
SiO2	39.57	0.35	39.64	0.35	39.46	0.35	39.59	0.35	39.46	0.35	39.26	0.35	39.62	0.35	39.78	0.35	39.55	0.35	39.72	0.35	39.60	0.35	50.93	0.43	39.56	0.35	39.40	0.35	39.51	0.35	39.71	0.35	39.65	0.35	39.68	0.35	39.67	0.35	39.83	0.35	39.85	0.35	39.67	0.35	39.51	0.35	39.84	0.35	39.74	0.35	39.62	0.35	39.61	0.35						
TiO2	0.02	0.03	0.02	0.03	0.02	0.03	0.03	0.03	0.01	0.03	0.05	0.03	0.04	0.03	0.00	0.00	0.00	0.00	0.06	0.03	0.01	0.03	0.66	0.05	0.02	0.03	0.02	0.03	0.02	0.03	0.01	0.03	0.02	0.03	0.01	0.03	0.02	0.02	0.02	0.02	0.03	0.02	0.03	0.02	0.00	0.00	0.03	0.03	0.02	0.03	0.00	0.00	0.00	0.00						
Al2O3	0.03	0.02	0.00	0.02	0.00	0.00	0.02	0.02	0.03	0.02	0.03	0.02	0.00	0.00	0.03	0.02	0.01	0.02	0.02	0.02	0.03	0.02	3.30	0.06	0.00	0.00	0.04	0.02	0.02	0.02	0.01	0.02	0.01	0.02	0.02	0.02	0.02	0.02	0.03	0.02	0.03	0.02	0.00	0.02	0.04	0.02	0.01	0.02	0.00	0.00	0.00	0.02	0.01	0.02	0.00	0.00				
Cr2O3	0.02	0.04	0.01	0.04	0.03	0.04	0.03	0.04	0.02	0.04	0.00	0.04	0.04	0.01	0.04	0.00	0.00	0.04	0.04	0.04	0.00	0.00	4.26	0.07	0.00	0.00	0.02	0.04	0.00	0.00	0.02	0.04	0.00	0.04	0.00	0.00	0.02	0.04	0.04	0.04	0.02	0.04	0.01	0.04	0.00	0.00	0.01	0.04	0.00	0.00	0.01	0.04	0.03	0.04	0.02	0.04				
FeO	15.08	0.25	15.03	0.25	15.08	0.25	15.04	0.25	14.99	0.25	15.14	0.25	15.15	0.25	15.08	0.25	14.96	0.25	14.86	0.25	14.84	0.25	4.61	0.13	14.56	0.24	14.89	0.25	14.62	0.24	14.71	0.25	14.73	0.25	14.90	0.25	14.90	0.25	14.81	0.25	14.68	0.25	14.87	0.25	15.03	0.25	14.82	0.25	14.78	0.25	14.86	0.25	14.66	0.25						
MnO	0.23	0.04	0.23	0.04	0.24	0.04	0.28	0.04	0.21	0.04	0.24	0.04	0.24	0.04	0.24	0.04	0.24	0.04	0.20	0.04	0.20	0.04	0.14	0.04	0.22	0.04	0.25	0.04	0.23	0.04	0.22	0.04	0.21	0.04	0.24	0.04	0.21	0.04	0.26	0.04	0.27	0.04	0.22	0.04	0.24	0.04	0.23	0.04	0.21	0.04	0.20	0.04	0.23	0.04						
MgO	44.14	0.89	44.48	0.89	44.35	0.89	44.80	0.90	44.76	0.90	44.08	0.88	44.19	0.89	44.38	0.89	44.90	0.90	44.32	0.89	44.66	0.89	16.05	0.41	44.85	0.90	44.22	0.89	44.48	0.89	44.14	0.88	44.43	0.89	44.30	0.89	44.57	0.89	44.51	0.89	44.73	0.89	45.00	0.90	44.07	0.88	44.66	0.89	44.29	0.89	44.94	0.90	44.59	0.89						
CaO	0.11	0.01	0.11	0.01	0.09	0.01	0.10	0.01	0.09	0.01	0.11	0.01	0.09	0.01	0.10	0.01	0.10	0.01	0.08	0.01	0.06	0.01	21.78	0.40	0.10	0.01	0.06	0.01	0.09	0.01	0.10	0.01	0.10	0.01	0.12	0.01	0.10	0.01	0.11	0.01	0.08	0.01	0.09	0.01	0.11	0.01	0.11	0.01	0.10	0.01	0.11	0.01	0.10	0.01	0.11	0.01				
Na2O	0.01	0.04	0.00	0.00	0.00	0.00	0.00	0.00	0.00	0.00	0.00	0.04	0.00	0.00	0.03	0.04	0.00	0.00	0.01	0.04	0.01	0.04	0.46	0.08	0.01	0.04	0.00	0.00	0.02	0.04	0.02	0.04	0.01	0.04	0.01	0.04	0.00	0.00	0.02	0.04	0.00	0.00	0.00	0.00	0.01	0.04	0.01	0.04	0.00	0.00	0.00	0.00	0.00	0.00						
K2O	0.01	0.01	0.00	0.00	0.00	0.00	0.00	0.00	0.00	0.01	0.01	0.01	0.00	0.00	0.00	0.00	0.00	0.00	0.00	0.00	0.00	0.01	0.00	0.01	0.00	0.00	0.00	0.00	0.00	0.00	0.00	0.00	0.01	0.00	0.00	0.00	0.00	0.01	0.00	0.00	0.00	0.00	0.00	0.01	0.01	0.00	0.00	0.01	0.01	0.00	0.00	0.01	0.00	0.00						
NiO	0.26	0.05	0.26	0.04	0.27	0.05	0.23	0.05	0.26	0.05	0.28	0.05	0.28	0.05	0.29	0.05	0.27	0.05	0.25	0.05	0.25	0.05	0.04	0.04	0.21	0.04	0.27	0.05	0.27	0.05	0.29	0.05	0.28	0.05	0.23	0.05	0.26	0.05	0.26	0.04	0.25	0.05	0.26	0.05	0.26	0.04	0.27	0.05	0.25	0.05	0.24	0.05	0.30	0.05						
Total	99.48	0.99	99.78	0.99	99.55	0.99	100.11	1.00	99.83	1.00	99.20	0.99	99.61	0.99	99.92	0.99	100.07	1.00	99.55	0.99	99.66	0.99	99.23	0.74	99.51	1.00	99.16	0.99	99.27	0.99	99.25	0.99	99.45	0.99	99.52	0.99	99.76	0.99	99.90	0.99	99.94	1.00	100.12	1.00	99.26	0.99	99.98	0.99	99.40	0.99	100.02	1.00	99.53	0.99						
Mg#	83.91	0.89	84.07	0.89	83.98	0.89	84.15	0.89	84.19	0.89	83.85	0.89	83.86	0.90	83.99	0.89	84.25	0.89	84.17	0.89	84.29	0.88	86.12	1.21	84.60	0.87	84.11	0.89	84.43	0.88	84.25	0.88	84.31	0.88	84.12	0.89	84.21	0.89	84.27	0.89	84.45	0.88	84.36	0.88	83.94	0.89	84.31	0.89	84.23	0.89	84.36	0.88	84.43	0.88						
Spot size			77						77						77				77																														77											
Li			1.80		0.14				1.60		0.13				1.78		0.15				1.72		0.15																												1.54		0.08							
B			11.24		2.04				12.00		2.27				11.83		2.34				10.60		2.19																												7.84		0.43							
Ca			649		30				597		28				562		27				396		20																												627		22							
Sc			7.68		0.31				7.55		0.31				7.52		0.31				7.28		0.31																														6.62		0.36					
Ti			87.67		3				81.89		2.82				80.12		2.78				83.82		2.93																														70.64		2.84					
V			6.5		0.2				6.4		0.2				6.0		0.2				5.7		0.2																														4.3		0.1					
Cr			98.37		4.41				97.06		4.42				93.53		4.34				82.27		3.89																														47.76		1.47					
Mn			1755		70				1726		69				1761		72				1778		74																																1828		57			
Co			156		8				156		8				159		9				154		9																																159		5			
Ni			1736		89				1731		91				1743		94				1783		99																																		1937		109	
Cu			0.236		0.014				0.242		0.014				0.182		0.012				0.083		0.010																																0.055		0.020			
Zn			85.29		2.97				83.87		2.94				83.38		2.94				84.73		3.01																																89.49		2.76			
Rb			0.0053		0.0013				<0.00		0.0014				0.0042		0.0014				<0.00		0.0015																																<0.00		0.0028			
Sr			<0.00		0.0022				<0.00		0.0022				<0.00		0.0023				0.0069		0.0025																																<0.00		0.0053			
Y			0.1499		0.0062				0.1544		0.0064				0.1200		0.0052				0.0974		0.0047																																0.0899		0.0073			
Zr			0.0913		0.0050				0.0749		0.0044				0.0738		0.0045				0.0723		0.0047																																		0.0222		0.0033	
Nb			0.0020		0.0005				0.0014		0.0005				0.0012		0.0004				0.0018		0.0005																																		0.0012		0.0006	
Sb			<0.00		0.0023				<0.00		0.0021				<																																													

Table A2.P (continued olivine in OI-T3)

Sample	anhedral undeformed area 1 n.d. core												anhedral undeformed area 2 n.d. core												anhedral undeformed area a n.d. rim																	
Shape	core												rim												rim																	
n. grain																																										
Location																																										
Dist. (mm)	1.00	σ	1.28	σ	1.47	σ	1.66	σ	1.81	σ	2.06	σ	2.25	σ	0.00	σ	0.19	σ	0.38	σ	rim	σ	0.56	σ	0.00	σ	0.13	σ	0.31	σ	0.41	σ	0.06	σ	0.40	σ	1.09	σ	core	σ	1.31	σ
SiO2	39.97		0.22	39.82	0.21	39.64	0.21	39.98	0.22	39.69	0.21	39.64	0.21	40.01	0.22	39.61	0.80	39.51	0.79	39.53	0.79	39.37	0.79	39.91	0.80	39.92	0.80	40.03	0.80	39.88	0.80	39.88	0.80	39.98	0.80	40.19	0.81	39.96	0.80			
TiO2	0.02	0.03	0.01	0.03	0.03	0.03	0.03	0.03	0.03	0.02	0.02	0.00	0.02	0.00	0.02	0.03	0.00	0.00	0.01	0.03	0.02	0.03	0.02	0.02	0.03	0.02	0.03	0.01	0.03	0.01	0.03	0.02	0.02	0.03	0.02	0.03	0.03	0.03	0.03	0.03	0.03	
Al2O3	0.01	0.02	0.00	0.00	0.03	0.02	0.02	0.02	0.02	0.02	0.01	0.02	0.00	0.02	0.02	0.02	0.00	0.02	0.01	0.02	0.00	0.00	0.00	0.03	0.02	0.00	0.02	0.02	0.02	0.02	0.02	0.02	0.02	0.02	0.02	0.01	0.02	0.01	0.02	0.01	0.02	
Cr2O3	0.03	0.03	0.00	0.00	0.00	0.00	0.03	0.03	0.03	0.00	0.03	0.00	0.00	0.00	0.00	0.00	0.00	0.02	0.03	0.01	0.03	0.00	0.00	0.02	0.03	0.03	0.03	0.01	0.03	0.00	0.03	0.00	0.03	0.02	0.03	0.05	0.03	0.02	0.03			
FeO	16.25	0.23	16.15	0.23	16.26	0.23	16.21	0.23	16.33	0.23	16.28	0.23	16.49	0.23	16.19	0.23	16.32	0.23	16.25	0.23	16.21	0.24	16.41	0.23	16.58	0.23	16.70	0.23	16.44	0.23	17.00	0.23	16.81	0.23	17.00	0.23	16.94	0.23				
MnO	0.25	0.04	0.22	0.04	0.26	0.04	0.23	0.04	0.25	0.04	0.23	0.04	0.25	0.04	0.25	0.04	0.24	0.04	0.25	0.04	0.23	0.04	0.25	0.04	0.25	0.04	0.26	0.04	0.23	0.04	0.25	0.04	0.25	0.04	0.25	0.04	0.25	0.04	0.26	0.04		
MgO	43.18	0.39	43.38	0.39	43.01	0.39	42.98	0.38	43.04	0.39	43.19	0.39	43.40	0.39	43.87	0.39	43.79	0.39	43.88	0.39	44.03	0.40	43.47	0.39	43.62	0.39	43.76	0.39	43.74	0.39	43.28	0.39	43.55	0.39	43.31	0.39	42.98	0.39				
CaO	0.10	0.01	0.09	0.01	0.09	0.01	0.10	0.01	0.09	0.01	0.05	0.01	0.06	0.01	0.08	0.01	0.06	0.01	0.09	0.01	0.07	0.01	0.07	0.01	0.07	0.01	0.05	0.01	0.06	0.01	0.05	0.01	0.08	0.01	0.09	0.01	0.09	0.01	0.09	0.01		
Na2O	0.00	0.00	0.00	0.00	0.00	0.03	0.02	0.03	0.02	0.03	0.00	0.04	0.01	0.03	0.00	0.03	0.01	0.03	0.00	0.01	0.03	0.00	0.01	0.03	0.01	0.03	0.00	0.00	0.00	0.00	0.00	0.03	0.00	0.00	0.00	0.00	0.00	0.00	0.00	0.00	0.00	
K2O	0.00	0.01	0.01	0.01	0.00	0.01	0.00	0.01	0.00	0.00	0.00	0.01	0.00	0.01	0.00	0.00	0.00	0.00	0.00	0.01	0.00	0.00	0.00	0.00	0.01	0.00	0.00	0.00	0.00	0.00	0.00	0.00	0.00	0.00	0.00	0.00	0.00	0.00	0.01	0.01		
NiO	0.20	0.04	0.25	0.04	0.17	0.04	0.17	0.04	0.19	0.04	0.21	0.04	0.20	0.04	0.19	0.04	0.22	0.04	0.22	0.04	0.23	0.04	0.23	0.04	0.20	0.04	0.22	0.04	0.19	0.04	0.19	0.04	0.19	0.04	0.23	0.04	0.23	0.04	0.21	0.04		
Total	100.01	0.50	99.93	0.50	99.48	0.50	99.75	0.50	99.64	0.50	99.62	0.50	100.43	0.51	100.23	0.92	100.17	0.92	100.26	0.92	100.17	0.92	100.41	0.92	100.68	0.92	101.09	0.93	100.54	0.92	100.69	0.92	100.92	0.93	101.14	0.93	100.52	0.92				
Mg#	82.57	0.71	82.72	0.70	82.50	0.71	82.54	0.71	82.45	0.71	82.55	0.70	82.43	0.71	82.85	0.70	82.71	0.71	82.80	0.70	82.89	0.73	82.53	0.71	82.42	0.71	82.37	0.72	82.59	0.71	81.95	0.72	82.20	0.72	81.95	0.72	81.89	0.72				
Spot size	77		77												77		77														77		77						77		77	
Li	2.53	0.16	2.20	0.14											1.98	0.16	2.03	0.16	2.60	0.19	2.20	0.17					2.09	0.18	2.11	0.17	2.04	0.16	2.20	0.17			2.20	0.17				
B	20.41	2.54	21.93	2.60											6.95	0.28	6.38	0.26	7.55	0.30	7.26	0.27					7.35	0.30	7.60	0.30	6.95	0.28	7.26	0.27			7.26	0.27				
Ca	791	32	790	32											486	19	668	19	518	23	512	18					328	14	618	22	687	24	802	27			802	27				
Sc	7.40	0.24	8.55	0.28											7.21	0.31	7.24	0.31	7.42	0.32	8.60	0.30					7.31	0.37	8.02	0.39	8.35	0.38	8.60	0.38			8.60	0.38				
Ti	131	6	150	7											138	18	128	17	128	18	248	18					121.62	22	146	25	136	21	248	37			248	37				
V	8.1	0.3	9.3	0.3											7.3	0.2	7.1	0.2	10.2	0.3	12.6	0.2					6.5	0.2	7.7	0.2	7.4	0.2	12.6	0.4			12.6	0.4				
Cr															52	5	47	5	67	7	72	5					37.14	6	51	7	41	5	72	9			72	9				
Mn	2073	97	2054	94											1962	59	1966	60	1975	60	2112	59					2117	64	2092	63	2109	64	2112	64			2112	64				
Co	184	6	185	6											166	5	167	5	168	5	175	5					175	5	177	5	175	5	175	5			175	5				
Ni	1762	121	1749	116											2694	743	2632	716	2540	688	2391	653					2060	614	2161	631	2309	640	2391	654			2391	654				
Cu	0.188	0.015	0.101	0.012											<0.00	0.018	<0.00	0.018	<0.00	0.017	0.185	0.017					0.145	0.021	<0.00	0.019	0.149	0.020	0.185	0.021			0.185	0.021				
Zn	102.24	12.08	103.26	11.79											99.39	4.02	99.40	4.06	99.55	4.11	100.77	4.06					97.91	4.70	99.64	4.66	99.28	4.32	100.77	4.30			100.77	4.30				
Rb	<0.00	0.0029	<0.00	0.0031											<0.00	0.0032	<0.00	0.0031	<0.00	0.0030	<0.00	0.0029					<0.00	0.0035	<0.00	0.0031	<0.00	0.0031	<0.00	0.0033				<0.00	0.0033			
Sr	<0.00	0.0033	<0.00	0.0034											<0.00	0.0031	<0.00	0.0030	<0.00	0.0027	<0.00	0.0027					0.0590	0.0042	<0.00	0.0029	<0.00	0.0029	<0.00	0.0029	<0.00	0.0029	<0.00	0.0030				
Y	0.1617	0.0072	0.1997	0.0086											0.1370	0.0075	0.1280	0.0072	0.2320	0.0120	0.2550	0.0074					0.1020	0.0069	0.1440	0.0090	0.1620	0.0094	0.2550	0.0140			0.2550	0.0140				
Zr	0.0634	0.0057	0.0375	0.0051											0.0380	0.0051	0.0490	0.0053	0.0560	0.0055	0.1560	0.0052					0.0310	0.0049	0.0650	0.0063	0.0460	0.0053	0.1560	0.0110			0.1560	0.0110				
Nb	0.0029	0.0006	0.0023	0.0006											<0.00	0.0008	<0.00	0.0007	0.0030	0.0007	0.0070	0.0006					0.0020	0.0007	0.0030	0.0008	0.0030	0.0009	0.0070	0.0011			0.0070	0.0011				
Sb	<0.00	0.0016	<0.00	0.0017											0.0050	0.0018	0.0070	0.0020	0.0100	0.0023	<0.00	0.0018					<0.00	0.0016	0.0040	0.0017	<0.00	0.0017	<0.00	0.0017	<0.00	0.0017	<0.00	0.0017	<0.00			
Ba	<0.00	0.0034	<0.00	0.0037											<0.00	0.0039	<0.00	0.0029	<0.00	0.0033	<0.00	0.0029					0.0150	0.0053	<0.00	0.0044	<0.00	0.0043	<0.00	0.0036				<0.00	0.0036			
La	<0.00	0.0004	<0.00	0.0004											<0.00	0.0006	0.0020	0.0009	<0.00	0.0008	<0.00	0.0006					<0.00	0.0009	<0.00	0.0008	<0.00	0.0008	<0.00	0.0009				<0.00	0.0009			
Ce	<0.00	0.0006	<0.00	0.0005											0.0030	0.0009	<0.00	0.0009	<0.00	0.0008	<0.00	0.0009					0.0030	0.0010	<0.00	0.0008	<0.00	0.0008	<0.00	0.0008				<0.00	0.0008			
Pr	<0.00	0.0003	<0.00	0.0002											<0.00	0.0003	<0.00	0.0004	<0.00	0.0003	<0.00	0.0003					<0.00	0.0004	<0.00	0.0003	0.0020	0.0005	<0.00	0.0004				<0.00	0.0004			
Nd	<0.00	0.0011	<0.00	0.0011											<0.00	0.0020	<0.00	0.0018	<0.00	0.0019	<0.00	0.0023																				

Table A2.P (continued plagioclase)

Sample Shape n. grain OI Location Dist. (mm)	305-U1309D-241R-2W, 89-91														305-U1309D-247R-3W, 16-18										305-U1309D-247R-3W, 22-25																																																																																																																																																																																																																																																																								
	interstitial							interstitial							interstitial					interstitial					interstitial																																																																																																																																																																																																																																																																								
	14							12							5					8					10					9																																																																																																																																																																																																																																																																			
	rim-wedge			core				rim			core				rim	rim				rim	rim				rim	rim		rim		rim		rim		rim		rim		rim																																																																																																																																																																																																																																																											
	0.06	σ		0.53	σ		0.66	σ		1.00	σ		rim	0.05	σ	core	0.15	σ	rim	-0.51	σ	-0.45	σ	-0.38	σ	-0.32	σ	-0.26	σ	0.13	σ	0.31	σ	0.56	σ	0.84	σ	1.81	σ	2.00	σ	2.13	σ	2.44	σ	2.66	σ	rim	0.06	σ	0.17	σ																																																																																																																																																																																																																																													
SiO ₂	49.50	0.99	48.12	0.96	47.47	0.95	47.66	0.95	49.22	0.24	49.65	0.24	49.83	0.24	49.46	0.24	48.45	0.23	49.88	0.24	49.58	0.24	47.25	0.95	47.33	0.95	47.21	0.95	48.61	0.97	47.46	0.95	47.55	0.95	47.41	0.95	48.00	0.96	48.30	0.97	48.58	0.41	48.24	0.41																																																																																																																																																																																																																																																					
TiO ₂	0.06	0.03	0.05	0.03	0.04	0.03	0.06	0.03	0.04	0.03	0.02	0.03	0.04	0.03	0.04	0.03	0.04	0.03	0.06	0.03	0.05	0.03	0.06	0.03	0.04	0.03	0.04	0.03	0.03	0.03	0.03	0.03	0.03	0.06	0.03	0.06	0.03	0.06	0.03	0.05	0.03	0.02	0.03	0.04	0.03																																																																																																																																																																																																																																																				
Al ₂ O ₃	31.16	0.26	31.91	0.27	32.19	0.27	32.39	0.27	31.92	0.19	32.05	0.19	31.67	0.19	31.85	0.19	30.78	0.19	31.77	0.19	31.87	0.19	32.26	0.28	32.51	0.28	32.56	0.28	31.65	0.27	32.13	0.27	32.46	0.27	32.22	0.27	31.99	0.27	32.04	0.27	31.69	0.19	31.71	0.19																																																																																																																																																																																																																																																					
Cr ₂ O ₃	0.00	0.00	0.01	0.03	0.01	0.03	0.01	0.03	0.00	0.00	0.00	0.00	0.00	0.00	0.04	0.04	0.01	0.04	0.00	0.00	0.03	0.04	0.00	0.03	0.00	0.00	0.01	0.03	0.03	0.02	0.03	0.00	0.00	0.00	0.00	0.00	0.00	0.00	0.00	0.00	0.00	0.02	0.04	0.02	0.04																																																																																																																																																																																																																																																				
FeO	0.29	0.04	0.30	0.04	0.27	0.04	0.27	0.04	0.28	0.04	0.30	0.04	0.31	0.04	0.24	0.04	0.41	0.04	0.24	0.04	0.24	0.04	0.27	0.04	0.27	0.04	0.20	0.04	0.43	0.05	0.26	0.04	0.22	0.04	0.24	0.04	0.21	0.04	0.25	0.04	0.28	0.04	0.27	0.04																																																																																																																																																																																																																																																					
MnO	0.00	0.00	0.01	0.03	0.00	0.00	0.00	0.00	0.01	0.03	0.00	0.00	0.01	0.03	0.00	0.00	0.02	0.03	0.01	0.03	0.01	0.03	0.00	0.01	0.00	0.01	0.03	0.00	0.00	0.00	0.00	0.00	0.00	0.00	0.00	0.00	0.00	0.00	0.00	0.01	0.03	0.01	0.03	0.01	0.03																																																																																																																																																																																																																																																				
MgO	0.04	0.02	0.05	0.02	0.05	0.02	0.04	0.02	0.04	0.02	0.06	0.02	0.03	0.02	0.04	0.02	0.13	0.02	0.04	0.02	0.05	0.02	0.04	0.02	0.04	0.02	0.05	0.02	0.05	0.02	0.05	0.02	0.05	0.02	0.05	0.02	0.05	0.02	0.05	0.02	0.05	0.02	0.20	0.05	0.09	0.04																																																																																																																																																																																																																																																			
CaO	15.35	0.29	16.30	0.30	16.71	0.31	16.70	0.31	15.75	0.28	15.50	0.27	15.47	0.27	15.69	0.28	16.35	0.29	15.43	0.27	15.66	0.28	16.83	0.30	16.98	0.30	17.00	0.30	15.98	0.28	16.79	0.29	16.84	0.30	16.74	0.29	16.56	0.29	16.30	0.29	15.28	0.29	15.95	0.30																																																																																																																																																																																																																																																					
Na ₂ O	3.35	0.15	2.60	0.13	2.45	0.13	2.58	0.13	2.81	0.15	3.00	0.16	2.97	0.16	2.85	0.15	2.77	0.15	2.90	0.15	2.82	0.15	2.23	0.13	2.19	0.13	2.18	0.13	2.81	0.14	2.41	0.13	2.37	0.13	2.45	0.13	2.58	0.13	2.75	0.14	2.95	0.20	2.83	0.19																																																																																																																																																																																																																																																					
K ₂ O	0.02	0.01	0.01	0.01	0.01	0.01	0.01	0.01	0.01	0.01	0.01	0.01	0.02	0.01	0.01	0.01	0.01	0.01	0.02	0.01	0.01	0.01	0.00	0.01	0.02	0.01	0.02	0.02	0.02	0.01	0.00	0.00	0.01	0.01	0.01	0.01	0.01	0.01	0.01	0.01	0.01	0.01	0.02	0.01	0.01	0.01																																																																																																																																																																																																																																																			
NiO	0.00	0.00	0.01	0.03	0.00	0.00	0.02	0.03	0.00	0.00	0.01	0.03	0.01	0.03	0.01	0.03	0.00	0.00	0.00	0.00	0.03	0.00	0.00	0.00	0.00	0.00	0.00	0.01	0.03	0.00	0.03	0.00	0.00	0.00	0.00	0.00	0.00	0.00	0.00	0.00	0.00	0.00	0.00	0.00	0.00	0.00	0.00																																																																																																																																																																																																																																																		
Total	99.78	1.07	99.37	1.05	99.20	1.04	99.75	1.05	100.09	0.44	100.61	0.44	100.37	0.44	100.23	0.45	98.98	0.45	100.36	0.44	100.35	0.45	98.94	1.04	99.40	1.04	99.28	1.04	99.61	1.06	99.16	1.04	99.57	1.04	99.18	1.04	99.47	1.05	99.76	1.05	99.03	0.58	99.17	0.58																																																																																																																																																																																																																																																					
An	71.71	1.67	71.71	1.42	77.61	1.46	79.02	1.53	75.56	1.70	74.05	1.73	74.23	1.73	75.28	1.70	76.55	1.62	74.61	1.72	75.41	1.69	80.67	1.47	81.07	1.47	81.19	1.47	75.85	1.60	79.34	1.47	79.73	1.46	79.07	1.47	78.01	1.50	76.58	1.54	74.13	2.08	75.72	2.02																																																																																																																																																																																																																																																					
Spot size	77	77	77	77	77	77	77	77	77	77	77	77	77	77	77	77	77	77	77	77	77	77	77	77	77	77	77	77	77	77	77	77	77	77	77	77	77	77	77	77	77	77	77	77	77	77																																																																																																																																																																																																																																																			
Li	<0.00	0.11	<0.00	0.12	4.18	0.21	2.69	0.16	<0.00	0.10	<0.00	0.09	<0.00	0.08	<0.00	0.08	<0.00	0.08	<0.00	0.07	<0.00	0.07	<0.00	0.07	<0.00	0.07	<0.00	0.07	<0.00	0.07	<0.00	0.07	<0.00	0.07	<0.00	0.07	<0.00	0.07	<0.00	0.07	<0.00	0.07	<0.00	0.07	<0.00	0.07	<0.00	0.07																																																																																																																																																																																																																																																	
B	4.06	0.27	7.19	0.42	7.02	0.41	6.01	0.36	5.63	0.51	5.92	0.52	5.85	0.51	4.85	0.45	8.09	1.29	11922	3550	112923	3584	113637	3605	110779	3514	113637	3600	113637	3600	113637	3599	113637	3599	113638	3602	113637	3602	113637	3602	113637	3602	113637	3602	113637	3602	113637	3602	113637	3602																																																																																																																																																																																																																																															
Ca	11922	3550	112923	3584	113637	3605	110779	3514	113637	3600	113637	3600	113637	3599	113637	3599	113637	3602	113637	3602	113637	3602	113637	3602	113637	3602	113637	3602	113637	3602	113637	3602	113637	3602	113637	3602	113637	3602	113637	3602	113637	3602	113637	3602	113637	3602	113637	3602																																																																																																																																																																																																																																																	
Sc	1.07	0.06	1.41	0.07	1.13	0.06	1.01	0.05	0.43	0.04	0.53	0.04	0.59	0.04	0.46	0.03	0.31	0.03	0.43	0.04	0.53	0.04	0.59	0.04	0.46	0.03	0.31	0.03	0.43	0.04	0.53	0.04	0.59	0.04	0.46	0.03	0.31	0.03	0.43	0.04	0.53	0.04	0.59	0.04	0.46	0.03	0.31	0.03																																																																																																																																																																																																																																																	
Ti	270	9	359	12	333	11	317	11	222	7	194	6	182	6	224	7	238	16	270	9	359	12	333	11	317	11	222	7	194	6	182	6	224	7	238	16	270	9	359	12	333	11	317	11	222	7	194	6	182	6	224	7	238	16																																																																																																																																																																																																																																											
V	1.57	0.06	2.18	0.08	1.84	0.07	1.48	0.06	2.88	0.10	3.27	0.11	3.30	0.11	2.92	0.10	2.65	0.19	1.57	0.06	2.18	0.08	1.84	0.07	1.48	0.06	2.88	0.10	3.27	0.11	3.30	0.11	2.92	0.10	2.65	0.19	1.57	0.06	2.18	0.08	1.84	0.07	1.48	0.06	2.88	0.10	3.27	0.11	3.30	0.11	2.92	0.10	2.65	0.19																																																																																																																																																																																																																																											
Cr	<0.00	0.41	6.01	0.48	5.95	0.45	<0.00	0.38	8.94	0.49	4.32	0.40	8.78	0.47	11.01	0.53	<0.00	<0.00	<0.00	0.41	6.01	0.48	5.95	0.45	<0.00	0.38	8.94	0.49	4.32	0.40	8.78	0.47	11.01	0.53	<0.00	<0.00	<0.00	0.41	6.01	0.48	5.95	0.45	<0.00	0.38	8.94	0.49	4.32	0.40	8.78	0.47	11.01	0.53	<0.00	<0.00	<0.00	0.41	6.01	0.48	5.95	0.45	<0.00	0.38	8.94	0.49	4.32	0.40	8.78	0.47	11.01	0.53	<0.00	<0.00	<0.00	0.41	6.01	0.48	5.95	0.45	<0.00	0.38	8.94	0.49	4.32	0.40	8.78	0.47	11.01	0.53	<0.00	<0.00	<0.00	0.41	6.01	0.48	5.95	0.45	<0.00	0.38	8.94	0.49	4.32	0.40	8.78	0.47	11.01	0.53	<0.00	<0.00	<0.00	0.41	6.01	0.48	5.95	0.45	<0.00	0.38	8.94	0.49	4.32	0.40	8.78	0.47	11.01	0.53	<0.00	<0.00	<0.00	0.41	6.01	0.48	5.95	0.45	<0.00	0.38	8.94	0.49	4.32	0.40	8.78	0.47	11.01	0.53	<0.00	<0.00	<0.00	0.41	6.01	0.48	5.95	0.45	<0.00	0.38	8.94	0.49	4.32	0.40	8.78	0.47	11.01	0.53	<0.00	<0.00	<0.00	0.41	6.01	0.48	5.95	0.45	<0.00	0.38	8.94	0.49	4.32	0.40	8.78	0.47	11.01	0.53	<0.00	<0.00	<0.00	0.41	6.01	0.48	5.95	0.45	<0.00	0.38	8.94	0.49	4.32	0.40	8.78	0.47	11.01	0.53	<0.00	<0.00	<0.00	0.41	6.01	0.48	5.95	0.45	<0.00	0.38	8.94	0.49	4.32	0.40	8.78	0.47	11.01	0.53	<0.00	<0.00	<0.00	0.41	6.01	0.48	5.95	0.45	<0.00	0.38	8.94	0.49	4.32	0.40	8.78	0.47	11.01	0.53	<0.00	<0.00	<0.00	0.41	6.01	0.48	5.95	0.45	<0.00	0.38	8.94	0.49	4.32	0.40	8.78	0.47	11.01	0.53	<0.00	<0.00	<0.00	0.41	6.01	0.48	5.95	0.45	<0.00	0.38	8.94	0.49	4.32	0.40	8.78	0.47	11.01	0.53	<0.00	<0.00	<0.00	0.41	6.01	0.48	5.95	0.45	<0.00	0.38	8.94	0.49	4.32	0.40	8.78	0.47	11.01	0.53	<0.00	<0.00	<0.00</

Table A2.P (continued plagioclase)

Sample	305-U1309D-247R-3W, 62-66																				305-U1309D-247R-3W, 76-81																											
Shape	interstitial										interstitial					interstitial					interstitial																											
n. grain Ol	11										5					6					10																											
Location	core					rim					core					rim					core					rim																						
Dist. (mm)	0.33 σ	0.47 σ	0.58 σ	0.67 σ	0.75 σ	0.81 σ	0.87 σ	0.97 σ	1.07 σ	1.16 σ	1.26 σ	1.36 σ	1.46 σ	1.55 σ	0.06 σ	0.16 σ	0.22 σ	0.28 σ	0.18 σ	0.25 σ	0.32 σ	0.31 σ	0.42 σ	0.41 σ	0.51 σ	0.61 σ	0.71 σ	0.81 σ	0.91 σ	1.01 σ	1.11 σ	1.21 σ																
SiO ₂	48.56	0.41	48.70	0.41	48.82	0.41	48.40	0.41	48.64	0.41	47.72	0.40	48.16	0.41	47.58	0.41	47.73	0.41	47.71	0.41	47.95	0.41	48.14	0.41	48.00	0.41	48.20	0.41	49.31	0.99	49.52	0.99	49.48	0.99	49.07	0.98	49.18	0.41	49.18	0.41	48.40	0.41	49.35	0.41	48.23	0.41		
TiO ₂	0.05	0.03	0.02	0.03	0.05	0.03	0.06	0.03	0.03	0.03	0.01	0.03	0.07	0.03	0.07	0.03	0.04	0.03	0.03	0.03	0.04	0.03	0.06	0.03	0.07	0.03	0.04	0.03	0.07	0.03	0.08	0.03	0.07	0.03	0.09	0.03	0.04	0.03	0.02	0.03	0.06	0.03	0.09	0.03	0.08	0.03		
Al ₂ O ₃	31.61	0.19	31.71	0.19	31.77	0.19	31.67	0.19	31.72	0.19	31.94	0.19	32.16	0.20	31.73	0.20	32.25	0.20	32.21	0.20	32.06	0.20	31.83	0.20	31.80	0.20	32.28	0.20	31.23	0.27	31.03	0.27	31.25	0.27	31.18	0.27	32.08	0.19	31.85	0.19	32.22	0.20	31.94	0.19	32.87	0.20		
Cr ₂ O ₃	0.01	0.04	0.00	0.00	0.02	0.04	0.02	0.04	0.00	0.00	0.00	0.00	0.00	0.00	0.00	0.00	0.00	0.00	0.00	0.00	0.00	0.00	0.00	0.00	0.00	0.00	0.00	0.03	0.03	0.00	0.00	0.00	0.00	0.01	0.03	0.02	0.03	0.00	0.00	0.02	0.04	0.00	0.00	0.00	0.00	0.00	0.00	
FeO	0.28	0.04	0.27	0.04	0.24	0.04	0.24	0.04	0.26	0.04	0.26	0.04	0.32	0.04	0.27	0.04	0.28	0.04	0.27	0.04	0.25	0.04	0.25	0.04	0.26	0.04	0.32	0.04	0.38	0.04	0.28	0.04	0.28	0.04	0.31	0.04	0.27	0.04	0.29	0.04	0.25	0.04	0.32	0.04	0.35	0.04		
MnO	0.00	0.00	0.01	0.03	0.00	0.00	0.00	0.00	0.00	0.03	0.01	0.03	0.00	0.03	0.01	0.03	0.01	0.03	0.00	0.00	0.00	0.00	0.00	0.00	0.00	0.00	0.00	0.00	0.00	0.00	0.02	0.03	0.00	0.00	0.01	0.03	0.01	0.03	0.00	0.00	0.00	0.00	0.00	0.00	0.00	0.00	0.00	0.00
MgO	0.08	0.04	0.06	0.03	0.03	0.04	0.01	0.03	0.06	0.04	0.05	0.04	0.05	0.04	0.14	0.04	0.02	0.04	0.04	0.04	0.04	0.04	0.06	0.04	0.05	0.04	0.08	0.04	0.09	0.02	0.07	0.02	0.06	0.02	0.07	0.02	0.12	0.04	0.07	0.04	0.08	0.04	0.07	0.04	0.08	0.04		
CaO	15.35	0.29	15.67	0.29	15.70	0.29	15.76	0.29	15.76	0.29	16.21	0.30	16.21	0.30	16.49	0.31	16.35	0.31	16.10	0.30	16.21	0.30	16.03	0.30	16.06	0.30	15.33	0.29	15.30	0.29	15.22	0.29	15.33	0.29	15.39	0.29	15.47	0.29	15.84	0.30	15.16	0.28	16.08	0.30				
Na ₂ O	2.86	0.19	3.06	0.20	3.08	0.20	2.97	0.20	3.04	0.20	2.84	0.19	2.69	0.19	2.54	0.18	2.41	0.18	2.54	0.18	2.75	0.19	2.64	0.19	2.62	0.19	2.89	0.20	3.05	0.15	3.15	0.15	3.15	0.15	3.07	0.15	3.07	0.20	3.02	0.20	2.81	0.19	3.25	0.21	2.54	0.18		
K ₂ O	0.02	0.01	0.02	0.01	0.01	0.01	0.01	0.01	0.01	0.01	0.01	0.01	0.02	0.01	0.02	0.01	0.02	0.01	0.01	0.01	0.01	0.01	0.01	0.01	0.01	0.00	0.00	0.01	0.01	0.03	0.01	0.04	0.01	0.03	0.01	0.03	0.01	0.04	0.01	0.03	0.01	0.02	0.01	0.03	0.01	0.03	0.01	
NiO	0.00	0.00	0.03	0.03	0.00	0.00	0.01	0.03	0.00	0.00	0.00	0.00	0.01	0.04	0.00	0.00	0.00	0.03	0.00	0.00	0.00	0.00	0.01	0.04	0.01	0.04	0.00	0.00	0.00	0.01	0.04	0.00	0.00	0.00	0.00	0.00	0.00	0.00	0.00	0.00	0.00	0.00	0.00	0.00	0.02	0.03	0.05	0.03
Total	98.82	0.57	99.54	0.58	99.71	0.58	99.16	0.58	99.53	0.58	99.07	0.58	99.69	0.59	98.58	0.58	99.26	0.58	99.17	0.58	99.20	0.58	99.20	0.58	98.84	0.58	99.88	0.59	99.51	1.08	99.50	1.08	99.53	1.08	99.18	1.07	100.21	0.58	99.93	0.58	99.71	0.59	100.25	0.58	100.29	0.57		
An	74.80	2.05	73.91	2.08	73.83	2.09	74.54	2.05	74.14	2.07	75.90	2.00	76.87	2.03	77.94	1.97	79.06	1.94	78.05	1.98	76.40	2.04	77.25	2.00	77.17	2.01	75.46	2.08	73.55	1.70	72.87	1.71	72.77	1.71	73.39	1.69	73.48	2.11	73.89	2.10	75.69	2.07	72.04	2.15	77.79	1.98		
Spot size																77						77	77						77																			
Li																<0.00	0.09						<0.00	0.08	<0.00	0.07	<0.00	0.07	<0.00	0.07	<0.00	0.06																
B																8.52	0.79						7.36	0.71	7.11	0.58	8.43	0.68	7.79	0.64																		
Ca																113637	3601						113637	3599	109992	3487	110564	3505	113209	3589																		
Sc																0.41	0.04						0.48	0.04	0.96	0.05	0.88	0.05	0.89	0.05																		
Ti																529	46						545	49	422	14	366	12	433	15																		
V																2.79	0.10						3.32	0.12	3.72	0.13	3.81	0.13	3.19	0.11																		
Cr																9.98	0.80						5.21	0.54	6.99	0.41	7.29	0.42	9.48	0.48																		
Mn																24.32	0.84						16.21	0.56	47.78	1.96	11.29	0.48	10.83	0.48																		
Co																0.52	0.03						0.45	0.03	0.81	0.04	0.43	0.03	0.35	0.03																		
Ni																<0.00	1.69						<0.00	1.59	5.71	0.99	<0.00	0.93	<0.00	0.90																		
Cu																<0.00	0.08						<0.00	0.07	0.44	0.05	0.39	0.05	0.32	0.05																		
Zn																4.65	0.20						2.04	0.11	8.40	0.33	2.77	0.14	2.67	0.13																		
Rb																0.22	0.02						0.18	0.01	0.13	0.01	0.10	0.01	0.09	0.01																		
Sr																165	5						172	5	159	5	160	5	157	5																		
Y																0.22	0.01						0.23	0.01	0.37	0.01	0.35	0.01	0.32	0.01																		
Zr																0.036	0.009						0.023	0.008	0.024	0.005	0.040	0.005	<0.00	0.004																		
Nb																<0.00	0.002						<0.00	0.002	0.004	0.002	<0.00	0.001	0.003	0.001																		
Sb																0.024	0.008						<0.00	0.007																								
Ba																4.40	0.19						4.40	0.19	3.50	0.15	3.07	0.14	3.09	0.14																		
La																0.523	0.023						0.554	0.024	0.444	0.020	0.416	0.019	0.450	0.021																		
Ce																1.140	0.042						1.124	0.040	1.028	0.036	0.983	0.035	0.995	0.036																		
Pr																0.137	0.008						0.146	0.008	0.135	0.007	0.141	0.007	0.143	0.007																		
Nd																0.557	0.034						0.692	0.037	0.678	0.037	0.633	0.036	0.612	0.036																		
Sm																0.097	0.013						0.128	0.014	0.083	0.013	0.153	0.017	0.162	0.018																		
Eu																0.415	0.021						0.393	0.019	0.424	0.020	0.396	0.019	0.452	0.021																		
Gd																0.083	0.013						0.090	0.012	0.109	0.015	0.152	0.017	0.122	0.016																		
Tb																0.012	0.002						0.011	0.002	0.013	0.002	0.013	0.002	0.011	0.002																		
Dy																0.053	0.006						0.066	0.006	0.055	0.008	0.065	0.009	0.065	0.009																		
Ho																0.009	0.001						0.011	0.001	0.014	0.002	0.015	0.002	0.009	0.002																		
Er																0.026	0.004						0.011	0.002	0.042	0.007	0.026	0.005	0.028	0.006																		
Tm																<0.00	0.001						0.003	0.001	<0.00	0.001	0.003	0.001	0.005	0.001																		
Yb																0.019	0.005						<0.00	0.004	<0.00	0.004	<0.00	0.003	<0.00	0.004																		
Lu																0.003	0.001						<0.00	0.001	<0.00	0.001	<0.00	0.001	<0.00	0.000																		
Hf																<0.00	0.002						0.010	0.003	<0.00	0.000	0.012	0.004	0.031	0.008																		
Ta																<0.00	0.002						<0.00	0.002	<0.00	0.002	<0.00	0.002	<0.00	0.001																		
Pb																0.122	0.009						0.077	0.007	0.128	0.010	0.098	0.009	0.172	0.012																		
Th																0.002	0.001						<0.00	0.000	0.003	0.001	<0.00	<0.00	<0.00	0.000																		

Table A2.P (continued clinopyroxene)

Sample Shape n. grain OI Location	305-U1309D-247R-3W, 16-18																	305-U1309D-247R-3W, 22-25																													
	interstitial 1					interstitial 1					interstitial 13					interstitial 5					interstitial 2																										
Dist. (mm)	rim			core		rim			core		rim			core		rim			rim			core		core		core		core																			
SiO ₂	52.07	0.24	52.59	0.24	52.91	0.24	51.58	0.25	51.94	0.25	51.53	0.25	52.04	0.24	51.58	1.03	51.27	1.02	51.40	1.03	51.72	1.03	51.62	1.03	52.09	1.04	51.60	1.03	51.42	0.43	50.85	0.42	50.73	0.42	51.18	0.43	50.95	0.42	51.15	0.43	50.93	0.42					
TiO ₂	0.67	0.05	0.60	0.05	0.47	0.04	0.46	0.04	0.40	0.04	0.39	0.04	0.37	0.04	0.46	0.04	0.50	0.04	0.43	0.04	0.40	0.04	0.37	0.04	0.38	0.04	0.41	0.04	0.41	0.04	0.42	0.04	0.39	0.04	0.42	0.04	0.43	0.04	0.41	0.04	0.40	0.04	0.37	0.04			
Al ₂ O ₃	3.44	0.06	3.38	0.06	2.60	0.06	3.73	0.07	3.67	0.07	3.55	0.07	3.64	0.07	3.56	0.06	3.29	0.06	3.69	0.07	3.59	0.06	3.57	0.06	3.53	0.06	3.46	0.06	3.71	0.07	3.97	0.07	3.74	0.07	3.73	0.07	3.64	0.07	3.71	0.07	3.71	0.07	3.71	0.07			
Cr ₂ O ₃	1.27	0.07	1.29	0.07	0.57	0.05	1.35	0.07	1.29	0.07	1.27	0.07	1.42	0.07	1.29	0.07	1.21	0.07	1.36	0.07	1.31	0.06	1.30	0.06	1.28	0.06	1.21	0.06	1.33	0.06	1.36	0.07	1.48	0.07	1.41	0.07	1.32	0.07	1.47	0.07	1.39	0.07	1.39	0.07			
FeO	5.21	0.13	5.40	0.13	3.50	0.11	4.23	0.12	4.64	0.12	4.39	0.12	4.47	0.12	4.20	0.11	4.53	0.13	4.36	0.12	4.44	0.12	5.25	0.13	5.00	0.13	5.43	0.13	4.91	0.12	5.43	0.13	4.52	0.12	4.24	0.12	4.28	0.12	4.42	0.12	4.52	0.12	4.45	0.12			
MnO	0.16	0.04	0.16	0.03	0.14	0.03	0.14	0.04	0.12	0.04	0.14	0.04	0.16	0.04	0.14	0.04	0.18	0.04	0.12	0.04	0.12	0.04	0.13	0.03	0.15	0.04	0.16	0.04	0.11	0.04	0.17	0.04	0.13	0.03	0.11	0.03	0.11	0.03	0.12	0.03	0.16	0.03	0.10	0.03	0.14	0.03	
MgO	17.59	0.19	18.00	0.19	16.82	0.18	15.96	0.18	16.69	0.19	16.32	0.19	16.82	0.19	16.42	0.18	17.03	0.19	16.24	0.18	16.56	0.18	18.27	0.20	17.48	0.19	19.17	0.20	17.71	0.19	18.31	0.44	16.63	0.41	16.13	0.40	16.09	0.40	16.76	0.41	17.19	0.42	16.61	0.41			
CaO	19.15	0.34	18.29	0.32	21.96	0.39	21.59	0.16	19.82	0.15	21.24	0.16	20.83	0.16	21.16	0.15	21.02	0.37	21.86	0.38	21.86	0.38	19.71	0.35	19.97	0.35	18.91	0.33	20.49	0.36	18.94	0.35	21.14	0.39	22.17	0.40	22.27	0.41	21.23	0.39	20.85	0.38	21.26	0.39			
Na ₂ O	0.38	0.07	0.39	0.07	0.51	0.07	0.44	0.06	0.44	0.07	0.42	0.07	0.39	0.06	0.41	0.06	0.41	0.06	0.42	0.06	0.39	0.06	0.38	0.06	0.36	0.06	0.29	0.05	0.33	0.06	0.33	0.07	0.32	0.07	0.35	0.07	0.35	0.07	0.34	0.06	0.37	0.07	0.35	0.07			
K ₂ O	0.01	0.01	0.00	0.00	0.01	0.01	0.00	0.00	0.00	0.00	0.00	0.00	0.00	0.00	0.00	0.01	0.01	0.01	0.01	0.00	0.01	0.00	0.00	0.00	0.00	0.00	0.01	0.01	0.00	0.00	0.00	0.01	0.00	0.01	0.00	0.01	0.00	0.01	0.00	0.00	0.00	0.00	0.01	0.00	0.00		
NiO	0.02	0.03	0.05	0.04	0.04	0.03	0.03	0.04	0.04	0.04	0.02	0.04	0.05	0.04	0.04	0.04	0.03	0.04	0.07	0.04	0.07	0.04	0.05	0.04	0.04	0.05	0.04	0.06	0.04	0.04	0.04	0.06	0.04	0.08	0.04	0.04	0.04	0.05	0.04	0.05	0.04	0.05	0.04	0.03	0.04		
Total	99.95	0.49	100.15	0.48	99.53	0.52	99.04	0.39	99.05	0.39	99.26	0.39	99.70	0.39	99.73	0.38	99.91	1.13	99.95	1.12	100.18	1.12	100.79	1.12	99.81	1.12	101.03	1.12	100.41	1.12	100.11	0.73	99.51	0.73	99.80	0.73	99.43	0.73	99.73	0.73	99.24	0.73	99.73	0.73	99.24	0.73	
Mg#	85.76	1.01	85.58	1.01	89.54	0.94	87.07	1.06	86.51	1.05	86.90	1.05	87.02	1.04	87.46	1.00	87.01	1.05	86.92	1.07	86.92	1.02	86.12	0.99	86.17	1.01	86.29	0.97	86.53	1.00	85.74	1.13	86.76	1.13	87.15	1.13	87.01	1.14	87.12	1.12	87.16	1.11	86.93	1.13			
Spot size		77			77			77			77			77			77			77			77			77			77			77			77			77			77			77			77
Li	4.69	0.21					2.92	0.17	2.86	0.16			2.75	0.16			3.02	0.38	2.79	0.35	2.52	0.32	2.33	0.30			2.40	0.14			3.24	0.18			3.12	0.18			3.08	0.18			3.08	0.18			
B	5.13	0.37					17.24	1.23	16.82	1.20			16.88	1.20			9.74	0.96	9.59	0.98	8.49	0.91	8.15	0.90			8.35	0.55			9.75	0.65			9.32	0.63			10.22	0.71			10.22	0.71			
Ca	156877	4970					154375	4884	150087	4748			148872	4710			156234	4943	140868	4457	142726	4516	135150	4276			135364	4284			158521	5015			151731	4801			151945	4808			151945	4808			
Sc	123.7	4.1					114.3	3.8	106.0	3.5			106.8	3.5			118.2	4.7	104.0	4.3	105.4	4.4	102.9	4.4			89.1	3.0			102.1	3.5			100.4	3.4			98.9	3.4			98.9	3.4			
Ti	4549	243					2949	97	2322	76			2406	79			2906	102	2468	87	2491	89	2647	95			2284	81			2515	90			2438	88			2402	88			2402	88			
V	375	12					386	13	316	10			326	11			373	12	326	11	330	11	332	11			310	10			360	12			364	12			349	12			349	12			
Cr	8367	465															7073	852	6199	786	6234	832	5647	793			7446	245			8884	293			8741	288			8562	283			8562	283			
Mn	1503	50					1138	41	1036	37			1060	38			1247	70	1129	66	1182	73	1099	71			951	35			1038	38			1049	39			1057	40			1057	40			
Co	33.56	1.07					32.99	1.15	32.18	1.12			32.18	1.12			32.81	1.56	31.81	1.56	32.63	1.65	28.03	1.47			27.23	0.96			33.74	1.20			32.88	1.18			32.26	1.18			32.26	1.18			
Ni	287	11					366	34	365	34			365	34			386	50	364	50	382	56	333	52			291	14			364	18			353	18			349	19			349	19			
Cu	0.86	0.06					0.05	0.02	0.02	0.02			0.29	0.02			0.02	0.02	0.08	0.02	0.02	0.06	0.02			1.44	0.06			2.64	0.11			1.36	0.06			1.15	0.01			1.15	0.01				
Zn	25.81	0.93					19.24	0.90	18.35	0.86			17.87	0.84			19.86	1.73	18.90	1.74	20.08	1.96	18.31	1.89			19.95	0.80			22.89	0.93			22.21	0.92			20.59	0.88			20.59	0.88			
Rb		0.01						0.00	0.00	0.00				0.00				0.00	0.00	0.00	0.00	0.03	0.00				0.03	0.00			0.01	0.00			0.02	0.00			0.01	0.00			0.01	0.00			
Sr	8.18	0.27					7.58	0.25	6.84	0.22			7.00	0.23			7.34	0.23	6.30	0.20	6.70	0.21	7.19	0.23			6.74	0.23			8.01	0.27			7.84	0.27			7.64	0.26			7.64	0.26			
Y	29.36	0.97					17.32	0.57	13.07	0.43			13.77	0.45			17.23	0.55	14.28	0.45	14.98	0.48	15.30	0.49			17.86	0.42			16.81	0.40			16.67	0.40			16.44	0.40			16.44	0.40			
Zr	36.92	1.25					10.04	0.34	5.76	0.20			6.50	0.22			7.95	0.32	5.28	0.22	5.91	0.25	7.64	0.33			13.54	0.31			7.58	0.18			7.68	0.18			7.37	0.17			7.37	0.17			
Nb	0.23	0.01					0.12	0.01	0.07	0.00			0.06	0.00			0.11	0.01	0.06	0.00	0.07	0.00	0.09	0.01			0.14	0.01			0.03	0.00			0.04	0.00			0.07	0.00			0.07	0.00			
Sb		0.00						0.00	0.00	0.00				0.00				0.00	0.00	0.00	0.00	0.00	0.00	0.00				0.00																			
Ba	0.18	0.03						0.01	0.01	0.01			0.03	0.01				0.01	0.00	0.02	0.01	0.10	0.01				0.12	0.01			0.07	0.01			0.08	0.01			0.08	0.01			0.08	0.01			
La	0.242	0.013					0.178	0.007	0.114	0.005			0.107	0.005			0.153	0.007	0.096	0.005	0.107	0.005	0.124	0.006			0.128	0.005			0.097	0.004			0.093	0.004			0.081	0.004			0.081	0.004			
Ce	1.590	0.059					0.929	0.031	0.613	0.021			0.624	0.021			0.798	0.035	0.539	0.025	0.6																										

Table A2.P (continued clinopyroxene)

Sample Shape n. grain OI Location	305-U1309D-247R-3W, 62-66													305-U1309D-247R-3W, 76-81																																
	interstitial				interstitial				interstitial				interstitial				interstitial																													
	rim	rim	core	core	rim	rim	core	core	rim	rim	core	core	wedge	rim	rim	core	core	rim	rim	core	core	core																								
Dist. (mm)	0.73	0.81	0.88	0.13	0.19	0.25	0.29	0.38	0.13	0.41	-0.06	-0.12	-0.24	-0.60	-0.19	-0.27	-0.48	-0.66	0.05	0.22	0.35	0.98																								
SiO ₂	50.94	0.42	50.82	0.42	51.35	0.43	51.53	0.43	51.64	0.43	51.15	0.04	50.77	0.42	56.18	1.12	51.66	1.12	51.66	1.03	51.54	1.03	52.09	1.04	51.41	1.03	49.56	0.99	51.89	1.03	51.35	1.02	51.57	1.03	51.63	1.03	51.34	0.43	51.21	0.43	51.32	0.43	51.23	0.43	51.23	0.43
TiO ₂	0.42	0.04	0.40	0.04	0.44	0.04	0.51	0.04	0.54	0.05	0.51	0.04	0.55	0.05	0.57	0.05	0.09	0.03	0.68	0.04	0.79	0.05	0.42	0.04	0.40	0.04	0.88	0.05	0.34	0.04	0.36	0.04	0.35	0.04	0.32	0.04	0.45	0.05	0.42	0.04	0.38	0.04	0.40	0.04	0.40	0.04
Al ₂ O ₃	3.73	0.07	3.69	0.07	3.66	0.07	3.43	0.06	3.58	0.06	3.52	0.06	3.60	0.06	3.43	0.06	1.50	0.04	5.69	0.08	3.29	0.06	3.43	0.06	3.70	0.07	3.02	0.06	3.50	0.06	3.51	0.06	3.71	0.06	3.53	0.06	3.71	0.07	3.83	0.07	3.81	0.07	3.70	0.07		
Cr ₂ O ₃	1.45	0.07	1.44	0.07	1.37	0.07	1.22	0.07	1.25	0.07	1.29	0.07	1.29	0.07	1.16	0.07	0.04	0.03	0.79	0.05	1.07	0.06	1.05	0.06	1.18	0.06	1.11	0.06	1.27	0.06	1.24	0.06	1.24	0.06	1.13	0.06	1.37	0.07	1.49	0.08	1.43	0.07	1.44	0.07		
FeO	4.34	0.12	4.36	0.12	4.35	0.12	4.35	0.12	4.11	0.12	4.49	0.12	4.50	0.12	3.94	0.11	4.63	0.12	4.58	0.12	4.92	0.12	5.95	0.14	4.97	0.13	4.89	0.13	4.75	0.12	4.62	0.12	4.32	0.12	4.35	0.12	4.24	0.12	4.56	0.13	5.10	0.14	4.72	0.13		
MnO	0.13	0.03	0.13	0.03	0.13	0.03	0.15	0.03	0.14	0.04	0.14	0.04	0.15	0.04	0.14	0.03	0.17	0.04	0.10	0.03	0.13	0.04	0.17	0.04	0.14	0.04	0.17	0.04	0.15	0.03	0.15	0.04	0.13	0.03	0.13	0.03	0.16	0.04	0.17	0.04	0.16	0.04	0.16	0.04		
MgO	16.10	0.40	16.48	0.41	16.76	0.41	17.54	0.42	16.50	0.41	16.29	0.40	16.53	0.41	17.05	0.42	21.82	0.22	20.10	0.21	16.67	0.18	18.82	0.20	16.60	0.19	16.19	0.19	16.77	0.18	16.14	0.18	15.85	0.18	15.96	0.18	16.68	0.42	16.19	0.41	17.46	0.43	16.27	0.41		
CaO	21.98	0.40	21.83	0.40	21.49	0.39	19.77	0.36	21.53	0.39	20.75	0.38	21.80	0.40	21.31	0.39	12.51	0.24	12.28	0.23	20.60	0.38	17.62	0.33	20.26	0.37	19.76	0.36	21.45	0.39	21.97	0.40	22.20	0.41	22.22	0.41	21.38	0.39	21.31	0.39	20.00	0.37	20.99	0.39		
Na ₂ O	0.39	0.07	0.40	0.07	0.41	0.07	0.39	0.07	0.42	0.07	0.42	0.07	0.43	0.07	0.45	0.07	0.65	0.07	1.42	0.10	0.37	0.06	0.33	0.06	0.36	0.06	1.87	0.12	0.39	0.06	0.40	0.06	0.41	0.06	0.38	0.06	0.37	0.07	0.41	0.08	0.33	0.07	0.41	0.08		
K ₂ O	0.00	0.00	0.00	0.00	0.00	0.00	0.00	0.00	0.00	0.01	0.00	0.00	0.00	0.00	0.00	0.01	0.01	0.03	0.01	0.01	0.00	0.01	0.00	0.00	0.00	0.00	0.00	0.33	0.02	0.00	0.01	0.00	0.01	0.00	0.00	0.00	0.00	0.00	0.00	0.00	0.00	0.00	0.00	0.00		
NiO	0.04	0.04	0.04	0.04	0.07	0.04	0.04	0.04	0.03	0.04	0.03	0.04	0.04	0.04	0.03	0.04	0.05	0.04	0.11	0.04	0.03	0.04	0.06	0.04	0.01	0.04	0.04	0.08	0.04	0.04	0.04	0.03	0.04	0.06	0.04	0.04	0.04	0.03	0.04	0.06	0.04	0.04	0.04	0.04	0.05	0.04
Total	99.52	0.73	99.58	0.73	100.02	0.73	99.65	0.73	99.73	0.73	98.59	0.72	99.66	0.73	98.89	0.73	97.65	1.18	97.44	1.10	99.42	1.12	99.93	1.12	99.05	1.12	97.76	1.09	100.54	1.14	99.77	1.13	99.83	1.13	99.70	1.13	99.72	0.74	99.65	0.74	100.05	0.74	99.37	0.74		
Mg#	86.86	1.15	87.06	1.12	87.29	1.12	86.04	1.13	87.73	1.11	86.61	1.14	86.74	1.14	88.52	1.05	89.37	0.84	88.67	0.88	85.79	1.03	84.93	1.00	85.61	1.08	85.52	1.08	86.29	1.03	86.17	1.04	86.72	1.04	86.74	1.03	87.53	1.15	86.34	1.21	85.91	1.19	86.00	1.21		
Spot size		77		77		77		77		77		77		77		77		77		77		77		77		77		77		77		77		77		77		77		77		77		77		
Li			3.00	0.18	2.28	0.15	2.44	0.17			2.70	0.19	2.72	0.20			2.68	0.15			2.70	0.16	2.14	0.13	2.27	0.13			2.10	0.12	1.94	0.12			2.77	0.17	1.99	0.12	1.89	0.12	1.60	0.10				
B			8.69	0.62	7.85	0.63	9.15	0.75			7.99	0.68	8.49	0.75			15.87	4.72	15.98	5.18	11.69	0.66			12.20	0.70	7.67	0.72			12.20	0.70	7.67	0.72			7.84	0.76	7.99	0.79						
Ca			153589	4860	141296	4471	153875	4869			155805	4930	152303	4820			150087	4749	150087	4749	150087	4749			150087	4749	150087	4836			150087	4749	152803	4836			152374	4822	142940	4524						
Sc			100.6	3.4	96.2	3.4	100.7	3.6			102.1	3.6	104.8	3.8			110.0	4.3			104.9	4.2	116.0	4.7	100.4	3.3			98.1	3.2	116.2	4.0			109.4	3.8	101.7	3.5								
Ti			2517	94	3481	138	3123	126			3204	132	3472	146			3693	863			2738	679	5165	1355	1940	63			1965	64	2900	95			2504	82	2302	75								
V			360	12	382	13	366	13			394	14	372	13			383	15			336	13	430	17	302	10			305	10	372	12			323	11	303	10								
Cr			8748	290	7375	247	7621	257			7572	256	7665	260			6562	1196			7101	1358	6504	1303	7266	240			6597	218	8601	437			8852	463	8164	440								
Mn			1128	44	1149	49	1191	52			1088	48	1200	55			1210	50			1175	49	1255	54	1102	36			1068	35	1251	49			1278	50	1181	47								
Co			31.91	1.18	29.40	1.18	30.79	1.26			28.54	1.20	33.14	1.43			33.37	1.76			33.06	1.81	31.17	1.77	28.35	0.91			30.70	0.99	30.66	1.21			32.55	1.31	30.09	1.23								
Ni			344	19	316	21	340	24			336	25	417	33			331	25			330	27	309	26	351	12			377	13	330	14			342	15	317	14								
Cu			0.43	0.02	0.11	0.01	0.12	0.01			0.23	0.02	0.54	0.03			0.11	0.03			5.62	0.36	1.15	0.08	0.37	0.04			0.18	0.03	1.08	0.05			0.10	0.02	0.28	0.02								
Zn			22.18	0.97	20.07	0.98	20.83	1.05			20.14	1.05	20.54	1.11			21.63	2.09			26.17	2.65	23.04	2.44	20.45	0.71			19.05	0.66	20.09	0.74			23.42	0.86	21.31	0.79								
Rb			0.02	0.00	0.02	0.00	0.02	0.00			0.02	0.00	0.02	0.00			0.00				0.11	0.01	0.07	0.01	0.02	0.01			0.00	0.01	0.00			0.01	0.00	0.01	0.00									
Sr			7.83	0.27	7.12	0.26	7.43	0.28			7.77	0.30	7.43	0.29			7.36	0.31			8.25	0.35	7.33	0.32	7.80	0.24			7.67	0.24	7.32	0.23			7.23	0.23	6.75	0.21								
Y			19.14	0.46	26.79	0.67	23.31	0.59			24.78	0.63	28.74	0.74			20.76	0.84			13.83	0.57	26.78	1.13	12.49	0.39			10.07	0.32	23.54	0.59			18.23	0.46	17.95	0.45								
Zr			12.21	0.29	30.91	0.74	17.49	0.42			19.88	0.49	31.39	0.77			16.83	0.61			6.97	0.26	28.80	1.07	5.74	0.18			4.00	0.13	12.95	0.31														

Appendix 3

Appendix 3 reports whole rock geochemical data of olivine-gabbro, olivine-bearing gabbro and disseminated-oxide gabbro from IODP Hole U1473A (Atlantis Bank).

Table A3.1 Whole rock composits of gabbroic samples from Atlantis Bank

Laboratory : Geosciences Montpellier

Expedition	360-U1473A	360-U1473A	360-U1473A	360-U1473A	360-U1473A	360-U1473A	360-U1473A	360-U1473A	360-U1473A	360-U1473A	360-U1473A	360-U1473A	360-U1473A	360-U1473A	360-U1473A	360-U1473A	360-U1473A		
Core section	3R-2	4R-1	4R-2	6R-2	8R-2	11R-2	18R-2	27R-1	28R-2	28R-3	29R-1	34R-1	37R-4	39R-3	43R-7	44R-4	45M-1		
Interval (cm)	55-62	34-41	45-52	33-40	59-66	75-82	98-105	33-40	55-62	247.29	247.29	248.76	36-43	86-93	140-147	43-50	102-109		
Depth CCSF (mbsf)	14.70	22.74	24.35	43.43	62.94	92.34	160.32	235.93	247.29	247.29	248.76	255.36	304.36	338.4	355.01	399.11	406.27		
Lithological Interval	4	7	8	15	24	43	99	121	125	125	125	156	169	169	201	203	204		
Lithological Unit	I	I	I	I	I	II	II	IV	IV	IV	IV	V	V	V	V	V	V		
Internal Standard (I.S.)																	I.S.		
Rock name	olivine gabbro	olivine-bearing gabbro	olivine gabbro	olivine gabbro	olivine gabbro	oxide-bearing olivine gabbro	olivine gabbro	olivine gabbro	olivine gabbro	olivine gabbro	olivine gabbro	olivine gabbro	olivine gabbro	olivine gabbro	olivine gabbro	olivine gabbro	olivine gabbro		
Alteration (%)	<5	<5	<5	15	<5	<5	<5	<5	15	10	<5	15	18	<5	<5	15	10		
Duplicate																	(1)	(2)	
Conc.	2.573	1.557	1.168	3.476	1.435	1.711	1.731	1.990	2.675	2.321	1.691	2.425	3.763	2.390	1.915	2.869	2.366	2.966	
σ	0.030	0.018	0.024	0.051	0.018	0.008	0.009	0.031	0.037	0.037	0.015	0.019	0.025	0.019	0.003	0.033	0.047	0.029	
Li	Conc.	43.13	27.52	56.02	42.00	32.90	41.66	42.97	37.24	43.42	39.28	43.89	40.44	44.95	42.59	47.23	52.74	39.97	38.49
σ	0.53	0.21	0.72	0.49	0.50	0.12	0.44	0.19	0.08	0.46	0.13	0.57	0.47	0.23	0.43	0.42	0.49	0.36	
Sc	Conc.	1819	1269	3715	1852	3788	5635	3390	2583	3063	2429	2646	2326	3602	2803	5084	3067	2445	2412
σ	7	3	35	13	21	20	20	12	139	36	14	7	44	5	47	43	15	35	
Ti	Conc.	167.6	103.5	277.6	160.2	171.5	252.5	218.8	181.6	177.6	181.5	175.0	208.7	190.0	220.4	243.1	179.0	179.0	176.6
σ	0.7	0.7	3.1	0.5	1.3	1.2	1.6	3.2	1.6	2.4	2.5	1.2	3.0	0.2	0.9	4.5	0.7	2.5	
V	Conc.	761.2	571.1	1189.8	786.5	992.5	1216.2	1240.0	940.0	1029.2	756.4	855.5	844.3	1123.5	957.8	1182.0	981.9	975.2	994.8
σ	3.6	5.2	8.5	2.9	15.8	10.5	10.4	8.2	5.6	12.7	9.5	1.6	9.9	3.4	6.3	9.2	7.8	15.8	
Mn	Conc.	32.9	26.3	33.3	37.4	34.1	40.0	46.0	37.9	44.3	27.5	30.2	37.0	36.8	36.9	40.2	29.9	40.1	41.3
σ	0.1	0.2	0.2	0.2	0.4	0.4	0.5	0.2	0.3	0.4	0.4	0.1	0.3	0.1	0.2	0.3	0.2	0.4	
Co	Conc.	142.3	119.1	38.3	326.0	46.8	91.9	63.8	109.5	138.6	75.9	88.9	143.4	59.5	87.2	76.4	54.7	84.0	85.1
σ	0.6	1.0	0.3	2.8	0.1	0.9	1.2	0.9	1.4	1.1	1.0	1.0	0.7	0.2	0.7	0.6	0.7	1.0	
Ni	Conc.	43.20	35.07	31.83	126.30	21.05	85.41	78.73	82.92	71.96	30.05	58.70	102.19	86.99	65.69	65.88	54.68	91.85	89.04
σ	0.19	0.28	0.14	0.86	0.25	0.52	0.88	0.50	0.42	0.52	0.58	0.47	1.01	0.12	0.10	0.50	0.80	1.07	
Cu	Conc.	28.25	21.14	40.22	34.68	33.63	56.20	55.76	42.97	47.34	26.60	34.59	34.92	47.24	36.43	54.17	32.29	38.73	37.96
σ	0.11	1.95	0.23	1.95	0.40	2.08	0.64	2.10	0.26	1.97	0.40	1.97	2.11	1.95	0.33	2.08	0.24	1.96	
Zn	Conc.	10.52	12.59	15.53	8.88	17.60	14.54	15.14	12.72	12.69	13.37	13.39	11.46	14.76	12.70	14.67	12.92	13.32	13.21
σ	0.05	0.10	0.11	0.19	0.20	0.26	0.25	0.17	0.25	0.43	0.07	0.04	0.16	0.20	0.21	0.14	0.08	0.32	
Ga	Conc.	0.0808	0.0867	0.1026	0.1668	0.1107	0.0821	0.2340	0.1490	0.1757	0.1955	0.1755	0.1045	0.7420	0.2922	0.1226	0.0946	0.1691	0.1625
σ	0.0041	0.0069	0.0014	0.0067	0.0013	0.0068	0.0014	0.0066	0.0040	0.0079	0.0036	0.0068	0.0146	0.0067	0.0044	0.0073	0.0010	0.0066	
Rb	Conc.	130.19	168.91	166.20	114.35	191.25	143.07	155.49	153.21	135.73	161.04	158.24	137.44	158.43	149.53	153.30	149.75	164.05	162.46
σ	0.66	1.20	0.59	0.76	0.42	1.18	1.24	1.60	1.35	2.99	1.48	0.35	2.40	1.42	1.28	2.23	2.13	2.43	
Sr	Conc.	8.69	6.06	16.64	8.79	15.57	17.90	14.36	15.28	19.67	15.37	15.60	10.57	18.54	14.65	20.77	14.76	11.34	11.57
σ	0.07	0.03	0.14	0.08	0.21	0.04	0.08	0.08	0.08	0.08	0.02	0.07	0.19	0.03	0.30	0.11	0.08	0.06	
Y	Conc.	11.73	6.19	19.11	9.37	32.43	24.78	23.40	33.20	45.05	25.30	30.96	15.30	21.45	31.63	30.78	16.75	17.08	14.18
σ	0.09	0.06	0.20	0.08	0.32	0.06	0.15	0.04	0.28	0.13	0.26	0.10	0.17	0.09	0.21	0.09	0.08	0.08	
Zr	Conc.	0.089	0.076	0.126	0.176	0.629	0.326	0.271	0.374	0.504	0.857	0.323	0.154	0.356	0.384	0.361	0.127	0.165	0.149
σ	0.001	0.002	0.002	0.004	0.005	0.007	0.003	0.004	0.005	0.005	0.005	0.004	0.004	0.005	0.005	0.001	0.001	0.002	
Nb	Conc.	0.189	1.091	0.569	0.427	0.452	0.371	0.266	0.458	0.520	0.622	1.439	0.217	0.710	0.519	0.336	0.208	0.227	0.218
σ	0.007	0.020	0.012	0.007	0.017	0.003	0.017	0.003	0.020	0.011	0.052	0.003	0.019	0.017	0.007	0.008	0.004	0.006	
Sb	Conc.	0.057	n.d.	0.013	0.006	0.022	0.003	0.009	0.002	0.005	0.004	0.005	0.003	0.005	0.005	b.d.l.	0.004	0.004	0.003
σ	0.002	n.d.	0.002	0.000	0.003	0.000	0.002	0.000	0.002	0.002	0.002	0.002	0.002	0.001	0.002	0.000	0.000	0.001	
Cs	Conc.	0.001	0.001	0.001	0.002	0.002	0.000	0.004	0.010	0.007	0.003	0.006	0.004	0.021	0.004	0.005	0.009	0.006	0.006
σ	0.000	0.000	0.000	0.000	0.000	0.000	0.000	0.000	0.001	0.001	0.000	0.000	0.000	0.000	0.000	0.000	0.000	0.000	
Ba	Conc.	2.678	1.879	2.586	1.688	3.702	3.500	2.976	3.166	2.826	3.715	2.919	1.996	4.459	2.441	3.269	2.447	2.739	2.697
σ	0.041	0.029	0.062	0.022	0.306	0.023	0.090	0.057	0.039	0.022	0.031	0.075	0.032	0.033	0.020	0.027	0.045	0.061	
La	Conc.	0.4635	0.3714	0.6258	0.6212	1.6172	0.9000	0.8654	1.4559	1.7437	1.5037	1.2493	0.5997	1.1250	1.1980	1.0747	0.6156	0.6989	0.6980
σ	0.0070	0.0023	0.0059	0.0054	0.0077	0.0036	0.0036	0.0116	0.0149	0.0106	0.0069	0.0077	0.0070	0.0047	0.0037	0.0057	0.0032	0.0065	
Ce	Conc.	1.4565	1.0990	2.0845	1.6816	4.6072	2.9489	2.6692	4.3284	5.3222	4.5244	3.7666	1.8914	3.4597	3.6780	3.4818	2.0547	2.1608	2.1217
σ	0.0106	0.0045	0.0163	0.0155	0.0525	0.0205	0.0141	0.0112	0.0560	0.0260	0.0106	0.0106	0.0248	0.0018	0.0172	0.0198	0.0170	0.0224	
Pr	Conc.	0.2862	0.2066	0.4338	0.2934	0.7850	0.5871	0.5022	0.7483	0.9569	0.7533	0.6822	0.3660	0.6413	0.6520	0.6980	0.4210	0.4090	0.3973
σ	0.0006	0.0010	0.0066	0.0030	0.0095	0.0022	0.0093	0.0035	0.0098	0.0035	0.0031	0.0025	0.0083	0.0095	0.0017	0.0040	0.0032	0.0063	
Nd	Conc.	1.7473	1.2544	2.7951	1.7678	4.2372	3.6743	2.9737	4.1337	5.3252	3.9279	3.8443	2.2546	3.8418	3.6684	4.3151	2.6884	2.4131	2.3707
σ	0.0100	0.0066	0.0292	0.0231	0.0394	0.0060	0.0121	0.0159	0.0524	0.0292	0.0407	0.0231	0.0480	0.0205	0.0302	0.0266	0.0115	0.0430	
Sm	Conc.	0.7485	0.5203	1.2504	0.7308	1.4533	1.5263	1.1919	1.4623	1.9082	1.3412	1.4273	0.9168	1.5472	1.3194	1.7708	1.1623	0.9893	0.9440
σ	0.0047	0.0087	0.0173	0.0145	0.0239	0.0040	0.0232	0.0112	0.0222	0.0099	0.0076	0.0218	0.0121	0.0289	0.0047	0.0090	0.0086	0.0164	
Eu	Conc.	0.4295	0.4524	0.7337	0.4496	0.8297	0.9338	0.7231	0.7218	0.7393	0.6030	0.7104	0.5325	0.9021	0.6056	0.9417	0.6525	0.5693	0.5603
σ	0.0037	0.00																	

Table A3.1 (continued)

Laboratory : Geosciences Montpellier

Expedition	360-U1473A	360-U1473A	360-U1473A	360-U1473A	360-U1473A	360-U1473A	360-U1473A	360-U1473A	360-U1473A	360-U1473A	360-U1473A	360-U1473A	360-U1473A	360-U1473A	360-U1473A	360-U1473A	360-U1473A	360-U1473A	360-U1473A	
Core section	46R-1	48R-3	50R-3	51R-4	52R-1	59R-1	60R-3	63R-1	65R-1	65R-6	66R-6	68R-5	72R-2	79R-8	80R-4	83R-1				
Interval (cm)	27-35	76-83	71-77	91-98	7-13	17-24	85-92	85-92	80-87	57-63	54-61	103-110	17-24	29-36	111-118	13-28				
Depth CFSF (mbsf)	411.07	433.96	453.26	464.65	469.07	529.37	541.98	568.65	586.5	593.43	603.15	621.53	649.06	701.35	706.52	730.85	733.21			
Lithological Unit	205	215	220	228	230	243	248	263	266	277	284	293	311	344	345	382				
Lithological Unit	V	V	V	V	V	VI	VI	VI	VII	VII	VII	VII	VIII	VIII	VIII	VIII	VIII	VIII	VIII	
Internal Standard (I.S.)																	I.S.			
Rock name	olivine gabbro	olivine gabbro	olivine gabbro	olivine gabbro	olivine gabbro	olivine-bearing gabbro	olivine gabbro	olivine gabbro	olivine gabbro	olivine gabbro	olivine gabbro	olivine gabbro	olivine gabbro	olivine gabbro	olivine gabbro	olivine-bearing			disseminated olivine gabbro	
Alteration (%)	15	10	10	10	10	<5	<5	<2	<2	<2	<2	<2	8	8	8	8			10	
Duplicate																(1)	(2)			
Conc.	2.804	1.925	1.868	2.014	1.418	2.036	1.140	2.021	2.030	3.004	1.080	2.261	2.611	2.971	2.366	1.397	1.919	3.016		
Li																				
σ	0.035	0.026	0.020	0.020	0.029	0.007	0.014	0.027	0.019	0.022	0.003	0.023	0.048	0.016	0.010	0.013	0.035	0.046		
Conc.	35.52	40.00	47.58	24.86	44.14	39.99	38.35	37.50	37.50	40.16	41.54	41.47	42.53	31.46	25.17	23.32	39.83			
Sc																				
σ	0.34	0.31	0.26	0.13	0.24	0.21	0.32	0.19	0.36	0.63	0.15	0.47	0.33	0.10	0.07	0.27	0.13	0.49		
Conc.	2438	2022	2399	1362	2469	2472	2636	2360	1983	1824	2152	1764	2647	2207	1684	19011	20448	1936		
Ti																				
σ	9	12	20	18	20	15	13	19	11	17	14	24	25	26	21	82	85	7		
Conc.	157.6	168.6	200.9	102.9	196.5	187.5	196.5	177.0	162.5	167.1	178.2	157.4	170.3	187.2	122.6	416.5	413.0	166.6		
V																				
σ	1.0	2.0	1.5	1.5	3.2	1.9	0.8	1.0	0.9	1.7	2.0	0.5	1.7	1.9	1.1	1.3	3.8	1.8		
Conc.	860.8	941.3	949.2	732.1	843.7	936.6	917.9	894.7	821.1	778.3	807.1	780.6	832.8	824.5	735.0	2288.7	2204.6	787.5		
Mn																				
σ	0.8	4.6	5.8	12.2	11.7	4.1	8.6	9.8	5.3	11.8	3.3	9.1	7.6	7.3	9.7	13.2	13.3	2.1		
Conc.	34.7	40.7	38.2	34.3	28.0	35.4	34.6	34.6	35.0	32.0	35.0	33.6	33.2	33.0	36.3	57.2	52.8	32.8		
Co																				
σ	0.0	0.1	0.2	0.3	0.2	0.3	0.3	0.2	0.1	0.2	0.3	0.3	0.3	0.2	0.2	0.3	0.2	0.1		
Conc.	67.0	122.0	98.4	87.3	63.5	82.3	92.2	82.6	109.5	102.9	124.1	113.4	129.8	115.9	128.2	58.1	53.6	137.7		
Ni																				
σ	0.4	0.4	0.9	1.3	1.0	0.3	0.6	0.7	0.5	0.9	0.2	1.3	0.2	0.8	1.1	0.6	0.6	0.7		
Conc.	50.44	70.41	62.69	46.55	49.54	31.13	76.42	35.10	52.86	89.38	122.82	96.53	79.79	71.30	47.18	145.30	140.10	73.37		
Cu																				
σ	0.25	0.24	0.56	0.59	0.31	0.33	0.40	0.17	0.10	0.72	0.66	1.53	0.56	0.58	0.48	0.80	1.10	0.52		
Conc.	38.15	35.98	34.89	29.87	29.76	35.60	35.00	33.99	30.62	25.07	29.31	29.09	32.91	29.77	31.13	294.99	269.23	28.29		
Zn																				
σ	0.31	2.04	0.36	2.12	0.53	1.96	0.47	1.96	0.40	1.94	0.20	1.95	0.69	2.06	2.07	1.20	1.97	1.97		
Conc.	14.37	10.95	11.68	12.98	13.70	12.94	13.04	13.28	12.36	12.03	11.69	11.62	11.63	11.04	11.01	37.19	35.80	11.08		
Ga																				
σ	0.13	0.19	0.08	0.11	0.14	0.13	0.11	0.03	0.17	0.07	0.16	0.21	0.22	0.20	0.15	0.16	0.10	0.24		
Conc.	0.1341	0.0668	0.1101	0.1077	0.1697	0.1189	0.1763	0.1124	0.0951	0.0585	0.1241	0.1084	0.0571	0.0397	0.0750	2.318	2.218	0.0417		
Rb																				
σ	0.0007	0.0072	0.0030	0.0068	0.0030	0.0075	0.0025	0.0078	0.0041	0.0067	0.0050	0.0068	0.0006	0.0068	0.0069	0.003	0.016	0.0066		
Conc.	181.50	134.68	137.41	187.30	161.87	147.71	137.85	152.20	144.32	142.50	141.54	158.72	140.77	145.59	156.57	134.68	131.08	148.89		
Sr																				
σ	0.68	0.29	0.47	2.31	1.57	0.86	0.32	2.08	1.52	1.30	0.41	1.54	2.23	0.96	2.49	0.54	0.91	0.19		
Conc.	9.47	9.58	13.04	6.13	12.62	11.50	11.84	9.70	8.90	8.91	9.51	8.51	11.03	11.00	7.50	213.81	214.64	9.28		
Y																				
σ	0.08	0.05	0.06	0.04	0.07	0.07	0.06	0.04	0.03	0.02	0.06	0.01	0.05	0.06	0.03	2.00	2.57	0.01		
Conc.	13.27	12.71	19.54	7.65	13.40	15.13	13.13	14.33	11.79	9.26	10.18	9.23	16.18	14.91	10.99	41.87	42.89	10.75		
Zr																				
σ	0.08	0.12	0.15	0.06	0.07	0.09	0.11	0.07	0.01	0.01	0.05	0.01	0.09	0.09	0.05	0.43	0.45	0.03		
Conc.	0.147	0.156	0.267	0.106	0.573	0.194	0.092	0.173	0.148	0.076	0.097	0.078	0.169	0.094	0.156	4.666	5.551	0.091		
Nb																				
σ	0.002	0.001	0.005	0.002	0.005	0.001	0.002	0.003	0.002	0.004	0.003	0.003	0.003	0.001	0.003	0.056	0.067	0.002		
Conc.	0.584	0.194	0.222	0.117	1.665	0.218	0.227	0.204	0.160	0.130	0.236	2.068	0.267	0.234	0.247	6.149	7.161	0.169		
Sn																				
σ	0.012	0.002	0.007	0.007	0.033	0.009	0.012	0.014	0.008	0.006	0.004	0.032	0.006	0.011	0.005	0.084	0.132	0.002		
Conc.	b.d.l.	0.002	0.004	0.003	0.008	0.002	0.007	0.002	0.005	0.003	0.005	0.002	b.d.l.	0.005	0.009	0.023	0.025	b.d.l.		
Sb																				
σ	0.002	0.000	0.002	0.001	0.002	0.001	0.002	0.000	0.002	0.000	0.002	0.001	0.002	0.002	0.002	0.002	0.002	0.002		
Conc.	0.004	0.004	0.004	0.015	0.037	0.004	0.006	0.004	0.001	0.000	b.d.l.	n.d.	0.001	n.d.	b.d.l.	0.016	0.016	0.000		
Cs																				
σ	0.000	0.000	0.000	0.001	0.001	0.000	0.001	0.000	0.000	0.000	n.d.	n.d.	0.000	n.d.	0.000	0.002	0.001	0.000		
Conc.	2.828	1.668	1.920	2.042	2.541	1.667	1.936	1.741	1.605	1.505	1.782	1.799	1.835	1.455	1.719	11.785	12.231	1.378		
Ba																				
σ	0.058	0.028	0.033	0.045	0.057	0.054	0.018	0.031	0.0											

Appendix 4

Appendix 4 reports average compositions of standards used to define the quality of *in situ* and whole rock geochemical analyses. Limit of detection are also reported.

Table S3 - Trace elements BIR (mean) composition, reproducibility, accuracy, sensitivity and detection limit.

Sensitivity is reported per single spot sizes.

Detection limit is for each phase (Ol=olivine; Plg=plagioclase; Cpx=clinopyroxene) and per single spot sizes.

Spot size	BIR		Accuracy %		USGS BIR-1G GeoRem		SENSITIVITY (cps/ppm) / spot size						Detection Limit (ppm)		
	Average (n. 92)	σ			Pref. Values	σ	102		77		51		102	77	51
							MEAN	σ	MEAN	σ	MEAN	σ			
Li	3.01	0.22	0.33		3.00	0.70	2290	639	2236	1292			0.1096	0.0684	
B	10.71	2.83	13.67		12.40	0.40	1047	446	1317	693			0.1283	0.1529	
Sc	42.82	3.56	0.41		43.00	3.00	4230	1129	6449	2406			0.0172	0.0221	
Ti	6959	423	7.05		5400	200	430	123	558	212	87	46	0.4627	0.3729	0.8910
V	335	13	0.98		326	32	4936	1346	6637	2506			0.0080	0.0099	
Cr	422	17	5.12		392	24	n.a.	n.a.	5547	2161			n.a.	0.1470	
Mn	1453	92	0.93		1472	77	4516	1401	6387	2398			0.0420	0.0530	
Co	54.19	1.74	4.21		52.00	5.00	6471	1971	7045	2684			0.0211	0.0180	
Ni	191.8	22.8	0.96		178.0	18.0	206	66	236	101	38	31	1.0101	0.7964	2.9200
Cu	114.9	4.8	3.43		119.0	12.0	3639	1105	4570	1707			0.0521	0.0360	
Zn	74.77	4.61	4.14		78.00	17.00	1198	380	1434	522			0.0493	0.0399	
Rb	0.20	0.02	1.08		0.20	0.01	8398	2743	7527	2404			0.0050	0.0067	
Sr	102.6	3.0	5.80		109.0	2.0	20939	6022	18325	5760			0.0089	0.0087	
Y	13.569	1.445	4.38		14.300	1.400	9737	2736	8112	2703			0.0022	0.0017	0.0042
Zr	12.536	1.208	0.27		14.000	1.200	4824	1341	3806	1287	1065	531	0.0148	0.0116	0.0257
Nb	0.507	0.023	2.45		0.520	0.040	8870	2532	7470	2435			0.0009	0.0009	
Sb	0.554	0.027	1.03		0.560	0.090	2864	947	2396	1690			0.0058	0.0045	
Ba	5.998	0.236	2.94		6.500	0.070	1166	371	1338	446			0.0158	0.0101	
La	0.586	0.017	3.75		0.609	0.020	7967	2324	8218	2734			0.0017	0.0012	
Ce	1.825	0.043	3.42		1.890	0.040	8511	2553	8903	2828			0.0023	0.0017	
Pr	0.345	0.011	6.67		0.370	0.020	10218	3245	11017	3600			0.0008	0.0006	
Nd	2.265	0.082	4.42		2.370	0.030	1533	492	1661	560	530	280	0.0044	0.0029	0.0077
Sm	1.038	0.043	4.75		1.090	0.020	1346	437	1454	497			0.0021	0.0016	
Eu	0.508	0.019	1.78		0.517	0.005	4267	1435	4787	1666			0.0011	0.0007	
Gd	1.837	0.058	0.68		1.850	0.020	1321	433	1346	488			0.0108	0.0067	
Tb	0.348	0.009	0.52		0.350	0.040	8175	2699	7896	2817			0.0011	0.0006	
Dy	2.546	0.049	0.14		2.550	0.020	3083	964	2342	759	573	332	0.0022	0.0013	0.0060
Ho	0.557	0.013	0.47		0.560	0.030	12507	4003	9456	3091			0.0003	0.0002	
Er	1.675	0.046	1.47		1.700	0.020	2834	927	2138	712			0.0011	0.0008	
Tm	0.241	0.007	0.60		0.240	0.030	12254	3986	9233	3107			0.0004	0.0002	
Yb	1.654	0.043	0.86		1.640	0.030	2005	647	1538	527	373	226	0.0010	0.0010	0.0047
Lu	0.247	0.007	0.50		0.248	0.009	11343	3710	8544	2958			0.0004	0.0003	
Hf	0.488	0.060	6.12		0.570	0.030	2021	667	1478	512			0.0014	0.0009	
Ta	0.035	0.004	3.47		0.036	0.006	9092	2900	7251	2632			0.0011	0.0009	
Pb	3.978	0.604	7.51		3.700	0.300	5206	1798	4707	1914			0.0029	0.0021	
Th	0.027	0.003	9.92		0.030	0.002	11415	3556	7865	2746			0.0001	0.0000	
U	0.017	0.002	26.53		0.023	0.006	12611	4083	10622	3823			0.0001	0.0001	

Table A4.2 Quality of Whole rock ICP-MS data

LOD = limit of detection calculated after blanks

ppm	LOD	Batch blanks n=8	UBN			BIR-1			PM-S			BHVO			BE-N		
			Average n=8	σ	Pref'd values GeoRem	Average n=8	σ	Pref'd values GeoRem	Average n=8	σ	Pref'd values GeoRem	Average n=8	σ	Pref'd values GeoRem	Average n=8	σ	Pref'd values GeoRem
Li	0.002	0.002	24.0	4.2	26.8	2.58	0.36	3.20	6.18	1.09	7.55	1.96	2.20	4.60	10.30	1.03	12.63
Sc	0.002	0.020	10.68	0.12	13.20	36.83	0.42	43.00	29.39	0.11	34.00	12.77	14.52	31.00	18.71	0.08	22.39
Ti	0.17	0.13	496	9	560	4901	33	5600	5970	65	6595	7054	7951	16300	13460	159	15659
V	0.006	0.007	67	1	71	334	2	319	201	4	186	164	185	318	238	14	234
Cr	0.001	0.179	1207	1012	2090	258	107	393	212	91	319	103	116	288	238	54	353
Mn	0.10	0.10	947	26	1028	1279	4	1363	1188	13	1224	635	718	1317	1495	11	1400
Co	0.004	0.003	99	3	99	49	1	52	48	1	49	21	24	45	58	0	56
Ni	0.057	0.076	1906	28	1966	161	1	166	116	1	118	57	63	118	254	2	263
Cu	0.020	0.066	23.9	1.0	27.5	111	3	119	55	1	57	64	72	137	64	1	69
Zn	0.1	0.4	74	0	85	65	0	72	55	1	60	48	54	106	113	4	123
<i>ppb</i>																	
Ga	2.3	1.4	2622	22	3157	14919	19	15300	15414	184	15600	10992	12435	21320	21748	665	17200
Rb	1.5	1.6	2993	63	3761	173	8	200	789	3	978	4202	4784	9190	43546	721	46670
Sr	5.0	10.2	6932	150	8169	100709	973	109000	262572	1447	279200	185386	212066	396000	1297739	13720	1391190
Y	0.3	0.4	2574	123	2584	15893	158	15600	10863	174	11310	12787	14679	26000	29628	795	29397
Zr	2.0	3.5	3324	138	3849	14085	256	14000	36361	370	38200	86895	99664	174000	271601	2375	270980
Nb	1.5	0.9	49.2	0.8	72.3	520	9	550	2235	20	2440	8751	9939	18600	103611	2151	110720
Sn	4.0	4.1	325	3	370	711	22	600	3726	2258	3000	953	1088	2100	1586	106	1900
Sb	1.9	2.2	77	13	180	510	20	460	30.3	2.0	28.0	74.7	85.4	150	233	14	260
Cs	0.2	0.2	10785	164	10835	5.30	0.06	7.00	317	2	372	45.3	50.1	101	686	14	700
Ba	5.1	35.7	20393	744	26859	6060	189	7140	138806	786	148100	61353	70361	133000	981807	7270	1035330
La	0.4	0.6	325	36	336	597	8	615	2555	49	2683	7535	8637	15500	84083	1962	79010
Ce	0.5	0.9	739	61	829	1720	16	1920	5973	120	6870	17980	20527	38100	142856	3977	151960
Pr	0.1	0.1	110	6	124	341	5	370	954	20	1069	2415	2780	5420	15612	335	17380
Nd	0.5	0.5	563	23	619	2184	30	2380	5022	65	5520	11227	12814	24700	60717	1031	66140
Sm	0.5	0.4	200	2	220	1011	21	1120	1610	37	1784	2776	3155	6120	11047	322	12120
Eu	0.1	0.2	76.1	1.0	82.7	497	9	530	997	12	1069	971	1111	2090	3460	80	3700
Gd	0.3	0.3	313	3	314	1815	2	1870	1975	5	2040	2937	3356	6330	9284	220	10200
Tb	0.1	0.1	58.7	0.2	60.4	347	4	360	317	1	338	439	499	960	1207	15	1320
Dy	0.4	0.3	415	9	416	2506	50	2510	2005	33	2095	2531	2862	5310	6111	161	6690
Ho	0.1	0.1	93	3	95	562	11	560	403	9	428	469	533	980	1028	28	1080
Er	0.2	0.2	272	4	283	1602	33	1660	1056	14	1140	1168	1322	2550	2450	47	2650
Tm	0.1	0.0	41.9	1.3	43.7	240	5	250	147	3	169	156	175	330	294	6	330
Yb	0.2	-	284	7	291	1578	19	1650	914	12	997	921	1046	2000	1676	27	1820
Lu	0.1	0.1	44.8	1.0	46.6	238	5	250	135	3	151	129	145	270	226	6	250
Hf	0.7	0.6	132	0	114	618	0	582	1108	7	1100	2293	2565	4460	5671	71	5770
Ta	0.6	0.5	16.18	1.73	26.22	41	1	36	173	0	190	593	657	1210	5221	267	5608
W	1.2	1.0	16777	2517	20138	74.3	-	70.0	215	2	300	175	186	210	31733	984	28000
Pb	2.7	29.3	11300	110	13132	3107	29	3100	2590	1295	2470	968	1112	2400	3907	27	4248
Th	0.2	0.1	67.0	23.6	72.1	28.65	1.27	32.00	43.38	3.86	53.00	579	625	1230	9733	217	10639
U	0.2	0.2	46.0	14.8	62.2	8.33	0.64	10.00	11.33	1.82	19.00	188	196	409	2099	301	2517

Appendix 5

Appendix 5 reports a compilation of partition and diffusion coefficients. Compositions of starting material used in the numerical modeling are also reported. These tables correspond to Supplementary Material Table T4, T5 and T6 in Ferrando et al. (2018).

Table S4 Selected partition coefficients

Elements	Partition coefficients							
	Olivine		Plagioclase		Clinopyroxene		Orthopyroxene	
	Pref. Values	Literature range [2,5,6,8-10]	Pref. Values	Literature range [1,3,5,11]	Pref. Values	Literature range [5-9]	Pref. Values	Literature range [3,5,6,8,9]
Ni	Equation from [4]	7.21 - 22.28	0.089	0.089	2.84	2.84-3.78	4.33	3.5-7.38
Co	5.21	2.28 - 5.21	0.042	0.042 - 3.2	0.95	0.95 - 1.18	2.48	1.46 - 2.48
Zn	1.16	1.16	1.8	1.8	0.5	0.5	0.72	0.72 - 0.79
Mn	1.15	0.73 - 1.63	0.031	0.029 - 0.031	1.02	1.02 - 1.16	1.41	1.05 - 1.41
La	3.60E-05		0.054	0.003 - 0.077	0.080	0.06 - 0.08	0.003	0.001 - 0.002
Ce	5.60E-05	5.60E-05 - 3.00E-04	0.040	0.004 - 0.054	0.105	0.031 - 0.16	0.004	0.004 - 0.005
Pr	1.00E-04	1.00E-04 - 1.70E-04	0.035	0.005 - 0.042	0.130	0.13	0.007	0.006 - 0.007
Nd	2.50E-04	1.70E-04 - 2.50E-04	0.030	0.01 - 0.054	0.180	0.067 - 0.273	0.020	0.01 - 0.02
Sm	4.50E-04	3.20E-04 - 1.30E-03	0.020	0.02 - 0.081	0.270	0.108 - 0.459	0.040	0.016 - 0.055
Eu	8.60E-04	3.60E-04 - 1.10E-03	0.378	0.02 - 0.378	0.354	0.354	0.046	0.016 - 0.059
Gd	1.30E-03	6.70E-04 - 2.90E-03	0.013	0.013 - 0.042	0.418	0.28 - 0.418	0.069	0.055 - 0.069
Tb	2.60E-03	2.60E-03	0.011	0.028 - 0.035	0.559	0.559	0.110	0.11
Dy	4.80E-03	4.80E-03	0.009	0.034 - 0.049	0.700	0.7	0.150	0.15
Ho	7.00E-03	7.00E-03	0.007	0.037 - 0.052	0.760	0.76	0.200	0.2
Er	1.32E-02	1.32E-02	0.005	0.04 - 0.057	0.760	0.23 - 0.76	0.240	0.038 - 0.24
Tm	2.00E-02		0.004	0.04 - 0.061	0.740	0.286 - 0.74	0.315	0.315
Yb	2.67E-02	2.67E-02 - 3.30E-02	0.003	0.003 - 0.05	0.740	0.442 - 0.74	0.320	0.091 - 0.39
Lu	3.30E-02	8.90E-03 - 3.30E-02	0.002	0.024 - 0.05	0.740	0.74	0.326	0.106 - 0.47

[1] Aigner-Torres et al. (2007)

[2] Beattie (1994)

[3] Bedard (2001)

[4] Hart and Davis (1978)

[5] Laubier et al. (2014)

[6] Le Roux et al. (2011)

[7] Lunstrom et al. (1998)

[8] McDade et al. (2003)

[9] Salters et al. (2002)

[10] Spandler and O'Neill (2010)

[11] Sun et al.(2017)

Table S5 Selected diffusion coefficients

Elements	Diffusion coefficients			
	Pref. Values	Olivine Literature range [13,15,17-22]	Plagioclase Literature values [12,24]	Clinopyroxene Literature Values [14, 16, 23]
Fe-Mg	-16	-16.94 / -14.82	-16.47	-15.08
Mn	-16.6	-17.25 / -14.88		
Ni	-15.8	-17.11 / -14.63		
Co	-16.4	-16.4 / -14.57		
Ti	-15.6	-20.71 / -14.41		-21.47
Li	-14.1	-14.82 / -14.1		
Sm		-19.15		
Eu		-19.1 / -14.89		
Dy		-2.06E+01	-19.75	-18.010
Lu		-19/ -14.95		

Diffusion coefficients (m/s^2) are reported in logarithmic scale; when reported in literature, diffusion in olivine is measured along [001]

[12] Cherniak (2003)

[13] Cherniak (2010)

[14] Cherniak and Liang (2012)

[15] Cherniak and Liang (2014)

[16] Dimanov and Wiedenbeck (2006)

[17] Dohmen et al. (2007)

[18] Jollands et al. (2014)

[19] Jollands et al. (2016)

[20] Spandler and O'Neill (2010)

[21] Spandler et al. (2007)

[22] Remmert et al. (2008)

[23] VanOrman et al. (2001)

[24] VanOrman et al. (2014)

Table S6 Chemical composition of melt and rock starting material for modeling performed in this study

Starting material for	Stage 1					Stage 2				
	Bulk Hzb 1274A [25]	Hole Ol	Opx	Cpx	Primitive MORB [26- 27]	Bulk Hzb output Stage 1	Ol	Opx	Cpx	N-MORB [28]
Modal %		80	17	3			97	1.5	1.5	
FeO TOT	7.53	8.11	5	3.05	9.74	7.9	-	-	-	9.74
MgO	40.69	52.17	34.74	17.5	8.05	40.7	-	-	-	8.05
Mg#	91.46	92	93	91	71	90.7	91	92	91	71
Ni	3172				350	1750-2000				200
La	0.0005				3.10	0.0002				4.19
Ce	0.0016				9.16	0.0008				12.42
Pr	0.0003				1.60	0.0003				1.98
Nd	0.0017				8.87	0.0035				10.66
Sm	0.0010				2.98	0.0021				3.48
Eu	0.0004				1.11	0.0015				1.26
Gd	0.0016				3.91	0.0080				4.55
Tb	0.0003				0.70	0.0028				0.82
Dy	0.0037				4.67	0.0348				5.50
Ho	0.0015				1.01	0.0108				1.18
Er	0.0063				2.88	0.0565				3.42
Tm	0.0016				0.43	0.0123				-
Yb	0.0159				2.82	0.1030				3.28
Lu	0.0041				0.42	0.0184				0.48

[25] Godard et al. (2008)

[26] Major elements - Presnall and Hoover (1987)

[27] Trace elements - Workman and Hart (2005)

[28] Gale et al. (2014)

Supplementary Material - References

- Aigner-Torres, M., Blundy, J., Ulmer, P., Pettke, T., 2007. Laser Ablation ICPMS study of trace element partitioning between plagioclase and basaltic melts: An experimental approach. *Contributions to Mineralogy and Petrology* 153, 647–667. doi:10.1007/s00410-006-0168-2
- Beattie, P., 1994. Systematics and energetics of trace-element partitioning between olivine and silicate melts: Implications for the nature of mineral/melt partitioning. *Chemical Geology* 117, 57–71. doi:10.1016/0009-2541(94)90121-X
- Bédard, J.H., 2001. Parental magmas of the Nain Plutonic Suite anorthosites and mafic cumulates: a trace element modelling approach. *Contributions to Mineralogy and Petrology* 141, 747–771. doi:10.1007/s004100100268
- Cherniak, D.J., 2010. Cation Diffusion in Feldspars. *Reviews in Mineralogy and Geochemistry* 72, 691–733. doi:10.2138/rmg.2010.72.15
- Cherniak, D.J., 2003. REE diffusion in feldspar. *Chemical Geology* 193, 25–41.
- Cherniak, D.J., Liang, Y., 2014. Titanium diffusion in olivine. *Geochimica et Cosmochimica Acta* 147, 43–57. doi:10.1016/j.gca.2014.10.016
- Cherniak, D.J., Liang, Y., 2012. Ti diffusion in natural pyroxene. *Geochimica et Cosmochimica Acta* 98, 31–47. doi:10.1016/j.gca.2012.09.021
- Dimanov, A., Wiedenbeck, M., 2006. (Fe,Mn)-Mg interdiffusion in natural diopside: effect of pO_2 . *European Journal of Mineralogy* 18, 705–718. doi:10.1127/0935-1221/2006/0018-0705
- Dohmen, R., Becker, H.W., Chakraborty, S., 2007. Fe-Mg diffusion in olivine I: Experimental determination between 700 and 1,200°C as a function of composition, crystal orientation and oxygen fugacity. *Physics and Chemistry of Minerals* 34, 389–407. doi:10.1007/s00269-007-0157-7
- Gale, A., Langmuir, C.H., Dalton, C.A., 2014. The global systematics of ocean ridge basalts and their origin. *Journal of Petrology* 55, 1051–1082. doi:10.1093/petrology/egu017
- Godard, M., Lagabriele, Y., Alard, O., Harvey, J., 2008. Geochemistry of the highly depleted peridotites drilled at ODP Sites 1272 and 1274 (Fifteen-Twenty Fracture Zone, Mid-Atlantic Ridge): Implications for mantle dynamics beneath a slow spreading ridge. *Earth and Planetary Science Letters* 267, 410–425. doi:10.1016/j.epsl.2007.11.058
- Hart, S.R., Davis, K.E., 1978. Nickel partitioning between olivine and silicate melt. *Earth and Planetary Science Letters* 40, 203–219. doi:10.1016/j.pcad.2011.11.003
- Jollands, M.C., Hermann, J., O'Neill, H.S.C., Spandler, C., Padrón-Navarta, J.A., 2016. Diffusion of Ti and some Divalent Cations in Olivine as a Function of Temperature, Oxygen Fugacity, Chemical Potentials and Crystal Orientation. *Journal of Petrology* 57, 1983–2010. doi:10.1093/petrology/egw067

- Jollands, M.C., O'Neill, H.S.C., Hermann, J., 2014. The importance of defining chemical potentials, substitution mechanisms and solubility in trace element diffusion studies: the case of Zr and Hf in olivine. *Contributions to Mineralogy and Petrology* 168. doi:10.1007/s00410-014-1055-x
- Laubier, M., Grove, T.L., Langmuir, C.H., 2014. Trace element mineral/melt partitioning for basaltic and basaltic andesitic melts: An experimental and laser ICP-MS study with application to the oxidation state of mantle source regions. *Earth and Planetary Science Letters* 392, 265–278. doi:10.1016/j.epsl.2014.01.053
- Le Roux, V., Dasgupta, R., Lee, C.T.A., 2011. Mineralogical heterogeneities in the Earth's mantle: Constraints from Mn, Co, Ni and Zn partitioning during partial melting. *Earth and Planetary Science Letters* 307, 395–408. doi:10.1016/j.epsl.2011.05.014
- Lundstrom, C.C., Shaw, H.F., Ryerson, F.J., Williams, Q., Gill, J., 1998. Crystal chemical control of clinopyroxene-melt partitioning in the Di-Ab-An system: Implications for elemental fractionations in the depleted mantle. *Geochimica et Cosmochimica Acta* 62, 2849–2862. doi:10.1016/S0016-7037(98)00197-5
- McDade, P., Blundy, J.D., Wood, B.J., 2003. Trace element partitioning on the Tinaquillo solidus at 1.5 GPa. *Physics of the Earth and Planetary Interiors* 139, 129–147. doi:10.1016/S0031-9201(03)00149-3
- Presnall, D., Hoover, J.D., 1987. High pressure phase equilibrium constraints on the origin of mid-ocean ridge basalts, in: B.O. Mysen (Ed.), *Magmatic Processes: Physicochemical Principles*, Special Publication-Geochemical Society. pp. 75–89.
- Salter, V.J.M., Longhi, J.E., Bizimis, M., 2002. Near mantle solidus trace element partitioning at pressures up to 3.4 GPa. *Geochemistry, Geophysics, Geosystems* 3, 1–23. doi:10.1029/2001GC000148
- Spandler, C., O'Neill, H.S.C., 2010. Diffusion and partition coefficients of minor and trace elements in San Carlos olivine at 1,300°C with some geochemical implications. *Contributions to Mineralogy and Petrology* 159, 1–28. doi:10.1007/s00410-009-0456-8
- Spandler, C., O'Neill, H.S.C., Kamenetsky, V.S., 2007. Survival times of anomalous melt inclusions from element diffusion in olivine and chromite. *Nature* 447, 303–306. doi:10.1038/nature05759
- Sun, C., Graff, M., Liang, Y., 2017. Trace element partitioning between plagioclase and silicate melt: The importance of temperature and plagioclase composition, with implications for terrestrial and lunar magmatism. *Geochimica et Cosmochimica Acta* 206, 273–295. doi:10.1016/j.gca.2017.03.003
- Van Orman, J.A., Cherniak, D.J., Kita, N.T., 2014. Magnesium diffusion in plagioclase: Dependence on composition, and implications for thermal resetting of the ^{26}Al - ^{26}Mg early solar system chronometer. *Earth and Planetary Science Letters* 385, 79–88. doi:10.1016/j.epsl.2013.10.026

Van Orman, J.A., Grove, T.L., Shimizu, N., 2001. Rare earth element diffusion: influence of temperature, pressure, and ionic radius, and an elastic model for diffusion in silicates. *Contributions to Mineralogy and Petrology* 141, 687–703.

Workman, R.K., Hart, S.R., 2005. Major and trace element composition of the depleted MORB mantle (DMM). *Earth and Planetary Science Letters* 231, 53–72. doi:10.1016/j.epsl.2004.12.005

Appendix 6

Appendix 6 reports geochemical compositions of minerals analysed to develop new secondary standards for LA-ICP-MS analyses. They include *in situ* major (EPMA) and trace elements analyses (LA-ICP-MS), and solution ICP-MS analyses. Finally, I report the compositions of standard used during the analyses.

Table A6.1 Major element compositions of all mineral samples

Proxy sample	15GLM01												15GLM01											
Phase	Olivine San Carlos												Magmatic olivine											
Location	rim	σ	core	σ	core	σ	rim	σ	rim	σ	core	σ	rim	σ	core	σ	rim	σ	core	σ	rim	σ		
SiO2	41.63	0.22	41.67	0.22	41.55	0.22	41.39	0.22	41.26	0.22	41.04	0.22	41.10	0.23										
TiO2	0.03	0.02	0.01	0.02	0.01	0.02	0.00	0.02	0.02	0.02	0.02	0.02	0.01	0.03										
Al2O3	0.04	0.02	0.01	0.02	0.01	0.02	0.01	0.02	0.00	0.00	0.00	0.02	0.02	0.02										
Cr2O3	0.05	0.03	0.03	0.03	0.03	0.03	0.01	0.03	0.02	0.03	0.02	0.03	0.04	0.03										
FeO	8.58	0.16	8.62	0.16	8.69	0.16	8.58	0.16	10.53	0.18	10.60	0.18	10.59	0.19										
MnO	0.08	0.03	0.12	0.03	0.14	0.03	0.13	0.03	0.15	0.03	0.16	0.03	0.13	0.04										
MgO	48.81	0.42	48.78	0.42	48.79	0.42	48.34	0.42	47.19	0.41	47.16	0.41	47.03	0.42										
CaO	0.07	0.01	0.08	0.01	0.08	0.01	0.08	0.01	0.13	0.01	0.13	0.01	0.12	0.01										
Na2O	0.02	0.03	0.00	0.00	0.01	0.03	0.00	0.00	0.00	0.00	0.00	0.03	0.00	0.03										
K2O	0.00	0.00	0.00	0.00	0.00	0.01	0.00	0.01	0.00	0.00	0.00	0.00	0.00	0.00										
NiO	0.35	0.05	0.37	0.05	0.39	0.05	0.34	0.05	0.35	0.05	0.38	0.05	0.36	0.05										
Total	99.67	0.51	99.70	0.51	99.71	0.51	98.89	0.51	99.65	0.51	99.51	0.51	99.41	0.52										
Mg#	91.02	0.55	90.98	0.55	90.92	0.55	90.94	0.54	88.87	0.60	88.80	0.60	88.78	0.62										

Proxy sample	15GLM01												15GLM01		15GLM01												15GLM01																	
Phase	Clinopyroxene Inagli												Diopside glass		Cr-diopside		Augite																											
Location	rim	σ	core	σ	core	σ	rim	σ	rim	σ	rim	σ	rim	σ	core	σ	rim	σ	rim	σ	core	σ	rim	σ	rim	σ	rim	σ	rim	σ	rim	σ	rim	σ										
SiO2	55.27	0.25	54.95	0.25	55.07	0.25	54.96	0.25	54.57	0.25	54.73	0.25	56.39	0.26	54.15			0.25	53.80	0.25	54.09	0.25	54.45	0.25	54.30	0.25	54.15	0.25	54.19	0.25	45.94	0.23	45.17	0.22	45.54	0.22	45.42	0.22	45.22	0.22	45.39	0.22		
TiO2	0.12	0.03	0.07	0.03	0.07	0.03	0.09	0.03	0.08	0.03	0.08	0.03	0.03	0.03	0.10			0.03	0.10	0.03	0.10	0.03	0.13	0.03	0.05	0.03	0.08	0.03	0.12	0.03	2.76	0.08	3.13	0.08	2.92	0.08	2.92	0.08	2.86	0.08	2.95	0.08		
Al2O3	0.20	0.02	0.16	0.02	0.17	0.02	0.18	0.02	0.20	0.02	0.17	0.02	0.63	0.03	0.93			0.03	1.12	0.04	1.06	0.04	0.84	0.03	1.15	0.04	1.20	0.04	1.30	0.04	8.14	0.09	8.55	0.10	8.37	0.09	8.58	0.10	8.65	0.10	8.72	0.10		
Cr2O3	0.29	0.04	0.27	0.04	0.27	0.04	0.32	0.04	0.33	0.04	0.29	0.04	0.00	0.00	0.00			0.03	0.01	0.03	0.02	0.03	0.01	0.03	0.00	0.00	0.01	0.03	0.01	0.03	0.02	0.03	0.04	0.03	0.05	0.03	0.04	0.03	0.04	0.03	0.04	0.03		
FeO	1.12	0.06	1.10	0.06	1.09	0.06	1.14	0.06	1.13	0.06	1.09	0.06	0.10	0.03	3.62			0.11	3.60	0.11	3.87	0.11	3.59	0.11	3.76	0.11	3.74	0.11	3.89	0.11	6.68	0.14	6.62	0.14	6.58	0.14	6.67	0.14	6.68	0.14	6.79	0.14		
MnO	0.06	0.03	0.05	0.03	0.05	0.03	0.03	0.03	0.04	0.03	0.06	0.03	0.00	0.03	0.14			0.03	0.10	0.03	0.12	0.03	0.08	0.03	0.09	0.03	0.10	0.03	0.11	0.03	0.08	0.03	0.07	0.03	0.09	0.03	0.09	0.03	0.11	0.03	0.06	0.03		
MgO	17.62	0.19	17.51	0.19	17.56	0.19	17.52	0.19	17.58	0.19	17.51	0.19	19.72	0.20	15.95			0.18	15.67	0.18	15.67	0.18	15.82	0.18	16.29	0.18	16.14	0.18	16.30	0.18	12.28	0.15	12.09	0.15	12.13	0.15	12.08	0.15	11.82	0.15	11.99	0.15		
CaO	25.55	0.18	25.32	0.18	25.26	0.18	25.10	0.18	25.10	0.18	25.00	0.17	23.85	0.17	24.86			0.17	24.50	0.18	24.72	0.17	24.92	0.17	24.12	0.17	24.00	0.17	23.95	0.17	23.40	0.17	23.39	0.17	23.38	0.17	23.10	0.16	23.34	0.17	23.25	0.16		
Na2O	0.22	0.05	0.22	0.05	0.24	0.05	0.24	0.05	0.22	0.05	0.27	0.05	0.00	0.03	0.32			0.06	0.39	0.06	0.35	0.06	0.40	0.06	0.47	0.06	0.43	0.06	0.47	0.06	0.44	0.06	0.44	0.06	0.42	0.06	0.48	0.07	0.39	0.06	0.41	0.06		
K2O	0.00	0.00	0.00	0.00	0.00	0.01	0.00	0.01	0.00	0.01	0.00	0.00	0.00	0.01	0.00			0.01	0.00	0.01	0.00	0.00	0.00	0.00	0.00	0.00	0.00	0.00	0.00	0.01	0.00	0.00	0.01	0.00	0.00	0.01	0.00	0.00	0.00	0.00	0.00	0.00	0.00	
NiO	0.01	0.04	0.03	0.04	0.01	0.04	0.02	0.03	0.00	0.04	0.00	0.04	0.02	0.03	0.00			0.00	0.02	0.04	0.00	0.03	0.00	0.00	0.01	0.03	0.03	0.04	0.03	0.04	0.00	0.00	0.03	0.03	0.01	0.03	0.02	0.04	0.01	0.03	0.01	0.04	0.01	0.04
Total	100.47	0.38	99.67	0.38	99.79	0.38	99.61	0.38	99.26	0.37	99.20	0.37	100.74	0.38	100.09			0.38	99.30	0.39	100.00	0.38	100.25	0.38	100.26	0.38	99.86	0.38	100.36	0.38	99.74	0.38	99.54	0.38	99.43	0.38	99.40	0.38	99.12	0.38	99.61	0.38	99.61	0.38
Mg#	96.54	0.62	96.61	0.63	96.63	0.62	96.47	0.63	96.53	0.62	96.62	0.62	99.71	0.32	88.70			0.99	88.57	1.03	87.83	1.02	88.70	0.99	88.53	0.98	88.51	0.98	88.20	0.99	76.63	1.29	76.49	1.29	76.67	1.29	76.36	1.29	75.93	1.31	75.88	1.31	75.88	1.31

Proxy sample	15GLM01												Chromite Cuba																																	
Phase	Chromite Madagascar												Chromite Cuba																																	
Location	rim	σ	core	σ	core	σ	rim	σ	rim	σ	rim	σ	rim	σ	rim	σ	rim	σ	core	σ	core	σ	rim	σ	rim	σ	rim	σ	rim	σ	rim	σ	rim	σ												
SiO2	0.12	0.02	0.13	0.02	0.09	0.02	0.09	0.02	0.08	0.02	0.10	0.02	0.03	0.02	0.06			0.02	0.05	0.02	0.03	0.02	0.06	0.02	0.39	0.03	0.08	0.02	0.03	0.02	0.04	0.02	0.04	0.02	0.04	0.02	0.04	0.02	0.04	0.02	0.04	0.02	0.04	0.02		
TiO2	0.06	0.03	0.10	0.03	0.10	0.03	0.09	0.03	0.10	0.03	0.09	0.03	0.33	0.04	0.26			0.03	0.27	0.04	0.24	0.03	0.20	0.03	0.24	0.03	0.26	0.03	0.23	0.03	0.23	0.03	0.23	0.03	0.23	0.03	0.23	0.03	0.23	0.03	0.23	0.03	0.23	0.03		
Al2O3	14.18	0.14	16.35	0.15	14.95	0.14	16.60	0.15	15.66	0.14	15.55	1.00	29.25	0.27	29.30			0.27	26.94	0.26	29.79	0.28	29.52	0.27	29.40	0.27	30.04	0.28	29.10	0.27	29.34	0.27	29.34	0.27	29.34	0.27	29.34	0.27	29.34	0.27	29.34	0.27	29.34	0.27	29.34	0.27
Cr2O3	58.01	0.94	55.31	0.90	56.33	0.91	54.74	0.89	55.18	0.89	55.91	1.31	38.82	0.40	38.48			0.39	39.00	0.40	38.69	0.40	38.87	0.40	38.22	0.39	37.41	0.39	38.21	0.39	39.03	0.40	39.03	0.40	39.03	0.40	39.03	0.40	39.03	0.40	39.03	0.40	39.03	0.40	39.03	0.40
FeO	14.15	0.21	14.48	0.21	14.48	0.21	13.86	0.21	14.47	0.21	14.29	0.28	15.18	0.23	14.86			0.23	15.75	0.23	14.53	0.22	14.99	0.23	15.10	0.23	15.03	0.23	14.97	0.23	14.85	0.23	14.85	0.23	14.85	0.23	14.85	0.23	14.85	0.23	14.85	0.23	14.85	0.23	14.85	0.23
MnO	0.28	0.04	0.24	0.04	0.23	0.04	0.29	0.04	0.27	0.05	0.26	0.03	0.20	0.04	0.19			0.04	0.26	0.05	0.24	0.04	0.19	0.04	0.22	0.04	0.22	0.04	0.22	0.04	0.23	0.04	0.23	0.04	0.23	0.04	0.23	0.04	0.23	0.04	0.23	0.04	0.23	0.04		
MgO	12.94	0.17	12.42	0.16	13.28	0.17	14.13	0.18	13.15	0.17	13.19	0.62	16.10	0.20	15.85			0.19	16.32	0.20	15.83	0.19	13.95	0.18	16.23	0.20	14.56	0.18	16.16	0.20	14.27	0.18	14.27	0.18	14.27	0.18	14.27	0.18	14.27	0.18	14.27	0.18	14.27	0.18	14.27	0.18
CaO	0.01	0.01	0.00	0.00	0.01	0.01	0.01	0.01	0.01	0.01	0.01	0.00	0.00	0.01	0.00			0.01	0.01	0.01	0.00	0.01	0.00	0.00	0.01	0.01	0.01	0.01	0.00	0.00	0.00	0.01	0.00	0.00	0.01	0.00	0.00	0.00	0.00	0.00	0.00	0.00	0.00	0.00	0.00	
Na2O	0.00	0.00	0.00	0.00	0.01	0.04	0.00	0.00	0.01	0.05	0.00	0.00	0.00	0.00	0.00			0.00	0.04	0.04	0.00	0.00	0.03	0.04	0.00	0.00	0.00	0.00	0.00	0.00	0.00	0.00	0.00	0.00	0.00	0.00	0.00	0.00	0.00	0.00	0.00	0.00	0.00	0.00	0.00	
K2O	0.00	0.01	0.00	0.00	0.00	0.00	0.00	0.01	0.00	0.01	0.00	0.00	0.00	0.00	0.01			0.02	0.0																											

Table A6.2 In situ (LA-ICP-MS) Trace element compositions of all mineral samples

n.d. = not detected b.d.l. = below detection limit values are reported in ppm

Poxy sample	15GLM01						15GLM01						15GLM01						15GLM01																	
	Olivine San Carlos						Magmatic olivine						Dioptside glass						Augite																	
Phase	rim	σ	core	σ	core	σ	rim	σ	core	σ	rim	σ	rim	σ	core	σ	rim	σ	rim	σ	core	σ	rim	σ	rim	σ	core	σ	rim	σ	rim	σ	core	σ	rim	σ
Li	2.09	0.087	2.09	0.089	1.97	0.09	2.04	0.099	1.60	0.1	1.77	0.084	1.76	0.097	1.60	0.1	1.77	0.084	1.76	0.097	1.60	0.1	1.77	0.084	1.76	0.097	1.60	0.1	1.77	0.084	1.76	0.097	1.60	0.1	1.77	0.084
B	24.87	1.05	25.03	1.1	24.78	1.14	24.39	1.16	22.38	1.33	23.27	1.3	24.30	1.45	22.38	1.33	23.27	1.3	24.30	1.45	22.38	1.33	23.27	1.3	24.30	1.45	22.38	1.33	23.27	1.3	24.30	1.45	22.38	1.33	23.27	1.3
Si	193987.4	6134.49	193987.36	6134.49	193987.36	6134.51	192117.59	6134.5	192117.6	6075.37	192117.6	6075.36	192117.61	6075.38	192117.6	6075.37	192117.6	6075.36	192117.61	6075.38	192117.6	6075.37	192117.6	6075.36	192117.61	6075.38	192117.6	6075.37	192117.6	6075.36	192117.61	6075.38	192117.6	6075.37	192117.6	6075.36
Ca	520.83	13.33	527.17	17.71	529.77	18.06	509.36	18.52	472.4	18.2	496.47	18.55	493.34	18.18	472.4	18.2	496.47	18.55	493.34	18.18	472.4	18.2	496.47	18.55	493.34	18.18	472.4	18.2	496.47	18.55	493.34	18.18	472.4	18.2	496.47	18.55
Sc	4.48	0.15	4.48	0.15	4.48	0.15	4.36	0.2	5.38	0.15	5.7	0.19	5.46	0.2	5.38	0.15	5.7	0.19	5.46	0.2	5.38	0.15	5.7	0.19	5.46	0.2	5.38	0.15	5.7	0.19	5.46	0.2	5.38	0.15	5.7	0.19
Ti	9.69	0.31	9.79	0.31	9.69	0.31	9.68	0.32	47.07	0.31	48.87	0.31	48.15	0.32	47.07	0.31	48.87	0.31	48.15	0.32	47.07	0.31	48.87	0.31	48.15	0.32	47.07	0.31	48.87	0.31	48.15	0.32	47.07	0.31	48.87	0.31
V	3.9	0.12	3.94	0.13	4.03	0.13	3.88	0.13	5.77	0.13	5.82	0.19	5.81	0.2	5.77	0.13	5.82	0.19	5.81	0.2	5.77	0.13	5.82	0.19	5.81	0.2	5.77	0.13	5.82	0.19	5.81	0.2	5.77	0.13	5.82	0.19
Cr	n.d.	n.d.	n.d.	n.d.	n.d.	n.d.	n.d.	n.d.	n.d.	n.d.	n.d.	n.d.	n.d.	n.d.	n.d.	n.d.	n.d.	n.d.	n.d.	n.d.	n.d.	n.d.	n.d.	n.d.	n.d.	n.d.	n.d.	n.d.	n.d.	n.d.	n.d.	n.d.	n.d.	n.d.	n.d.	n.d.
Mn	979.19	32.51	987.56	33.17	984.35	33.54	982.36	33.75	1152.25	35.5	1141.84	42.63	1158.8	43.33	1152.25	35.5	1141.84	42.63	1158.8	43.33	1152.25	35.5	1141.84	42.63	1158.8	43.33	1152.25	35.5	1141.84	42.63	1158.8	43.33	1152.25	35.5	1141.84	42.63
Co	154.65	4.93	155.12	4.98	152.74	4.95	154.21	5.01	166.74	5.19	166.18	5.7	166.51	5.78	166.74	5.19	166.18	5.7	166.51	5.78	166.74	5.19	166.18	5.7	166.51	5.78	166.74	5.19	166.18	5.7	166.51	5.78	166.74	5.19	166.18	5.7
Ni	2891.74	205.06	2845.4	209.75	2782.07	214.78	2673.36	224.8	2407.13	241.6	2413.93	229.43	2390.87	242.36	2407.13	241.6	2413.93	229.43	2390.87	242.36	2407.13	241.6	2413.93	229.43	2390.87	242.36	2407.13	241.6	2413.93	229.43	2390.87	242.36	2407.13	241.6	2413.93	229.43
Cu	0.908	0.029	0.915	0.029	0.889	0.029	0.901	0.03	0.827	0.029	0.855	0.027	0.864	0.029	0.827	0.029	0.855	0.027	0.864	0.029	0.827	0.029	0.855	0.027	0.864	0.029	0.827	0.029	0.855	0.027	0.864	0.029	0.827	0.029	0.855	0.027
Zn	52.08	1.59	51.65	1.58	50.78	1.56	50.14	1.56	73.49	1.54	73.94	2.26	72.48	2.28	73.49	1.54	73.94	2.26	72.48	2.28	73.49	1.54	73.94	2.26	72.48	2.28	73.49	1.54	73.94	2.26	72.48	2.28	73.49	1.54	73.94	2.26
Rb	b.d.l.	0.001	b.d.l.	0.001	b.d.l.	0.001	b.d.l.	0.001	b.d.l.	0.001	b.d.l.	0.001	b.d.l.	0.001	b.d.l.	0.001	b.d.l.	0.001	b.d.l.	0.001	b.d.l.	0.001	b.d.l.	0.001	b.d.l.	0.001	b.d.l.	0.001	b.d.l.	0.001	b.d.l.	0.001	b.d.l.	0.001	b.d.l.	0.001
Sr	0.019	0.0012	0.009	0.001	0.011	0.001	0.00999	0.006	0.006	0.00999	0.006	0.0099	0.006	0.00991	0.006	0.00999	0.006	0.0099	0.006	0.006	0.00999	0.006	0.0099	0.006	0.00991	0.006	0.00999	0.006	0.0099	0.006	0.00991	0.006	0.00999	0.006	0.0099	
Y	0.036	0.0016	0.031	0.0014	0.031	0.0015	0.029	0.0014	0.06	0.0014	0.063	0.0027	0.066	0.003	0.06	0.0014	0.063	0.0027	0.066	0.003	0.06	0.0014	0.063	0.0027	0.066	0.003	0.06	0.0014	0.063	0.0027	0.066	0.003	0.06	0.0014	0.063	0.0027
Zr	0.012	0.0021	0.017	0.0021	0.017	0.0023	0.018	0.002	0.017	0.0021	0.016	0.002	0.016	0.0021	0.017	0.0021	0.016	0.002	0.016	0.0021	0.017	0.0021	0.016	0.002	0.016	0.0021	0.017	0.0021	0.016	0.002	0.016	0.0021	0.017	0.0021	0.016	0.002
Nb	b.d.l.	0.001	0.009	0.00059	0.009	0.00065	0.008	0.00097	0.004	0.00057	0.004	0.00037	0.004	0.00042	0.004	0.00057	0.004	0.00037	0.004	0.00042	0.004	0.00057	0.004	0.00037	0.004	0.00042	0.004	0.00057	0.004	0.00037	0.004	0.00042	0.004	0.00057	0.004	0.00037
Sb	b.d.l.	0.00096	0.003	0.00096	b.d.l.	0.00088	b.d.l.	0.00083	b.d.l.	0.00098	b.d.l.	0.00088	b.d.l.	0.00082	b.d.l.	0.00098	b.d.l.	0.00088	b.d.l.	0.00082	b.d.l.	0.00098	b.d.l.	0.00088	b.d.l.	0.00082	b.d.l.	0.00098	b.d.l.	0.00088	b.d.l.	0.00082	b.d.l.	0.00098	b.d.l.	0.00088
Ba	b.d.l.	0.0015	b.d.l.	0.0015	b.d.l.	0.0017	b.d.l.	0.0016	b.d.l.	0.0016	b.d.l.	0.0015	b.d.l.	0.0014	b.d.l.	0.0016	b.d.l.	0.0015	b.d.l.	0.0014	b.d.l.	0.0016	b.d.l.	0.0015	b.d.l.	0.0014	b.d.l.	0.0016	b.d.l.	0.0015	b.d.l.	0.0014	b.d.l.	0.0016	b.d.l.	0.0015
La	0.001	0.00024	b.d.l.	0.00015	b.d.l.	0.00018	b.d.l.	0.00019	b.d.l.	0.00016	b.d.l.	0.00019	b.d.l.	0.00016	b.d.l.	0.00016	b.d.l.	0.00019	b.d.l.	0.00016	b.d.l.	0.00016	b.d.l.	0.00019	b.d.l.	0.00016	b.d.l.	0.00016	b.d.l.	0.00019	b.d.l.	0.00016	b.d.l.	0.00016	b.d.l.	0.00019
Ce	0.001	0.00022	b.d.l.	0.00021	b.d.l.	0.00023	b.d.l.	0.00022	b.d.l.	0.00022	b.d.l.	0.0002	b.d.l.	0.00019	b.d.l.	0.00022	b.d.l.	0.0002	b.d.l.	0.00019	b.d.l.	0.00022	b.d.l.	0.0002	b.d.l.	0.00019	b.d.l.	0.00022	b.d.l.	0.0002	b.d.l.	0.00019	b.d.l.	0.00022	b.d.l.	0.0002
Pr	b.d.l.	0.00007	0.0002	0.00009	b.d.l.	0.00009	b.d.l.	0.00008	b.d.l.	0.00008	b.d.l.	0.00007	b.d.l.	0.00008	b.d.l.	0.00008	b.d.l.	0.00007	b.d.l.	0.00008	b.d.l.	0.00008	b.d.l.	0.00007	b.d.l.	0.00008	b.d.l.	0.00008	b.d.l.	0.00007	b.d.l.	0.00008	b.d.l.	0.00008	b.d.l.	0.00007
Nd	b.d.l.	0.00057	b.d.l.	0.00044	b.d.l.	0.0004	b.d.l.	0.00035	0.00044	0.00045	b.d.l.	0.00052	b.d.l.	0.00042	0.00044	0.00045	b.d.l.	0.00052	0.00044	0.00045	0.00044	0.00045	0.00042	0.00052	0.00044	0.00045	0.00044	0.00045	0.00042	0.00052	0.00044	0.00045	0.00044	0.00045	0.00042	0.00052
Sm	0.0022	0.00055	b.d.l.	0.00045	b.d.l.	0.00031	b.d.l.	0.00027	0.0009	0.00019	b.d.l.	0.00031	0.001	0.00027	0.0009	0.00019	b.d.l.	0.00031	0.001	0.00027	0.0009	0.00019	b.d.l.	0.00031	0.001	0.00027	0.0009	0.00019	b.d.l.	0.00031	0.001	0.00027	0.0009	0.00019	b.d.l.	0.00031
Eu	b.d.l.	0.00015	b.d.l.	0.00017	b.d.l.	0.00015	b.d.l.	0.00011	0.0004	0.00011	b.d.l.	0.00013	b.d.l.	0.00017	0.0004	0.00011	b.d.l.	0.00013	0.0004	0.00011	0.0004	0.00011	b.d.l.	0.00013	0.0004	0.00011	0.0004	0.00011	b.d.l.	0.00013	0.0004	0.00011	0.0004	0.00011	b.d.l.	0.00013
Gd	b.d.l.	0.00073	b.d.l.	0.00062	b.d.l.	0.00061	b.d.l.	0.00063	b.d.l.	0.00059	b.d.l.	0.00065	b.d.l.	0.00065	b.d.l.	0.00059	b.d.l.	0.00065	b.d.l.	0.00065	b.d.l.	0.00059	b.d.l.	0.00065	b.d.l.	0.00065	b.d.l.	0.00059	b.d.l.	0.00065	b.d.l.	0.00065	b.d.l.	0.00059	b.d.l.	0.00065
Tb	b.d.l.	0.00009	0.0003	0.00011	b.d.l.	0.0001	b.d.l.	0.0001	0.0005	0.00011	b.d.l.	0.00011	b.d.l.	0.00009	0.0005	0.00011	b.d.l.	0.00011	0.0005	0.00011	0.0005	0.00011	b.d.l.	0.00011	0.0005	0.00011	0.0005	0.00011	b.d.l.	0.00011	0.0005	0.00011	0.0005	0.00011	b.d.l.	0.00011
Dy	0.0025	0.00036	0.0032	0.00042	0.0025	0.00043	0.00044	0.00061	0.0004	0.0004	0.00059	0.00056	0.00059	0.0006	0.0004	0.0004	0.00059	0.00056	0.00059	0.0006	0.0004	0.0004	0.00059	0.00056	0.00059	0.0006	0.0004	0.0004	0.00059	0.00056	0.00059	0.0006	0.0004	0.0004	0.00059	0.00056
Ho	0.0012	0.00012	0.0008	0.00012	0.0012	0.00014	0.0009	0.00012	0.0022	0.00011	0.0016	0.00018	0.0023	0.00016	0.0022	0.00011	0.0016	0.00018	0.0023	0.00016	0.0022	0.00011	0.0016	0.00018	0.0023	0.00016	0.0022	0.00011	0.0016	0.00018	0.0023	0.00016	0.0022	0.00011	0.0016	0.00018
Er	0.005	0.00055	0.0075	0.00067	0.0053	0.00058	0.00055	0.00064	0.0107	0.00058	0.0113	0.00084	0.0132	0.00093	0.0107	0.00058	0.0113	0.00084	0.0132	0.00093	0.0107	0.00058	0.0113	0.00084	0.0132	0.00093	0.0107	0.00058	0.0113	0.00084	0.0132	0.00093	0.0107	0.00058	0.0113	0.00084
Tm	0.0014	0.00014	0.0013	0.00013	0.0009	0.00012	0.00012	0.00015	0.0028																											

Table A6.2 continued (Chromites)

Poxy sample 15GLM01		Chromite Cuba																														
Phase	Chromite Madagascar																															
Location	rim	σ	core	σ	core	σ	rim	σ	rim	σ	rim	σ	core	σ	core	σ	rim	σ	rim	σ	core	σ	core	σ	rim	σ						
Li	8.75	0.38	7.59	0.41	7.23	0.32	9.74	0.30																								
B	8.46	0.5	10.85	0.48	8.85	0.59	8.36	0.49																								
Si	318	14	889	66	238	34	1701	11	68	22	455	32	230	25	1446	78	762	46	117	24	11231	624	115	22	84	23						
Ca	196	17	231	18	60	16	259	15	703	43	797	46	1042	54	1072	58	1073	57	423	44	670	48	999	55	1141	62						
Sc	1.576	0.065	1.318	0.055	0.748	0.056	1.131	0.043	3.89	0.19	3.55	0.18	3.91	0.19	2.52	0.16	2.96	0.17	4.72	0.23	3.83	0.2	3.14	0.18	3.09	0.18						
Ti	907	29	770	26	778	24	803	25	1397	46	1372	45	1554	52	1480	49	1711	57	1936	67	1466	51	1453	51	1483	53						
V	814	26	721	23	729	23	720	23	944	31	942	31	1005	33	985	32	1068	35	1039	34	949	32	971	33	984	33						
Cr	383083	12114	383083	12114	383083	12114	383083	12114	265559	8398	263233	8324	266790	8437	264670	8370	265901	8409	261454	8268	255913	8093	261386	8266	266995	8443						
Mn	1450	46	1499	47	1402	47	1509	44	1272	41	1225	39	1339	43	1300	41	1290	41	1246	40	1346	43	1325	43	1353	44						
Co	273	8	248	8	244	8	260	8	214	7	216	7	229	7	220	7	214	7	208	7	221	8	220	8	223	8						
Ni	901	28	718	23	902	22	740	28	1495	50	1589	53	1673	56	1657	56	1542	53	1435	51	1987	70	1548	56	1502	55						
Cu	0.213	0.048	0.563	0.056	1.145	0.052	0.736	0.066	0.36	0.099	b.d.l.	0.1	b.d.l.	0.11	1.36	0.14	n.d.	0.12	0.9	0.13	2.33	0.16	0.47	0.12	b.d.l.	0.13						
Zn	436	14	388	13	391	12	412	12	419	15	423	15	447	16	436	16	427	16	411	17	431	18	433	18	427	18						
Rb	0.433	0.017	0.411	0.017	0.278	0.017	0.400	0.015																								
Sr	0.898	0.031	0.380	0.015	0.155	0.015	0.384	0.010	0.081	0.029	0.349	0.036	n.d.	0.028	0.296	0.039	n.d.	0.032	n.d.	0.037	1.460	0.074	n.d.	0.033	n.d.	0.037						
Y	0.0210	0.0029	0.0410	0.0029	0.0130	0.0034	0.0230	0.0025	n.d.	0.0084	0.0540	0.0110	0.0370	0.0110	n.d.	0.0091	n.d.	0.0085	0.0290	0.0120	0.1060	0.0160	0.0490	0.0120	0.0600	0.0140						
Zr	2.906	0.097	2.415	0.064	1.442	0.080	1.870	0.051	0.948	0.069	0.867	0.067	1.135	0.081	1.143	0.084	1.020	0.077	2.210	0.140	1.089	0.084	1.001	0.081	0.783	0.072						
Nb	1.284	0.043	1.217	0.040	1.153	0.041	1.171	0.039	0.886	0.047	0.900	0.048	0.855	0.047	0.849	0.048	0.873	0.049	0.868	0.050	0.704	0.043	0.672	0.042	0.810	0.049						
Sb	b.d.l.	0.004	0.046	0.009	b.d.l.	0.005	0.119	0.004																								
Ba	3.210	0.120	1.416	0.068	0.438	0.057	1.724	0.028	b.d.l.	0.039	0.455	0.061	n.d.	0.035	n.d.	0.040	0.102	0.039	0.187	0.054	1.700	0.120	n.d.	0.040	b.d.l.	0.038						
La	0.1221	0.0060	0.0233	0.0027	0.0097	0.0022	0.0324	0.0016	n.d.	n.d.	n.d.	n.d.	n.d.	n.d.	n.d.	n.d.	n.d.	n.d.	n.d.	n.d.	n.d.	n.d.	n.d.	n.d.	n.d.	n.d.						
Ce	0.1595	0.0072	0.0332	0.0037	0.0121	0.0037	0.0362	0.0040	n.d.	n.d.	n.d.	n.d.	n.d.	n.d.	n.d.	n.d.	n.d.	n.d.	n.d.	n.d.	n.d.	n.d.	n.d.	n.d.	n.d.	n.d.						
Pr	0.0091	0.0013	b.d.l.	0.0011	b.d.l.	0.0010	b.d.l.	0.0011	n.d.	n.d.	n.d.	n.d.	n.d.	n.d.	n.d.	n.d.	n.d.	n.d.	n.d.	n.d.	n.d.	n.d.	n.d.	n.d.	n.d.	n.d.						
Nd	b.d.l.	0.0046	0.0100	0.0033	b.d.l.	0.0034	b.d.l.	0.0032	n.d.	n.d.	n.d.	n.d.	n.d.	n.d.	n.d.	n.d.	n.d.	n.d.	n.d.	n.d.	n.d.	n.d.	n.d.	n.d.	n.d.	n.d.						
Sm	0.0083	0.0031	0.0069	0.0030	b.d.l.	0.0026	0.0071	0.0020	n.d.	n.d.	n.d.	n.d.	n.d.	n.d.	n.d.	n.d.	n.d.	n.d.	n.d.	n.d.	n.d.	n.d.	n.d.	n.d.	n.d.	n.d.						
Eu	0.0047	0.0012	b.d.l.	0.0012	0.0050	0.0010	0.0030	0.0015	n.d.	n.d.	n.d.	n.d.	n.d.	n.d.	n.d.	n.d.	n.d.	n.d.	n.d.	n.d.	n.d.	n.d.	n.d.	n.d.	n.d.	n.d.						
Gd	b.d.l.	0.0045	b.d.l.	0.0046	b.d.l.	0.0037	b.d.l.	0.0043	n.d.	n.d.	n.d.	n.d.	n.d.	n.d.	n.d.	n.d.	n.d.	n.d.	n.d.	n.d.	n.d.	n.d.	n.d.	n.d.	n.d.	n.d.						
Tb	b.d.l.	0.0007	b.d.l.	0.0007	b.d.l.	0.0006	0.0025	0.0007	n.d.	n.d.	n.d.	n.d.	n.d.	n.d.	n.d.	n.d.	n.d.	n.d.	n.d.	n.d.	n.d.	n.d.	n.d.	n.d.	n.d.	n.d.						
Dy	b.d.l.	0.0015	b.d.l.	0.0015	b.d.l.	0.0015	b.d.l.	0.0016	n.d.	n.d.	n.d.	n.d.	n.d.	n.d.	n.d.	n.d.	n.d.	n.d.	n.d.	n.d.	n.d.	n.d.	n.d.	n.d.	n.d.	n.d.						
Ho	b.d.l.	0.0004	b.d.l.	0.0002	0.0006	0.0003	b.d.l.	0.0002	n.d.	n.d.	n.d.	n.d.	n.d.	n.d.	n.d.	n.d.	n.d.	n.d.	n.d.	n.d.	n.d.	n.d.	n.d.	n.d.	n.d.	n.d.						
Er	0.0477	0.0046	0.0718	0.0043	0.0391	0.0055	0.0428	0.0047	n.d.	n.d.	n.d.	n.d.	n.d.	n.d.	n.d.	n.d.	n.d.	n.d.	n.d.	n.d.	n.d.	n.d.	n.d.	n.d.	n.d.	n.d.						
Tm	0.1501	0.0057	0.2090	0.0062	0.1719	0.0073	0.1683	0.0066	n.d.	n.d.	n.d.	n.d.	n.d.	n.d.	n.d.	n.d.	n.d.	n.d.	n.d.	n.d.	n.d.	n.d.	n.d.	n.d.	n.d.	n.d.						
Yb	0.0038	0.0018	0.0083	0.0023	b.d.l.	0.0024	0.0084	0.0016	n.d.	n.d.	n.d.	n.d.	n.d.	n.d.	n.d.	n.d.	n.d.	n.d.	n.d.	n.d.	n.d.	n.d.	n.d.	n.d.	n.d.	n.d.						
Lu	0.0018	0.0005	b.d.l.	0.0003	b.d.l.	0.0003	b.d.l.	0.0004	n.d.	n.d.	n.d.	n.d.	n.d.	n.d.	n.d.	n.d.	n.d.	n.d.	n.d.	n.d.	n.d.	n.d.	n.d.	n.d.	n.d.	n.d.						
Hf	0.0426	0.0053	0.0420	0.0040	0.0158	0.0048	0.0263	0.0032	n.d.	0.0100	n.d.	0.0043	n.d.	0.0160	n.d.	0.0170	n.d.	0.0049	n.d.	0.0330	n.d.	0.0130	n.d.	0.0170	n.d.	0.0150						
Ta	b.d.l.	0.0011	b.d.l.	0.0010	b.d.l.	0.0010	b.d.l.	0.0010	n.d.	0.0024	n.d.	0.0029	n.d.	0.0038	b.d.l.	0.0030	0.0117	0.0051	0.0191	0.0060	n.d.	0.0040	n.d.	0.0041	n.d.	0.0037						
Pb	0.0800	0.0051	0.0507	0.0046	0.0596	0.0039	0.0679	0.0044	0.0235	0.0099	n.d.	0.0088	0.0230	0.0100	0.0320	0.0120	b.d.l.	0.0086	n.d.	0.0110	0.0580	0.0130	n.d.	0.0094	b.d.l.	0.0110						
Th	0.0206	0.0017	0.0016	0.0005	0.0015	0.0004	0.0024	0.0004	n.d.	0.0030	0.0000	b.d.l.	n.d.	0.0034	n.d.	0.0025	n.d.	0.0007	0.0000	b.d.l.	n.d.	0.0010	b.d.l.	0.0034	0.0460	0.0100						
U	0.0174	0.0014	0.0036	0.0008	0.0025	0.0006	0.0059	0.0005	n.d.	0.0010	<	0.00055	0.0005	n.d.	0.0016	0.0098	0.0032	n.d.	0.0017	n.d.	0.0018	n.d.	0.0016	n.d.	0.0004	0.0013						

Table A6.3 Solutions ICP-MS - Trace element compositions of silicate mineral

n.d. = not detected b.d.l. = below detection limit

Mineral	Olivine San Carlos				Clinopyroxene Inagli				Clinopyroxene Madagascar				Cr-Diopside		Diopside glass		
	<i>ol SC 1</i>	σ	<i>ol SC 2</i>	σ	<i>cpx INA 1</i>	σ	<i>cpx INA 2</i>	σ	<i>cpx MAD 1</i>	σ	<i>cpx MAD 2</i>	σ	<i>Cr-diop</i>	σ	<i>diop</i>	σ	
Cr	178	1	173	2	2015	17	2024	20	28.04	0.35	24.99	0.41	190	2			
(ppb)																	
Li	2159	111	2041	103	608	103	629	104	956	105	910	102	2300	101	7843	103	
Sc	4025	43	3829	31	58739	531	61117	323	7271	173	7318	134	76760	617	1221	24	
Ti	42013	516	39942	462	510525	6050	526418	2680	1220492	16088	1193139	6791	1248448	10157	122155	754	
V	4608	43	4400	56	5688	85	5850	15	25530	309	25034	129	23623	110	29082	87	
Mn	997689	817	955459	8971	340577	3847	349611	804	473402	4944	455393	1493	911973	4020	7093	102	
Co	142495	943	139019	1506	15303	41	15716	83	4184	93	4102	7	43385	213	1323	10	
Ni	2982726	16912	2930049	43642	220152	1376	223797	726	5492	405	5475	365	149637	1378	42163	501	
Cu	7668	70	7884	99	422	73	117	70	418	87	884	81	9659	141	59680	188	
Zn	50119	12648	64872	12683	b.d.l.	12651	b.d.l.	12644	33628	12654	32358	12659	b.d.l.	12645	b.d.l.	12644	
Ga	98.2	1.5	94.1	10.8	1280	45	1296	29	10398	114	10021	160	2858	38	4348	59	
Rb	39.5	2.8	37.9	2.6	28.5	2.3	41.3	2.2	89	2	103	4	2260	9	509	2	
Sr	691	23	584	30	1867257	11015	1885115	4310	76752	882	71975	351	597550	2394	229129	1692	
Y	68	2	58	1	4133	33	4169	10	14033	115	13220	116	5568	16	470	3.93	
Zr	273	3	244	2	3371	37	3476	19	192598	2558	180318	739	5864	7	205536	792	
Nb	122	2	116	1	21	1	22	1	832	12	736	4	104	2	403	11	
Cd	137	9	300	11	58	9	46	9	414	15	385	9	103	9	2447	21	
Sn	2155	121	4718	119	b.d.l.	119	b.d.l.	118	2417	119	2157	122	654	119	6315	126	
Sb	27.4	1.0	53.0	1.0	b.d.l.	21.93	b.d.l.	1.09	52.2	2.1	55.2	1.3	12.7	1.1	451	4	
Cs	1.33	0.24	1.38	0.13	4.21	0.23	3.73	0.39	4.60	0.10	4.18	0.16	44.76	0.52	24.86	0.51	
Ba	929	61	513	63	4932	79	4414	67	2161	74	2105	62	45758	197	51862	275	
La	22.3	1.1	27.8	1.2	6130	44	6106	10	32473	216	29619	242	5677	27	926	2.89	
Ce	41	1	51	1	15350	224	15301	53	87282	756	79553	888	13775	66	1655	4.17	
Pr	4.94	0.20	6.20	0.19	2349	21	2311	19	11716	83	10667	81	2184	17	167	0.69	
Nd	18.88	1.28	24.27	0.74	10769	43	10681	30	44233	212	40408	418	10469	42	582	4.88	
Sm	4.60	0.26	5.41	0.91	2351	36	2332	5	6765	54	6159	104	2413	24	95	0.76	
Eu	1.91	0.15	1.97	0.12	731	4	724	9	1118	11	1023	8	734	4	26	0.79	
Gd	5.62	0.95	5.87	1.23	1840	31	1827	4	4614	17	4204	23	2142	8	92	1.11	
Tb	1.13	0.07	1.06	0.04	197	2	192	2	546	4	500	6	244	0	13	0.53	
Dy	7.94	0.33	8.18	0.34	894	11	872	7	2719	17	2457	38	1181	3	73	0.52	
Ho	2.10	0.21	1.80	0.05	138	2	136	2	467	1	419	4	192	1	14	0.31	
Er	7.24	0.72	6.53	0.78	288	7	285	4	1042	12	934	11	386	2	34	1.61	
Tm	1.46	0.09	1.39	0.14	39	1	38	1	138	1	124	2	48	1	5	0.21	
Yb	12.06	0.24	12.10	0.85	278	7	274	2	848	4	759	21	273	7	43	1.00	
Lu	2.74	0.21	2.80	0.11	50	1	49	1	117	2	104	1	40	0	5	0.15	
Hf	5.55	0.32	5.05	0.09	144	3	142	2	4390	10	3942	48	186	3	3482	25.15	
Ta	2.71	0.03	3.69	0.05	1.77	0.11	1.50	0.06	183	3	143	1	6.35	0.19	1037	n.d.	
Pb	4614	33.52	7506	91.22	956	28	870	31	1503	21	1384	8	2359	11	22313	183.50	
Th	5.14	0.35	5.08	0.45	22.7	1.3	20.9	1.1	3380	49	3133	44	225	1	169	1.42	
U	3.84	0.32	3.85	0.30	12.6	0.5	10.7	0.2	141	2	130	3	276	3	3430	19.70	

Table A6.4 Solutions ICP-MS - Trace element compositions of chromites

n.d. = not detected b.d.l. = below detection limit

Mineral	Chromite Madagascar												Chromite Cuba											
	chr MAD 1	σ	corrected	chr MAD 2	σ	corrected	chr MAD 3	σ	corrected	chr MAD 4	σ	corrected	CU 1	σ	corrected	CU 2	σ	corrected	CU 4	σ	corrected			
Cr	294231	3433		265816	3829		283472	4053		232585			142774			188968			65613					
Cr-yield																								
Digestion (ppb)	77			69			73			60			54			72			25					
Li	7244	199	9420	5647	109	8232	5774	127	7920	4671	107	7798	478	2	883	528	12	736	476	3	1913			
Sc	4857	148	6316	4073	101	5937	4094	47	5616	3509	26	5857	3175	29	5860	3678	26	5130	2391	32	9604			
Ti	722268	8289	939231	545986	5574	795898	572580	5024	785432	454190	3343	758248	887136	6978	1637550	1026373	2945	1431435	365853	4532	1469514			
V	571304	8447	742918	411647	5402	600068	440524	4361	604286	353258	5156	589746	624224	3826	1152245	722140	1563	1007135	240647	1387	966603			
Mn	976228	8814	1269478	750975	7869	1094715	792565	10273	1087195	657678	9087	1097960	751972	1914	1388054	862231	7293	1202513	364973	2740	1465980			
Co	179106	1727	232907	132373	1642	192963	142238	1464	195114	115828	1539	193369	139336	826	257198	151227	1104	210910	54602	689	219319			
Ni	936711	12326	1218090	759437	6305	1107051	788721	7417	1081922	640033	8495	1068503	1436335	8928	2651308	1528806	10078	2132156	740104	8899	2972757			
Cu	7110	116	9246	7296	119	10636	6927	149	9503	6008	106	10030	4448	33	8210	4898	45	6831	4314	14	17328			
Zn	306915	13148	399109	225201	12801	328281	235160	13030	322579	189940	13234	317095	229933	1788	424429	257442	1299	359043	90278	1471	362616			
Ga	22528	518	29295	16010	218	23338	17749	231	24347	14122	159	23576	31772	302	58647	38700	10	53973	13781	147	55356			
As	718	20	934	642	35	936	669	47	918	554	33	925	-	-	-	-	-	-	-	-	-			
Rb	157	7	205	185	7	269	211	7	290	193	3	322	159	3	293	175	5	244	59	2	237			
Sr	1044	36	1357	1110	44	1618	1189	52	1631	1066	33	1779	2101	32	3877	2617	14	3650	2266	26	9103			
Y	316	3	411	323	3	471	336	6	461	291	4	485	626	5	1156	792	9	1105	672	1	2698			
Zr	1739	12	2261	1726	57	2516	1881	23	2580	4139	19	6910	571	8	1053	696	5	970	429	18	1723			
Nb	281	6	366	256	2	374	282	5	388	240	3	401	89.2	1.7	165	107	2	150	39.1	1.7	157			
Cd	52.5	8.6	68.2	51.2	10.4	74.6	58.8	8.8	80.6	45.7	8.8	76.3	-	-	-	-	-	-	-	-	-			
Sn	412	118	536	478	119	697	448	119	615	357	118	596	171	2	316	132	2	184	125	1	501			
Sb	201	6	261	213	2	311	223	1	306	212	5	354	36.44	3.16	67.27	52.53	5.89	73.26	42.81	2.18	171.97			
Cs	14.97	0.16	19.47	15.49	0.91	22.58	16.52	1.22	22.66	13.12	0.73	21.90	-	-	-	-	-	-	-	-	-			
Ba	3138	72	4081	3164	75	4612	3321	96	4556	3160	71	5275	2628	48	4851	3518	78	4906	3061	52	12295			
La	327	29	426	323	5	470	343	2	471	297	3	496	5696	24	10515	7371	63	10280	6520	39	26188			
Ce	657	6	855	691	11	1007	740	6	1014	628	2	1048	12084	62	22305	15535	180	21665	13713	30	55079			
Pr	71	1	93	76	1	110	80	2	109	69	0	115	1179	2	2177	1533	17	2137	1354	6	5437			
Nd	264	5	343	278	4	405	302	6	415	255	5	425	4295	21	7928	5606	29	7818	4941	17	19846			
Sm	46.9	0.7	61.0	50.0	0.6	72.8	52.9	0.6	72.5	43.6	1.3	72.8	621	5	1146	799	1	1115	712	12	2860			
Eu	18.4	0.9	23.9	19.1	0.6	27.8	20.2	0.2	27.8	18.0	0.6	30.0	125	1	230	159	3	222	146	3	584			
Gd	45.6	1.3	59.3	50.5	2.3	73.7	50.6	4.2	69.3	45.3	3.3	75.6	347	6	641	452	9	631	406	4	1629			
Tb	7.21	0.42	9.38	7.74	0.40	11.28	8.29	0.30	11.37	8.06	0.11	13.46	37.34	0.41	68.93	48.10	0.25	67.09	42.99	0.68	172.69			
Dy	47.8	1.2	62.2	54.1	2.3	78.8	55.8	2.5	76.6	49.3	1.1	82.4	153	2	283	202	3	282	181	3	727			
Ho	10.78	0.04	14.02	11.89	0.34	17.33	12.53	0.29	17.19	11.34	0.17	18.93	21.54	0.09	39.76	29.26	0.85	40.81	26.13	0.74	104.95			
Er	32.1	1.5	41.8	36.0	1.3	52.4	36.6	1.1	50.2	33.3	1.6	55.6	54	2	100	70	2	98	59	3	238			
Tm	5.23	0.18	6.80	5.62	0.21	8.19	6.29	0.06	8.63	5.91	0.17	9.87	6.83	0.28	12.61	8.31	0.45	11.58	6.42	0.18	25.78			
Yb	37.5	1.4	48.7	44.7	1.3	65.2	44.1	2.0	60.5	41.9	2.0	70.0	31.7	0.4	58.6	38.1	0.6	53.1	33.5	0.9	134.7			
Lu	6.59	0.22	8.57	7.00	0.40	10.20	7.88	0.11	10.81	7.21	0.29	12.04	4.13	0.16	7.62	5.31	0.44	7.41	4.96	0.03	19.90			
Hf	59.2	0.9	77.0	62.8	1.3	91.5	69.6	1.6	95.4	126.1	0.5	210.5	11.13	0.29	20.55	13.10	0.51	18.27	9.47	0.94	38.05			
Ta	4.73	0.22	6.15	5.25	0.64	7.65	5.18	0.35	7.11	9.54	0.53	15.93	0.63	0.11	1.17	0.51	0.12	0.71	b.d.l.	0.12	b.d.l.			
Pb	486	10	632	525	11	766	515	9	706	362	9	605	557	3	1028	693	5	967	558	3	2240			
Th	31.6	1.7	41.1	31.9	1.1	46.6	32.8	0.6	44.9	27.7	0.5	46.3	732	3	1351	944	9	1317	789	5	3170			
U	118	4	154	124	1	180	126	3	173	113	2	189	74	1	137	95	1	132	78	2	313			

Table A6.5 Quality of LA-ICP-MS data

Spot size	BIR mean (ppm)		USGS BIR-1G GeoRem		Reproducibility %	Accuracy %	SENSITIVITY (cps/ppm) / spot size				Detect. Limit (ppm)	
	Average		Pref. Values				102		77		102	77
	(7 spots)	σ	(ppm)	σ			MEAN	σ	MEAN	σ		
Li	3.15	0.12	3.00	0.70	3.87	0.33	6756	641	2863	445	0.0185	0.0527
B	17.10	4.97	12.40	0.40	29.06	13.67	8708	1338	2553	1024	0.0529	0.1090
Sc	44.83	1.00	43.00	3.00	2.23	0.41	17611	1268	7754	1071	0.0166	0.0271
Ti	7231	493	5400	200	6.82	7.05	1462	78	661	109	0.1470	0.3180
V	353	11	326	32	3.13	0.98	16200	981	7616	926	0.0034	0.0072
Cr	369	n.d.	392	24	n.d.	5.12	n.d.	n.d.	5167	625	n.d.	n.d.
Mn	1375	39	1472	77	2.85	0.93	18850	1401	8168	1258	0.0214	0.0394
Co	55.15	0.61	52.00	5.00	1.11	4.21	21795	1592	9219	1644	0.0033	0.0097
Ni	161.6	15.3	178.0	18.0	9.50	0.96	810	40	357	33	0.3040	0.6170
Cu	116.2	5.8	119.0	12.0	4.95	3.43	13499	916	5935	939	0.0101	0.0237
Zn	75.09	4.52	78.00	17.00	6.02	4.14	3622	144	1767	203	0.0195	0.0337
Rb	0.193	0.010	0.197	0.007	5.42	1.08	22506	1511	10211	1286	0.0026	0.0060
Sr	104.6	2.4	109.0	2.0	2.32	5.80	58595	4643	25942	3870	0.0022	0.0096
Y	13.72	0.36	14.30	1.40	2.61	4.38	27879	1929	12426	2200	0.0007	0.0011
Zr	12.58	0.35	14.00	1.20	2.74	0.27	12844	816	5807	1057	0.0050	0.0095
Nb	0.493	0.017	0.520	0.040	3.36	2.45	23214	1525	10638	1850	0.0005	0.0002
Sb	0.569	0.020	0.560	0.090	3.46	1.03	9584	437	4533	497	0.0025	0.0045
Ba	6.097	0.113	6.500	0.070	1.85	2.94	4130	286	1827	251	0.0039	0.0062
La	0.582	0.007	0.609	0.020	1.19	3.75	23894	1093	11598	1593	0.0006	0.0006
Ce	1.844	0.029	1.890	0.040	1.56	3.42	24809	1119	12276	1404	0.0004	0.0008
Pr	0.348	0.004	0.370	0.020	1.19	6.67	34507	2066	15931	2187	0.0002	0.0002
Nd	2.217	0.083	2.370	0.030	3.74	4.42	5733	375	2519	392	0.0008	<0.00000
Sm	1.031	0.027	1.090	0.020	2.58	4.75	5265	431	2241	369	0.0009	<0.00000
Eu	0.490	0.025	0.517	0.005	5.20	1.78	17000	1298	7242	1122	0.0003	<0.00000
Gd	1.836	0.064	1.850	0.020	3.46	0.68	5816	623	2181	431	0.0017	0.0029
Tb	0.348	0.006	0.350	0.040	1.79	0.52	31461	2368	13092	2372	0.0003	0.0003
Dy	2.568	0.030	2.550	0.020	1.17	0.14	10282	815	4270	779	0.0005	0.0003
Ho	0.561	0.009	0.560	0.030	1.56	0.47	41441	3339	17246	3181	0.0001	<0.00000
Er	1.712	0.042	1.700	0.020	2.47	1.47	9511	759	3954	731	0.0006	0.0005
Tm	0.241	0.002	0.240	0.030	1.02	0.60	41150	3275	17101	3061	0.0001	<0.00000
Yb	1.645	0.029	1.640	0.030	1.74	0.86	7159	608	2868	527	0.0005	0.0006
Lu	0.250	0.007	0.248	0.009	2.99	0.50	38768	3138	15963	2896	0.0001	<0.00000
Hf	0.509	0.025	0.570	0.030	4.85	6.12	6529	485	2749	484	0.0002	0.0004
Ta	0.035	0.002	0.036	0.006	6.29	3.47	30561	2450	12480	2557	0.0004	0.0007
Pb	3.407	0.075	3.700	0.300	2.19	7.51	17522	1418	7487	1011	0.0013	0.0021
Th	0.028	0.002	0.030	0.002	6.42	9.92	33666	2262	14776	2362	0.0000	<0.00000
U	0.017	0.000	0.023	0.006	2.48	26.53	39000	2776	16678	2247	0.0001	<0.00000

Table A6.6 Quality of ICP-MS data

	LOD	Batch blanks <i>n</i> = 3	UBN		BIR-1			DT-S		
			Average <i>n</i> = 3	σ	Pref'd values	Average <i>n</i> = 3	σ	Pref'd values	<i>n</i> = 1	Pref'd values
<i>ppm</i>										
Li	0.004	0.05	26.0	1.5	26.8	2.6	0.7	3.2	1.9	2.0
Sc	0.002	0.0004	15.2	0.7	13.2	49.0	6.8	43.0	4.2	3.5
Ti	0.1	0.06	733	38	560	6684	905	5600	21.3	19.0
V	0.004	0.004	64.8	3.7	71.4	315.3	42.4	319.0	6.2	9.3
Mn	0.03	0.09	919	49	1028	1218	135	1363	915	912
Co	0.003	0.007	98	6	99	49	5	52	133	133
Ni	0.07	0.7	1912	101	1966	163	17	166	2331	2319
Cu	0.003	0.2	24.1	0.1	27.5	112	12	119	5.7	6.0
Zn	0.2	7.2	84	6	85	72	10	72	40	45
<i>ppb</i>										
Ga	3.6	0.7	2558	81	3157	14716	1032	15300	291	0
Rb	2.7	6.2	3206	156	3761	186	12	200	49	61
Sr	2.8	49.7	7774	405	8169	105788	7526	109000	331	343
Y	0.4	1.3	2482	89	2584	14461	933	15600	31	33
Zr	1.6	9.1	3487	187	3931	14514	1281	14000	134	198
Nb	0.4	4.4	55.7	2.6	61.0	608.4	22.2	550.0	13.3	17.6
Cd	0.3	5.2	57.1	5.1	49.3	150.3	3.7	97.0	28.5	6.4
Sn	14	64.5	172	2	370	576	68	600	309	583
Sb	0.9	3.7	276	71	243	422	25	460	401	518
Cs	0.2	0.4	9800	414	10835	5.5	0.6	7.0	7.0	6.3
Ba	3.8	136.0	23974	1274	26859	5935	153	7140	292	340
La	0.2	1.2	311	1	336	572	17	615	23	33
Ce	0.5	1.5	704	6	829	1623	58	1920	42	56
Pr	0.1	0.2	103	1	124	314	13	370	4.9	6.2
Nd	1.3	0.7	517	10	619	2013	84	2380	19.0	24.2
Sm	0.3	0.2	182	6	220	908	28	1120	3.2	4.7
Eu	0.1	-	74	3	83	477	34	530	0.8	1.1
Gd	0.3	0.2	306	10	314	1753	114	1870	3.9	4.3
Tb	0.0	0.0	55	2	60	333	22	360	0.7	0.7
Dy	0.2	0.1	399	14	416	2416	173	2510	4.2	4.8
Ho	0.1	0.0	89	3	95	537	40	560	1.1	1.3
Er	0.2	-	232	11	283	1389	111	1660	4.1	4.9
Tm	0.1	-	35.2	1.7	43.7	205	16	250	0.9	1.1
Yb	0.1	0.1	238	8	291	1344	124	1650	7.8	9.4
Lu	0.0	0.0	36.8	1.6	46.6	201	17	250	1.7	2.4
Hf	0.4	0.2	109	5	130	531	44	582	4.3	6.6
Ta	0.0	-	18	1	21	69	7	36	1.3	1.3
Pb	7.3	41.3	12851	133	13132	2817	144	3100	7126	9279
Th	0.3	0.4	53.4	2.4	72.1	28.6	2.5	32.0	8.2	9.8
U	0.1	0.1	47.0	3.0	62.2	9.9	0.5	10.0	2.9	3.3

CURRICULUM VITAE CARLOTTA FERRANDO

Address	VIA PREMANICO 37, GENOVA (ITALY)
Tel.	+393288006689
E-mail	carlotta.ferrando@gm.univ-montp2.fr
Nationality	Italian
Date of birth	04/01/1990

RESEARCH INTEREST

Oceanic lithosphere petrology, major and trace elements geochemistry, microstructural geology, structural geology, geological mapping

CURRENT PROFESSIONAL STATUS

PhD degree in igneous petrology in the framework of the Marie-Curie Initial Training Network ABYSS: “Melt transport and dissolution-precipitation processes through the heterogeneous lower oceanic crust: microstructural and petro-geochemical constraints from drill cores” at Geosciences Montpellier, CNRS, University of Montpellier

Contract started : **15 November 2014** , Defended : **6 December 2017**

EDUCATION

23/10/2014 - Master's Degree in Geology and Geological Techniques (Earth Science, Genova)

University: Università degli Studi di Genova (Italia)

Thesis subject: Microstructural and petrological investigations on troctolites, olivine gabbros and peridotites in ophiolites outcrop Erro Tobbio (Piani di Praglia, Genova)

EXPERIENCE

Field work: **30/11/2015-30/01/2016** – Member of the Shipboard Scientific Party (structural geology team) of IODP Expedition 360 “SW Indian Ridge Lower Crust and Moho” *Preliminary research project:* Slow-spread lower crust accretion: insights on processes recorded by petro-structural and chemical variations in olivine-rich gabbroic rocks from Hole U1473A.

Teaching and mentoring: **01/08/2015-15/11/2016** - Master student monitoring (Monika Dolinska): Crystallographic Preferred Orientation and In-situ chemical analyses

Erasmus experience: **19/09/2011-14/07/2012** - Universidad de Zaragoza (España); 3rd year Bachelor's Degree in Geology Sciences

SKILLS

EBSD and microstructural analyses; EPMA analyses; ICP-MS and LA-ICP-MS analyses; field mapping; Microsoft office (Word, Excel, and PowerPoint); Adobe Illustrator; Corel Draw; MATLAB; ImageJ

TRAINING

ABYSS short courses

26/04-02/05/2015 - Formation and evolution of the Ocean Crust including everyday field trip and calculation exercises on “thermal aspects of mid-ocean ridges” and “magma chambers modelling”, *ABYSS Short-Course 1* by D. Teagle and T. Henstock, Troodos ophiolite (Cyprus);

25-26-30/05/2015 - Experimental geology, *ABYSS Short-Course 4a* by J. Koepke and R. Almeev, University of Hannover (Germany);

5-9/10/2015 - Imaging and analytical techniques for (bio)petrology, *ABYSS Short-Course 3* by B. Ménez, IPGP, Paris (France);

4-6/04/2016 - Course on experimental geology, *ABYSS Short-Course 4b* by P. Fumagalli, University of Milan, Milano (Italy);

7-9/09/2016 – Microstructures and modelling reaction driven fracturing, *ABYSS Short-Course 5* by H. Austrheim and B. Jamtveit, Oslo (Norway).

Other short courses

24-28/08/2015 - Application of diffusion studies to the determination of timescales in geochemistry and petrology, *DMG/MSA Short-Course*; S. Chakraborty and Dohmen R., Bochum (Germany);

31/08-11/09/2015 - Ocean crust processes: magma, faults, fluxes and life, *ECORD Summer School 2015* by W. Bach, G. Früh-Green, C. Garrido, F. Klein, B. Menez, A. Morris, U. Röhl, T. Schroeder, D. Teagle, R. Tribuzio et al., MARUM - IODP Bremen Core Repository, Bremen (Germany);
12-18/02/2017 - School on MELting and fluid/melt-rock REactions in the MAntle, *Winter School MEREMA* G. Ceuleneer, M. Ghiorso, K. Hidas, Y. Liang, A. Luguét, C. Marchesi, A. Montanini, O. Müntener, E. Rampone, A. Sanfilippo, A. Stracke et al., Pavia (Italy).

PARTICIPATION TO WORKSHOPS AND CONFERENCES

ABYSS workshops

23-27/11/2014- *ABYSS Workshop 1*, Montpellier (France);
27-29/05/2015 - *ABYSS Workshop 2* - invited speakers P. Kelemen and G. Früh-Green, Institut für Mineralogie, Hannover (Germany);
12-13/10/2015 - *ABYSS Mid-Term Meeting1* and *Outreach Workshop*, IPGP, Paris (France);
7-10/04/2016 - *ABYSS Mid-Term Meeting2* and *Outreach Workshop* - invited speakers M. Scambelluri & R. Tribuzio, Sestri Levante (Italy);
1-2/09/2016 - *ABYSS Workshop 3*, Oslo Science Park (Norway);
2-6/04/2017 - *ABYSS Mid-Term Meeting 3*, Centro Tecnológico IACT, CSIC, Granada (Spain);
27/09-30/10/2017 - *ABYSS Workshop 4* and *Final ABYSS Meeting*, NOCS, Southampton (England).

International workshops, conferences and meetings

02-03/04/2015 - Introduction to MTEX open source and free texture analysis training, *MTEX Workshop at ESF-MicroDICE conference* by D. Mainprice, Montpellier (France);
13-16/05/2015 - Indian Ocean Crust and Mantle Drilling - IODP Expedition 360, *US-CHINA IODP Joint Drilling Workshop* by H. Dick, C. MacLeod et al., Woods Hole MA (USA);
11-15/09/2016 - 2nd European Mineralogical Conference (EMC2) - Rimini, Italy;
23-28/04/2017 - EGU General Assembly 2017, Vienna, Austria.
11-15/12/2017 - AGU Fall Meeting 2017, New Orleans, USA.

MISCELLANY

Outreach activity

9/10/2015 - "La Fête de la Science" and launch of the Searocks Blog, *ABYSS Outreach event*, IPGP, Paris (France).

Grants

- ECORD Scholarship to attend the ECORD Summer School 2015 in Bremen;
- Ecole Doctoral GAIA Scholarship to attend the AGU Fall Meeting 2017 in New Orleans.

Language: Italian (mother tongue), English (fluent, written); Spanish (fluent, written); French (fluent), Courses: French, A2B Immersion B2 (01/01-30/03/2015)

LIST OF PUBLICATIONS

Reports

MacLeod, C.J., Dick, H.J.B., Blum, P., and the Expedition 360 Scientists, **2017**. Southwest Indian Ridge Lower Crust and Moho. *Proceedings of the International Ocean Discovery Program, 360: College Station, TX (International Ocean Discovery Program)*. <http://dx.doi.org/10.14379/iodp.proc.360.101.2017>

Ciążela, J., Dick, H. J. B., MacLeod, C. J., Blum, P. and the Expedition 360 Scientists, **2016**. ARTYKUŁY INFORMACYJNE, Ekspedycja IODP 360: pierwszy etap odwiertu do płaszcza Ziemi. *Przegląd Geologiczny, vol. 64, nr 1*.

Peer Reviewed Journals

Ferrando, C., Godard, M., Ildefonse, B., Rampone, E., **in press**. Melt transport and mantle assimilation at Atlantis Massif (IODP Site U1309): constraints from geochemical modeling. In Press LITHOS6645 (submitted Sept 2017, Accepted Jan 2018). doi:10.1016/j.lithos.2018.01.012

Basch, V., Rampone, E., Crispini, L., **Ferrando, C.**, Ildefonse, B., Godard, M., 2018. From mantle peridotites to hybrid troctolites: textural and chemical evolution during melt-rock interaction history (Mt.Maggiore, Corsica, France). In press Lithos, Special Volume "ABYSS".

Ferrando, C., Godard, M., Ildefonse, B., in prep. Ca and REE chemical profiles: a record of subsolidus re-equilibration in Olivine-rich troctolites from Hole U1309D?

Abstracts

Ferrando, C., Ildefonse, B., **2015**. Microstructural analysis of olivines in Erro-Tobbio troctolites: crystallographic preferred orientations and misorientation patterns, in MicroDICE Final conference - ESF research networking Programme on the Micro-Dynamics of Ice, 30 March - 1st April 2015, Montpellier, France. (poster)

Basch, V., Rampone, E., Ferrando, C., Ildefonse, B., Crispini, L. and Godard, M., **2015**, Microstructural variations in lower crustal oceanic troctolites: an indicator of melt-rock interactions (Erro Tobbio, Ligurian ophiolites, Italy), in A dynamic planet: developments and perspectives 100 years after Wegener, 02-04 September 2015, Florence, Italy. SIMP-SGI-AIV-SoGei Congress - Rendiconti Online Soc. Geol. It. Volume 35 Suppl. 2, p. 38. (poster)

Ferrando, C., Godard, M., Ildefonse, B., **2016**. New constraints on the formation of heterogeneous oceanic crust at slow spreading ridges: a detailed petro-geochemical study of the olivine-rich troctolites from Atlantis Massif (MAR, IODP Hole U1309D, 30°N), in EMC (European Mineralogical Conference), 10-17 September 2016, Rimini, Italy. EMC Book of abstract, p.42. (oral).

Deans, J.R., Cheadle, M.J., Ferrando, C., Plümpner, O., Viegas, G., **2016**. Insights into oceanic core complex formation from structural studies of IODP Hole U1473A, Expedition 360 Atlantis Bank, Southwest Indian Ridge, in AGU Fall Meeting (American Geophysical Union), 12-16 December 2017, San Francisco, USA; AGU Abstract OS23F-03.

MacLeod, C.J., Deans, J.R., Morris, A., Evans, A., Cheadle, M.J., Ferrando, C., Dick, H.J.B., **2016**. Contrasting Modes of Detachment Faulting at Slower-Spreading Mid-Ocean Ridges, in AGU Fall Meeting (American Geophysical Union), 12-16 December 2017, San Francisco, USA; AGU Abstract T33A-2992.

Ferrando, C., Godard, M., Ildefonse, B., Rampone, E., **2017**. Chemical profiles along olivine crystallographic axes: a record of the melt-rock interaction sequence forming Hole U1309D Olivine-rich troctolites (Atlantis Massif, MAR, 30°N), in EGU General Assembly, 22-30 April 2017, Vienna, Austria. Geophys. Res. Abs., Vol. 19, EGU2017-5127, 2017. (poster)

Ferrando, C., Godard, M., Ildefonse, B., Rampone, R., **2017**. Melt Transport and Mantle Assimilation at Atlantis Massif (IODP Site U1309): Evidence from Chemical Profiles along Olivine Crystallographic Axes, in AGU Fall Meeting (American Geophysical Union), 11-15 December 2017, New Orleans, USA; AGU Abstract n°226523. (oral)

Basch, V., Rampone, E., Crispini, L., Ferrando, C., Ildefonse, B. and Godard, M., **2017**, From mantle peridotites to hybrid troctolites: Textural and geochemical evolution during multi-stage melt-rock interaction history, in AGU Fall Meeting (American Geophysical Union), 11-15 December 2017, New Orleans, USA; AGU Abstract n°215571. (poster)